



Characterization of down-valley winds in stable stratification from the KASCADE field campaign and WRF mesoscale simulations

Gert-Jan Duine

► To cite this version:

Gert-Jan Duine. Characterization of down-valley winds in stable stratification from the KASCADE field campaign and WRF mesoscale simulations. Ocean, Atmosphere. Université Toulouse III Paul Sabatier, 2015. English. NNT: . tel-01263986

HAL Id: tel-01263986

<https://theses.hal.science/tel-01263986>

Submitted on 28 Jan 2016

HAL is a multi-disciplinary open access archive for the deposit and dissemination of scientific research documents, whether they are published or not. The documents may come from teaching and research institutions in France or abroad, or from public or private research centers.

L'archive ouverte pluridisciplinaire **HAL**, est destinée au dépôt et à la diffusion de documents scientifiques de niveau recherche, publiés ou non, émanant des établissements d'enseignement et de recherche français ou étrangers, des laboratoires publics ou privés.



THÈSE

En vue de l'obtention du

DOCTORAT DE L'UNIVERSITÉ DE TOULOUSE

Délivré par : *l'Université Toulouse 3 Paul Sabatier (UT3 Paul Sabatier)*

Présentée et soutenue le 12/10/2015 par :

Gert-Jan DUINE

**Caractérisation des vents de vallée en conditions stables à partir de la
campagne de mesures KASCADE et de simulations WRF à
mésos-échelle**

JURY

FRANK ROUX

BERTRAND CARISSIMO

ERIC PARDYJAK

PIERRE DURAND

THIERRY HEDDE

PIERRE ROUBIN

INVITÉ:

JORDI VILA-GUERAU DE

ARELLANO

Président du Jury

Rapporteur

Rapporteur

Directeur de thèse

Co-directeur de thèse

Co-directeur de thèse

Rapporteur

École doctorale et spécialité :

SDU2E : Océan, Atmosphère et Surfaces Continentales

Unités de Recherche :

Laboratoire d'Aérodynamique (UPS - CNRS) et

Laboratoire de Modélisation des Transferts dans l'Environnement (CEA)

(Co-)directeurs de Thèse :

Pierre DURAND, Thierry HEDDE et Pierre ROUBIN

Rapporteurs :

Bertrand CARISSIMO, Eric PARDYJAK et Jordi VILA-GUERAU DE ARELLANO

<http://kascade.sedoo.fr/>



Characterization of down-valley winds in stable stratification from the KASCADE field campaign and WRF mesoscale simulations

Author:

Gert-Jan DUINE

Supervisors:

Pierre DURAND

Thierry HEDDE

Pierre ROUBIN

A collaboration between:

Laboratoire de Modélisation des Transferts dans l'Environnement (CEA Cadarache) and
Laboratoire d'Aérodynamique (University of Toulouse)



To cite this version:

Duine, G. (2015). *Characterization of down-valley winds in stable stratification from the KASCADE field campaign and WRF mesoscale simulations*. Ph.D. thesis, Université Toulouse III Paul Sabatier.

Acknowledgements

The last three years went quickly. I need to say I felt privileged to work in a very interesting project, on very interesting places: where in the world can you enjoy sunny afternoons in your t-shirt after a freezing early morning of measurements? Sometimes progress was slow, either through personal 'speed' but sometimes because of bureaucracy, for which at Cadarache it seems that they are about to win the world championship's soon. Also, learning - well.. understanding - another language caused quite a headache in the beginning, but luckily everyone helped me greatly by achieving this goal. Other goals were achieved as well, and here I would like to thank the people involved.

En premier lieu, je tiens à remercier mes encadrants. Merci à Thierry qui m'a chaleureusement accueilli chez lui au début de ma thèse le temps que je trouve un logement. J'ai également apprécié nos échanges, ton sens pratique, ainsi que ton sens de l'humour. Merci aussi à Pierre (Roubin) avec qui j'ai beaucoup rigolé et scientifiquement beaucoup échangé au cours de ces trois années de thèse. Je n'oublierai jamais la matinée qui a suivi ton retour du Canada! En plus, un grand merci pour tous tes conseils bureaucratiques (je te dois pas mal de chose sur ce point là). Enfin je tiens à remercier Pierre (Durand) pour ses conseils avisés, ainsi que de m'avoir guider sur le bon chemin. Merci également pour toutes nos riches et productives discussions, et plus particulièrement pour la calibration des instruments ainsi que la rédaction des articles. Je pense au final que j'ai été extrêmement chanceux de travailler avec chacun d'entre vous. Vous avez des spécialités différentes, mais elles ont été très complémentaires pour ce travail de thèse.

Vivre à deux endroits différents n'est pas toujours facile, mais il y a aussi des avantages: on apprend à mieux connaître le pays et ses coutumes. J'ai apprécié de travailler au LMTE à Cadarache. Je me suis aperçu que l'on pouvait également aimer son lieu de travail bien que l'on reste la plupart du temps (enfermé) dans un centre nucléaire. Mais s'il vous plaît, arrêtez de faire des mots-croisés, vous aurez le temps d'en faire plus tard. Au laboratoire d'Aérodynamique les choses sont différentes mais tout aussi sympathiques qu'au LMTE. Merci à tous les doctorants et contractuels pour avoir rendu cette aventure si enrichissante (bien que cela soit une honte de ne pas avoir un terrain de volley durant l'hiver - heureusement j'ai passé la plupart de mes hivers en Provence). Merci à mes "colocs" à Toulouse et Aix pour tous les non-sens que j'ai dû essayer de comprendre. J'espère pouvoir vous rendre visite très prochainement.

I would also like to thank the 'rapporteurs' for reviewing the PhD-thesis. For sure this was not an easy one, as it is quite long. I liked the fact you were available Jordi, although it was not practical at all, but the circle is round now. Eric en Bertrand, thanks for making the trip to Toulouse. Also the thesis committee (Chantal Staquet, Alexandre Paci en Gert-Jan Steeneveld) helped greatly by giving confidence that we were on the right track. Especially Gert-Jan I encountered a lot during the last three years, and luckily you were always available for some advice. This remains one of the strongest points of the Wageningen University.

Ook Peter wil ik bedanken: goed van je dat je het hebt aangedurfd om naar Frankrijk te komen. Erg grappig ook, Provençaals spreken op het werk, hertjes spotten op het centrum en fontijnen die maar heel kort oranje werden. Een groot deel van de pagina's hierna zijn ook jouw verdienste. Succes met je vervolg PhD.

Deze drie jaren waren niks geweest zonder m'n rode, ijzeren ros. Maar deze vreugde heb ik vooral mogen delen met vrienden. Na jarenlang trainen heb ik nog steeds moeite om Joep de les te lezen, een natuurtalent. Kenny, de magistrale rit door de Vogezes (met dubbele pizzabodem) was toch wel een hoogtepunt. Beiden bedankt voor de verkenningstochten in de Pyreneeën, de Alpen of de Vogezes, en alles daaromheen. En natuurlijk niet te vergeten de andere mooiweerrijders Florian, Faycal, Simon, Marcia, Benoit, Christian, het bejaardenclubje van CSPA, Paco en dan vergeet ik er vast nog wel een paar. Ook alle Hollanders die me een bezoekje hebben gebracht verdienen een bedankje. Het was fijn om eens af en toe wat langer

in de moerstaal te spreken dan alleen een skype-gesprekje. Ik kom snel langs als ik weer in Nederland ben.

Mick, ook al ben je familie, toch een bedankje van professionele aard: dat prachtige projectlogo was er zonder jou niet geweest. En ook al waren het er niet veel, de snelle hulp voor het bijpoetsen van enkele figuren zijn een opmerking waard. Inge, je had ineens eerder een publicatie in een tijdschrift dan ik! Helaas is je overredingskracht nog niet groot genoeg om me te overtuigen een eigen onderzoeksgroep in Breda te beginnen. Ik twijfel er in ieder geval niet aan dat je boek een groot succes wordt, al was het alleen maar door de toevallige Franse input die ik kon geven. Pa en ma, wie had dat nou gedacht dat ik na de wens om mijn profielrichting te wijzigen halverwege de middelbare school, waar niet direct gehoor aan werd gegeven, uiteindelijk in Frankrijk terecht zou komen? Bedankt in ieder geval voor alle steun, en dan vooral in de immateriële zin. Ik denk dat jullie wel hebben genoten van het eindelijk dan ontdekken van dat vreemde, enge land.

Gert-Jan (of zoals men mij prefereerde te noemen): Gert, Gerardus, Gérard-Jean, gardian, Christian, chrétien, monsieur G., Jère-Jean, of de fonetische correcte Rert-Yann

Abstract

This thesis investigates down-valley wind characteristics in complex terrain of moderate orography for a mid-latitude area. The work was motivated by safety regulation in the context of sanitary impact of the Cadarache centre on its close surroundings. Cadarache is one of the research centres of 'Commissariat à l'Énergie Atomique et aux Energies Alternatives' (CEA), located in southeastern France. It is embedded in a small valley, the Cadarache Valley (CV), which is one of the tributaries of the larger Durance Valley (DV). The two valleys are distinct in width (1 - 2 vs. 5 km for CV and DV, respectively), length (5 vs. more than 60 km), depth (100 vs. 200 m and higher) and slope angle (1° vs. 0.2° on average along the valleys main axis), and therefore react differently under stable conditions. Stable stratifications regularly occur in the region due to frequent weak synoptic forcing and clear sky conditions. During such conditions, dilution of pollutants can become weak; this is one of the major motivations of the present study.

To investigate the valley wind behaviour, the KASCADE (KAtabatic winds and Stability over CAadarache for Dispersion of Effluents) campaign has been designed. It was conducted in the winter of 2013 including continuous observations (flux tower, Sodar and Cadarache observational network) covering a 3-month period and 23 intensive observation periods (IOPs). During the IOPs tethered balloon experiments were conducted and radio-soundings were launched. An IOP was carried out when weak synoptic forcing periods and clear skies were expected, started at 12 UTC and lasted 24 hours. A calibration experiment served for sensor correction purposes, resulting in a high quality data set of a well-documented campaign (<http://kascade.sedoo.fr/>). The valley flows at the local and regional scale are characterized from observations analysis and IOP simulations with the non-hydrostatic WRF model.

The analysis shows that the Cadarache and Durance down-valley (CDV and DDV, respectively) winds are both dominating flows during the period of investigation. Once stable stratification has set around sunset, CDV wind continuously grows and thickens. The profile forms in a jet which is mostly observed at around 30 m agl with $2 - 3 \text{ m s}^{-1}$. CDV wind is a thermally driven flow, which persists regularly throughout the night and disappears in the early morning alongside stable stratification. Though the Cadarache current observational network lacks means of measurement for inside CDV wind, this work shows that it can be nowcasted from available meteorological tower observations. Although the forecast of CDV wind is out of reach of mesoscale modeling on a kilometer-scale resolution, the nowcasting methodology developed here could be used to forecast it by means of a combination of dynamical and statistical downscaling.

The DDV wind has been investigated by means of observations and modeling - all IOPs were simulated with an optimized WRF configuration at a 1-km horizontal grid spacing. The DDV wind has been recognized as down-valley oriented, and strongly related to stability at a regional scale, as it exists only after sunset when synoptic forcing is very weak. On the one hand, though highly variable, the DDV wind arrival at Cadarache is mostly observed 6 to 9 hours after sunset. On the other hand, it is dominantly present around sunrise, when convectively driven processes are not yet established. Jets are observed mostly at around 175 - 225 m agl with wind speeds between 4 and 8 m s^{-1} . DDV wind depth appears to be closely related to valley depth, which varies throughout the DV. Some deficiencies of the simulations are found, including underestimations of diurnal temperature ranges, overestimations of atmospheric turbulent fluxes, too early timing for onset and cessation of DDV wind. Despite these, the DDV wind is simulated close to reality thanks to the 1-km resolution allowing a correct representation of the Durance valley orography. Spatial characteristics show different types of DDV winds: it may appear as shallow drainage, but also as channelled flow resulting from a mountain-to-plain circulation. The latter finds its origin in low level jets (LLJs) simulated at the sloping plateau in between Southern Alps and DV itself. High wind speeds within the valley are seen in LLJs especially after tributary valley inlets. Data was not abundant enough to fully clarify the most dominant mechanism that causes the flow, but drainage and flow channelling are the most important candidates.

Résumé

Cette thèse est dédiée à la caractérisation des vents descendants de vallée dans une région de moyenne latitude caractérisée par un terrain complexe d'orographie modérée, et dans le contexte de la réglementation des rejets atmosphériques du centre de Cadarache. Cadarache est un des centres de recherche du 'Commissariat à l'Énergie Atomique et aux Énergies Alternatives' (CEA), installé dans une petite vallée (CV) confluyente à la vallée majeure de la Durance (DV). Ces deux vallées se distinguent par leur largeur (1 à 2 kms et 5 kms respectivement pour CV et DV), leur longueur (5 kms et plus de 50 kms), leur profondeur (environ 100 m et plus de 200 m) et leur pente moyenne (1.2° et 0.2°), et par conséquent sont le siège d'écoulements aux caractéristiques différentes en stratification stable. En effet, un forçage synoptique faible associé à un ciel dégagé sont dans la région des conditions fréquentes qui favorisent la stabilité atmosphérique et consécutivement la mauvaise dispersion des polluants, faisant de cette situation un sujet d'intérêt majeur pour l'impact sanitaire et environnemental du centre.

La campagne de mesure KASCADE (KAtabatic winds and Stability over CAdarache for Dispersion of Effluents) constitue le volet expérimental de l'étude. Réalisée pendant l'hiver 2013 elle a couvert 3 mois d'observation continue (avec un mât pour la mesure des flux turbulents et radiatifs, un sodar et les observations météorologiques du site de Cadarache) complétée de 23 périodes d'observation intensive (POI). Pendant ces POI des profils ont été réalisés par ballon captif et radiosondages. Une POI était déclenchée en conditions de forçage synoptique faible et de ciel clair, démarrait à 12 UTC et durait 24 heures. Une phase de calibration des capteurs a permis les corrections nécessaires à la qualité des données et la constitution d'une base de données bien documentée (<http://kascade.sedoo.fr/>). Les analyses ont été basées sur ces observations et sur un volet de simulation numérique de la météorologie régionale avec le code WRF.

L'analyse montre que les écoulements descendant les vallées de Cadarache (CDV) et de la Durance (DDV) dominent pendant toute la période d'étude. La stabilité s'installant dès le coucher du soleil, le courant CDV s'établit et s'épaissit progressivement. Le profil de vent en forme de jet présente son maximum à environ 30 m où il atteint 2 à 3 m s⁻¹. C'est un courant de densité qui se maintient toute la nuit et disparaît avec l'inversion de stabilité au lever du soleil. Comme la station météorologique du centre manque de capteur de vent dans la CV même, une méthode a été développée pour diagnostiquer le CDV en exploitant l'instrumentation disponible. Ainsi, si la prévision de ce vent n'est pas à la portée du modèle méso-échelle WRF avec une résolution kilométrique, cette méthode le permet en combinant une descente d'échelle dynamique et statistique.

Le vent DDV a été étudié grâce aux observations et aux simulations - toutes les POI ont été simulées avec une résolution de 1 km. C'est un vent qui suit l'axe de la vallée, fortement corrélé à la stabilité à l'échelle régionale car il n'apparaît que la nuit lorsque le forçage synoptique est faible. Ce vent n'arrive à Cadarache que 6 à 9 heures après le coucher du soleil avec une grande variabilité. D'un autre côté, il est à son maximum au lever du soleil avant que les processus convectifs ne démarrent, et présente un jet entre 175 et 225 m avec des vitesses de 4 à 8 m s⁻¹ et dont la hauteur est corrélée à la profondeur variable de la vallée. Les simulations s'avèrent imparfaites avec une sous-estimation de l'amplitude diurne de température, une surestimation des flux turbulents et un décalage dans la chronologie du DDV par rapport à l'observation. Mais malgré ces défauts, la DV étant bien résolue avec une maille de 1 km, l'occurrence de ce vent est assez bien simulée. Par ailleurs l'examen de ses caractéristiques spatiales montre qu'il s'agit soit d'un écoulement de drainage, soit d'un écoulement canalisé forcé. Ce dernier trouve son origine dans des jets de basse couche naissant sur les plateaux inclinés situés entre la vallée même et les montages voisins des Préalpes du sud. Ces jets présentent des vitesses significatives, principalement au niveau des confluences de la Durance et de ses affluents. Bien qu'on ne dispose pas de données suffisantes pour élucider le mécanisme dominant de déclenchement du vent DDV, il est clair que les deux précédemment identifiés sont de bons candidats.

Table of Contents

General introduction	1
Introduction en Français	5
1 Stable boundary layers over complex terrain	9
1.1 Basic principles of the atmosphere	9
1.1.1 Structure	9
1.1.2 Length and time scales	10
1.1.3 Stability	10
1.1.4 Governing equations	12
1.1.5 Energy transport	14
1.2 The atmospheric boundary layer over land	17
1.2.1 Convective boundary layer	17
1.2.2 Processes in the stable boundary layer	17
1.3 Implications of stability over complex terrains	19
1.3.1 Thermally driven downslope winds	20
1.3.2 Valley systems	21
1.3.3 Various origins of valley flows	22
1.4 Summary	24
2 Methodology: observations	27
2.1 Introduction	27
2.2 Site characteristics	27
2.2.1 Durance Valley	27
2.2.2 Cadarache Valley	28
2.2.3 Other orographic features	29
2.2.4 Typical meteorological phenomena	29
2.3 Instrumentation and measurement strategy	29
2.3.1 Continuous observations	30
2.3.2 Intensive observational periods	33
2.4 Data post-processing	35
2.4.1 Evaluation method	35
2.4.2 Sensor corrections summary	36
2.4.3 Tethered balloon: Height correction and measurement uncertainties . . .	37
2.4.4 Sodar: validation	42
2.4.5 M30	46

3	Methodology: Mesoscale modeling with WRF	51
3.1	Introduction	51
3.2	The WRF-model: basic set-up	51
3.2.1	Basic principles of WRF	51
3.2.2	The study area	52
3.2.3	Orography	53
3.2.4	Land use	54
3.3	Configurations	55
3.3.1	Model sensitivity to subgrid-scale processes	56
3.3.2	Configuration 1: The optimized set-up	59
3.3.3	Configuration 2: Increase of vertical resolution	59
3.3.4	Configuration 3: Extension of the inner domain	60
4	Characterization of down-valley winds by observations	63
4.1	Abstract of the article	63
4.2	Article	63
5	Cadarache down-valley wind nowcast	81
5.1	Abstract of the article	81
5.2	Article	81
6	Model set-up and evaluation	93
6.1	Introduction	93
6.2	Model sensitivity	93
6.2.1	Set-up of the reference configuration	94
6.2.2	Influence of grid spacing and domain size	102
6.3	Evaluation of the reference configuration	110
6.3.1	Strategy	111
6.3.2	Fluxes and turbulence parameters	112
6.3.3	Temperature and humidity	114
6.3.4	Wind speed and direction	116
6.3.5	Summary of the model performance	123
6.4	Conclusions	124
7	Durance down-valley wind	127
7.1	Introduction	127
7.2	Durance down-valley wind characteristics	127
7.2.1	Timing and height	127
7.2.2	General characteristics along the Durance valley	129
7.3	Analysis of two remarkable IOPs	135
7.3.1	Methodology	135
7.3.2	IOP 16	136
7.3.3	IOP 21	138
7.3.4	Summary	141
7.4	The origin of the flow	141
7.5	Summary and conclusions	144

General conclusions and perspectives	145
Conclusions générales et perspectives	151
References	156
Appendices	163
A Terminology	165
B Background for Chapter 6	169
B.1 IOP descriptions	169
B.2 Figures	173
C Technical Report: Instruments calibration experiment and results	193

General introduction

Context

One of the important factors that determine the environmental impact of particles and gases is their atmospheric dispersion, which itself is largely controlled by the stability of the atmosphere. During the day, due to surface heating by solar radiation, convective boundary layers develop up to around 1 - 2 km agl. This layer is efficiently mixed, transporting heat, moisture and atmospheric trace species vertically throughout the boundary layer depth by means of turbulent convection. Once they have reached higher layers, these trace species can be transported by larger scale winds. During such convective situations, the atmospheric dilution is relatively large, and thus the atmospheric concentrations are lower. On the contrary, during clear nights as the ground surface is cooled, stratified stable layering develops which can extend up to a few hundreds of meters. Furthermore, turbulence is generally weak or even absent, and the dilution of pollutants is weak. Therefore concentrations can be high during such conditions, making the stable boundary layer the most penalizing situation for impact assessment.

Complex terrains are those regions which are characterized by shallow or deep valleys progressing among hills and mountain ranges. During the day, horizontal temperature gradients create pressure gradients leading to upslope flows. The trace species released at the valley bottom can reach even higher altitudes than for a convective boundary layer over flat terrain. During the night, the opposite occurs, horizontal temperature and pressure gradients form, causing the denser air close to the surface to flow downslope, similarly to water runoff on sloping terrain. Then pollutants can stagnate in the valley bottoms, where high concentrations can be observed.

The conditions suitable for these penalizing situations, associated with atmospheric stability, are found under weak synoptic forcing and clear-skies. Such conditions frequently occur in Provence, whose orography is complex, hence the interest of studying the valley winds in the middle Durance valley and its tributaries.

Motivation

The 'Laboratoire de Modélisation des Transferts dans l'Environnement' (LMTE) is the reference unit for impact assessment on the local and regional environment for the 'Commissariat à l'Énergie Atomique et aux Energies Alternatives' (CEA) facilities belonging to the 'Direction de l'Énergie Nucléaire' (DEN). As such, the LMTE perform calculations for chemical and radiological contaminants transport in soil, surface and ground waters, and in the atmosphere.

The models currently in use at LMTE for impact assessment are mostly of the Gaussian type. These are among the earliest dispersion models, which assume that pollutants within plumes have a gaussian distribution in their cross-section. Such models are computationally not expensive, which is very beneficial for emergency risk management. However, the meteorology description is often minimal in the earliest models, with the use of only one wind vector plus an atmospheric stability class. At best the more advanced gaussian models (e.g. ADMS, AERMOD) benefit from a continuous description of the atmospheric stability based on similarity theory

and can be forced with non-uniform wind fields although with serious limitations on their 3-dimensionality and the underlying orographic complexity.

This is why LMTE has shifted to deterministic models that resolve the turbulent wind field and the thermodynamic state of the atmosphere from the local scale to the mesoscale. Besides, the hydrostatic assumption is no longer realistic when one wants to solve the flow with a kilometre or sub-kilometer horizontal resolution. Among the non-hydrostatic models widely used in the boundary-layer, the Weather & Research Forecasting (WRF) model is available for free and offers many advantages, among others the fact that it can be run for research studies as well as in operational mode. The increase of computational resources in the last decades allowed this to a large extent. These types of model can simulate a real atmosphere, with its stacked layers, and do include vertical motions. Orography is described in the model, however its representation is dependent on the horizontal resolution. Besides, the WRF model can be coupled to global circulation models, and so is capable to capture the state of the atmosphere in real time. It further includes modules that account for soil processes which lead to a better representation of surface-atmosphere exchanges.

Using WRF as a tool for environmental impact calculations has several advantages: firstly, research can be performed on dominant meteorological events occurring in the area of interest. As such, it can serve to a better regional impact assessment of the Cadarache site. Secondly, the model can be used in an operational mode, thus it can respond to the question of direct local and regional risk management. In the future, it is planned to feed a dispersion model with the meteorological fields computed by the mesoscale model. In this regard WRF has the advantage of being easily coupled to the FLEXPART Lagrangian dispersion code, which will allow to finely describe the transport of the released contaminants in the atmosphere.

Cadarache is situated in southeastern France, in the Prealps, at the lower end of the middle Durance Valley (DV). The region can be characterized as fairly complex regarding orography and land use. The Southern Alps, Rhône Valley and Mediterranean Sea are at no more than 60 km as the crow flies. Clear skies and calm winds are regularly observed in the region which therefore is very susceptible to stable boundary layer (SBL) evolution and development of local wind systems. Understanding the patterns of near-surface flows and cold-pool build up in the valleys is thus a major issue for assessing the sanitary and environmental impact of Cadarache.

The valleys of interest for Cadarache are cross-oriented, and of different size and depth. Therefore they both act differently on SBL development and dispersion. The existence of down-valley wind patterns can be detected by the two Cadarache permanent weather stations, but their standard and minimal instrumentation neither allows for their complete description nor gives us access to their governing factors. Previous works have been done to survey down-valley winds in complex terrains (e.g. POVA, COLPEX, TRANSFLEX), but as valley geometries are very distinct, these could not be used for the current study.

The KASCADE (KAtabatic winds and Stability over CAdarache for Dispersion of Effluents) field measurement campaign was conducted in the winter of 2013 and was designed to characterize the local SBL and the associated thermally driven winds to feed numerical simulations of pollutant dispersion for impact studies. Continuous observations were obtained from December 2012 to March 2013. The campaign also included 23 intensive observational periods (IOPs) in January and February.

This work constitutes a direct contribution to the operational requirements of the CEA. However, the studies were conducted and the tools developed with a view to improve the general knowledge of boundary-layer processes in complex areas. The significance of this thesis cannot therefore be restricted to the Cadarache specific area but is of general interest for boundary-layer related flows in stable conditions and moderate orography.

Thesis objectives

As a first step, the Durance down-valley (DDV) wind and the Cadarache down-valley (CDV) wind have to be characterized by measuring their height, strength, and timing of occurrence. Then, understanding the phenomena and their causes should be searched by a combined analysis of, and a comparison between the measurements and the WRF simulations.

To attain these objectives, the KASCADE field experiment has been conducted and the mesoscale model WRF has been set up and run. They constitute the main means of this thesis which unfolds according to the following content:

Chapter 1 contains a general introduction to atmospheric governing equations, important scales, and more in-depth explanations about stability, boundary layer, orography influences and their impact on dispersion.

Chapter 2 describes in more detail the topography and the specific meteorology of the region. The KASCADE experiment is detailed, with the measurement strategy and the instrumentation used. To guarantee the data quality, an inter-calibration campaign between various sensors was conducted shortly after KASCADE. Its methodology and results are also described in this chapter.

The strategy for the modelling contribution is presented in Chap. 3. It contains further explanations on the mesoscale model WRF, its difficulties when used over complex terrain and several additional implementations done to better cover the regional topography. It further describes the model evaluation strategy and the sensitivity studies performed to come up with an optimum set-up dedicated to the regional weather forecast.

The results regarding the first objective of the PhD-thesis - analysis and characterization of the down-valley winds - are presented in the form of an article in Chap. 4. It contains an overview of the observations collected during the campaign and proves that stability and the DDV and CDV winds are very dominant throughout the full campaign period. A good characterization of the CDV wind could be made, and the campaign's intensive part served as the basis to derive a conceptual picture of the valley winds during weak synoptic forcing.

Apart from KASCADE, which were temporary observations, no direct measurements of the CDV wind are routinely available. Chapter 5 presents an original methodology with which the CDV wind can be nowcasted by using other data from the existing system. Thanks to this method, a climatology has been made.

The overall spatial characteristics of the DDV wind could not be researched by means of the KASCADE observations only. Therefore, the WRF model has been set up to address this shortcoming. In the first part of Chap. 6, the model is evaluated for the calmest IOP, evaluated by testing different set-ups in order to find an optimized configuration for the study area. This work has been done by supervising the Master student P. Kalverla (Wageningen University). Then, sensitivity tests are performed concerning vertical resolution, horizontal domain extension and horizontal resolution. In a next step, the model performance is evaluated in a more general way, through the simulation of all IOPs.

The spatial characteristics of the DDV wind are examined along the DV in Chap. 7. Also its time evolution for different IOPs is investigated in this chapter. Finally, possible origins of the DDV wind are explored.

It is reminded that treating pollutant dispersion in the area of Cadarache was not among the thesis objectives. After a short recollection of the methodologies employed and the main results presented in the various chapters, the conclusion will give some insights on possible future works to perpetuate the know-how that has been presented in this thesis, and to further improve the knowledge of processes and tools developed.

Introduction en Français

Contexte

Un des facteurs primordiaux qui contribuent à l'impact environnemental de la dispersion des particules et gaz polluants dans l'atmosphère est la stabilité de l'atmosphère. Ainsi pendant la journée, en raison du chauffage du sol par insolation, une couche limite convective se développe jusqu'à 1 ou 2 km d'altitude. La convection turbulente qui y règne la brasse efficacement, en sorte que chaleur, humidité, gaz ou particules sont mélangés verticalement sur toute la hauteur de la couche limite. Une fois en altitude, les vents reprennent les particules et les transportent sur de plus grandes échelles de temps et d'espace. Aussi en situation convective, la dilution atmosphérique est relativement importante, et les concentrations sont plus basses. En revanche, pendant la nuit quand le terrain se refroidit, une stratification de couches stables se développe au-dessus du sol, s'élevant jusqu'à une centaine ou quelques centaines de mètres de hauteur. De plus, la turbulence y est généralement peu intense voire même absente, et la dilution des polluants est faible. Les concentrations sont par conséquent élevées dans de telles conditions, ce qui fait de la couche limite stable la situation la plus pénalisante du point de vue de l'impact.

On appelle terrain complexe toute région marquée par un réseau de vallées plus ou moins ouvertes et profondes, progressant parmi des collines ou chaînes de montagne ou entaillant un plateau. Dans la journée, les gradients horizontaux de température génèrent des gradients de pression responsables d'écoulements qui remontent les pentes (anabatiques). Les rejets en fond de vallée peuvent alors atteindre des altitudes plus élevées que dans une couche limite convective en terrain plat. Pendant la nuit, le contraire se produit, les gradients horizontaux de température et pression provoquent des écoulements d'air vers les bas des pentes (catabatiques), à l'image de l'eau ruisselant vers l'aval. Les polluants peuvent alors stagner dans les fonds de vallées, où il est possible d'observer des concentrations élevées.

Les conditions propices à ces situations pénalisantes, avec une stratification stable de l'atmosphère, se rencontrent lorsque le forçage synoptique est faible avec un ciel dégagé. De telles conditions se produisent fréquemment en Provence, région dont l'orographie est complexe, d'où l'intérêt d'étudier les vents de vallée dans la région de la moyenne de la Durance.

Motivation

Le 'Laboratoire de Modélisation des Transferts dans l'Environnement' (LMTE) du centre de Cadarache est l'unité de référence pour les études d'impact locales ou régionales des installations du "Commissariat à l'Énergie Atomique et aux Energies Alternatives" (CEA) relevant de la Direction de l'Énergie Nucléaire (DEN). Par conséquent une de ses missions consiste en la simulation du transport de contaminants chimiques et radiologiques dans les sols, les eaux de surface ou souterraines et l'atmosphère.

Les modèles couramment utilisés au LMTE pour les études d'impact sont pour l'essentiel de type gaussien. Ils figurent parmi les premiers modèles de dispersion, supposant que les polluants se distribuent dans une coupe du panache selon une loi gaussienne. De tels modèles

sont économiques du point de vue du temps de calcul, ce qui est un avantage pour la gestion du risque en situation d'urgence. Cependant, la description météorologique est minimale avec les modèles les plus anciens, le vent y étant décrit par une seule direction et une seule vitesse et la stabilité atmosphérique paramétrée selon des classes discrètes. Au mieux les modèles gaussiens les plus avancés (par exemple ADMS, AERMOD) bénéficient d'une description non par classe mais continue de la stabilité et peuvent exploiter des champs de vent et de turbulence tridimensionnels bien qu'avec des limitations quant à leur tridimensionnalité et la complexité orographique.

C'est pourquoi le LMTE s'est tourné vers les modèles déterministes qui résolvent le champ de vent turbulent et l'état thermodynamique de l'atmosphère, de l'échelle locale à la méso-échelle. Avec cet objectif l'hypothèse hydrostatique n'est pas réaliste si l'on résout le vent à une échelle horizontale kilométrique ou sub-kilométrique. Parmi les modèles non-hydrostatiques largement utilisés pour la couche limite, le code "Weather & Research Forecasting" (WRF) est librement accessible et offre de nombreux avantages, parmi lesquels la possibilité de pouvoir servir aussi bien pour la recherche que pour la prévision opérationnelle du temps. Ce type de modèle peut simuler l'atmosphère réelle, avec ses stratifications, et prend en compte les mouvements verticaux et l'orographie dont la qualité de représentation dépend naturellement de la résolution horizontale. De plus, le modèle WRF peut être couplé à un modèle global de la circulation atmosphérique, et ainsi suivre l'état de l'atmosphère en temps réel. Un module décrivant les échanges dans le sol et entre la surface et l'atmosphère est aussi couplé au modèle atmosphérique.

Utiliser WRF pour les études d'impact présente plusieurs avantages: premièrement, on peut faire de la recherche sur les phénomènes météorologiques dominants qui se produisent dans la région d'intérêt et par conséquent mieux appréhender l'impact régional dans la zone de Cadarache. Deuxièmement, l'accroissement de la puissance de calcul acquise ces dernières décennies permet d'exploiter le modèle dans une mode de prévision opérationnelle. Il peut donc répondre aux questions de gestion du risque à l'échelle locale et régionale. Ainsi dans le futur, il sera possible d'alimenter un modèle de dispersion avec les champs météorologiques calculés par le modèle méso-échelle. WRF offre ici l'avantage d'être facilement couplé au code de dispersion lagrangienne FLEXPART, ce qui permettra de décrire finement les panaches de gaz et particules.

Le centre de recherche de Cadarache est situé dans les Préalpes du Sud-Est de la France, les Préalpes, à l'extrémité aval de la moyenne vallée de Durance (DV). La région présente une orographie assez complexe et une occupation des sols variée. Les Alpes du sud, la vallée du Rhône et la mer Méditerranée n'en sont pas à plus de 60 km à vol d'oiseau. On y observe régulièrement un ciel dégagé et des vents faibles, ce qui l'expose au développement de couches limite stables et de vents locaux. Comprendre l'organisation des vents de vallée et la formation des couches froides dans les vallées affluentes est donc une question essentielle pour l'évaluation de l'impact sanitaire et environnemental de Cadarache.

Au niveau de Cadarache, deux vallées jouent un rôle essentiel: la vallée de Cadarache même où se trouvent la plupart des installations du centre, et la large vallée de la Durance où débouche la précédente. Ces deux vallées perpendiculaires et de géométries très différentes sont le siège d'écoulements aux caractéristiques spécifiques en stratification stable. Ces flux de vallée sont certes vus par les stations permanentes de Cadarache, mais insuffisamment connus au regard des besoins des études d'impact. Des études en terrain complexe ont été réalisées auparavant (par exemple les projets POVA, COLPEX, TRANSFLEX), mais les géométries des vallées étaient très différentes, et les résultats ne sont pas forcément transposables à cette étude.

C'est pourquoi la campagne de mesures sur le terrain KASCADE (vents KAtabatiques et Stabilité sur CAdarache pour la Dispersion d'Effluents atmosphériques) conduite pendant l'hiver 2013 a été conçue pour caractériser la couche limite stable locale et les vents thermiques associés.

Des mesures en continu ont été acquises de Décembre 2012 à Mars 2013, complétées par 23 périodes d’observation intensive (POI) en Janvier et Février.

Ainsi doit-on reconnaître dans ce travail une contribution directe aux besoins opérationnels du CEA. Cependant, les études ont été réalisées et des outils développés de façon à améliorer notre connaissance des couches limites stables en terrain complexe si bien que la portée de cette thèse n’est pas restreinte spécifiquement à la seule région proche de Cadarache ni à la thématique des études d’impact.

Objectifs

Dans une première étape, les écoulements canalisés dans les vallées de Durance et de Cadarache doivent être identifiés et caractérisés. Leur caractérisation consiste en la détermination de leur hauteur, vitesse et développement au cours du temps. Ensuite, lorsque leurs caractéristiques sont connues, la compréhension des phénomènes et de leurs causes est recherchée dans l’analyse conjointe des données expérimentales et des simulations numériques. Une retombée de cette étude est la mise au point d’une version optimisée du modèle WRF à même de prévoir l’apparition de ces écoulements.

Pour atteindre ces objectifs, la campagne d’observations KASCADE et le modèle à méso-échelle WRF constituent donc les principaux outils. Le travail de thèse sera présenté dans ce manuscrit de la manière suivante :

Le chapitre 1 comporte une introduction générale aux équations qui gouvernent le comportement de l’atmosphère, les échelles importantes, des explications approfondies sur la stabilité, la couche limite, l’influence orographique et ses conséquences sur la dispersion.

Le chapitre 2 décrit en détail la topographie de la région et sa météorologie spécifique. La campagne KASCADE, l’instrumentation utilisée et la stratégie d’observation sont détaillées. Pour s’assurer de la qualité des données et optimiser la calibration des capteurs, une série d’inter-comparaisons entre différents instruments a été réalisée peu après KASCADE. Sa méthodologie et ses résultats figurent également dans ce chapitre.

La stratégie employée dans la démarche de modélisation est présentée au chapitre 3. Il fournit la description nécessaire du modèle à méso-échelle WRF, ses difficultés d’emploi en terrain complexe, et les adaptations réalisées pour mieux couvrir la topographie régionale. Y est décrite la stratégie d’évaluation du modèle ainsi que l’étude de sensibilité effectuée pour aboutir à un paramétrage optimum pour la région.

Les résultats relatifs au premier objectif de la thèse, l’analyse et la caractérisation des vents de vallée, sont présentés sous la forme d’un article dans le Chapitre 4. Il comporte une vue d’ensemble des observations effectuées pendant la campagne. Il montre que les conditions de stabilité sont bien appréhendées et que les vents catabatiques de CV et DV sont dominants sur toute la durée de KASCADE. En particulier le vent de la vallée de Cadarache a pu être bien décrit, et la phase intensive des observations a servi de base à l’élaboration d’un schéma conceptuel synthétique du cycle des vents de vallée au niveau de Cadarache pendant les épisodes de faible forçage synoptique.

En dehors de la campagne KASCADE, aucune mesure directe du vent de vallée de Cadarache n’est disponible en continu. Le chapitre 5 présente une méthodologie originale permettant de diagnostiquer la présence d’un écoulement dans cette vallée en utilisant les mesures météorologiques continues d’une station du site. Grâce à cette méthode, une climatologie de ce vent peut être établie.

Enfin les caractéristiques spatiales du vent de la vallée de Durance dans son ensemble ne pouvant pas être appréhendées au moyen de la seule instrumentation mise en œuvre localement

pendant KASCADE, le modèle WRF a été utilisé afin de combler cette lacune. Les résultats sont présentés au chapitre 6 et 7. Dans le chapitre 6, le modèle a été configuré sur une POI, et différents paramétrages afin de définir une configuration réglage optimal pour la région étudiée. Des tests de sensibilité portant sur la résolution verticale, horizontale et la taille du plus petit domaine imbriqué ont également été effectués, ces derniers en collaboration étroite avec un étudiant de Master (P. Kalverla, Université de Wageningen). Dans un deuxième temps, la performance du modèle a été évaluée plus systématiquement en simulant tous les POI de KASCADE. Dans le chapitre 7, les caractéristiques spatiales du vent ont alors été examinées sur toute la longueur de la moyenne vallée, mais également son évolution temporelle. Pour finir, les origines possibles du vent de vallée de Durance ont été explorées.

On rappelle qu'il n'était pas dans les objectifs de cette thèse d'aborder les questions de dispersion atmosphérique autour de Cadarache. Après un bref rappel des méthodologies, outils et principaux résultats présentés dans les divers chapitres, la conclusion indique quelques perspectives de travail futur afin de pérenniser le savoir-faire qui a été emmagasiné au cours de cette étude, et de poursuivre l'amélioration de la connaissance des processus et des outils développés.

Chapter 1

Stable boundary layers over complex terrain

This chapter is dedicated to the laws ruling the atmosphere, its structure and scales and governing equations. The most important processes within the boundary layer are developed, with an emphasis on the stable boundary layer. As down-valley winds can be the consequence of stability over complex terrain and form the core of this thesis, these are detailed with a synthesis on the onset of the different flow origin. Also the complications for dispersion studies and modeling simulations concerning stable boundary layers over complex terrains are given.

1.1 Basic principles of the atmosphere

1.1.1 Structure

The Earth is surrounded by the atmosphere, which is bounded to the Earth by gravity. The atmosphere comprises a mixture of numerous gases, with respect to their volume fraction, the most important gases are nitrogen (0.78), oxygen (0.21) and water vapor (0 to 0.07). The atmosphere can be partitioned into five layers (Fig. 1.1): troposphere (0 to 6 - 18 km), stratosphere (6 - 18 to 50 km), mesosphere (50 to 85 km), thermosphere (85 to about 700 km) and exosphere (700 km and higher - Stull, 2000). These layers are characterized by different vertical temperature gradients, the top of each layer is indicated by its 'pause'. Within the troposphere the temperature and pressure decrease with height. Pressure decreases from the surface to outer space. The temperature in the stratosphere increases with height and therefore weather phenomena are mainly constricted to the troposphere and exchanges between the troposphere and the stratosphere are scarce.

The depth of the troposphere varies with latitude. It is at its highest around the equator, and at its the lowest around the Earth's poles. The troposphere itself can be divided in the planetary boundary layer (PBL) and the free atmosphere. The PBL encounters a strong diurnal pattern, it directly feels the effect of the sun's presence or absence. The free atmosphere comprises the layer above the PBL up to the tropopause. It is a layer which is not directly controlled by the Earth's surface. The PBL is that layer of the atmosphere which exerts the biggest influence on our daily life. It controls stability and influences local wind patterns in combination with the heterogeneous surface. It is one of the drivers for mechanisms strongly controlling dispersion and so knowledge increase of dominant processes in the boundary layer is of high importance for the quality of daily life.

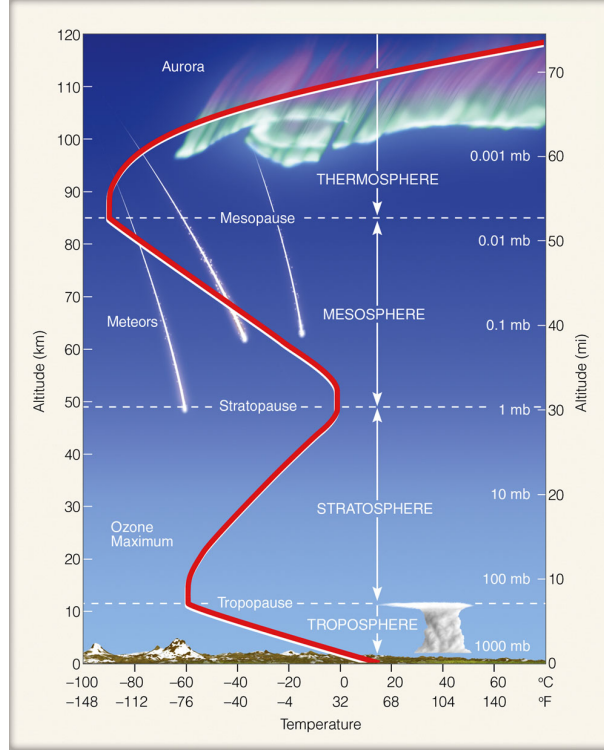


Figure 1.1: The Earth's atmosphere as partitioned into its most important layers (source: <http://www.geogrfy.net/GEO1/>).

1.1.2 Length and time scales

The troposphere comprises the complex interplay of processes at multiple lengths and time scales (Fig. 1.2). For most processes, the length and time scales are approximately correlated: a process with a longer length scale covers a longer time period. Excluding the time scales lasting longer than a week, the scales can be distinguished into several classes. The synoptic or macroscale acts at length scales of 1000 km and time scale of 1 day to several days. Examples of systems acting at the synoptic scale are high or low pressure areas, or hurricanes. At the smallest scale in the atmosphere, the microscale is defined. Here for example, turbulence is a dominant mechanism. Turbulence is the chaotic mixture of swirls acting at scales from a few centimeters to several kilometers with an associated time scale of less than a second to several minutes. In between macroscale and microscale, mesoscale processes take place. They act on the scales of several kilometers to tens of kilometers, span a lifetime from hours to one day and can be strongly linked to diurnal cycles. Mesoscale processes include phenomena such as, among others, land/sea breeze effects, thunderstorms, mountain and lee waves, foehn and valley winds. They can be affected by the microscale and the macroscale processes and therefore it is important to take into account processes on the microscale and macroscale when dealing with valley winds.

1.1.3 Stability

The basic principles of the processes in the atmosphere are presented here, through the basic equations of fluid mechanics that describe dynamics and thermodynamics of the gases in the atmosphere. First, we treat the basics of thermodynamics. The state of gases in dry air is well described with the ideal gas law, also known as the equation of state:

$$p = \rho R_d T \quad (1.1)$$

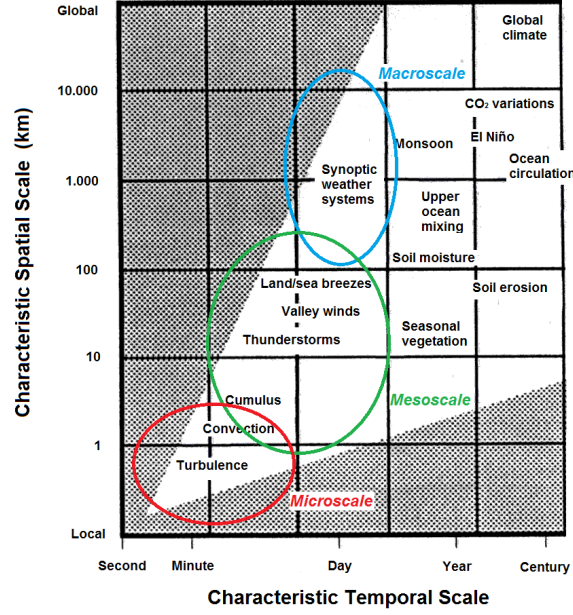


Figure 1.2: Typical length and time scales of processes occurring in the atmosphere. Adapted from Holtslag (2003).

where p represents the atmospheric pressure, ρ the density of dry air in kg m^{-3} , R_d the gas constant for dry air ($287 \text{ J K}^{-1} \text{ kg}^{-1}$) and the absolute temperature T in Kelvin. As pressure decreases with height, from the ideal gas law it follows that for fixed volumes temperature decreases with height. In dry air, to account for the effect of temperature changes that air parcels experience during vertical motions, the potential temperature θ is introduced:

$$\theta = T \cdot \left(\frac{p_0}{p} \right)^{R_d/C_p} \quad (1.2)$$

Here T is observed at pressure level p , with a reference level p_0 . T must be given in Kelvin. C_p is the specific heat of dry air at constant pressure ($1004.7 \text{ J kg}^{-1} \text{ K}^{-1}$). Generally, 1000 hPa is chosen for p_0 which is close to sea level pressure. θ is a conserved variable, which means it remains constant for dry adiabatic processes. The temperature change that a dry air parcel experiences, can also be expressed with respect to the dry adiabatic lapse rate Γ_d . In the troposphere this value is fixed at $-9.8^\circ\text{C km}^{-1}$. This is an idealized value, the actual lapse rate of temperature in the troposphere can take a wide range of values. For example, by radiosondes, it averages to $6\text{-}7 \text{ K km}^{-1}$. Γ_d can be used to approximate the potential temperature θ from temperature T depending on height z (instead of p):

$$\theta(z) = T(z) + \Gamma_d \cdot z \quad (1.3)$$

here both temperature variables can be expressed in $^\circ\text{C}$ and K.

Having defined θ the atmospheric static stability can be defined in three different states:

$$\begin{aligned} \frac{\partial \theta}{\partial z} < 0 & \quad \text{statically unstable layer} \\ \frac{\partial \theta}{\partial z} > 0 & \quad \text{statically stable layer} \\ \frac{\partial \theta}{\partial z} \simeq 0 & \quad \text{neutral layer} \end{aligned}$$

The stability is a result from the buoyancy effect, based on Archimede's principle. It is one of the most important drivers of vertical motions in the atmosphere. A buoyant force exerted

on an air parcel can be written as:

$$F = g \cdot \left(\frac{T}{T_0} - 1 \right) \quad (1.4)$$

Here F reflects the buoyancy force per unit mass, g is the gravitational constant of 9.81 m s^{-2} , and T and T_0 are temperatures of the heated or cooled air and that of the environment, respectively. Due to resulting density differences the air moves vertically, stays at or returns to its initial location when displaced from it. For the statically unstable air, the warmer air is below the colder air. From buoyancy effects it follows that air rises in unstable air until it reaches an equilibrium state higher. For a statically stable layer the colder air is below the warmer air, the layers do not tend to mix and so there is little if any exchange between them. Air flow is or becomes turbulent when the air is unstable and it tends towards a laminar state when it is stable. However, turbulent flow can exist even in stable stratification as a consequence of mechanical friction. Neutral profiles are those with a vertical profile close to Γ_d . In general, an atmospheric vertical profile is built up as a superposition of stable, unstable and neutral profiles.

Water vapor accounts for a substantial part of the gases in the atmosphere, 0 to 7%. Water vapor is less dense than dry air. To account for buoyancy effects of water vapor in non-cloudy air, the virtual potential temperature θ_v is introduced and reads as:

$$\theta_v = \theta \cdot (1 + 0.61 \cdot r) \quad (1.5)$$

with r being the humidity mixing ratio in kg kg^{-1} . A similar expression follows for the virtual temperature T_v .

Static stability only considers buoyancy effects. Dynamic stability includes both wind shear and buoyancy effects. This is expressed in a gradient Richardson number:

$$Ri_g = \frac{\frac{g}{T_v} \frac{\partial \theta_v}{\partial z}}{\left(\frac{\partial U}{\partial z} \right)^2 + \left(\frac{\partial V}{\partial z} \right)^2} \quad (1.6)$$

It is often approximated as a bulk Richardson number Ri_B

$$Ri_B = \frac{g \cdot (\Delta T_v + \Gamma_d \Delta z) \cdot \Delta z}{T_v \cdot (\Delta U)^2} \quad (1.7)$$

Δz corresponds to the height difference of the temperature (θ) and wind (U) observations, with $\Delta z = z_2 - z_1$ (level 2 being higher than level 1). Dry air is often assumed so that $T_v \simeq T$. Flow becomes statically stable for $Ri_B > 1$ and it becomes dynamically unstable for $Ri_B < 0.25$. Ri_B is classically used to define stability inside air masses and as such is a good indicator for stability, as it relates wind speed to buoyancy effects. However, through the difference between both thresholds from laminar to turbulent regimes and vice versa, a hysteresis effect occurs (McTaggart-Cowan and Zadra, 2014). Besides, the uncertainty of Ri_B is strongly related to the depth of the bulk; the larger the bulk, the larger the uncertainty (Stull, 1988).

1.1.4 Governing equations

For the fluid mechanics, and its combination with thermodynamics, we introduce the equations of motion. These are mainly based on three conservation principles: conservation of mass, momentum and on scalar species (e.g. heat and moisture). Conservation of mass, also known as the continuity equation, in a fully compressible form reads as

$$\frac{\partial \rho}{\partial t} + \frac{\partial(\rho U_j)}{\partial x_j} = 0 \quad (1.8)$$

where j refers to the Einstein's summation notation. For typical length scales within the boundary layer, the fluid is generally assumed to be incompressible and Eq. 1.8 reduces to (Businger, 1982):

$$\frac{\partial(\overline{U_j})}{\partial x_j} = 0 \quad (1.9)$$

The bar denotes a generic mean. In practice it is identified with an average over time or space, depending on its application. An intermediate form between fully compressible and incompressible systems has been derived in anelastic form (e.g. Ogura and Phillips, 1962), which will not be considered here. A traditional equation for conservation of momentum reads as (Stull, 1988, Eq. 3.4.3c):

$$\frac{\partial \overline{U_i}}{\partial t} + \overline{U_j} \frac{\partial \overline{U_i}}{\partial x_j} = -\delta_{i3}g + f_c \epsilon_{ij3} \overline{U_j} - \frac{1}{\bar{\rho}} \frac{\partial \overline{P}}{\partial x_i} + \frac{\nu \partial^2 \overline{U_i}}{\partial x_j^2} - \frac{\partial(\overline{u'_i u'_j})}{\partial x_j} \quad (1.10)$$

where the first term on the left hand side represents storage of mean momentum, the second term represents advection of mean momentum by the mean wind. On the right hand side, the first term allows gravity to act in the vertical direction only, the second term describes the apparent force which acts on the movement of the body as a result of the rotation of the Earth with the Coriolis parameter f_c ; it strongly depends on latitude, is zero around the equator and strongest around the poles. The third term describes mean pressure-gradient forces, the fourth term represents the influence of viscous stress on mean motions with ν being the kinematic viscosity in $\text{m}^2 \text{s}^{-1}$ and the last term represents the influence of Reynolds' stress on the mean motions with the primed variables being perturbations to the mean state ($u = \bar{u} + u'$). In a simplified form, neglecting molecular diffusion and viscosity, making the hydrostatic and Boussinesq approximations and rotating the coordinate along the mean wind component, the conservation of momentum can be written as (Stull, 1988):

$$\frac{\partial \overline{U}}{\partial t} + \overline{U_j} \frac{\partial \overline{U}}{\partial x_j} = -f_c(\overline{V_g} - \overline{V}) - \frac{\partial(\overline{u'_j u'})}{\partial x_j} \quad (1.11)$$

where $\overline{V_g}$ is the mean geostrophic wind, that follows from horizontal pressure gradient forces.

Heat conservation is approximated as

$$\frac{\partial \overline{\theta}}{\partial t} + \overline{U_j} \frac{\partial \overline{\theta}}{\partial x_j} = -\frac{1}{\bar{\rho} C_p} \left[L_v W + \frac{\partial \overline{Q_j^*}}{\partial x_j} \right] - \frac{\partial(\overline{u'_j \theta'})}{\partial x_j} \quad (1.12)$$

here latent heat L_v is introduced for the phase changes for water. $L_v = 2.5 \cdot 10^6 \text{ J kg}^{-1}$ at 0°C , W representing the water vapor mass per unit volume per unit time created from a phase change. Q_j^* represents the mean net body source associated with radiation divergence. Equation 1.12 can also be used for conservation of moisture q or any other extensive quantity (e.g. CO_2), it then should be replaced for θ . Hence, the first term on the right hand side would then be replaced for a net moisture term, or other gaseous source term and the radiation term should be omitted.

There are some generalities for the terms in Eqs. 1.11 and 1.12, and they are physically explained as follows. The first term on the left hand side represents local storage for heat, momentum or moisture. The second term is advection of a scalar, i.e. U or θ . The first term on the right hand side represents different body forcings and are the source and sink terms. The last term represents the turbulent flux divergence terms. On the latter two, radiation and turbulence, we will elaborate more in Sect. 1.1.5.

1.1.5 Energy transport

An evaluation of processes in the boundary layers by means of the Reynolds number shows that for typical length scales in the boundary layer, the main driving process is turbulence. The Reynolds number Re is defined as:

$$Re \equiv \mathbf{V}\mathbf{L}/\nu_{air} \quad (1.13)$$

where \mathbf{V} and \mathbf{L} are velocity and length scales in the boundary layer. The kinematic viscosity of air is $\nu_{air} \cong 1.5 \times 10^{-5} \text{ m}^2 \text{ s}^{-1}$. With typical scaling values $\mathbf{V} = 5 \text{ m s}^{-1}$ and $\mathbf{L} = 100 \text{ m}$ in the surface layer, $Re = 3 \times 10^7$.

However, before going to the processes generated by turbulence, we shall explain the role of heat transfer in the atmosphere. Like in any other physical systems heat transfer in the atmosphere is represented through radiation, conduction, convection and advection. Here we briefly point out the basic principles which are important to our study.

1.1.5.1 Radiation

Each body with a temperature above zero Kelvin emits electromagnetic energy. Wien's law states that for a given black body at temperature T (in Kelvin) the maximum of the emitted wavelength λ_m is given by:

$$\lambda_m T = c \quad (1.14)$$

with the constant $c = 2897 \text{ } \mu\text{m K}$. Mainly, two bodies influence the radiative processes in the atmosphere: the Sun and the Earth itself. Observed from the Earth, the Sun's temperature at the surface is around 6000 K. The Earth's surface temperature is 288 K on average. Applying Wien's law gives corresponding values of 0.5 and 10 μm for λ_m . These are the peaks of the Planck curve, visible in Fig. 1.3. The peak for solar radiation is in the visible range of wavelengths, between 0.4 and 0.7 μm . For the Earth's surface, this peak is in the infrared range, i.e. between 8 and 18 μm . Therefore the wavelengths for both emitters are clearly separated. The two components are solar or short-wave radiation (SW) and infrared or long-wave radiation (LW). Consequently, four components can be defined, leading to a surface radiation budget Q^* :

$$Q^* = SW^\downarrow - SW^\uparrow + LW^\downarrow - LW^\uparrow \quad (1.15)$$

Where the arrows designate either an upwelling \uparrow or downwelling \downarrow part of its component, with a direction perpendicular to the Earth's surface. All radiation components are fluxes, the rate of transfer of a quantity per unit area per unit time, and can be expressed in W m^{-2} . At the top of the atmosphere the solar 'constant' is 1368 (± 7) W m^{-2} (Stull, 2000). At the surface however, SW^\downarrow is less, it depends largely on the solar angle with respect to the surface and the atmosphere transmissivity. SW^\uparrow is the direct reflection of SW^\downarrow by the surface to the atmosphere. It strictly depends on SW^\downarrow , the slope angle and the surface type. Their relation can be expressed in the albedo α . LW emission of either the surface or the sky are related to the temperature through the Stefan-Boltzmann relationship:

$$LW = \sigma \epsilon T^4 \quad (1.16)$$

where σ is the Stefan-Boltzmann constant of $5.67 \times 10^{-8} \text{ W m}^{-2} \text{ K}^{-4}$. ϵ is the surface emissivity, which is between 0.9 and 0.99 for most natural surfaces. For upwelling radiation T is the surface temperature, for downwelling radiation T is the sky temperature (both in Kelvin). The balance between LW^\uparrow and LW^\downarrow is greatly dependent on the presence of clouds and on their base temperature. They have a low transmissivity and high emissivity thus absorb the emitted Earth's surface radiation. Therefore, one of the conditions for strong cooling of the Earth's surface is the absence of clouds. Altogether, the incoming solar radiation controls heating during the day. During the night however, when the solar radiation is absent, the atmosphere experiences radiative heat loss as it is generally colder than the surface.

The radiation components can be observed by pyranometers (shortwave radiation) and pyrgeometers (longwave radiation). In models these are estimated by the use of parameterization schemes.

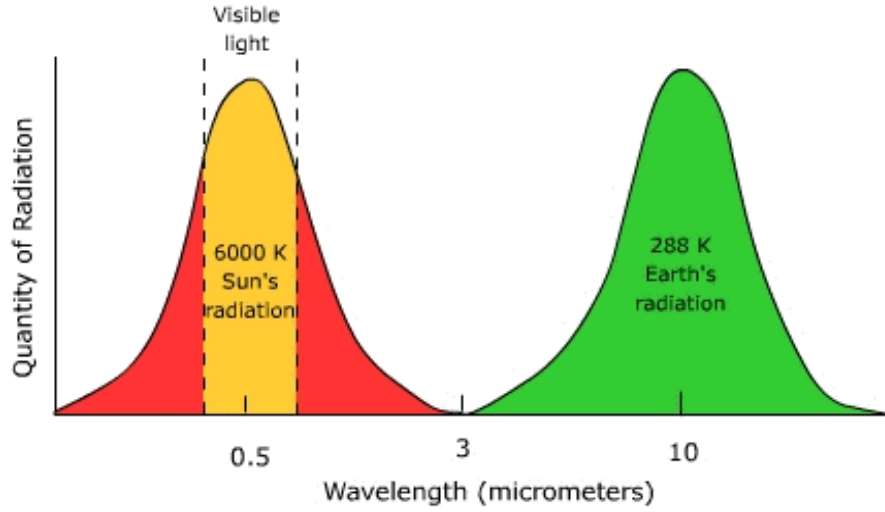


Figure 1.3: Emission spectra of the Sun and the Earth (source: <http://www.earthonlinemedia.com/>).

1.1.5.2 Conduction

The energy at the surface is re-distributed into radiation (*LW*-components), conductive or convective transport, in the form of heat. The soil conductivity controls the transport of heat from the atmosphere into the soil, or vice versa, and is expressed as the soil heat flux G , which is approximated by Fourier's law:

$$G = -\lambda \frac{\partial T}{\partial z} \quad (1.17)$$

λ is the thermal heat conductivity in $\text{W m}^{-1} \text{K}^{-1}$, which is dependent on the soil type and its water content.

1.1.5.3 Turbulent transport

For turbulent flow, the turbulent transport flux can be approximated in terms of vertical gradients of mean quantity (or any other scalar like moisture). Here sensible heat flux H , latent heat flux $L_v E$ and momentum flux τ are defined according to K-theory (Moene and van Dam, 2014). As such, they are seen as vertical transport proportional to their respective scalar vertical gradient. H is expressed as:

$$H = -\rho C_p K_h \frac{\partial \bar{\theta}}{\partial z} \quad (1.18)$$

ρ being the density of air in kg m^{-3} , K_h is a turbulent exchange coefficient in $\text{m}^2 \text{s}^{-1}$. H takes care for temperature change and can be sensed by the human body, therefore is named sensible heat. On the contrary, latent heat is heat which is hidden until water phase changes occur and is expressed as:

$$L_v E = -\rho L_v K_e \frac{\partial \bar{q}}{\partial z} \quad (1.19)$$

where K_e is again a turbulent exchange coefficient. q is the specific humidity in kg kg^{-1} . Latent energy becomes important whenever phase changes occur. Then the available energy goes into the $L_v E$ term at the cost of H . This is why dry environments tend to warm more quickly than wet environments. Note that other gases, such as CO_2 , are transported with turbulence as well.

To capture these, the same procedure is followed as for $L_v E$. Lastly, we define the momentum transport:

$$\tau = -\rho K_m \frac{\partial \bar{U}}{\partial z} \quad (1.20)$$

It is a measure for stress, one of the initiations for mechanical turbulence. Here again, K_m is an exchange coefficient. In the end the Eqs. 1.18 to 1.20 are mathematically similar to that of conduction.

Turbulence implies a large spectrum of eddies of different sizes and types. For observations, sonic anemometers are used to capture the momentum and temperature changes at high frequencies of usually 10 Hz. For water vapor, a gas analyzer is added to the measurement set-up. This set-up enables to capture the eddies on a wide spectrum of frequencies, therefore H , $L_v E$ and τ are usually averaged over 30 min. For this eddy covariance techniques are used, and the quantities can be computed directly from the fluctuations:

$$H = \bar{\rho} C_p \overline{w' \theta'} \quad (1.21)$$

$$L_v E = \bar{\rho} L_v \overline{w' q'} \quad (1.22)$$

$$\tau = -\bar{\rho} \overline{w' u'} \quad (1.23)$$

From a modelling perspective, the turbulent variables are parameterized (see Chap. 3). Finally, we introduce the friction velocity u^* . It is a velocity scale related to mechanically generated turbulence:

$$u^* = \sqrt{\frac{\tau}{\rho}} \quad (1.24)$$

The turbulent kinetic energy (TKE) is a measure of turbulence intensity. It controls the exchanges of moisture, heat and momentum. The TKE, per unit mass e , can be written in a more easier form as: $\bar{e} = 0.5(\overline{u_i'^2})$. So it represents the summed velocity variances, divided by 2. In a coordinate system aligned with the mean wind, assuming horizontal homogeneity and neglecting subsidence, its conservation equation reads :

$$\frac{\partial \bar{e}}{\partial t} = \frac{g}{\theta_v} (\overline{w' \theta'_v}) - \overline{u' w'} \frac{\partial \bar{U}}{\partial z} - \frac{\partial (\overline{w' e})}{\partial z} - \frac{1}{\bar{\rho}} \frac{\partial (\overline{w' p'})}{\partial z} - \epsilon_d \quad (1.25)$$

Here again, the first term represents local storage or time rate of change. The second term is a buoyancy term and so can be either a production or consumption term, depending on the stability of the atmosphere, i.e. whether the sensible heat flux component is positive or negative. The third term is a production term due to shear. Momentum of wind is lost downward to the ground, so multiplied by minus one results in a positive term. Term four is the vertical turbulent transport of TKE. Integrated over the boundary layer, it is 0. Term five is the pressure correlation term and can transport TKE in either turbulence or waves. The last term is the viscous dissipation term, i.e. the conversion of TKE into heat. Hence TKE is a non-conserved variable.

1.1.5.4 Surface energy budget

The definitions given in the latter sections lead to the surface energy budget:

$$Q^* = H + L_v E + G \quad (1.26)$$

For sign convention, non-radiative fluxes (terms on the right-hand side) directed away from the surface are positive. So, these terms are positive if they represent losses of heat for the surface and negative when they are gains. The radiation budget Q^* is positive as a gain and negative as a loss. During the day, when solar radiation is dominant, the terms on both sides of the equation

are generally positive. H and $L_v E$ transport heat away from the surface to the atmosphere and G transports heat away into the soil. During the night, both sides of the equation are usually negative. The surface radiative deficit (left hand side) leads to subtraction of heat from the sub-surface and the atmosphere. Despite many efforts, the surface energy balance in observations remains unclosed (Foken, 2008; Cuxart et al., 2015).

1.2 The atmospheric boundary layer over land

As explained in Sect. 1.1.1, the lowest part of the troposphere is called the boundary layer. It is that layer which reacts directly on processes occurring at or close to the surface. We can define two types of boundary layers over land, which both have their specific dominant processes. The convective or mixed boundary layer (CBL), which is mostly present during the day, and the stable boundary layer (SBL), which mostly develops during the night. For CBL the turbulence dominates the flow patterns. For SBL however, turbulence is suppressed and therefore other mechanisms can become dominant. For the latter, the complex interplay of processes remains a challenge (Steenefeld, 2014). The diurnal time pattern from SBL to CBL is shown in Fig. 1.4.

1.2.1 Convective boundary layer

For CBL development, turbulence is the main process for heat and moisture exchange. During the day when the sky is clear, the Earth's surface is heated due to solar insolation. As a consequence of the surface heating, the atmosphere close to the surface is heated and becomes warmer than the air layer above: instability is formed and due to buoyancy air parcels rise from the surface up to a height at which they reach stability with their surroundings, the entrainment zone. Above this zone is the free troposphere, potential temperature increases with height, and the atmosphere is drier. Due to convection turbulent eddies penetrate into the free atmosphere, but descend again due to stability in the free troposphere. With their return, they take back a bit of the warmer and drier free troposphere. Therefore, processes of the entrainment zone take care for transport of heat during the day. Overall, processes within the boundary layer are directly controlled by the transport of heat, momentum, water vapor, from the surface.

When CBL is formed, the layer from the surface up to the entrainment zone is well mixed: θ and q are nearly constant with height. The mixed boundary layer height varies strongly, and depends, among others, on solar insolation and moisture availability. It is usually the highest around noon or in the afternoon. During the afternoon, eddies are still generated but do not reach the noon mixed layer height anymore. Turbulence decays, leaving a layer of air with the initial mean state variables which are the same as those of the recently-decayed mixed layer, the residual layer. The residual layer is neutral or slightly stable. Typical heights of the convective mixed layer at noon are between 1 and 2 km in height.

1.2.2 Processes in the stable boundary layer

During the night the contrary happens. From sunset, or even before, when the sky is clear the Earth's surface is cooled by the radiative heat loss. The air layer in contact with the ground becomes denser than the layer above. Buoyancy weakens the turbulence, and if synoptic forcing is sufficiently weak a stable boundary layer (SBL) forms. As the night develops the cooling continues and a stably stratified layering develops and extends upward. It can grow up to 200 or 300 m. Turbulence is no longer the dominant mechanism for heat transfer, and so a complex interplay of other mechanisms develops (Mahrt, 2014; Steenefeld, 2014).

The stable boundary layer can be classified into weakly stable and very stable regime (Mahrt et al., 1998; Van de Wiel et al., 2003). During the weakly stable regimes, continuous turbulence overcomes the radiative heat loss. The turbulence is generated by shear (Eq. 1.25), which implies strong mechanical mixing, i.e. high values for u^* . Similarity theory can be applied

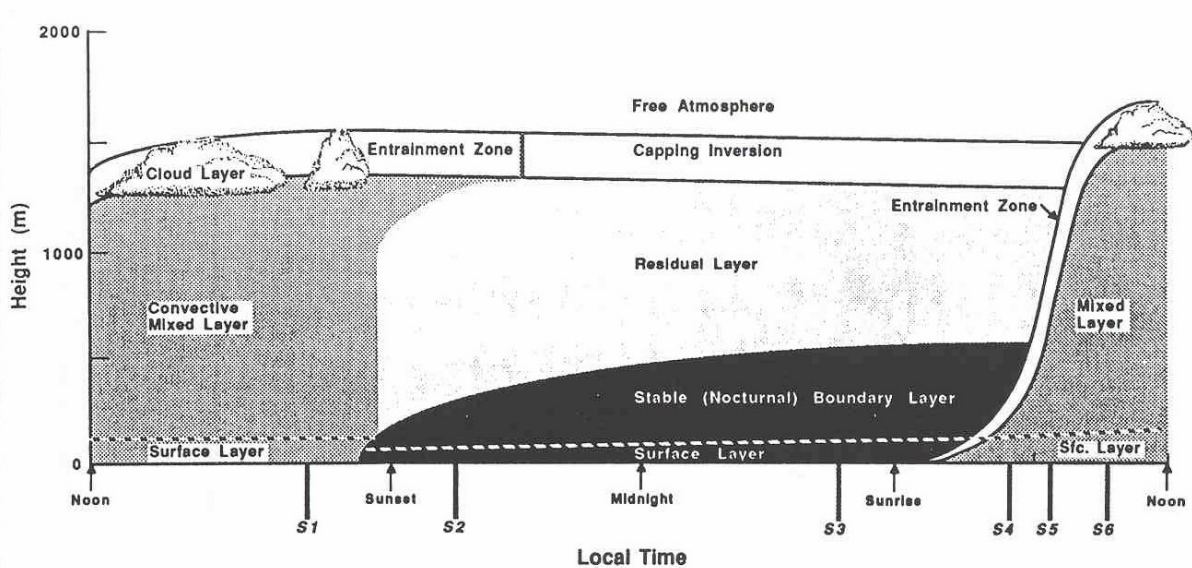


Figure 1.4: A representation of the diurnal cycle of the atmospheric boundary layer. Adopted from (Stull, 1988)

during such regimes (Nieuwstadt, 1984). For the very stable regime however, the turbulence is strongly diminished. This regime remains poorly understood because of the complex interactions between turbulence, radiative flux divergence (Brutsaert, 1972), gravity waves (Nappo, 2012; Largeron et al., 2013) and other submeso-scale motions (Mahrt, 2014). Intermittency behavior of turbulence is observed for the very stable regime. Figure 1.5 shows a representation of the physical processes involved during SBL formation and their interactions (Steeneveld, 2014). We pick up some of these processes important for our study.

One of the features developing regularly in SBLs over flat terrain which are directly important to our study are low level jets (LLJs - Blackadar, 1957). Due to weakening of turbulence, air layers get decoupled to a limited interaction between them (ReVelle, 1993; Delage et al., 2002). LLJs are represented by a localized maximum in the wind speed profile. The peak of the wind is typically larger than the geostrophic wind speed and can be regularly found at SBL depth. LLJs occur in a periodic behavior, as they tend to destroy the stability: at the onset of LLJs turbulent mixing is enhanced, which can destroy the stability needed for the onset of LLJs (Fig. 1.5). Other types of LLJs are found as well, under the forcing of baroclinicity over sloping terrain, land/sea breezes and inertial oscillation (Kraus et al., 1985). Although in general turbulence is reduced inside SBLs, elevated shear may occur in regions below a LLJ (Smedman, 1988; Mahrt, 1999). LLJs can be found throughout the year and all over the world (Tuononen et al., 2015).

One of the principal variables controlling the temperature tendency in SBL is radiative flux divergence, i.e. the third term in Eq. 1.12. As pointed out earlier, every object with a temperature above zero Kelvin emits radiation, depending on its temperature and emissivity. When vertical gradients of temperature close to the ground in SBL become very large, the radiative emission differs strongly between the different layers. Thus, the temperature evolution is governed amongst other by the divergence of the net longwave radiative flux (Anfossi et al., 1976), which is reported to be substantial, with values of several K h^{-1} (Hoch et al., 2007; Steeneveld et al., 2010). The understanding of it, both on observational and modelling side, still remains a challenge (Steeneveld, 2014).

Modeling the SBL is a challenging, but necessary task for dispersion studies (Hanna and Yang, 2001; Milliez and Carissimo, 2007). In addition to the fore-mentioned unsatisfactory understanding of the most important processes, these are incompletely represented in physical

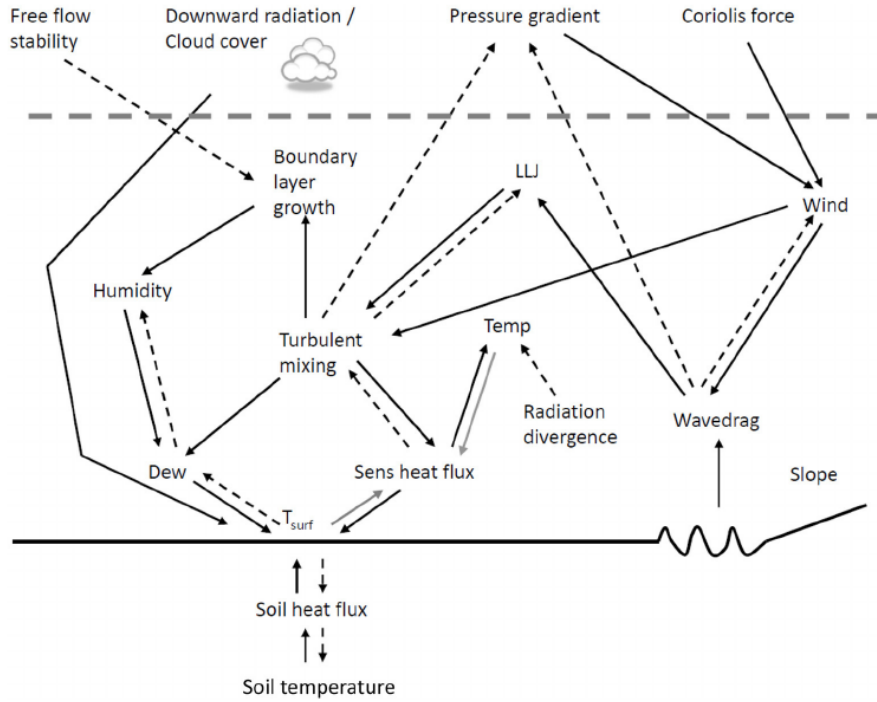


Figure 1.5: Schematic overview of the physical processes for a SBL over land, their interactions including positive (full lines) and negative (dashed lines) feedbacks. Gray lines indicate processes that can either have positive or negative feedbacks, depending on the boundary layer state. Adopted from Steeneveld (2014).

parameterization schemes (Sterk et al., 2013). Model performance for the SBL has been investigated for homogeneous conditions in the model intercomparison studies of GABLS (Svensson et al., 2011; Holtslag et al., 2013), showing the difficulties to adequately represent key parameters for boundary layers.

Over complex terrain the challenge is even harder (Arnold et al., 2012), as the local-scale inhomogeneities require subkilometer resolution, which is nowadays still inadequate for operational use. Besides, SBLs are much more thinner than convective boundary layers, increasing the difficulty. Consequently, for both understanding and modeling purposes, atmospheric observations remain a necessity for future performance (García-Díez et al., 2013), particularly over complex areas (Rotach et al., 2004).

1.3 Implications of stability over complex terrains

25% of the Earth’s land surface is mountainous (Barry, 2013). Relatively to this important part in the environment, little is known about the meteorology in such areas. Mainly because of practical issues, weather stations are scarce in mountainous areas and mainly situated in accessible valleys and plains where they better represent the synoptic pattern. Besides, mountain ranges can be at such distance from human activity that this lowers the economic interest for a dense weather station network. Nevertheless, the understanding of processes related to the orography is necessary on all scales. Orography can modify the synoptic pattern, the mean atmospheric flow (e.g. Mistral), cause flow blocking or wind acceleration.

For dispersion studies, characterizing the SBL is of extreme importance and not the least in regions of orographic complexity. Although pollutants are mostly emitted during daytime, the nighttime concentration of contaminants can be substantially high (Vecchi et al., 2007) as they can be trapped in the SBL. Therefore the SBL is recognized as one of the most penalizing atmospheric conditions for air quality (Zanetti, 1990). In regions of orographic complexity,

mountains and valleys modify the flow and thus strongly influence the dispersion (Bowen et al., 2000; Triantafyllou and Kassomenos, 2002) which can have a severe consequence on air quality (Pardyjak et al., 2009; Salmond and McKendry, 2005; Largeron, 2010). The direct relation of orographically induced flows to air quality has been investigated recently in TRANSFLEX, approving the implications for health regulation (Fernando et al., 2013).

This thesis treats the local flows under calm, stably stratified conditions, hence we elaborate on the most important patterns found in these.

1.3.1 Thermally driven downslope winds

One of the most prominent modifications of orography to wind patterns are named thermally driven winds. The simplest example of a thermally driven wind is exerted by slopes. Over slopes, strong diurnal patterns concerning the wind direction can be found, as a consequence of the day-night insolation pattern. During the night, downslope winds develop. These katabatic winds are gravity flows initiated by nocturnal radiative surface cooling, under calm clear-sky conditions (Fig. 1.6). The layer at the surface is denser than the layer at the same altitude away from the slope. The negative buoyancy experienced by the air layer at the surface, causes the air to flow downslope (Manins and Sawford, 1979; Mahrt, 1982; Horst and Doran, 1986; Haiden and Whiteman, 2005). During the day, the opposite occurs. The surface is heated, and a less dense air layer close to the surface develops, relative to the air layer at the same altitude away from the surface.

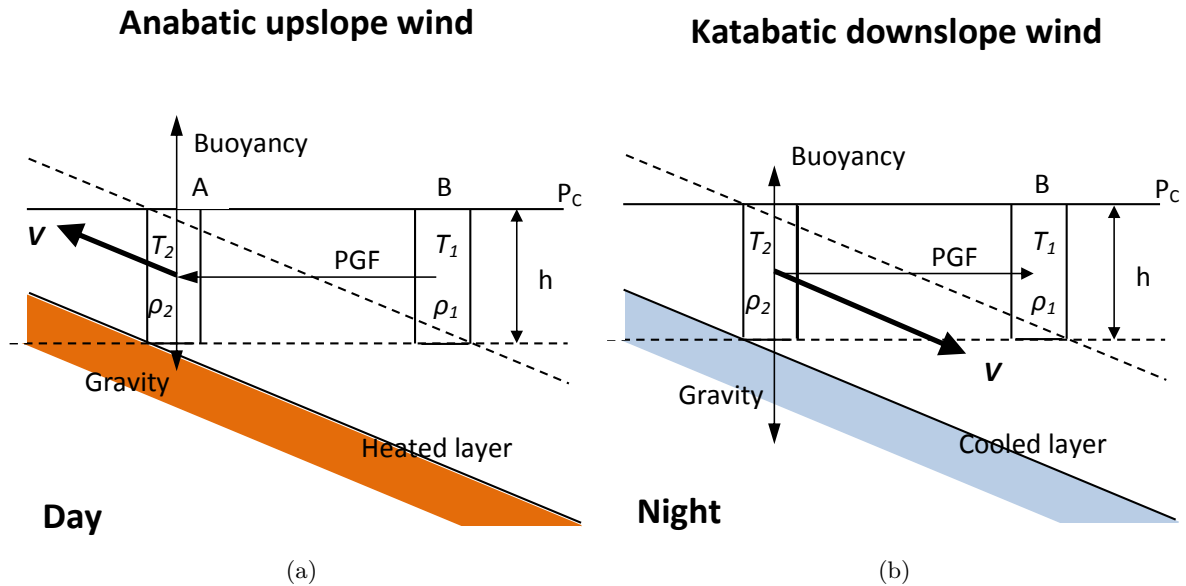


Figure 1.6: Schematic overview of forces involved in anabatic upslope (a) and katabatic downslope (b) winds (V). The air temperature in columns A and B determines their density (ρ) and pressure gradient force (PGF). After Barry (2013) and adapted.

Gentle slopes with angles as low as 1° can induce downslope flows (Mahrt and Larsen, 1990; Skillingstad, 2003). Downslope flows start mostly when sensible heat flux becomes negative. Consequently, it is very much related to the slope angle and orientation and depend on local sunset (Nadeau et al., 2013). These flows are mostly found throughout the night, as long as stability occurs. In this way, they are more stationary than LLJs. Through their momentum they tend to mix the boundary layer, but this depends on flow depth and speed. Many external factors driving the flow speed and height have been proposed, including slope angle (Smith and Skillingstad, 2005), ridge-top wind speed and inversion depth (Horst and Doran, 1986). A general idea for the typical depth h of slope flows is 0.05 times the altitude drop from the top of

the slope (Horst and Doran, 1986). A more comprehensive approach from Monti et al. (2002) includes the along slope distance from the top s and the slope angle α to calculate h .

Improper and ambiguous terminology is found widespread in the literature (see also Appendix A). The thermally driven downslope wind is often referred to as katabatic wind, although katabatic is generic and simply means going downward, irrespective of the cause. However, downslope winds also refer to winds that are forced over topography by large-scale pressure gradients (Durran, 2002), e.g. the foehn winds (Swiss, Austria) and Bora winds (Croatia). The term has also been used for downslope winds at high latitudes for which wind speeds can go up to 30 m s^{-1} (Bromwich, 1989). To complicate matter, thermally driven winds can also be land and sea breezes.

1.3.2 Valley systems

Also inside mountain or valley systems, strong diurnal wind patterns are found. The valley winds are produced likewise the slope flows, by horizontal temperature gradients. The reversal of the wind happens twice a day. Within valleys the diurnal signature as induced by (in)stability is present as well, although in a more complex form (see Fig. 1.7). Likewise to thermally driven slope winds, upslope and up-valley winds are found during the day, and downslope and down-valley winds occur during the night. Inside deep or shallow valley systems, the downslope flows from the sidewalls can feed the momentum of the down-valley flow. Drainage occurs and the cold air that converges to the valley bottom often results in a weak lifting motion, creating return currents at approximately the valley height (Oke, 1987). Valley drainage can be thought of as a river of cold and dense air flowing down the valley. Down-valley flows can be strongest with clear skies when wind aloft is weak. Similar but opposite patterns are found during the day. Most downslope flows are found with speeds of $2 - 3 \text{ m s}^{-1}$, but depend greatly on the slope angles, slope shapes, stability strengths and valley depths. Also the onset of slope and valley flows within a valley is very much related to the valley geometry, notably its depth.

Scale analysis shows that the large number of different flow types requires different approaches and thus not one single universal solution applies (Mahrt, 1982), as for example the flow depends greatly on the valley geometry (Atkinson, 1995; Monti et al., 2002). This is one of the reasons why local field measurement observations remain necessary for unexplored regions. Thermally driven slope and valley flows were investigated extensively during the VTMX-campaign (Doran et al., 2002) while cold pooling is documented by the METCRAX (Whiteman et al., 2008) and COLPEX (Price et al., 2011) campaigns.

One of the additional features of the valley meteorology is its influence on temperature near the ground, as it enhances the diurnal temperature range (DTR). The cold and dry air drained into the valley lowers the minimum temperature (Geerts, 2003). The colder air stagnates at the valley bottom and consequently a cold pool develops below a valley inversion (Clements et al., 2003). These cold pools can persist a long time during the early morning. The subsequent break-up of these inversions, leading to the daily mixed boundary layer, is more complex than over flat land. Inversion breakup begins at (local) sunrise (Fig. 1.8). Mass and heat are entrained from the stable core and transported up the sidewalls by the upslope flows. The stable core shrinks due to subsidence and sinks until it is broken. From this time, a turbulent well mixed layer is established up to valley depth.

So, the boundary layer evolution is somehow different between complex and flat terrain. In general, during the day, the PBL can be higher than on flat terrains as a consequence of the upslope winds (part A in Fig. 1.9), air can penetrate more easily into the free troposphere than for flat terrains. From sunset, part B, convection has vanished and the stable stratification starts building up with the consequent downslope flows. However, the up-valley flow remains aloft. Generally, the stable layer grows up to valley depth (part C). After sunrise, the morning

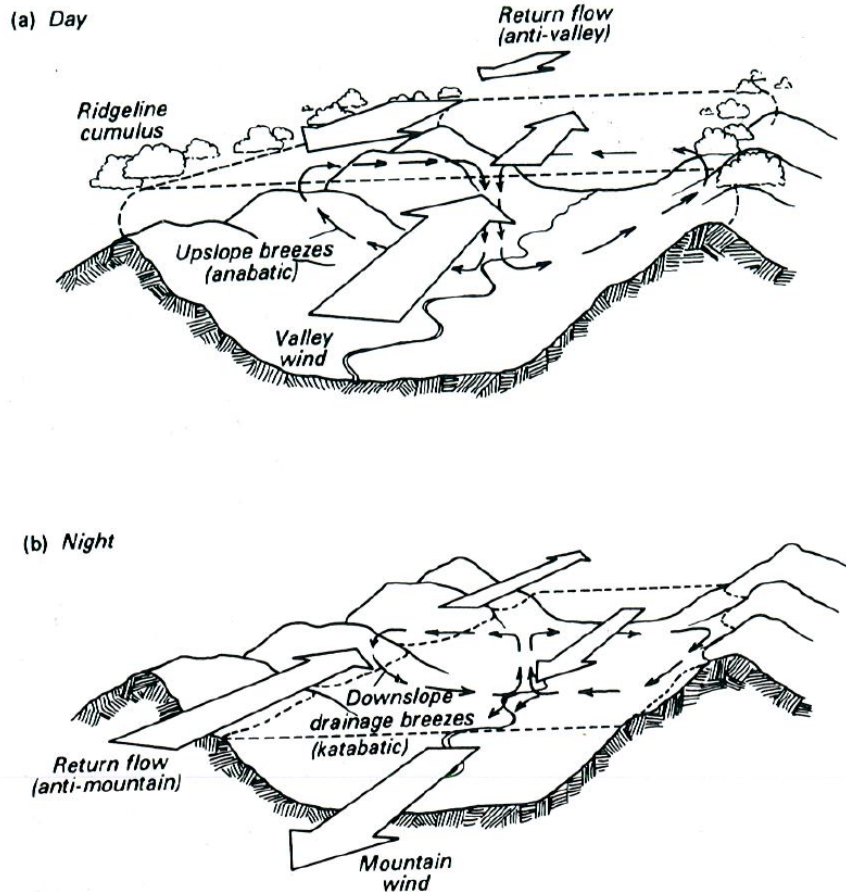


Figure 1.7: The diurnal wind pattern for valley winds. Source: Oke (1987).

transition (from part D) contains a stable core disconnected from the surface which has a longer lifetime than over flat land (Fig. 1.4). The CBL grows gradually from the surface, above the stable core the large scale CBL from the plain can already be found. Within the stable core, the down-valley wind remains until the CBL has taken over the full vertical profile in part E. Consequently, the onset of the full-mixed layer comes with a great delay in comparison to the flat land mixed boundary layer (Fig. 1.4).

1.3.3 Various origins of valley flows

The thermal driving force is not the only (possible) origin for valley flows. They can be multiple, some related to above-valley conditions. Whiteman and Doran (1993) classified four distinct relationships between valley flow and above-valley flow. The proposed mechanisms are either fully independent or (quasi-) dependent flows (Fig. 1.10). The cases presented here are idealized. Besides, other mechanisms may exist. Note that the above-valley wind is preferably the geostrophic wind.

Thermally driven The first class is the fully independent, thermally driven flow. This flow is completely disconnected from the above-valley flow, and shows the clear diurnal pattern which was described in the previous section. It is considered as thermal forcing, and is generated by along-valley pressure gradients. Such systems produce up-valley winds during the day and down-valley winds during the night, and are mechanisms found for many valleys. Fig. 1.10a shows the idealized dependency for the Cadarache Valley, which is the smallest valley under study with southeast-northwest axis orientation. Mostly, the thermally driven flows are found during weak synoptic forcing situations, when upper-level winds are weak but the valley geometry plays a

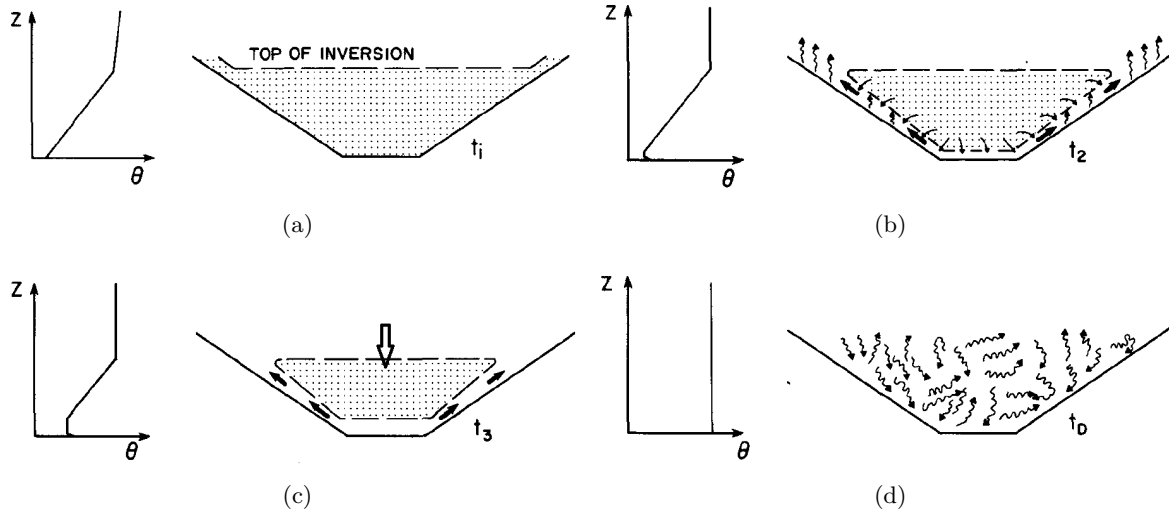
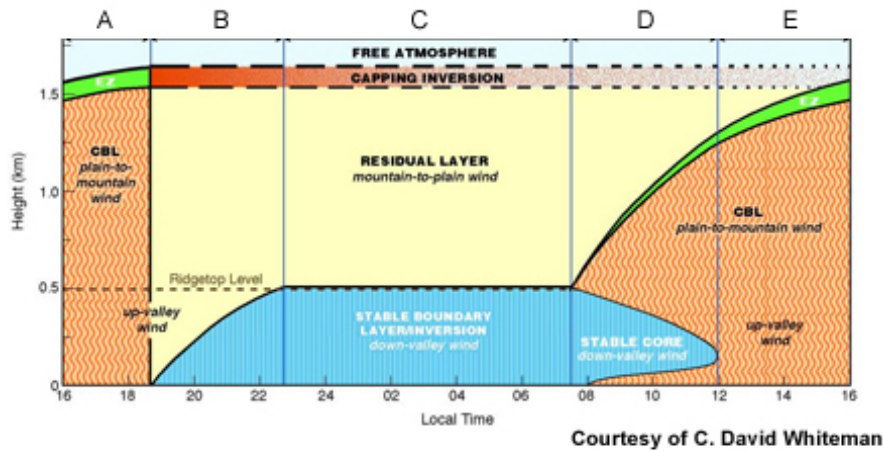


Figure 1.8: Time evolution of temperature inversion break-up after sunrise with potential temperature (θ) profile on the left. a: Nocturnal valley inversion at initial time, b: start of surface warming, c: slope wind and stable core shrinking start, d: end of inversion, turbulent well mixed layer throughout valley depth. Source: Whiteman (1982).



Courtesy of C. David Whiteman

Figure 1.9: The evolution of the boundary layer for a mountain plain system for five different stages: A: the full mixed afternoon boundary layer, extends over the valley, B: around (local) sunset stability and down-valley winds gain in depth from the surface until stability reaches valley depth in C: down-valley winds and SBL up to valley depth, D: CBL develops after sunrise, a stable core remains until E: a full-mixed has developed with up-valley winds.

role as narrower valleys do favor the mechanism.

Downward momentum transport The second important mechanism is downward momentum transport, presented as the diagonal line in Fig. 1.10b. For this mechanism, the valley wind is totally dependent on the above-valley wind. Assuming the latter is however a geostrophic wind, a slight turning would be expected at the surface due to friction effect. The downward momentum is mainly caused by vertical turbulent mixing or gravity waves (Whiteman and Doran, 1993). The phenomenon is mostly present during unstable and neutrally stratified conditions. Moreover, shallow and wide flat-bottomed valleys favor this mechanism. Low sidewalls cause wind channeling to be fairly ineffective and a flat bottom does not promote thermally driven winds.

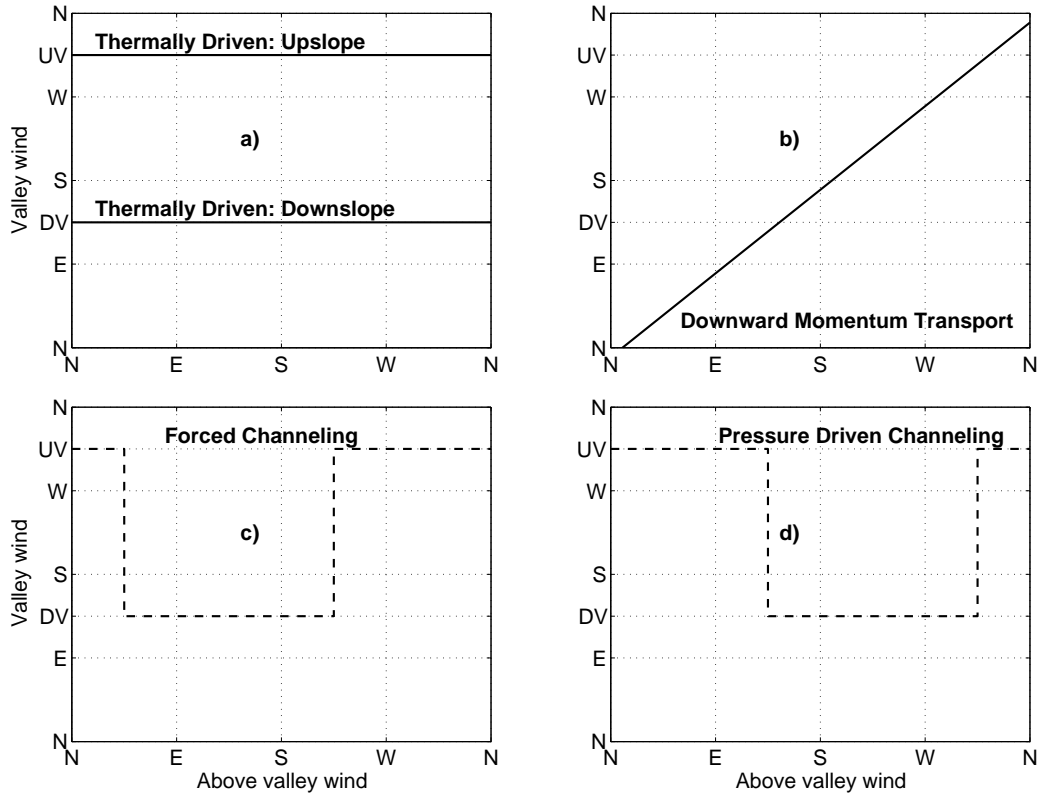


Figure 1.10: Valley wind direction and its relation to above valley wind according to Whiteman and Doran (1993), adapted for a valley with a southeast-northwest direction, up-valley (UV) and down-valley (DV) indicated on the y-axis.

Forced channeling The third class is forced channeling (Fig. 1.10c). It occurs when above-valley flows are re-directed by the valley sidewalls into the valley axis direction. The valley wind then depends on the direction of the above-valley wind. Upslope (downslope) winds are expected when the upper flow direction departs by less than 90° from the UV (DV) axis direction. Narrow valleys during unstable or neutral conditions facilitate the forced channeled flow (Weber and Kaufmann, 1998).

Pressure-driven channeling The fourth mechanism is pressure-driven channeling (Fig. 1.10d). Valley winds are driven by the component of the geostrophic pressure gradient along the valley's axis. Winds in the valley turn from up to down-valley or down to up-valley wind when geostrophic wind direction crosses the valley axis. Countercurrents can occur for this mechanism, i.e. in opposite direction from that observed within the valley with respect to the above valley direction (Weber and Kaufmann, 1998). Pressure-driven channeling can be of importance in wide and shallow valleys under slightly to moderately stable atmospheric conditions (Carrera et al., 2009) and has been reported for the wide Rhine Valley (Gross and Wippermann, 1987).

1.4 Summary

This chapter comprises a brief overview of the atmosphere, stable boundary layers, valley winds in particular and their complexities. We explained the atmosphere's structure, length and time scales, and governing equations. Then, we have seen that the boundary layer structure can be partitioned into two completely different ones: firstly the deep convective boundary layer which is mostly dominated by turbulence and fairly well understood following turbulence theories, and secondly the more shallow stable boundary layer for whose behavior is more complex,

especially when turbulence is not significantly present. Studying the latter structure in the valleys comprising the Cadarache site is the topic of this thesis.

Hence the last part of the chapter contains the consequences of stability over complex terrain. We briefly set out the current challenges for modeling the stable boundary layer over complex terrain. The consequence for atmospheric dispersion in such conditions is also explained. Mechanisms on slope flows, valley wind systems and their typical boundary layers are explained, with more detail for thermally driven down-valley winds. Mechanisms driving valley flows other than thermal effects are also presented.

The influence of stability over complex terrain on the regional wind pattern is investigated for southeastern France. This is done by means of observations (campaign KASCADE), and numerical modeling on the mesoscale. The methodology for both can be found in Chaps. 2 and 3 respectively. The results of KASCADE and the dominance of the down-valley winds under investigation are set out in Chap. 4. The down-valley flow for the smallest valley examined (Cadarache Valley) is further investigated on its characteristics related to stability in Chap. 5. The KASCADE data is used to set-up and evaluate the Weather Research and Forecasting model for the region in Chap. 6. Spatial characteristics of the larger scale down-valley flow related to the Durance Valley are investigated by means of numerical modeling in Chap. 7.

Chapter 2

Site description, measurement set-up and inter-comparison

2.1 Introduction

This chapter contains the methodology used for observations. The first section is dedicated to the Cadarache site description and highlights the dominant meteorology at the site and its close surroundings (Sect. 2.2). A detailed description of the KASCADE-campaign is given, including the measurement strategy, measurement locations and sensors used, operation schedule and other details important for later analyses (Sect. 2.3). The last section of this chapter (Sect. 2.4) is dedicated to the results after the inter-comparison, and concerns specific data treatment necessary before phenomenological analyses can start.

2.2 Site characteristics

2.2.1 Durance Valley

The Durance Valley (DV) has been formed by the Durance river, a braided river flowing from the Southern Alps to the Rhône Valley (Warner, 2006). The Cadarache research center is situated on the east bank of DV, close to Clue de Mirabeau (Fig. 2.1a). The middle valley of the Durance is the part from Sisteron to the Clue de Mirabeau and has a length of 67 km with a mean slope angle of 0.2° . The valley bottom itself is nearly flat (Fig. 2.1c). The along-valley direction downslope is around 30° from the north, as indicated by the red line in Fig. 2.1a. Close to Sisteron the DV is 5 km wide, but it widens to 8 km close to Cadarache. The DV narrows abruptly to 200 m at the Clue de Mirabeau, where the lower DV starts. The valley depth close to Cadarache is 200 m. The aspect ratio, defined as the ratio of the valley depth to the valley width, close to Cadarache is 0.04. However, it varies along the part between Sisteron and Clue de Mirabeau.

The DV facilitates a wind which is frequently measured by the Cadarache meteorological observational network (Margerit, 2004). This wind, with a direction of around 30° , is recognized as the Durance down-valley (DDV) wind and is one of the two valley winds under investigation. Previous studies in literature have been done on DV meteorological phenomena, and have shown the existence of down-valley winds; Kalthoff et al. (2005) showed the existence of the along-valley oriented wind in the early morning during ESCOMPTE, a campaign focused on the land/sea breeze effect on photo-oxidant pollution during summer (Cros et al., 2004; Mestayer et al., 2005). Quénol and Beltrando (2008) investigated the effect of spring frost on the DV wind system in the lower part of the DV. However, a thorough phenomenological study in literature is lacking, though the importance of a DDV wind documentation was crucial for dispersion on a larger

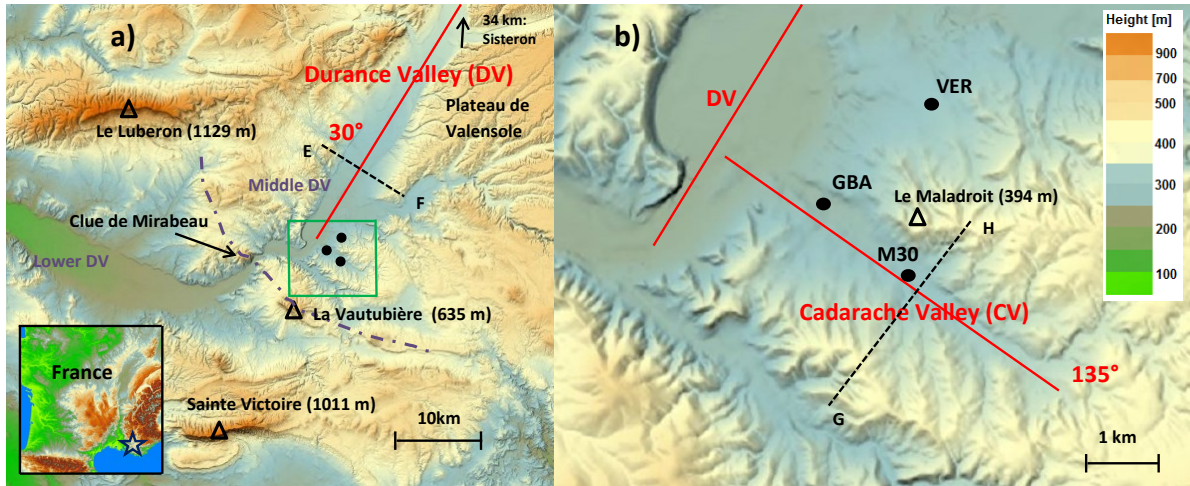


Figure 2.1: The study area. a) provides a zoom on the area indicated by the star in the lower left frame, b) is the enlargement of the green square in a). The red lines indicate the Durance (DV) and the Cadarache (CV) valleys with their down-valley directions marked in degrees from north (in red), the dash-dot line separates the middle and lower DV sections in a). Measurement locations are indicated by black dots. The most important orographic features and their maximum altitude are indicated. The height scale applies to both frames. c) and d) provide valley cross sections for DV and CV, respectively. Locations of cross sections are given in a) and b) by dashed lines. Source maps: Geoportail.gouv.fr

scale. Knowledge on its characteristics by means of observations leads to better evaluation and understanding of model behavior and so to improved dispersion calculations on a regional scale.

2.2.2 Cadarache Valley

The Cadarache Valley (CV) is a side valley of the DV. Its along-valley orientation is 135° , which is almost perpendicular to the DV. It is 2 km wide, 5 km long, with a slope angle of 1.2° and a depth of ≈ 100 m. The width and depth lead to an aspect ratio of 0.05. The sidewalls have an average slope angle of around 6° . The land use in the CV is a mixture of broad-leaved and mixed forests, grasslands, artificial surfaces and buildings.

The valley is shallow but narrow and long enough to facilitate the Cadarache down-valley (CDV) wind. The CDV wind existence has never been documented in literature before. However, its characteristics should be known as most of the facilities of the Cadarache site are embedded within this valley. Regarding the valley's size, this is mainly important for risk management on a local scale.

2.2.3 Other orographic features

The local wind patterns may be modified due to the presence of other orographic features of different scales (Fig. 2.1a). The Southern Alps, situated northeast of Cadarache, reach 1500 m asl at about 70 km distance and attain up to 3000 m at 140 km. Jiménez and Cuxart (2014) show that in very calm synoptic conditions mountain systems of this scale develop drainage currents that can modify the flow more than 100 km downstream. A sloping plateau with an average angle of 1° is situated in between the Southern Alps and Cadarache on the DV left bank. This Plateau de Valensole could enhance LLJ-formation during stable situations and therefore could contribute to flow-channeling in the DV. The Luberon and Sainte Victoire mountains are two east-west oriented ridges at moderate distance from the site: They have heights of 900-1100 m, and modify flows on a regional scale. Closer to Cadarache, the narrow Clue de Mirabeau divides the DV in its middle and lower part. Especially in winter situations, it facilitates cold air pool formation. Finally, situated within the Cadarache site boundaries, the Maladroit hill is part of the CV northeastern sidewall with a height of 394 m asl, around 110 m above the valley bottom.

2.2.4 Typical meteorological phenomena

Various important meteorological phenomena are typical for the region, notably the Mistral wind, land/sea breeze effects and heavy precipitation events. Although they are not directly linked to the aim of the study it is worth mentioning them, as these phenomena can interfere with valley winds and were sometimes present during the KASCADE experiment. The Mistral is a cold, strong and dry wind that flows down the Rhône Valley (Guenard et al., 2005) and can occur throughout the year, with possible strong diurnal variation close to the ground (Reiter, 1971). At the Cadarache site the Mistral comes from a northwesterly direction. Not all Mistral events, however, reach Cadarache. During afternoons, due to solar insolation and proximity to the Mediterranean Sea, land/sea breezes develop (Cros et al., 2004; Mestayer et al., 2005). Sometimes these breezes are coupled with the Mistral (Bastin et al., 2005) and reach Cadarache approaching from the west. Precipitation events in the region usually come from the southeast (Margerit, 2006). They occur mainly during Fall and early Spring months although they are observed outside these seasons as well. Heavy precipitation events around the Mediterranean Sea have been intensively investigated during the HYMEX-campaigns (Drobinski et al., 2013).

The study area is protected from western oceanic influences by the surrounding mountain as Massif Central. Due to meteorological mesoscale phenomena mentioned (e.g. Mistral), clear skies occur frequently in the region. Wrathall (1985) reports more than 2500 hours of sunshine per year.

2.3 Instrumentation and measurement strategy

To investigate the valley flow onset, their occurrence and interactions during stable conditions, the KASCADE campaign was conducted during the winter of 2013¹. Nocturnal stability in the region occurs throughout the year, but shorter days and longer nights of winter enhance SBL formation. The campaign collected continuous observations that were supplemented by special intensive observational periods (IOPs).

¹Thanks to all participating colleagues from Laboratoire de Modélisation des Transferts dans l'Environnement and Laboratoire d'Aérodynamique, the campaign was a success. A special thanks goes to Dr. Thierry Hedde, who took the part of administrative matters concerning CEA, and more importantly, direct problem-solving for issues occurring during the campaign.

2.3.1 Continuous observations

The data for continuous observations were collected between 13th December 2012 and 18th March 2013 at three different sites: La Grande Bastide (GBA), La Verrerie (VER) and M30. A detailed description of the instrumentation deployed during KASCADE is given in Table 2.1. Sensor descriptions can be found in the Technical Note (Appendix C).

2.3.1.1 GBA and VER

Cadarache has two permanent weather stations, La Grande Bastide (GBA - Fig. 2.2a) and La Verrerie (VER - Fig. 2.2b). Both measure temperature at 2 m agl. GBA also observes temperature at 110 m. Wind speed and direction are observed at 110 m (GBA) and 15 m (VER). Additionally, atmospheric pressure and relative humidity observations are available. The top of the GBA-mast extends above the CV sidewalls and its stable boundary layer and thus can sense the overlying winds. GBA has been operated for several years and can be used as a long term reference for the dataset.

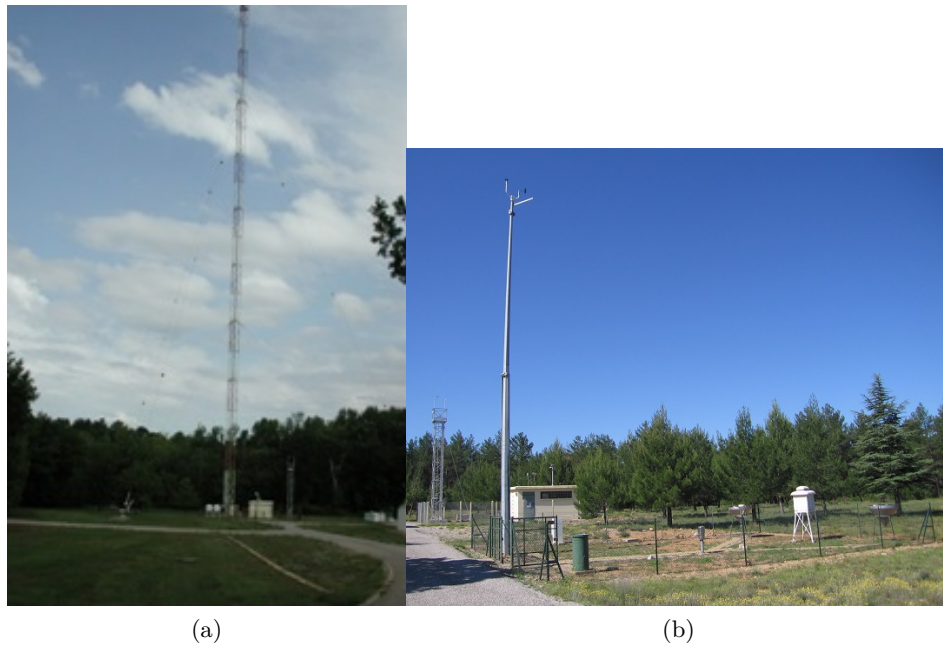


Figure 2.2: The permanent measurement stations a: La Grande Bastide and b: Xaria at La Verrerie (photo: Y. Margerit).

2.3.1.2 30 m flux tower

At the M30 site in the CV (Fig. 2.1b), a flux divergence tower has been installed with sensors at different heights (Fig. 2.3a): sonic anemometers at 2, 10 and 30 m, one fast hygrometer at 30 m, longwave and shortwave radiation sensors at 2 and 20 m and two thermohygrometers at 2 and 30 m. To avoid that the tower influences the lower radiation sensor, the latter was placed on a separate mast at approximately 25 m from the M30 tower. The three sonic anemometers were oriented to the southeast to better capture the down-valley wind. M30 was placed in the middle of the CV on a flat open area with a 600 m fetch in the along-valley upslope direction. The site is mostly a grass prairie with patches of bare soil.

By deploying M30, wind components, heat and momentum fluxes can be calculated at three levels, and evaporation at one level. The goals for measurements by the flux tower at this location were multiple:

Table 2.1: Summary of measurements at the sites shown in Fig. 2.1b, and their stations: geographical coordinates, base elevation above sea level (asl), measurement height above ground level (agl), instruments used, measured parameters, sampling frequency. Abbreviations include T : temperature, RH : relative humidity, U' , V' , W' : sonic wind speed components, T' : sonic temperature, H_2O' : humidity, CO_2' : carbon dioxide concentration, SW^\downarrow , SW^\uparrow , $SW^\downarrow, LW^\downarrow, LW^\uparrow$: incoming- and outgoing shortwave and longwave radiation, PP : atmospheric pressure, FF : wind speed, DD : wind direction, T_d : dew point temperature, v_z ascending/descending speed. # denotes the number of measurements at different heights.

Site	Station	Coordinates (°N, °E)	Elev base (m asl)	Meas hgt (m agl)	Instrument	Variable	Acq. freq.(Hz)	Additional information
M30	id.	43.68550 5.76169	286	30.36	Campbell Sci. HMP45 thermohygrometer	T, RH	0.1	$T \#2, RH \#2$
				30.29	Campbell Sci. CSAT sonic anemometer	$U'V'W'T'$	10.0	sonic #3
				30.29	LI-COR LI-7500A open path analyzer	$H_2O'CO_2'$	10.0	
				20.11	Kipp & Zonen CNR4 net radiometer	$SW^\downarrow, SW^\uparrow, LW^\downarrow, LW^\uparrow$	0.1	radiation #2
				10.50	Young 81000 sonic anemometer	$U'V'W'T'$	10.0	sonic #2
CNR1		43.68564 5.76147	286	1.90	Campbell Sci. HC2S3 thermohygrometer	T, RH	0.1	$T \#1, RH \#1$
				1.90	Young 81000 sonic anemometer	$U'V'W'T'$	10.0	sonic #1
				1.18	Kipp & Zonen CNR1 net radiometer	$SW^\downarrow, SW^\uparrow, LW^\downarrow, LW^\uparrow$	0.1	radiation #1
				2-300	Vaisala TTS111 tethersondes (3)	T, RH, PP, FF, DD	0.25	3 profiling sensors
				1.50	Vaisala TTS111 tethersonde (1)	T, RH, PP, FF, DD	0.25	$v_z = 30 \text{ cm s}^{-1}$
RS		43.68550 5.76169	286	0-5000	MODEM M2K2-DC Radiosonde system	T, RH, PP, FF, DD	1.0	Height correction sensor
								Balloon type cosmo-
								prene KE 45 g
VER	id.	43.70744 5.76514	295	15.0	Dégréane DEOLIA96 cup anemometer	FF, DD	0.1	
				2.0	Vaisala PT100 thermometer	T	0.1	
					Vaisala hygrometer	RH	0.1	
					Vaisala barometer	PP	0.1	
					PréciMéca R30295 rain gauge	RR	0.1	
SODAR		43.70697 5.76531	297	75-400	Remtech PA2 Sodar	FF, DD	0.001	
						$\sigma_u, \sigma_v, \sigma_w$		
GBA	id.	43.69442 5.74614	265	110.0	PT100 thermometer	T	0.1	
					Metek sonic anemometer	FF, DD		
				2.0	PT100 thermometer	T	0.1	
					Rotonic hygrometer	RH		

1) Direct observations of stability by means of temperature observations at the top and bottom of the tower. At the same heights, relative humidity is available.

2) Continuous observations of the onset and decay of the Cadarache down-valley wind at three levels.

3) Model validation for numerical studies.

4) Heat budget calculations. With sonic anemometers and net radiometers at different levels, radiation divergence and heat flux divergence can be determined. Radiation divergence is a crucial parameter for SBL-formation which is still relatively unexplored (Sun et al., 2003; Savijärvi, 2006; Hoch et al., 2007; Steeneveld et al., 2010). Furthermore, the relation of these budgets to down- and up-valley wind onset and decay can be used to generalize the study.

Further details on M30 measurement equipment can be found in Table 2.1. Details on data treatment are given in Sect. 2.4.5.

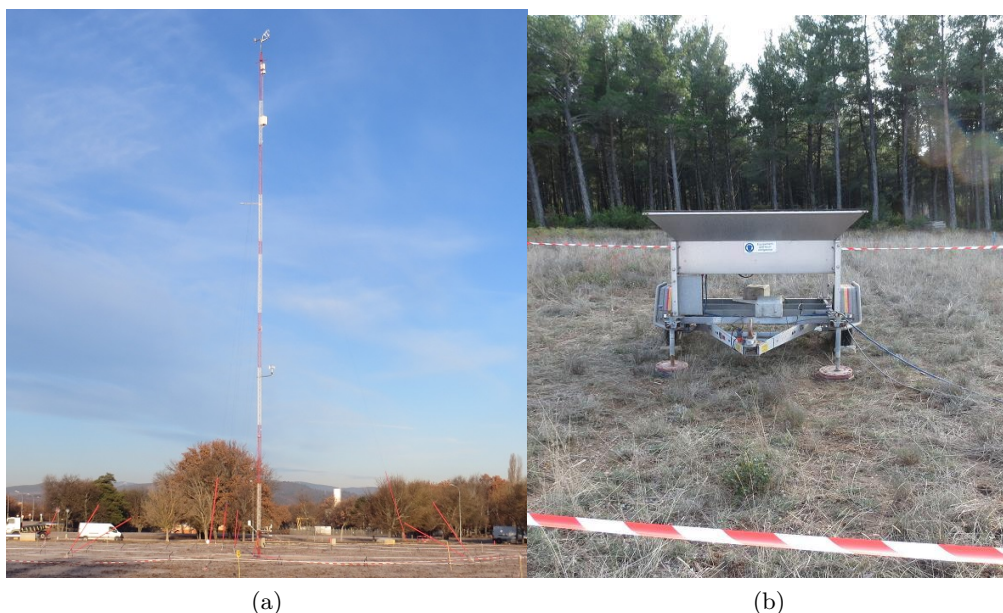


Figure 2.3: a: The site of the 30 meter flux tower at M30 and b: the Sodar at VER.

2.3.1.3 Sodar

At VER (Fig. 2.1) a Remtech PA2 Sodar provides averages of wind speed and direction and turbulence characteristics every 15 minutes with a vertical resolution of 25 m (Fig. 2.3b)². VER is located outside the CV, and so is disconnected from the CV boundary layer. The Sodar provides continuous information on the DDV flow from 100 to 500 m agl. Potentially characteristics on the onset, decay, depth and strength of this flow can be derived. Besides, it gives insight on the dominant wind patterns associated with larger scales as mentioned in Sect. 2.2. It therefore can point out the dominance of the DDV wind over the Cadarache site relatively to other winds. As it is based on indirect measurements, a validation of these measurements is necessary. This is done by evaluating them against the tethered balloon and GBA-observations (Sect. 2.4.4).

The Sodar has some limitations in its usage. It performs badly when wind speeds are over 20 m s⁻¹. Also during rain events the retrieval of backscattered signals is poor. Besides, information

²The Sodar equipment has been provided by the Laboratoire de Physico-Chimie de l'Atmosphère, Université du Littoral Côte d'Opale, Dunkerque, France.

is obtained only between 100 and 500 m. However only strong Mistral events could come close to the Sodar wind speed limitation, and as our main interest are dry periods during weak wind situations, the Sodar operational limitations were not problematic.

2.3.2 Intensive observational periods

An intensive observational period (IOP) consisted in tethered balloon soundings and releases of radiosondes. The target period to carry out an IOP was between half January and March. On a daily basis, forecasts for stability occurrence were made for the days ahead based on the actual synoptic situation. An IOP was planned when clear skies and weak synoptic forcing were expected, but were actually executed when the wind was weak enough for tethered balloon operation (i.e. $U < 12 \text{ m s}^{-1}$ and low turbulence), making these periods inherently related to weak wind conditions. Altogether, 23 IOPs were carried out between 15 January and 2 March 2013, listed in Table 2.2. When triggered, an IOP started at 12:00 UTC and lasted for 24 hours.

2.3.2.1 Tethered balloon

Tethered balloon soundings were achieved around sunset and sunrise, to capture at least the daytime to nighttime and nighttime to daytime boundary layer transitions. When conditions were favorable, i.e. weak winds and weak turbulence, measurements were realised, and in the last week of the campaign, full-night measurements were obtained³. The goal was to profile the evolution of the boundary layer up to 300 meter. The tethered balloon was equipped with up to three Vaisala probes on the line, vertically spaced 50 m apart (Fig. 2.4a). Each probe measures temperature, relative humidity, wind speed and direction and pressure. Ideally, a ground level probe was set nearby in the field to capture continuously the atmospheric pressure, as that is needed to obtain the correct height for probes in flight (Fig. 2.4b).

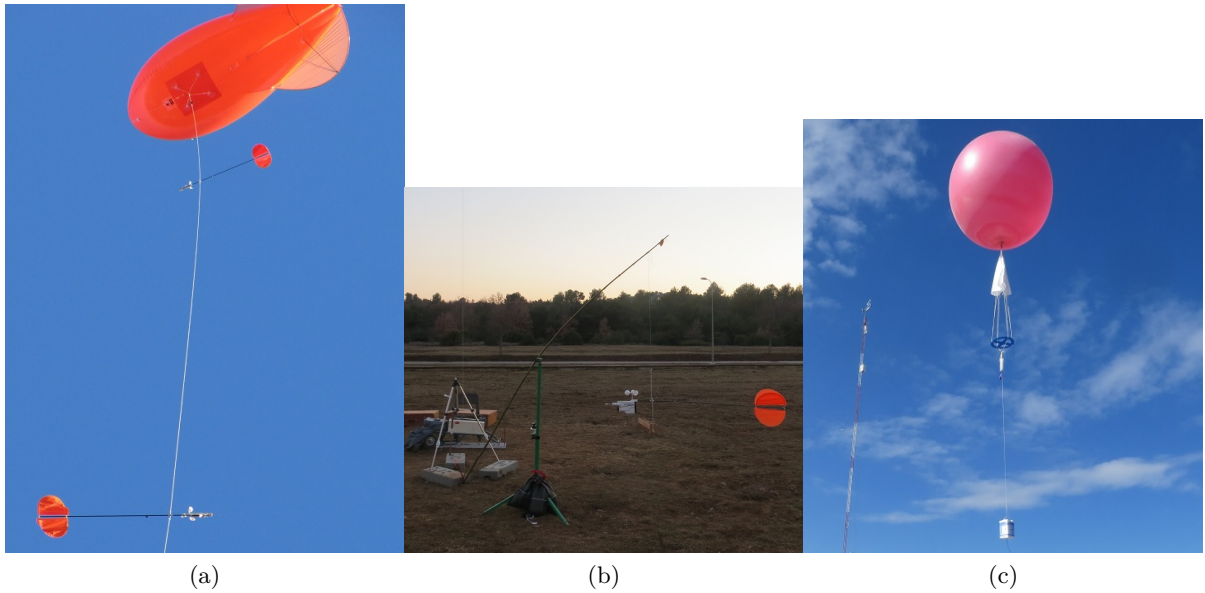


Figure 2.4: Illustration of the intensive observations. (a) the tethered balloon and two tethersondes; (b) the ground level probe and; (c) a radio-sounding just after launch.

Figure 2.5 shows an example of a TB-session with several consecutive scans having one ground level probe and three probes in flight. The acquisition system worked on a frequency of 1 Hz. In the ideal set-up, 3 to 4 probes are connected to the acquisition system. A set-up of 4 probes results in observations for each probe every four seconds. To obtain a profile of sufficient

³Unfortunately, due to administrative constraints working on-site during the other weeks was only allowed until 23:00 and from 04:00 local time.

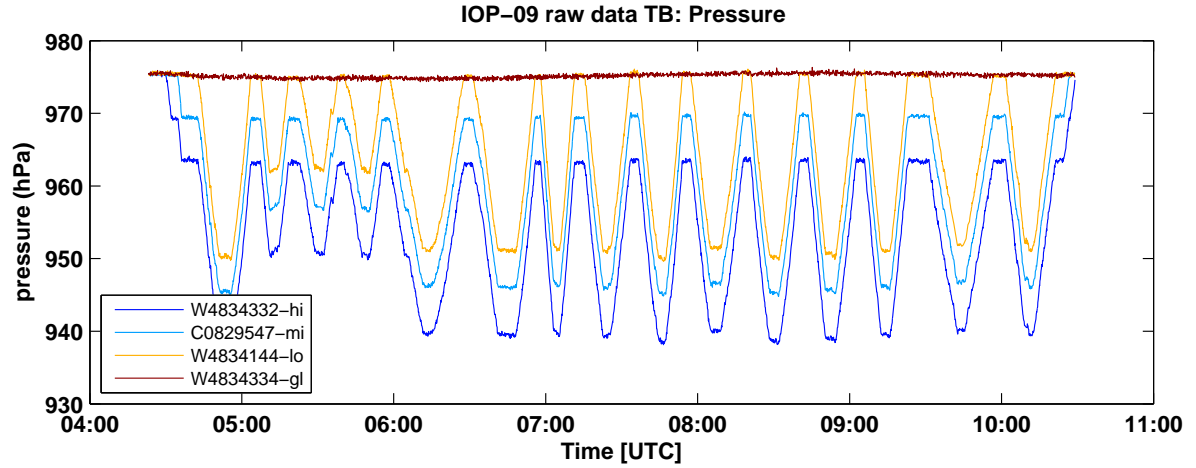


Figure 2.5: Example of scans made during an IOP. Each line represents a tethersonde pressure measurement where *hi*, *mi*, *lo* and *gl* stand for higher, middle, lower and ground level probe, respectively. The numbers correspond to the sonde ID-nr.

vertical resolution, the ascend and descend speed was restricted to around 30 cm s^{-1} . Doing so, it takes around 15 minutes to obtain a full scanned profile of 300 m. After every ascent or descent, a plateau level was maintained. After three minutes, the profiling procedure continued with either an ascent or descent. The numbers of profiles completed during each IOP are shown in Table 2.2.

Table 2.2: Summary of KASCADE IOPs. IOPs start at 12:00 UTC and last 24 hours. Full-night measurements were made on IOPs 19-23. The number of radiosondes (RS) launches and tethered balloon (TB) profiles (either ascent or descent) are indicated.

IOP nr	start date	# RS	# TB-profiles
1	14/01/2013	2	6
2	21/01/2013	2	-
3	22/01/2013	2	6
4	23/01/2013	2	42
5	24/01/2013	3	50
6	28/01/2013	2	20
7	29/01/2013	3	54
8	30/01/2013	2	16
9	07/02/2013	2	30
10	08/02/2013	1	10
11	11/02/2013	2	20
12	12/02/2013	3	36
13	13/02/2013	3	34
14	14/02/2013	3	42
15	18/02/2013	3	42
16	19/02/2013	3	38
17	20/02/2013	2	48
18	21/02/2013	3	30
19	25/02/2013	3	52
20	26/02/2013	4	46
21	27/02/2013	4	66
22	28/02/2013	4	46
23	01/03/2013	3	26
Total		61	760

2.3.2.2 Radio-soundings

To probe the troposphere above 500 m, radiosondes were launched close to M30 for each IOP (Fig. 2.4c). The radiosondes were of the recovery type, reaching an average altitude of around 5 km. Therefore they do not drift too far from the launch site, and so they could be recovered. Normally, the RS releases were at 12:00, 18:00 and 06:00 UTC and during the campaign's last week when full-night measurements were deployed, the RSs were also launched at 00:00 UTC. The list of radiosonde releases can be found in Table 2.2.

2.4 Data post-processing

Before phenomenological analysis can start several processing tasks need to be made, including sensor calibration, corrections, validations and specific data treatments. Sensors are inter-compared for relative inconsistencies by means of an inter-comparison campaign. The strategy on this campaign and the procedures for sensor corrections are explained in Appendix C and summarized in Sect. 2.4.2. Specific data treatment includes height correction of the tether sondes (Sect. 2.4.3), validation of Sodar observations against other available measurements (Sect. 2.4.4) and fast response raw data treatment, turbulent fluxes calculation and refinements of longwave radiation measurements obtained at M30 (Sect. 2.4.5).

2.4.1 Evaluation method

For the evaluation of the difference between two measurement sensors o and m , or between observations and model output, several statistical parameters are used:

$$MBE = \frac{\sum_i (m_i - o_i)}{n} \quad (2.1)$$

$$MAE = \frac{\sum_i |m_i - o_i|}{n} \quad (2.2)$$

$$RMSE = \left(\frac{\sum_i (m_i - o_i)^2}{n} \right)^{0.5} \quad (2.3)$$

$$\sigma_o = \left(\frac{\sum_i (o_i - \bar{o})^2}{n} \right)^{0.5} \quad (2.4)$$

$$\sigma_{diff} = \left(\frac{\sum_i (m_i - o_i - MBE)^2}{n} \right)^{0.5} \quad (2.5)$$

MBE stands for mean bias error and MAE for mean absolute error. These statistical measures can be used to evaluate the discrepancy on for example temperature, humidity, pressure and wind speed and direction. The standard deviation σ is a measure for the scatter of one population, either o or m . We introduce an additional quality index called the directional accuracy $DACC$ (Santos-Alamillos et al., 2013), which is appropriate for angle evaluation, in our case DDV wind

direction. The method is based on the circular difference $\Delta\Theta$ between two observed direction angles α and β (Jammalamadaka and Sengupta, 2001):

$$\Delta\Theta(\alpha, \beta) = |\min[\alpha - \beta, 360^\circ - (\alpha - \beta)]| \quad (2.6)$$

\min represents an operator, giving the minimum value. Then we define the *DACC* that accounts for the percentage of times in which Θ is lower than a chosen threshold (30°):

$$DACC = \frac{\sum_{1(if 0^\circ \leq \Delta\Theta_i \leq 30^\circ)} 0(else)}{n} \cdot 100\% \quad (2.7)$$

The *DACC* gives an indication on the agreement between the sensors without restrictions on wind direction. For an evaluation dedicated to a specific direction, in our case DDV wind direction, we slightly adapt Eq. 2.7 by defining a dedicated *DACC_{DDV}*, in this case between 10° and 50° :

$$DACC_{DDV} = \frac{\sum_{1(if 10^\circ \leq \alpha_i \& \beta_i \leq 50^\circ)} 0(else)}{\sum_{1(if 10^\circ \leq \beta_i \leq 50^\circ)} 0(else)} \cdot 100\% \quad (2.8)$$

Equations 2.1 to 2.8 give a framework to evaluate discrepancies either between sensors, or quality between model output and observations.

2.4.2 Sensor corrections summary

Shortly after KASCADE inter-comparisons on the sensors have been conducted. The full methodology and results can be found in the Technical Report KASCADE 2013 Instruments Calibration Campaign (Appendix C). A summary of the most prominent results is given in this section:

- Two complementary inter-comparison (IC) experiments have been conducted: at Centre de Recherche Atmosphérique (Lannemezan) from late April to early June 2013 and at Laboratoire d'Aérodynamique (Toulouse) in June 2013. The tethersondes are calibrated by using both inter-comparison and KASCADE datasets.
- A resolution issue for the net radiometer CNR1 has been identified. 10-minute averaging is sufficient to suppress the sampling resolution issue.
- The longwave components of the net radiometer CNR4 have been checked for inconsistencies on the calibration coefficients k supplied by the manufacturer. For this check, a CG4-pyrgeometer, kindly supplied by CNRM, was used as a reference since it had been recently calibrated. The provided k 's were found correct, hence the CNR4 could be used as a reference for relative calibration against the net radiometer CNR1.
 - Relative calibration of CNR1 for longwave radiation has been done in two steps: a correction for k and a body temperature (T_{body}) correction. These lead to stepwise improvements for mean differences from -4.53 (no correction applied) to -3.22 (k -corrected) to 0.03 W m^{-2} (both k - and T_{body} -corrected) for the calibration of the downward facing sensor. Upward facing sensor: -4.17 to -2.80 to -0.07 W m^{-2} .
 - After relative correction, uncertainties for the radiation difference between two levels and longwave heating rate are estimated at 0.93 W m^{-2} and $0.15^\circ\text{C h}^{-1}$ respectively. Considering separately incoming and outgoing longwave radiation, these quantities can be calculated at 1.36 and 0.69 W m^{-2} and 0.21 and $0.11^\circ\text{C h}^{-1}$ respectively. These uncertainties do not include a bias estimation. Bias sources on the uncertainty for radiation divergence include artificial objects like the tower itself, the surrounding buildings and roads. These contributions are further explored in Sect. 2.4.5.2.

- Shortwave radiation for CNR1 has been calibrated against CNR4 for both incoming and outgoing components. Both are estimated by a 2nd order polynomial fit (Eqs. 11 and 12 in the Technical Report).
- Using the inter-comparison dataset from the IC-campaign in Lannemezan, the two thermohygrometers, installed at M30, have been calibrated relatively against their average for relative humidity only (Eqs. 17 to 19 in the Technical Report), for temperature no correction was needed.
- The tethersonde probes were corrected using the KASCADE dataset in an innovative way. All probes were corrected for relative humidity and pressure. For relative humidity a relative correction was applied in two steps. Firstly, probe 402 was corrected against the thermohygrometer at 2 m at M30 during neutral conditions determined by M30 observations. Probe 402 was used throughout the campaign as a ground level probe and provided the dataset for correction (Eq. 20 in the Technical Report). Before and after each IOP, all tethersondes were installed side by side on a bench for intercomparison (Fig. 2 in Technical Report). Each bench inter-comparison lasted at least 3 minutes. At the end of the campaign, this data was used to calibrate the tethersondes against probe 402 (Table 14 in the Technical Report). No correction was necessary for temperature after it followed the same procedure. As no absolute reference existed for pressure measurement, the various probes were adjusted on their average (Table 15 in the Technical Report). For wind speed, no correction was necessary. As the full KASCADE dataset has been used for the tethersonde probe inter-comparisons, the range of values of the variables was representative of the KASCADE campaign.

2.4.3 Tethered balloon: Height correction and measurement uncertainties

A proper data treatment for the Vaisala tethersondes is important as the tethered balloon data will serve as a validation tool for the Sodar (Sect. 2.4.4.1) but also as an analysis tool. This section explains the data treatment for the tethersonde profiles once the measurements of all the sensors have been corrected. In particular, the methodology for profiles separation, height correction due to atmospheric pressure evolution, and averaging procedure for noise removal are discussed. A final short analysis on measurement uncertainties is also made.

2.4.3.1 Height correction procedure

The Vaisala acquisition system computes directly the height for all tethersondes using a constant pressure reference. For this, the very first pressure value measured by the first connected sonde when the software is started is used. As atmospheric pressure evolves in a time lapse of several hours (e.g. red line in Fig. 2.5), the height given by the acquisition system drifts along with this evolution. To correct this, we use the pressure of a ground level probe, which was ideally installed every IOP at a height of around 1.5 m (Fig. 2.4b). When no ground level probe was available, a ground level signal for pressure and temperature was deducted from the lowest sonde. The correction method assumes the equation of state (Eq. 1.1) and the hydrostatic equilibrium:

$$\frac{dp}{dz} = -\rho |g| \quad (2.9)$$

where z is the height in m agl. By combining Eqs. 1.1 and 2.9, neglecting the moisture contribution, we come to an approximated hypsometric equation (Stull, 2000):

$$(z_2 - z_1) = \frac{R_d}{|g|} \cdot \bar{T} \cdot \ln \left(\frac{p_1}{p_2} \right) \quad (2.10)$$

The overbar for T signifies an average temperature between the heights z_1 and z_2 , p_1 and p_2 are the corresponding pressure values at these heights. We can rearrange Eq. 2.10 to serve directly our purpose:

$$z_s = \frac{R_d}{|g|} \cdot \frac{T_s + T_{gl}}{2} \cdot \ln\left(\frac{p_{gl}}{p_s}\right) + z_{gl} \quad (2.11)$$

here s stands for the sonde in flight and gl for the sonde at ground level ($z_{gl} = 1.5$ m).

Due to technical problems of some of the tethersondes and to weather conditions, the order and the number of tethersondes on the tethered balloon line was modified at each IOP, see Appendix A in the Technical Report.

Uncertainty for pressure Before height correction, one should take into account the measurement uncertainty on pressure of Vaisala tethersondes. A random noise is present of around 1.5 hPa (see Appendix C-3 in the Technical Report). However, Fig. 2.6 shows the erratic behavior of pressure measured by the ground level probe during a part of IOP 9. Here a maximum uncertainty of 0.75 hPa is estimated, an equivalent of 6 meters in height. This maximum uncertainty applies to all tethersondes. Consequently, an explicit minimum threshold for vertical resolution of 6 m should be applied to the TB-profiles. For the ground level probe however, a moving average is used which provides a safe reference.

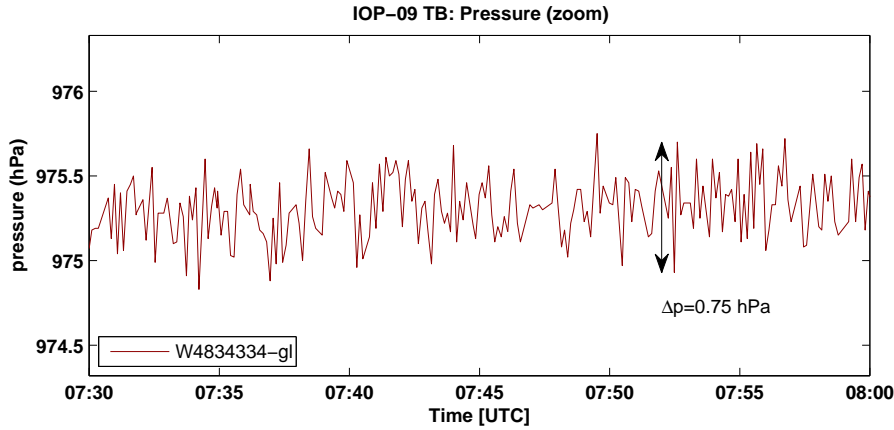


Figure 2.6: Estimation of the maximum uncertainty for pressure values measured by the ground level probe.

Estimated ground level pressure and temperature Ideally, IOPs were conducted with a ground level probe. Unfortunately, several IOPs have been conducted without this sensor; in these cases we lack the evolution of temperature and pressure needed for correction (see Eq. 2.11). Consequently, an estimated value for ground level pressure and temperature is defined, based on the linear interpolation between the periods of time when the lower probe is brought to the ground level (~ 2 m). As there is some random noise in the temperature and pressure values, a smoothed average of three values is used. See Fig. 2.7b for an example of pressure interpolation (the blue line indicates the linearly interpolated signal of the estimated ground level pressure).

The height correction Figure 2.8 shows measurements in meters agl for the lower tether-sonde before and after height corrections for IOP5. It is clear that along this IOP, due to the evolving pressure the original raw height leads to errors of more than 20 m. The corrected values however stay around their aimed height at the 'Down Plateau' state throughout the IOP. Finally, from the figure it becomes clear that idealized profiles were hard to construct. Throughout this IOP, scan heights and tethersonde staggering varied, which makes generalization for all IOPs difficult.

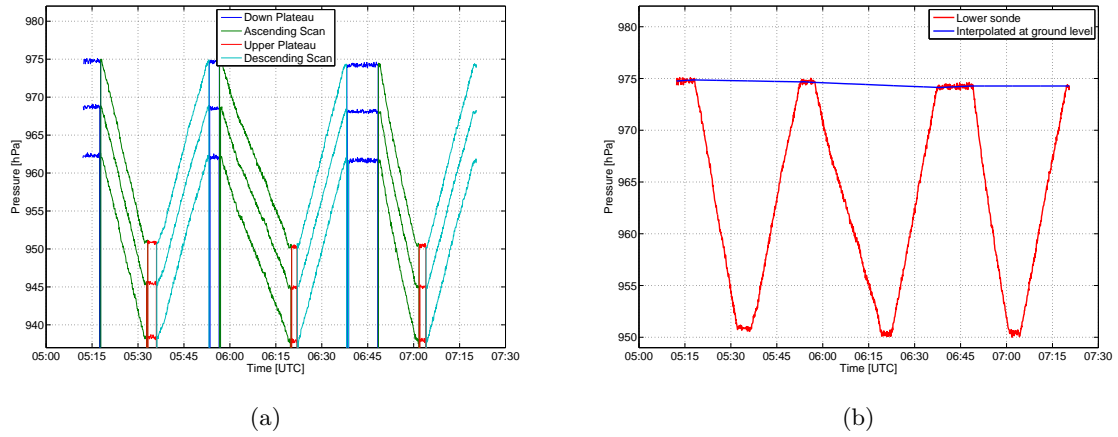


Figure 2.7: a: Scan separation into 4 different states for 3 sondes in flight. b: Pressure measured by the lowest flying tethered sonde and the interpolated signal for pressure during IOP1 (no ground probe available).

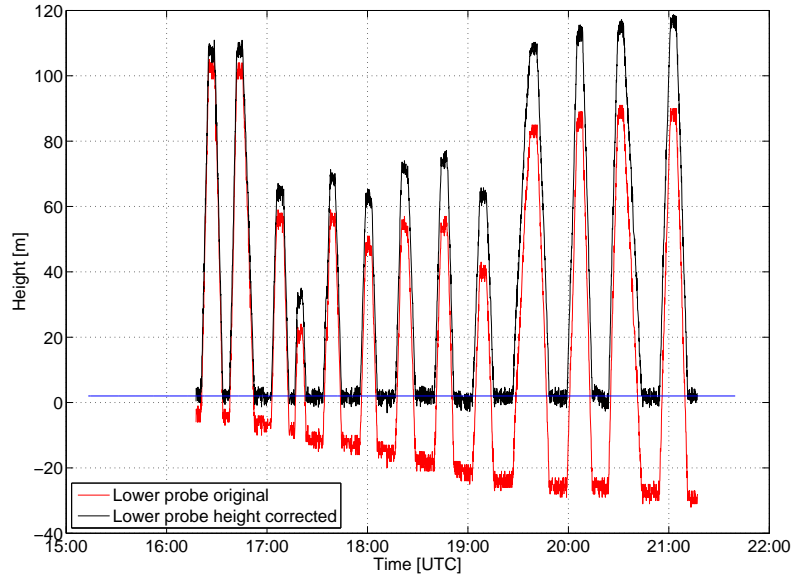


Figure 2.8: Example of corrected and non-corrected tethered sonde heights showing the characteristics of 15 TB flights of IOP 5. As reference, a blue line is drawn at 2 m, this is the ideal height during 'Down Plateau' for the lower tethered sonde. Note that during the session three sondes were attached, but for clarity only one is shown.

2.4.3.2 Scan separation

The tethered balloon profiling strategy has been explained in Sect. 2.3.2.1. The profiling procedure led to a total 760 scans, in ascending and descending motion. To obtain final profiles ready to analyse, these scans should be identified in the whole data set and separated. To fulfill an automatic separation procedure, four different 'states' are defined during a tethered balloon session (see Fig. 2.7a):

- 1) a lower level station called "Down Plateau" where the sondes are at starting height (i.e. 2 m, 52 m, 102 m),
- 2) an ascending scan called "Ascending Scan",

- 3) an upper level station called "Upper Plateau" where the three sondes are at their highest (i.e. 200 m, 250 m and 300 m),
- 4) a descending scan called "Descending Scan".

Each of these states can be distinguished by the pressure change Δp in time:

$$\Delta p(t) = p(t + \Delta t) - p(t) \quad (2.12)$$

where p is measured by each sonde at time t . Δt stands for each next incremental time the pressure signal is sent to the acquisition systyem. As stated before, the noise on pressure is quite high, therefore a moving average is needed to obtain a proper evolution for Δp . After several empirical tests, an optimal combination of a moving average of 19 values with threshold values Δp for finding a scan state as defined in Table 2.3 have been defined to make proper scan separations. For 4 attached sondes, this corresponds to a time interval of around 80 seconds and so we do not pass the 3-minute time lapse in between two scans. Note that the moving average for pressure is used for the cutting procedure only and does not influence the original pressure values. Nevertheless, three problems should be kept in mind when applying the procedure, some of them can be distinguished from Fig. 2.5:

- 1) Every IOP has different tethered balloon operators, leading to ascent and descent speeds being person-dependent, even if all targeted the 'ideal' 30 cm s^{-1} . In Fig. 2.5 this is represented by the different angles of the ascending and descending scans. It also leads to different values of $\Delta p(t)$.
- 2) Some scans were stopped in mid-ascent/descent and restarted after some time due to gusty periods or winch problems. Here the signal can be erroneously assigned to a plateau state. As the reasons for a stop are multiple, it is impossible to automatize fully.
- 3) Very turbulent conditions lead to a bigger uncertainty in pressure values due to balloon oscillations. Therefore scan samples can be erroneously recognized as upwards or downwards. As the desired conditions of KASCADE are mostly non-turbulent, the problem is rare, but nevertheless occurs.

To avoid erroneous state allocation, whether a full scan has been assigned correctly is checked visually. If not assigned correctly, the scans are re-assigned manually. Figure 2.7a shows an example of a finished scan separation applied directly to measured data. Each IOP is processed accordingly and balloon trajectories separated in a number n of scans and plateaus.

Table 2.3: Definition for a scan state, Δp is introduced in Eq. 2.12.

State	Smoothed $\Delta p[hPa]$
Down Plateau	< 0
Ascending	< -5
Upper Plateau	≥ 0
Descending	> 5

2.4.3.3 Uncertainty of other variables

After height correction and scan separation, separate profiles can be obtained. However, uncertainties are still measured when the sondes are in flight, i.e. sensor uncertainty and measurement variability. Sensor uncertainties are generally provided by the manufacturer. For temperature and relative humidity these are reported at 0.5°C and 5% , respectively. For wind speed and

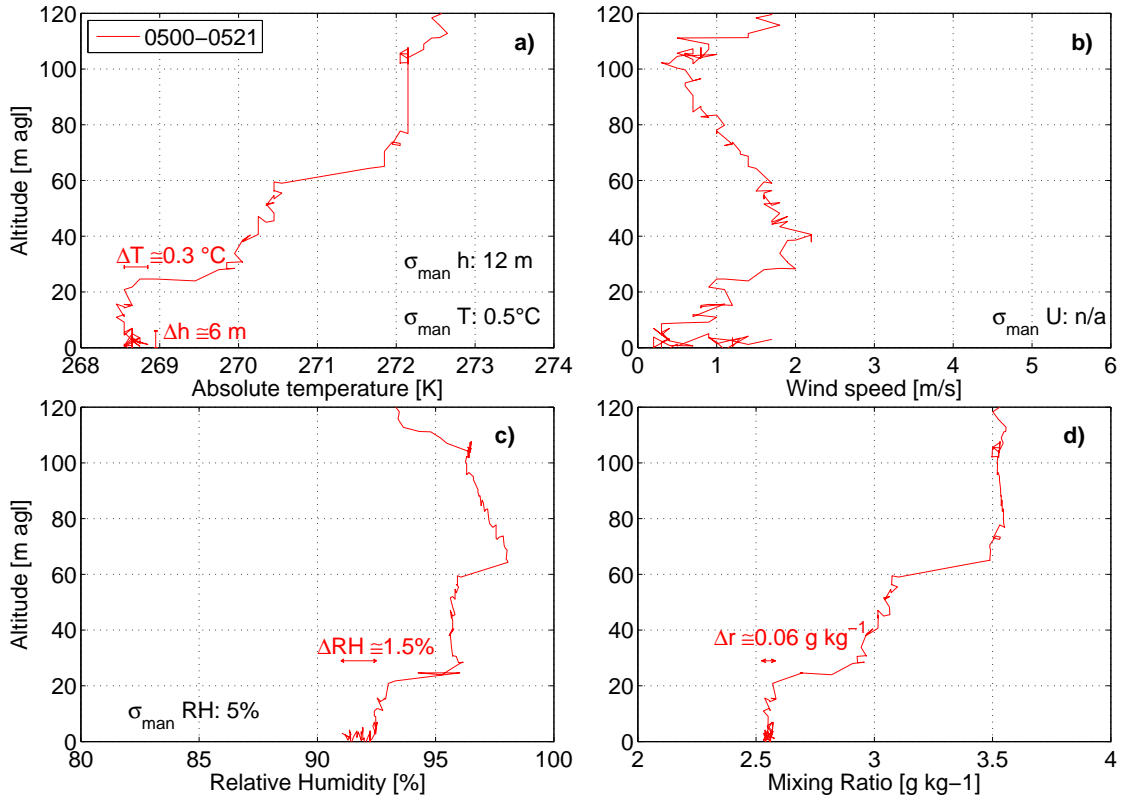


Figure 2.9: Zoom of a tethersonde profile with uncertainty estimations Δ for temperature (T), height (h), wind speed (U), relative humidity (RH) and humidity mixing ratio (r). The profile was a combination of a scan and its preceding ‘Down Plateau’ during IOP 15, the legend in the top left diagram indicates the time lapse for the profile (in UTC). σ_{man} indicates the uncertainty given by manufacturer.

direction, no indications of uncertainty are given, only measurement resolutions of 0.1 m s^{-1} and 1° respectively. Figure 2.9 shows an example of the lower part of a tethered balloon profile for temperature, wind speed, relative humidity and mixing ratio after inter-calibration and height corrections. On purpose an ascending motion and its preceding plateau are shown, which gives a qualitative insight in the uncertainties after height correction, when sondes are in flight. Note that only measurements of the lowest tethersonde are shown. Several remarks can be made:

Height: The uncertainty in height is created mainly by measurement uncertainty on pressure. For confirmation of the estimated uncertainty on height ($0.75 \text{ hPa} \simeq 6 \text{ m}$, see Sect. 2.4.3.1), we can check a consecutive plateau and ascent of a profile (Fig 2.9a). The lower part of the profile shown represents a plateau of around three minutes at 2 m height, and includes erratic behavior of height. The Δh drawn reflects the maximum uncertainty measured during this plateau. It confirms the estimated uncertainty, as Δh for the lower sonde plateau is 6 m. Checks for the other middle and upper tethersonde for the same profile (i.e. 52 and 102 m height) showed uncertainties of 7 and 5 m respectively. This confirms that the average of 6 m should be used.

Temperature: The uncertainty for a sonde in flight as given by the manufacturer is 0.5°C . However, uncertainty on temperature is strongly dependent on the local state of the atmosphere. We try to give an estimate of the lower tethersonde measurement variability by taking only its down plateau (Fig. 2.9a). From measurements, the estimation of the uncertainty is around 0.3°C .

Wind speed: An estimation of wind speed uncertainty is complicated, mainly in low wind speed conditions (Fig. 2.9b). We therefore show it as an illustration only. During the down

plateau for example, which lasted for three minutes, the wind speed was varying between 0.2 and 1.6 m s⁻¹.

Relative Humidity: RH is a directly measured value from the TSs and is quite consistent in terms of uncertainty during the down plateau, 1.5%. The manufacturer gives a sensor variability of 5%.

Mixing Ratio: r is an estimated variable from T , p and RH , so this value includes all uncertainties. We detect the same profile as for T and a relative small uncertainty for the lower probe.

Keeping the uncertainties for variables of the tethered balloon sondes in mind, we continue our study with the Sodar validation.

2.4.4 Sodar: validation

The Sodar has been installed at VER (Fig. 2.1) on the 21st November 2012. It was at the same location for one full year to obtain a seasonal pattern of the wind profile. After this period it has been moved to the M30 site where it operated also for more than one year. Finally, to make a comparison with the GBA tower, it has been moved to this location from the 18th of February 2015 up to now. See Table 2.4 for the exact locations and the period of observations at each location. The principle of Sodar measurements is based on remote sensing. For later analysis, it is important to test the reliability of these observations. In this section we validate the Sodar against tethered balloon and GBA tower. So we use the data observed during the IOPs of KASCADE and during the intercomparison set-up with GBA.

Table 2.4: Sodar availability on the several locations

<i>Location</i>	<i>Coordinates</i>	<i>Elevation (m asl)</i>	<i>Period</i>
VER	43.70744 5.76514	295	21/11/2012 - 06/01/2014
M30	43.68546 5.76171	287	06/01/2014 - 18/02/2015
GBA	43.69526 5.74329	265	18/02/2015 - ...

2.4.4.1 Sodar vs. tethered balloon

After the corrections for the tethered balloon observations in Sects. 2.4.2 and 2.4.3, we can use this database to validate the Sodar observations. To this purpose, the tethered balloon profiles have been averaged to obtain a vertical resolution similar to that of the Sodar (25 m). the tethered balloon was installed close to the M30 location *inside* the CV, whereas the Sodar was located at VER, *outside* the CV. The horizontal distance between the both sites is approximately 2.5 km (Fig. 2.1). The CV sidewalls are around 100 m higher than the valley's bottom, so the Sodar observations cannot be validated below this height by means of tethered balloon profiles. Besides, the reliability of the Sodar observations below 100 m is questionable. All tethered balloon profiles obtained during KASCADE are used to evaluate the Sodar observations to a height of at least 300 m. Some tethered balloon profiles have been made up to 400 m, but such profiles are too scarce to draw direct conclusions.

The statistics parameters used for evaluation have been introduced in Sect. 2.4.1. We use the tethered balloon profiles as a reference (i.e. o in Eqs. 2.1 to 2.8). Only winds with a speed faster than 1 m s⁻¹ are retained.

Table 2.5 shows the results for wind speed for all available heights. The heights of interest are indicated between the dashed lines, for these the errors are lowest. Below 125 m, the difference

Table 2.5: Evaluation of the wind speed of Sodar (SOD) against all 760 Tethered Balloon (TB) profiles as obtained during 22 IOPs. n denotes the number of observations available for validation. A minimum threshold of 1 m s^{-1} for wind speed is taken. Details on the calculations for statistical variables given are explained in the text. The dashed lines mark the lower and upper heights of interest.

Height [m]	n -	Mean Sodar [m s^{-1}]	Mean TB [m s^{-1}]	MBE [m s^{-1}]	MAE [m s^{-1}]	$RMSE$ [m s^{-1}]	σ_{diff} [m s^{-1}]	σ_{SOD} [m s^{-1}]	σ_{TB} [m s^{-1}]
25	447	2.84	1.84	1.01	1.27	1.66	0.07	1.29	0.75
50	394	3.28	2.17	1.11	1.47	1.82	0.09	1.53	1.09
75	397	3.58	2.51	1.07	1.34	1.70	0.11	1.65	1.34
100	482	3.75	3.05	0.71	1.11	1.46	0.10	1.71	1.54
125	616	3.72	3.16	0.55	1.14	1.48	0.10	1.71	1.66
150	672	3.99	3.68	0.31	1.07	1.37	0.09	1.71	1.65
175	617	4.35	4.22	0.12	0.92	1.21	0.10	1.72	1.74
200	608	4.59	4.53	0.06	0.91	1.15	0.11	1.84	1.96
225	406	4.56	4.50	0.06	0.96	1.23	0.13	1.82	2.01
250	373	4.61	4.63	-0.02	1.00	1.27	0.13	1.72	1.93
275	364	4.59	4.69	-0.10	0.97	1.26	0.14	1.75	1.93
300	320	4.51	4.54	-0.03	0.91	1.20	0.15	1.76	1.96
325	55	4.39	4.44	-0.05	0.79	1.10	0.33	1.60	1.86
350	18	4.97	4.99	-0.02	1.15	1.61	0.69	1.72	2.39
375	9	4.12	4.32	-0.20	0.85	1.21	0.81	1.80	1.62
400	7	4.53	4.17	0.37	0.55	0.59	0.91	1.68	1.72

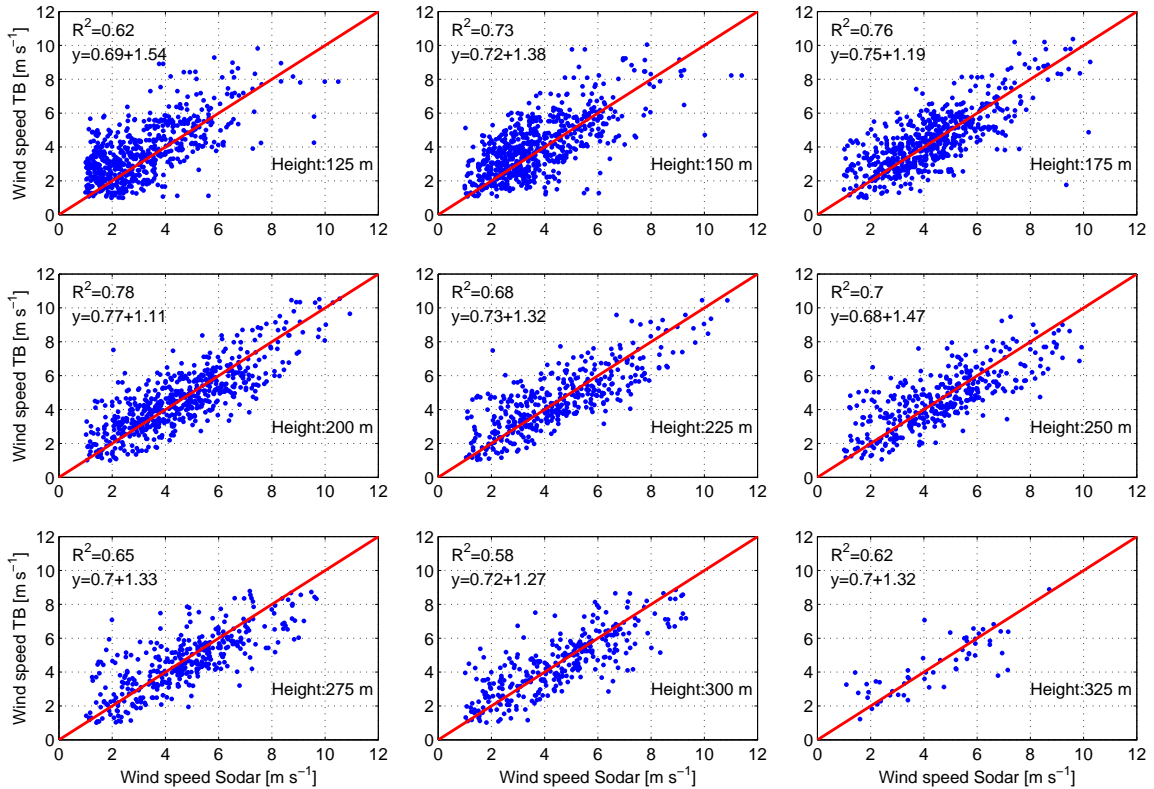


Figure 2.10: Wind speed scatter plots and regression coefficients between Sodar and tethered balloon (TB) for given heights.

in measurement location strongly influences the comparison. Besides, this Sodar does not give trustworthy measurements below 100 m. Above 300 m, the number of values available is not high enough for a valuable statistical comparison. We show all heights as reference, but we will

Table 2.6: Same as Table 2.5 but for wind direction

Height [m]	n	MBE deg	MAE deg	DACC %	DACC _{DDV} %
25	447	0.64	73.99	23.3	57.1
50	394	-6.08	57.69	32.0	100.0
75	397	1.51	38.78	46.9	69.2
100	482	-0.09	24.42	68.5	72.7
125	616	-0.74	18.69	78.7	81.3
150	672	0.86	16.63	84.7	88.0
175	617	0.34	15.45	85.9	89.7
200	608	-0.95	15.47	86.3	92.9
225	406	0.80	14.90	86.0	90.0
250	373	2.08	14.98	86.3	92.2
275	364	3.79	16.16	84.9	92.7
300	320	6.08	18.66	81.6	89.6
325	55	11.96	16.80	90.9	90.9
350	18	8.08	19.21	88.9	100.0
375	9	-10.88	21.07	66.7	100.0
400	7	-22.98	22.98	71.4	100.0

focus on the layers between 125 and 300 m.

Mean wind speeds are comparable, however, standard deviations are high. The scatter for relevant heights in Fig. 2.10 shows that this is a rather high random noise. However, the noise for tethered balloon is systematically higher than for Sodar (σ_{TB} vs. σ_{SOD}). This can be explained by the smoothing character of Sodar profiles. Highest scores for R^2 are in the layers between 150 and 275 m. Biases are low. A slight over- and underestimation for the Sodar can be noted below and above 250 m, respectively, but this is of negligible value.

For wind direction, the same conclusions as for wind speed can be drawn, see Table 2.6 and Fig. 2.11. Lowest errors and highest accuracies are found within 125 and 300 m. This is very convenient, as the DDV wind is largely constricted within this range, as will be seen later on in Chap. 4. As expected, below 125 m and above 300 m, the errors are much larger than within the range of interest. This is also reflected in the $DACC$ and the $DACC_{DDV}$, the latter being relevant for the DV orientation, i.e. between 10° and 50° . Regarding the scatter plots it should be noted that at some directions, winds are deflected, e.g. westerly winds for the tethered balloon are in the northwestern range for the Sodar. This can be very well caused by local orographic effects. Outside the range of interest, most $DACC$ values are lower than 80%.

We have checked the Sodar data against the tethered balloon profiles for wind speed and direction, at least between 125 and 300 m. This range does not exclude the applicability of the Sodar-observations above it. Above 300 m we can use the data, but these could not be checked statistically. However, above 500 m the availability of observations becomes scarce. Altogether, we can rely on the Sodar measurements between 125 and 300 m.

2.4.4.2 Sodar vs. GBA

The Sodar has been installed at the GBA site from 18 February 2015 (Fig. 2.1b). Due to practical purposes, the Sodar could not be installed closer than 250 m horizontal distance. The installation close to the GBA tower gives an opportunity to cross check the validity of both devices. The time for intercomparison has been set from 19 February to 17 March 2015. The 110 m high GBA tower is situated at the lower end of the CV. For comparison, we use the Sodar at a level of 100 m. Contrary to the previous section, this is a valid height for comparison as both devices are practically at the same location.

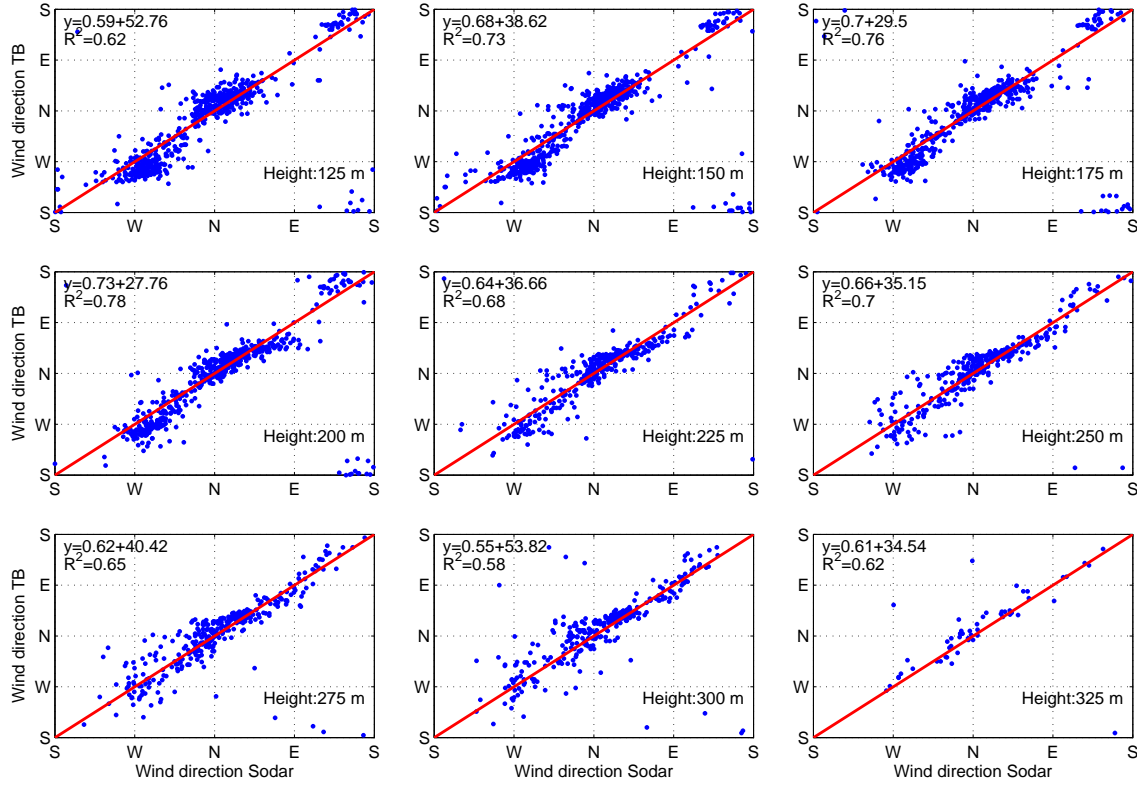


Figure 2.11: Wind direction scatter plots and regression coefficients between Sodar and tethered balloon (TB) for given heights.

The Sodar and GBA-tower have different measurement intervals (15 min vs. 10 min). For comparison, we select the closest value. Only winds with a speed higher than 1.0 m s^{-1} are retained. For GBA, there is missing data around the northern direction. This results from an averaging error in the acquisition system. For proper comparison, we then omit the northern winds (i.e. between 330° and 30°) from the Sodar data set and remove the corresponding GBA observations. For the selected period, wind roses are given in Fig. 2.12 and results are given in Table 2.7. The statistics do not show big differences between both devices. Winds with components other than North, are reliably measured. However, still some differences in wind direction are observed.

Table 2.7: Statistics for GBA and Sodar when they were at the same location between 19th February and 17th March 2015. The northern winds are excluded for proper statistical comparison (see text for explanation)

summary	wspd [m s^{-1}]	wdir [$^\circ$]
<i>BIAS</i>	0.11	6.56
<i>MAE</i>	0.73	14.29
<i>RMSE</i>	1.01	24.04
<i>DACC</i> ($< 30^\circ$)	-	89.96%

2.4.4.3 Summary

We can conclude that we can safely use the Sodar measurements for observational studies between 100 and 300 m. Below and above its validity could not be checked. However, there is no direct reason why the Sodar would give bad values above this range.

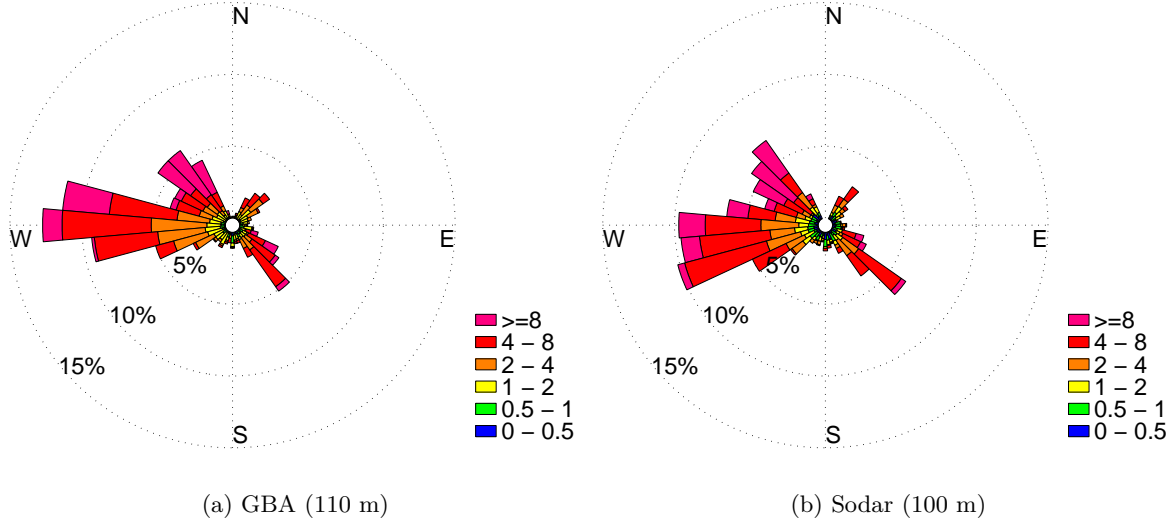


Figure 2.12: Wind roses for GBA and Sodar when they were at the same location between 19 February and 17 March 2015. The northern winds are excluded for proper comparison (see text for explanation).

2.4.5 M30

An ensemble of sensors were installed at different levels at M30 (Sect. 2.3.1.2). Here we explain shortly some additional treatments done to their data in order to obtain a high-quality dataset. Among them are flux data and radiation treatments.

2.4.5.1 Turbulent fluxes

Sonic raw data treatment During the campaign, it was noticed that the lower two sonic anemometers (both Young 81000) showed notorious spikes in the raw measurement signals (Fig. 2.13a). These problems did not occur for the upper sonic (CSAT). It was suspected that the spikes originated from serial writing in the data logger. In the raw data of sonic anemometers, it is very common to have short term spikes coming from several sources. However, the spikes observed lasted several seconds, and returned periodically, i.e. ~ 13 s. They showed up on every variable: u' , v' , w' , T'_s , influenced heavily their variances over longer time periods and so must be suppressed before further flux calculations. Therefore a de-spiking procedure has been developed⁴.

For the de-spiking procedure, it appeared that for each separate 30-minute sample, both the spike return period and the spike time length were variable. The period of spike return however, was detectable using an automated procedure. As the time length of the spike was highly variable, a sensitivity test was performed for several time lengths from 2 to 6 s. The final window size chosen for the de-spiking period was 5.0 s. There was no interpolation nor replacing procedure, so erroneous data was removed, and the chronological continuity of the time series is lost. Therefore no spectral analysis can be done on the lower two sonics. The method is rigorous, but necessary. Overall, around 40% of the raw data is instant data loss, but turbulent structures are maintained (Fig. 2.13b).

The CSAT did not have spikes, and so the influence of the de-spiking procedure on calculated fluxes has been checked by applying the same procedure. On the CSAT time series the same periods of time are removed as has been done for the Young time series. After calculation of the sensible and latent heat fluxes for both complete and shortened CSAT time series are compared,

⁴The procedure has been developed by people of Laboratoire d'Aérodynamique

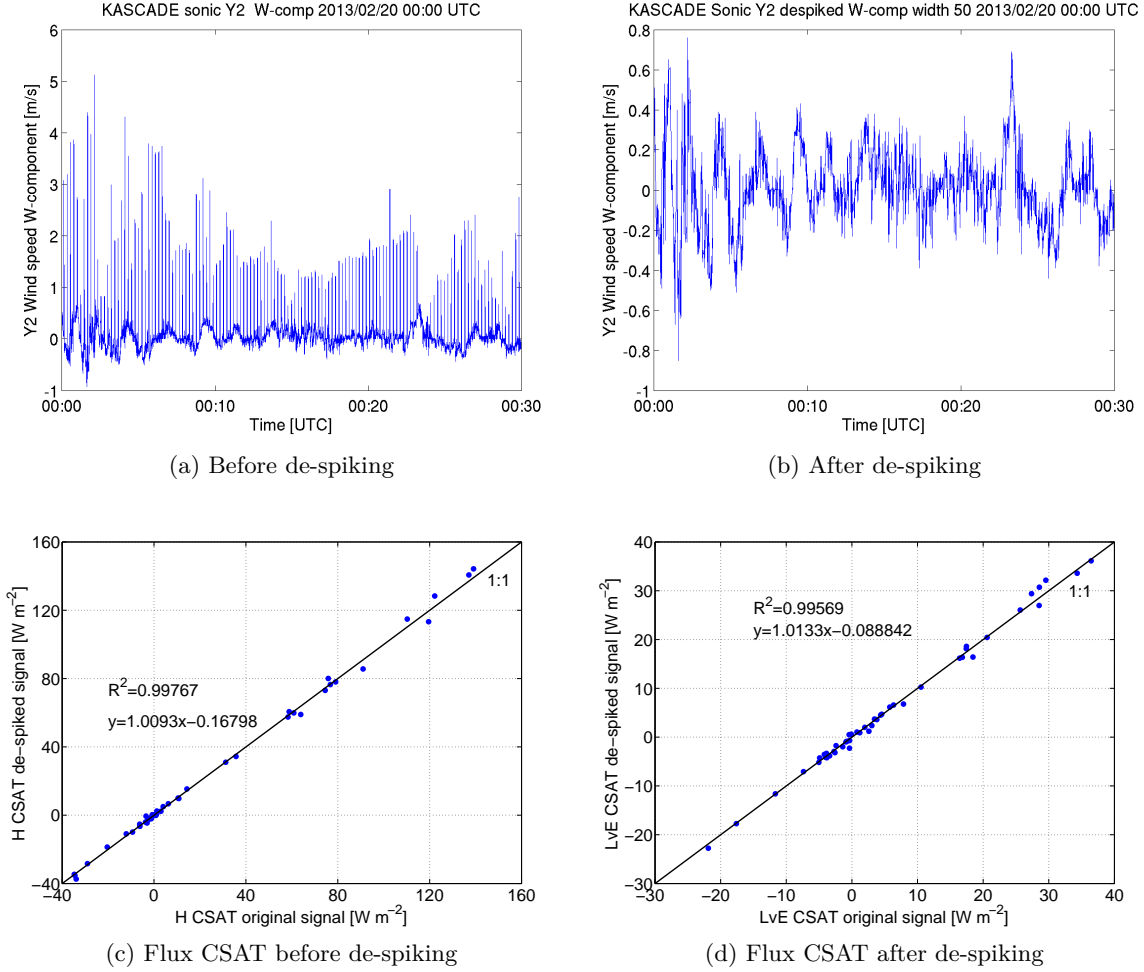


Figure 2.13: 30-minute samples of the W-component of Young 2 (Y2) at 10.50 m, before (a) and after (b) de-spiking the signal. The obtained sensible (c) and latent heat (d) fluxes for the CSAT (not affected by the spikes) when using the original and an artificial de-spiked signal, for 20 February 2013.

no big discrepancies are noted (Fig. 2.13c and d). The de-spiking procedure for the Young sonics has then been applied to the full-campaign data.

Flux package and calculations The three sonic anemometers were oriented to the southeast to better capture the down-valley wind. For flux calculations, the flux package EddyPro v4.2.0 from LI-COR has been used with a linear detrending, on a time scale of 30 min. A time lag compensation is applied by covariance maximization. A tilt correction in the sense of a planar fit has been applied for the CSAT. Available mast data are considered for turbulent and radiative flux calculations.

The validity of the calculated fluxes was checked for both initial and de-spiked signals during the inter-comparison (Sect. 2.4.2) with another eddy-covariance package (Baghi et al., 2012). No inexplicable deficiencies were found for the de-spiked signals.

2.4.5.2 Radiation - bias estimation

The tower was equipped with two net radiometers at different levels: a CNR4 at 20.11 m agl and a CNR1 at 1.18 m on a distant mast. The lower radiometer is installed away from the tower to reduce artificial, and so biased, influences on radiation measurements. We can use this set-up to estimate the radiation divergence, which is one of the crucial parameters for stable boundary layer formation. In the set-up, it is rather a finite difference approximation of the

divergence as it comes from a bulk for the 1.18 - 20.11 layer. Radiation divergence is difficult to estimate because of the large measurement uncertainties and the subtraction of quantities with the same magnitude. To reduce uncertainties, a calibration has been performed which resulted in a relative uncertainty (Sect. 2.4.2). Moreover, a bias estimation of the artificial objects is necessary⁵.

Sources of the biases origin in different footprints for both downward facing radiometers. For the downward facing radiometers, it comes mainly from interposed objects as seen by the higher (CNR4) but not the lower sensor (CNR1). As both see the grass, we assume that the bias on ΔLW^\uparrow comes mainly from the presence of roads and a concrete canal in the vicinity of M30. Figure 2.14 shows the estimated footprint for the CNR4 at 20.11 m, following the approach of (Schmid et al., 1991) which obeys Lambert's cosine law by:

$$r = h_s \left(\frac{1}{F} - 1 \right)^{-0.5} \quad (2.13)$$

where r is the radius in m of a circular area contributing to the radiometer located at height h_s . F designates the view factor of the radiometer. For example, $F=50\%$ corresponds to the area which contributes for 50% to the signal of CNR4. For $F=50\%$, r equals h_s , for $F=80\%$, r equals $2h_s$ and for $F=90\%$, r equals $3h_s$.

In the defined footprint area we recognize three different objects that may affect the CNR4 radiometer (neglecting the trees):

- 1) Dirt and asphalt roads between the 80%- 90% circles.
- 2) Ditch and concrete slab path between 80%- and 90% circles.
- 3) The tower itself in the inner circle.

The first two types of objects are surface objects emitting towards the sky, and are estimated in a same manner. The tower influences the CNR4-measurements in a different way.

Influence of artificial surface objects on LW upwelling radiation For the middle circle in Fig. 2.14, which represents 80% - 50% $\simeq 30\%$ of the footprint, roads and the concrete path together have an influence of 1.04%. For the outer circle (90%), objects influence around 1.7% of the total footprint. Therefore, the total contribution of the roads α to the footprint of the radiometer CNR4 is $1.04\% + 1.68\% = 2.72\%$.

Influence of the tower The tower M30 itself is an artificial object which will lead to different longwave radiation measurements between CNR1 and CNR4. As the CNR4 is located just above the middle of the mast, both upper and lower sensor longwave radiation measurements will experience an artificial influence. Sun et al. (2003) provides the following formula, which is adapted for our purpose:

$$LW_{CNR4}^\uparrow = \frac{1}{4\pi} \langle 2 \cdot LW_t \cdot \phi_w [1 - \cos(2\phi_b)] + LW_g \{2\pi [(1 + \cos(2\phi_b)) + 4(\pi - \phi_w)]\} \rangle \quad (2.14)$$

ϕ_w being the horizontal angle relative to the mast width w and ϕ_b being the angle of the boom with respect to the tower foot (Fig. 2.15). To estimate the influence of the upper part of the tower on LW_{CNR4}^\uparrow the equation can be used by replacing ϕ_b by ϕ_t , the latter representing the angle of the boom with respect to the tower top.

By applying Eq. 2.14 on our set-up, we find a relative contribution of the tower of the form:

$$LW_{CNR4}^\uparrow = \gamma_t LW_t + \gamma_g LW_g \quad (2.15)$$

where γ_t signifies the relative contribution of the tower to the signal measured by CNR4, γ_g represents the contribution of the grass surface. The total contributions are listed in Table 2.8.

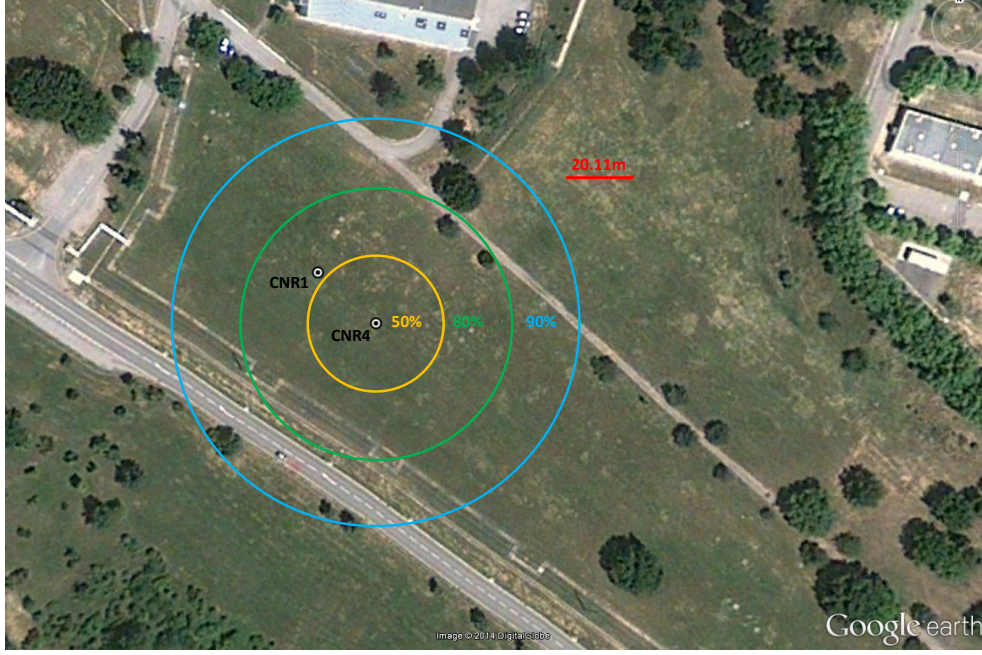


Figure 2.14: Estimation of the footprint for the CNR4. Also the location of CNR1 is shown.

Table 2.8: Relative contribution of the tower to longwave radiation measurement

Quantity	Tower contribution γ_t	Grass or sky contribution γ_g
LW_{CNR4}^{\uparrow}	2.70%	97.30%
LW_{CNR4}^{\downarrow}	2.59%	97.41%
LW_{CNR1}^{\uparrow}	negligible	negligible
LW_{CNR1}^{\downarrow}	negligible	negligible

We recall that this is a beginning framework for the radiation divergence calculations, which needs to be taken into account for its future estimations.

⁵However the results are not treated in this thesis, the work done is presented as it provides crucial information for future radiation divergence estimations

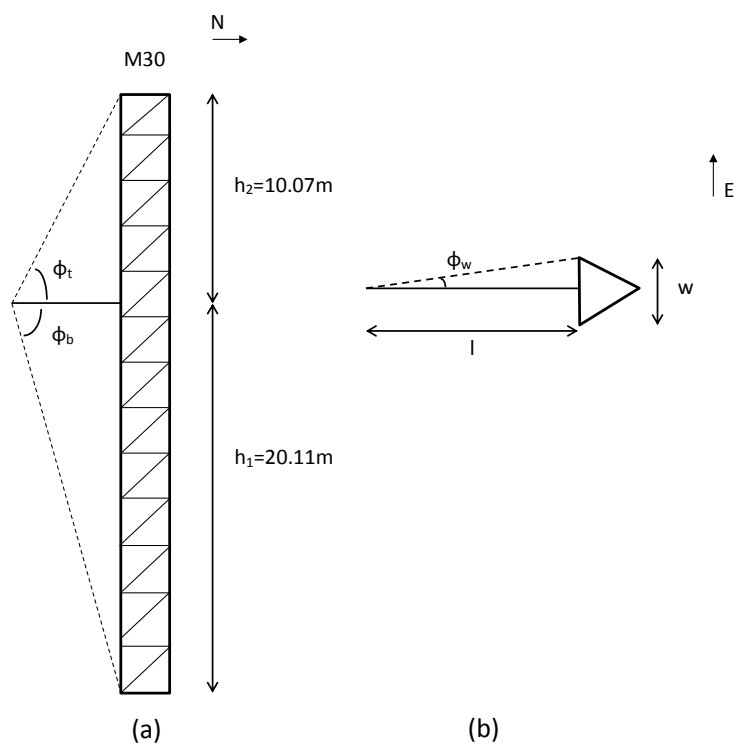


Figure 2.15: Schematic diagram of the tower dimensions and angles relative to the net radiometer when looking westward (a) and downward (b)

Chapter 3

Methodology: Mesoscale modeling with WRF

3.1 Introduction

The goal of the simulation part of the thesis is to set up a numerical model which is capable of simulating the DDV wind. Then, we could use the model simulations to investigate the DDV wind in its spatial characteristics and possibly its origin. In this chapter we elaborate on the methodology used to achieve this set of goals.

3.2 The WRF-model: basic set-up

3.2.1 Basic principles of WRF

We use the Weather Research & Forecasting (WRF) model. The WRF model is a fully compressible, non-hydrostatic numerical model used to simulate processes in the atmosphere from the global scales to local scale (Sect. 1.1.2). The governing equations included in the model are the perfect gas law, the Navier-Stokes equations, the conservation of scalars like turbulent kinetic energy, heat, water and aerosols (Pielke, 2013). Model variables are pressure, the three wind components, radiation, temperature and those related to water transport.

The governing equations are finite volume approximated in space (e.g. Fig. 3.1). The variables are discretized over a finite number of grid cells. In each grid cell, atmosphere processes are calculated separately during a time step. To maintain numerical stability, this time step is strongly linked to the grid cell size, making the full simulation time greatly dependent on the grid cell size. A mesoscale model like WRF is typically used with grid cell sizes bigger than 1 km in horizontal resolution. Subgrid scale processes are parameterized, which will be dealt with in Sect. 3.3.1.

To simulate atmospheric processes the full system should normally be taken into account, i.e. the full globe. However, the time scales of the processes studied are typically no longer than several days (see Fig. 1.2) and the horizontal scales involved at this time scale are typically around 1000 km, at maximum size. This makes it possible to focus on a certain region of interest by the use of nested domains, and to save computational time. In several steps, the processes are dynamically downscaled to the innermost domain, which is the region of interest. In our case, this domain is the middle section of the Durance Valley and its surroundings, see Fig. 3.2. The outermost domain is forced with variables from a global circulation model, for this we use re-analysis data of the European Centre of Medium-Range Weather Forecasts (ECMWF). These type of models are run on an operational basis but on a lower resolution, generally between 16 -

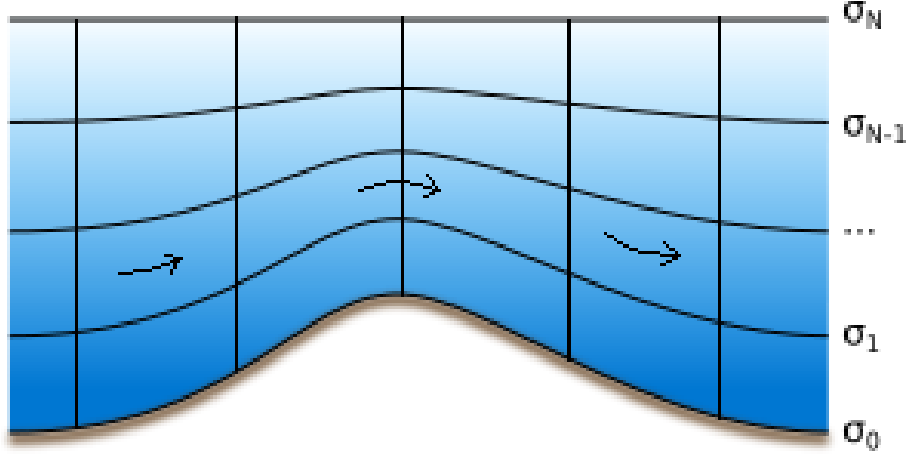


Figure 3.1: Representation of vertical (sigma co-ordinates) and horizontal resolution over complex terrain. Source: Wikipedia and adapted.

90 km. Numerous types of observational data are assimilated into the global circulation model, which gives the most up-to-date information on the synoptic scale. The global model provides the initial and boundary conditions to the WRF outer domain, and updates the boundary conditions regularly, in our case every 6 hours. The nested domains work in parallel, and are restricted to work on integer (preferably odd) parent ratio. Information exchange between the nested domains is possible in the form of one-way or two-way nesting. In one-way nesting this is strictly in the down-scaling direction. In two-way nesting there is bi-directional information exchange between parent and nested domains. The parent domain is then influenced by the calculations from its nested domain. We use two-way nesting in this study.

The vertical co-ordinate of the WRF-model is given by sigma-levels σ which are introduced to avoid numerical problems caused by orography (Fig. 3.1): they are terrain-following, and defined for each pressure level p with the pressure at the surface p_s and the pressure at the top of the atmosphere p_{top} :

$$\sigma = \frac{p - p_{top}}{p_s - p_{top}} \quad (3.1)$$

The bottom of the model is near the Earth's surface ($\sigma = 1$). The top of the model is set to very small pressure values ($\sigma = 0$). The use of the sigma-levels is one of the reasons why the WRF-model is very well adapted for winds initiated over slopes and in valleys. However, high horizontal resolutions are needed for small scale valleys, which can be typically out of reach. There are limitations in the use for sigma co-ordinates and finite different schemes regarding steep slopes and cliffs. The orography in our study area is dominated by low slope angles, so no problems are expected here. The vertical resolution in our case is detailed in Sect. 3.3.3.

3.2.2 The study area

The study area is fitted into four nested domains (Fig. 3.2). The outer domain has a resolution of 27 km, this corresponds to the resolution of the used re-analysis data. By dynamical downscaling with a parent ratio of 3, the inner domain has a horizontal resolution of 1 km. The domain sizes are chosen so that all important meteorological phenomena related to orographic features are captured. The outer grid covers the biggest part of the continent, including the Alps massif, the Pyrenees and a portion of the Mediterranean Sea and of the Atlantic Ocean. The second domain includes the western part of the Alps, the full Pyrenees and the Massif Central. With a horizontal resolution of 9 km it should be able to represent regional meteorological events such as the Mistral and the frequent low pressure area between Corsica and the continent, also known as the Genoa low. The third domain covers the Provence and should solve mesoscale

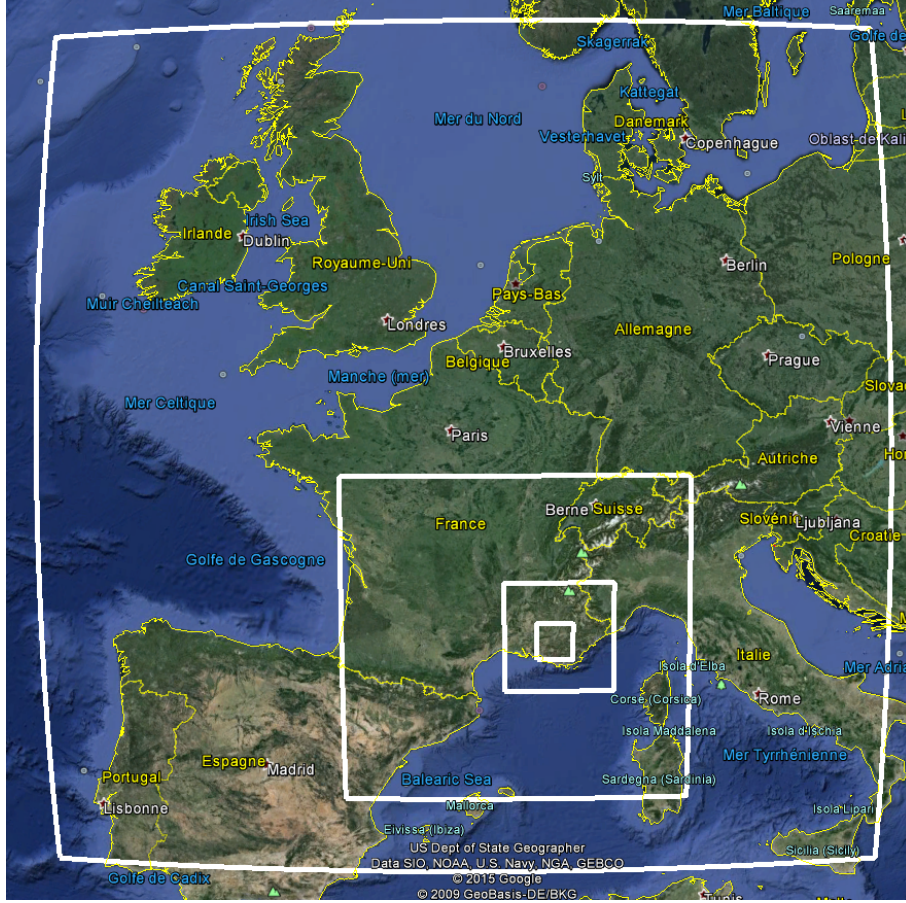


Figure 3.2: The four domains in WRF with the boundaries in white. Horizontal resolutions are 27, 9, 3 and 1 from the outer to the inner domain. Source: Google Earth

phenomena like sea breezes, redirected Mistral wind and anabatic events on slopes and in valleys resolved. Finally, the fourth domain represents the Durance valley area and includes the highest surrounding mountains like Luberon and St. Victoire, see Fig. 3.3a for their representation.

3.2.3 Orography

To cover the orography with the highest possible resolution, data from the Shuttle Radar Topography Mission (SRTM - Farr et al., 2007) is embedded in WRF¹. SRTM comprises a global database for terrain height with a horizontal resolution of 3" (equivalent to 90 m at the equator). Regarding the horizontal resolution used for the four domains in WRF, the orography is largely smoothed. This is a well-known issue in modelling over complex orography (Jiménez and Dudhia, 2012). However, the Durance Valley, 5 (bottom width) to 8 (ridge to ridge) km in width and 60 km in length, is reasonably represented in the inner domain (Fig. 3.3b and c). The valley depth is also captured to a good extent with a depth of 200 m in the model, see Fig. 3.5b. On the contrary, the smaller Cadarache Valley (1 - 2 km wide and 5 km long) is not fully resolved (Fig. 3.3d). To resolve the CV we would need to go to subkilometer horizontal resolution, which is computationally very expensive and reaches physical limitations of the model (Arnold et al., 2012). Similarly the small size of the Clue de Mirabeau (200 m wide and deep) results in misrepresentation at 1 km resolution. Other important orographic features influencing the region meteorology as the Luberon, Vautubiere and St. Victoire mountains are resolved.

Considering the scope of the thesis, performing simulations on subkilometer scale would have

¹Work done by Dr. T. Hedde

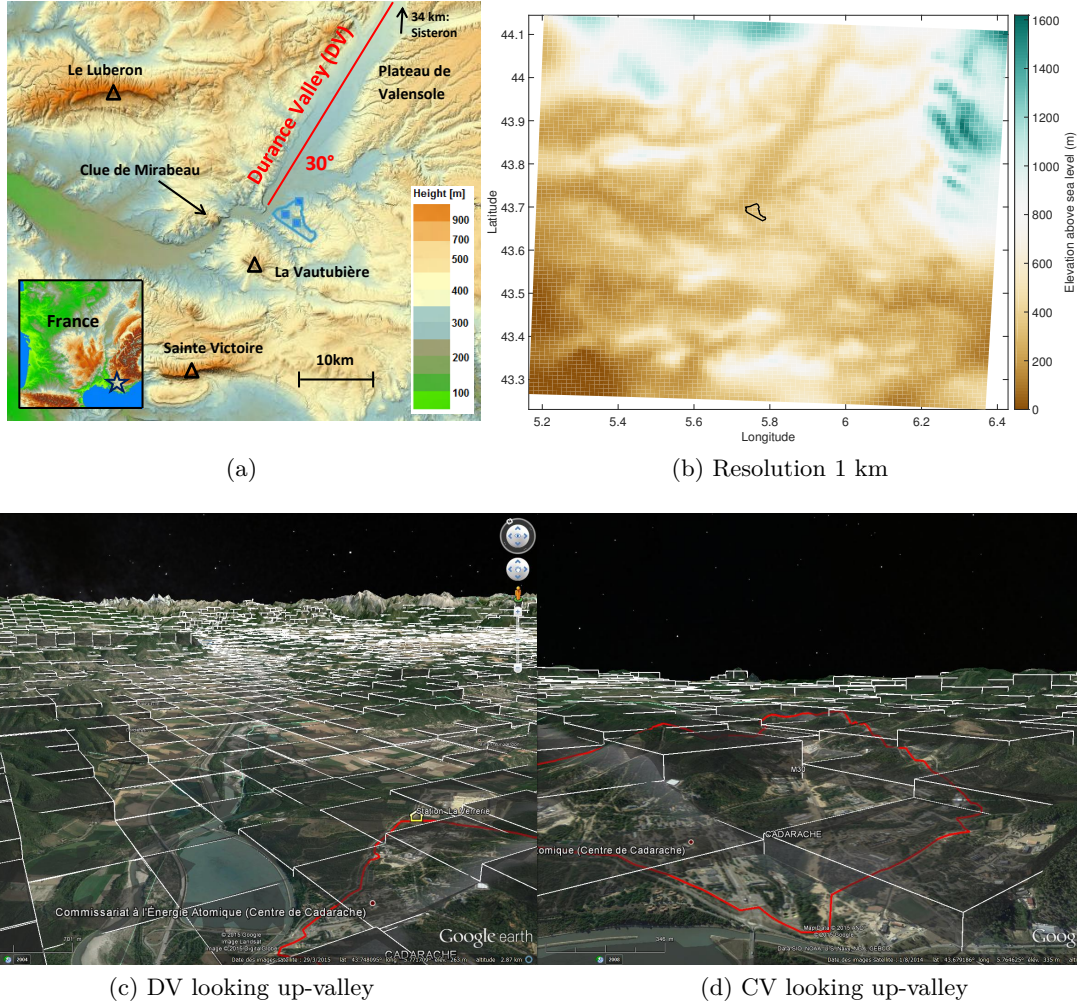


Figure 3.3: The orography of the study area. *a*: Original data (Source: IGN; Geoportail.gouv.fr). *b*: the inner 4th domain with a resolution of 1 km. For reference, the Cadarache site boundaries are given in (a) in blue and (b) in black. *c* and *d*: impression on different representation of the valleys at 1 km resolution (white blocks), Cadarache site boundaries are given in red.

been interesting. However, regarding the technical complexity of the simulations, this would have lead to 1 or 2 case studies only. In a first approach it was chosen to define an appropriate model configuration by simulating the IOPs of the campaign on 1 km resolution, and to evaluate the model performance to reproduce the major flow characteristics, but at the local scale.

Consequently, as both the regional orography and DV itself are well resolved, this domain set-up should be suitable to capture and investigate the DDV wind onset and development.

3.2.4 Land use

Key parameters in the model essential for energy and momentum partitioning at the surface, such as roughness length, albedo, soil moisture, emissivity and thermal inertia, are coming from land use (Pineda et al., 2004). On a 1 km resolution, an adequate representation of these land surface properties is a main issue, as for example the roughness length of surface terrain affects the intensity of turbulence properties (Sertel et al., 2010).

For our study, the land use of the Corine Land Cover 2006 (CLC) data (Büttner et al., 2007) is incorporated in the model². This database is more recent than the standard one incorporated

²Work done by Dr. T. Hedde

in WRF, the USGS (1992), and has a higher resolution (100 m versus 900 m). Figure 3.4a shows the variety of land use for the region of Cadarache as represented in the CLC database. The Cadarache area is a mix of buildings, roads, grass fields but is dominated by deciduous forest. The use of the CLC database better reflects the heterogeneity than the too homogeneous USGS-database. The improvement on the heterogeneity realism of the land surface obtained by implementing the CLC is shown in Figs. 3.4c (USGS) and 3.4d (CLC). Note that this is an example with a resolution of 667 m.

The use of a higher resolution land map considerably improves the representation of the land use with the 1 km grid (Santos-Alamillos et al., 2015). Improvements for wind, temperature and precipitation forecast on high resolution (1 km) simulation using the CLC have been obtained (De Meij et al., 2014). However, areas with high spatial variability do not necessarily show an improvement, as the interpolation after translation from the 100 m to 1 km grid does not necessarily give the best land use classification for the grid cell concerned. This further affects the wind speed and direction in such cells for these regions.

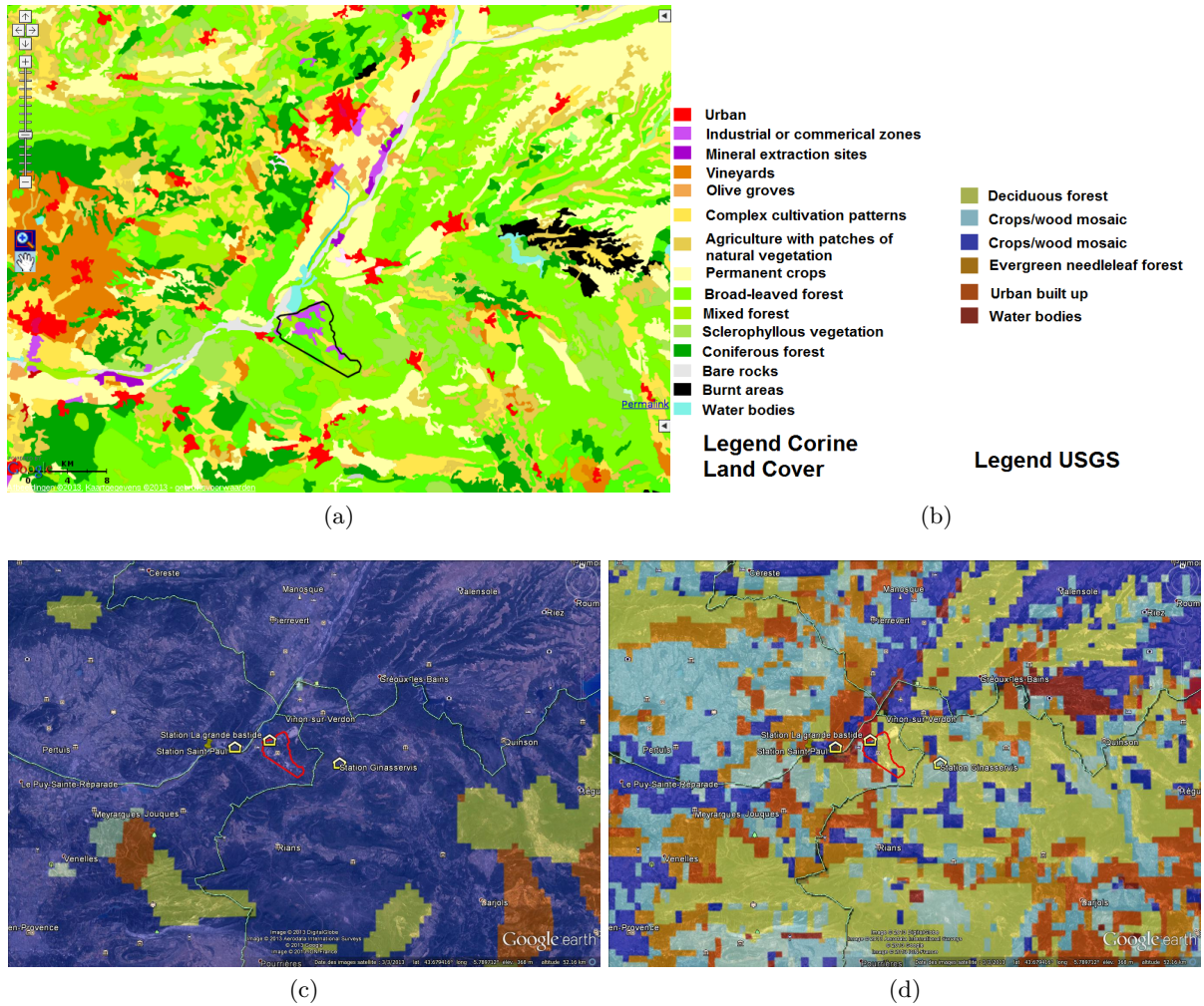


Figure 3.4: a: Land use of the region around Cadarache as given by CLC 2006 database; b: color codes used in the CLC and USGS land use; c: land use according to the USGS database with 667 m horizontal resolution (USGS color code); d: land use according to the CLC database with a 667 m horizontal resolution (USGS color code).

3.3 Configurations

In this section we describe the various set-ups of modelling parameters tested to improve the comparisons with observations.

3.3.1 Model sensitivity to subgrid-scale processes

The atmosphere is the scene where processes interact from the global scale to the micro-scale. Important processes to invoke at subgrid scale (i.e. <1 km in our case) are, among others, turbulence, convection, moisture transfer which need to be parameterized through optional schemes available in WRF. Some processes are always parameterized whatever is the resolution (e.g. radiation), and some schemes are turned off when resolution is high (e.g. cumulus). The choice of the schemes depends on the specific region under study and the dominating conditions. Therefore, to optimize a set-up, one needs to determine the most relevant schemes and to test the model for sensitivity. As a first step, two land surface and five planetary boundary layer (PBL) schemes were tested. We will briefly introduce these two groups of schemes and the processes involved. Part of this work is adapted from a Master thesis (Kalverla et al., 2015)³.

3.3.1.1 Sensitivity to land surface schemes

The land surface scheme plays a very important role in the partitioning of available energy. It computes sensible, latent and soil heat fluxes, as well as skin and soil temperatures. Surface characteristics like albedo, emissivity, soil moisture, roughness length, zero-plane displacement and conductivity are either read from climatological lookup tables or computed interactively. Most computed quantities have an improved estimation linked to the increasing complexity of the model. Two schemes of contrasting complexity are tested: the MM5 5-layer thermal diffusion (TD) scheme (Dudhia, 1996) and the unified NOAH land surface model (Tewari et al., 2004). TD is an elementary model which computes only temperature exchange between different soil layers. It does not include canopy, and soil moisture is read from a look-up table. The NOAH scheme is more advanced. It predicts soil moisture, includes canopy, root penetration depth, frozen soil, a layer of snow and surface runoff. It also includes soil freezing feedbacks. In the study area during winter situations, temperatures easily drop below 0°C and so the top layer of the soil freezes regularly. It is an important feedback to account for (Viterbo et al., 1999). The NOAH model should thus be closer to reality but this is at the cost of computational effort.

3.3.1.2 Sensitivity to planetary boundary layer schemes

The PBL scheme calculates the transport of heat, water vapor and momentum as an effect of turbulent mixing. The contribution of turbulence to the rate of change of any mean atmospheric variable C is expressed in a prognostic equation as:

$$\left(\frac{\partial C}{\partial t}\right)_{turb} = -\frac{\partial \overline{w'C'}}{\partial z} \quad (3.2)$$

where $\overline{w'C'}$ is the vertical turbulent transport flux which is computed as a correlation between the fluctuations of w and C . In observations, this quantity is derived by time averaging second moments of the fluctuations, typically averaged over 30 minutes. Mesoscale models cannot estimate the fluctuation terms, but only compute the mean flow and so the turbulent transport needs to be parameterized. However, turbulent scales of more than 1 km could exist in convective boundary layers, some turbulence may be resolved by the model. We are focused on stable situations, which have thin boundary layers and smaller size characteristic scales, therefore we assume that the turbulence contribution is completely parameterized.

Typically, the number of unknowns in the set of turbulent flow equations is larger than the number of equations (a variable is considered to be unknown when neither a prognostic nor a diagnostic equation defines it). To eliminate the unknown in the correlation of Eq. 3.2 requires to close the equation system by expressing the correlation term. Closure can be done in several

³Under supervision of G.J. Duine and G.J. Steeneveld (Wageningen University)

ways, either local or nonlocal. Nonlocal closure assumes that the unknown quantity at a given point is parameterized by values of known quantities at several points in space, whereas for local closure an unknown quantity at any point in space is parameterized by values or gradients of known quantities at the same point. Closure assumptions made to model turbulence are named after the highest order prognostic equations retained. In first-order closure, as in Eq. 3.2, the second moments are approximated (e.g. $\overline{w'C'}$). Second-order closure involves approximation terms on third moments (e.g. $\overline{u'v'C'}$). It is expected that the higher the order, the better the approximation becomes, but this adds complexity and computational expenses (Stull, 1988). In this study, we checked the sensitivity to nonlocal closure and local TKE-closure schemes.

For nonlocal closure, two schemes have been tested, YSU (Hong et al., 2006) and ACM2 (Pleim, 2007). These are first-order schemes, relating the turbulent flux term to the gradient of the considered variable (e.g. C):

$$\overline{w'C'} = -K_C \frac{\partial C}{\partial z} \quad (3.3)$$

where K_C is the eddy diffusivity coefficient for C . Based on the consideration that large eddies of the order of the boundary layer height account for an important part of the total transport, both schemes incorporate nonlocal mixing terms. In YSU this is done by adding a countergradient term. In ACM2 nonlocal fluxes are accounted for by transilient turbulence theory. Further details can be found in (Kalverla et al., 2015) and the references given for these schemes.

For TKE-closure, a local 1.5 order closure, three other schemes are considered, namely the MYJ (Janjic, 1994), MYNN2.5 (Nakanishi and Niino, 2006) and QNSE (Sukoriansky et al., 2005). In these schemes extra prognostic terms for mean turbulent kinetic energy and for mean variance of potential temperature and humidity are added. This leads to more unknowns, but also more information on mixing characteristics. For example, in the first order closure K_C is an empirically derived value, depending on the state of the atmosphere. In 1.5 order closure it is a function of the TKE, approximately represented by:

$$K_C = \lambda \bar{e}^{0.5} \quad (3.4)$$

where λ is a length-scale depending on the height above the surface and atmospheric stability. \bar{e} is the mean TKE. Definitions of λ differ between the different schemes, about which more details can be found in the given references.

There are large differences between the PBL schemes and each one has its strengths and weaknesses. Generally, nonlocal mixing schemes perform better in convective boundary layers (García-Díez et al., 2013), whereas the TKE schemes are often better in simulating stable boundary layers (Kleczeck et al., 2014). When flows are anisotropic, or when internal waves occur, which is often the case in stable boundary layers, the validity of the YSU, ACM2, MYJ and MYNN2.5 schemes are limited due to the fact that the physical reasoning on which K_C is based does not hold. The QNSE scheme is based on a spectral analysis to distinguish effects of internal waves and turbulence, and so is expected to give better results during stable conditions (Sukoriansky et al., 2005). However, large biases are obtained during daytime situations (Shin and Hong, 2011).

Processes in the surface layer, the lowest part of the boundary layer, are accounted for in surface layer schemes. These are generally based on the Monin-Obukhov similarity theory. The choice of surface layer schemes in WRF is tied to PBL scheme options as listed in Table 3.1.

3.3.1.3 Other sensitivity tests

With the NOAH + YSU set-up (run 1 in Table 3.1), a configuration commonly used in modelling studies, other sensitivity tests have been performed:

Table 3.1: The different combinations of land surface schemes and PBL schemes tested with their corresponding surface layer schemes. References for the schemes in the first two columns are given in the text.

Run #	Land surface scheme	PBL scheme	Surface layer scheme
Run 1	NOAH	YSU	MM5 (Beljaars, 1995)
Run 2	NOAH	MYJ	Eta (Janjic, 1994)
Run 3	NOAH	QNSE	QNSE (Sukoriansky et al., 2005)
Run 4	NOAH	MYNN2.5	MYNN (Nakanishi and Niino, 2006)
Run 5	NOAH	ACM2	Pleim-Xiu (Pleim, 2006)
Run 6	TD	YSU	MM5
Run 7	TD	MYJ	Eta
Run 8	TD	QNSE	QNSE
Run 9	TD	MYNN2.5	MYNN
Run 10	TD	ACM2	Pleim-Xiu

- The representation of soil moisture becomes more important when the model resolution increases (Chen and Dudhia, 2001; Angevine et al., 2014). The latent heat flux and soil heat conductivity influence the boundary-layer growth and mixed-layer temperature (Van Heerwaarden et al., 2009). Unfortunately, no observations of soil moisture are available in our case. However, to test its influence, the soil moisture content in the model is manually reduced by a factor of 2.
- It has been shown that the role of the land-atmosphere coupling is of major importance (Chen et al., 1997). To explore this role, an attempt was made to modify the land-surface coupling through the Zilitinkevitch empirical coefficient C_{zil} (Zilitinkevich, 1995) that relates the momentum roughness length z_0 to the roughness length for heat z_{0h} . The coefficient was set at its reported range limits, i.e. 0.01 (strong coupling, large z_{0h}) and 1 (weak coupling, small z_{0h}). More details on this approach can be found in Kalverla et al. (2015).
- Concerning atmospheric radiation, three combinations for shortwave and longwave schemes have been tested: 1) the Goddard shortwave (Chou and Suarez, 1994) and RRTM longwave (Mlawer et al., 1997); 2) CAM (Collins et al., 2004) shortwave and longwave; 3) RRTMG (Iacono et al., 2008) shortwave and longwave. These are compared with the 'Reference radiation' configuration (see below for its definition).
- To test the sensitivity to initial and boundary conditions the Global Forecast System (GFS) is used in one run. The horizontal resolution of GFS is 0.25° .

To parameterize microphysical processes the WSM 6-class Graupel scheme has been chosen (Hong and Lim, 2006). The Kain-Fritsch scheme (Kain, 2004) is chosen for cumulus parameterization for the outer domain only, so it is explicitly resolved in our model for the three inner domains. The 1 - 10 km resolution is a gray zone concerning the scales belonging to convective processes (Kain, 2004). No sensitivity tests on microphysics nor cumulus parameterizations are done. For radiation options, in all runs for shortwave radiation the Dudhia scheme is used (Dudhia, 1989) and for longwave radiation the RRTM scheme (Mlawer et al., 1997). In the radiation sensitivity test this combination is called 'Reference'.

Table 3.2 recapitulates the sensitivity tests proposed. To come out with an ideal configuration, we need to compare our sensitivity tests against a chosen IOP. Based on a nearly perfect radiation balance, IOP 16 was chosen. This IOP was carried out at between 19 February 12:00 UTC 2013 and 20 February 12:00 UTC 2013 and took place during calm synoptic forcing under weak southeasterly flow over the study area. We take 24 hours as spin-up time, and use the operational analysis input data of the ECMWF, having a horizontal resolution of 0.25° on 20 pressure levels. The horizontal resolution of the ECMWF matches the resolution of the outer domain. However, the grid type is not the same: ECMWF is a geographical latitude/longitude

projection whereas for WRF this is a Lambert projection. The vertical ECMWF data are also interpolated to the levels used in WRF.

Table 3.2: Model configuration used to test the model’s sensitivity. The IOP start and end times are indicated in Table 2.2

Model version	WRF v3.5.1
Start date simulation	18 February 2013 12:00 UTC
End date	20 February 2013 12:00 UTC
Spin-up time	24 hours
Time step	120 seconds
Domains configuration	4 domains
Parent-child ratio	1 : 3
Nesting	Two-way nesting
Grid size inner domain	1 x 1 km
Vertical (sigma) levels	35 levels
Land use	Corine land cover (2006) (Büttner et al., 2007)
Orography	SRTM (Farr et al., 2007)
Global data input	ECMWF re-analysis 0.25°
Microphysics	WSM 6-class Graupel
Longwave (LW) radiation	Varied with run 1 schemes fixed (Table 3.1)
Shortwave (SW) radiation	Varied with run 1 schemes fixed (Table 3.1)
Cumulus scheme	Kain-Fritsch for D01
Planetary boundary layer	Varied (with Dudhia (SW) & RRTM (LW))
Surface layer	Varied (with Dudhia (SW) & RRTM (LW))
(land) Surface scheme	Varied

3.3.2 Configuration 1: The optimized set-up

An optimized set-up should come out from the results obtained in the comparison with IOP 16 (Sect. 3.3.1). To investigate the DDV wind, its governing processes and its regional behavior, we need a DDV wind which has developped in the model. Therefore the next step is to simulate all IOPs in order to select those where a correctly simulated DDV wind has been obtained. This configuration can be used to simulate all 23 IOPs to test the model’s general capability to model the DDV wind. The simulations are started 24 hours (spin-up time) before the IOP starting time. Each IOP is simulated individually to avoid divergence effect that could happen if simulating the KASCADE observation period at once in only one run.

3.3.3 Configuration 2: Increase of vertical resolution

The model sensitivity runs in the first configuration used 35 logarithmically spaced vertical sigma-levels, with highest density near the surface. In this second configuration, we added 11 vertical layers. The aim is to increase the vertical resolution and see the effect on the DDV wind. This is done with the purpose to improve two aspects: firstly a higher resolution close to the surface should improve boundary-layer representation; secondly mixed layer properties (e.g. entrainment) are expected to be better represented when increasing the number of model levels around the boundary-layer height. Therefore we introduce 14 instead of 9 sigma-levels in the lowest 400 m. The increase of model layers at the surface will also increase the number of layers in the DV itself. Inside the DV, which is around 200 m deep, in configuration 2 there are 10 layers instead of 6 (see Fig. 3.5b). The maximum PBL heights observed during IOPs varied to a large extent, but were mostly in the range of 1000 to 1500 m. With the configuration 1 set-up, the thickness of the layers dramatically increases to 200 m above 1000 m agl. Therefore the increase of the number of sigma-levels is focused between 1000 and 2000 m height, with 9 layers instead of 4. The thickness of these 9 layers is now around 100 m. See Table 3.3 for a comparison between the first two configurations for the lower 30 sigma-levels (Eq. 3.1). To

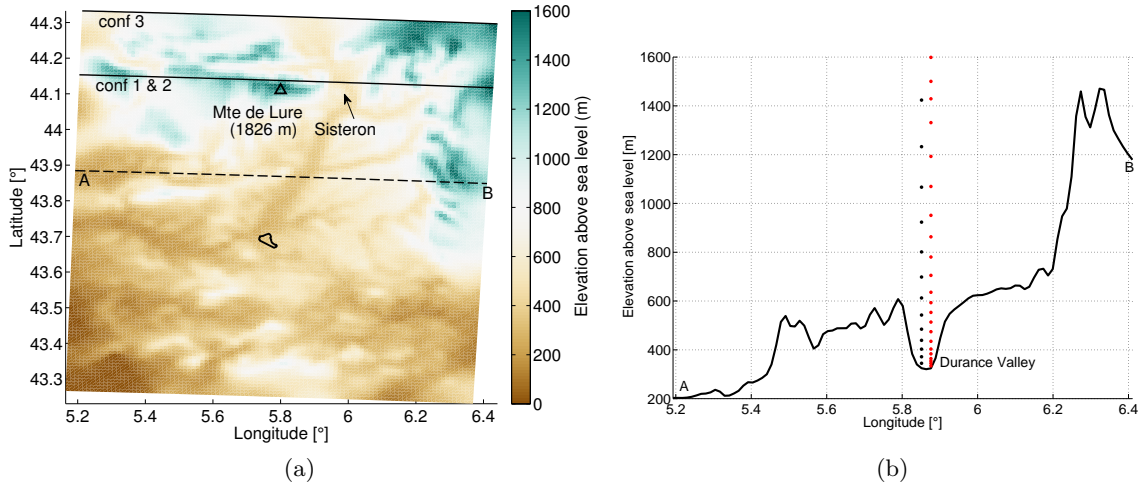


Figure 3.5: a: the innermost domain's northern borders for different configurations. b: a horizontal cross section of the ground altitude from the 1 km resolution grid, the horizontal dashed line from (a) shows its location. The dots show the heights of the sigma-levels in conf1 (black) and conf2 (red). The black line on (a) show the upper limit for innermost domain used with configurations 1 and 2.

maintain numerical stability (i.e. $(w_{max}\Delta t)/\Delta z < 1$), the time step is decreased from 120 to 90 s.

This configuration has been simulated for a selection of IOPs. The selection is based on the model's capability to model the DDV wind (see Chap. 6).

3.3.4 Configuration 3: Extension of the inner domain

In the first set of simulations from configuration 1, the choice of the innermost domain northern border is questionable, as the 'Montagne de Lure' is cut into half, see Fig. 3.5a. Also the 'Clue de Sisteron' is not fully incorporated. To investigate this as a source of influence, the inner domain of the third configuration is extended 21 km to the North to include the full mountain ridge and the 'Clue de Sisteron'. For vertical resolution, the sigma levels of the first configuration are taken. Doing so, a sensitivity study on the difference in simulated wind patterns is performed for the same selection of IOPs as for the second configuration.

Table 3.3: Sigma levels with their approximate corresponding model heights h (agl) and thickness of the layer immediately above each level for configurations (conf) 1 and 2.

level #	conf 1			conf 2		
	σ -level	h [m]	Thickness [m]	σ -level	h [m]	Thickness [m]
1	1.0000	0.0	-	1.0000	0.0	-
2	0.9974	20.6	21	0.9987	10.2	10
3	0.9940	47.6	27	0.9974	20.5	10
4	0.9900	79.6	32	0.9962	29.9	9
5	0.9854	116.4	37	0.9949	40.2	10
6	0.9796	162.9	47	0.9924	60.0	20
7	0.9723	221.8	59	0.9899	79.9	20
8	0.9635	292.9	71	0.9859	111.6	32
9	0.9528	380.0	87	0.9809	151.2	40
10	0.9401	484.3	104	0.9759	190.8	40
11	0.9252	608.4	124	0.9709	230.5	40
12	0.9079	754.8	146	0.9659	270.3	40
13	0.8882	924.6	170	0.9606	312.7	42
14	0.8659	1120.6	196	0.9520	381.9	69
15	0.8410	1344.3	224	0.9427	457.2	75
16	0.8133	1600.4	256	0.9326	539.6	82
17	0.7828	1891.7	291	0.9219	627.6	88
18	0.7494	2221.9	330	0.9077	745.6	118
19	0.7133	2592.5	371	0.8931	868.4	123
20	0.6742	3010.8	418	0.8769	1006.5	138
21	0.6323	3480.5	470	0.8656	1104.0	97
22	0.5876	4008.2	528	0.8574	1175.3	71
23	0.5406	4596.1	588	0.8462	1273.6	98
24	0.4915	5251.3	655	0.8351	1371.9	98
25	0.4409	5977.4	726	0.8235	1475.8	104
26	0.3895	6776.6	799	0.8113	1586.2	110
27	0.3379	7653.6	877	0.7958	1728.3	142
28	0.2871	8607.3	954	0.7756	1916.7	188
29	0.2378	9641.8	1035	0.7494	2166.8	250
30	0.1907	10762.3	1121	0.7133	2522.5	356

Chapter 4

Characterization of down-valley winds by observations

4.1 Abstract of the article

The main part of this section is constituted by a paper reproduced below¹. The first sections of this paper summarize the theoretical background, the geographical characteristics of the area investigated, and give an overview of the observation strategy, as has been detailed in Chap. 2 of the thesis. The result section starts with a characterization of the down-valley flows by means of the measurement campaign KASCADE. A general overview of dominant weather patterns is given, from which is concluded that DDV wind is a dominant wind, as compared to other regional phenomena like Mistral wind, afternoon westerly winds and southeasterly cloud (and precipitation) events. However, stable stratification is observed throughout the campaign, and leads to the direct onset of the CDV wind. This wind persists throughout the night, shows characteristic depths up to half the valley depth and jets around 30 m height for 2 - 3 m s⁻¹. The CDV ceases when stable stratification is eroded in the valley, firstly at the ground and just above it, before the stable core is diminished gradually. Generally, within 2 hours after sunrise stable stratification has overcome.

DDV wind acts on larger scales than CDV wind, and so sets in 6 - 9 hours after sunset. The high variability for the onset is probably explained by the demand of large scale stability, though this cannot be proven by the very local observations. However, the dominance of the DDV wind, during weak synoptic forcing periods, is mostly prominent around sunrise, when convectively driven winds are weakest. Its momentum forces the continuation of the flow up to 4.5 hours after sunrise (on average). Jets are found at 175 - 225 m agl with speed mostly found between 4 and 8 m s⁻¹. From then, the daily pattern is picked up again by generally observed westerly anabatic winds coming in.

The Southern Alps and a sloping plateau on the DV east bank as aspects of influence could not be determined nor excluded as governing processes for DV wind origin. In between the two valley winds, a shear layer is observed whose possible origin could be a combination of a valley return current and a DV wind stream re-directed by orography. The paper concludes with the synthesis of the diurnal wind cycle by means of a conceptual diagram.

In the conclusion of the paper, it is indicated that additional modeling studies are expected to better explain the governing processes of the DDV wind development. Such studies will be presented in Chap. 6.

4.2 Article

¹This chapter under revision:

Duine G., T. Hedde, P. Roubin, P. Durand, M. Lothon, F. Lohou, P. Augustin and M. Fourmentin (2015). Down-valley flows in stable stratification: Observations in complex terrain during the KASCADE field experiment, *Quarterly Journal of the Royal Meteorological Society*, under review.



Down-valley flows in stable stratification - Observations in complex terrain during the KASCADE field experiment

Gert-Jan Duine,^{a,b*} Thierry Hedde,^a Pierre Roubin,^a Pierre Durand,^b Marie Lothon,^b Fabienne Lohou,^b Patrick Augustin^c and Marc Fourmentin^c

^aLaboratoire de Modélisation des Transferts dans l'Environnement, CEA Cadarache, France

^bLaboratoire d'Aérodynamique, University of Toulouse, CNRS, Toulouse, France

^cLaboratoire de Physico-Chimie de l'Atmosphère, Université du Littoral Côte d'Opale, Dunkerque, France

*Correspondence to: T. Hedde, Laboratoire de Modélisation des Transferts dans l'Environnement, CEA Cadarache, 13108 St. Paul ls Durance cedex, France. E-mail: Thierry.Hedde@cea.fr

The field experiment KASCADE (KAtabatic winds and Stability over Cadarache for Dispersion of Effluents) has been conducted in South-Eastern France during the winter of 2013 and has revealed the dominant presence of nocturnal valley flows during stable conditions in two cross-oriented valleys with gentle slopes, the DV and its smaller side valley, the CV. Within the narrow (1 km width) and shallow (100 m depth) CV, which has an average slope angle of 1.2° along the valley axis (6 km length), a downslope drainage flow is instantly generated once nocturnal stability has formed. This katabatic wind is generally observed with maximum wind speeds of $2 - 3 \text{ m s}^{-1}$ at around 30 m height above ground level. It can reach depths of half the valley sidewalls height but is largely dependent on above-valley wind conditions. The wind persists throughout the night and remains typically 1.5 - 2 hours after sunrise. The wider (5 km) and deeper (200 m) DV presents a lower slope angle (0.2°) and a larger fetch ($> 50 \text{ km}$) in which the DV wind develops during stable conditions. This valley wind has been mostly observed with jets around 175 - 225 m above ground level and wind speeds of $4 - 8 \text{ m s}^{-1}$. It commonly sets with a time delay of 6 - 9 hours after sunset, this uncertainty can be related to the larger scales involved. The Southern Alps and a sloping plateau on the DV east bank as aspects of influence could not be determined nor excluded as governing processes for DV wind origin. In between the two valley winds, a shear layer is observed whose possible origin could be a combination of a valley return current and a DV wind stream re-directed by orography.

Key Words: Nocturnal valley flows; stable boundary layer; complex orographic region; field experiment KASCADE; katabatic winds

Received ...

1. Introduction

During the night when skies are clear and synoptic forcing is weak the Earth's surface is cooled by radiative heat loss and the air layer in contact with the ground becomes denser than the layer above: a stable boundary layer (SBL) forms (Stull 1988). As the night evolves, the cooling continues and a stably stratified layering extends upward. The different layers get decoupled due to the limited interaction between them (ReVelle 1993; Delage *et al.* 2002), leading to the onset of low level jets (LLJs) over flat terrain (Blackadar 1957). LLJ can also develop under baroclinic forcing over sloping terrain, in land and sea breezes, and with valley winds and inertial oscillations (Kraus *et al.* 1985). Although in general turbulence is reduced inside SBLs, elevated shear may occur in regions below a LLJ (Smedman 1988; Mahrt 1999) which often has peak winds at the top of SBL. The SBL can

be classified into the weakly stable, intermittent and very stable regimes (Mahrt 1998; van de Wiel 2003). The first two regimes are well described by similarity theory, but the third is not (Nieuwstadt 1984). The very stable boundary layer however remains poorly understood because of complex interactions between turbulence, radiative flux divergence (Brutsaert 1972), gravity waves (Nappo 2012; Largeron *et al.* 2013) and other submesoscale motions (Mahrt 2014). Among other campaigns, SBLs have been observed to a large extent during SABLES98 (Cuxart *et al.* 2000) and CASES99 (Poulos *et al.* 2002).

Over sloping terrain in stable conditions horizontal temperature gradients, initiated by radiative surface cooling, tend the air to flow downslope as a consequence of negative buoyancy (Manins and Sawford 1979; Mahrt 1982; Horst and Doran 1986; Haiden and Whiteman 2005). A thermally driven downslope or katabatic wind develops, although katabatic simply means going

downward, irrespective the cause. However, downslope winds also refers to winds that are forced over topography by large-scale pressure gradients (Durran 2002), e.g. the foehn winds and Bora winds (Croatia). The term has also been used for downslope winds at high latitudes for which wind speeds can go up to even 30 m s^{-1} (Bromwich 1989). Gentle slopes with angles as low as 1° can induce downslope flows (Mahrt and Larsen 1990; Skillingstad 2003). Many external factors for the flow speed and height have been proposed, including slope angle (Smith and Skillingstad 2005) and ridge-top wind speed and inversion depth (Horst and Doran 1986). Scale analysis shows that the large number of different flow types require different approaches and thus not one single universal solution applies (Mahrt 1982), as for example the flow depends greatly on the valley geometry (Atkinson 1995; Monti et al. 2002). Inside deep or shallow valley systems, drainage occurs and the converging cold air reaching the valley bottom often results in a weak lifting motion, creating return currents at approximately the valley height (Oke 1987). The colder air stagnates at the valley bottom and consequently a cold pool develops below a valley inversion (Clements et al. 2003). Thermally driven valley and slope flows were investigated extensively during the VTMX-campaign (Doran et al. 2002) while cold pooling is documented by the METCRAX (Whiteman et al. 2008) and COLPEX (Price et al. 2011) campaigns.

Valley flows can have multiple origins, some related to above-valley conditions. Consequently, Whiteman and Doran (1993) classified them into a fully independent thermally driven flow and three (quasi-) dependent flows: downward momentum transport, forced channeling and pressure driven channeling were proposed. Downward momentum transport plays a large role in unstable and neutral stratification in wider valleys (Whiteman and Doran 1993). Narrow valleys during unstable or neutral conditions experience the forced channeled flow (Weber and Kaufmann 1998) and pressure-driven channeling can be of importance in wide and shallow valleys under slightly to moderately stable conditions (Carrera et al. 2009).

For dispersion studies, characterizing the SBL is of extreme importance and especially in regions of orographic complexity, the SBL is recognized as one of the more serious atmospheric conditions for air quality (Zanetti 1990). In regions of orographic complexity, mountains and valleys modify the flow and thus strongly influence dispersion (Bowen et al. 2000; Triantafyllou and Kassomenos 2002; Salmond and McKendry 2005; Largeron 2010). Besides, modeling the SBL is a challenging, but necessary task for dispersion studies (Hanna and Yang 2001). However, governing processes are poorly understood and incompletely represented in physical parameterization schemes (Sterk et al. 2013). Over complex terrain the challenge is difficult (Arnold et al. 2012). Consequently, both for understanding and modeling purposes, observations are still needed over complex areas (García-Díez et al. 2013).

When contaminants are released in a complex area, there is a need to document both local and regional flows, especially for stable conditions where vertical dilution is very weak and modifies the horizontal transport and dispersion relative to convective conditions. Cadarache is a research centre of the "Commissariat à l'Energie Atomique et aux Energies Alternatives" (CEA), located in South-Eastern France (see Fig. 1) at the lower end of the middle Durance Valley (DV) (Warner 2006). The operation of several facilities there requires control of pollutant emission control and impact assessment. Clear skies and calm winds are regularly observed in the region (Wrathall 1985), which is very susceptible to SBL-development and development of local wind systems. Understanding the patterns of valley flows and cold pool build up in the smaller valleys confluent to the DV is thus a major issue for assessing the sanitary and environmental impact of Cadarache.

The KASCADE (KAtabatic winds and Stability over CADarache for Dispersion of Effluents) field measurement campaign was conducted in the winter of 2013 and was designed to characterize the local SBL and the associated thermally driven winds to feed future numerical simulations of pollutant dispersion for impact studies. Continuous observations were obtained from December 2012 to March 2013 including 23 intensive observational periods (IOPs) in January and February. More details on the campaign can be found in Sect. 2.

This paper focuses mainly on the first goal of the campaign: to understand and characterize the valley flow patterns that develop under stable conditions. Two valleys are under study; the large DV and its smaller side valley, the Cadarache Valley (CV). Their widths (5 vs. 1.5 km, respectively), depths (200 vs. 100 m), average slope angles (0.2° vs. 1.2°) and lengths (67 vs. 5 km) are distinctly different, making them behave differently under stratified conditions in terms of timing and flow characteristics. The winter season in 2013 was characterized as having strong diurnal patterns during weak synoptic forcing. Valley flows were dominant, and large differences were found in the timing of onset and duration, in the two valleys related to their respective geometries and sensitivity to large-scale stability. Typical jet depths and wind speeds were related to the valley depths and above valley wind conditions. The paper is organized as follows: First, a detailed description of the study area and the KASCADE-campaign are provided in Sect. 2. For general understanding, the observations of regional weather phenomena and stability are described in Sect. 3.1, whereas we focus on typical valley flow development during two different synoptic situations in Sect. 3.2. Then, the DV and CV flows are characterized in terms of timing (Sect. 3.3), and a phenomenology is given in Sect. 3.4. Finally, a summary of the work and future prospects related to the campaign are given in Sect. 4.

2. Experiment design

2.1. Site characteristics

The CV meets the larger DV at the "Clue de Mirabeau" (Fig. 1). The DV has been formed by the Durance river, a braided river flowing from the Southern Alps to the Rhône Valley. The valley is 5 km wide with an average depth of 200 m. This middle part of the valley between Sisteron and Clue de Mirabeau has a length of 67 km with a mean slope angle of 0.2° . The aspect ratio, defined as the ratio of the valley depth to the valley width, is 0.04. The along-valley direction is around 30° from the North, as indicated by the red line in Fig. 1a. The valley narrows from 5 km to 200 m at the Clue de Mirabeau, where the lower part of the DV starts. The CV is a side valley of the DV with an orientation of 135° from the North, almost perpendicular to the DV. The valley is 1 to 2 km wide, 5 km long, with a slope angle of 1.2° , a depth of ≈ 100 m and an aspect ratio of 0.05. The sidewalls have an average slope angle of around 6° . The land use in the CV is a mixture of broad-leaved and mixed forests, grasslands, artificial surfaces and buildings. Previous studies have been done in the DV, Kalthoff et al. (2005) showed the existence of an along valley oriented wind only in the early morning during the ESCOMPTE-campaign, which was focused on the land-sea breeze effect during summer (Cros et al. 2004; Mestayer et al. 2005). Quénot and Beltrando (2008) investigated the effect of spring frost on the DV-wind system in the lower part of the DV.

Other orographic features of different scales (Fig. 1) may modify the local wind patterns. The Southern Alps, about 70 km northeast of Cadarache, reach heights of at least 1500 m MSL and attain heights up to 3000 m at a distance of 140 km. In very calm synoptic conditions mountain systems of this size develop drainage currents that can modify the flow more than 100 km

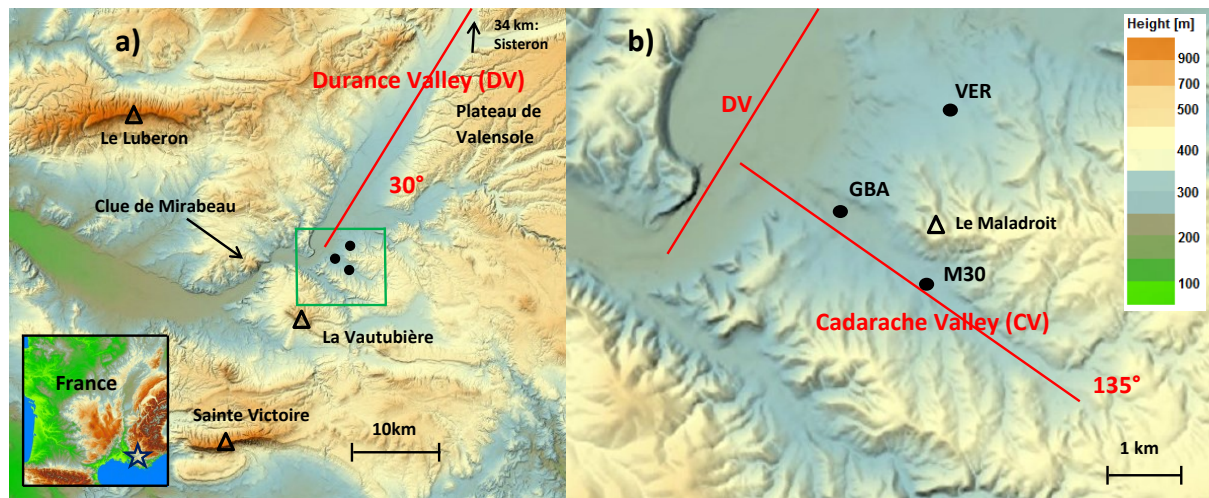


Figure 1. The study area. a) provides a zoom on the area which indicated by the blue star in the lower left frame, b) is the enlargement of the green square in a). The red lines indicate the Durance (DV) and the Cadarache (CV) valleys with their down-valley directions marked in degrees from North (in red). Measurement locations are indicated by black dots. The most important regional orographic features are also indicated. The height scale applies on all frames. Source maps: Geoportail.gouv.fr

downstream (Jiménez and Cuxart 2014). A sloping plateau with an average angle of 1° lies in between the Southern Alps and Cadarache on the DV left bank. This Plateau de Valensole can enhance LLJ-formation during stable situations and therefore can contribute to flow-channeling in the DV. Two east-west oriented mountain ridges are at moderate distance from the site: The Luberon and the Sainte Victoire. Both have heights of 900-1000 m, and modify flows on a regional scale. Especially in winter situations, the narrow Clue de Mirabeau facilitates cold air pool formation. Finally, situated within the Cadarache site boundaries, the Maladroit hill is part of the valley's northeastern sidewall with a height of 394 m, being 110 m higher than the valley bottom. The Maladroit is suspected to play an important role in the interaction of the CV and DV in terms of height for both flows.

Various important local meteorological phenomena are typical for the region, notably the Mistral wind, the land-sea breeze effect and heavy precipitation events. Although they are not directly linked to the aim of the study it is worth mentioning them, as these phenomena can interfere with the valley winds and were sometimes present during the KASCADE-experiment. The Mistral is a cold and dry wind that flows down the Rhône Valley (Guenard *et al.* 2005) and can occur throughout the year (Reiter 1971). At the Cadarache site the Mistral comes from a northwesterly direction. Not all Mistral events, however, reach Cadarache. During the afternoons, due to solar insolation and proximity to the Mediterranean Sea, land-sea breezes develop (Cros *et al.* 2004; Mestayer *et al.* 2005). Sometimes the breezes are coupled with the Mistral wind (Bastin *et al.* 2005) and reach the Cadarache site where they approach from the west. Precipitation events usually come from the southeast from the Mediterranean Sea (Margerit 2006) mainly during the Fall and early Spring months although they are observed in winter as well and have been intensively investigated during the HYMEX-campaigns (Drobinski *et al.* 2013).

Due to the orographic features and meteorological mesoscale phenomena mentioned (e.g. Mistral), clear skies occur frequently in the region. Wrathall (1985) reports more than 2500 hours of sunshine per year.

2.2. Instrumentation and measurement strategy

To investigate the onset of the valley flows and their occurrence and interactions during stable conditions, the KASCADE-campaign was conducted during the winter of 2013. Nocturnal stability in the region occurs throughout the year, but the

Table 1. Summary of KASCADE IOPs. IOP start at 12 UTC and last 24 hours. Full-night measurements were made on IOPs 19-23. The number of radiosondes (RS) launches and tethered balloon (TB) profiles are indicated.

IOP nr	start date	# RS	# TB-profiles
1	14/01/2013	2	6
2	21/01/2013	2	-
3	22/01/2013	2	6
4	23/01/2013	2	42
5	24/01/2013	3	50
6	28/01/2013	2	20
7	29/01/2013	3	54
8	30/01/2013	2	16
9	07/02/2013	2	30
10	08/02/2013	1	10
11	11/02/2013	2	20
12	12/02/2013	3	36
13	13/02/2013	3	34
14	14/02/2013	3	42
15	18/02/2013	3	42
16	19/02/2013	3	38
17	20/02/2013	2	48
18	21/02/2013	3	30
19	25/02/2013	3	52
20	26/02/2013	4	46
21	27/02/2013	4	66
22	28/02/2013	4	46
23	01/02/2013	3	26
Total		61	760

shorter days and longer nights of winter enhance SBL formation. The campaign collected continuous observations that were supplemented by special IOPs. The data were collected between 13th December 2012 and 18th March 2013. 23 IOPs were carried out between 15 January and 2 March 2013. An IOP was planned when clear skies and weak synoptic forcing were expected, but were actually executed when the wind was weak enough for the tethered balloon to be operated, making these periods inherently related to weak wind conditions. A full list of IOPs can be found in Table 1.

Measurements were made at different locations (Fig. 1), a detailed description of the instrumentation is given in Table 2. Cadarache has two permanent weather stations, La

Grande Bastide (GBA) and La Verrerie (VER), which measure temperature at 2 m and wind speed and direction at 110 m (GBA) and 15 m (VER) agl. The top of the GBA-mast extends above the CV sidewalls and its stable boundary layer and thus can sense the overlying DV winds. GBA has been operated for several years and can be used as a long term reference for the dataset.

The M30-site (Fig. 1) has a 30 m flux tower with sonic anemometers at 2, 10 and 30 m, one fast hygrometer at 30 m, longwave and shortwave radiation sensors at 2 and 20 m and two thermohygrometers at 2 and 30 m. M30 was placed in the middle of the CV on a flat open section with a 600 m fetch. The site is dominated by grass with patches of bare soil. The flux tower was installed to collect data for model validation for planned numerical studies. Turbulent fluxes of sensible heat, latent heat and momentum have been calculated with the open-source flux calculation package EddyPro® (LI-COR Biosciences, USA), version 4.1.2. The radiometers at two different heights (the lower one on a nearby mast) provide measurements of the radiation divergence, a crucial parameter for SBL-formation which is still relatively unexplored (Sun *et al.* 2003; Savijärvi 2006; Hoch *et al.* 2007; Steeneveld *et al.* 2010).

At VER a Remtech PA2 Sodar provides averages of wind speed and direction and turbulence characteristics every 15-min with a vertical resolution of 25 m. This Sodar provides continuous information on the timing and depth of the DV flow from 100 to 500 m agl.

During IOPs, a tethered balloon was deployed and radiosondes (RSs) were launched at a site close to M30. The tethered balloon was equipped with up to three Vaisala probes, on a vertical distance of 50 m, measuring temperature, relative humidity, wind speed and direction and pressure. The tethered balloon was deployed to make measurements during the sunset and sunrise transitions, but in the last week of the campaign full-night measurements were also made. In general, profiles were measured up to 300 m agl at an average scanning vertical speed of 0.3 m s^{-1} , completing profiles every 15-min. Ideally, at the surface an extra ground-level probe was installed to give a pressure reference for height correction. To cover the troposphere above 500 m, RSs were launched in every IOP, reaching an average altitude of around 5 km. Normally, the RS releases were at 12, 18 and 06 UTC and during the last campaign week when full-night measurements were deployed, the RSs were also launched at 00 UTC.

All sensors were checked for inconsistencies and re-calibrated during a two-month inter-comparison experiment right after KASCADE at *Centre de Recherches Atmosphériques*, Lannemezan, France. For the two net radiometers, a relative calibration was needed for all radiation components, with the newest radiometer CNR4 as a reference. The thermohygrometers from M30 were corrected for relative humidity only as no correction was needed for temperature. For relative humidity the tethersondes were corrected against the M30-thermohygrometers, while for pressure their average was taken as a reference for correction. At every start of a tethered balloon experiment, the tethersondes were calibrated for wind direction. Prior to the flux calculations, an additional despiking procedure was developed for the two lower sonic anemometers. The validity of calculated fluxes was checked for both normal and de-spiked signals during the inter-comparison with another eddy-covariance package (Baghi *et al.* 2012) and no inexplicable deficiencies were found for the de-spiked signal. Additional information on the correction procedures can be found in a KASCADE technical report (Duine 2014).

3. Flow characterization

3.1. Overview of flows and prominent meteorological conditions

The last 24 days of the campaign are presented in Fig. 2. A diurnal temperature range (DTR) of 15°C was observed regularly with a peak of 20°C on 17 February. For midlatitude areas in winter time these values are rather extreme (Wallace and Hobbs 2006), but can be explained by several regional factors and characteristics. The distance from the Mediterranean Sea, a general lack of cloud cover and a low soil moisture generally have an amplifying effect on DTR (Jackson and Forster 2010). Also the complex topography could partly explain the high DTR; Geerts (2003) showed that the tendency of cold air to drain from higher slopes to the valley bottom creates strong inversions and increases DTR. Large scale advection of cold air masses coming from the Southern Alps should also be taken into account as a factor for DTR-enhancement. Another important factor is the contribution of the Mistral to lower the aerosol concentration (Salameh *et al.* 2007), which enhances DTR citepHansen1995. During the day temperature differences ($T_{110\text{m}} - T_{2\text{m}}$) are negative whenever a clear sky is present. Positive temperature differences persist from before sunset until after sunrise whenever a negative radiation budget is present and wind speeds are low. Positive temperature differences between 110 and 2 m can easily go up to 5°C .

The wind directions measured at the stations show different patterns. Westerly winds prevail during the afternoon in clear sky and unstable conditions at both GBA and M30. Once the sun sets, a stable layer forms rapidly and at M30 (black dots in Fig. 2) in the CV the observed wind direction turns to the SE, i.e. down-valley and opposite of the daytime direction. This weak drainage flow will, hereafter, be named Cadarache down-valley (CDV) wind. Whenever rain (10th February) or strong Mistral (8th February) events occur, no stable layer forms and no CDV wind is measured. But, during cloudy (and rainy) periods SE-winds often occur (e.g. the nights from 10 to 11 and 17 to 18 February), as can be seen from the 110 m measurements (blue dots). These events happen coincidentally in the same direction as CDV wind, but the temperature gradient indicates that those are not linked to the thermally driven flow. Another regional feature is clear from the wind direction measurements of GBA at 110 m height. At this height well above the valley, the westerly daytime flow often persists into the early evening but turns progressively into a NE-direction aligned with the DV. This wind, hereafter called DDV wind, is initiated about 6 to 9 hours after sunset and persists until a few hours after sunrise. We will elaborate more on the timing of the DDV wind in Sect. 3.3.

Atmospheric stability information from the M30 flux tower is given by median values for the full campaign including both IOPs and non-IOPs Fig. 3. For Figs. 3b, 3c and 3d, the variability is shown by means of probability density functions. Taking astronomical sunset time as the reference time, the stability forms before sunset and ceases after sunrise. Temperature measurements at 2 and 30 m provide insight on the diurnal development of local stability at the surface in the CV (Fig. 3a). A stable layer forms around 1.5 hour before sunset and persists throughout the night until sunrise, which is in the time frame 12 - 15 hours after sunset due to different night lengths. This layer disappears typically 1 hour after astronomical sunrise (not shown). Sensible heat flux H (Fig. 3b) becomes negative 1 hour before sunset and reaches its minimum value at half an hour after sunset. In this shallow, narrow valley the sidewalls are able to create shading effects leading to negative values for H before sunset (Nadeau *et al.* 2013). After this minimum the negative H smoothly increases to 0, and becomes positive 1 hour after sunrise (not shown). So, the delay between the zero-buoyancy flux and the zero temperature gradient

Table 2. Summary of measurements at the sites shown in Fig. 1b, and their stations: geographical coordinates, base elevation above sea level (asl), measurement height above ground level (agl), instruments used, measured parameters, sampling frequency. Abbreviations include T : temperature, RH : relative humidity, U , V , W : sonic wind speed components, T' : sonic temperature, H_2O' : humidity, CO_2' : carbon dioxide concentration, SW^\downarrow , SW^\uparrow , LW^\downarrow , LW^\uparrow : incoming- and outgoing shortwave & longwave radiation, PP : atmospheric pressure, FF : wind speed, DD : wind direction, T_d : dew point temperature, v_z ascending/descending speed. # denotes the number of measurements at different heights.

Site	Station	Coordinates (°N, °E)	Elev base (m asl)	Meas hgt (m agl)	Instrument	Variable	Acq. freq.(Hz)	Additional information
M30	id.	43.68550 5.76169	286	30.36	Campbell Sci. HMP45 thermohygrometer	T, RH	0.1	$T\#2, RH\#2$
				30.29	Campbell Sci. CSAT sonic anemometer	$U'V'W'T'$	10.0	sonic #3
				30.29	LI-COR LI-7500A open path analyzer	$H_2O'CO_2'$	10.0	
				20.11	Kipp & Zonen CNR4 net radiometer	$SW^\downarrow, SW^\uparrow, LW^\downarrow, LW^\uparrow$	0.1	radiation #2
				10.50	Young 81000 sonic anemometer	$U'V'W'T'$	10.0	sonic #2
				1.90	Campbell Sci. HC2S3 thermohygrometer	T, RH	0.1	$T\#1, RH\#1$
CNRI		43.68564 5.76147	286	1.90	Young 81000 sonic anemometer	$U'V'W'T'$	10.0	sonic #1
				1.18	Kipp & Zonen CNR1 net radiometer	$SW^\downarrow, SW^\uparrow, LW^\downarrow, LW^\uparrow$	0.1	radiation #1
TB		43.68511 5.76233	287	2-300	Vaisala TTS111 tethersondes (3)	T, RH, PP, FF, DD	0.25	3 profiling sensors $v_z = 30 \text{ cm s}^{-1}$
				1.50	Vaisala TTS111 tethersonde (1)	T, RH, PP, FF, DD	0.25	Height correction sensor
RS		43.68550 5.76169	286	0-5000	MODEM M2K2-DC Radiosonde system	T, RH, PP, FF, DD	1.0	Balloon type cosmo- prene KE 45 g
				.			.	
VER	id.	43.70744 5.76514	295	15.0	Dégréane DEOLIA96 cup anemometer	FF, DD	0.1	
				2.0	Vaisala PT100 thermometer	T	0.1	
					Vaisala hygrometer	RH	0.1	
					Vaisala barometer	PP	0.1	
					PréciMéca R30295 rain gauge	RR	0.1	
				75-400	Remtech PA2 Sodar	FF, DD	0.001	
GBA	id.	43.69442 5.74614	265	110.0	PT100 thermometer	T	0.1	
					Metek sonic anemometer	FF, DD		
				2.0	PT100 thermometer	T, RH	0.1	
					Rotonic hygrometer	RH		

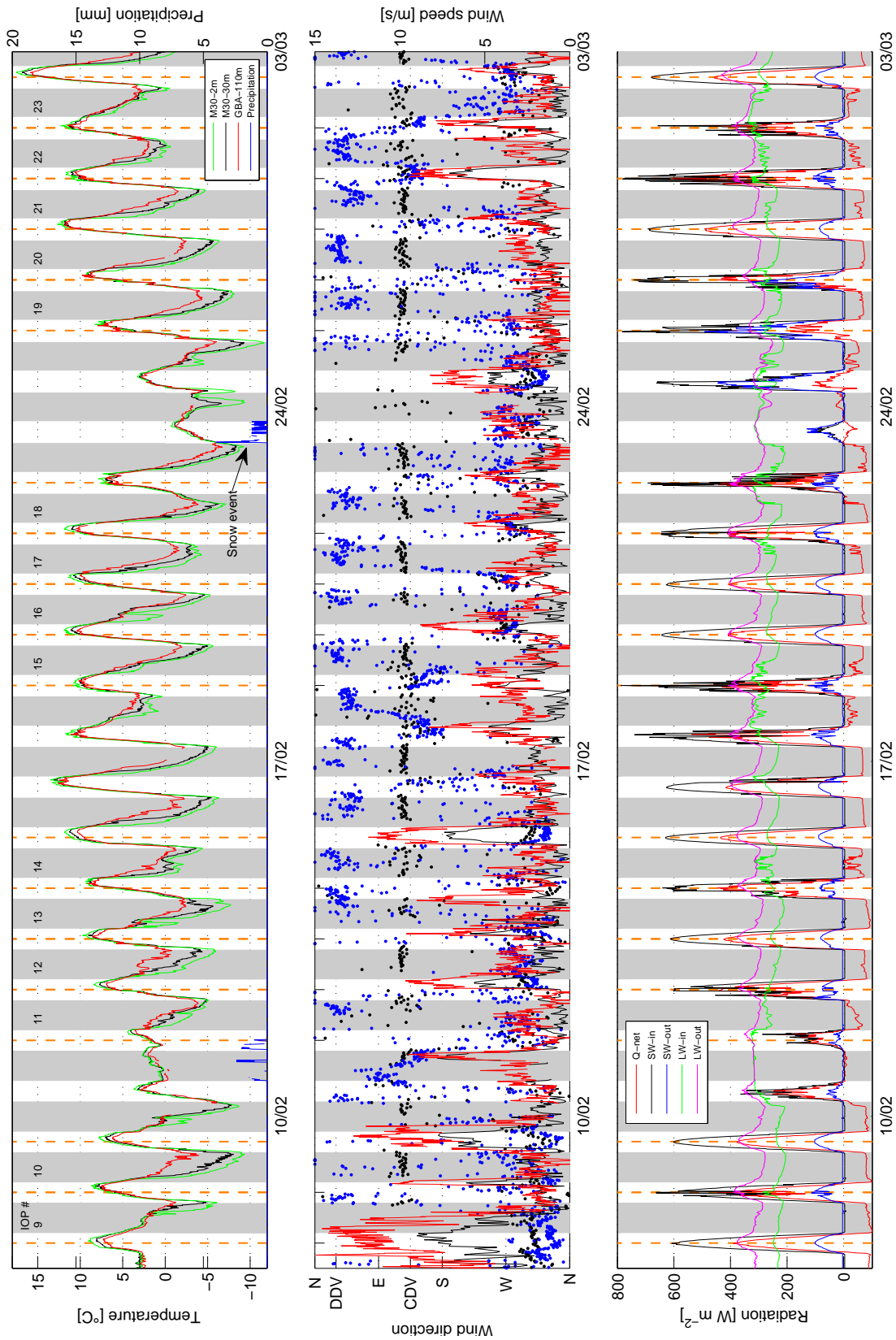


Figure 2. Continuous observations during the 24 last days of KASCADE of: temperature at three different heights and precipitation (top), wind speed & direction (lines and dots, respectively) at two heights (middle), radiation components (SW stands for short-wave, LW for long-wave, in and out for incoming and outgoing, respectively, and Q-net is net-radiation, bottom). In the middle diagram the black line and dots are observations at M30 at 30 m height, the red line (wind speed) and blue dots (wind direction) are observed at GBA at 110 m height. Precipitation was measured with a rain gauge at 1.2 m height, other measurement locations and heights are indicated in the corresponding boxes. The gray shaded areas indicate nighttime periods, note that the date labels are centered on the night. In the top diagram the IOPs are indicated by their number, the orange lines designating the start and end time of each IOP. In the middle diagram the left axis also shows the downslope direction for CV and DV. All quantities shown are 10-min averages, except for precipitation which is a 30-min averages, except for precipitation which is a 10-min averages, except for precipitation which is a 10-min averages. See Fig. 1 for the location of the measurements.

is approximately half an hour. Another measure of stability is the stability index (inverse of the scaled Obukhov-length z/L) and is computed at 30 m height (Fig. 3c). Like for H , around 1 hour before sunset a crossover can be determined for the median value of the dataset. The stability index then remains positive until 15 hours after sunset. The return to negative (unstable) values occurs about 1 hour after sunrise. The distribution and median value of friction velocity u^* clearly illustrate the transition from typical daytime mixing values to non-mixed conditions during the night when stability is established (Fig. 3d). Wind speed diminishes and weak turbulent mixing is observed during the night until sunrise. At night, u^* rarely exceed 0.2 m s^{-1} and often is less than 0.1 m s^{-1} , indicating that turbulent shear stresses are suppressed, a feature regularly found in SBL-measurements (e.g. Monti *et al.* 2002). Mixing increases again after 1.5 hours after sunrise.

The predominant wind patterns during the 3-month dataset from Sodar-measurements at VER are shown in Fig. 4. The wind direction is classified in 10° bins, with frequencies shown every three hours relative to sunrise or sunset. VER is north of the Maladroit hill (Fig. 1) which is outside the CV. Thus, a CDV wind cannot be observed there. The figure reveals the relative importance of the DDV wind. Four typical wind patterns appear: the DDV wind from 30° , the cloudy weather wind with possible rain events from the SE, the Mistral from the N to NW and an afternoon and evening WSW wind. Westerly winds prevail before sunset, denoting a mixture of Mistral and general westerly circulation during daytime. This wind direction is predominant before sunset and just after sunrise. Southeasterly winds from the cloudy and rainy events are also measured before sunset. As the night falls, the downward momentum flux enhanced by convective mixing during the day ceases, causing the retreat of the NW or SE winds higher up. As the stable conditions settle in, the DDV flow can develop and strengthen. The DDV flow appears 6 to 9 hours after sunset. Before and around sunrise the NW and SE-direction are very low in frequency, but do re-appear from 3 to 6 hours after sunrise. Then, after 6 to 9 hours after sunrise the general pattern repeats from the top left picture (not shown). Now that we have a feeling of the different predominant wind patterns, we will investigate the circumstances under which the valley winds tend to develop.

3.2. Focus on specific situations

This section investigates two different IOPs to gain insight on stability and valley flow development during relatively weak easterly synoptic forcing on the one hand (IOP 21) and during a stronger northwesterly synoptic forcing on the other hand (IOP 5). We will describe the general behavior during an IOP by means of the tethered balloon profiles.

3.2.1. IOP 21

Although no ideal IOP existed, IOP 21 had typical CDV and DDV wind development and thus can be used as an illustrative example. The IOP was conducted in the last week of KASCADE, starting at 12 UTC on the 27th February 2013, astronomical sunset and sunrise were at 17:21 and 06:16 UTC respectively. During this last week, full-night measurements of SBL-formation were made with the tethered balloon.

Four days before the IOP start, on the 23rd February, a precipitation event covered the region with a 10 cm snow layer, see Fig. 2. The values of SW^\uparrow indicate that the snow had mostly melted by the start of the IOP, with patches remaining only in shadow areas. The synoptic situation was dominated by a high pressure area over the United Kingdom that extended eastward over Europe with a low pressure area over southern Spain moving slowly eastward, driving an easterly flow over southern France.

The synoptic easterly flow is confirmed by all RSs launched during the IOP (Fig. 5). High altitude cirrus at the IOP-start gradually dissipated with time (Fig. 2). The 2 m DTR of 16°C (Fig. 2) agreed well with the noon and early morning RSs. A dry mixed layer extended to 1400 m at 12 UTC. By the next morning (06 UTC), a SBL-depth of around 400 m was reached, which is beyond the height range of the tethersondes. A very high value of 12°C was observed in the 06 UTC profile (the temperature difference between the SBL-top and surface level). The mixing ratio profile indicates moisture advection during the IOP with dew formation in the early morning as result of the strong stability. A strong westerly jet developed below 1000 m in the 18 UTC-sounding. Observations of Sodar at VER, and the GBA and M30 stations confirm that the onset of this westerly wind at Cadarache was at 17 UTC and lasted for several hours. Westerly flows in the region are observed frequently in the late afternoon and early night, as shown in Fig. 4.

Up to 66 tethersonde profiles were achieved during IOP 21, from which 14 are selected and shown in Fig. 6. The potential temperature profile showed that 8 minutes before sunset a stable layer had already formed below 30 m. Above this height, the residual layer from the afternoon convective boundary layer was still present. The corresponding wind profile showed a westerly direction, the typical afternoon wind direction as seen before in Figs. 4 and 5. 80 minutes after sunset (18:43 UTC) the atmosphere had cooled by 2°C , but surface cooling was stronger with a SBL strength of 3°C . The stability facilitates the onset of the downvalley flow (i.e. SE). Wind speeds were still low, but the southeasterly flow extended to 60 m AGL. As already mentioned in Sect. 3.1, this CDV wind is typically found during nights with weak synoptic forcing and surface cooling.

The SBL-height grows steadily throughout the night while the wind profile changes dramatically within the first hours. Higher up in the profile, between 100 and 300 m, three hours after sunset the wind speed drops from 5 to less than 0.5 m s^{-1} . The weak wind speeds aloft at 21:40 and 22:31 UTC allow the CDV wind to grow to the full 100 m valley depth. The CDV wind takes the shape of a jet, its height of maximum speed growing from 30 to 40 m AGL. Maximum wind speeds were around 2.5 m s^{-1} . During the extremely calm period the wind at around 175 m turns to the north-northeasterly DDV wind direction. At 23:52 UTC, the DDV wind was initiated at about 175 m height, forming a jet with a maximum wind speed of 3 m s^{-1} . So, in this night the DDV wind began 6.5 hours after sunset. Later we will show that this is a typical value for the DDV wind onset. Meanwhile, the CDV wind keeps flowing steadily, implying ongoing relative cooling at the valley bottom (Thompson 1986), a clear signature of a katabatic or drainage flow.

During the second part of the night (lower sub-figures), the cooling at the surface continues until a minimum temperature of -3°C is reached at around sunrise (06:16 UTC). The DDV had attained wind speeds up to 4 m s^{-1} , a value which is exceeded in other IOPs. Above the DDV wind (e.g. higher than 200 m) an easterly flow is observed which aligns with the earlier-mentioned synoptic situation and makes flow channeling one of the explanations for the continuation of the DDV flow. After 4 UTC a shear layer is observed between 50 and 100 m: the wind rotates clockwise with altitude from SE to NNE, viz. a 255° rotation instead of 125° . This typical behavior was measured during nighttime in other IOPs featuring both DDV and CDV winds. Hypotheses for the origin of this shear layer include: i) a return current flowing just above the CDV flow, ii) a deflection of the DDV flow by the Maladroit hill or iii) a combination of i) and ii). Comparison of GBA- and tethersonde measurements at these heights shows agreement supporting the spatial homogeneity of the flow (not shown). The complexity of the layer between 50

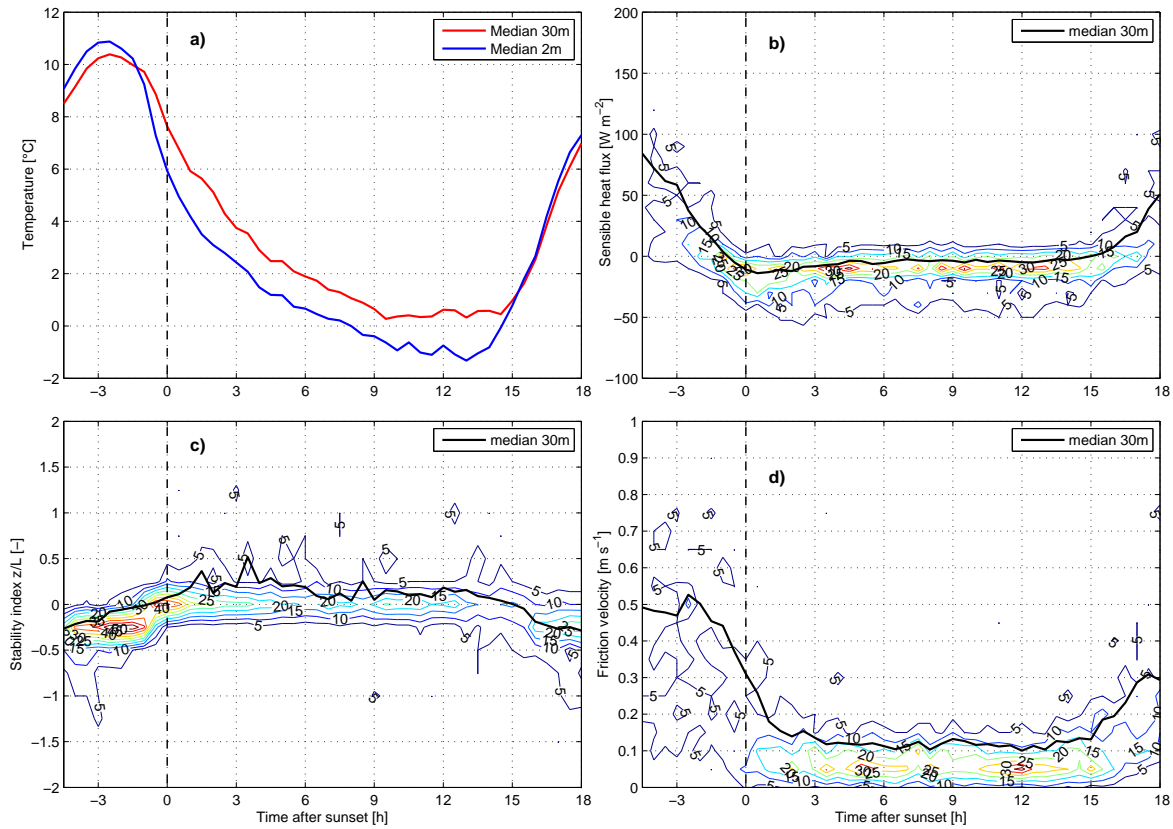


Figure 3. Time series measured at M30 in the Cadarache Valley (medians in bold lines and pdf-distribution in thin lines) of a) temperature difference between 2 and 30 m height, b) sensible heat flux (at 30 m), c) stability index z/L (at 30 m) and d) friction velocity (at 30 m). For this data the full campaign period has been used, that is from 13 December 2012 to 18 March 2013. All data is sunset referenced, which is indicated by the dashed lines.

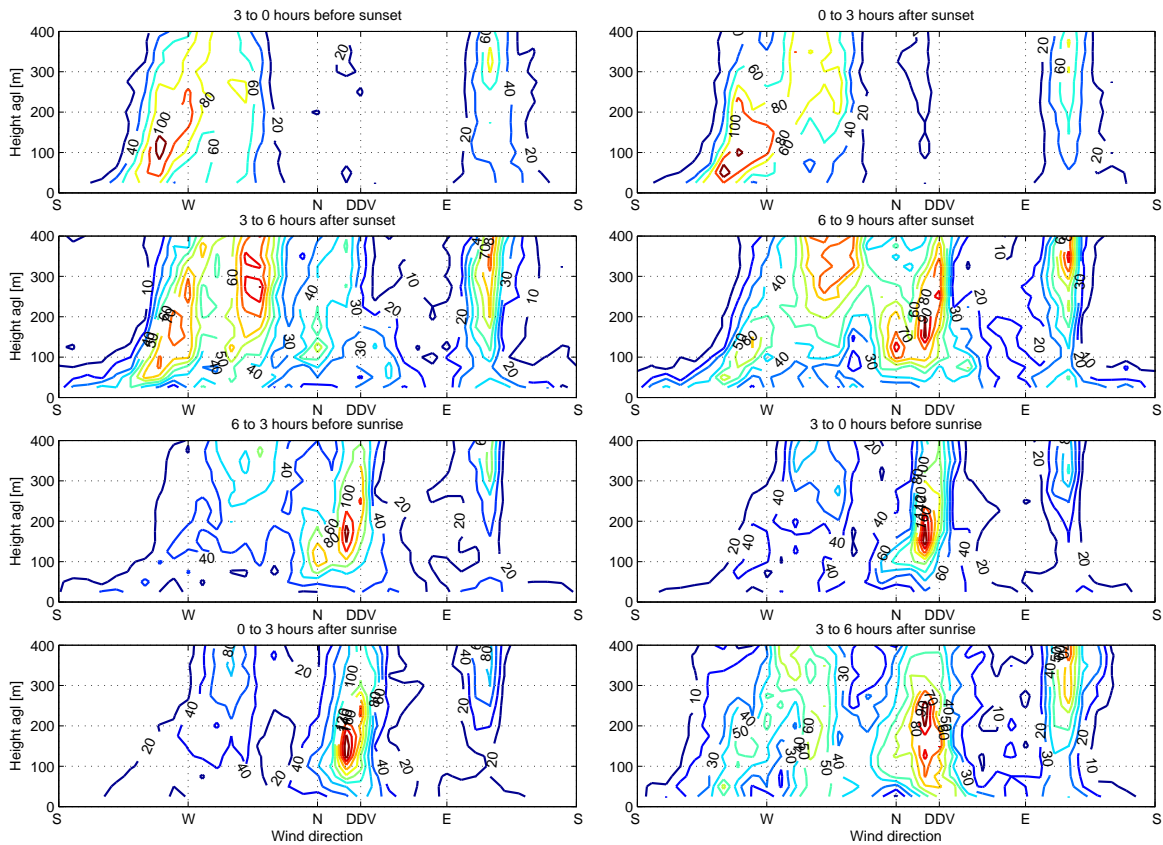


Figure 4. Frequencies of Sodar wind direction profiles above ground level (agl) observed at VER (Fig. 1) for the period of 13 December 2012 to 15 March 2013. The top and bottom four figures are sunset and sunrise referenced, respectively. On the x-axis we have indicated the downslope direction for Durance Valley (DDV).

and 100 m is demonstrated by the profile at 07:41 UTC, where in this layer a fully westward wind has developed. As this is already

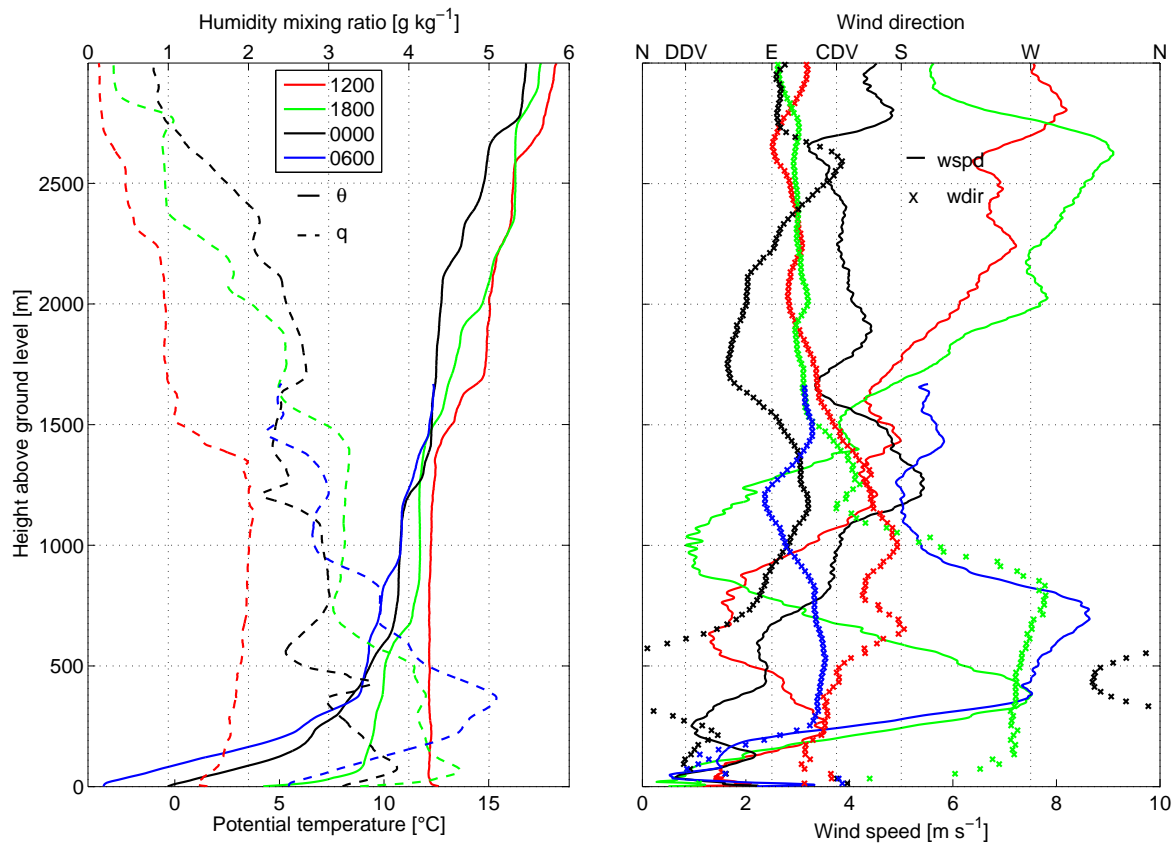


Figure 5. 6-hourly RSs launched near the M30-site during IOP 21 (27 to 28 February 2013) with the mixing ratio q (dashed lines) and potential temperature θ (solid lines) in the left panel and wind speed (solid lines) and wind direction (crosses) in the right panel. The launch times are indicated in the legend on the left panel. The downslope direction for Durance and Cadarache valleys are indicated on the wind direction axis by DDV and CDV, respectively.

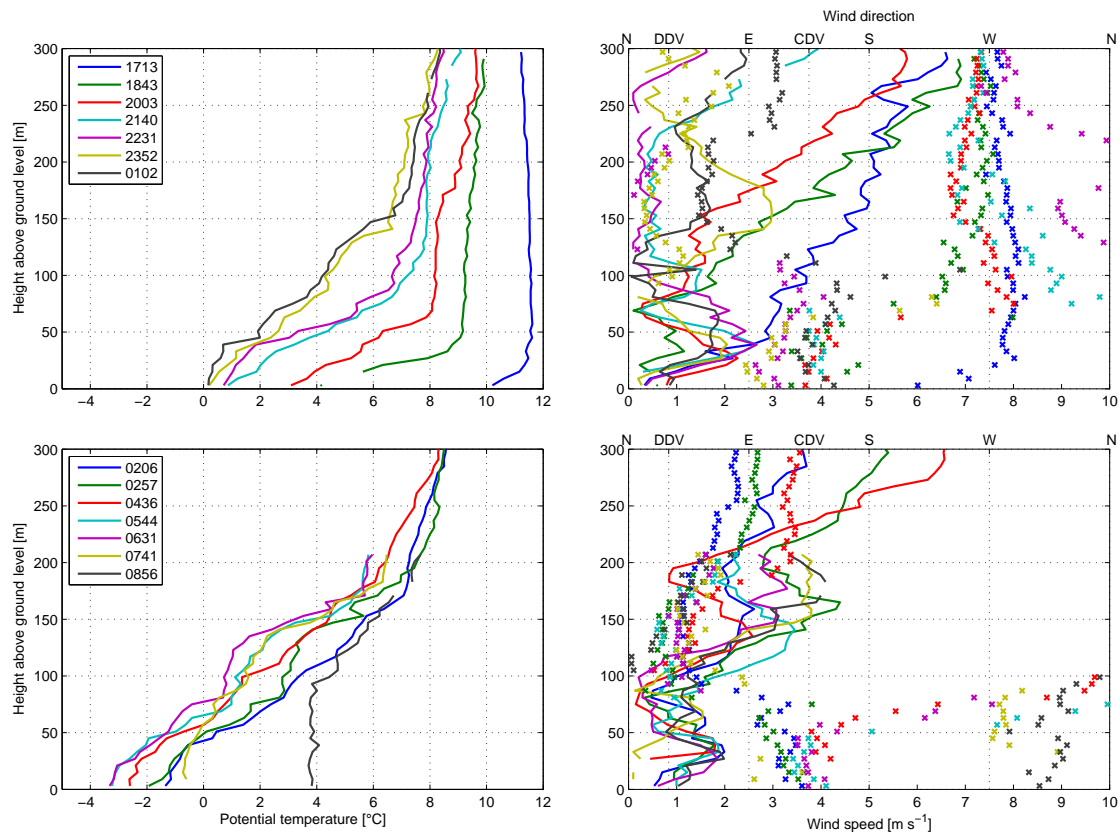


Figure 6. Selection of tethered sonde profiles near the M30-site, averaged over 6 m, as measured during IOP 21 (27 to 28 February 2013) for potential temperature (left) and wind speed and direction (lines and crosses, respectively, right). The Durance and Cadarache Valley's downslope directions are indicated on the wind direction axis. The times (UTC) are indicated in the temperature diagrams.

1.5 hours after sunrise and it is an upvalley direction, this can be attributed to the early onset of an anabatic upvalley flow which has developed starting further downstream in the valley. When the anabatic flow meets the katabatic wind, it is lifted because of its lower density. This feature is similar to that found by [Monti et al. \(2002\)](#) and [Brazel et al. \(2005\)](#) and has been observed during morning transitions in several IOPs. At the surface, the CV wind shifted from downvalley to upvalley at 07:50 UTC (not shown). The DDV wind lasted until around 10 UTC as determined by Sodar-measurements. Following this, the SE-direction returned reflecting the synoptic conditions.

IOP 21 is one of the many examples with a co-existence of the CDV and DDV winds. The CDV wind flows throughout the night, but with variable depths from case to case. Its depth depends on the above-valley wind direction and wind speed, but reaches the full valley depth when winds are very calm above the valley. The DDV wind however forms as a LLJ, may be influenced by flow channeling, has a maximum depth of 200 m with its jet maximum at around 175 m and a wind speed of 4 m s^{-1} .

3.2.2. IOP 5

In this section we examine SBL development and the corresponding wind flow patterns during the non-typical IOP 5 which started on 24th January 2013. Astronomical sunset was at 16:36 UTC and sunrise at 07:01 UTC. A low pressure system was present above Italy creating a weak pressure gradient and so a northerly wind pattern, and weak Mistral wind conditions. No clouds were observed during the IOP. The northerly wind is well visible in the RS-profiles (Fig. 7). The 12 UTC temperature profile shows a convective layer of around 1000 m height. Note that the lower part is not totally mixed; this can be attributed to an internal layer specific to the CV which is not mixed with the larger scale boundary layer. At this time the layer below 1300 m is extremely calm, with wind speeds below 1 m s^{-1} , but in the lowest layers northwest winds with wind speeds of around 3 m s^{-1} . At 18 UTC, the wind has turned and strengthened, and the air layer up to 800 m has already cooled. Two inversion layers are observed with a neutral layer in between, the lowest one with its top around 100 m and the upper one at 800 m height. Because this second layer is at considerable height and the sun set just 1.5 hours before, this inversion layer developed due to cold air advection and is linked to the Mistral wind. By the early morning (06 UTC), the lowest stable layer has grown to 250 m, with a continuing NW-flow; the upper inversion has also strengthened. This second upper stable layer has a top height of 750 m, and again a N-flow with a strong jet at 500 m and a maximum wind speed of around $9\text{--}10 \text{ m s}^{-1}$. A DTR of 16°C is observed, similar to IOP 21. The SBL-strength for the lowest layer is 10°C , somewhat less than during IOP 21. The decrease in q reflects dew formation which is constrained to CV-depth only.

The RS-profiles show clearly that during IOP 5 Mistral-conditions were predominant, but because of its weak nature a total of 50 tethersonde profiles were obtained from which 7 evening and 7 morning transition profiles were selected (Fig. 8). During the afternoon, the wind below 200 m has turned from NW to Westerly direction at 14 UTC, as investigation of Sodar measurements and the VER and M30 stations showed. This wind continued until the first available tethersonde profile at 16:23 UTC. This shift to westerly was during the afternoon, likewise IOP 21, and a typical feature for the region as shown in Sect. 3.1. At 16:48 UTC, 8 minutes after sunset, the surface cooling started, causing the surface wind to become light and variable. After 18 UTC, the westerly wind shifted to northwesterly and winds became down-valley in the lower layers. By approximately 3 hours after sunset (19:31 UTC), a fully developed CDV wind

was observed with a jet maximum at 30 m height. The onset of the CDV wind during this IOP is later than observed during IOP 21 and several other IOPs (not shown). The delay is related to the stronger synoptic forcing, which sustains mixing in the lower layers and so delays a possible onset of the CDV wind. Meanwhile in the upper air the wind has turned from westerly to north-northwesterly, the SBL steadily grows to a depth of 125 m with a strength of 6°C .

The morning profiles in the lower two sub-figures (Fig. 8) show that a steady SBL depth of about 150 m has developed. The Sodar-observations reveal that this northerly wind was observed during the full night period, with speeds of around $4\text{--}6 \text{ m s}^{-1}$ up to 500 m agl (not shown). No clear DDV wind (e.g. 30°) was observed below 300 m, as was the case for IOP 21. A steady CDV wind persisted near the surface, although it was less deep than during IOP 21. It is generally observed with a depth of 50 m and has its maximum speed at 25 m agl, with weaker wind speeds of $1\text{--}2 \text{ m s}^{-1}$. Also the CDV flow is more variable than in IOP 21, because of the lower wind speed. Just above the CDV flow a shallow return current is observed that turns to form a northerly component above 100 m. The NW-direction above the CDV flow prevents the thickening of the drainage flow as its upper part is eroded.

To summarize, during IOP 5 the CDV flow was weak, but still present. Due to the synoptic forcing during the evening and morning, no DDV wind was present up to the DV sidewall height. The CDV wind can exist when synoptic forcing is of considerable strength, however its height and wind speed are strongly dependent on the wind conditions aloft. The DDV wind however, is more susceptible to synoptic conditions and its onset is less evident than that for the smaller scale CDV flow. In the next two sections we will elaborate more on both flows in terms of timing (Sect. 3.3) and depth (Sect. 3.4).

3.3. Valley-flow timing

To investigate the timing for the onset of the nocturnal CDV and DDV winds and to extract general patterns in these, we use the full campaign dataset for M30, GBA and VER. Figure 9 shows wind direction as a frequency distribution on a time scale referenced to sunset at 2, 10 and 30 m for M30 and 110 m for GBA. The medians for the wind directions at 2, 10 and 30 m are given in Fig. 9d and come from a vector average.

The most frequent wind direction is WNW at all heights in the afternoon. This is upvalley for CV, a behavior previously seen in Figs. 2, 4, 6 and 8. It is not necessarily a local valley effect as it is also present at 110 m. The wind turns to SE at 2 and 10 m heights at sunset, indicating the onset of the CDV wind. One hour after sunset the 30 m wind turns to SE as well, as indicated by the median value. The CDV wind at 2 m fluctuates more, but this is caused by the low wind speed near the surface and the downslope contribution from the sidewalls. The CDV flow persists at all heights until after sunrise (Fig. 10). The medians indicate that it takes approximately 2 hours after sunrise to generate a fully developed upvalley flow. The transition to upslope is earlier at 30 m than at 2 m. While the figure deals only with the medians this feature was observed regularly during tethersonde morning transition measurements (e.g. IOP 21 in Sect. 3.2.1), and may be explained by the valley shading effect leading to earlier surface heating at the lower end of the CV than in the valley itself. This creates an anabatic current which is lifted once it meets the colder, denser katabatic flow. Thus, erosion of the katabatic current can start from the top, initiated by the re-established WNW flow aloft. During nighttime (Fig. 9), for the 2, 10 and 30 m heights an infrequent NW-signal is found, related to Mistral events. These events were episodically present during the entire

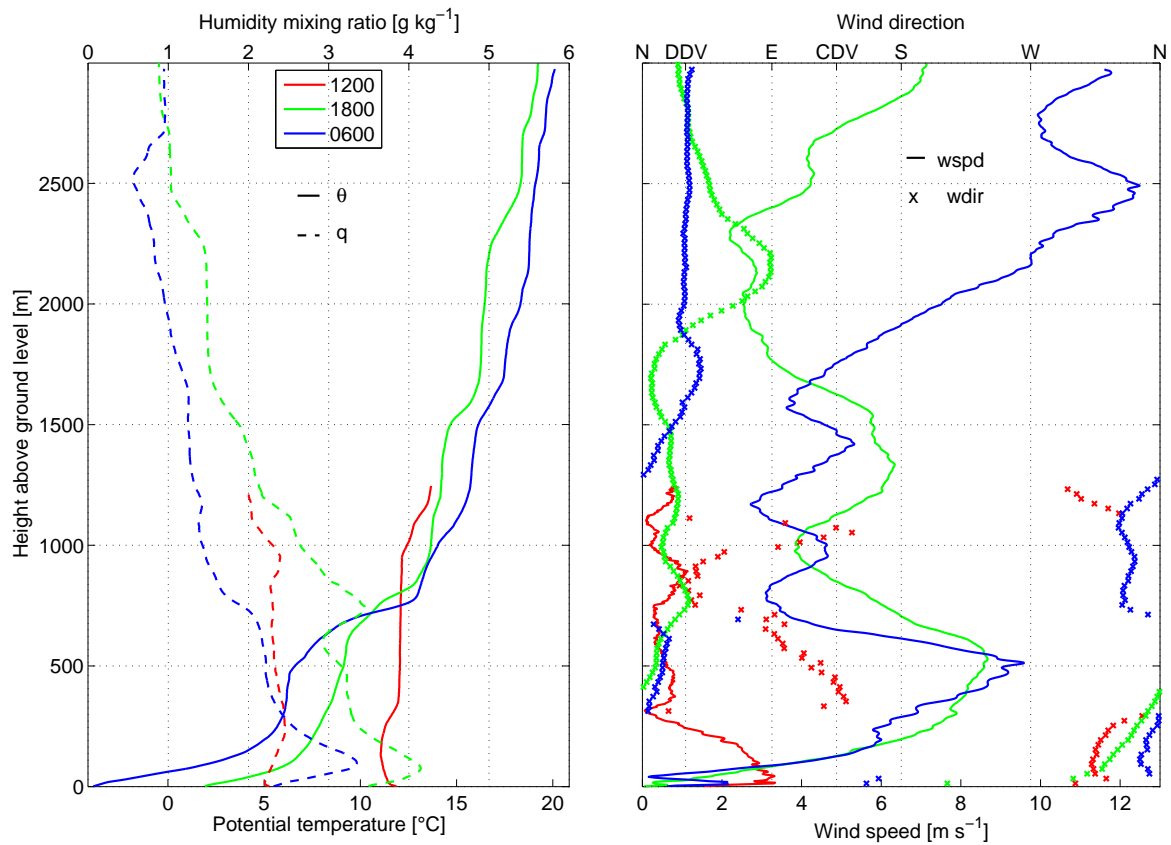


Figure 7. Same as Fig. 5 but for IOP 5 (24 to 25 January 2013).

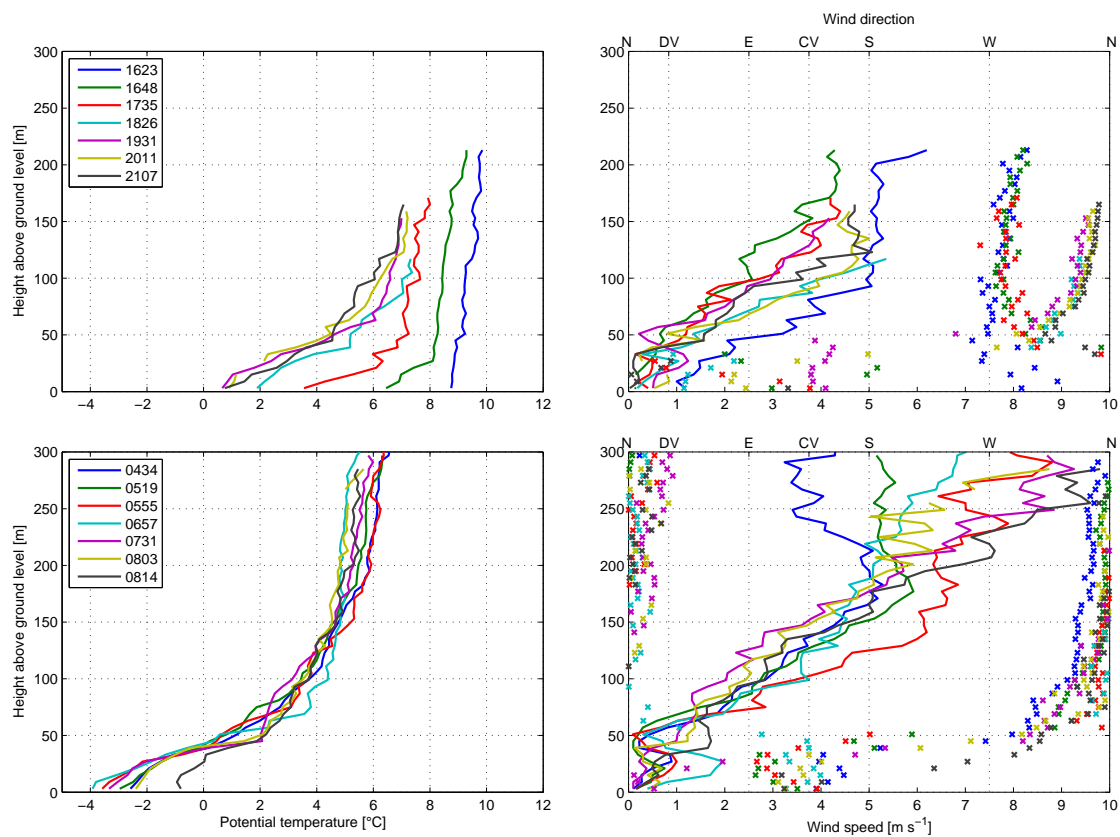


Figure 8. Same as Fig. 6, but for IOP 5 (24 to 25 January 2013).

campaign. The figure highlights the occurrence of the CDV flow, which is dominant in the CV.

The timing of the onset of the DDV flow can be seen in the 110 m measurements at GBA (Fig. 9). This tower is situated above the

CV-depth (Fig. 1) it therefore captures better the DV influence. Wind events from the SE are entirely rain- and cloud-related (Fig. 2). These events are also present at 2, 10 and 30 m but are then mixed with the drainage flow signal. After sunset, the daytime

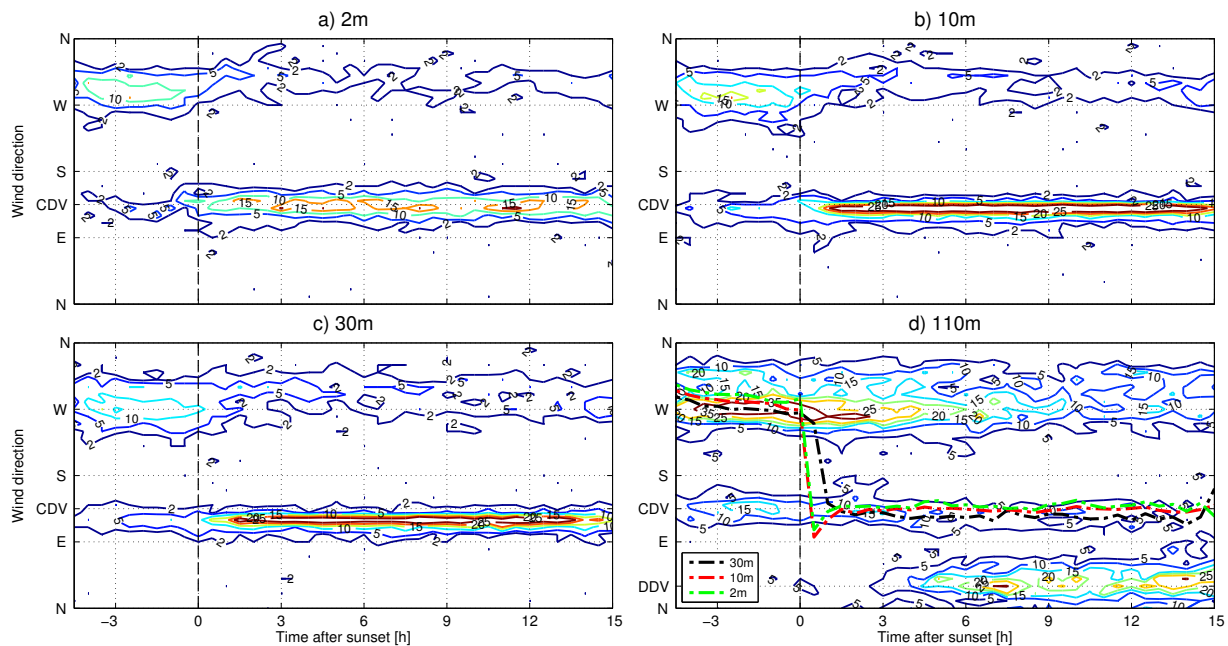


Figure 9. Sunset referenced distribution of wind direction at several heights, the 110m height is taken at GBA, the others at M30 (see Fig. 1 for the location). CV and DV denote the downslope direction of the Cadarache and Durance valleys, respectively. The data period was 13 December 2012 to 18 March 2013 except for the 2 m which was until 23 February 2013. On the lower right diagram the medians for the 2, 10 and 30 m levels are indicated.

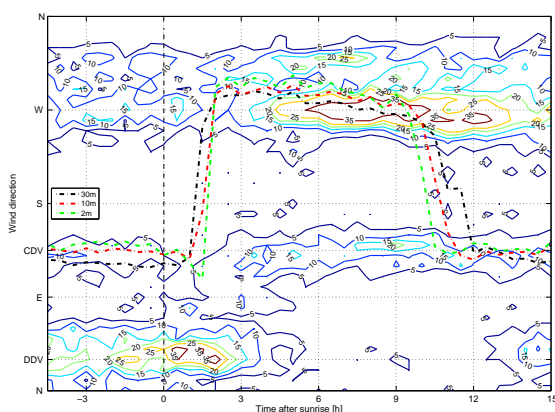


Figure 10. Same as lower right diagram of Fig. 9 but sunrise referenced.

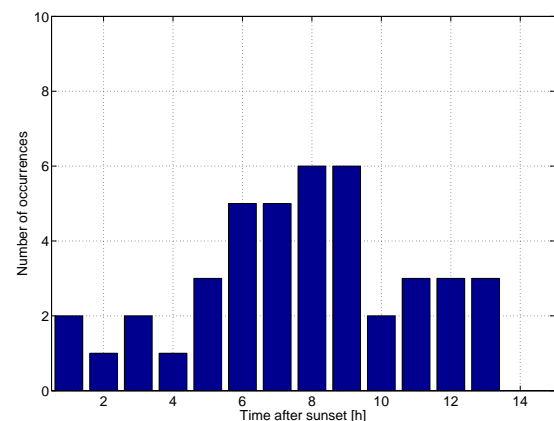


Figure 11. Histogram of the sunset-related onset time of the DDV wind observed at 225 m agl for the period of 13 December 2012 to 15 March 2013.

WNW wind continues steadily into the night. The first signals of the DDV flow are visible about 4.5 hours after sunset when the wind shifts to around 30° . From this time on both WNW and NNE-directions co-exist but as the night continues the frequency in the downvalley direction increases. After sunrise the DDV wind continues longer than the CDV wind (Fig. 10), shifting back to the daytime WNW direction around 4.5 hours after sunrise. The probability of having a downvalley wind after sunrise is highest, perhaps because other dominant convectively driven mesoscale phenomena (e.g. weak Mistral and anabatic effects) are at their lowest intensity at this time.

To be more precise about the time delay in the onset of the DDV winds, we consider the Sodar-measurements at VER (Fig. 1). Figure 11 shows the timing of the onset of a wind oriented in the 10° - 50° direction range, i.e. along the DDV direction as measured by the Sodar at a height of 225 m. From Fig. 4 the core of this wind is between 100 and 300 m agl. We restrict our analysis to winds lasting at least 1.5 hours to exclude coincidental occurrences in the same wind direction range during extreme low wind speed conditions. The figure shows that DDV winds can start throughout the night at this height, but the highest probability

for the DDV wind onset is between 6 and 9 hours after sunset, although the onset at lower heights could be earlier than this.

Figures 9, 10 and 11 demonstrate that the two valleys have their own timing relative to sunset and sunrise for downvalley wind onset and cessation. Wind reversals in the smaller CV occur at sunset and sunrise transitions. Onset occurs when a stable layer forms at the surface and cessation occurs shortly after sunrise when stability diminishes. The DV has a longer fetch; the measurement site is on a sidewall of the DV at its lower end so that this transition takes time to reach the site's elevation. Besides, other mesoscale forcings can influence this site and the larger valley. Thus, the origin of this flow is quite hard to determine by means of the local KASCADE measurements only. Altogether, several origins for the DDV flow are possible: local valley drainage, channeling effects from larger scale synoptic winds, channeling effects of drainage currents and LLJs originating from the Plateau de Valensole (see Sect. 2.1). Also gravity currents coming from the Alps can play a major role in the onset and delay for the DDV wind. Jiménez and Cuxart (2014) reported this for the Pyrenees, where the mountain ridge can affect flows on horizontal plains more than 100 km away with time delays of more than 6

hours. Future numerical modeling is expected to help reveal the governing and dominant mechanisms and their interactions.

3.4. Valley-flow phenomenology

Up to now we have focused on the general conditions under which the valley flows are able to develop. In this section we focus on the data from the large scale low wind speed IOP conditions, pointing out typical flow depths and interactions, as well as local feature influences. We have disregarded IOP 2, which had a very strong Mistral event that precluded tethersonde measurements.

The CDV wind is only present at nighttime (Sect. 3.3), so for height characterization we can restrict our analysis to nighttime periods. Figure 12 shows the tethersonde wind roses at various heights. The highest frequency of down-valley winds occur at around 33 m agl. At 51 m height there is still a high frequency of down-valley winds, along with a smaller frequency of up-valley winds. At higher elevations (e.g. 75 m) the down-valley is barely present and at 111 m it is absent. Typical values for the wind speed in the jet can be around 2 to 3 m s⁻¹.

At the end of the night during IOP 21 a shear layer was observed between 50 and 100 m (Sect. 3.2.1). This layer, situated between the zones of the DDV and CDV winds, was observed in other IOPs and therefore appears in Fig. 13. In the shear layer the winds turn clockwise with elevation by 255° and is typically present in the late night and believed to represent the erratic large horizontal motions generated by the mixing of the CDV and DDV flows when stratification is at its strongest. In spite of its low frequency it is readily identifiable in the IOP mean data and is especially apparent during IOPs when both winds are present.

The Maladroit hill (Fig. 1), which lies north of the tethersonde site, creates a sheltering effect and thus influences the CV wind measurements. Striking differences are observed between the 111 m tethersonde wind rose and the 110 m GBA measurements (Fig. 12). During nighttime at GBA the northeasterly DDV wind is present while it is lacking in the tethersonde wind roses. We can determine the height up to which the hill has influence on the DDV wind as observed at the tethersonde location. The first wind rose that resembles the GBA one is at 135 m, which is 25 m higher than the hill itself. Note, however, that only one location in the CV was sampled and that the exact spatial distribution of the influence of the sidewalls remains unknown.

The influence of clear skies and relatively weak synoptic forcing on the diurnal wind pattern can be demonstrated by comparing Sodar observations at VER for the full winter period (Fig. 4) with Sodar observations at the same site for IOPs in Fig. 14. Figure 13 provides tethersonde data for IOPs at M30 inside the CV. The biggest differences between the full winter period and the IOP-period are only to be found in the SE and NW-sections. Both sections encounter winds which are principally synoptically driven; recall SE large-scale winds mainly bring cloudy and rainy periods and the strong NW-winds originate mostly from Mistral events. These features are lacking under the weak synoptic conditions of the IOPs. However, note that the SE-flow in the upper air is partly present in the figures from IOP 15 (see Fig. 2). Nevertheless, it is clear that in weak synoptic forcing during the afternoon, westerly winds are predominant. This is possibly related to the local orographic features tending to dominate the low altitude wind pattern. Note, by comparing Figs. 13 and 14, that there is a difference between the measurements inside and outside the CV during IOPs. The Sodar-observations are divided into two groups: WSW and NW, whereas inside the CV the tethersonde measurements lack this bi-directional behavior. Right after sunset inside the valley, the CDV flow has developed near the surface and remains well established throughout the night. The onset of the CDV flow is consistent with the mast measurements

in Sect. 3.3 and shown in Fig. 9. Figures 13 and 14 further imply that the westerlies remain just after sunset, but later than 3 to 6 hours after sunset a transition point can be observed as the general pattern shifts towards the DDV direction. This confirms the uncertainty on the timing of the DDV wind onset from Sect. 3.3. In the period from 6 hours before sunrise to the moment of sunrise, the DDV flow is fully developed between 100 and 300 m, the core being mainly below DDV depth, i.e. 300 m. Once the DDV wind is set, it flows at speeds of 4–8 m s⁻¹ (Fig. 12). LLJs are frequently found during IOPs and were always in the range of 175–225 m agl (not shown). It takes around 3 hours before sunrise for the DDV wind to take over the general pattern, but in any case we conclude that during calm wind conditions the DDV wind is a dominant feature, however strongly influenced by the prevailing synoptic conditions.

4. Summary and conclusions

This paper uses the field measurements from the KASCADE campaign to measure and characterize the atmospheric stability and resulting valley winds that develop under the influence of orography during winter over the Cadarache site in Southeastern France. The nearby perpendicularly oriented CV and DV are both shallow, with average depths of 100 and 200 m, and gentle slopes of 1.2° and 0.2°, respectively. Nonetheless, they develop local winds under weak synoptic forcing. KASCADE investigated the nocturnal valley winds and their importance at the Cadarache site, providing data to increase understanding of their occurrence, timing, strength and depth. Two interacting valley flow systems are recognized, the CDV and DDV winds. These winds occur when atmospheric stability is high. During the winter of 2013, these down-valley flows are more dominant than other meteorological winds typical for the region, e.g. the Mistral wind, up-valley winds and winds related to precipitation events. Moreover, the fact that these valley flows occur under stable conditions which are penalizing for air quality concerns, stresses the need for their characterization (Bowen *et al.* 2000).

The strong diurnal pattern during weak synoptic forcing under clear sky conditions for the Cadarache site as presented in this study is further conceptualized in Fig. 15. Typically, westerly winds are observed in the afternoon as a consequence of synoptic forcing combined with up-valley flow development. After sunset, in the CV a down-valley flow is initiated quite rapidly, typically reaching depths of 50 m with its profile 'nose' at around 25–30 m agl with wind speed maxima of 2–3 m s⁻¹. This flow requires the development of a stable atmosphere in the valley and can be characterized as a small scale drainage flow. Its flow depth is governed by above valley conditions (Barr and Orgill 1989). For example, stronger above-valley winds can decrease the CDV wind depth. The sheltering effect of the relatively narrow CV easily allows the CDV wind to survive near the surface. The CDV flow typically begins within one hour after sunset. It persists throughout the night and ceases within 2 hours after sunrise. This cessation typically starts from the top as the up-valley flows above the valley erode the stability and work their way downward into the valley.

The DDV wind, as seen from the Cadarache site, is likewise tied to the times of sunset and sunrise, but with an onset delay of 6 hours after sunset, although the variability is very high. Furthermore, the wind speed increases towards sunrise, and the maximum wind speeds can even occur after sunrise. Generally it is found that the DDV wind ceases 3 to 6 hours after sunrise, after heating of the surface triggers the onset of convectively driven flows, which develop a turbulent mixed layer that overcomes stability and takes over the wind pattern. For the DDV wind, LLJs were frequently observed with peak speeds of 4–8 m s⁻¹

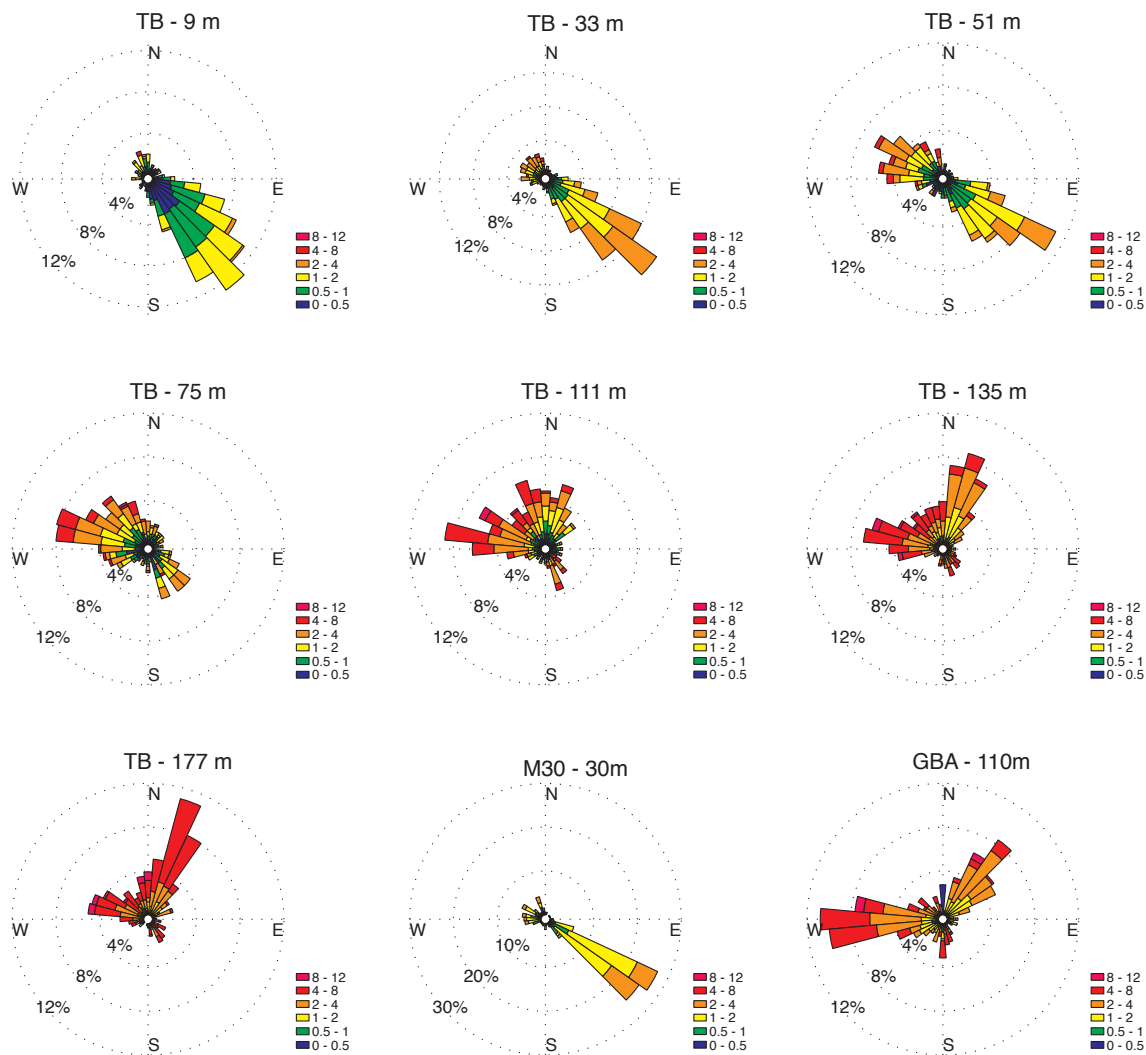


Figure 12. Wind roses (in m s^{-1}) at several heights constructed from TB, M30 and GBA measurements for all nighttime periods of tethered scans during all IOPs.

at 175 - 225 m agl. Driving forces behind the DDV flow are multiple, e.g. flow channeling, synoptic forcing, drainage current. Typical DDV flows are observed up to 300 m, but can sometimes extend up to 500 m or higher. Unfortunately RSs were not released frequently enough to characterize the flow at this depth. Besides, the Alpine influence could be of importance, as this mountain ridge is approximately 70 km from the measurement site, possibly partly explaining the typical time delay we find for the onset of the DDV wind (Jiménez and Cuxart 2014). Because a variety of scales may play a role, future numerical simulations should clarify the factors governing the onset of the DDV wind.

A complex interplay at the Cadarache site between these two valley flows results in a transition or shear layer that can be affected by the existence of a CDV return current and a re-directed DDV flow due to the presence of a hill. GBA and tethered measurements at 110 m height at M30 show considerable agreement whenever this upslope current was present at valley depth, supporting the spatial homogeneity of the flow. The identification of these directional shear layers is of importance for impact studies (Bowen *et al.* 2000).

To increase the understanding of the general wind pattern in the Cadarache region during stable conditions, numerical modeling and dispersion studies are currently in progress. Recently, the WRF numerical code has been tested and partly validated with the field campaign data to study the ability of the code to simulate

the DDV wind, among other processes (Kalverla 2014). In a next step, additional modeling studies are expected to better explain the governing processes of the DDV wind development. Moreover, the KASCADE dataset showed great potential to study other mechanisms important for SBL formation, like radiation divergence. This dataset can contribute to both observational and modeling studies of boundary-layer processes over complex terrain and is now open to the scientific community*.

Acknowledgements

The authors gratefully thank S. Derrien, E. Pique, C. Jarnot, P. Medina, C. Darbieu, G. Bret from Laboratoire d'Aérodynamique for their support on the technical or observational basis, as well as F. Jourdain, Y. Margerit, S. Bontemps and E. Cohenny from Laboratoire de Modélisation des Transferts dans l'Environnement for their invaluable support during the progress of the KASCADE-experiment. H. Delbarre from Laboratoire de Physico-Chimie de l'Atmosphère is acknowledged for his effective support in the provision of the Sodar equipment. The KASCADE campaign and the PhD grant were funded by the CEA.

*Interested scientists are invited to contact Dr. Thierry Hedde (Thierry.Hedde@cea.fr)

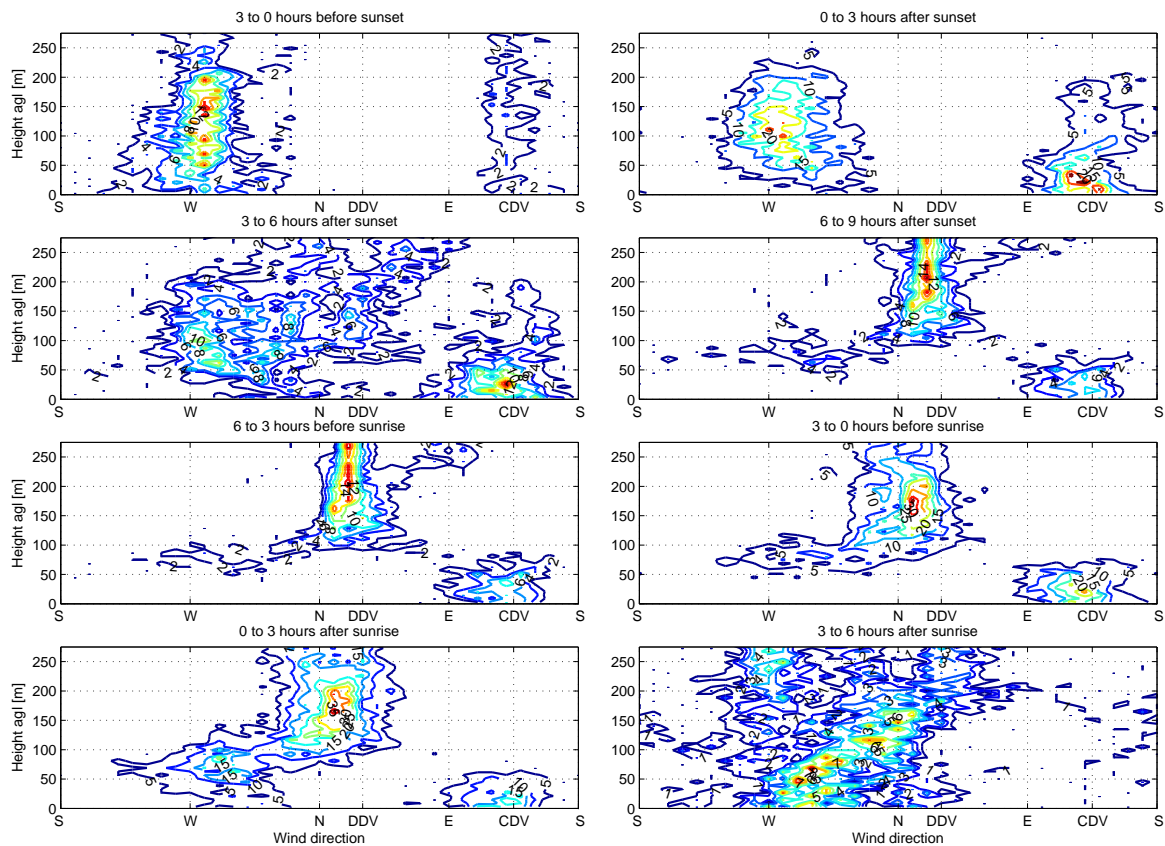


Figure 13. Same as Fig. 4 but for tethered sonde measurements near the M30-site during IOP days only (see Table 1 for dates) and with the indication of the downvalley winds in the Cadarache Valley (CDV) and Durance Valley (DDV) directions.

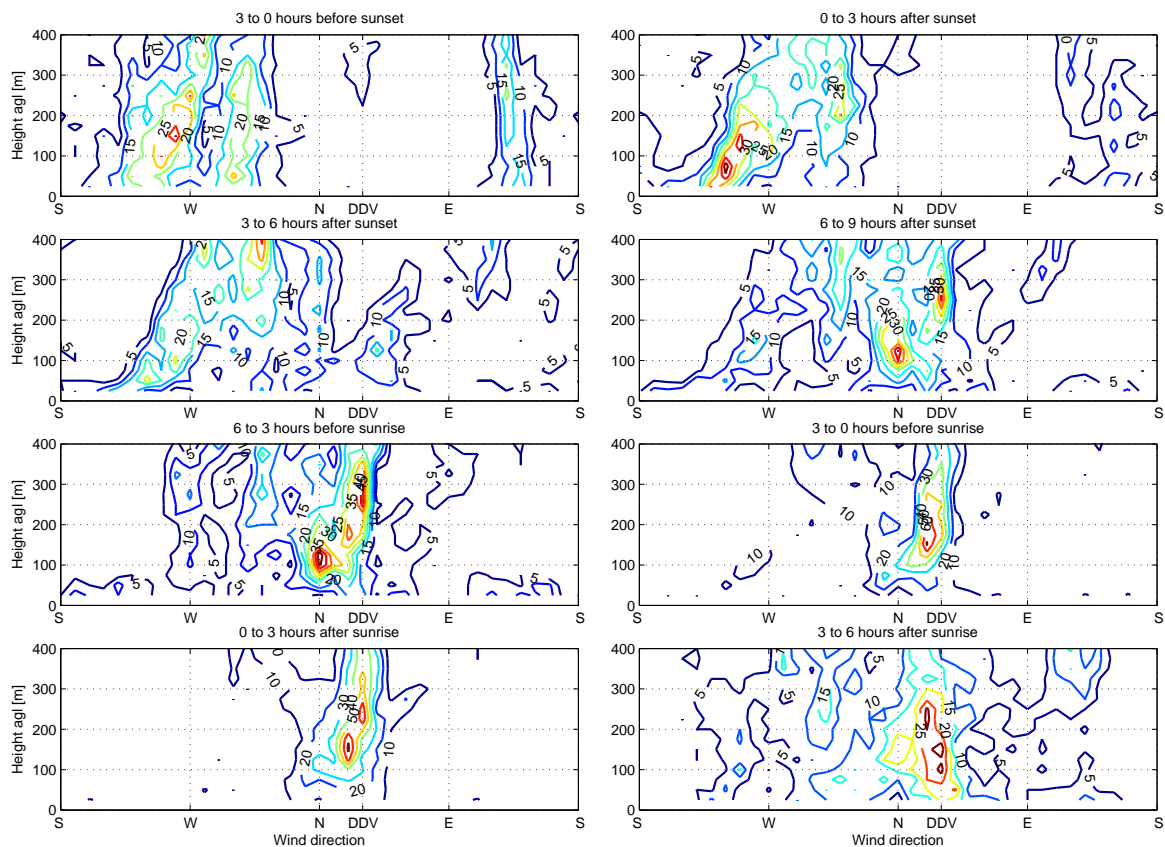


Figure 14. Same as Fig. 4 but for IOP days only (see Table 1 for dates).

References

Arnold D, Morton D, Schicker I, Seibert P, Rotach M, Horvath K, Dudhia J, Satomura T, Müller M, Zängl G, *et al.* 2012. *High resolution modelling*

in complex terrain: report on the HiRCot 2012 Workshop, Vienna, 21-23 February 2012. Institut für Meteorologie, Department Wasser-Atmosphäre-Umwelt, Univ. f. Bodenkultur.

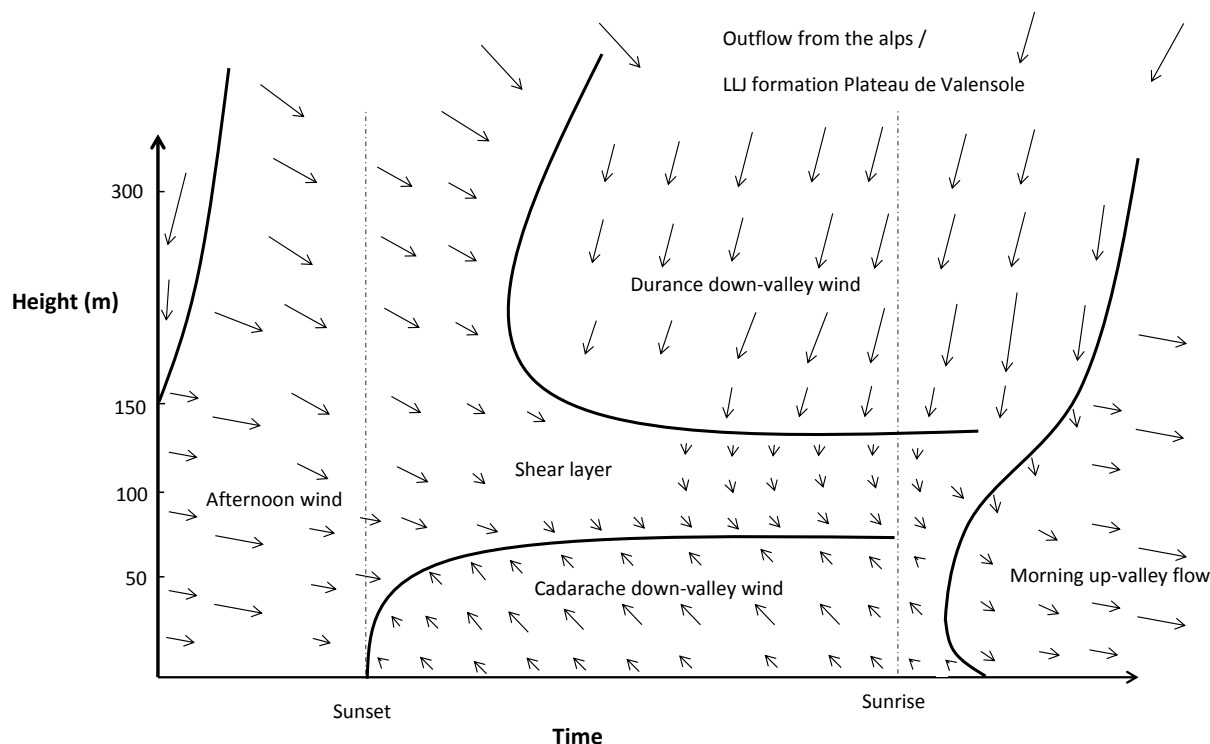


Figure 15. Conceptual drawing of the diurnal wind pattern in and above the Cadarache valley during typical KASCADE conditions (clear sky and weak synoptic forcing).

- Atkinson B. 1995. Orographic and stability effects on valley-side drainage flows. *Bound.-Lay. Meteorol.* **75**(4): 403–428.
- Baghi R, Durand P, Jambert C, Jarnot C, Delon C, Serça D, Striebig N, Ferlicq M, Keravec P. 2012. A new disjunct eddy-covariance system for BVOC flux measurements - validation on CO₂ and H₂O fluxes. *Atmospheric Measurement Techniques* **5**(12): 3119–3132, URL <http://www.atmos-meas-tech.net/5/3119/2012/>. 10.5194/amt-5-3119-2012.
- Barr S, Orgill MM. 1989. Influence of external meteorology on nocturnal valley drainage winds. *J. Appl. Meteorol.* **28**(6): 497–517.
- Bastin S, Drobinski P, Dabas A, Delville P, Reitebuch O, Werner C. 2005. Impact of the Rhône and Durance valleys on sea-breeze circulation in the Marseille area. *Atmos. Res.* **74**(1): 303–328.
- Blackadar AK. 1957. Boundary layer wind maxima and their significance for the growth of nocturnal inversions. *B. Am. Meteorol. Soc.* **38**(5): 283–290.
- Bowen BM, Baars JA, Stone GL. 2000. Nocturnal wind direction shear and its potential impact on pollutant transport. *J. Appl. Meteorol.* **39**(3): 437–445.
- Brazel A, Fernando H, Hunt J, Selover N, Hedquist B, Pardyjak E. 2005. Evening transition observations in Phoenix, Arizona. *J. Appl. Meteorol.* **44**(1): 99–112.
- Bromwich DH. 1989. An extraordinary katabatic wind regime at Terra Nova Bay, Antarctica. *Mon. Wea. Rev.* **117**(3): 688–695.
- Brutsaert W. 1972. Radiation, evaporation and the maintenance of turbulence under stable conditions in the lower atmosphere. *Bound.-Lay. Meteorol.* **2**(3): 309–325.
- Carrera ML, Gyakum JR, Lin CA. 2009. Observational study of wind channeling within the St. Lawrence River Valley. *J. Appl. Meteorol. Clim.* **48**(11): 2341–2361.
- Clements CB, Whiteman CD, Horel JD. 2003. Cold-air-pool structure and evolution in a mountain basin: Peter Sinks, Utah. *J. Appl. Meteorol.* **42**(6): 752–768.
- Cros B, Durand P, Cachier H, Drobinski P, Frejafon E, Kottmeier C, Perros P, Peuch VH, Ponche JL, Robin D, et al. 2004. The ESCOMPTE program: an overview. *Atmos. Res.* **69**(3): 241–279.
- Cuxart J, Yagüe C, Morales G, Terradellas E, Orbe J, Calvo J, Fernández A, Soler M, Infante C, Buenestado P, et al. 2000. Stable atmospheric boundary-layer experiment in Spain (SABLES 98): a report. *Bound.-Lay. Meteorol.* **96**(3): 337–370.
- Delage Y, Bartlett PA, McCaughey JH. 2002. Study of 'soft' night-time surface-layer decoupling over forest canopies in a land-surface model. *Bound.-Lay. Meteorol.* **103**(2): 253–276.
- Doran J, Fast JD, Horel J. 2002. The VTMX 2000 campaign. *B. Am. Meteorol. Soc.* **83**(4): 537–551.
- Drobinski P, Ducrocq V, Alpert P, Anagnostou E, Béranger K, Borga M, Braud I, Chanzy A, Davolio S, Delrieu G, et al. 2013. HyMeX, a 10-year multidisciplinary program on the Mediterranean water cycle. *B. Am. Meteorol. Soc.* .
- Duine GJ. 2014. Kascade 2013 instruments calibration campaign. Technical Report CEA DEN CAD DTN SMTA LMTE NT 2014(11) 11, Commissariat à l'Energie Atomique.
- Durrán DR. 2002. Downslope winds. In: *Encyclopedia of Atmospheric Sciences*, Holton JR, Curry JA, Pyle JA (eds), Elsevier Science Ltd: London, UK, pp. 644–650.
- García-Díez M, Fernández J, Fita L, Yagüe C. 2013. Seasonal dependence of WRF model biases and sensitivity to PBL schemes over Europe. *Q. J. Roy. Meteor. Soc.* **139**(671): 501–514.
- Geerts B. 2003. Empirical estimation of the monthly-mean daily temperature range. *Theor. Appl. Climatol.* **74**(3–4): 145–165.
- Guenard V, Drobinski P, Caccia JL, Campistron B, Bench B. 2005. An observational study of the mesoscale mistral dynamics. *Bound.-Lay. Meteorol.* **115**(2): 263–288.
- Haident T, Whiteman CD. 2005. Katabatic flow mechanisms on a low-angle slope. *J. Appl. Meteorol.* **44**(1): 113–126.
- Hanna SR, Yang R. 2001. Evaluations of mesoscale models' simulations of near-surface winds, temperature gradients, and mixing depths. *J. Appl. Meteorol.* **40**(6): 1095–1104.
- Hoch S, Calanca P, Philipona R, Ohmura A. 2007. Year-round observation of longwave radiative flux divergence in Greenland. *J. Appl. Meteorol. Clim.* **46**(9): 1469–1479.
- Horst T, Doran J. 1986. Nocturnal drainage flow on simple slopes. *Bound.-Lay. Meteorol.* **34**(3): 263–286.
- Jackson LS, Forster PM. 2010. An empirical study of geographic and seasonal variations in diurnal temperature range. *J. Climate* **23**(12): 3205–3221.
- Jiménez MA, Cuxart J. 2014. A study of the nocturnal flows generated in the north side of the Pyrenees. *Atmos. Res.* **145**: 244–254.
- Kalthoff N, Kottmeier C, Thürauf J, Corsmeier U, Said F, Fréjafon E, Perros P. 2005. Mesoscale circulation systems and ozone concentrations during ESCOMPTE: a case study from IOP 2b. *Atmos. Res.* **74**(1): 355–380.
- Kalverla P. 2014. Evaluation of the weather research and forecasting model for contrasting diurnal cycles in the durance valley complex terrain during the kascade field campaign. *MSc Thesis Wageningen University* .
- Kraus H, Malcher J, Schaller E. 1985. A nocturnal low level jet during PUKK. *Bound.-Lay. Meteorol.* **31**(2): 187–195.
- Largeroy Y. 2010. Dynamique de la couche limite atmosphérique stable en relief complexe. application aux épisodes de pollution particulière des vallées alpines. PhD thesis, Grenoble University.

- Largerone Y, Staquet C, Chemel C. 2013. Characterization of oscillatory motions in the stable atmosphere of a deep valley. *Bound.-Lay. Meteorol.* **148**(3): 439–454.
- Mahrt L. 1982. Momentum balance of gravity flows. *J. Atmos. Sci.* (39): 2701–2711.
- Mahrt L. 1999. Stratified atmospheric boundary layers. *Bound.-Lay. Meteorol.* **90**(3): 375–396.
- Mahrt L. 2014. Stably stratified atmospheric boundary layers. *Annu. Rev. Fluid Mech.* **46**: 23–45.
- Mahrt L, Larsen S. 1990. Relation of slope winds to the ambient flow over gentle terrain. *Bound.-Lay. Meteorol.* **53**(1–2): 93–102.
- Manins P, Sawford B. 1979. Katabatic winds: A field case study. *Q. J. Roy. Meteor. Soc.* **105**(446): 1011–1025.
- Margerit Y. 2006. Analyse des données météorologiques, gradient thermique, pluviométrie et humidité sur la zone de Cadarache. Technical Report CEA DEN CAD DTN SMTM LMTE NT 2006(07) 30, Commissariat à l’Energie Atomique.
- Mestayer PG, Durand P, Augustin P, Bastin S, Bonnefond JM, Bénech B, Campistron B, Coppalle A, Delbarre H, Dousset B, *et al.* 2005. The urban boundary-layer field campaign in Marseille (UBL/CLU-ESCOMPTE): set-up and first results. *Bound.-Lay. Meteorol.* **114**(2): 315–365.
- Monti P, Fernando H, Princevac M, Chan W, Kowalewski T, Pardyjak E. 2002. Observations of flow and turbulence in the nocturnal boundary layer over a slope. *J. Atmos. Sci.* **59**(17): 2513–2534.
- Nadeau DF, Pardyjak ER, Higgins CW, Huwald H, Parlange MB. 2013. Flow during the evening transition over steep alpine slopes. *Q. J. Roy. Meteor. Soc.* **139**(672): 607–624.
- Nappo CJ. 2012. *An introduction to atmospheric gravity waves*, vol. 102. Academic Press.
- Nieuwstadt FT. 1984. The turbulent structure of the stable, nocturnal boundary layer. *J. Atmos. Sci.* **41**(14): 2202–2216.
- Oke TR. 1987. *Boundary layer climates: second edition*. Routledge, London, ISBN 0-415-04319-0.
- Poulos GS, Blumen W, Fritts DC, Lundquist JK, Sun J, Burns SP, Nappo C, Banta R, Newsom R, Cuxart J, *et al.* 2002. CASES-99: A comprehensive investigation of the stable nocturnal boundary layer. *B. Am. Meteorol. Soc.* **83**(4): 555–581.
- Price J, Vosper S, Brown A, Ross A, Clark P, Davies F, Horlacher V, Claxton B, McGregor J, Hoare J, *et al.* 2011. COLPEX: field and numerical studies over a region of small hills. *B. Am. Meteorol. Soc.* **92**(12): 1636–1650.
- Quénol H, Beltrando G. 2008. Impact of a new railway line embankment (Mediterranean TGV) on the frequency of spring frosts in a fruit-growing area of the Durance Valley (south of France). *Meteorol. Appl.* **15**(3): 389–398.
- Reiter E. 1971. Digest of Selected Weather Problems of the Mediterranean. Technical Report 9-71, Navy Weather Research Facility.
- ReVelle DO. 1993. Chaos and “bursting” in the planetary boundary layer. *J. Appl. Meteorol.* **32**(7): 1169–1180.
- Salameh T, Drobinski P, Menut L, Bessagnet B, Flamant C, Hodzic A, Vautard R. 2007. Aerosol distribution over the western Mediterranean basin during a Tramontane/Mistral event. *Ann. Geophys.* **25**(11): 2271–2291, URL <https://hal.archives-ouvertes.fr/hal-00330152>.
- Salmond J, McKendry I. 2005. A review of turbulence in the very stable nocturnal boundary layer and its implications for air quality. *Prog. Phys. Geog.* **29**(2): 171–188.
- Savijärvi H. 2006. Radiative and turbulent heating rates in the clear-air boundary layer. *Q. J. Roy. Meteor. Soc.* **132**(614): 147–161.
- Skyllingstad ED. 2003. Large-eddy simulation of katabatic flows. *Bound.-Lay. Meteorol.* **106**(2): 217–243.
- Smedman AS. 1988. Observations of a multi-level turbulence structure in a very stable atmospheric boundary layer. *Bound.-Lay. Meteorol.* **44**(3): 231–253.
- Smith CM, Skillingstad ED. 2005. Numerical simulation of katabatic flow with changing slope angle. *Mon. Wea. Rev.* **133**(11): 3065–3080.
- Steenekveld G, Wokke M, Zwaafink CG, Pijlman S, Heusinkveld B, Jacobs A, Holtslag A. 2010. Observations of the radiation divergence in the surface layer and its implication for its parameterization in numerical weather prediction models. *J. Geophys. Res.* **115**: D06107. Doi:10.1029/2009JD013074.
- Sterk H, Steenekveld G, Holtslag A. 2013. The role of snow-surface coupling, radiation, and turbulent mixing in modeling a stable boundary layer over arctic sea ice. *J. Geophys. Res.-Atmos.* **118**(3): 1199–1217.
- Stull RB. 1988. *An introduction to boundary layer meteorology*. Kluwer Academic Publishers, ISBN 90-277-2769-4.
- Sun J, Burns S, Delany AC, Oncley S, Horst T, Lenschow D. 2003. Heat balance in the nocturnal boundary layer during CASES-99. *J. Appl. Meteorol.* **42**: 1649–1666.
- Thompson B. 1986. Small-scale katabatics and cold hollows. *Weather* **41**(5): 146–153.
- Triantafyllou A, Kassomenos P. 2002. Aspects of atmospheric flow and dispersion of air pollutants in a mountainous basin. *Sci. Total Environ.* **297**(1): 85–103.
- Wallace JM, Hobbs PV. 2006. *Atmospheric science: an introductory survey*, vol. 92. Academic press.
- Warner RF. 2006. Natural and artificial linkages and discontinuities in a Mediterranean landscape: Some case studies from the Durance Valley, France. *Catena* **66**(3): 236–250.
- Weber RO, Kaufmann P. 1998. Relationship of synoptic winds and complex terrain flows during the MISTRAL field experiment. *J. Appl. Meteorol.* **37**(11): 1486–1496.
- Whiteman CD, Doran JC. 1993. The relationship between overlying synoptic-scale flows and winds within a valley. *J. Appl. Meteorol.* **32**(11): 1669–1682.
- Whiteman CD, Hoch SW, Hahnenberger M, Muschinski A, Hohreiter V, Behn M, Cheon Y, Zhong S, Yao W, Fritts D, *et al.* 2008. METCRAX 2006: Meteorological experiments in Arizona’s Meteor crater. *B. Am. Meteorol. Soc.* **89**(11): 1665–1680.
- Wrathall J. 1985. The Mistral And Forest Fires In Provence - Côte D’Azur, Southern France. *Weather* **40**: 119–124. Doi: 10.1002/j.1477-8696.1985.tb07493.x.
- Zanetti P. 1990. Air pollution modelling. *Southampton-UK: Comp. Mech. Publications*.

Chapter 5

Cadarache down-valley wind nowcast

5.1 Abstract of the article

The latter section has shown that the Cadarache down-valley (CDV) wind was a dominant wind during the KASCADE observation period. The Cadarache meteorological instrumentation network lacks observations in the range of the CDV wind, i.e. between the surface and 50 m no valid wind measurements are available. However, it is essential to know its occurrence, as some of Cadarache research installations are embedded in the Cadarache Valley. This paper¹ investigates the possibility to use the observations directly available from the 110 m tower GBA in order to nowcast the CDV wind.

The valley winds observed during the campaign are first categorized according to the work of Whiteman and Doran (1993), in order to determine what are the main drivers of the CDV wind. To nowcast this wind, a methodology is developed using a dichotomous forecast verification principle (Wilks, 2011). This method allows to optimize a threshold on a parameter, being able to nowcast the drainage flow as observed at 10 m agl in the middle of the CV (M30 location). Among the potential predictors available from the continuously operating GBA tower, three candidates were chosen based on the various possible forcings (dynamical or thermal): a vertical temperature difference (ΔT between heights of 110 m and 2 m), wind speed U at 110 m (U_{110m}) and their combination in the form of a bulk Richardson number (Ri_B). The method is based on a forecast verification principle, for which throughout the range of predicted variables the statistics 'proportion correct' and 'bias' are calculated. Using this method gives insight into the predictability of the CDV wind.

The results demonstrate that CDV wind is a thermally driven flow. For an observed 10 m wind, the ΔT value of 1.5°C scores highest (0.91), better than the Ri_B value of 0.8 (0.86) and the U_{110m} value of 3.4 m s^{-1} (0.72). The applicability of the threshold is also demonstrated for winds observed at a height of 2 and 30 m during the KASCADE campaign, and even for summer conditions thanks to complementary observations done in the CV during the mid-July to end of September period.

The general applicability of the found threshold allowed a reconstruction of the CDV flow in the form of a 5-year monthly climatology. It shows that the CDV flow exists throughout the year and is strongly related to night duration. The representativeness of the 3-month stability occurrence during the KASCADE campaign is analysed relative to the 2007 - 2011 period, showing that December 2012 and February 2013 had more than 'normal' stable periods. During January and especially March 2013 stable periods were less frequent.

Daily operational forecasts are necessary to anticipate the behaviour of potentially hazardous emission. However, the CV is too small for mesoscale meteorological models at 1 kilometer resolution to forecast the drainage wind. The methodology presented in the paper can be used to infer the CDV wind by a combination of dynamical and statistical downscaling.

5.2 Article

¹This chapter is under revision:

Duine G., T. Hedde, P. Roubin and P. Durand (2015). A simple method based on routine observations to nowcast down-valley flows in shallow, narrow valleys, *Journal of Applied Meteorology and Climatology*, under review.

A simple method based on routine observations to nowcast down-valley flows in shallow, narrow valleys

Gert-Jan Duine^{1,2}, Thierry Hedde¹, Pierre Roubin¹, and Pierre Durand²

¹Laboratoire de Modélisation des Transferts dans l'Environnement, CEA Cadarache, France

²Laboratoire d'Aérodynamique, University of Toulouse, Toulouse, France

Abstract

A simple relation to diagnose the existence of a thermally driven down-valley wind in a shallow (100 m deep) and narrow (1 - 2 km wide) valley based on routine weather measurements has been determined. The relation is based on a method which has been derived from a forecast verification principle. It consists in optimizing a threshold of permanently measured quantities to nowcast the Cadarache (southeastern France) down-valley wind. Three parameters permanently observed at a 110-m high tower have been examined: the vertical temperature difference (between 110 m and 2 m), the wind speed at 110 m and a bulk Richardson number. The thresholds are optimized thanks to the wind observations obtained within the valley during the field experiment KASCADE, which was conducted in the winter of 2013. The highest predictability (correct nowcasting ratio of 0.91) was found for the temperature difference at a threshold value of 1.5°C (or 2.6°C for potential temperature). The applicability of the method to other heights (2 and 30 m) and to summer conditions is also demonstrated. This allowed a reconstruction of the climatology of the down-valley wind which demonstrates that the wind exists throughout the year, and is strongly linked to nighttime duration. This threshold technique will allow to forecast the subgrid-scale down-valley wind from operational numerical weather coarse grid simulations by means of statistical downscaling.

1 Introduction

Under clear skies and weak synoptic forcing, stable stratification develops during the night. Due to surface radiative heat loss, the air layer close to the ground becomes denser than the layer above (Stull, 1988). Over sloping terrain a horizontal temperature gradient forms and the air will start to flow downslope as a consequence of negative buoyancy

(Manins and Sawford, 1979; Haiden and Whiteman, 2005). The valley and drainage winds appearing on scales from meters (Mahrt et al., 2001) to tens of kilometers (Jiménez and Cuxart, 2014) have been studied all over the globe (Barry, 2013). The down-valley flows are mostly independent of above-valley wind conditions (Whiteman and Doran, 1993), especially in narrow valleys. They have been documented in climatological studies for valley systems at different scales (Stewart et al., 2002), or categorized as a combination of several parameters, such as net radiation, cooling rate and a temperature difference (Gudiksen, 1989; Amanatidis et al., 1992).

Local measurements and observational analyses of down-valley flows remain necessary due to distinct valley geometries and their influences on the flow pattern (Atkinson, 1995; Sheridan et al., 2014), especially under stable stratification conditions where pollutant concentration can be highest due to weak dilution. Methods to analyze and predict the down-valley flow characteristics by means of observations have been developed to a large extent, in the form of a radiation Richardson number (Mahrt et al., 2001) or a temperature difference on the vertical (Amanatidis et al., 1992). Drainage depths are determined by means of ambient wind conditions (Barr and Orgill, 1989) or with a combination of ridge top wind speed and strength and depth of the inversion (Horst and Doran, 1986). However, the studies devoted to predict the down-valley flows are mostly based on observations which are rarely available on a routine basis.

The KASCADE-campaign has been conducted in southeastern France during the winter of 2013 and revealed the dominant existence of a down-valley flow in a shallow and narrow valley, the Cadarache Valley (CV - Duine et al., 2015). This Cadarache down-valley (CDV) wind has been characterized as a thermally driven wind. It occurs mostly during stable stratification periods and is restricted to the valley depth, which is around 100 m. Many facilities of the Cadarache site, one of the research centers

of the Commissariat à l’Energie Atomique et aux Energies Alternatives (CEA), lay in the CV, and could potentially emit pollutants in the atmosphere. No measurements are available on a routine basis at the height and location of this CDV wind, but its conditions of existence are to be known for risk management purposes.

Consequently, a methodology has been developed using a dichotomous forecast verification principle (Wilks, 2011) to optimize a threshold, enabling to nowcast the down-valley flow presence or absence. As within narrow valleys local meteorology and cold pools can be dominant and do not always reflect the regional meteorology, this method could be generally applied, although its performance highly depends on the valley geometry. To verify the method, a combination of permanent and temporary measurements has been used. From the permanently installed 110 m tower, three potential quantities to nowcast the down-valley flow are available: a vertical temperature difference (between the top of the tower and 2 m), the wind speed at the top of the tower and a combination of the previous two data in the form of a bulk Richardson number. For validation, a temporarily installed mast in the valley is used, equipped with sonic anemometers at three levels from which the CDV wind can be characterized. This 30-m high tower has been deployed during the KASCADE campaign and enabled continuous observations of the valley winds in the CV. The computed thresholds are evaluated at the three several levels and for different seasons.

The paper is organized as follows. In Sects. 2.1 and 2.2 the measurement strategy and the general wind behavior in the CV observed during the KASCADE-campaign are explained. The methodology to optimize the threshold is presented in Sect. 2.3 and the candidates for down-valley wind predictors are introduced in Sect. 2.4. Results for the optimized thresholds are given in Sect. 3. The choice for the best predictor, its applicability to different heights of the CDV wind and to seasons other than winter is discussed in Sect. 4. Applications of this threshold methodology including a 5-year climatology are given in Sect. 5, and final conclusions and perspectives are given in Sect. 6.

2 Site, observations and methodology

2.1 Valley description and measurement set-up

The CV constitutes the main part of the Cadarache site (Fig. 1). The valley axis is indicated by the

red arrow pointing downslope. Its length is around 6 km until it meets the Durance Valley which is much larger and oriented almost perpendicularly to the CV. The CV is shallow (100 m) and narrow (1 - 2 km), which leads to an aspect ratio (valley depth to its width) of 0.04. The average slope along the valley bottom is 1.2° , whereas the slope of the side-walls is estimated at around 6° . The land use in the valley is a mixture of deciduous forest, grass, buildings and artificial surfaces, but grass dominates in the valley bottom and deciduous forest on the side-walls.

Two measurement towers deployed during KASCADE are used in this study: the permanently installed 110-m high tower at La Grande Bastide (GBA) and the 30-m flux tower (M30), installed for the campaign duration only. Both towers are situated on the axis of the CV, the GBA near to the lower end, and the M30 halfway of the valley length. The GBA-tower is only equipped with sensors at its top and bottom: wind and temperature are measured at 110 m, and temperature at screen level (2 m). The top level of the GBA-tower is situated above the CV sidewalls and therefore does not experience the inside-CV processes. M30 was instrumented with sonic anemometers at heights of 2, 10 and 30 m. A full list of the other M30-sensors, and other details and results of the campaign can be found in Duine et al. (2015).

2.2 Wind behavior in the Cadarache Valley

The flow within a valley has been related to the above-valley wind conditions by Whiteman and Doran (1993) who classified this relationship into four types: thermally driven, downward momentum transport, forced channeling and pressure driven channeling. These relationships are indicated by the lines in Figs. 2a to 2c, after adaptation to the CV orientation, i.e. SE for down-valley winds and NW for up-valley winds. The behavior of our observations with respect to this theoretical framework is presented in Fig. 3, which shows the wind direction measured within the CV at 10 m from the M30 tower and above the valley at 110 m from the GBA tower. Figure 3a shows the occurrences of the wind direction at 110 m, with a classification of the wind origin on the mesoscale. The three lower pictures show inside valley (M30) against above-valley wind directions (GBA). They all show the same data but are further classified with respect to a threshold defined either on the wind speed at 110 m at GBA U_{110m} (Fig. 3b), or the atmospheric stratification as characterized by the temperature difference ΔT between 110 and 2 m at GBA (Fig. 3c), or a bulk Richardson number Ri_B (Fig. 3d):

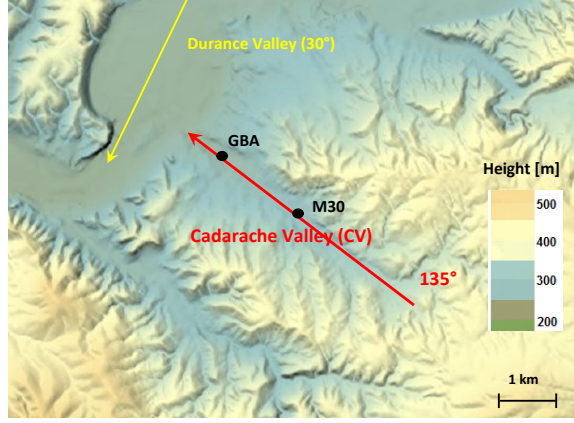


Figure 1: The Cadarache Valley (CV) and the middle Durance Valley. The red line indicates the CV axis orientation and length. The downslope directions of the bottom of the two valleys are marked by the arrow heads. The 110-m high tower La Grande Bastide (GBA) and the 30-m high tower M30 are both on the axis of the CV. Source: Geoportail.gouv.fr (IGN).

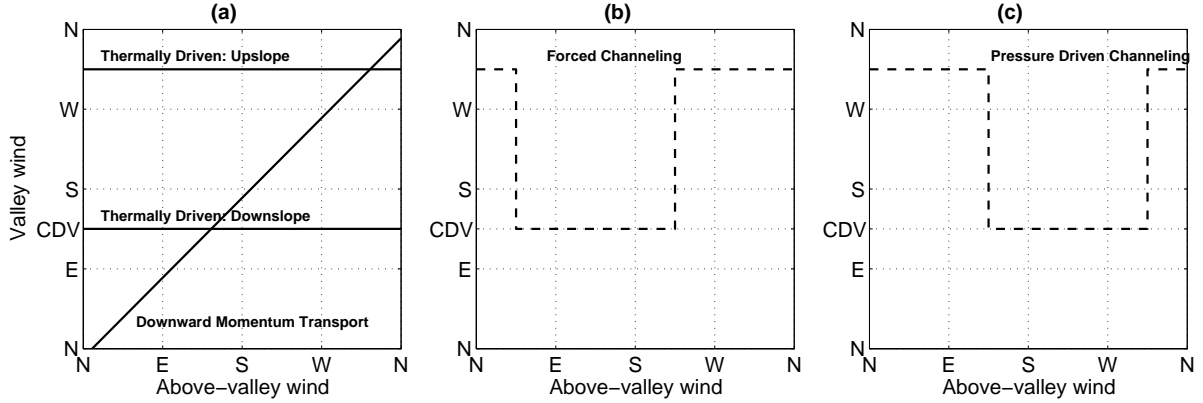


Figure 2: Inside-valley wind direction against above-valley wind direction according to Whiteman and Doran (1993), adapted to the CV. The direction for the Cadarache down-valley (CDV) is indicated on the y-axis. The different configurations are split in three diagrams (a, b and c) for a better legibility.

$$Ri_B = \frac{g \cdot (\Delta T + \Gamma_d \Delta z) \cdot \Delta z}{T_{110m} \cdot (\Delta U)^2} \quad (1)$$

with g being the gravitational acceleration of 9.81 m s^{-2} and Γ_d the dry adiabatic lapse rate of 9.8 K km^{-1} for potential temperature calculation. Δz corresponds to the height difference between the temperature measurements. The usage of Ri_B to our purpose is further detailed in Sect. 2.4. The classifications used in the figure are used as a first step in the analysis to describe the important features of the valley adapted to the theoretical framework presented in Fig. 2. The fixed thresholds are arbitrarily chosen and relatively simple, i.e. an arbitrary wind speed threshold, stable vs. unstable conditions and turbulent vs. laminar regime. Picking up the theoretical framework of Whiteman and Doran (1993) from Fig. 2 and the combination with our measurements (Fig. 3), enables to determine under which conditions the CDV wind develops.

The first group given in Whiteman and Doran (1993) classification of valley winds is a thermally

driven flow, which has an upslope direction during the day, and a downslope direction in the night. This theoretical relationship is indicated in Fig. 2a. Typically, the thermally driven flow is fully independent of above-valley wind conditions. It is especially observed during weak synoptic forcing in combination with clear skies. Relatively narrow valleys like the CV favor the existence of thermally driven flows during such conditions. Figure 3 reveals that during low wind speed conditions (Fig. 3b) or stable periods (Fig. 3c and Fig. 3d) there is a high preference for a down-valley flow within the CV, as a higher density of blue dots can be observed in the CDV direction. The up-valley channeled wind, i.e. NW wind, presents a much more scattered direction than the CDV wind. There are two possible reasons for that: firstly, the orography SE to the M30 location resembles a well-defined valley, whereas NW flows experience a more complex area, composed of the Durance and Cadarache valleys and local hills, before arriving at the M30 site (see Fig. 1); secondly, up-valley, northwesterly winds are generally observed either during high wind speed events such

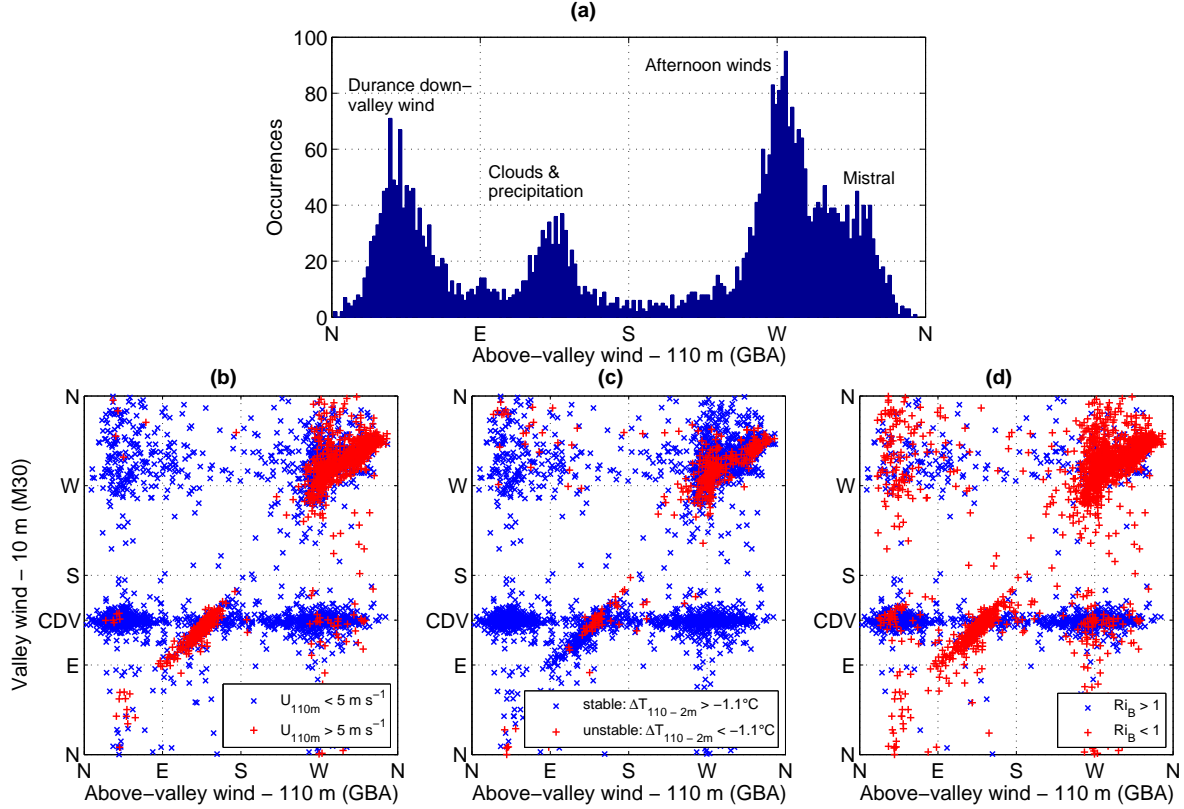


Figure 3: (a) Above-CV wind direction occurrence measured at 110 m, and (b) to (d): wind direction in the CV at 10 m against the above-valley wind direction at 110 m, divided into two classes according to threshold values (defined in the text). Data is from 13 December 2012 to 16 March 2013.

as a Mistral, or during neutral to moderately stable situations, i.e. conditions with sufficient vertical transfer of momentum to imprint the above-valley wind direction into the CV.

Another origin for valley winds is identified by Whiteman and Doran (1993) as downward momentum transport. For this relationship, the flow within the valley is totally dependent on the above-valley wind. The theoretical relationship is indicated by the diagonal line in Fig. 2a. It is favored by a wide valley (Whiteman and Doran, 1993) and can be mostly observed during unstable and neutral conditions. Such situations are highlighted by the red dots for either high wind speeds (Fig. 3b) or unstable conditions (Figs. 3c and 3d). In the CV, downward momentum transport occurs mostly for SE and NW upper winds, as the highest occurrences are found in these quadrants. The westerly directions are mostly measured during daytime, when instability is causing upslope anabatic flows, and/or during Mistral events which have west to northwest directions in the region. The SE-directions are typically observed during cloudy or precipitation events (Duine et al., 2015). Note that the latter conditions cause a direction which is intermingled with the CDV wind, but can be very well distinguished by means of the colors (e.g. red crosses on Fig. 3d).

Two other relationships are indicated by Whiteman and Doran (1993) as forced channeling and pressure driven channeling. Forced channeling (Fig. 2b) is favored during unstable and neutral conditions within narrow valleys (Weber and Kaufmann, 1998) while pressure driven channeling (Fig. 2c) typically occurs when moderately stable conditions are dominant in wide and shallow valleys (Carrera et al., 2009). Based on the figures, as the typical relation for forced or pressure-driven channeling are not visible, we conclude that these relationships are non-dominant mechanisms for a CDV wind to develop.

Thus, it is clear that the CDV wind mainly develops during stable conditions and low wind speeds. Although the GBA-tower does not provide wind measurement inside the CV, Fig. 3 reveals the plausibility of a relationship between the GBA-tower measurements and the occurrence of the CDV wind. The objective is now to find an optimal threshold under which the CDV wind can be inferred from GBA-observations only and without any wind measurement in the valley.

Table 1: Contingency table for verification of CDV wind occurrence. See text for the criteria used.

Criterion (GBA): ΔT , U_{110m} or Ri_B	Wind observations (M30)		
	CDV wind		No CDV wind
	Satisfied	a	b
	Not satisfied	c	d

2.3 Procedure for threshold optimization

To optimize a threshold based on the GBA observations, we use a procedure that defines a quality index based on contingency table values. The method is used for verification of non-probabilistic forecasts of bilateral events (Wilks, 2011). The principle relies on dichotomous predictors, so by using a threshold on GBA observations we define a bilateral predictor with which we can nowcast the CDV wind. In our case, the bilateral event is the CDV wind presence or absence. The threshold candidates coming from GBA observations are introduced in the next section.

We define the contingency table (Table 1). The letters a to d in the table are the count of occurrences for each couple of events, i.e. CDV wind observed or no CDV wind observed vs. CDV wind nowcasted or no CDV wind nowcasted. The thermally driven CDV wind is diagnosed from M30 observations when the wind direction is in the range $[90^\circ - 180^\circ]$. A sensitivity study to restrict the down-valley wind to smaller direction ranges, e.g. between 110° and 160° , did not influence the final results. The letters in the contingency table are described as follows:

- a) Correct nowcast or hit: A CDV wind is nowcasted and has been observed at M30.
- b) False alarm: a CDV wind is nowcasted but has not been observed.
- c) Missed nowcast: a CDV wind is not nowcasted, but has been observed.
- d) Correct rejection: a CDV wind is neither nowcasted nor observed.

To find the optimal threshold for the predictor criteria given in Table 1 we use the combined counts of the contingency table values by applying two different tests (Wilks, 2011)

$$PC = \frac{a + d}{a + b + c + d} \quad (2)$$

$$bias = \frac{a + b}{a + c} \quad (3)$$

where the "Proportion Correct" PC represents the fraction of the total number of events n ($n =$

$a + b + c + d$) for which the threshold correctly classified an event (a) or non-event (d). To optimize the PC , a and d should be as high as possible, and b and c as low as possible. It is a ratio ranging from 0 to 1, the higher the value for PC , the better the threshold-value for a given criterion. The $bias$ is used to evaluate the balance between the number of nowcasted CDV wind events to the number of observed CDV wind events. It is expressed as overnowcasting (>1) or undernowcasting (<1) of the event and should therefore be as close to 1 as possible. Equations 2 and 3 are the framework for choosing an optimized threshold.

All data of the winter of 2013 collected during the KASCADE continuous measurement period are used, i.e. from 13 December 2012 to 16 March 2013. The values are 30-minute averaged. A minimum threshold of 0.5 m s^{-1} is applied to wind speed because for lower wind speeds the wind direction is ill-defined. All values inside the SE-SE quadrant are discarded because this quadrant is blurred with two types of conditions: the stable conditions which favor a thermally driven CDV wind on the one hand and the cloudy weather and precipitation events which typically occur under southeasterly winds (Duine et al., 2015) on the other hand.

2.4 Threshold candidates

The purpose is to find which measured quantity at GBA can be best used to nowcast the CDV wind. The threshold optimization procedure (see Sect. 2.3) is applied to quantities derived from the GBA available measurements:

- 1) a vertical temperature difference $\Delta T = T_{110m} - T_{2m}$
- 2) the wind speed at 110 m U_{110m}
- 3) a combination of ΔT and U_{110m} in the form of a bulk Richardson number Ri_B (see Eq. 1).

The Richardson number is a good indicator for stability, as it relates wind speed to buoyancy and is classically used to assess stability inside air masses. It has been used before as a predictor for shallow drainage flows (Mahrt et al., 2001), with the addition of longwave radiation, which defines a radiation Richardson number. Unfortunately, there are no routine observations of net longwave radiation,

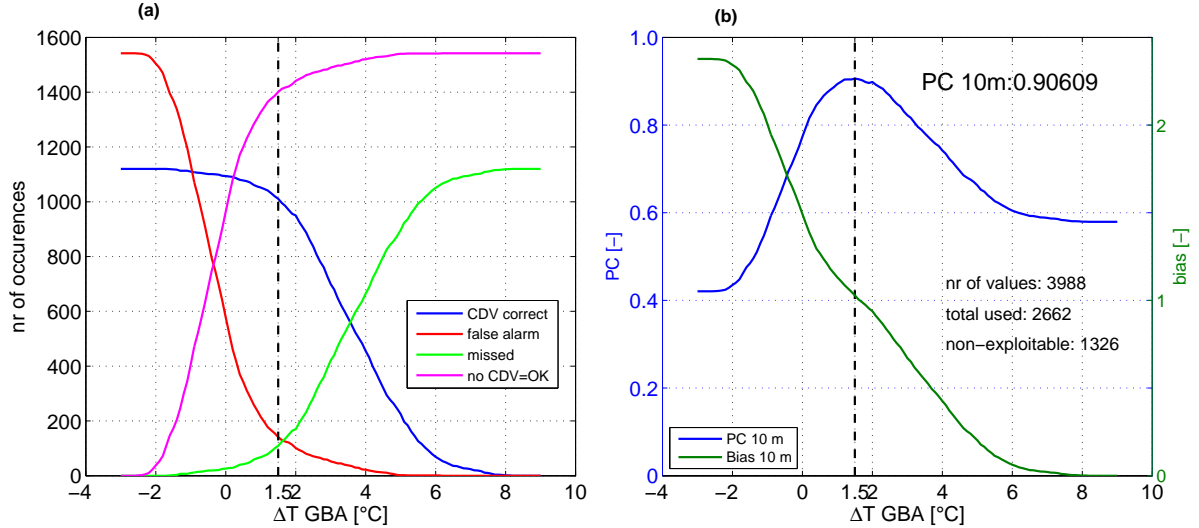


Figure 4: (a) Contingency table values for the different events as defined in Table 1, calculated for the ΔT criterion and (b) values of PC (blue line, left scale) and $bias$ (green line, right scale). The vertical dashed lines indicate the threshold value for which the best score is obtained. Data from 13 December 2012 to 16 March 2013.

thus we must rely on wind speed and a vertical temperature difference only.

Note that we have adapted the classical Ri_B to the availability of observations: humidity measurements at the GBA-site are only available at 2 m. Thus, we cannot determine a virtual temperature T_v at 110 m so we must base ourselves on the difference in absolute temperature T alone. The influence of neglecting the humidity variation in Eq. 1 has been checked by tethered balloon measurements which were deployed at location M30 (Fig. 1) during the KASCADE-campaign and showed little difference between the use of T vs. T_v : a relative error of around 2% on Ri_B is determined. The Ri_B increment used for optimization was taken as 0.1 and so in the range of interest for Ri_B (i.e. -1 to 5) the moisture-related error is lower than this increment and therefore does not affect the result. Furthermore, wind speed observations are only available at the height of 110 m. Consequently, we will assume that $U(2m) = 0$, so that $\Delta U \sim U_{110m}$. This assumption is probably not a major source of error, because a study of the GBA site characteristics, based on wind profiles from a SODAR and two measurement stations at the Cadarache site, has shown that the roughness length z_0 is 1.03 m and the zero-plane displacement height is of the order of 5 m. The 2-m level is therefore in the local roughness sub-layer, whereas the 110-m level observations are representative of a much larger area.

3 Results

3.1 Threshold ΔT_T

The contingency table values of PC and $bias$, as defined in Table 1 and in Eqs. 2 and 3, are presented in Figs. 4a and 4b for the temperature difference ΔT varying in the range -3 to 9°C by increments of 0.1°C. The optimized values are given in Table 2.

A maximum score of 0.91 for PC is obtained for the temperature difference threshold $\Delta T_T = 1.5^\circ\text{C}$ (vertical dashed line in both pictures). The value of ΔT_T represents the best separation value for which a thermally driven CDV wind (i.e. not thermally driven) is nowcasted when $\Delta T > \Delta T_T$ or a non-CDV wind is nowcasted if $\Delta T < \Delta T_T$. The high value for PC at ΔT_T reflects the relevance of the criterion and the threshold chosen. It further indicates that ΔT_T is a good candidate for this procedure. This is emphasized by the small but relatively high peak of the PC curve. This threshold is a rather safe one, as PC drops quickly when the value is set at higher or lower temperature differences. The skill of the optimum threshold is further reflected in the $bias$ of 1.03, which is very close to 1, the optimal value. The ratio of missed events $b + c$ is 0.09, see Sect. 4.1 for more details.

The value of 1.5°C corresponds to a potential temperature difference of approximately 2.6°C . This quite high value confirms that the wind inside CV is primarily thermally driven and can be linked to very stable situations.

Table 2: Optimized threshold values and contingency table values for the candidate criterions.

Type	ΔT	U_{110m}	Ri_B
Threshold unit	[°C]	[m s ⁻¹]	[-]
Height [m]	10	10	10
Season	winter	winter	winter
Threshold	1.5	4.0	0.8
PC	0.91	0.72	0.86
Bias	1.03	1.43	1.15
a	1011	993	1029
b	141	601	273
c	109	144	108
d	1401	961	1289
n	2662	2699	2699

3.2 Threshold U_T

The second criterion under investigation to nowcast the CDV wind is based on the wind speed at 110 m. The same procedure is followed as for ΔT_T (Sect. 3.1) with increments of 0.1 m s⁻¹ in the range 0.5 m s⁻¹ to the maximum observed wind speed. The results are shown in Fig. 5 and Table 2.

We find an optimal threshold for U_T at 4.0 m s⁻¹, with a PC of 0.72. This is the highest score at which a separation can be made to nowcast either a thermally driven CDV wind ($U < U_T$) or a non-CDV wind ($U > U_T$). The maximum value for PC based on U_{110m} is lower than based on ΔT_T . It indicates that a threshold based on wind speed is not as good as when using ΔT_T as a CDV wind predictor. The respective higher and lower counts for false alarm b and correct rejection d (Table 2) point out why the skill is lower for U_T than for ΔT_T . Besides, at the optimal threshold, the false alarm value b is 4 times higher than the missed value c . This indicates that a CDV wind is nowcasted too leniently, which is also reflected in the *bias*-value of 1.43, translating as an overforecast of the event. Note also that the peak for PC is flatter than for ΔT_T , which means that using U_T alone as a predictor for the CDV wind is not an indisputable method. Overall, the wind speed at 110 m does play a role in the existence of a CDV wind, but is not as relevant as the vertical temperature difference.

3.3 Threshold Ri_{B_T}

The last quantity we check is the bulk Richardson number Ri_B (Eq. 1). The results are shown in Fig. 6 and Table 2. A PC -score of 0.86 is found at the threshold $Ri_{B_T} = 0.8$. The corresponding PC -value of 0.86 is high, but still lower than for ΔT_T . It is remarkable that the PC -value sharply rises when passing the zero-line of Ri_B , confirming

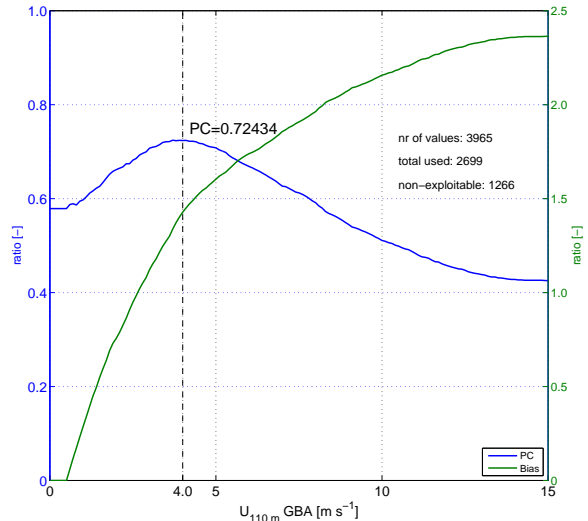


Figure 5: Same as Fig. 4b but for a criterion based on 110 m wind speed measurements at GBA. The optimal threshold is found at 4.0 m s⁻¹. Data from 13 December 2012 to 16 March 2013.

the fact that the CDV wind is indeed strongly related to stability. The values of PC at the right side of the peak are relatively high with respect to the peak value itself, which is an extra indication that the Ri -criterion may work less good. At the threshold-value of Ri_B , the number of false alarms b is twice as large as missed classifications c (Table 2). Therefore, the optimal threshold Ri_{B_T} of 0.8 results in some overnowcasting of the CDV wind, as is also indicated by the quite high value of the *bias* (1.15).

The value of $Ri_{B_T} = 0.8$ is a little lower than the threshold value of 1.0 which theoretically marks the transition from turbulent to non-turbulent regime in stable conditions. It is difficult to ascertain whether the difference between these two values is significant, because the height range in which Ri_B is computed is quite large (108 m), and the uncertainty on Ri -estimates through a 'bulk' assumption increases with the thickness of the layer, especially close to the surface where the vertical gradients are the highest (Stull, 1988). Furthermore, another reason of the lesser success for Ri_{B_T} than for ΔT_T may lie in the hysteresis behavior of critical Ri -thresholds, i.e. different values when passing from laminar to turbulent regime or vice versa (McTaggart-Cowan and Zadra, 2014). In this study, both transitions are mixed, and so could lower the score.

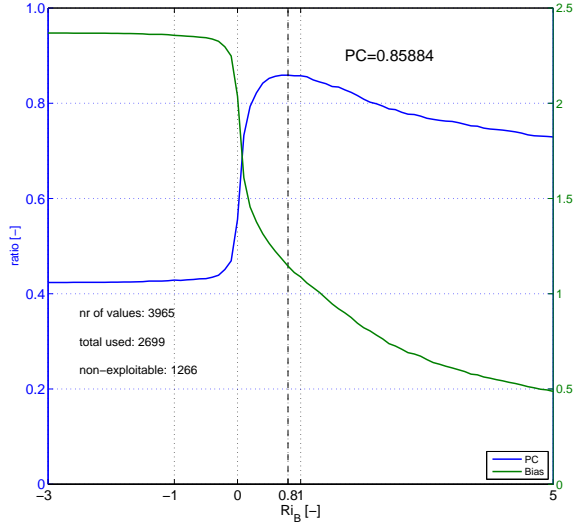


Figure 6: Same as Fig. 4b but for an optimization by means of a bulk Richardson number. The optimal threshold is found at 0.8. Data from 13 December 2012 to 16 March 2013.

4 Discussion

4.1 Choice of the predictor

The temperature difference threshold proved to be the best predictor of CDV winds. The PC -value of 0.91, which is close to, but somewhat lower than 1, means that some events are badly nowcasted. In this section we try to find out for which types of conditions the ΔT_T -criterion fails.

Figures 7a and 7b illustrate the performance of the temperature threshold to nowcast the CDV wind: in Fig. 7a, only the data for which the condition is valid ($\Delta T > 1.5^\circ\text{C}$) are shown. The result is compared to the actually observed winds at 10 m in the CV. The data falling outside the CV direction ($135^\circ \pm 45^\circ$), i.e. for which the nowcast fails, are plotted on the gray-shaded areas, whereas the successful data fall in the white area. On the contrary, in Fig. 7b the data for which the condition is not valid are plotted. The gray and white area are thus reversed with respect to Fig. 7a, with the exception of the CDV wind conditions inside as well as above the CV. This is because, in this case, the observed wind with a SE-direction at 10 m is due to the momentum transfer from the above-valley wind (see Fig. 2 and Fig. 3d), and not to the stability conditions. Furthermore, the data are sorted according to the hour of the day. In Figs. 7c and 7d, the same plots are shown as in Figs. 7a and 7b, but the data are sorted according to the wind speed at 110 m. During the period of measurement, sunsets were in the range 0540 and 0702 UTC, and sunrises between 1600 and 1748 UTC.

By applying ΔT_T of 1.5°C we miss 9% of the thermally driven CDV wind events and the non-CDV

wind events. The false alarms (i.e. $\Delta T_T > 1.5^\circ\text{C}$ and no CDV wind observed) have to be analyzed according to the wind speed: wind speeds higher than 4 m s^{-1} occur mainly in the NW-NW quadrant and are found during nighttime periods. These valley winds are related to downward momentum transport where turbulent motions are transported downwards (hence, Fig. 2). As such they oppose the onset of stability and so the formation of a CDV wind. Wind speeds lower than 4 m s^{-1} are mostly observed during the morning and evening transitions. Here stable stratification has already developed on the GBA-site close to the surface, but the down-valley wind at M30 has not set yet (during evening transition), or the stability at GBA is still present, but the down-valley jet has already been eroded (morning transition). To conclude, for a thermally driven CDV wind nowcast, one should be careful at applying the threshold when the wind speed at GBA is higher than 4 m s^{-1} and accompanied by a northwesterly direction.

On the other hand, missed nowcasts occur primarily during low wind speed conditions at 110 m (i.e. $< 4 \text{ m s}^{-1}$) and, although these misses have been observed throughout the full 24-hour period of the day, they are mostly frequent during the sunrise transition period.

4.2 Wind prediction at other heights

The tethered balloon observations during the KASCADE campaign have shown that the CDV wind can frequently grow up to a height of 50 m (Duine et al., 2015). In addition to the 10 m height, sonic anemometers were also installed at 2 and 30 m so the validity of the threshold can also be checked at these heights. This is done by applying the same procedure as for the 10 m CDV wind. At the 2 m level however, due to equipment malfunctioning, the dataset is 3 weeks shorter.

At 2 m comparable values for PC (0.91) and $bias$ (1.04) are found, but for a slightly higher ΔT -value of 1.6°C (Fig. 8 and Table 3). At 30 m the optimal score for PC is also shifted to a ΔT -value of 1.6°C , but with a score of 0.87 and a $bias$ of 1.04. However, due to the flatness of the PC peak, we can consider the threshold on ΔT is identical for the three heights.

4.3 Summer conditions

A mobile 2-m wind mast has been installed in the CV from 18 July to 25 September 2014 on M30 site so we can check the validity of the ΔT threshold at 2 m (1.6°C) during summer conditions.

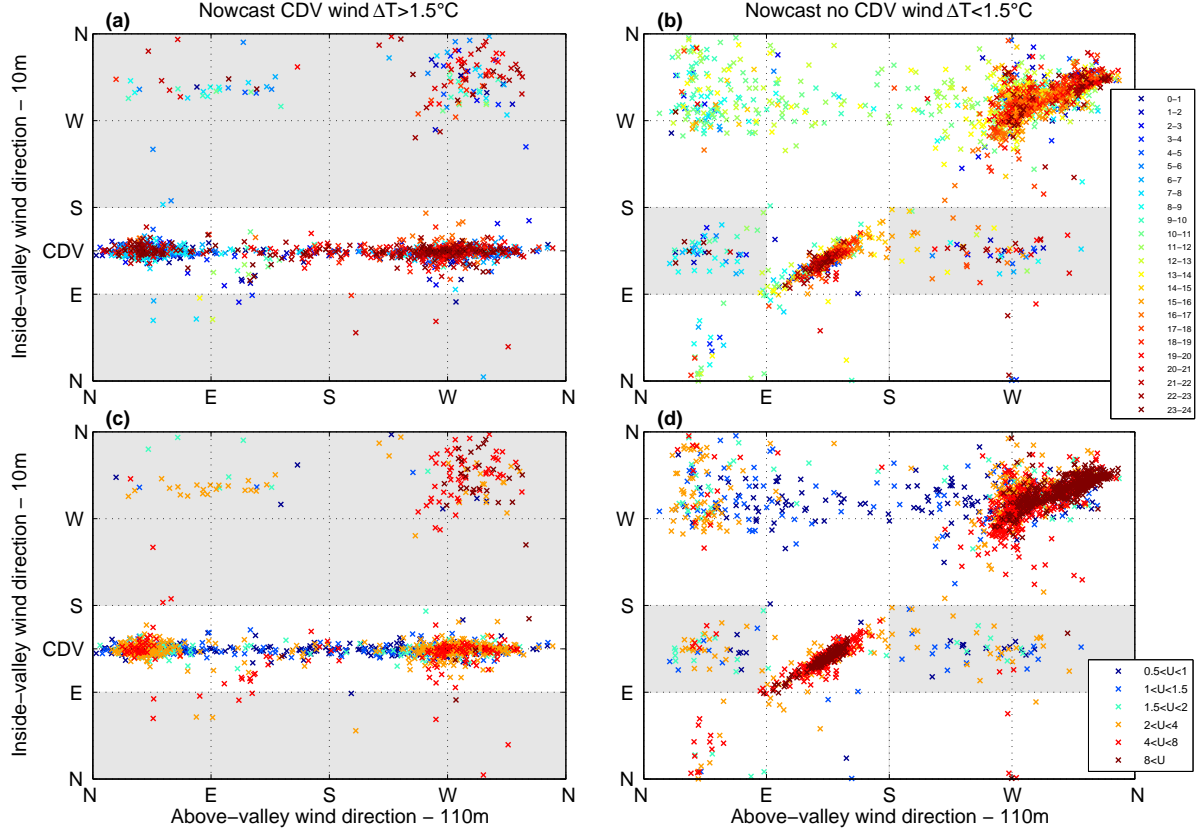


Figure 7: Relation between wind directions inside (10 m) and above (110 m) the valley, according to whether ΔT_T exceeds (left diagrams) or is below (right diagrams) the optimal threshold of 1.5°C . In the two upper diagrams (a and b), the plots are sorted according to the hours (UTC) and in the two lower diagrams (c and d) according to the wind speed observed at 110 m. White and gray backgrounds denote good and bad nowcast, respectively. The color scales on the right textboxes are also valid for the corresponding left diagram. Data from 13 December 2012 to 16 March 2013.

The results (Table 3) show that the CDV wind can be forecasted in summer as well and confirms the general applicability of the index. Interestingly, in spite of approximately the same sample size (2002 observations during summer vs. 1946 during winter) the number of *a* (good hits) events occurred half as often as in winter. In summer, this event is mostly replaced by correctly rejected events (*d*: non-CDV wind and $\Delta T < 1.6^\circ\text{C}$) and sometimes by false alarms (*b*). Therefore, the high value of *PC* comes from a high number of up-valley winds being correctly classified ($\Delta T < 1.6^\circ\text{C}$). Note that more than 72% of the values are below the threshold in summer, whereas this is 58% for winter conditions (ratio $(c+d)/n$). Non-thermally driven CDV wind observations ($((b+d)/n)$) are less frequent in winter (59%) than in summer (78%). A connection to the respective length of day and night for valley winds is worth considering (Giovannini et al., 2015) and could be checked on a year-long sample in the next section.

Table 3: *PC*, *bias* values, and contingency table of ΔT criterion for three different heights in winter and at 2 m in summer.

Height [m]	10	30	2	2
Season	winter	winter	winter	summer
Threshold [$^\circ\text{C}$]	1.5	1.6	1.6	1.6
<i>PC</i>	0.91	0.87	0.91	0.87
<i>Bias</i>	1.03	1.12	1.04	1.27
<i>a</i>	1011	926	708	372
<i>b</i>	141	250	104	185
<i>c</i>	109	120	76	67
<i>d</i>	1401	1513	1058	1378
<i>n</i>	2662	2809	1946	2002

5 Climatology of ΔT_T

The previous sections have shown the general applicability of the vertical temperature difference at GBA to nowcast the CDV wind by means of the GBA-tower observations with a relatively low uncertainty. The GBA-tower has been installed for many years already and a long-term dataset is available.

We apply the ΔT_T threshold of 1.5°C to ob-

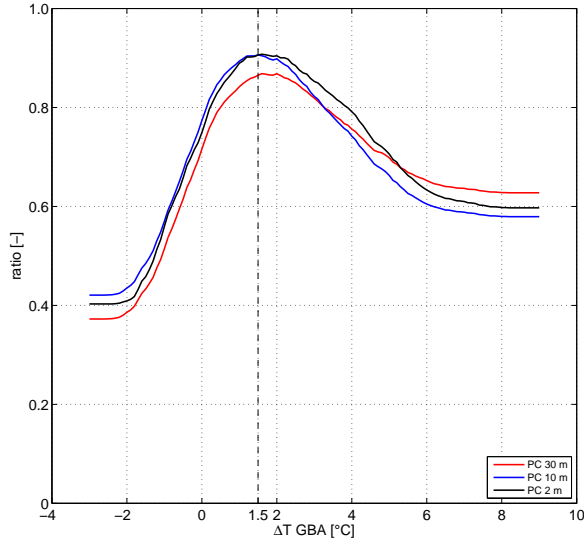


Figure 8: Same as Fig. 4 but for the other two measurement heights, 2 m (in black) and 30 m (in red). For comparison, the 10 m result from Fig. 4 is also reproduced. Data from 13 December 2012 to 16 March 2013 (30 m and 10 m) and to 23 February 2013 (2 m).

tain a climatology for thermally driven CDV wind occurrences at 10 m, for the years 2007 to 2011. Figure 9 shows monthly statistics on CDV wind and non-CDV wind occurrences. During the winter months, values of ΔT favoring a CDV wind are present almost half of the time and shows that the CDV wind is a dominant wind in winter. The occurrence diminishes gradually to a minimum in June, where conditions favoring thermally driven downslope winds are present during a third of the time. Consequently, the occurrence of this wind is strongly related to the length of the night which confirms the conclusion of Sect. 4.3.

The occurrences of the temperature threshold for the KASCADE period (December 2012 - March 2013) are also shown in Fig. 9. Note that the measurement period for KASCADE in December and March has been approximately only half of the month. Against the climatology reconstructed for 2007 - 2011, the months of December and February in particular show a higher occurrence of the CDV wind, whereas in January and in March the occurrences of non-CDV winds have been particularly higher.

6 Conclusions & perspectives

A forecast verification principle has been used in a methodology that determines an optimum threshold to nowcast a down-valley wind in a minimally-instrumented shallow valley. The method is able to identify the best performing quantity to nowcast the down-valley winds. The best predictor, a vertical temperature difference, has been tested for

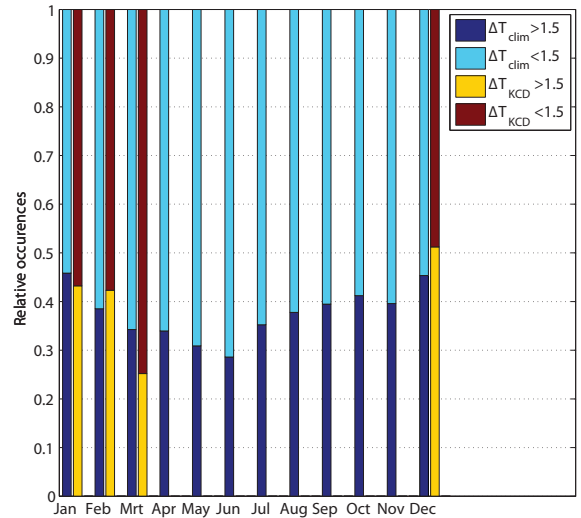


Figure 9: Monthly climatology of ΔT_T for the years 2007-2011 (clim) and the period of KASCADE (KCD), the latter from December 2012 to March 2013.

different valley wind heights and seasons. Consequently, it can be used as a nowcasting tool for the thermally driven down-valley flow but also to reconstruct the valley climatology, and it can serve as a tool for statistical downscaling in operational forecasting.

To carry out the threshold optimization, temporary observations of the down-valley wind were combined with measurements of a permanently installed 110-m high tower. The observations were taken from the KASCADE-dataset, a field experiment conducted in the winter of 2013 at the Cadarache site in southeastern France. Cadarache, one of the research centers of the CEA, lays along the shallow and narrow (100 m deep, 2 km wide) CV and comprises several facilities whose operation requires an assessment of atmospheric release dispersion. As in the CV itself no real-time monitoring is available to fully capture the dominant CDV wind, the method presented has been developed to take advantage of the existing instrumentation.

Three quantities have been tested to identify the most reliable predictor; a vertical temperature difference ΔT , a wind speed above the valley walls U_{110m} and a bulk Richardson number Ri_B . For a down-valley wind occurrence at 10 m, the ΔT came out as the best predictor index at a threshold value ΔT_T of 1.5°C, achieving a PC of 0.91. It defeats the Ri_B threshold of 0.8 ($PC=0.86$) and U_{110m} -threshold of 4.0 m s⁻¹ ($PC=0.72$), and confirms that the CDV wind is primarily thermally driven. Explanations why ΔT_T performs better than Ri_{BT} in predicting a drainage wind are the large bulk of measurements at the GBA-tower (108 m) and the hysteresis behavior of Ri . However, the applicability of the found optimal threshold is not fully

exclusive and needs some caution. For example, when $\Delta T < \Delta T_T$ under weak wind situations, CDV winds could be present. Furthermore, situations when $\Delta T > \Delta T_T$ with high wind speeds during nighttime, or low wind speed conditions around the sunset and sunrise transitions needs caution as well.

In addition to the 10 m wind nowcast, ΔT_T has been optimized for 2 and 30 m CDV winds. Similar values were found for the temperature difference: 1.6°C, with high values for PC of 0.91 and 0.87, respectively. A comparison with available measurements at 2 m in the summer of 2014 confirmed the found threshold value at this height, and so approved the general applicability of this threshold throughout the year. By means of the long-lasting availability of temperature measurements at the GBA-tower, a 5-year climatology could be made based on the found threshold, and revealed the existence of the thermally driven CDV wind throughout the year. Its occurrence is largely dependent on the night length. It further showed the relative importance of strong stability during the December and February months of the KASCADE-campaign.

Finding that a high-score nowcasting can be achieved through the use of only three routinely accessible parameters is of great practical importance for impact assessment and local risk management of pollutant dispersion. Moreover, daily operational forecasts are necessary for sanitary and safety purposes. However, the current operational forecasts are calculated with meteorological models on a relatively coarse grid (i.e. 1 - 3 km) which do not resolve the small valleys as the CV and so do not meet the requirement to forecast thermally driven down-valley winds at such small scales. In this instance, the identification of the vertical temperature difference as a threshold to nowcast the down-valley wind opens perspectives to forecast it by completing dynamical simulations with the statistical downscaling illustrated by this method.

Acknowledgements This work has been funded by the CEA in the form of a PhD-grant and the financing of the KASCADE-campaign. Laboratoire d'Aérodynamique is acknowledged for the provision of measurement material during the campaign.

References

- Amanatidis, G., K. Papadopoulos, J. Bartzis, and C. Helmig (1992). Evidence of katabatic flows deduced from a 84 m meteorological tower in Athens, Greece. *Bound.-Layer Meteorol.* 58(1-2), 117–132.
- Atkinson, B. (1995). Orographic and stability effects on valley-side drainage flows. *Bound.-Layer Meteorol.* 75(4), 403–428.
- Barr, S. and M. M. Orgill (1989). Influence of external meteorology on nocturnal valley drainage winds. *J. Appl. Meteorol.* 28(6), 497–517.
- Barry, R. G. (2013). *Mountain weather and climate, 3rd edition*. Cambridge University Press.
- Carrera, M. L., J. R. Gyakum, and C. A. Lin (2009). Observational study of wind channeling within the St. Lawrence River Valley. *J. Appl. Meteorol. Clim.* 48(11), 2341–2361.
- Duine, G.-J., T. Hedde, P. Roubin, P. Durand, M. Lohon, F. Lohou, P. Augustin, and M. Fourmentin (2015). Valley-driven flows in stable stratification - Observations in a complex orography area during the KASCADE field experiment. *submitted to Q. J. Roy. Meteor. Soc.*
- Giovannini, L., L. Laiti, D. Zardi, and M. de Franceschi (2015). Climatological characteristics of the Ora del Garda wind in the Alps. *Int. J. Climatol.* doi:10.1002/joc.4270.
- Gudiksen, P. H. (1989). Categorization of nocturnal drainage flows within the Brush Creek Valley and the variability of sigma theta in complex terrain. *J. Appl. Meteorol.* 28(6), 489–495.
- Haiden, T. and C. D. Whiteman (2005). Katabatic flow mechanisms on a low-angle slope. *J. Appl. Meteorol.* 44(1), 113–126.
- Horst, T. and J. Doran (1986). Nocturnal drainage flow on simple slopes. *Bound.-Layer Meteorol.* 34(3), 263–286.
- Jiménez, M. A. and J. Cuxart (2014). A study of the nocturnal flows generated in the north side of the Pyrenees. *Atmos. Res.* 145, 244–254.
- Mahrt, L., D. Vickers, R. Nakamura, M. Soler, J. Sun, S. Burns, and D. Lenschow (2001). Shallow drainage flows. *Bound.-Layer Meteorol.* 101(2), 243–260.
- Manins, P. and B. Sawford (1979). A model of katabatic winds. *J. Atmos. Sci.* 36(4), 619–630.
- McTaggart-Cowan, R. and A. Zadra (2014). Representing Richardson Number Hysteresis in the NWP Boundary Layer. *Mon. Wea. Rev.* 143(4), 1232–1258.
- Sheridan, P., S. Vosper, and A. Brown (2014). Characteristics of cold pools observed in narrow valleys and dependence on external conditions. *Q. J. Roy. Meteor. Soc.* 140(679), 715–728.
- Stewart, J. Q., C. D. Whiteman, W. J. Steenburgh, and X. Bian (2002). A climatological study of thermally driven wind systems of the US Intermountain West. *B. Am. Meteorol. Soc.* 83(5), 699–708.
- Stull, R. B. (1988). *An Introduction to Boundary Layer Meteorology*. Kluwer Academic Publishers.
- Weber, R. O. and P. Kaufmann (1998). Relationship of synoptic winds and complex terrain flows during the MISTRAL field experiment. *J. Appl. Meteorol.* 37(11), 1486–1496.
- Whiteman, C. D. and J. C. Doran (1993). The relationship between overlying synoptic-scale flows and winds within a valley. *J. Appl. Meteorol.* 32(11), 1669–1682.
- Wilks, D. S. (2011). *Statistical methods in the Atmospheric Sciences*, Volume 100. Academic press.

Chapter 6

Model set-up and evaluation

6.1 Introduction

The valley winds under study are of different scales and do behave differently under stable conditions, as was seen in Chap. 4. The Durance down-valley (DDV) wind was characterized as a dominant wind for the winter of 2013, especially during weak synoptic forcing events. The DDV wind appeared to be mostly present and at its strongest around and even after sunrise, when convectively driven processes are at their weakest. However, a big variability in the onset and cessation times of the DDV wind was noted. Observations of DDV wind are only available at one site, therefore its spatial extent could not be investigated. This is one of the reasons to set up a mesoscale model: to gain more insight in the spatial structure of the DDV wind, and possibly clarify its origin. In this chapter we focus on the first step: the set-up of the model and to test its sensitivity. To study the characteristics of the DDV wind in time and space, we use the mesoscale numerical model WRF. The model has been described in Chap. 3.

As a first step, for one IOP undergoing relatively weak synoptic forcing with a clear sky, the model is tested against several parameterization schemes and other model parameters. This leads to a reference configuration, chosen as the 'best one', i.e. closest to the observations: configuration 1. We explain the strategy, and the most important results in Sect. 6.2; more details can be found in Kalverla et al. (2015). Taking up this reference configuration, we extend the investigation on model sensitivity for the DDV wind development by simulating it for all 23 IOPs. From these simulations, a selection of 13 IOPs is further tested for model sensitivity on DDV wind development for two more configurations: with an increase of vertical grid spacing (configuration 2) and with an extension of the inner domain (configuration 3). A final sensitivity test on horizontal grid spacing is performed for one IOP.

The reference configuration is evaluated for all 23 IOPs by means of all available measurement devices on a local scale and the evaluation is extended regionally by including a meteorological network (Sect. 6.3). Also an analysis is made of the model capability to simulate each IOP individually. Figures for background information can be found in Appendix B.

6.2 Model sensitivity

To start the investigation of the DDV wind, its evaluation, its characteristics and to finally point out its origin we devise with a reference run. Its definition is based on the use of several parameterization schemes. This investigation also allows to test the model's sensitivity to several parameters and to point out its strengths and weaknesses. For the strategy itself we refer to Sect. 3.3.1.

6.2.1 Set-up of the reference configuration

To define the reference configuration¹, IOP 16 was selected as a benchmark. The IOP started at 19 February 2013 12:00 UTC and lasted 24 hours. IOP 16 was conducted under relatively weak synoptic forcing (Fig. 6.1b). Besides, it had a nearly perfect radiation balance for a stable boundary layer study (Fig. 2 of Chap. 4), and so presumably formed a good period to define a reference configuration. For model spin-up 24 hours are taken into account, so the simulation started at 18 February 2013 12:00 UTC and lasted 48 hours.

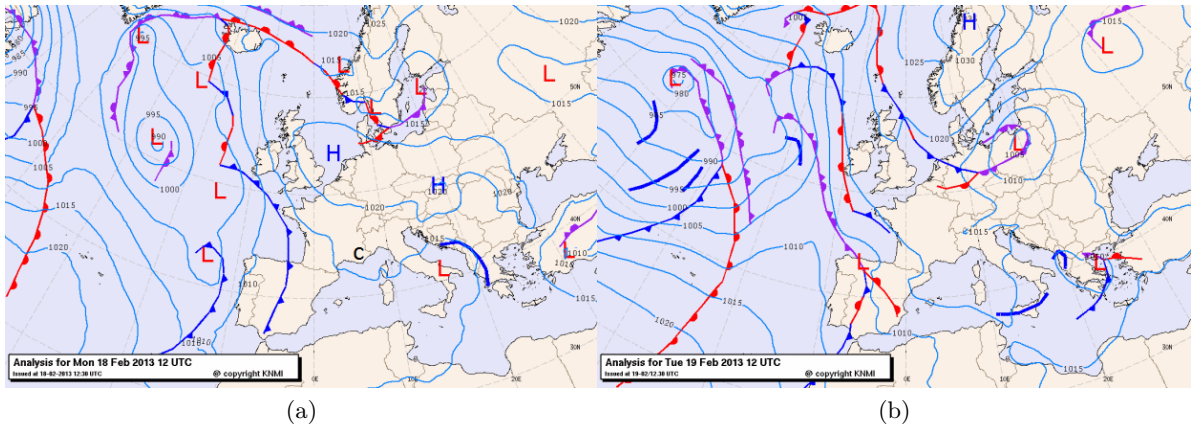


Figure 6.1: Synoptic situation at the start of the simulation (a) and 24 hours later at the start of IOP 16 (b). 'C' in (a) indicates the location of Cadarache.

6.2.1.1 Observations

Throughout the period, from the start of the simulations to the end of IOP 16, a synoptic northerly pattern is found above 2 km (radiosoundings, not shown). This flow becomes not directly visible from Fig. 6.1, as the synoptic pattern is relatively weak in the study area: a maximum wind speed of 15 m s^{-1} was observed in one radiosounding at 2 km, on other radiosoundings the winds up to 2 km height stayed below 10 m s^{-1} . On Fig. 6.2, obtained from interpolations of the radio-sounding data, large drying and warming is seen. A HYSPLIT backward trajectory analysis (Draxler and Rolph, 2003) run for IOP 16 showed that the air mass above 2 km was advected from southern Germany over the Alps to the study area (not shown). Consequently, the subsidence explains the warming and drying found during the period of investigation.

We highlight some important phenomena observed closer to the ground during the IOP. Although northwesterly winds were found aloft throughout the 48-hour period, strong diurnal patterns were found close to the ground for temperature and humidity from the radiosoundings (Fig. 6.2) and for wind as observed by the Sodar (Fig. 6.3). A thick mixed boundary layers is observed at noon; around 1400 m at the start of IOP 16. Some clouds were observed in the beginning of the IOP, but these gradually disappeared. This did not prevent the surface cooling during the night as stable boundary layers form and grow to a maximum depth of around 200 m in the early morning. This depth was confirmed by tethered balloon soundings (not shown). The SBL depth is determined following the temperature profile from the surface up to the height at where the steepness of the positive gradient diminishes (e.g. Fig. 6.4 for IOP 16). Also concerning humidity (Fig. 6.2b), close to the surface a strong diurnal pattern is observed, with evaporation in the afternoon and dew formation in the night.

¹The optimization for one IOP and sensitivity tests on different parameterization schemes (Sect. 6.2.1) are primarily based on the work done by P. Kalverla, a Master student of the Wageningen University.

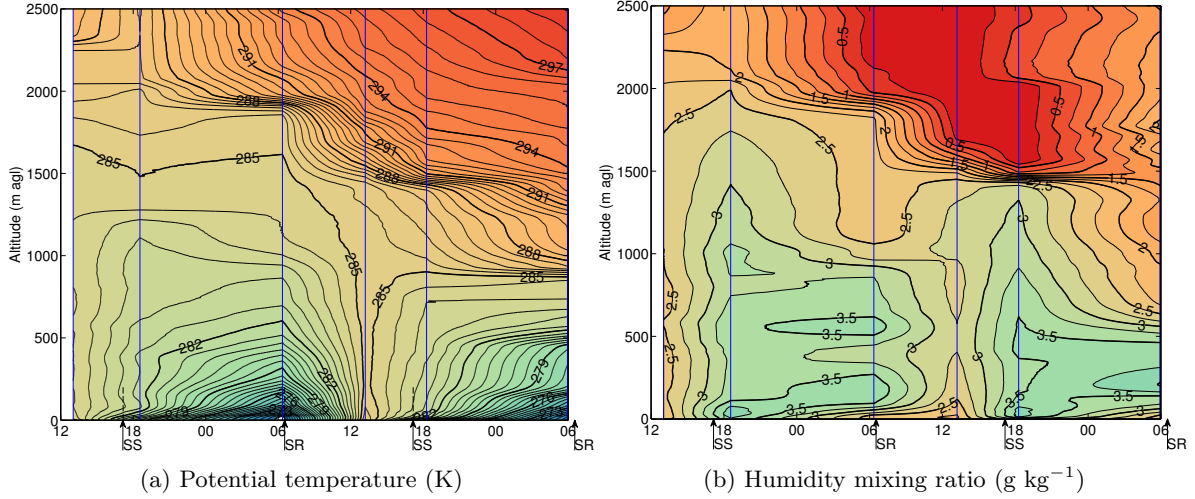


Figure 6.2: Observations during spin-up period and IOP 16 as interpolated from radio-sonde observations (time axis shown is in UTC between 18 February and 20 February 2013). a: potential temperature and b: humidity mixing ratio. Time of release indicated by the blue vertical lines. The sunset (SS) and sunrise (SR) times are indicated by the arrows below the time axis.

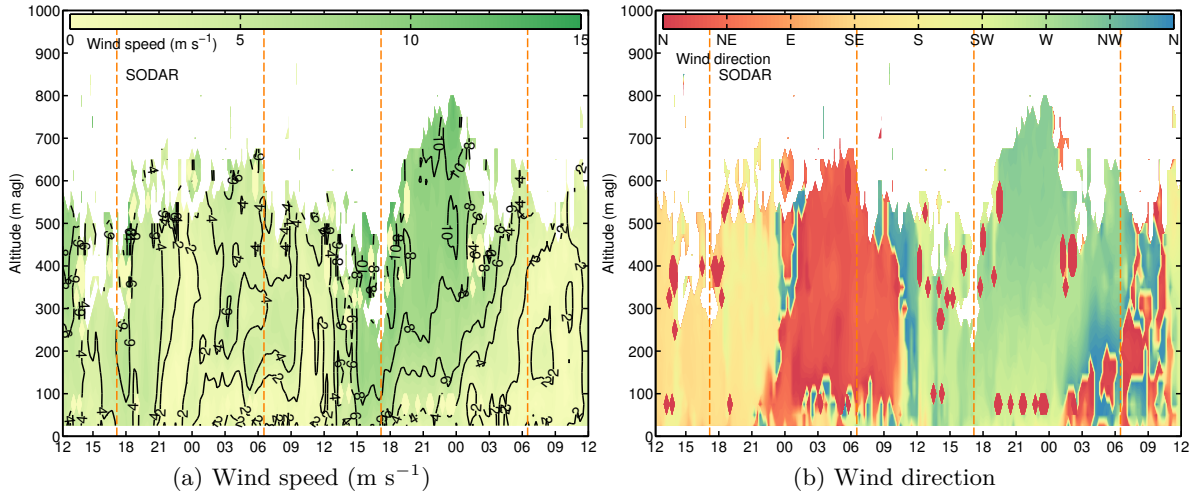


Figure 6.3: Sodar observations during spin-up and IOP 16 (time axis shown is in UTC between 18 February and 20 February 2013). The orange dashed lines represent the sunset and sunrise times.

In the afternoon during IOP 16 the wind, measured by the Sodar, was northwesterly. The wind speed at the surface quickly dropped after sunset due to the near-surface cooling (Fig. 6.3a). During the night a DDV wind developed. The wind direction remains northwesterly for a long period after sunset, but from around 01:00 UTC the wind starts turning to a DDV direction near the ground and then gradually grows in depth. A jet appears, around 200 m agl. However it is weak and shows up only after sunrise. The wind behavior is typical, although the cessation of the afternoon northwesterly wind and the onset of the DDV wind during IOP 16 are later than the average cessation and onset times. However, the fact that the DDV wind is stronger around sunrise is generally found during KASCADE (see Chap. 4).

6.2.1.2 Sensitivity to parameterization schemes

A sensitivity study has been performed on the land surface parameterization and the planetary boundary layer schemes, see Sect. 3.3.1 and Tables 3.1 and 3.2 for its definition. Two con-

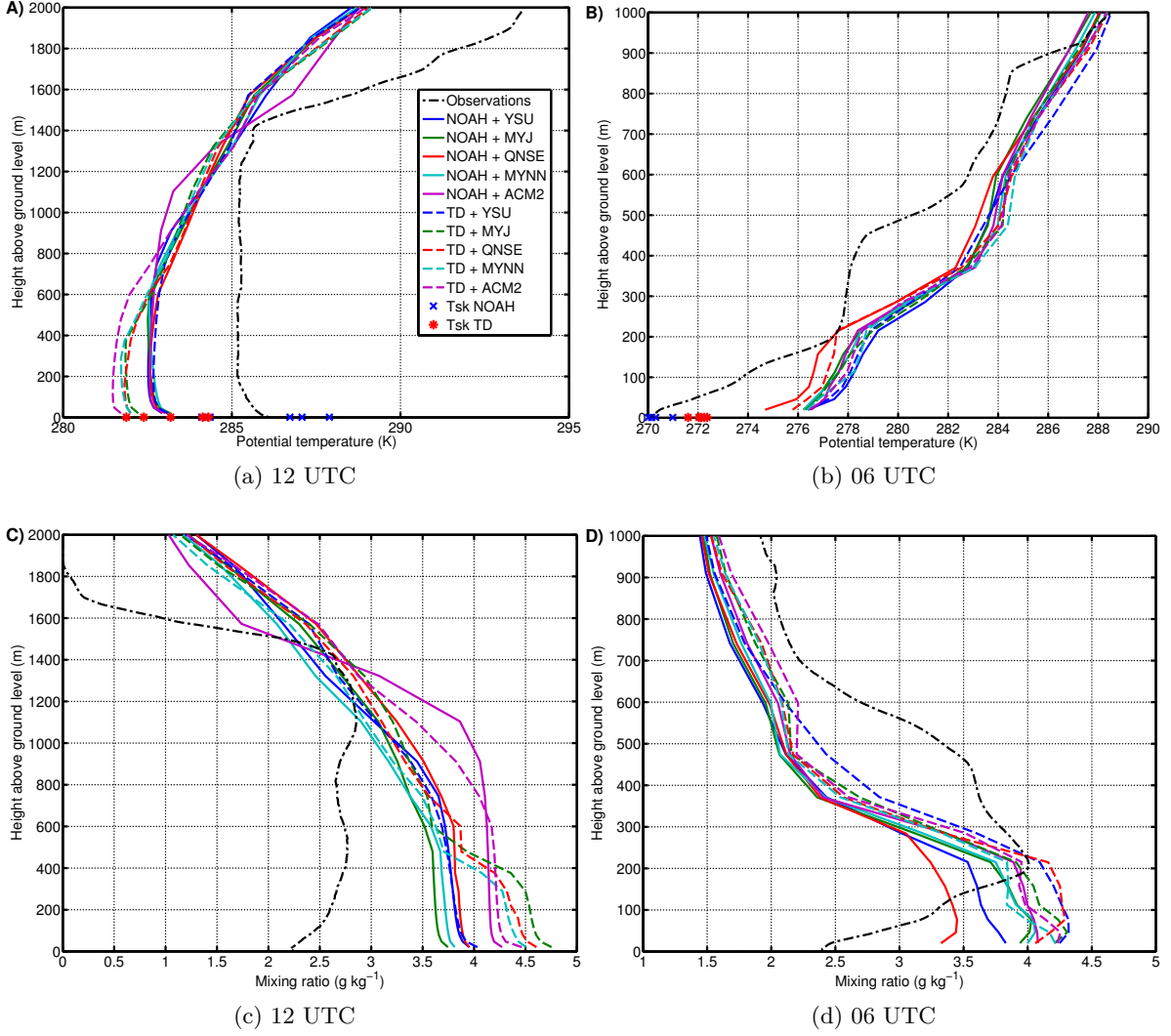


Figure 6.4: Measured and modeled profiles for the parameterization schemes sensitivity study at the start of IOP 16 (19 February 2013 12:00 UTC - left pictures) and IOP 16 early morning (20 February 2013 06:00 UTC - right pictures). Observations come from radiosoundings.

trasting states of the atmosphere were observed by the radio-sondes at the start of the IOP 16 (19 February 2013 12:00 UTC) and its early morning (20 February 2013 06:00 UTC): a well developed mixed-layer and a stably stratified boundary layer (Fig. 6.4). The vertical profiles from the ten paramaterization scheme combinations are compared for the same times.

It is clear that all runs fail to simulate the mixed-layer height (1400 m for observations vs. 500 - 1000 m for all simulations) and its strong inversion (Fig. 6.4a and 6.4c). Advection of dry and warm air is simulated, but with a delay which partly explains the colder and moister profiles at 12:00 UTC. The mixed layer is too cold and too moist in all simulations. The underestimation of the mixed layer height could be related to a too small (resp. large) sensible (resp. latent) heat flux and/or a too low entrainment of warm and dry air at the PBL top. The less distant profile is found by the NOAH+ACM2 combination which shows the highest mixed layer and the strongest inversion at the PBL top. Overall, the skin temperatures are highly underestimated with the TD scheme and cold and moist biases are larger with NOAH.

At 06:00 UTC, several layers are observed (Fig. 6.4b). A very stable layer is observed below 200 m, from 200 to 450 a near neutral profile is found. Another stable layer is observed between 450 and 600, from 600 to 900 m again a near neutral profile is found. Then around 900 m

another strong inversion is observed. The model reproduces in all simulations similar layering, but misses the upper stable stratification at 900 m and underestimates the altitude of all layers. The stratified layer closest to the ground is too thin and too weak. Weak coupling between the atmosphere-surface for all configurations results in a large gradient between the lowest model layer and skin temperature. Dew formation was observed, and this could be a possible explanation for drying in the lower 200 m, whereas above this height advection of dry air seems a logical explanation. Overall, little difference is visible between the model configurations, even if the NOAH+QNSE partly succeeds in representing the cold stratified layer near the surface. Finally, the diurnal temperature range is highly underestimated, which is a known problem in mesoscale modeling (Zhang and Zheng, 2004).

The time evolution of temperature, atmospheric fluxes (sensible and latent heat, incoming and outgoing longwave radiation) and wind observations is presented in Fig. 6.5. This gives a complementary insight in the evolution of the profiles of Fig. 6.4, for both observations and modeling. The 110 m temperature is shown as it is less sensitive to unresolved local effects inside the CV (Fig. 6.5a). Even at this height, the observations show a diurnal temperature range (DTR) of 12°C whereas the simulations come to only 7°C at best. Clouds are observed in the beginning of the simulation time, they are revealed in the increase of LW^\downarrow . The model fails to reproduce these (Fig. 6.5b).

However, our focus is from 12:00 UTC on 19 February. A large part for the DTR underestimation comes from the temperature underestimation at noon. The surface temperature can be estimated from the observed LW^\uparrow by applying the Stefan-Boltzmann law (Eq. 1.16): about 400 W m⁻² was observed which corresponds to about 295 K. The corresponding modeled values are on average 350 W m⁻² and 285 K: an underestimation of 10 K. Part of this high bias can be attributed to a too cold atmospheric profile. It can be explained either by an underestimation of warm air advection or entrainment at the PBL top, or by an erroneous partitioning of the energy at the surface, or even by the soil-surface scheme. Night-time net radiation is observed at about -60 W m⁻², a typical value for SBL development (Van de Wiel et al., 2003).

The 10 m wind at VER is highly overestimated in the model (Fig. 6.5c). However, the general pattern is caught by the simulations, as reflected by the 110 m observations (the open circles in the figure). At 110 m in the model (not shown), wind speeds of the order of 10 m s⁻¹ are simulated until around 03:00 UTC (20 February), after which the wind speed drops. This is much later than in observations. The friction velocity shows the same pattern as the wind (Fig 6.5d): mixing is overestimated from the early morning and continues until 03:00 UTC. In general, the decay of turbulence occurs earlier with the NOAH schemes than with the TD schemes.

The too-high mixing is reflected in the sensible and latent heat fluxes (Figs. 6.5e and 6.5f, respectively), with especially large overestimations in the afternoon and after sunset. H is strongly related to the existence of turbulence, and the very stable boundary layer observed may cause the very low H . A big difference is remarked between the NOAH and TD schemes: at noon NOAH gives higher sensible heat flux, whereas TD gives higher latent heat fluxes than observed. However, $L_v E$ is overestimated in both schemes and could explain the differences in the moisture profiles of Fig. 6.4. This is confirmed when we compare the Bowen ratio ($H/L_v E$) for observations and model schemes. Regarding the maximum values in the afternoon, for observations we find a Bowen ratio of 2.8 (140 W m⁻² / 50 W m⁻²), whereas for an average of the NOAH schemes we find 1.7 (170/100), and for TD schemes we find 0.5 (100 / 200). Note that the moisture bias in these profiles was larger for the TD schemes as well. From this we conclude that the NOAH schemes work best for energy partitioning at the surface.

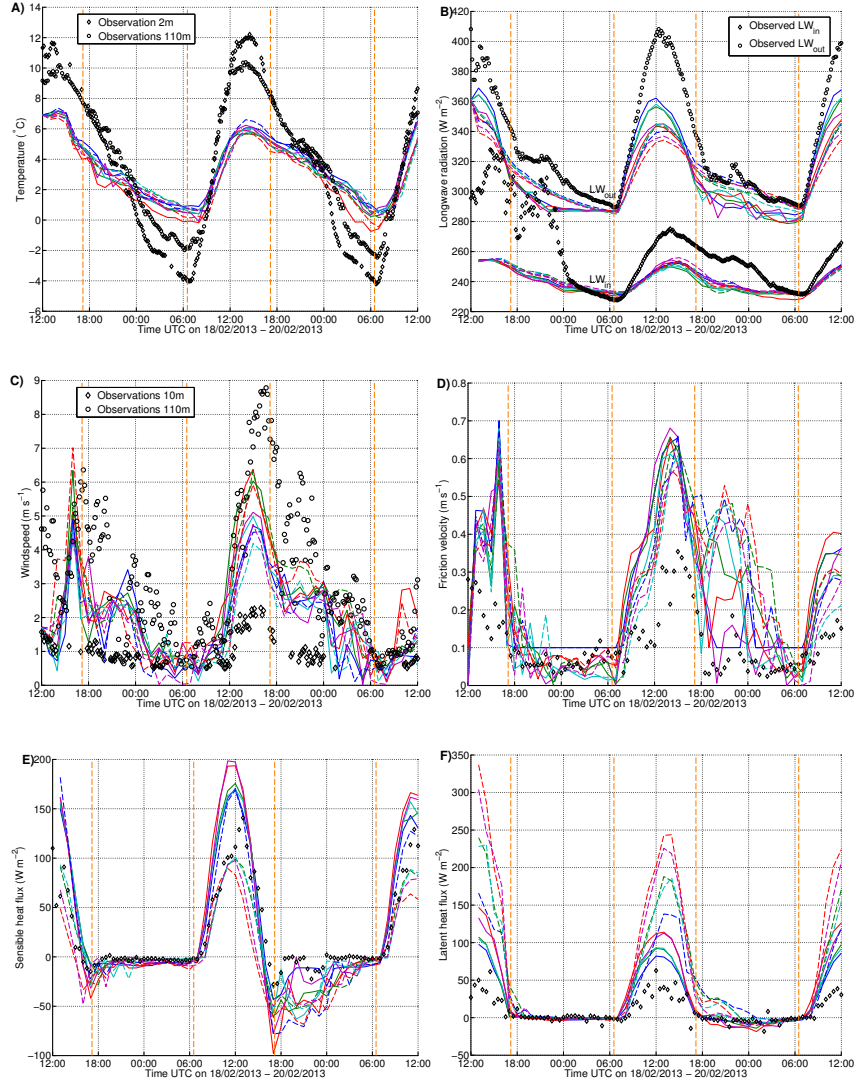


Figure 6.5: Observed and modeled evolution of a: 110 m temperature at GBA (2 m for observations is also shown), b: longwave radiation components, c: 15 m wind observations and 10 m wind model at VER (110 m wind for observations GBA is also shown), d: friction velocity, e) sensible heat flux and f) latent heat flux. Legend is the same as in Fig. 6.4

6.2.1.3 Tests of other configurations

To evaluate the model sensitivity and to improve the boundary layer profiles and atmospheric fluxes for IOP 16, other tests were executed. For this the combination of the NOAH+YSU schemes was used. To summarize:

- Evaporation was too high in the model, making the vertical profiles too moist. Soil moisture plays a crucial role in humidity availability at the surface, especially for high horizontal grid spacing (Angevine et al., 2014). In the study area, especially after Mistral conditions, the soil can be very dry whereas soil models not necessarily reproduce this drying process to a proper extent. The sensitivity test to soil moisture content showed that its reduction mainly re-partitioned the heat fluxes (not shown). The already overestimated sensible heat fluxes increased by around 50% and latent heat fluxes are reduced by a factor of 4, leading to a Bowen ratio of more than 10. This however improved the representation of the atmospheric profiles and diurnal temperature range. But the soil moisture content required for

improving the atmospheric profiles cannot be justified by means of the observations, even if a large uncertainty is accounted for.

- Atmosphere-surface coupling has been tested by varying the Zilitinkevitch parameter in the YSU scheme (c.f. Kalverla et al. (2015)). Very strong coupling enhances dew formation at night. The daytime profile slightly improved with a thicker mixed layer and stronger inversion. But, again, these improvements generated unrealistic sensible and latent heat fluxes.
- Several radiation schemes have been used, showing only improvements for cloud observations at the beginning of IOP 15 with the CAM-scheme (Fig. 6.6). However, the bias of LW^\downarrow for this scheme is larger than for the other schemes. Very small differences were noted between the other schemes used with the overall bias lowest in the RRTMG schemes. However, the differences are still large with a bias of -15.9 W m^{-2} and a maximum difference of 20 W m^{-2} . Compared to the reference run (NOAH + YSU schemes and the combination of the Dudhia (SW) and RRTM (LW) schemes) the results do not improve. The RRTMG scheme performs slightly better for longwave radiation, a crucial parameter for SBL formation.
- The initial and boundary conditions used were ECMWF re-analysis data. The case has also been simulated with GFS data on a 0.25° horizontal grid spacing. The GFS data turned out to contain a snow layer, which was not present at the time of observations. The snow merely caused changes in albedo and net radiation which resulted in lower sensible heat fluxes (50 W m^{-2} in comparison to 145 W m^{-2} in observations). Consequently, the boundary-layer growth was less, with lower temperatures and a smaller DTR. The misrepresentation of a snow layer appears more often, and therefore we cannot use the GFS initial and boundary conditions for the case studies presented here.

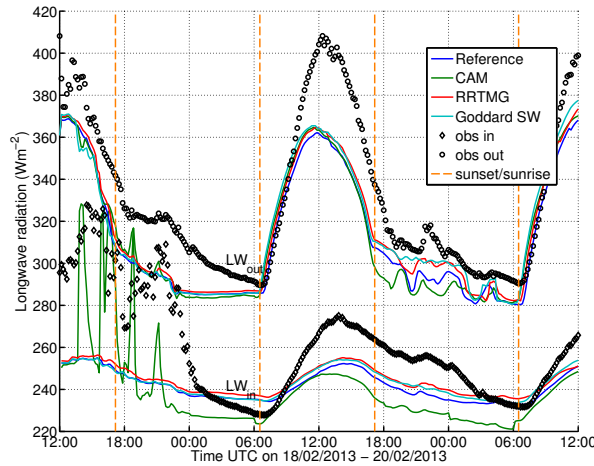


Figure 6.6: Simulated and observed LW^\downarrow and LW^\uparrow for configurations presented in Sect. 3.3.1.3. 'Reference' represents the configuration with NOAH+YSU (soil and PBL schemes), and Dudhia (SW) and RRTM (LW) radiation schemes.

6.2.1.4 Choice of a reference configuration

The sensitivity analysis using several combinations of five different PBL schemes and two different land surface schemes has shown that the model is quite insensitive to the choice of boundary layer scheme. For land surface, the NOAH scheme performs better concerning the skin temperatures. Also considering the Bowen ratio, the NOAH group of configurations performed more closely to observations. Considering the stable profiles, especially the QNSE scheme proved to be

Table 6.1: Optimal model configuration used for the first step of the modeling procedure. The IOP start and end times are indicated in Table 2.2

Model version	WRF v3.5.1
Start date simulation	IOP start minus spin-up time
End date	IOP end time
Spin-up time	24 hours
Time step	120 seconds
Domains configuration	4 domains
Parent-child ratio	1 : 3
Nesting	Two-way nested
Grid size inner domain	1 x 1 km
Vertical (sigma) levels	35 levels
Land use	Corine land cover (2006) (Büttner et al., 2007)
Orography	SRTM (Farr et al., 2007)
Global data input	ECMWF analysis 0.25°
Microphysics	WSM 6-class Graupel (Hong and Lim, 2006)
Longwave radiation	RRTMG (Iacono et al., 2008)
Shortwave radiation	RRTMG (Iacono et al., 2008)
Cumulus scheme	Kain-Fritsch (Kain, 2004)
Planetary boundary layer	QNSE (Sukoriansky et al., 2005)
Surface layer	QNSE
(land) Surface scheme	NOAH (LSM) (Tewari et al., 2004)

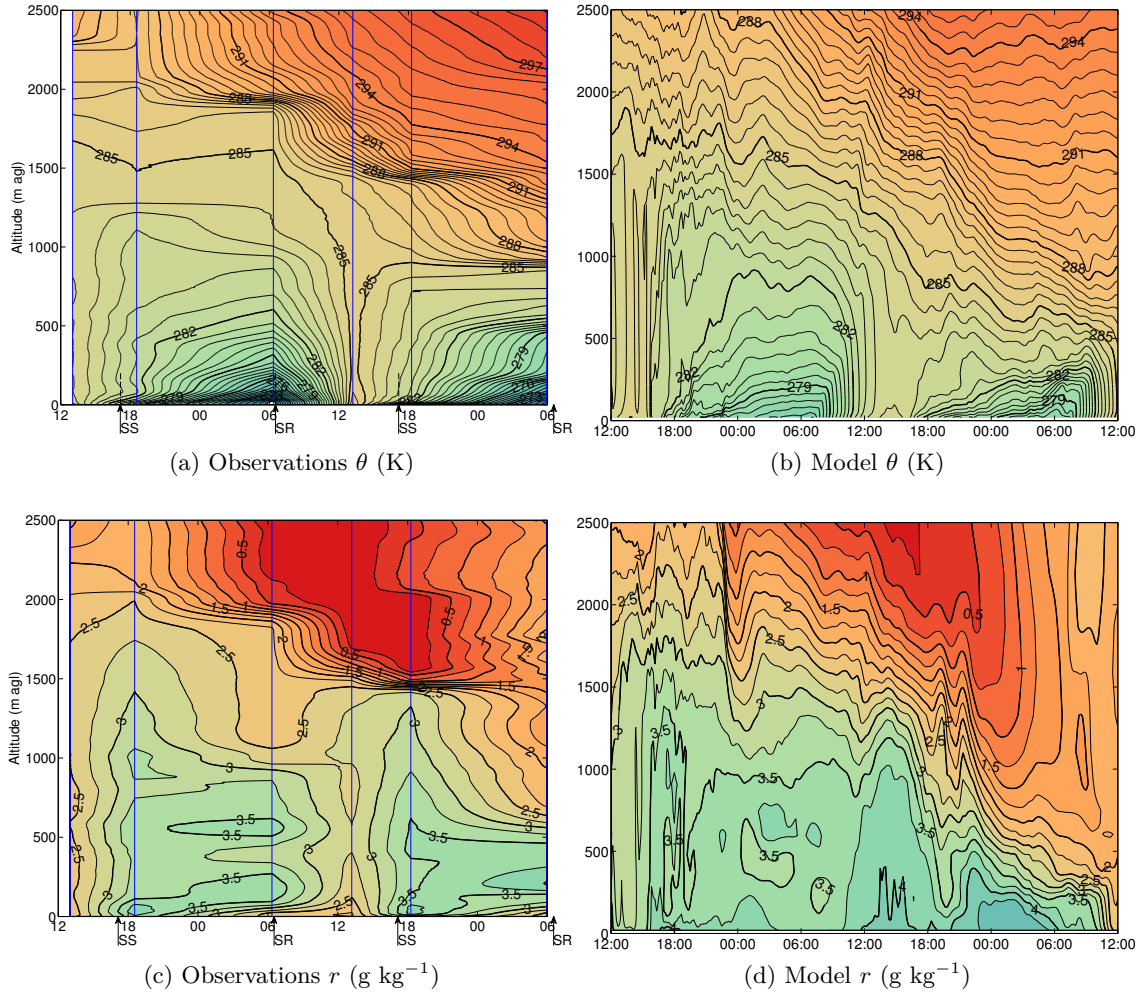


Figure 6.7: Potential temperature θ and humidity mixing ratio r from observations (left) and model (right) for the optimized set-up described in Table 6.1. The time axis is between 18 February 2013 12:00 UTC to 20 February 2013 06:00 UTC.

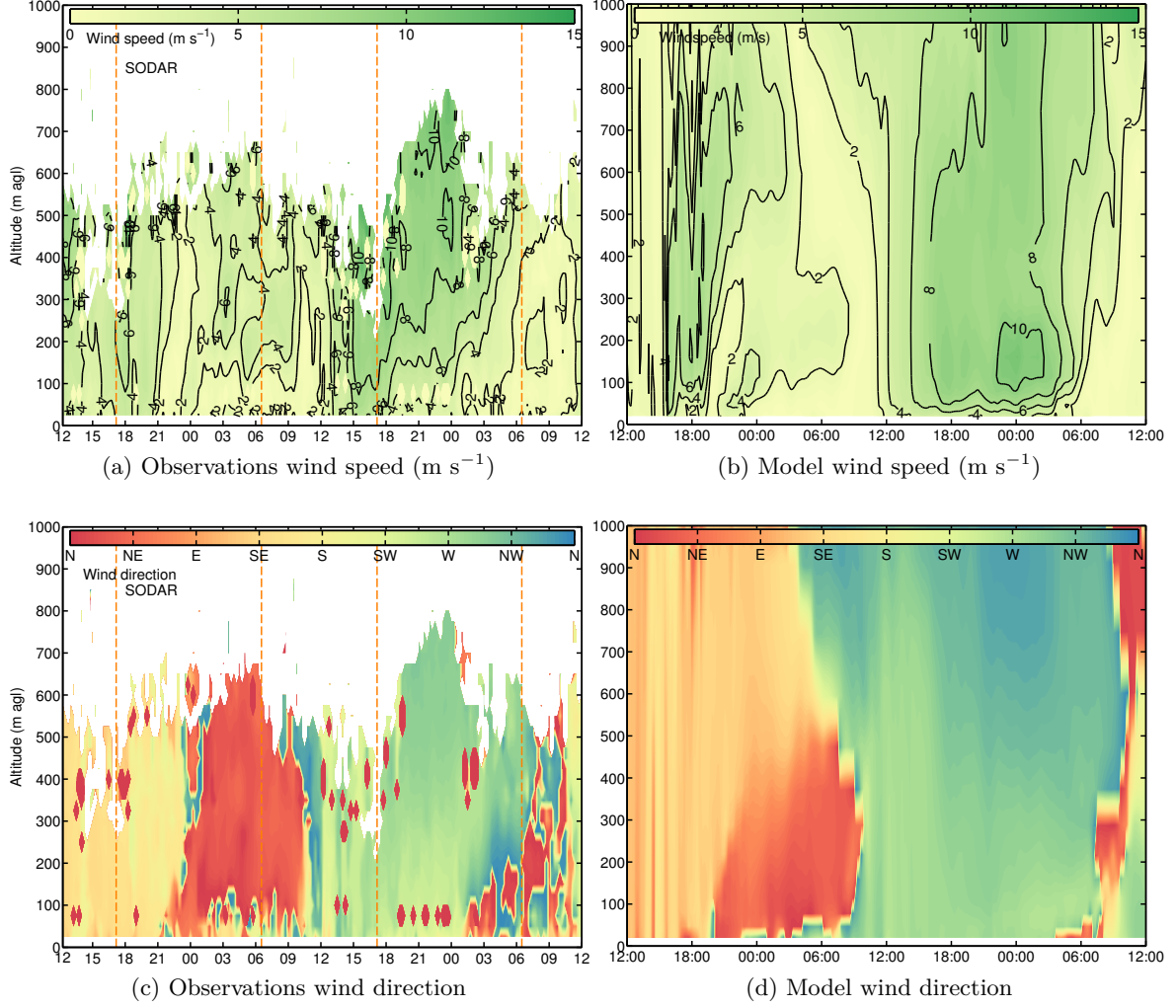


Figure 6.8: Wind speed and direction from observations (left) and model (right) for the optimized set-up described in Table 6.1. The time axis is between 18 February 2013 12:00 UTC to 20 February 2013 12:00 UTC.

able to simulate a stable layer. Although the layer was very shallow, it was simulated with both land surface options. Therefore the NOAH+QNSE simulation is the best set-up. For the radiation option, we choose the RRTMG longwave and shortwave schemes, which performed slightly better in simulating the longwave radiation. The modeling analysis results in a configuration presented in Table 6.1, it will be used for simulating the other IOPs.

This reference configuration and its resulting profiles are compared with observations for temperature and humidity in Fig. 6.7 and for wind speed and direction in Fig. 6.8. Dry and warm air advection is simulated, although with a large delay. Regarding the wind profiles, the general pattern is well reflected. However, the wind speed in the daytime to night-time transition is largely overestimated by the model. In observations, the wind speed quickly drops after sunset, but in the model this wind speed continues until around 03:00 UTC. The quick drop of wind speed after sunset is explained as the consequence of turbulent decay on downward momentum transport. For example, u^* also shows high mixing values whereas the observations show very low values from sunset. This transition is typically missed or delayed in models and forms the basis for the BLLAST-campaign (Lothon et al., 2014). Regarding the DDV wind, it ultimately reaches the Cadarache center at around sunrise, which is three hours after observations.

Some remarks about the choice of the reference configuration should be made. Energy balance closure remains a problem. It should be noted that the observations lack measurements

of the soil heat flux. Besides, the observations were done inside the Cadarache Valley, which is dominated by processes on a scale out of reach of the current horizontal grid spacing. Overall, the large scale wind speed and direction were simulated to a good extent. Warm and dry air advection is also simulated, although it is not strong enough and it comes with a delay. Most of the variables within the PBL follow the good pattern, but the diurnal range of temperature and humidity is underestimated, while turbulent fluxes are overestimated. Keeping these flaws in mind, we extend our research by simulating all IOPs in order to simulate the DDV wind, then we can check whether the flaws found are generic.

6.2.2 Influence of grid spacing and domain size

6.2.2.1 Approach

This section treats the sensitivity of the model on the DDV wind development. In a more general way we test the model sensitivity for its boundary-layer representation, surface cooling effect on the wind and valley representations: we investigate the influences of a higher vertical resolution, the model inner domain size and a coarser horizontal (3 km) grid spacing. For the vertical resolution and inner domain size this has been done by the simulation of 13 IOPs. The influence of the horizontal grid spacing is treated for IOP 21 only.

Two modifications to the model were proposed to see the influence on the DDV wind development in the model. This gives a total of three configurations:

- Configuration 1: The reference configuration proposed as the optimized configuration based on IOP 16 (see Table 6.1)
- Configuration 2: Increase of vertical resolution close to the ground and around CBL height (see Sect. 3.3.3 for details). It is expected to improve the surface cooling and mixed layer properties.
- Configuration 3: Increase of inner domain size to include important orographic features 'Montagne de Lure' and 'Clue de Sisteron' which are thought to influence the DDV wind origin (see Fig. 3.5 in Sect. 3.3.4 for details).

All 23 IOPs have been simulated for the first configuration. A selection of 13 IOPs for which a DDV wind has been correctly modeled has been again simulated with two additional configurations of the model. However, an exclusion was made on DDV winds which were recognized as flow channeling under high wind speed forcing aloft. We have chosen not to consider these as we are firstly interested to improve the model for the DDV wind when stability is the main driver. These criteria leave the IOPs listed in Table 6.2.

The IOPs which were not considered for the next configurations, are IOPs 1, 2, 3, 5, 8, 9, 12, 17, 18 and 22. They were rejected for different reasons. IOP 1 had a snow event in the early morning which has not been simulated. IOP 2 has been canceled due to a strong Mistral which was also modeled and therefore was not interesting for our purpose. Rain was observed during IOP 3 and no considerable DDV wind was simulated. IOP 5 showed some DV-directed wind in the model, but these were of the order of 12 m s^{-1} . IOP 8 was not selected because of the absence of DDV wind in both observations and model simulations. IOP 9 was marked by a strong Mistral and so has been rejected due to the absence of considerable DDV wind development in the late night. IOP 12 was not chosen because in the simulations the DDV wind only showed up late after sunset for a very short amount of time. Although a considerable DDV wind development has been observed during IOP 17, this has not been modeled at all. IOP 18 was not considered because of poor wind speed simulations in general. Finally, IOP 22 was modeled with very high wind speeds, and little channeling is observed.

Table 6.2: Summary of the IOPs simulated for each configuration.

		<i>IOPs simulated</i>
Configuration 1	Reference configuration (Table 6.1)	1 - 23
Configuration 2	Increase vertical resolution	4, 6, 7, 10, 11, 13-16, 19-21, 23
Configuration 3	Domain 04 extension	4, 6, 7, 10, 11, 13-16, 19-21, 23

Background information per IOP and important features are given in Appendix B. Here we continue the sensitivity study on configurations 2 and 3.

6.2.2.2 Boundary-layer representation

We first focus on IOP 16, for the first two configurations only. Figure 6.9 shows the profiles up to 3 km every 6 hours for temperature, humidity and wind speed and direction. No sounding was available at 00:00 UTC. Note that we do not show the extended domain configuration (configuration 3) in this figure as we do not expect big improvements on boundary layer profiles. The profiles for temperature show that at 12:00 and 18:00 UTC the temperature jump around the mixed layer top is slightly improved. For the early morning profile no clear improvement is made between the configuration 1 and 2. The signal of warm and dry upper air is also improved, but just slightly. However, improvements for humidity are barely made close to the surface. This can again be explained considering the Bowen ratio for the two different configurations: for configuration 1 this is around 1.7 (for values for H and $L_v E$ at noon of IOP 16), whereas for configuration 2 this is 1.6. Recall that for observations the Bowen ratio was higher than 2.0. Consequently, the second configuration does not improve the repartition of the energy at the surface.

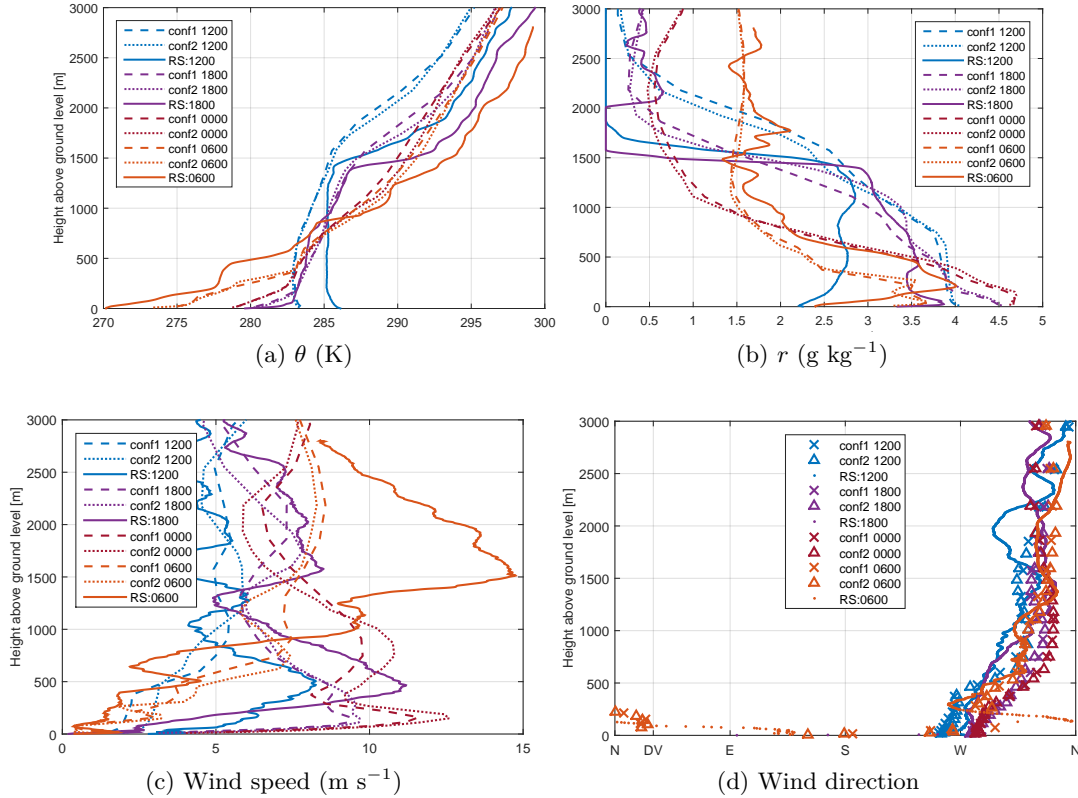


Figure 6.9: Sounding profiles at four times (in UTC) during IOP 16 of potential temperature θ , humidity mixing ratio r , wind speed and direction for the observations (RS), the first (conf1) and second (conf2) configuration. No observation was available at 00:00 UTC.

One of the problems when simulating IOP 16 is the evening transition, when the atmosphere turns from a turbulent behavior to relatively calm periods. At first sight, on the wind speed and direction profiles no real improvements are made. A LLJ with a westerly direction slightly increases in speed at 00:00 UTC, for the second configuration compared to the first one. Also the big jet observed at 1500 m at 06:00 UTC is missed by both configurations. Despite the flaws of the model to represent the boundary layer and even the upper air motions, the wind direction is modeled to a good extent already in the reference case (configuration 1). No big changes are found for the high vertical grid spacing run. To judge improvements for a DDV wind development a statistical approach involving more cases is needed, this will follow in Sect. 6.2.2.4.

6.2.2.3 Surface cooling

Figure 6.10 shows the vertical potential temperature difference between 110 and 2 m ($\Delta\theta$) for observations (GBA) and model configuration 1. For the model the considered upper level is around 110 m, with an uncertainty of 5 m, hence an interpolation here would not influence the results we show. All 23 simulated IOPs are shown. They are further classified per hour in the day (UTC). No extra selection is made on data quality. During the day and night large spreadings are found. It is clear that the biggest discrepancy occurs during the night when the difference between the GBA top and bottom can go up to more than 6°C, which is beyond of reach for the model. This difference comes mainly from the fact that the surface does not cool enough in the model. The disagreement is enhanced by the fact that the tower is situated in the CV, where during nights cold pools develop regularly which cannot be resolved by the model. Nevertheless, stability in the profiles (i.e. $\Delta\theta > 0$) is reached, but barely reaches for example the threshold value of 2.6°C which we computed to be the threshold for the onset of CDV wind from the GBA measurements (Chap. 5). However, the goal of the simulations at this grid spacing firstly is to look at DDV wind onset.

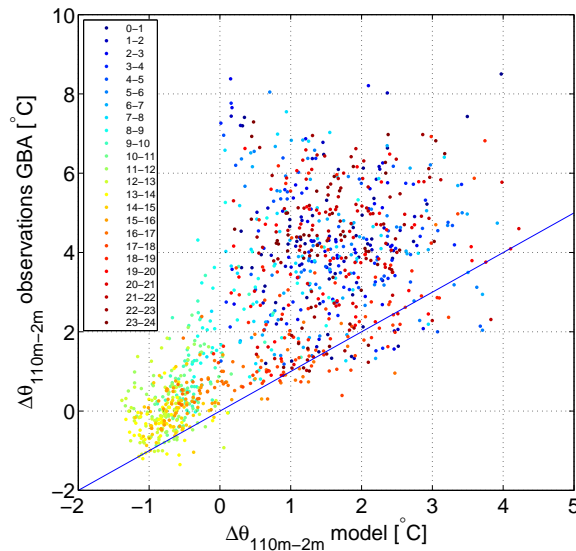


Figure 6.10: Difference of potential temperature $\Delta\theta_{110m-2m}$ for observations and model at GBA, the colors correspond to the hour of the day. The blue line represents a 1:1 line.

One of the reasons for increasing the vertical resolution (i.e. configuration 2) is to enhance surface cooling. The idea is that increased surface cooling should enhance stability and so the formation of thermally driven flows. For the 13 IOPs simulated in this configuration, we see that we do increase cooling at the surface (Fig. 6.11a). The inner domain size extension (configuration 3) does not enhance surface cooling (Fig. 6.11b). The pictures further show an

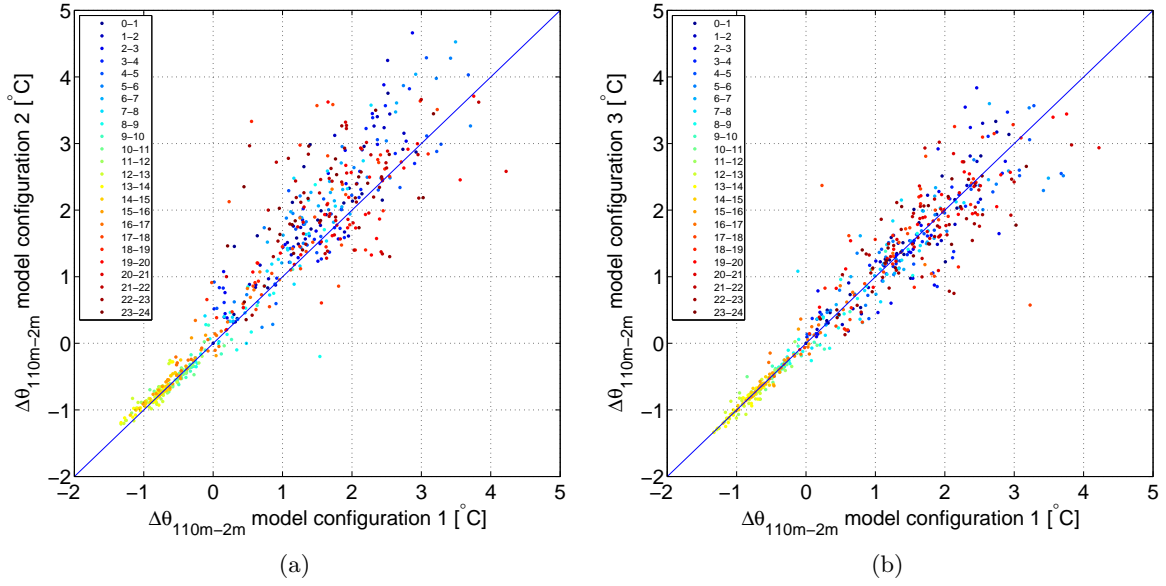


Figure 6.11: Same as Fig. 6.10 but for comparisons between different configurations of the model

heteroscedastic behavior: unstable conditions are less noisy and more locally dependent, whereas stable conditions are more sensitive to initial condition perturbations and are non-local, most likely due to stability driven winds.

A calculated bias for the minimum temperature showed a slight improvement: it goes from 2.0°C for the first configuration to 1.7°C for the second configuration. The third configuration with 2.0°C showed no improvement. Despite the improvement of the surface cooling, a correct estimate of the 2 m temperature in general requires a high vertical resolution of the order of less than 5 m (Largerón, 2010; Jiménez and Cuxart, 2014; Burns and Chemel, 2014); the vertical resolution in configuration 2 was only about 10 m close to the surface.

6.2.2.4 Wind development

To investigate the influences of the different configurations for wind forecast, we study the DDV wind development in greater detail for a single IOP and then for all 13 IOPs.

Simulation of IOP 7

IOP 7 has been conducted from 7 February to 8 February 2013 and has been marked as one with a DDV wind development in the early morning well observed and simulated. The IOP was subjected to synoptic forcing however, with a low pressure system present between Corsica and Italy at the start of the IOP at 12:00 UTC (Fig. 6.12a). It is a typical pattern for the Mistral wind onset. During the next 24 hours of the IOP however, the low pressure area proceeded eastwards and relatively calm winds were found consequently in the second course of the night over the study area at 06:00 UTC (Fig. 6.12b). Stable stratification could develop; a maximum SBL-depth of 250 m was observed by means of tethered balloon profiles in the early morning (not shown).

The Mistral conditions generally bring northwesterly winds in the study area, this is well visible in Fig. 6.13. The picture shows the wind speed and direction from the Sodar and model configurations 1 to 3 up to 800 m at the VER site for the full IOP development. The graph shows that the wind is captured quite well by all configurations. Before sunrise, a westerly circulation is observed and simulated, and after sunset (at 16:43 UTC) the wind speed at the surface quickly diminishes. A LLJ with a westerly direction is quickly formed with its nose around 300 m height

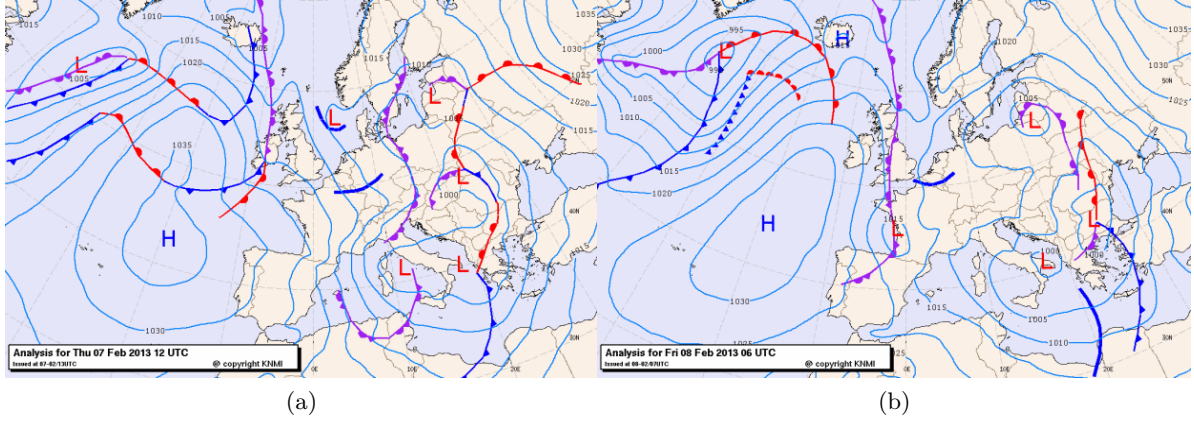


Figure 6.12: Synoptic situation at (a) the start of IOP 7 (7 February 2013 12:00 UTC) and (b) at the next morning 06:00 UTC.

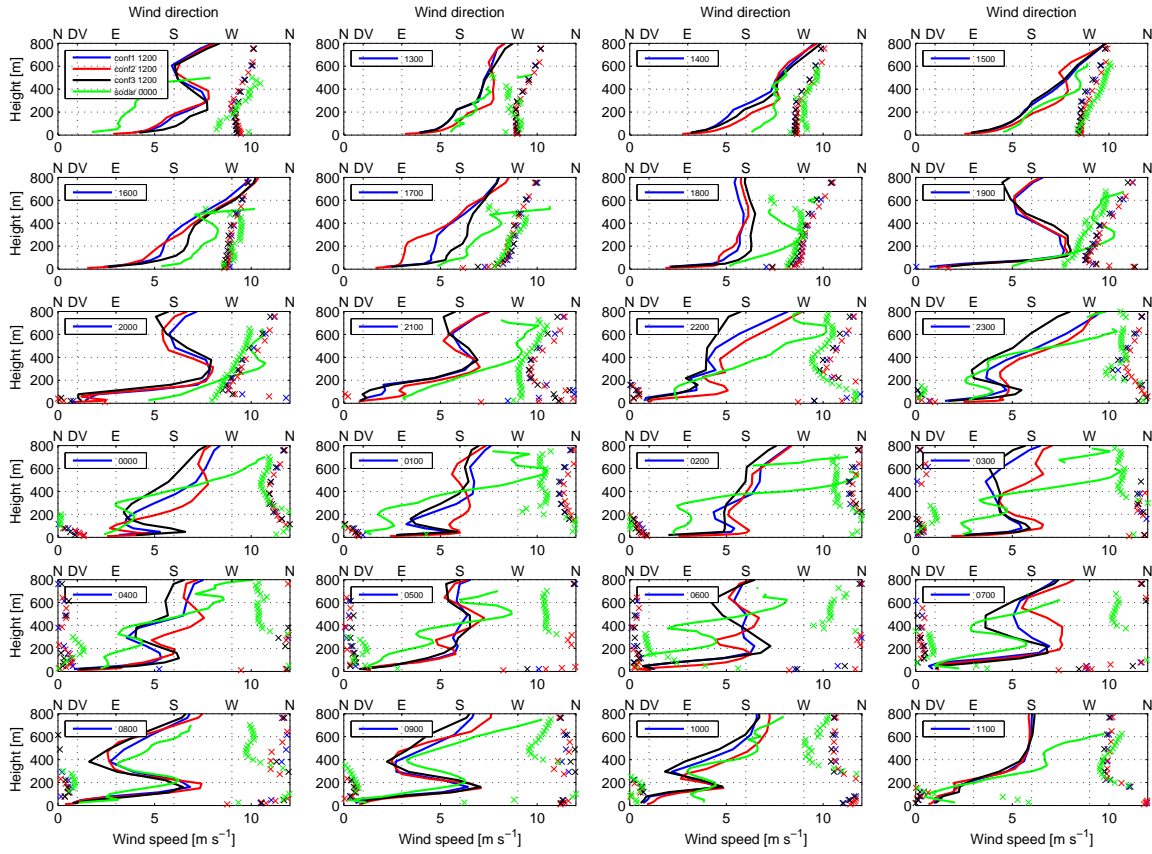


Figure 6.13: Comparison for wind speed (lines) and wind direction (crosses) between Sodar observations (green) and simulations for all configurations (red, black, blue) during IOP 7, the times (in UTC) are indicated in each box. Note that Sodar is not trustworthy below 100 m.

(20:00 UTC), but at the surface the wind already turns to the DDV wind direction in the form of a shallow jet in all configurations. The Sodar observations below 100 m are questionable and so we cannot check the validity of the onset of this jet by means of observations directly. However, GBA (110 m) and VER (15 m) wind observations show a gradual change in wind direction starting at 21:00 UTC for both stations and reaching a DDV wind direction at 21:30 UTC (VER) and 22:00 UTC (GBA). This DDV wind direction appears later on in a weak jet, whose speed continuously increases throughout the IOP, and finally reaches 7 m s^{-1} at an approximate height of 200 m in all configurations between 07:00 and 09:00 UTC. Furthermore,

Table 6.3: Summary of model performance evaluated with $DACC$ and $DACC_{DDV}$ (both in %) for wind direction. The results are presented for IOP 7 and for the ensemble of IOPs simulated with the three configurations of the model.

	IOP7		13 IOPs	
	$DACC$	$DACC_{DDV}$	$DACC$	$DACC_{DDV}$
Configuration 1	77.9	73.1	48.7	46.0
Configuration 2	74.6	72.9	46.8	48.0
Configuration 3	78.8	71.8	48.7	50.0

it compares very well with observations. Above 400 m agl, i.e. well above the valley depth at the VER site, the wind stays westerly to northwesterly in the observations, whereas in the model it turns from NW to NE and back for all configurations. It takes more than 3 hours after sunrise (06:56 UTC) in both model and observations for the DDV wind to diminish.

So, in general for this IOP the wind pattern and DDV wind characteristics are simulated to a good extent for all configurations. This is reflected in the $DACC$ and $DACC_{DDV}$ (Eqs. 2.7 and 2.8). $DACC$ indicates the accuracy of the prediction of wind direction and should be as close to 100% as possible. It is defined as the percentage of occurrences when the angular distance between two directions (e.g. observed and modeled) is less than a chosen threshold, set at 30° in our case (Santos-Alamillos et al., 2015). $DACC_{DDV}$ reflects the same value, but it is dedicated to the DDV wind direction selected from observations. This is based on the DV axis direction of 30° . A spread of 20° is accepted, which means that simulated winds within the $[10^\circ, 50^\circ]$ interval pass the test. The results are summarized in Table 6.3. The differences for the scores are minor between the configurations.

Model performance in the simulation of 13 IOPs

No real improvements appeared with the configuration tests as calculated for IOP 7. To see whether an increase of vertical resolution, or the inclusion of the mountain ridge around the 'Clue de Sisteron' in the inner domain have influence on the wind and notably the DDV wind onset during other IOPs, we present the statistical results for $DACC$ and $DACC_{DDV}$ in Figs. 6.14 and 6.15. The figures compare the observations of GBA at 110 m and Sodar at different heights (100, 150, 200, 275, 350, 450 and 600 m) to their corresponding closest model layers for the different IOPs. Some differences are found between IOPs, but no significant ones.

Table 6.3 summarizes the scores for all IOPs and again small differences are noted. The overall wind direction $DACC$ does not change: 48.7% (conf 1), 46.8% (conf 2) and 48.7% (conf 3) for the three configurations when averaged over the tested layers. The extended model domain did not improve greatly the occurrence of the simulated DDV wind. Averaged for all IOPs with DDV wind onset, and over all layers tested, the improvement for $DACC_{DDV}$ is just from 46% (conf 1) to 48% (conf 2) to 50% (conf 3). Although the surface layer cooling is enhanced with the second configuration, this does not improve significantly the representation of the DDV wind. Also for the third configuration, minor improvements are found. Note that the full inclusion of the Montagne de Lure and the Clue de Sisteron is not harmful either.

6.2.2.5 DDV wind development on lower horizontal grid spacing

Results so far have shown that the model set-up as proposed in Sect. 6.2.1, on a horizontal grid spacing of 1 km in the inner 4th domain and 35 layers in the vertical, is able to simulate the DDV wind to some extent. The third domain is on a horizontal grid spacing of 3 km, which suffices to roughly resolve the Durance valley (see Fig. 6.16 for the orography in the third domain) and prompts to check whether the DDV wind can develop at that grid spacing. To avoid feedback from the 4th to the 3rd domain, as we use two-way nesting in our study, we simulate IOP 21 with three domains only. IOP 21 was conducted under easterly synoptic conditions as



Figure 6.14: DACC for the DDV wind IOPs with the three different model configurations.

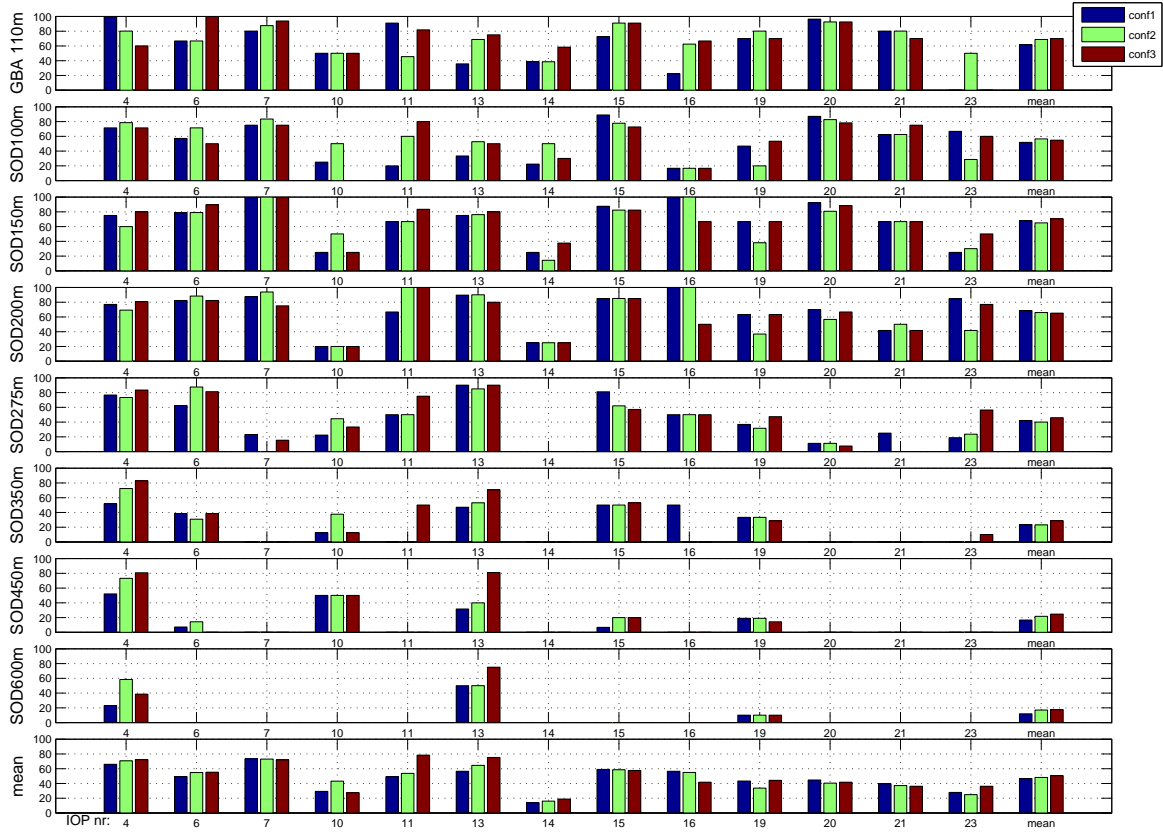


Figure 6.15: Same as Fig. 6.14 but for $DACC_{DDV}$.

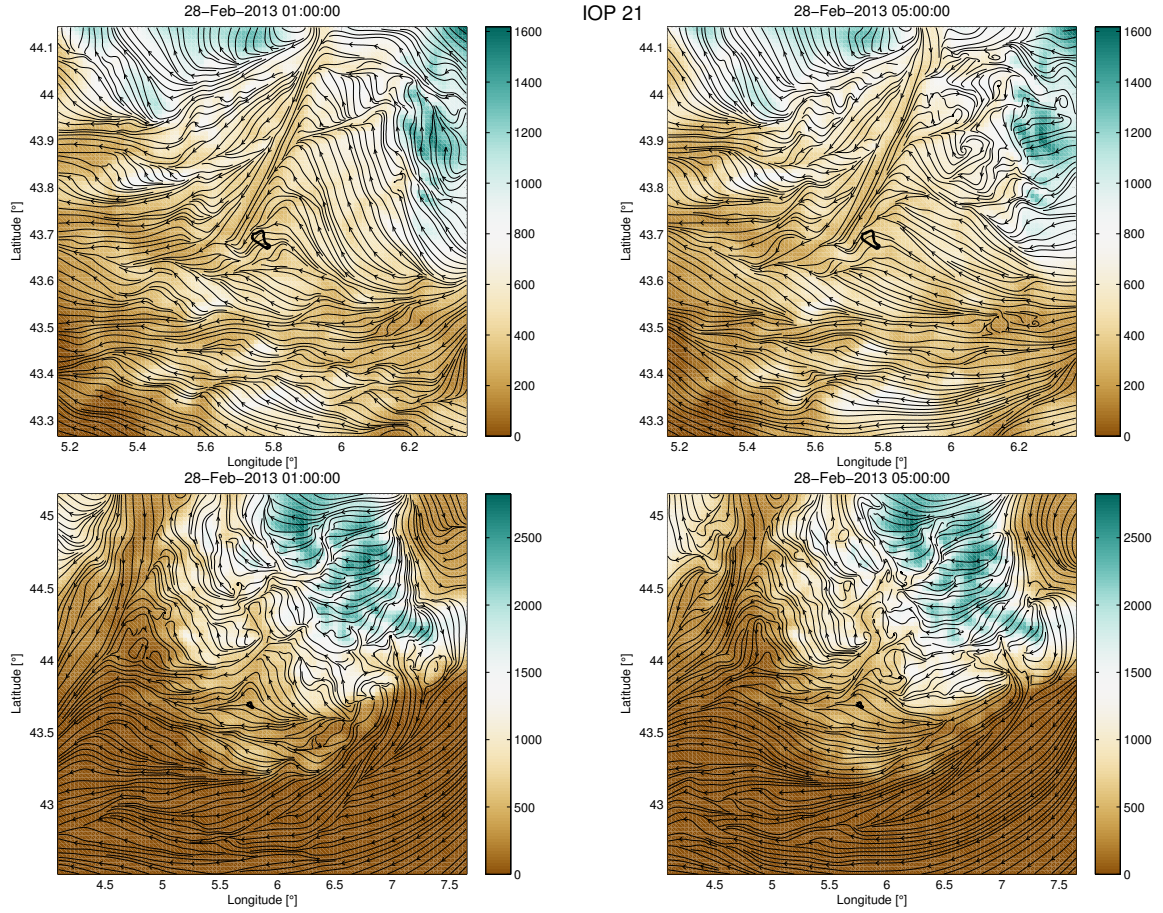


Figure 6.16: Streamlines at the 6th sigma-level (~ 220 m agl) during IOP 21 for the third domain with 1 km grid spacing (two upper figures) and 3 km grid spacing (two lower figures) and at two different times. Terrain height is in meters agl. Cadarache site is outlined in the middle of each map.

determined from radio-soundings (see Chap. 4, Sect. 3.2.1 for a thorough description of the synoptic situation during this IOP).

Figure 6.17 shows the wind direction during IOP 21 for sodar observations and for simulations at 1 km and 3 km grid spacing at different heights. At 100 m depth, the wind directions for the 1 and 3 km grid spacing are mostly close to a DDV wind. At the 150 and 200 m layers however, at 1 km grid spacing a DDV wind is simulated whereas at 3 km grid spacing an easterly wind is seen, which corresponds more to the synoptic situation. From 300 m high, the 1 and 3 km grid spacing both see this synoptic wind and come close to observations. These differences between the 1 and 3 km simulations result from the resolved DV depth at the Cadarache site. On a 3 km grid spacing, only up to three grid cells are available for a valley with a width of 5 to 8 km. In the 3 km grid spacing the DV at the Cadarache site is only 100 m deep, whereas in the 1 km grid spacing it is 200 m deep which enables getting a valley wind.

However, north of Cadarache, the depth of the valley on a 3 km grid spacing is resolved to a value closer to reality, and the DDV wind is seen deeper. This is reflected in the streamlines picture (Fig. 6.16) shown at a height of 220 m. Modeling correctly the depth of the DDV wind at the Cadarache site is crucial for the prediction of atmospheric dispersion calculation, consequently the horizontal grid spacing must be kept at 1 km for studies related to the DV.

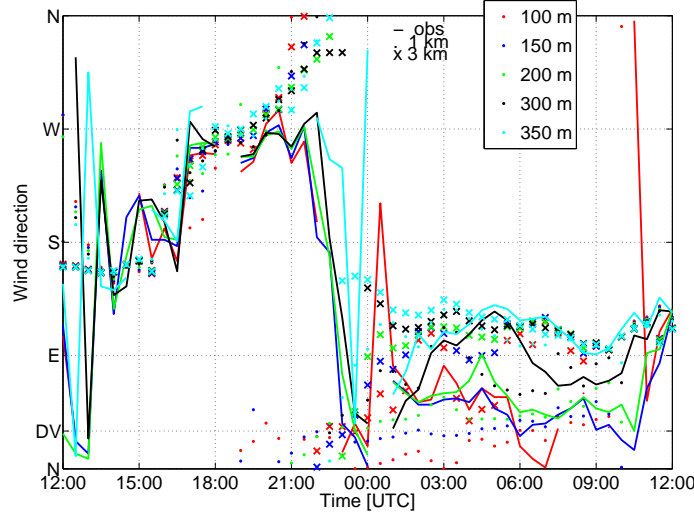


Figure 6.17: Wind direction observations (Sodar), simulations at 1 and 3 km horizontal grid spacing at different heights for IOP 21.

6.2.2.6 Concluding remarks

The sensitivity tests on vertical resolution and inner size domain show only little improvements. For the increase in vertical resolution, the boundary-layer representation just slightly improves the simulation of IOP 16 for warm air advection. Energy partitioning at the surface is not greatly improved, as compared to observations. But the vertical temperature difference close to the surface largely improves, which was one of the goals of the tests. Despite these efforts, the vertical resolution does not seem to be the crucial factor to enhance the DDV wind development in the model. This can lead to two conclusions: either the DDV wind comes from stability at a large scale for which low vertical resolution is sufficient; or the vertical resolution in the basic model set-up was already sufficient so that little improvement could be made by further refinement. It should be noted that the vertical discretization was chosen such that the resolution was highest close to the surface, i.e. below 50 m. The DV depth is around 200 m in reality and in the model, it is then possible that a higher vertical resolution between for example 100 and 200 m, could influence the DDV wind development.

On a 3 km horizontal grid spacing the model roughly resolves the DV, but only two grid cells are available within the valley which is not enough to match close to reality, especially close to the Cadarache site. Although this has been tested only for one IOP, the implication of an insufficiently resolved DV close to the Cadarache site is important for dispersion calculations. Therefore it is recommended to use a 1 km resolution.

At this point the model appears to be rather insensitive to tested schemes and grid modifications. The reference configuration shows overall good results for the DDV wind onset. Before investigating into detail the DDV wind by means of simulations, we will evaluate all 23 IOPs first.

6.3 Evaluation of the reference configuration

The reference configuration was determined against a single IOP. In a second step, minor improvements could be made on DDV wind development. We now evaluate this reference configuration (Table 6.1) for all 23 simulated IOPs in order to get a better view on the model general performance. Moreover, insight will be gained in the model capability to simulate the distinctive features of each IOP, which is needed for the ultimate goal: investigation of the DDV

wind. Meteograms as back-up for this section are provided in Appendix B.

6.3.1 Strategy

Although made at several sites, the KASCADE observations remain within a 1.2 km radius circle (see Fig. 6.18b). Additionally, the flux tower was placed in the small Cadarache Valley which is not described by the WRF model with a 1 km horizontal grid spacing. Therefore, these observations are inevitably influenced by local meteorological processes and are not necessarily representative of the region meteorology. To enlarge our vision, we include data of 7 permanent meteorological stations for the model evaluation in addition to the KASCADE observations. Six of these are maintained by Météo France (these are hourly averages), and the seventh is on the site of the Observatoire de Haute-Provence. However, it should be kept in mind that several of these stations are also situated at particular locations, undergoing local influences not seen by the model. All stations available for model evaluation are listed in Table 6.4. They are situated in or around the Durance valley (see Figs. 6.18a and 6.18b).

Table 6.4: Stations used for validation, their IDs and names, locations and height above sea level (asl) and in the model. The locations of the stations on a map are given in Fig. 6.18a and b.

Station ID	Name	Location [$^{\circ}$ N; $^{\circ}$ E]	Height asl [m]	Height asl in model [m]
M30	M30	43.68550; 5.76169	286	328
GBA	La Grande Bastide	43.69442; 5.74614	269	300
VER	La Verrerie	43.70744; 5.76514	295	326
StA	Saint Auban	44.06215; 5.98964	443	447
VAL	Valensole	43.83943; 6.00086	599	572
DAU	Dauphin	43.90982; 5.76719	443	408
BdJ	Bastide des Jourdans	43.78725; 5.61503	385	361
VIN	Vinon-sur-Verdon	43.73411; 5.78245	271	264
PEY	Peyrolles	43.65668; 5.60693	215	215
OHP	Observatoire Haute Provence	43.93301; 5.71468	650	602

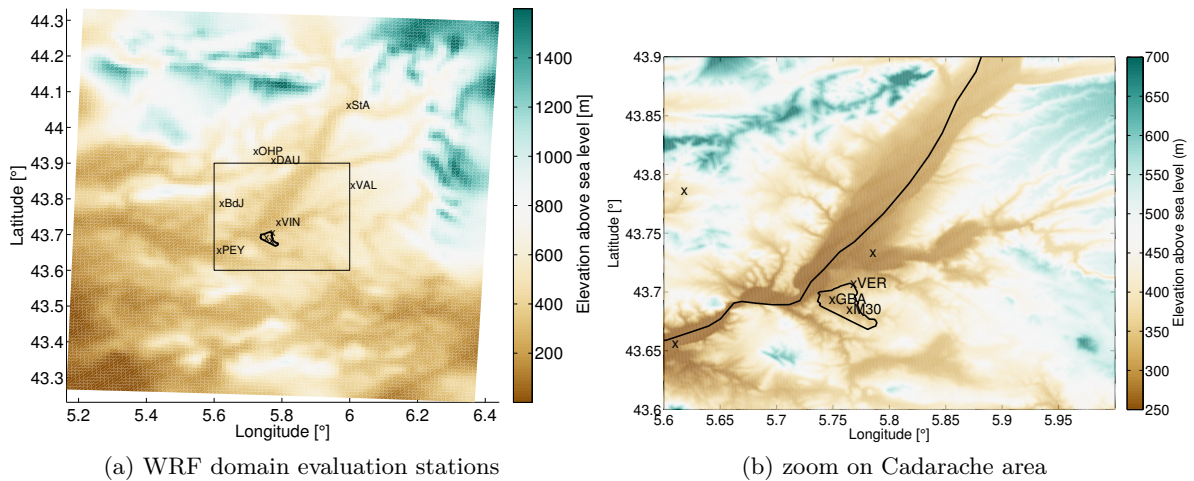


Figure 6.18: Stations used for model evaluation, a: the external stations for a large scale pattern and b: the stations used in KASCADE.

To evaluate the model against observations we use the framework presented in Sect. 2.4.1, notably Eqs. 2.1 to 2.8. In these equations 'o' stands for observations and 'm' for model output. In a first step, the evaluation is done for temperature, humidity (all stations) and atmospheric fluxes (M30). Then, special attention is given to wind speed and direction at 10 m (all stations) and aloft (Sodar and GBA tower), as the final goal is the DDV wind behavior for its implication in dispersion studies. The *DACC*, which gives a good indication on the accuracy of the model to forecast the wind direction whatever the direction, is the appropriate tool. All meteorological conditions (not only stable ones) are accepted for this evaluation.

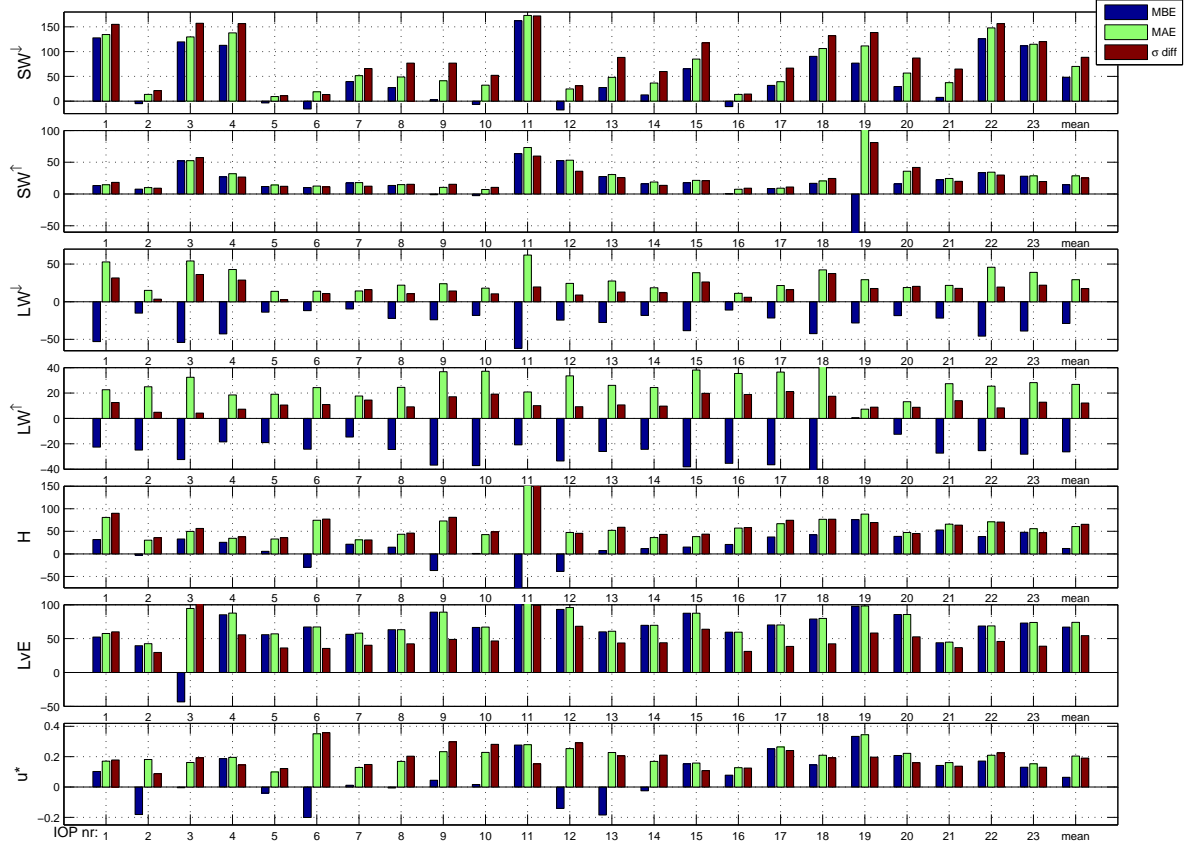


Figure 6.19: Estimations of daytime model errors for each IOP: mean bias error (MBE), mean absolute error (MAE) and standard deviation of the difference (σ_{diff}) against observations at station M30, for atmospheric fluxes ($W m^{-2}$) and friction velocity ($m s^{-1}$). The last column gives the mean value for all IOPs for each variable.

For this analysis we develop a subset of figures to deduce the model general behavior and its ability to simulate the IOPs. All IOPs are described separately and analyzed, this information can be found in Appendix B

6.3.2 Fluxes and turbulence parameters

To distinguish between the unstable and stable conditions, we present the atmospheric fluxes and friction velocity for daytime and night-time periods separately (Figs. 6.19 and 6.20). The bars give estimates of the bias, mean absolute error and standard deviation of the discrepancies (see Sect. 2.4.1 for their definition).

Shortwave radiation

As we have seen in Sect. 6.2 clouds can be easily missed by the model; the radiation scheme showed sensitivity on resolving clouds in the spin-up time of IOP 16 (Fig. 6.6). We chose the scheme with the lowest bias, and this scheme showed no clouds in its spin-up time. Hence that only for the outer domain a cumulus scheme has been used. In Fig. 6.19 the difference is clearly seen in errors for the shortwave incoming and outgoing components SW^\downarrow and SW^\uparrow , respectively; the errors for IOP 16 are relatively low, whereas for IOP 15 an overestimation of more than $50 W m^{-2}$ is found. Clouds or rain, which sometimes occurred along an IOP, are more often missed by the model, i.e. IOPs 1, 3, 4, 11, 15, 18, 19, 22 and 23 show the largest errors; it results in model overestimation. IOPs which have very low errors for the shortwave radiation components, notably IOPs 2, 5, 6, 12 and 16 were totally cloud-free in both observations and simulations. For example, especially IOP 2 was heavily influenced by Mistral and so the sky was clear in both observations and simulations. It can be seen as a confirmation that the parameterization

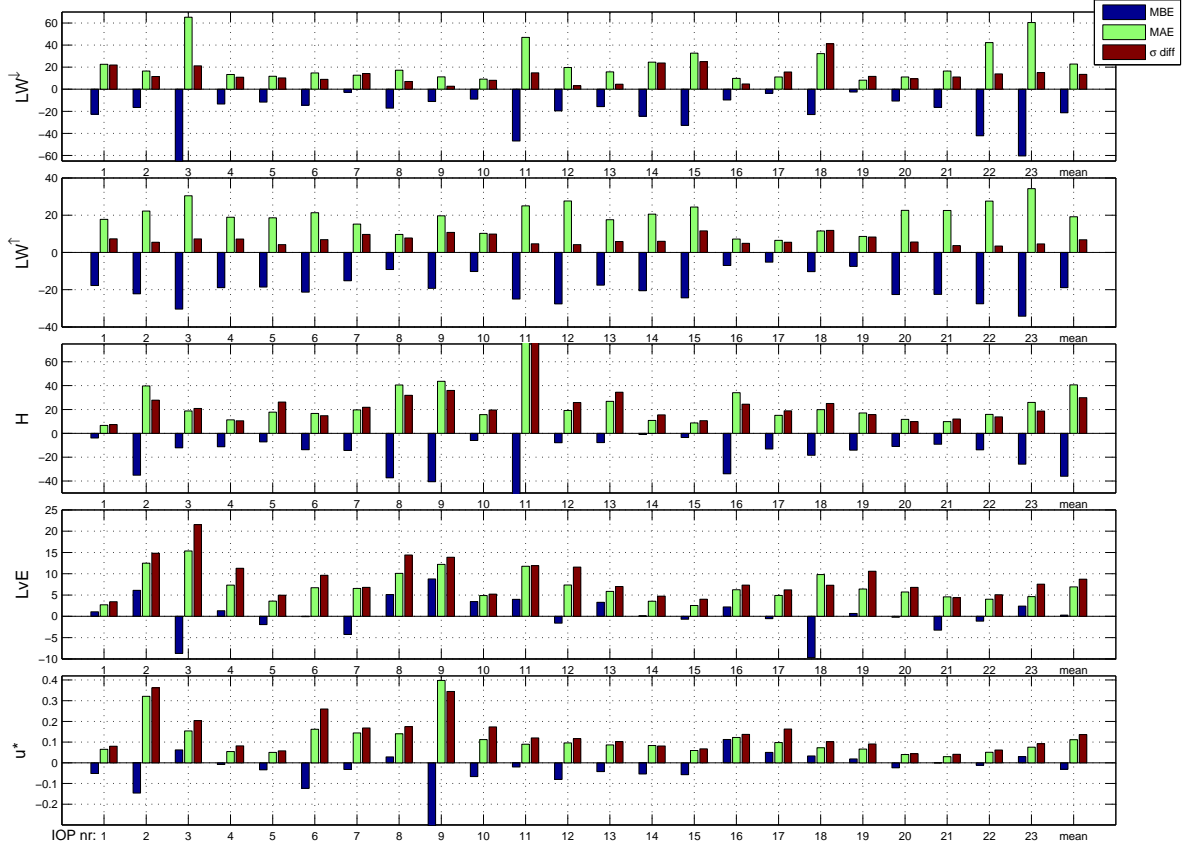


Figure 6.20: Same as Fig. 6.19 but for night-time data.

of shortwave radiation works properly. A special remark on SW^\uparrow goes to IOP 19, where SW^\uparrow is underestimated heavily, this is due to a snow layer being present in observations (see Chap. 4, Fig. 2), but not in the model. Largest errors for SW^\uparrow are obtained when rain events are encountered. Other IOPs very badly representing the SW^\uparrow are IOPs 3 (rain in the second half), 11 (rain at the start) and 12.

Longwave radiation

The influence of the lack of clouds is directly represented in the longwave components, during the day and night. Generally, the IOPs with clouds in the observations but not in the model perform very poorly for LW^\downarrow during day and night. LW^\downarrow is always underestimated in IOPs for which the observed clear sky is correctly simulated (e.g. IOPs 2, 5, 6 and 16). This means that the model atmosphere is always too cold and/or too dry. The same occurs for LW^\uparrow , where the skin temperature of the model is much lower during the day and the night. These results generalize the findings of Sect. 6.2.1. Note that, surprisingly, the errors for LW^\uparrow are lowest for surprisingly IOP 19 during the day, though the snow layer present in observations but not in the model. When we restrict to night-time clear sky cases without snow layers (i.e. IOPs 2, 5, 6, 7, 9, 10, 12, 13, 16, 17 and 20), average biases are found of -11.36 and -17.00 $W\ m^{-2}$ for LW^\downarrow and LW^\uparrow , respectively.

So, in some cases the biases of LW^\downarrow result from the presence of clouds not simulated by the model. It should be noted however that, for investigation of the DDV wind, the missing clouds are not a major problem. These IOPs are simulated with clear skies, and stability can form anyway in the model when winds drop during the night.

Friction velocity

For friction velocity u^* we take the observations from the CSAT sonic anemometer, installed at a

height of 30 m at M30 (see Sect. 2.3.1.2). We must be cautious in analysing the performance of the simulations because the measurements were conducted in a small valley which is not resolved by the model (Sect. 6.2). Big differences for the biases are found between night- and daytime values. u^* is largely underestimated for IOPs which were subject to heavy wind conditions, like IOP 2, 6 and 9. For the other IOPs, which were calmer, overestimations are generally found, especially from IOP 16 and during the day. During the night the errors are smaller, the values for u^* are generally smaller as well. However, u^* is represented relatively well at night except for IOPs 2, 6 and 9.

Heat fluxes

The under- or overestimation of u^* is reflected in the errors for H and partly for $L_v E$ during daytime. These are taken from the CSAT and the Li-COR at 30 m. The highest errors for these occur mainly when rain was observed (i.e. IOPs 3 and 11). High underestimations of H are mainly found for the IOPs with strong winds, i.e. IOPs 2 and 9. Excluding these IOPs, we see that $L_v E$ especially is largely overestimated during daytime, almost always by 50 to 100 W m⁻². Moreover, $L_v E$ is constantly overestimated, while the bias for u^* is variable and if it is overestimated it does not reach the same relative amounts as $L_v E$. This means that too much moisture is available in the model. By having too high values for $L_v E$, less energy is available for H and so suppresses mixed-layer growth, then entrainment is less and cooler PBL profiles are found. This might partly explain the negative bias found for LW^\downarrow . However, it should be noted that most of the time the energy balance is not closed from observations (Cuxart et al., 2015), and without soil heat flux observations it is hard to draw definitive conclusions on this.

For the heat fluxes during night-time, errors are largely controlled by the timing of decay of turbulence. IOPs 5, 20, 21 and 22 perform not too bad for the heat fluxes.

6.3.3 Temperature and humidity

The measured fluxes in the previous paragraphs were coming from local CV measurements, which can bias the conclusions especially for the heat fluxes and friction velocity. For the radiation components this problem is less important as they depend less on orography (the observations took place on flat terrain with a very low slope angle). To check the model performance for each IOP for a larger part of the innermost domain we compare temperature and humidity at 2 m for the 10 stations shown in Fig. 6.18.

The sensitivity tests presented in Sect. 6.2 already pointed out that the model underestimates the DTR, resulting from an underestimation of the maximum temperature and an overestimation of the minimum temperature. One can conclude that this occurs throughout almost all IOPs and for all stations, regarding the inconsistencies in the model by comparing with the observations the maximum, minimum and daily mean temperature (Fig. 6.21). Although between IOPs large differences are found, generalizations can be made.

The combination of the 110 and 2 m temperature at GBA gives an insight of valley effects and of its misrepresentation in the model. The foot of this mast is located inside the Cadarache Valley, unresolved by the model. Its top is above the valley sides, remote from ground influence, and therefore is expected to represent the meteorology at a larger scale. Between the IOPs large differences are noted, but the errors in the simulated temperature are always larger at 2 m than at 110 m (e.g. 4°C vs. 1.5°C for the mean temperature averaged over all the stations - last column of the figure). We have seen in Fig. 6.10 that a large bias was found for the temperature difference between 110 m and 2 m height, here it is confirmed that the bias is mainly caused by the 2-m temperature. For the minimum temperature difference, the stations M30, VER, VIN and PEY show the same behavior as GBA 2 m. M30 and VER show the highest mean overestimations (4°C) and VIN and PEY experience around 2°C. Note that VIN and PEY are in the resolved DV, unlike M30 and VER. Remarkably, DAU shows the same behavior as these

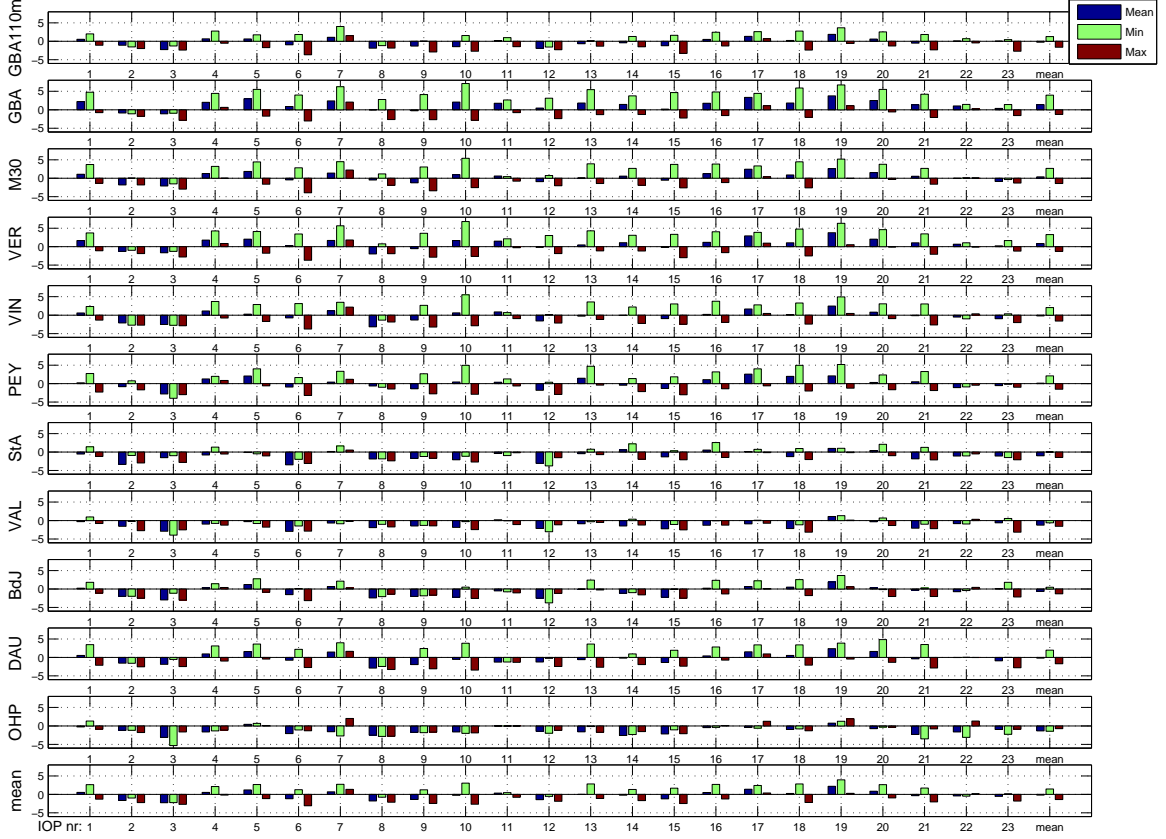


Figure 6.21: Model to observation differences in mean, maximum and minimum temperature (in °C) for each IOP at 2 m for all stations, and additional 110 m for the GBA location. The last column indicates the mean for all IOPs for each station. The last row reflects the mean for each IOP regarding all stations, without the 110 m values. An overall mean is given in the lower right corner.

sites. This station is far from the Cadarache site, but in a valley that is resolved. The other stations show irregular values at each IOP for the minimum temperature differences.

A quite homogeneous behavior is shown for the maximum temperature GBA 2 m and 110 m. The results are of the same sign, but the 2 m temperature is more underestimated. In general, all other stations show similar differences. The model is frequently underestimating the maximum temperature. This is true for all stations, and all IOPs, with the exception of IOP 7. Altogether the last column shows that at 2 m, on average, the minimum temperature is overestimated and the maximum temperature is slightly underestimated.

To summarize, the average of all stations and all IOPs, the global bias (MBE) for temperature is around zero (Fig. 6.22). This is however with an accompanying uncertainty σ_{diff} of 2°C. Values of MBE , MAE and σ_{diff} are different for each station and IOP (Fig. 6.22). Errors at the surface are higher than at 110 m (GBA 2 m vs. 110 m). Stations close to Cadarache also show the highest errors, with the most extreme ones in the second part of the campaign (i.e. from IOP 15). These show mainly positive biases, and are mainly controlled by the high overestimation of the minimum temperature (see Fig. 6.21).

Again, between stations large differences are found for each IOP. The means of MAE and σ_{diff} are all around 2°C. Regarding σ_{diff} especially VAL and StA score better. Temperatures are mainly underestimated for high wind speed conditions (IOPs 2, 3, 8 and 9 were (partly) subjected to Mistral conditions), but σ_{diff} are among the lowest especially for IOP 2. It is a signature of our model to have more difficulties with the cooling than with mixing. The positive biases for the Cadarache stations are mainly found for IOPs 1, 4, 5, 7, 10, 11, 13, 14, 16 to 22. These were IOPs with considerable formation of stable stratification in the observations. They

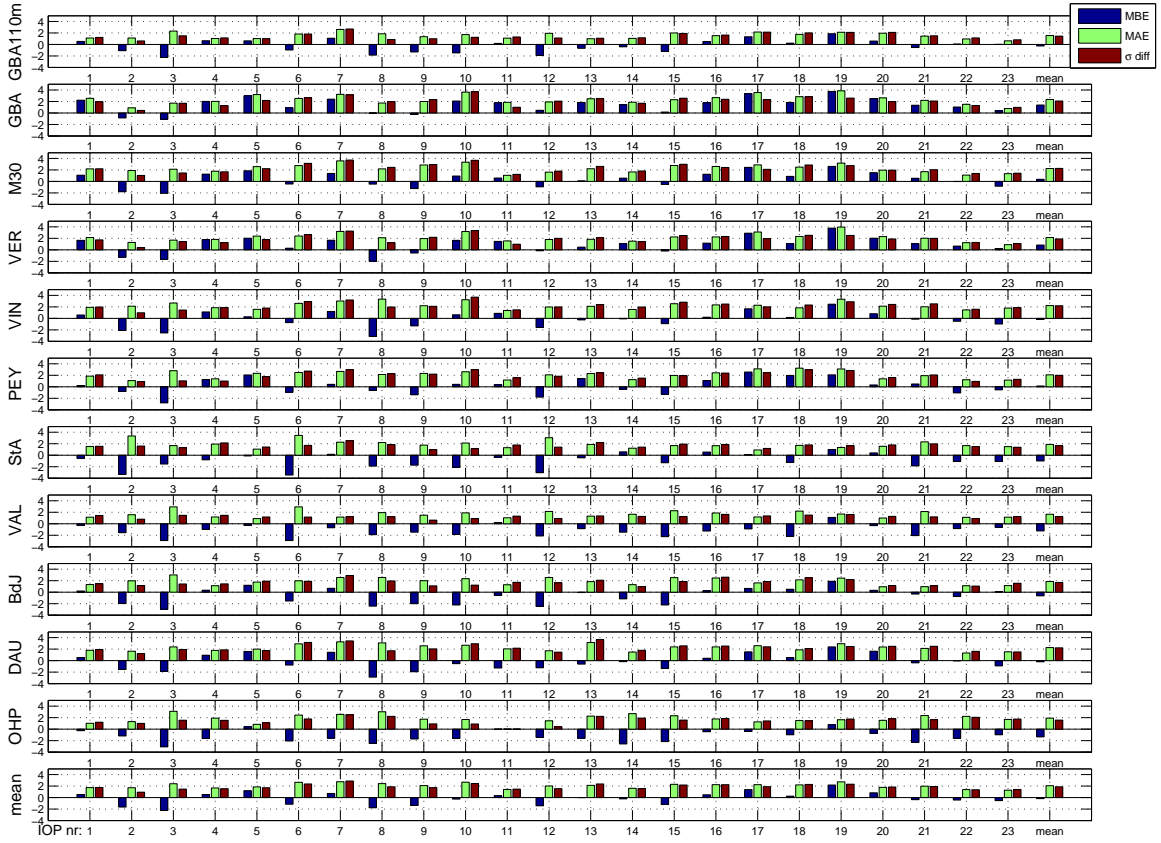


Figure 6.22: Same as Fig. 6.21 but for mean bias error (MBE), mean absolute error (MAE) and standard deviation of the difference (σ_{diff}).

are also the IOPs which show the highest errors for MAE and σ_{diff} . Regarding the fact that we are dealing with stations observing in unresolved valleys, these results are not surprising.

For the evaluation of humidity, we use the 2-m mixing ratio (g kg^{-1}) for the model and observations at all stations. The variability from one IOP to another is larger than the variability between the stations for a given IOP (Fig. 6.23). Generally, the model overestimates the humidity which can be related to too moist soils, leading to too moist profiles. The errors per station are of the same order. IOPs with the highest errors are 7, 8, 14, 17 and 18, from which IOP 7 is the worst. Data for IOP 11 are lacking. The general overestimation in the model is around 0.3 g kg^{-1} .

6.3.4 Wind speed and direction

The most important expectation from the model is that it should be capable of simulating the DDV wind. The initial study of the optimal configuration for the region, which involved IOP 16, showed that the model was able to represent this wind. In this section, we test the model for all IOPs.

6.3.4.1 Available observations

The validations for temperature and humidity at screen level have shown that the model is capable to get the general patterns of the IOPs, but has trouble with unresolved orographic local effects. We now want to test the model on its capability to simulate the general wind pattern, especially the DDV wind. For that purpose we use the GBA data at 110 m and the Sodar values at 100, 150, 200, 275, 350, 450, 600 m agl. No means is available to test the Sodars capability above 400 m, so the upper two heights remain questionable. The DDV wind appeared

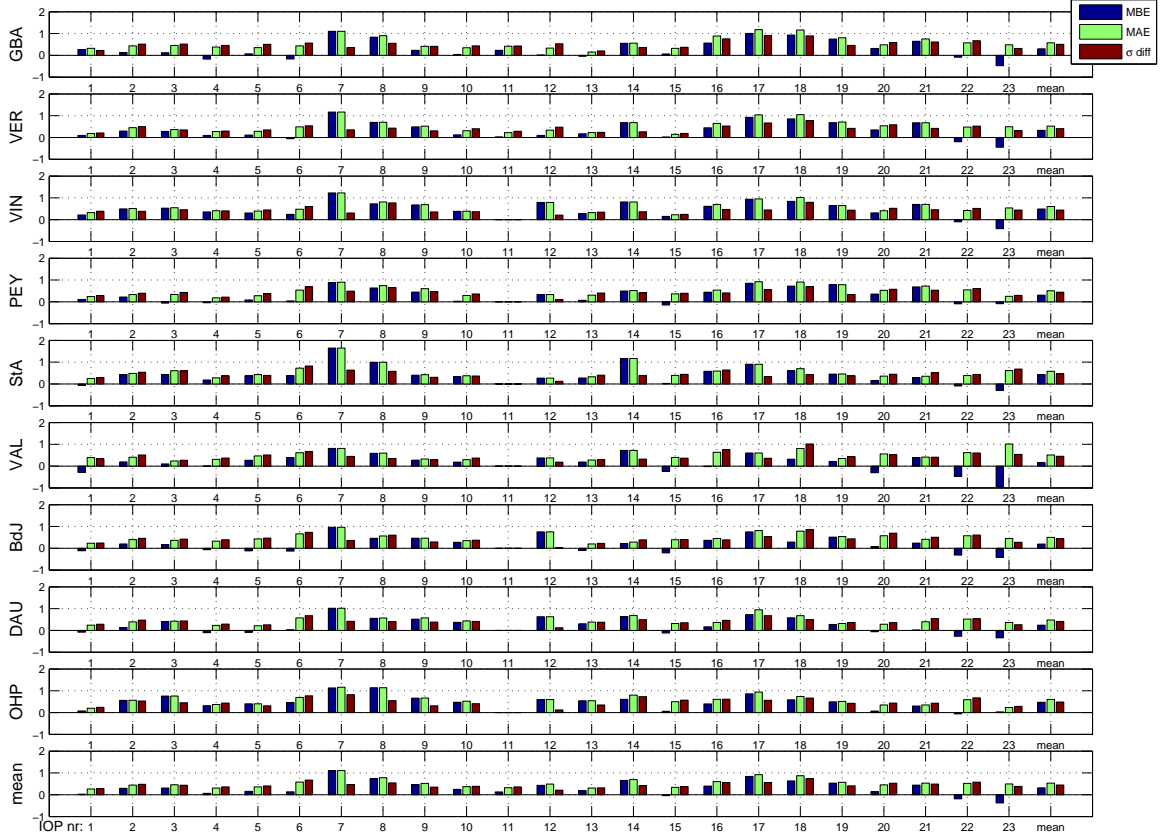


Figure 6.23: Same as Fig. 6.22 but for the humidity mixing ratio at 2 m (g kg^{-1}) at all stations. No data available for GBA at 110 m.

to be mostly present between 100 and 300 m (see Chap. 4). It should be remarked however that observations were rarely available outside this range. The GBA measurements are 10 min averaged, the Sodas give averages on a frequency of 15 min.

Additionally, measurements are available at a height of 10 m for 9 stations (all but GBA). Only a general check will be made: firstly, because the local orography at the stations is not always resolved by the model; secondly because the purpose is to evaluate the model for the DDV wind. Other winds important for dispersion, are driven at the mesoscale (see Chap. 4) and this mostly requires a validation against observations aloft rather than at 10 m. The data of these 9 stations are averaged over an hour.

The use of the Sodar as a validation tool is also beneficial, regarding the local measurements of KASCADE. The layers reached by the Sodar are representative of winds mostly advected at a regional scale, which indirectly permits validation for a larger area than the Cadarache site. Moreover, as we validate the model against observations at 110 m and higher, no drag effect is expected (Santos-Alamillos et al., 2013).

6.3.4.2 The use of instantaneous variables vs. average model output

Before an evaluation is made for wind, an important feature concerning the use of instantaneous model data should be clarified. The IOPs were simulated with an output resolution of 30 minutes, and for analysis instantaneous output variables are used. Even though the output value is already an average over the time step used (120 s in configuration 1) and over a grid cell size of 1 km^2 , using instantaneous variables for wind is not the most convenient method in the boundary layer as this can be rather noisy, especially in the lower layers.

To check the validity of using instantaneous variables from the WRF-output, we compare

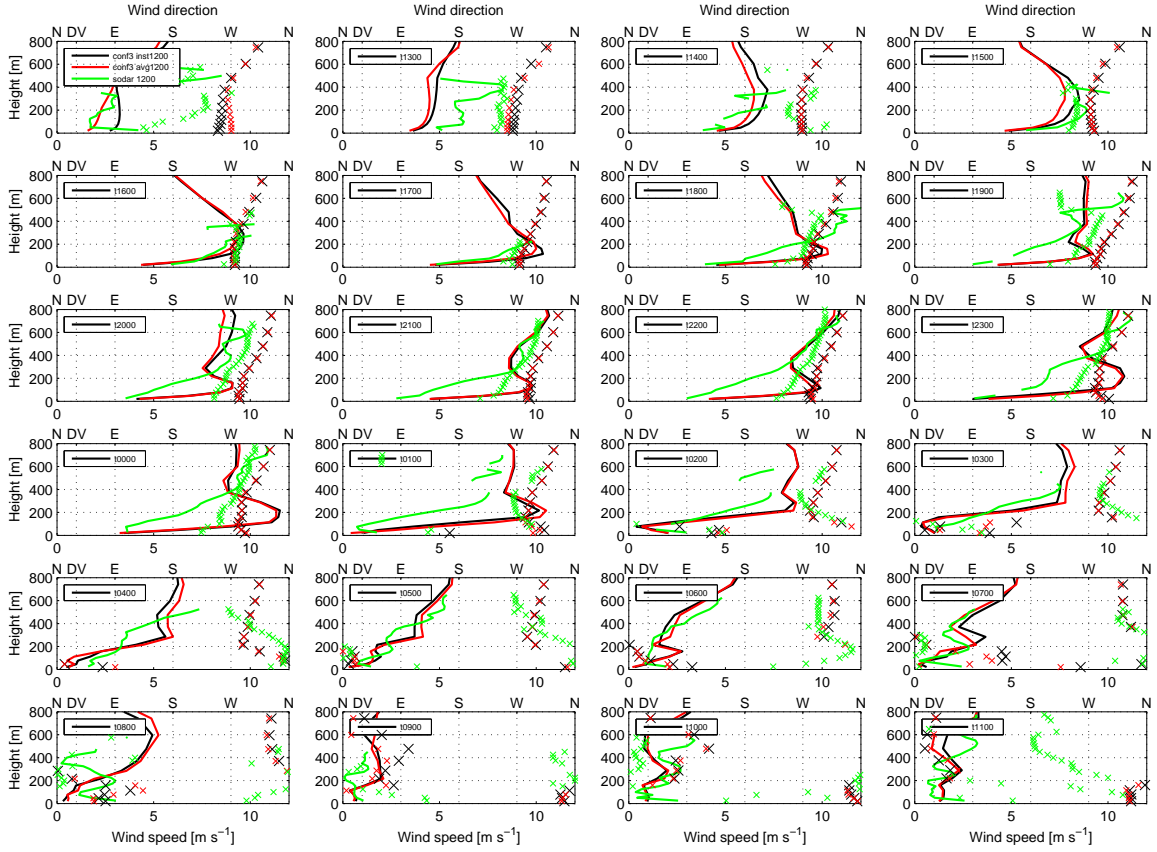


Figure 6.24: Comparison of average and instantaneous wind speed (lines) and direction (crosses) for different times during IOP 16. For reference, the sodar observations are given as well.

them with winds averaged over the output time interval which are available using the mass-weighted time-averaged winds on the given sigma-levels². Especially for vertical wind speed averages, the improvement is significantly large and its use is strongly recommended. On the other hand, for horizontal wind speed there is little improvement when using the output resolution-averaged rather data than the instantaneous output (Brioude et al., 2012). Anyway, we will compare for one IOP the differences between the instantaneous and averaged winds.

Figure 6.24 shows these differences for wind speed and direction, at each hour during IOP 16. For reference, the Sodar observations are given as well. The instantaneous value is the model output at a given time, whereas the average is done on all time steps of the preceding half hour. Qualitatively, we can conclude that the differences are small, for both wind speed and direction. Note that the largest differences are found during transitional periods, and especially when wind speeds are weak, a well known issue. That is why for the validation of wind direction, wind speeds below 0.5 m s^{-1} were eliminated. Table 6.5 quantifies the validation and confirms that differences are negligible. The bias (*MBE*) and mean absolute error (*MAE*) for wind speed are less than 5% of the total mean value ($=5.45 \text{ m s}^{-1}$). *MBE* and *MAE* for direction are of the same order. The coherence between the instantaneous and averaged wind is also reflected in the directional accuracy *DACC*, which shows a very high value.

We conclude that there are differences for wind speed and direction when using the instantaneous values, but these are negligible compared to the differences found between observations and simulations. Besides, most of the winds between 100 and 400 m are well developed. So,

²An additional option is available from WRF v3.3 to get output called *AVGFLXRUM* and *AVGFLXRVM*. These fluxes are coupled to the dry air mass in the column, so units are $\text{Pa m}^{-1} \text{ s}^{-1}$. *AVGFLXRUM* and *AVGFLXRVM* should be uncoupled by dividing them by the mass-factor MU and MUB (units in Pa), which are the perturbation and base state dry air mass of a column, respectively.

the use of the instantaneous output rather than the time-averaged output will not influence our conclusions for validating the wind simulation.

Table 6.5: Summary statistics between the instantaneous and averaged values for wind speed direction for IOP 16. The model levels 4, 5, 6, 7, 8, 9 and 10 at VER-site and the level 4 at the GBA-site are considered. These are the levels used for further model validation against observations.

summary	Wind speed [m s^{-1}]	Wind direction [$^{\circ}$]
<i>MBE</i>	0.017	1.43
<i>MAE</i>	0.283	4.37
<i>DACC</i> ($< 30^{\circ}$)	-	98.21%

6.3.4.3 Wind speed

Figure 6.25 shows the statistical errors of model wind speed for each IOP and several heights. In configuration 1, the heights correspond to the model layers 4, 5, 6, 7, 8, 9 and 10 corresponding to heights of 120, 160, 220, 290, 380, 480 and 610 m agl, respectively. No interpolation procedure has been followed. Negligible difference between the errors is found for the wind speed at 110 m at GBA and 100 m at VER. Again the differences between the IOPs are large. The largest errors are found for IOPs 2, 9 (both with Mistral winds), 13, 17, 18 and 22. At heights below 350 m it is slightly underestimated, but with a large spread. IOPs 17, 18 and 22 were synoptically driven with southeasterly flow, which was highly overestimated by the model at all heights. Channeling of the DV direction was observed and modeled, and so within the DV itself (i.e. below 300 m) the errors are relatively low. During IOP 13 a DDV wind occurred but the jet was highly underestimated. Regardless the Mistral-subjected IOPs, the model overestimates wind but with a large scatter (i.e. high σ_{diff}). IOPs 7, 14, 16 and 21 perform relatively well, with small errors for all estimators.

6.3.4.4 Wind direction

The directional accuracy *DACC* (see Eq. 2.7) is a proper parameter to evaluate our simulations for wind direction. We do this with an allowed difference of 30° between model and observations. The same layers as in the section for wind speed are used. *DACC* being a percentage, the higher the score, the better the model performs, with an optimum at 100%.

We highlight some features of the results presented in Fig. 6.26 that shows on one hand the *DACC* (red bars), and on the other hand two useful values: the total measurements population used to compute the *DACC* (green bars) and the number of successful values for *DACC* (yellow bars). The higher the population the higher the *DACC* reliability. The Sodar has good data availability up to 500 m, above that data is missing regularly (Sect. 2.4.4), consequently the observations for validation at 600 m are not numerous. The closer to 100 m the higher the number of observations, and so the representativeness to test with *DACC* increases.

For wind direction in general, the highest scores are found for IOP 2, 7, 16 and 22, with values over 90% for GBA, around 70% for other layers and an average value of around 70%. For IOP 2 this is not a surprise, as this is an IOP subjected to strong Mistral, in other words, strong synoptic forcing. However, errors for wind speed were considerably high. IOP 7 and 22 show high scores, on average even higher than IOP 2. This is promising, because, as noticed before, DDV winds were present during these IOPs. IOP 16 is performing relatively well.

Very low scores are found for IOPs 1, 10, 17 and 23. IOP 1 had a precipitation event in the early morning with some DDV wind onset just before. IOP 10 was subjected to clear skies and westerly winds; a DDV wind was not observed but simulated. IOP 17 showed a high overestimation of the wind speed (Sect. 6.3.4.3); a DDV wind was observed whereas the model simulated a southeasterly winds. During IOP 23 synoptical southeasterly winds were the

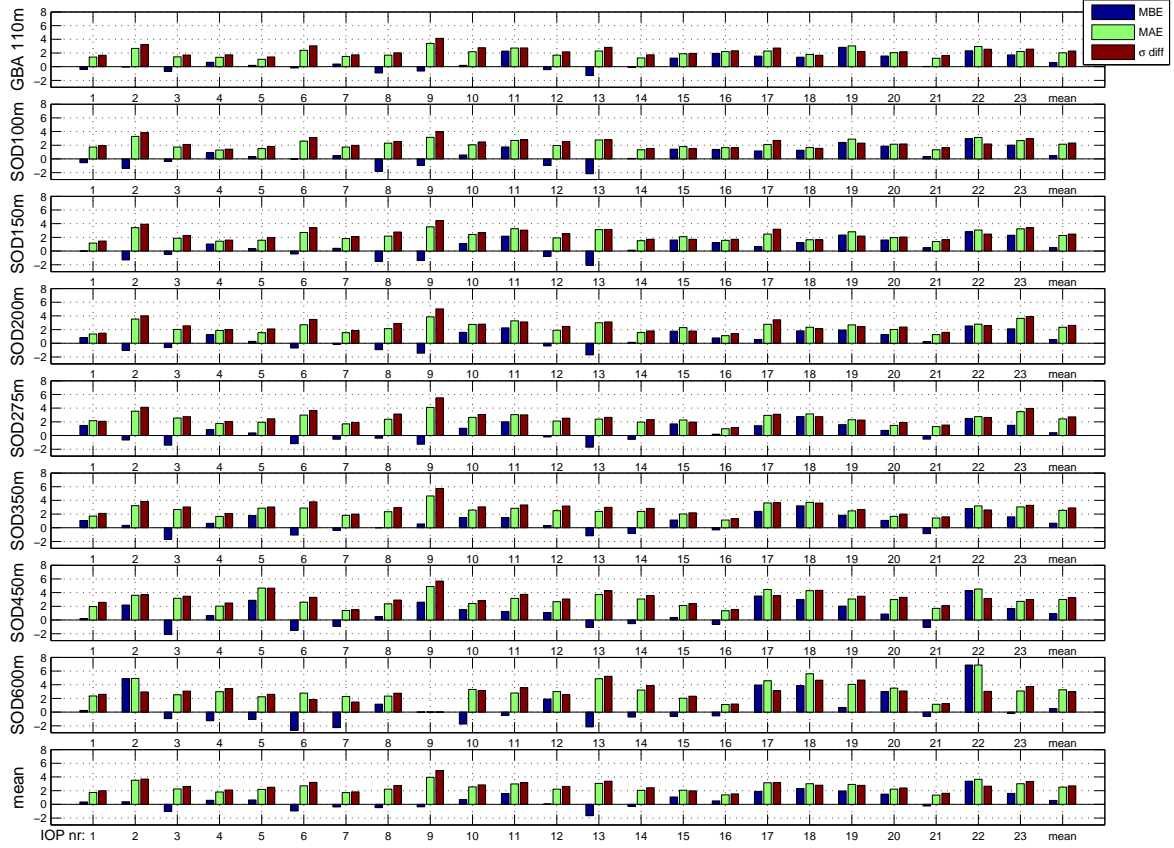


Figure 6.25: Wind speed model errors ($m s^{-1}$) for all simulated IOPs with respect to GBA (110 m) and Sodar (located at VER) at various heights. The same statistical criteria as in Fig. 6.19 are used.

driving forces, but in the end of the night a DDV wind settled and extended even up to 500 m agl, whereas in the model the wind direction was easterly at the beginning of the IOP, and a DDV wind sets in only below than 200 m.

Overall, the $DACC$ gives a good insight on which layers are modeled best. Also between the layers the differences are large. On average the layers at 150, 200 and 275 m show the highest scores. Above 350 m the scores drop. The variability is large for these layers among different IOPs.

6.3.4.5 Skill for Durance down-valley wind direction

The previous sections have shown that there are several layers in which the model simulates the wind rather well. As we are interested in the DDV wind, we use the $DACC_{DDV}$ from Eq. 2.8 that focuses on the DV orientation at Cadarache. Note that we accept values between 10 and 50° to smooth out some fluctuations from observations as well as from the model. The score for $DACC_{DDV}$ for all IOPs at the same heights as in the previous section is shown in Fig. 6.27. The occurrences of the DDV wind in observations and simulations are shown by the green and yellow bars. The latter are given to obtain more insight in the strength of the $DACC_{DDV}$ as a relevant value for assessing the model performance. For example, $DACC_{DDV}$ for IOP 16 is 100% at 150 and 225 m, but it seems to be rather a lucky shot regarding the total number of observations and simulations, i.e. only 3 and 4 times, respectively. However, regarding Fig. 6.26, these layers are simulated to a good extent for IOP 16 in general. This suggests that the 100% score for $DACC_{DDV}$ might not just be a lucky shot after all.

0% scores correspond to scarcely or no DDV wind observations at all and indicate that no DDV wind occurred during that IOP. This was the case for IOP 2, 8 and to a lesser extent

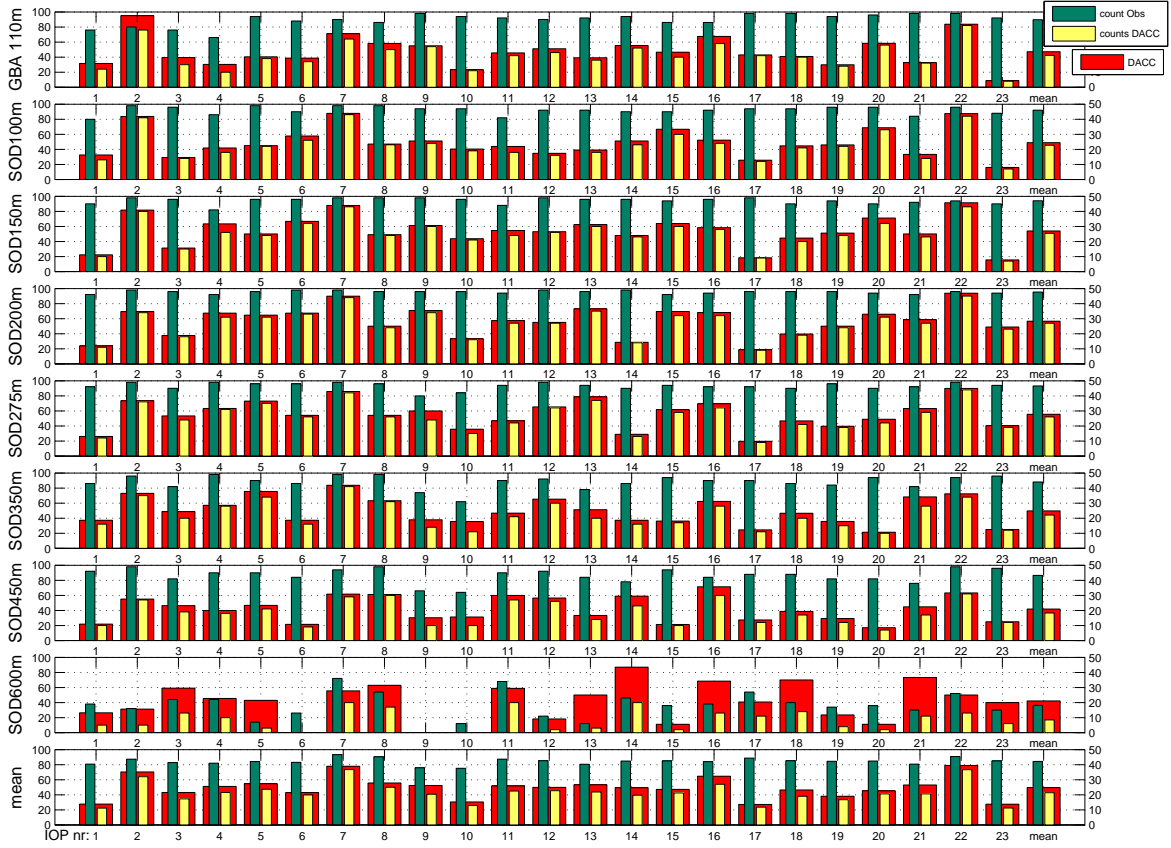


Figure 6.26: Model evaluation for wind direction against observations at GBA and several heights of the Sodar for each IOP by means of a DACC of 30° . On the left axis are DACC percentages, on right axis data counts. The last right column gives the average over all IOPs per selected height, the last row gives the average over all heights per IOP.

during IOP 9. 0% scores *with* DDV wind observations however also reveal the model failure to forecast the DDV wind. A good example for this situation is IOP 17, where we directly see that up to 600 m DDV wind directions are observed that are completely missed by the model. Considering the low $DACC$ for this IOP (Fig. 6.26), we conclude that this IOP is simulated very badly.

In general, $DACC_{DDV}$ is especially high for the levels 100, 150 and 200 m. Channeling effects are likely at these heights in both observations and simulations and probably explain the high scores within the valley. But, DDV directed winds are simulated and observed not only within the valley, as winds above the valley do occur as well. For example, at 450 m agl the DDV wind is observed and modeled during IOPs 4, 5 and 19.

The use of $DACC_{DDV}$ directly gives a good insight into the IOPs for which the model is capable of simulating a DDV wind. The best ones are IOPs 4, 6, 7, 13, 15, 19, 20, 21, 22 and 23, which have both high $DACC$ and occurrences. Ranking second are IOPs 5, 11, 12, 16 and 18, which have rather high $DACC$ s, but do lack a high number of occurrences. However, IOP 16 scores very well also for all wind directions, and the $DACC_{DDV}$ is a very good result. Lastly, the high score of IOP 7 is remarkable because it showed very large errors for the minimum temperature and humidity (Sect. 6.3.3).

Note on DACC A flaw in using this method is that we give the model a 'correct' hit when observations and simulations DDV wind direction match at the same time. This method does not count a 'correct' hit when there is a delay in onset or cessation of the DDV wind in the model. These situations are not reflected by the $DACC_{DDV}$ indicator and should then be

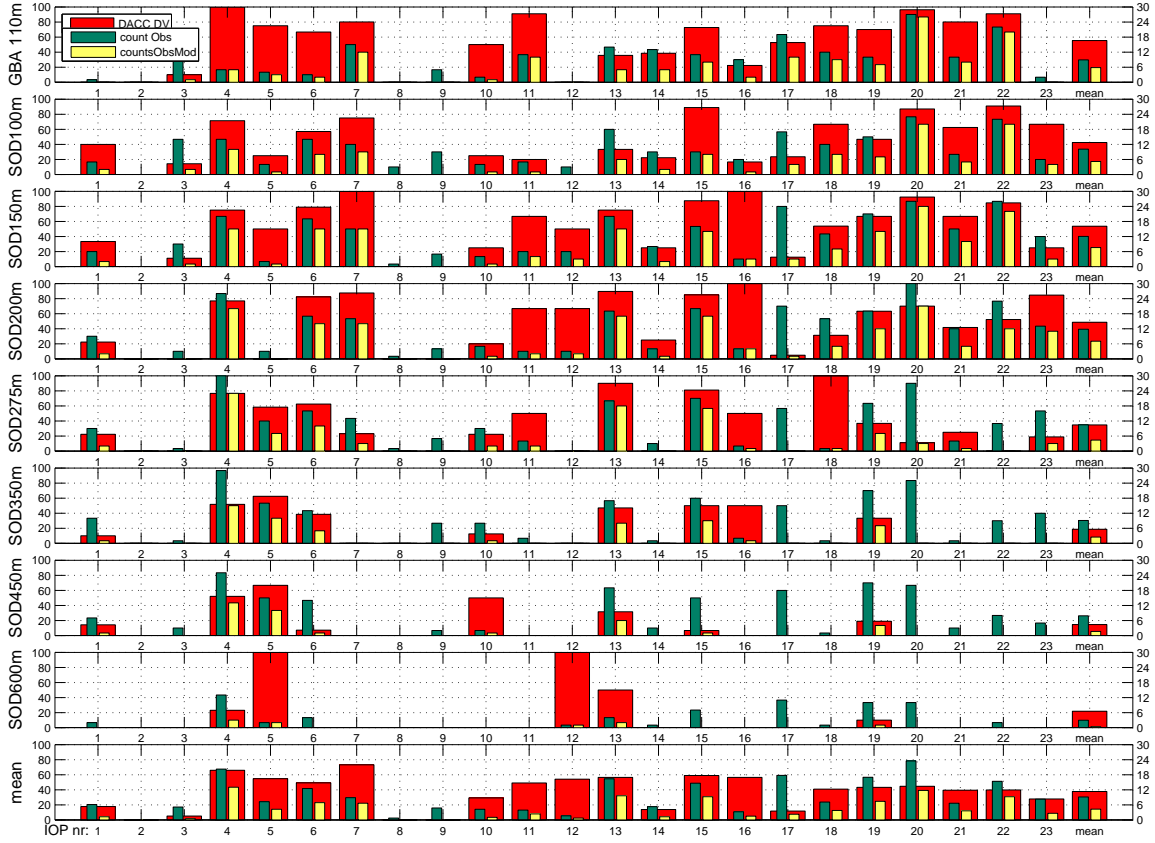


Figure 6.27: Same as Fig. 6.26, but restricted to the observed wind directions in the range $[10 - 50^\circ]$.

analysed differently through daily occurrence and daily duration time for instance.

6.3.4.6 10 m wind

For model evaluation at 10 m high, local effects become more important. For example, a misrepresentation of the valleys in the model itself, bearing either on orography or landuse (Santos-Alamillos et al., 2013). A second problem is that the use of instantaneous variables becomes more influencing at 10 m high than above. Figure 6.28 shows the errors for wind speed at all stations, for reference the GBA at 110 m is plotted as well (no observations at 10 m are available at this site). Errors are largest for some of the stations close to or inside the Cadarache valley (M30, VER, PEY). IOP 9 (a weak Mistral IOP) is one of the worst simulated in this comparison for all stations. Winds are overestimated mostly at Cadarache stations (M30, VER), which increases the suspicion of a local valley effect which is not resolved.

Figure 6.29 shows the *DACC* for all stations at 10 m. Here relatively high scores are found for 110 m. This is strongly related to the fact that the observations *and* the simulations are not affected by unrepresented valleys. The OHP station lacks a representative amount of values for wind direction; the source for its low availability is unknown. M30 is situated in the Cadarache valley, thus the *DACC* is very low for this station. A station which is relatively well represented by the model is station VAL, situated on the Plateau de Valensole: it shows even higher scores than GBA at 110 m.

Particular interest goes out to VER, VIN, PEY and StA as they are situated inside the DV which is sufficiently large to be rather well resolved at 1 km grid spacing. From these stations, the closest to Cadarache VER and VIN score very badly. Especially the low score for VIN is surprising, as this station is situated in the heart of the Durance Valley. However, it is at the confluence of the Verdon Valley, which may play a role in dominant wind patterns.

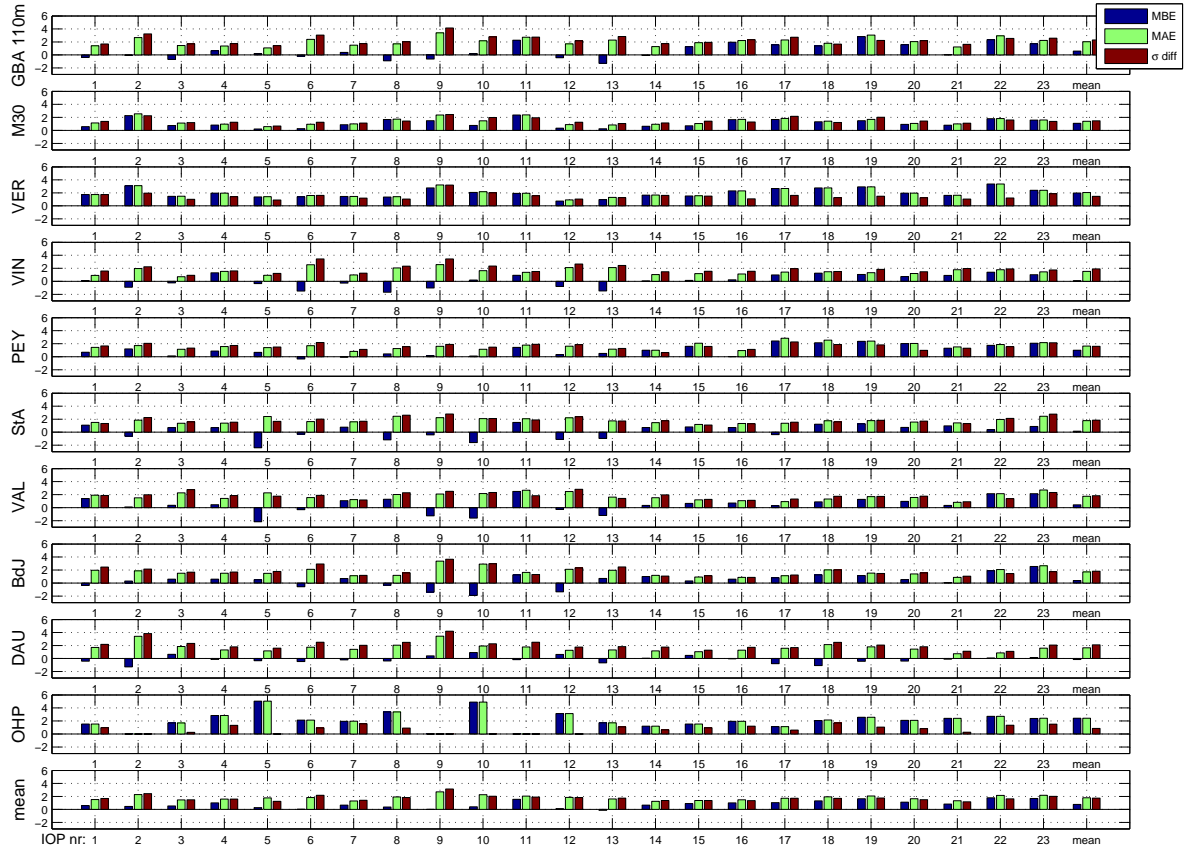


Figure 6.28: Same as Fig. 6.25 but for all available stations with 10 m wind speed observations ($m s^{-1}$), except for the GBA tower where the 110 m height is shown.

6.3.5 Summary of the model performance

The model is evaluated in the reference configuration against observations. As the KASCADE observations were very localized, this evaluation has been extended with the observations of seven distant meteorological stations. Although IOPs were conducted in very different circumstances which were not necessarily present in the simulations, generalizations could be made. In general, for clear sky situations both components of longwave radiation are underestimated. During weak synoptic forcing, sensible heat fluxes are overestimated and generally the same is found for the friction velocity. Considering a general higher overestimation of $L_v E$ (i.e. relatively), the conclusion of Sect. 6.2.1 that the model is too moist is confirmed.

Temperature and humidity at 2 m have been evaluated on a spatial scale in the Cadarache surroundings. The model has the highest difficulties during cold periods, the minimum temperature at 2 m is largely overestimated (i.e. by more than $2^\circ C$) for all stations. The largest biases come from stations close to Cadarache. Note that a correct estimate of the 2 m temperature, besides a good representation of the observational site in the model, would also require a higher vertical resolution (Larger0n, 2010; Jiménez and Cuxart, 2014; Burns and Chemel, 2014). We recall that an increase in vertical resolution enhanced the cooling at the surface, but this did not improve the results regarding our goal: prediction of the DDV wind. Humidity is generally overestimated (by $0.3 g kg^{-1}$), confirming the high positive biases of $L_v E$ and the confirmation that the model is too moist in the inner domain.

Wind speed and direction are evaluated against Sodar observations and the GBA tower at 110 m, and at 10 m for a total of 9 meteorological stations. In general, the wind speed is overestimated at all levels. Lowest errors and biases for wind speed are found within the DV itself, although differences are small in comparison with the errors above the valley. For

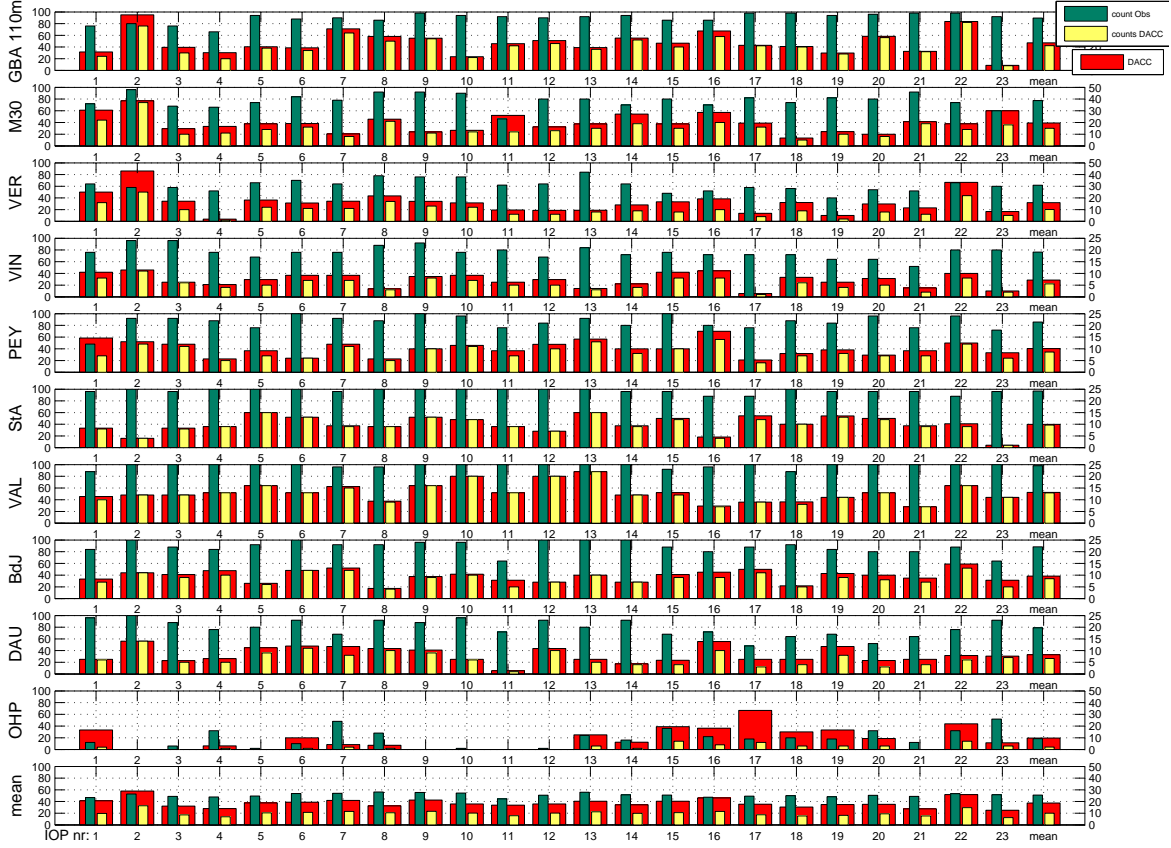


Figure 6.29: Same as Fig. 6.26 but for all available stations with 10 m wind observations.

wind direction, a similar pattern is found. Within the DV the model shows the highest values for $DACC$ and $DACC_{DDV}$. On a regional scale, the model overestimates the wind speed, with again, the highest biases for stations close to Cadarache, with the exception of the Vinon station, but at this location the model performs poorly for wind direction.

For the DDV direction, the model performs quite well, although during some IOPs it can be totally missed, or simulated when not observed. However, in 15 IOPs the development of a DDV wind is obtained, with different types of appearances; sometimes it is present as a channelled flow in the DV, sometimes present up to 600 m well above the DV depth. The latter occurs mostly in the observations and less in the model.

6.4 Conclusions

The mesoscale numerical model WRF has been used in a downscaling procedure on a 1 km horizontal grid spacing for the inner domain to explore the characteristics of the DDV wind. In a first step, the model has been set-up to a reference configuration by means of IOP 16 simulations. This IOP was recognized as one of the calmer IOPs concerning synoptic forcing, had a nearly perfect radiation balance, without disturbances of external influences such as a snow layer. The model performance has been evaluated by using several combinations of PBL, land surface and radiation schemes. The various tests revealed small variations in the model performance, but, anyway, it was capable of simulating the DDV wind. However, several problems concerning modeling performance were recognized. In general, the model fails to predict the high diurnal temperature range, mixed layer profiles are too cold and moist, and the PBL is not deep enough. The warm and dry upper air advection has been simulated, but with some delay. Stable boundary layers are well simulated, but processes related to the small Cadarache Valley were not simulated, as they cannot be resolved with a 1 km horizontal grid

spacing. Both a stronger land surface coupling and a decrease in soil moisture content lead to better atmospheric profiles, but also to unrealistic repartition of the atmospheric fluxes. The study of IOP 16 resulted in a combination of parameterization schemes, which constitutes the reference configuration. It should be noted that this choice was based rather more on experience than on performance for the IOP simulation, because of the model's relative insensitivity to the various configurations.

Then all 23 IOPs were simulated in the reference configuration. Based on the presence of a DDV wind in the model, a selection of 13 IOPs was made. These were simulated with a second and third model configuration: the increase of vertical resolution and the extension of the inner domain, respectively. The increase of vertical resolution resulted in minor improvements of the boundary layer profiles, but the surface cooling is enhanced. This did however not improve the DDV wind representation by the model. The extension of the inner domain only resulted in some improvement of the wind profiles. An additional test with a 3 km horizontal grid spacing showed the importance of using a higher grid spacing for DDV wind development in the model, especially close to the Cadarache site. It should be noted that this was tested only for IOP cases.

The reference configuration was chosen as being good enough to investigate the DDV wind. First, a full model evaluation has been done on all the 23 IOPs against the KASCADE observations and 7 meteorological stations. In general, clouds are not simulated when observed. For the clear sky periods in observations and simulations, incoming and outgoing longwave radiation are underestimated. No direct conclusions could be made on the turbulent fluxes as these observations were made locally in the CV. However, the overestimations found for IOP 16 do show a general pattern valid for all IOPs. Especially the latent heat fluxes are overestimated, which is not always found for u^* and H , and therefore the soil moisture treatment is a potential problem. Seven additional regional stations completed the assessment of the model inner domain capability to simulate 2 m temperature and humidity. In general the model highly overestimates the minimum temperature, especially close to the Cadarache site. However, local patterns particular to our measurement site could cause larger errors. Maximum temperatures are found to be spatially homogeneous but generally underestimated (i.e. the value for underestimation is of the same order for all stations). Biases for temperature were found to be very different for each IOP. The model overestimates the 2 m humidity mixing ratio with large differences between IOPs but with coherent patterns between the stations.

During IOPs which are subjected to strong winds as Mistral, the model underestimates the wind in the lower 300 m. For IOPs which are subjected to DDV winds the model generally overestimates the wind in the lower 300 m. The wind direction is captured with the highest performance at 275 m. The directional accuracy defined to identify the DDV wind, pointed out that the layers within the DV are simulated best. Above the DV depth, DDV directed winds are regularly observed, but not simulated. The IOPs performing best in simulating the DDV wind showed the highest errors for minimum temperatures. 10 m wind has been checked for all available stations, with the highest scores for the Plateau de Valensole station. But, as observed for 2 m temperature and humidity, local effects play a large role in the model's scores.

After the sensitivity tests and their thorough evaluation performed, in the next chapter we continue the DDV wind investigation on a regional scale by means of the simulations done in the reference configuration.

Chapter 7

Durance down-valley wind

7.1 Introduction

In the previous chapter we have determined a reference configuration, which has been evaluated against observations for all IOPs. In the model evaluation it was shown that it is capable to simulate the DDV wind. This chapter is devoted to explore the DDV wind in time and space to point out its origin. For this, we use the 23 IOPs as simulated in the reference configuration.

First, the the simulations are used to figure out DDV wind characteristics in time and space along the DV (Sect. 7.2). This analysis resulted in a method to study the DDV wind along its valley for IOPs individually (Sect. 7.3). Then, the origin of the DDV wind is clarified by relating the valley wind to above-valley winds (Sect. 7.4). Concluding remarks are given in Sect. 7.5.

7.2 Durance down-valley wind characteristics

7.2.1 Timing and height

The phenomenological study done by means of observations, presented in Chap. 4, has shown that the DDV wind could be related to sunset and sunrise times. It proved further that during most IOPs other relative important mesoscale phenomena were of second order importance. To increase the knowledge on the model's capability to simulate the DDV wind, we shall make use of wind direction probability density function (pdf) diagrams based on the 23 IOPs simulations done with the reference configuration (Fig. 7.1). Note that this is the same type of figure as Fig. 14 of Chap. 4, which we have reproduced in Fig 7.2 but with a lower time resolution since the Sodar output was twice as high as the model output (15 vs. 30 minutes). Furthermore, the vertical resolution is different between the model and the Sodar. Within the lower 400 m the Sodar gives output at 16 levels whereas the WRF configuration has only 8 grid levels, shown by the red dots in the top left diagram of Figs. 7.1 and 7.2. Nevertheless, these figures can give an idea of the model's capabilities to capture the regional meteorology and help to discuss some general patterns and differences between model and observations.

During the afternoon, the typical westerly wind is well captured by the model. The south-easterly events occurring during some IOPs are also well simulated. Normally, the latter winds are synoptically driven, which proves that synoptical patterns for these IOPs are simulated to a good extent. Also the DDV direction is set in both figures from 6 to 9 hours after sunset. The model also represents the pattern found for the timing around sunrise, when the DDV wind is at its strongest and the daily driven flows are at their weakest. Overall, the core of the DDV wind in the model is around the same direction and same height as in observations. However, some differences between simulations and observations can be noted concerning onset, cessation and the vertical structure.

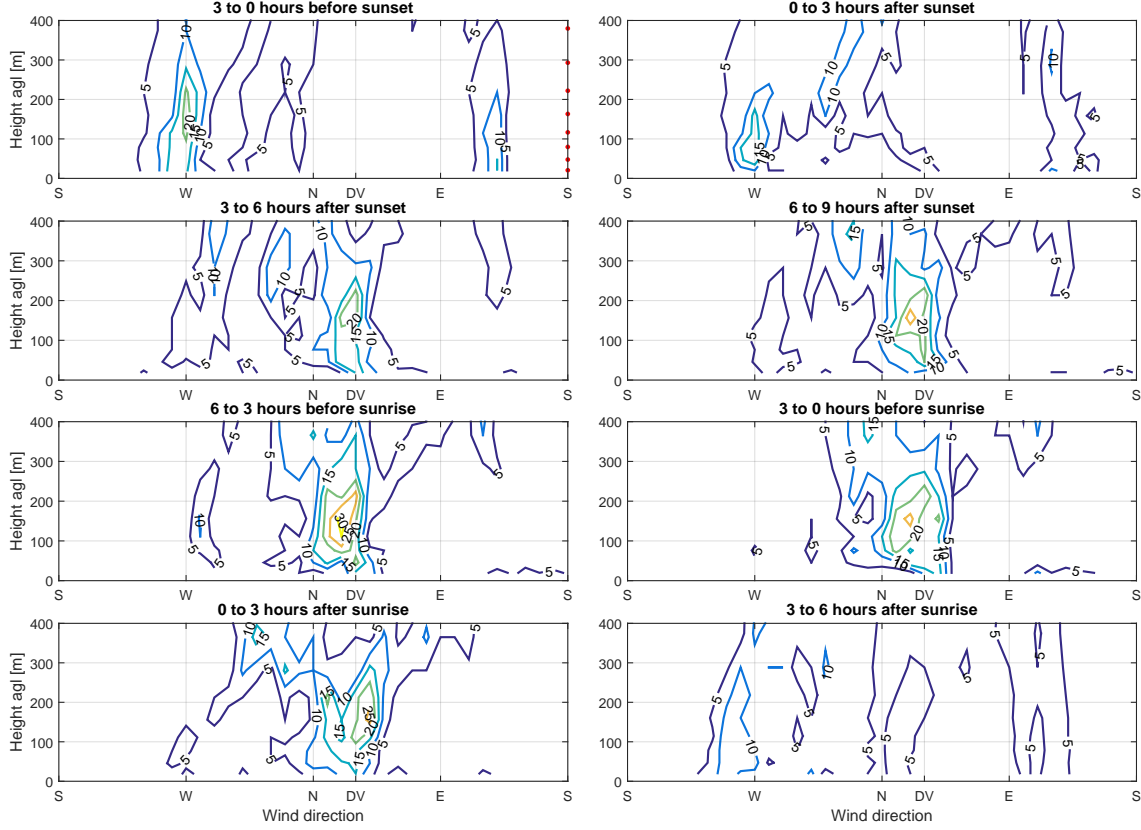


Figure 7.1: Pdf-frequencies of model wind direction at the VER location for 23 simulated IOPs. The top and bottom four figures are sunset and sunrise related respectively. On the x-axis the down-valley direction for Durance Valley (DV) is indicated.

Onset

There is a difference in the onset of the DDV wind. A relatively high occurrence of DDV wind direction is present in the simulations from 3 to 6 hours after sunset, whereas this pattern in the observations starts in the next time frame, i.e. 3 hours later. When assuming that IOPs are related to relative calm synoptic situations where stability easily forms, it seems that turbulence decay is not a problem in the simulations. A case-to-case study is needed to point out the most dominant problem in the model.

Cessation

There is also a difference in the cessation of the DDV wind. The DDV wind persists in the observations 3 hours after sunrise, whereas it has already diminished in the model even if it remains still dominant. In the next time frame, 3 to 6 hours after sunrise, the DDV wind in the model has already disappeared, whereas still high occurrence frequencies are found by the Sodar: the onset of the diurnal convective processes is too early in the model. As the DDV wind is at its strongest at this time of the day, this difference is of considerable importance for dispersion studies and impact calculations.

To sum up, both the onset and the cessation are too early in the model. The difference in timing for DDV wind cessation is remarkable. However, the observations could be biased, as the last 5 IOPs were conducted after a snow event which was not present in the model. Besides, without snow layers during clear skies in the region the temperature drops easily to around or below zero degrees. Around sunrise transition the ground surface and top soil were frequently frozen, which has not necessarily been seen in all simulations. Frozen soils can cause a great delay in cessation of the stability-related DDV wind. Hence the change from stable to unstable

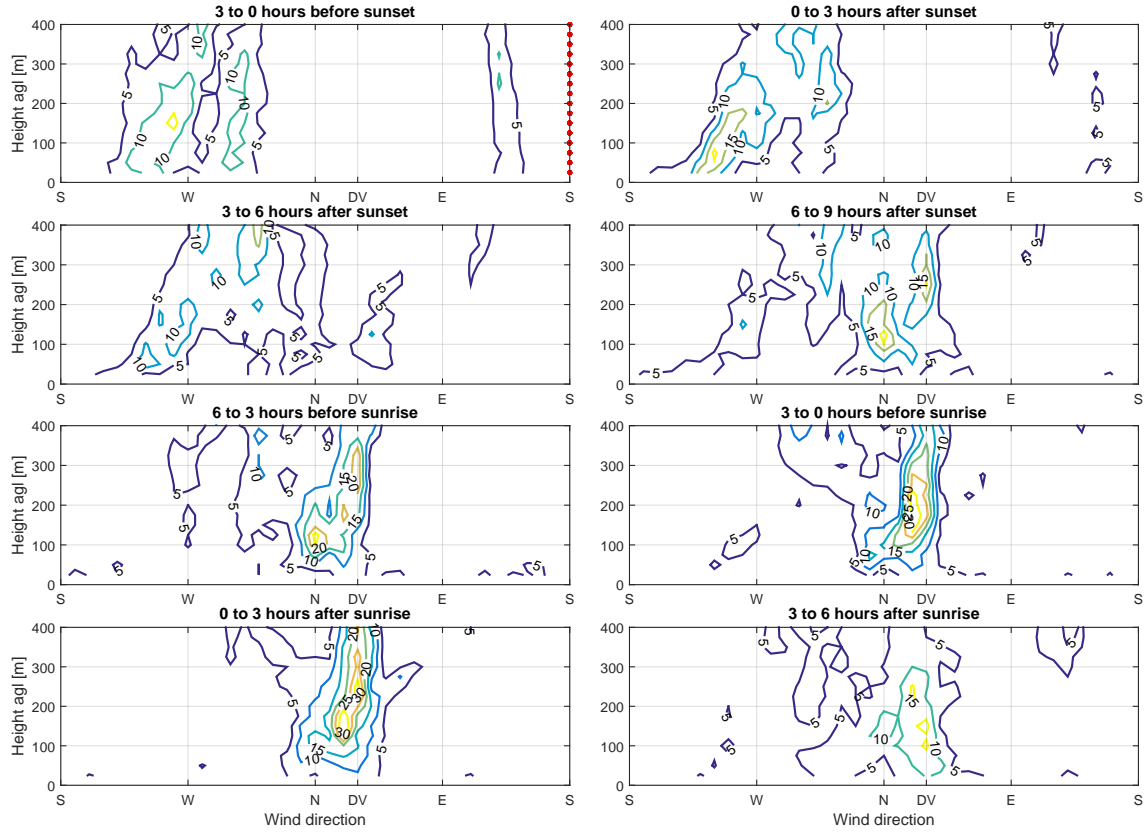


Figure 7.2: Same as Fig. 7.1 but for Sodar observations during the 23 IOPs at the same location (VER).

conditions can be delayed and explain the different timing of the cessation of the DDV wind. To investigate the timing difference more properly, year-round observations of the DDV wind should be compared with simulations.

Vertical structure

There are also differences in the structure of the core and its depth. The depth of the DDV wind core can be estimated between 100 and 300 m in the simulations, whereas in the observations it can be deeper. This could be linked to either a misrepresentation of the DV depth, or a too coarse vertical resolution of the model at these levels, or to a combination of both. The same graph for the high vertical resolution configuration has been checked but did not show big differences with the reference run. Therefore, a misrepresentation of the valley depth seems a reasonable explanation for this difference. It should be noted however that during the observations a DDV directed wind above the DV is much more present than in the model (see Fig. 6.27). Finally, the northwesterly flow above 300 m, linked to a Mistral context is more present in the model than in the observations which could be caused by a too strong synoptic forcing in the model.

To summarize, in the ensemble of the 23 case studies, it is clear that the model is able to represent the DDV wind as compared to observations. Nevertheless, differences are noted regarding flow depth and timing. The causes of this too early timing for both the onset and cessation can be numerous and would need to be investigated. Hence, this is an ensemble of 23 case studies, which points out the robustness of the chosen configuration in general. But this does not necessarily mean an accurate forecast for individual cases.

7.2.2 General characteristics along the Durance valley

The statistics of Sect. 6.3.4.5 and the results of Sect. 7.2.1 showed the general performance of the model to simulate the wind observations at the Sodar location (VER). It showed however

that the model has difficulties in sunset and sunrise transitions: the DDV wind starts and ceases too early. However, the general behavior is well captured by the model and therefore we can enlarge the spatial study to one horizontal dimension by picking up several locations along the DV: 29 points are defined, all well situated inside the DV (see Fig. 7.3).

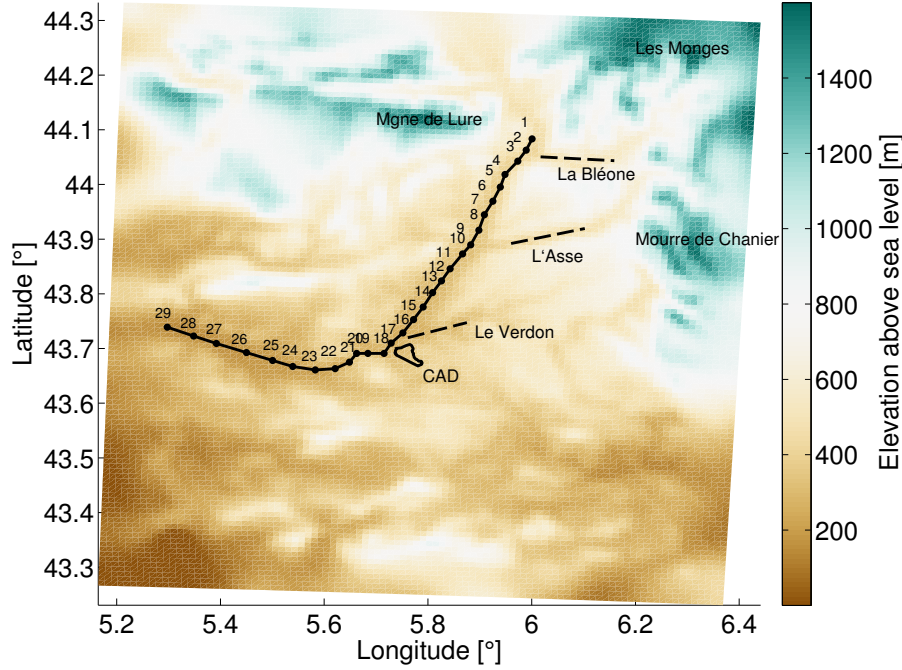


Figure 7.3: The 29 points situated in the centre of the valley (across the valley axis), these are numbered DV_n in the text. The most important side valleys (---) and orography features are indicated. Also the boundary of the Cadarache site (CAD) is outlined.

Figures 7.4 to 7.7 show the DDV wind in the model simulations at the locations DV1, DV3, DV6, DV13 and DV24. They represent the beginning of the straight fetch just downstream Clue de Sisteron (DV1), a location where effects from a side valley (la Bléone) can be seen (DV3), a point within the valley without influences of side valleys (DV6), a location 20 km north of the Cadarache site (DV13) and the lower part of the DV (DV24), where the valley turns to an east-west direction. The figures are made with the same scope as Fig. 7.1, i.e. they are compositions of the 23 IOP simulations in the first model configuration and focus on the sunset and sunrise transitions. Note that the top height for these figures is 800 m, and not 400 m as in Fig. 7.1 which is the upper limit of confidence in the Sodar observations. We comment the features for each location in the next sections.

DV1

Location DV1 is just south of the Clue de Sisteron and around 50 km north of Cadarache. The DV draws a bend at this location (Fig. 7.3), but at the location itself the down-valley direction roughly points to the south. The daily pattern found in Fig. 7.1 for the VER location is partly missing at DV1, whereas a down-valley wind direction is mostly dominant. The up-valley wind signal on the southwesterly quadrant just before sunset is much weaker, and the DDV wind signature is already visible. The lack of a strong diurnal pattern may be linked to the location of the surrounding mountains. For example, the vicinity of the Montagne de Lure may shield the DV1 location from western influences. Besides, the valley is relatively deep at this location, and with quite asymmetric valley sidewalls: the top of the west bank is 700 m higher than the valley bottom but the east bank is only 200 m higher. With a depth of almost 600 m, the core of the DDV wind is higher than at other locations. More important, the DDV wind is already well visible before sunset. The onset of the DDV wind at this location therefore is early. Another

important feature visible from the figures is that the DDV wind is northwesterly. Because of the bend described before, the valley steers the wind to a large extent, as we will see for the next locations as well.

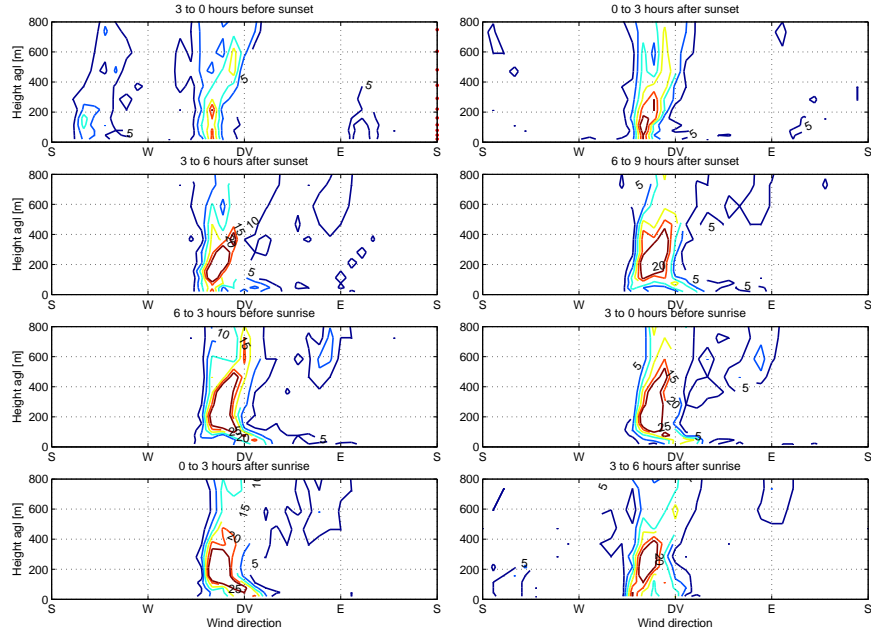


Figure 7.4: Wind direction of the WRF model for all observations, at location DV1.

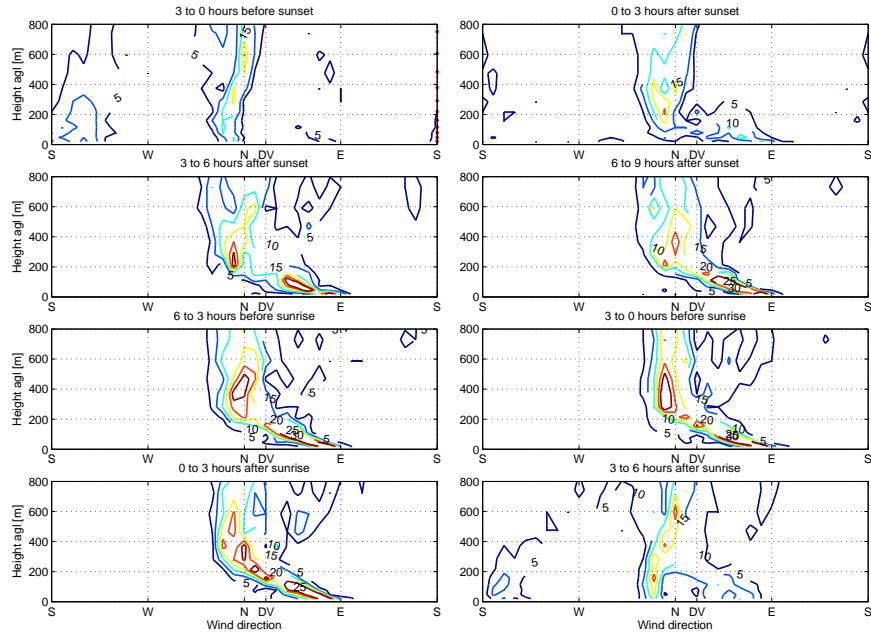


Figure 7.5: Same as Fig. 7.5, but for location DV3.

DV3

Location DV3 is around 5 km south of DV1 and at the confluence of la Bléone with the Durance. Bléone valley is oriented east-northeast and is around 200 m deep. The DV draws a curve there but the valley bottom is already oriented around 30° . Figure 7.5 shows the pattern found for the 23 simulated IOPs. The biggest difference between DV1 and DV3 lies in the effect of the side valley. It is clear that, mainly during the nights a direction change with height is found in the lower 200 m. Going upward in the profile, the wind becomes oriented along the DV. Above

200 m the pattern becomes similar to that of DV1. The figure shows that the side valley brings its westward component momentum while feeding the DDV stream downslope in the lower parts of the profile.

DV6

Location DV6 is 15 km south of DV1, and chosen so that it was undisturbed by the confluence of side valleys such as those of l'Asse and la Bléone. At DV6 the down-valley direction is oriented around 20° . Its depth is around 350 m, the east sidewall is very close to the valley center whereas the west sidewall reaches its top several kilometers westward from the valley bottom. Consequently, the valley is less protected from external influences than at DV1. Figure 7.6 shows that the depth of the core is similar to that at DV1, but develops later. For example, a DDV wind is visible before sunset, but is less frequent than for DV1. Shortly after sunset, it is also less frequent. Between 3 and 9 hours after sunset, the patterns are similar to a large extent, although the DDV wind thickens from 200 m to 400 m. The mountains around the DV, such as Montagne de Lure, Les Mouges and Mourre de Chanier are relatively close to DV6 and may create a sheltering effect that favors the thickening of the DDV wind.

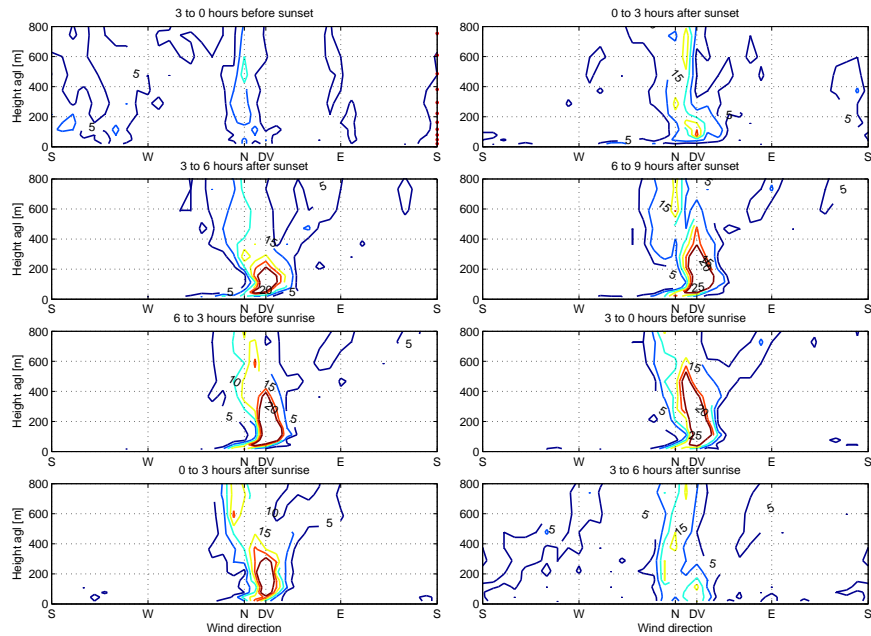


Figure 7.6: Same as Fig. 7.4, but for location DV6.

DV13

The more down along the valley we go, the more open it becomes, i.e. the valley widens and gets shallower. At DV13 the valley is around 200 m deep, approximately symmetric, and the sidewalls are less steep. These influences are visible in the pdf of the wind direction for location DV13, see Fig. 7.8. The core of the wind is much less high, and above the valley the scatter for wind direction is higher. We may conclude that the processes occurring inside the valley do undergo here a larger influence of the above valley conditions. This is visible in the onset, development and continuation of the DDV wind. In comparison with DV1 and DV6, the timing for the onset is later. The cessation of the wind also occurs earlier than upstream in the valley.

DV24

Location DV24 is situated in the lower DV where the valley is close to east-west oriented. The depth is now only 100 m and the valley has widened to approximately 20 km. This clearly has an impact on the daily pattern (Fig. 7.7): before sunrise a westerly wind and after sunrise an easterly wind are frequently simulated in all IOPs. After sunrise the westerly pattern takes over

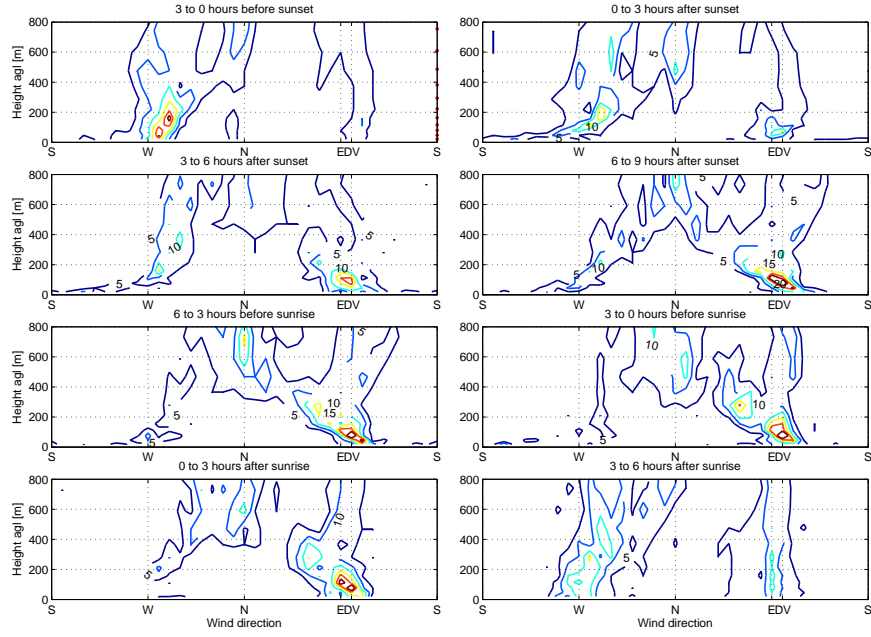


Figure 7.7: Same as Fig. 7.4, but for location DV24.

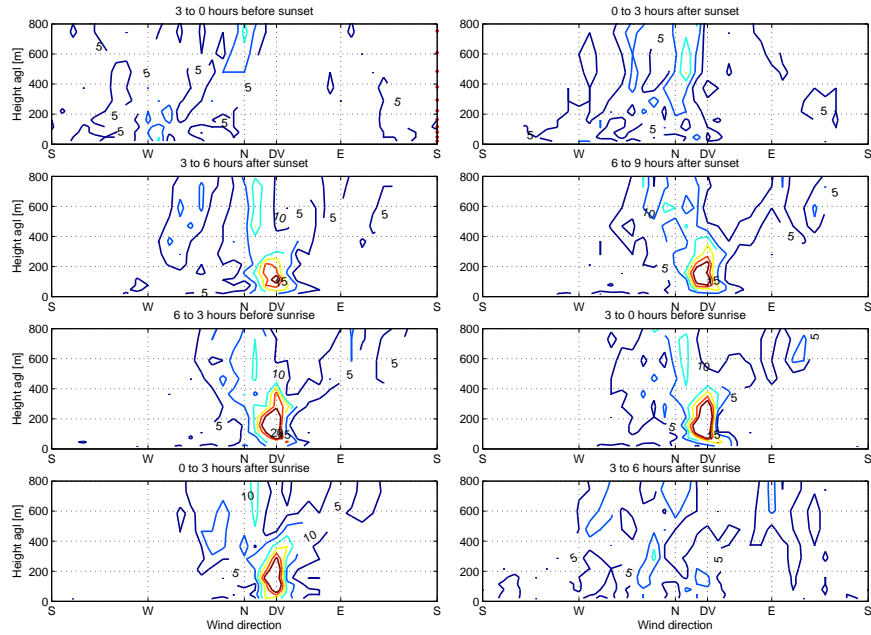


Figure 7.8: Same as Fig. 7.4, but for location DV13.

again, with some delay. The core of the DDV wind again is very well constricted to the DV depth. Above the core, the scatter of wind direction is high.

Summary

The combination of the pictures reveals that the diurnal pattern is more visible in the more downstream section of the DV than in the upstream part close to Sisteron. This can be linked to the valley shallowing and the absence of high mountains in the downstream area. The Durance basin becomes wide and large, hence synoptic patterns play a bigger role. This is an important feature for the onset of the DDV wind. In the upper part of the DV, closer to the higher surrounding mountains, the DDV wind is already visible around or even before sunset

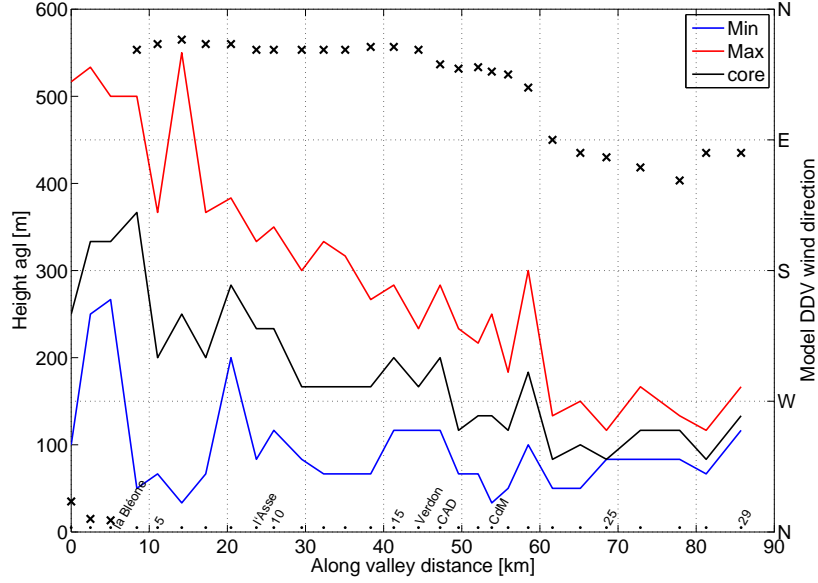


Figure 7.9: Evolution along the valley of maximum, minimum and core of the DDV wind height (lines) and core direction (crosses, right scale) at its mature state. The selected locations and important features (e.g. side valleys) along the axis are indicated by the dots and labels in the lower part of the figure, these locations can be found on the maps in Figs. 7.3 and 7.10.

whereas at location DV13 and more to the south, for example at Cadarache, the DDV wind shows up much later. Besides, the side valleys which are not deeper than the DV itself obviously contribute to the momentum for a DDV wind.

Figures 7.4 to 7.7 also reveal an important feature regarding the general depth of the DDV wind, once it is in a mature state. The more downstream in the valley, the thinner the depth of the DDV wind. Figure 7.9 shows the maximum, minimum and core depth at all different locations investigated along the valley axis. The DDV wind being strongest around sunrise, the time frame 3 to 0 hours before sunrise has been retained to construct Fig. 7.9. Note that the core depth is restricted to the 'red core' but using other maximum occurrence would result in a similarly shaped graph. The figure clearly shows that, once it is in its full mature state, the DDV wind diminishes in depth downstream. This is related to the lesser depth of the valley and the fact that the sheltering effect from the surrounding mountains diminishes. In the figure also a signal of the two side valleys of la Bléone and l'Asse is visible. At these locations the minimum height (blue line) of the DDV wind presents a peak so is higher than just upstream or downstream of their confluences. In the lower 100 m of the model, high occurrences of easterly winds are found, which correspond to the down-valley direction of these two side valleys. Closer to Cadarache at the confluence with the Verdon Valley, the Durance Valley is shallower and widening. This is why the graphs do not show the same peaks as for la Bléone and l'Asse.

The wind pattern in the valley is largely related to the surrounding topography (Fig. 7.10). Close to Clue de Sisteron, the mountains Montagne de Lure and Les Monges are 1000 m higher than the DV basin and relatively close to the valley bottom. The decreasing depth and a wider basin downstream strongly control the winds above the valley. Thus a current coming from the valley north of location DV1 would only survive on very weak synoptic forcing situations. During stronger synoptic forcings in the lower basin, this current only survives within the valleys, and not above. Consequently, the possibility for other winds aloft to erode the upper edge of the DDV wind increases.

Once the DDV wind is in its mature state, around sunrise, a clear dependency on the valley

axis is found. This is further shown by the black crosses in Fig. 7.9, which show the direction of the core for all locations around sunrise based on the figures like Fig. 7.4. We use this DDV wind direction from the model for our next section to put up an approach to investigate the development of the DDV wind along the valley for each IOP.

7.3 Analysis of two remarkable IOPs

7.3.1 Methodology

The previous sections have shown the general capability of the model to capture the essential features of the DDV wind. The last section showed the large variability along the valley axis, but a clear signal of the DDV wind existence. In the region of Cadarache, the DV axis presents a curve: it turns from south-southwesterly to west-northwesterly direction within 100 km distance (Fig. 7.10). To study the development of the DDV wind along the line of its axis, we introduce an approach following the different directions down the valley. An attempt was made by taking the terrain slope within the model as a reference for the Durance down-valley direction, but as the slope angles of the sidewalls towards the center of the valley are much larger than the slope of the DV main axis itself, this approach did not provide a clean result. Finally, we based ourselves on the DDV wind direction as found by its highest occurrence around sunrise, from the figures presented in Section 7.2.2. These figures are calculated for all 29 points along the DV axis as given in Fig. 7.3. In fact, this is how the model solves the DDV wind.

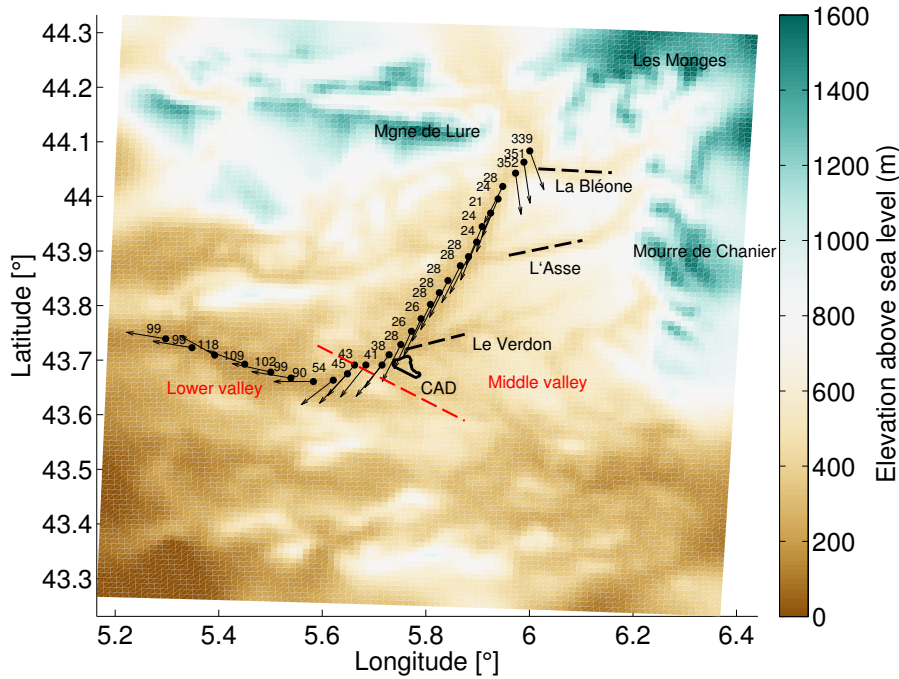


Figure 7.10: The 29 points as given in Fig. 7.3, embedded in the DV, with their local down-valley wind direction (determined as the highest occurrence for DDV wind direction) indicated by arrows and degrees from north. The most important side valleys are indicated (black dashed lines), as well as the Cadarache site (CAD) and other major orography features. The red dashed line indicates the transition from middle to lower Durance valley (Warner, 2006).

Knowing the core of the DDV wind direction simulated for 23 IOPs, we can define unit vectors \hat{D} aligned with the wind along the valley. Note that these are the wind directions picked at the heights of the core, as shown by the black line in Fig. 7.9. We consider these directions to define the wind component along the valley as the scalar product of the modeled wind vector U with the DDV wind direction vector \hat{D} . The units for this scalar product are m s^{-1} . This quantity is positive for down-valley directed winds and negative for up-valley directed winds.

It does not have a specified range as it is dependent on the wind speed and can be primarily used inside the DV to detect the evolution of the jets in time and along the valley axis. Above the DV, a very strong wind with a direction in between parallel and perpendicular to the DDV wind direction could show high values as well.

Then we normalize the scalar product by the simulated wind speed: this is the 'normalized scalar product of the DDV wind direction': $\hat{U} \cdot \hat{D}$. It is unitless, and ranges between -1 (up-valley winds) and 1 (down-valley winds) and therefore is a convenient value to follow the evolution in time and height of the DDV wind inside but also *above* the valley. Now we expect to be able to detect up to what height the DDV wind is formed. Ideally we can detect drainage due to surface cooling in the valley or large scale drainage as being produced by the mountains north of the valley. We can also detect until which model height the wind was directed in the down-valley direction. However, as the quantity is unit-less, we lose information on possible jets. Therefore we should use both scalars for a proper study on the evolution of the DDV wind to extend its characterization from a localized study to a regional study.

7.3.2 IOP 16

In Sect. 6.3 we concluded that, among others, IOP 16 and 21 were relatively well simulated IOPs concerning the DDV wind occurrence and timing at the Cadarache site. From this section we try to point out differences in DDV wind onset and development as seen from the modeling perspective. We refer to astronomical sunsets and sunrises. We take IOP 16 as a reference case.

The vectorial approach allows to leave the localized comparisons of IOP 16 presented earlier in Sects. 6.2.1 and 6.3.4. Figure 7.11 shows six typical times (a - f) during IOP 16 for the normalized scalar product (upper) and scalar product (lower) of the modeled wind. Positive values for both quantities indicate down-valley wind pattern, whereas negative values indicate up-valley winds. The along-valley distance is plotted with DV1, close to St. Auban, as the starting point. Note that the part between St. Auban and Clue de Mirabeau (CdM) belongs to the 'middle valley', and that downstream CdM (i.e. distance 55 - 85 km in the figure) we refer to the 'lower valley' (see Fig. 7.10). Figure 7.12 completes the view by showing streamlines at 160 m agl at four times.

We start our analysis at 12:00 UTC, the start time of the IOP (Fig. 7.11a). Negative values are found within the valley, which means an up-valley wind. It corresponds well with the streamline pattern shown in Fig. 7.12a at the same time. In the upper air northwesterly flows are simulated which is roughly in a down-valley direction. Nevertheless, at the surface up-valley winds exist between CAD and CdM.

5 hours later, around sunset (17:13 UTC) the westward winds still exist in the lower part of the DV, i.e. CdM and further down the valley (Fig. 7.11b). However, in the upper part of the DV, a down-valley current has already developed between St. Auban to l'Asse confluence at the surface, and extends up to 1200 m agl with wind speeds around 5 m s^{-1} . At the Cadarache site, up-valley winds are still simulated, which are more developed than at noon reaching around 5 m s^{-1} .

Half an hour after midnight the down-valley current aloft in the middle valley has been disconnected from the down-valley current close to the surface (Fig. 7.11c). In between them an up-valley current persists, although not very developed. However the DDV wind close to the surface has developed till the Verdon confluence. This very shallow flow is therefore not seen in the streamlines pictures (Fig. 7.12b). What both pictures do show at this time is the low wind speeds, represented as sinuous lines in streamlines pictures. In the upper air no big differences are found with respect to the sunset figure, in the lower valley westerly winds are still simulated.

At 04:00 UTC, the down-valley wind has thickened to more than 200 m (7.11d), and the DDV wind is also well visible in Fig. 7.12c. A stronger LLJ is found, especially between l'Asse

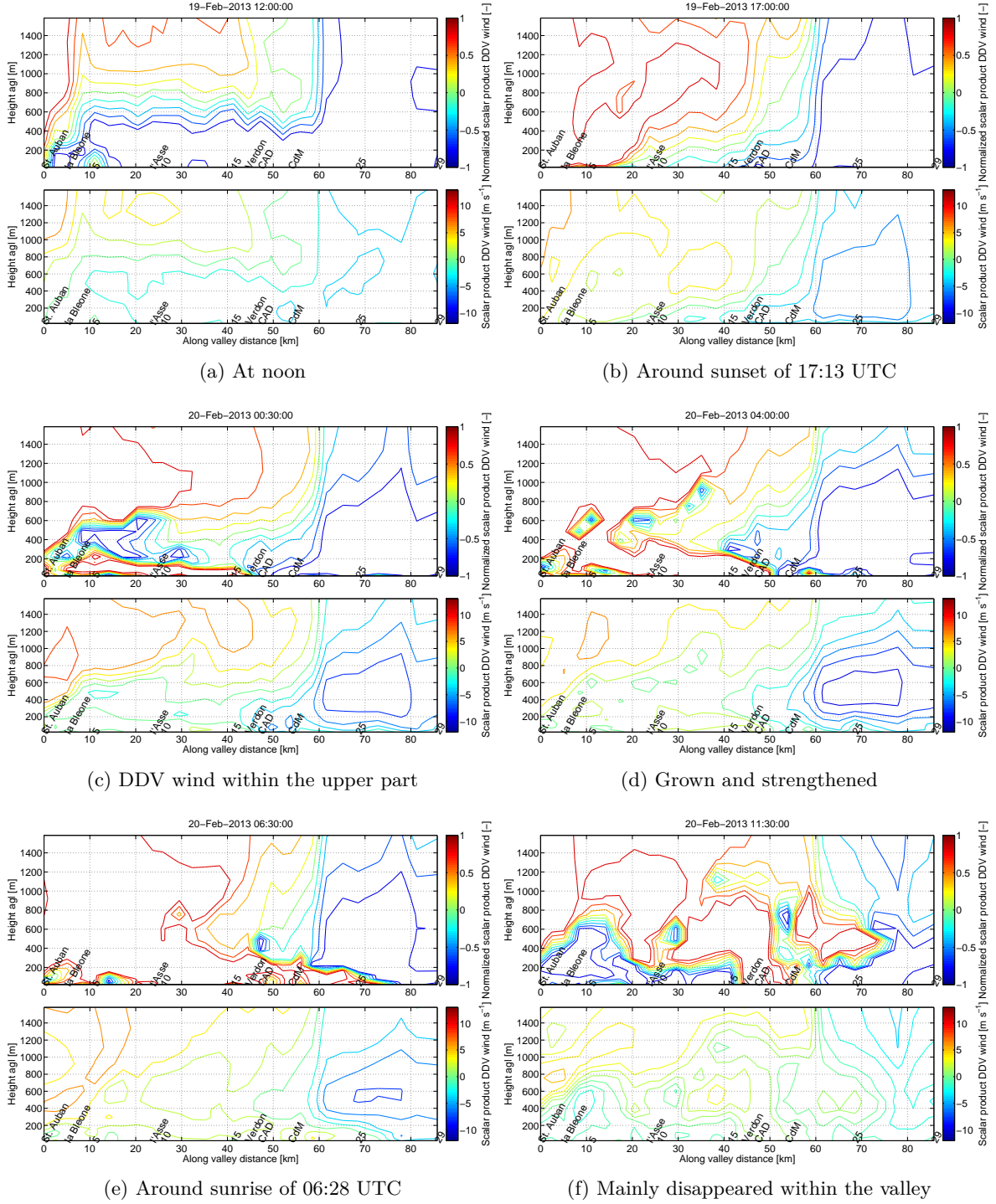


Figure 7.11: Valley wind components along the Durance valley for 6 different times characterizing typical features of the flow during IOP 16. The along valley distance is taken from DV1. Above the x-axis, the locations of the sidevalleys (la Bléone, l'Asse and Le Verdon), the Cadarache site (CAD) and the Clue de Mirabeau (CdM) are marked, the other slanted numbers correspond to the DV point numbers. See Figs. 7.3 and 7.10 for their location on a map.

and Le Verdon. The DDV wind has ultimately reached the Cadarache site, but not above 100 m agl. In the upper part of the middle valley, a down-valley wind is still found in altitude, but less strong. Westerly winds still prevail in the lower valley.

Around sunrise (06:28 UTC), the DDV wind has penetrated the lower part of the valley

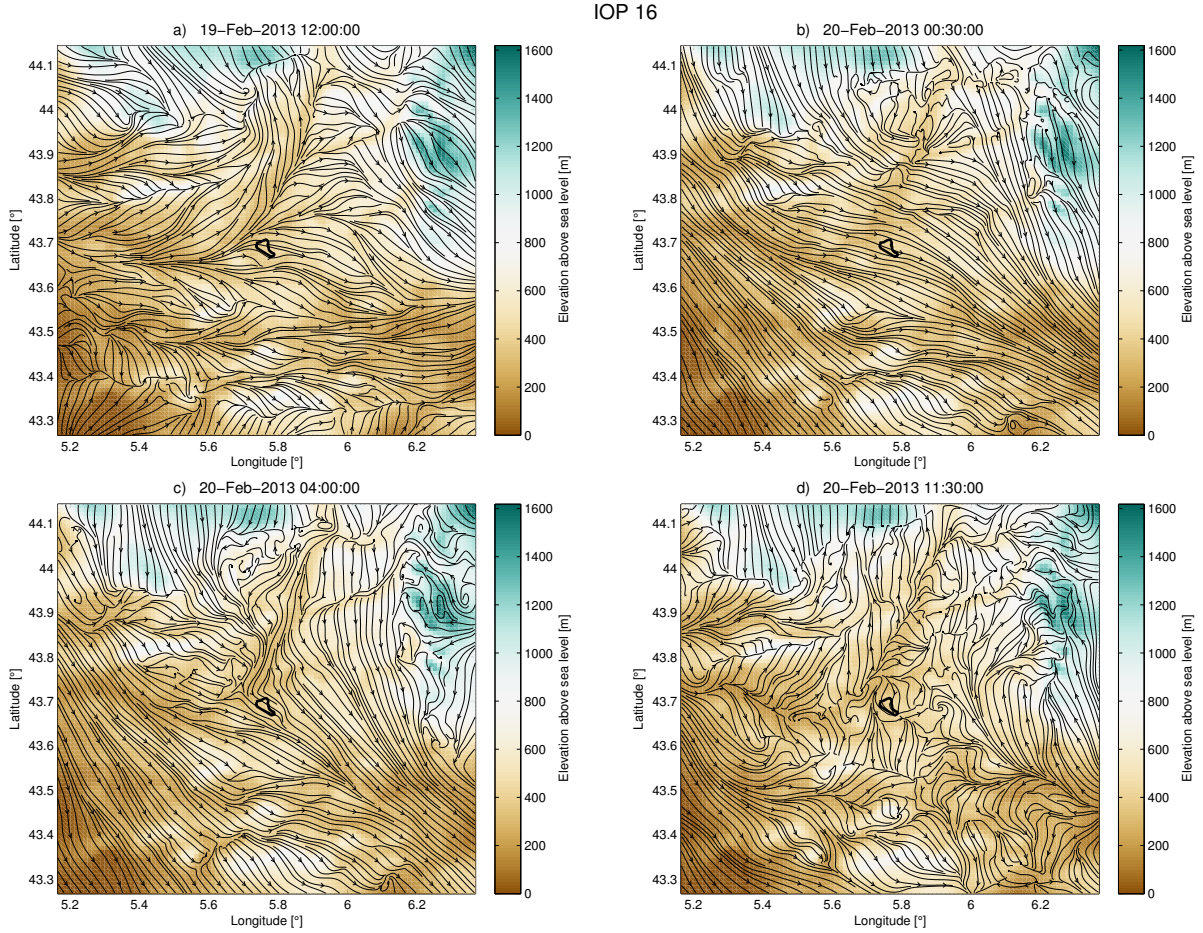


Figure 7.12: Streamlines at the 5th sigma-level (~ 160 m agl) during IOP 16 at four times, indicated above the graph.

down to location 25, but it is very thin (Fig. 7.11d). The DDV wind has thickened in the middle DV, between 30 and 50 km and even filled the air column up to 1600 m on the first 40 km downstream.

At 11:30 UTC, the down-valley wind has mostly disappeared with the exception of the Cadarache area (7.11f), which is confirmed by the streamlines picture (Fig. 7.12d). A down-valley component is found above Cadarache up to 800 m, which corresponds well to the Sodar measurements or model pictures (see Appendix). North of Cadarache, an up-valley wind has already formed, whereas down-valley components above 400 m are still observed.

The spatial characteristics presented in this section confirm that a DDV wind can develop as a drainage flow. Aloft a down-valley directed wind also develops, but both flows are clearly disconnected, which confirms that the DDV wind is a shallow drainage flow for IOP 16. It even develops weak LLJs within the DV between L'Asse and Le Verdon confluents. An influence of westerly winds close to Cadarache prevents the DDV wind from thickening and reaching the site until the early morning. Simulated winds are weak, around 3 m s^{-1} , which corresponds very well to observations (Fig. 6.3).

7.3.3 IOP 21

IOP 21 has been thoroughly described in the chapter dedicated to observations (see Sect. 3.3.1 in Chap. 4). It was chosen for investigation as its observations showed typical patterns and LLJs with typical wind speeds, with respect to other IOPs. The IOP was conducted under eastern

synoptic forcing with observed wind speeds between 4 and 9 m s⁻¹ at around 2500 m agl (Fig. 5, Chap. 4). Below at around 300 m agl westerly winds of 6 m s⁻¹ were observed and from midnight winds slowed down and a DDV wind set in (Fig. 6, Chap. 4). We explain now the onset from a spatial perspective and put it in relation to IOP 16, previously considered.

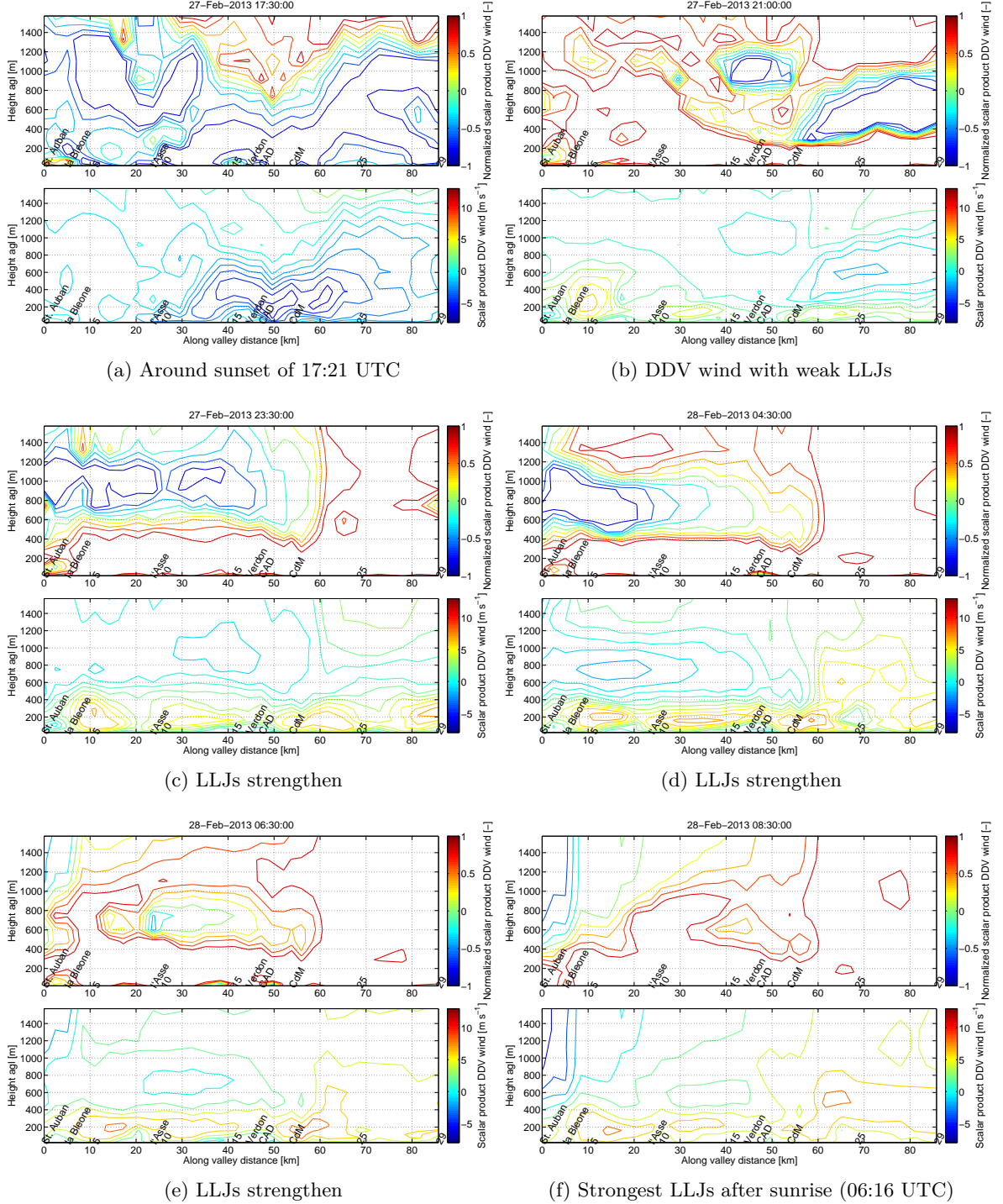


Figure 7.13: Same as Fig. 7.11 but for different times during IOP 21.

At sunset (17:21 UTC) the wind at the Cadarache site is upvalley (Fig. 7.13a) with maximum wind speeds of more than 5 m s⁻¹ at around 200 m agl (Fig. 7.14). At the Cadarache site, a 1 km thick jet with westerly direction was observed (see Fig. 5 in Chap. 4), which is not simulated at the Cadarache site but in the lower valley. The upvalley pattern simulated at Cadarache is

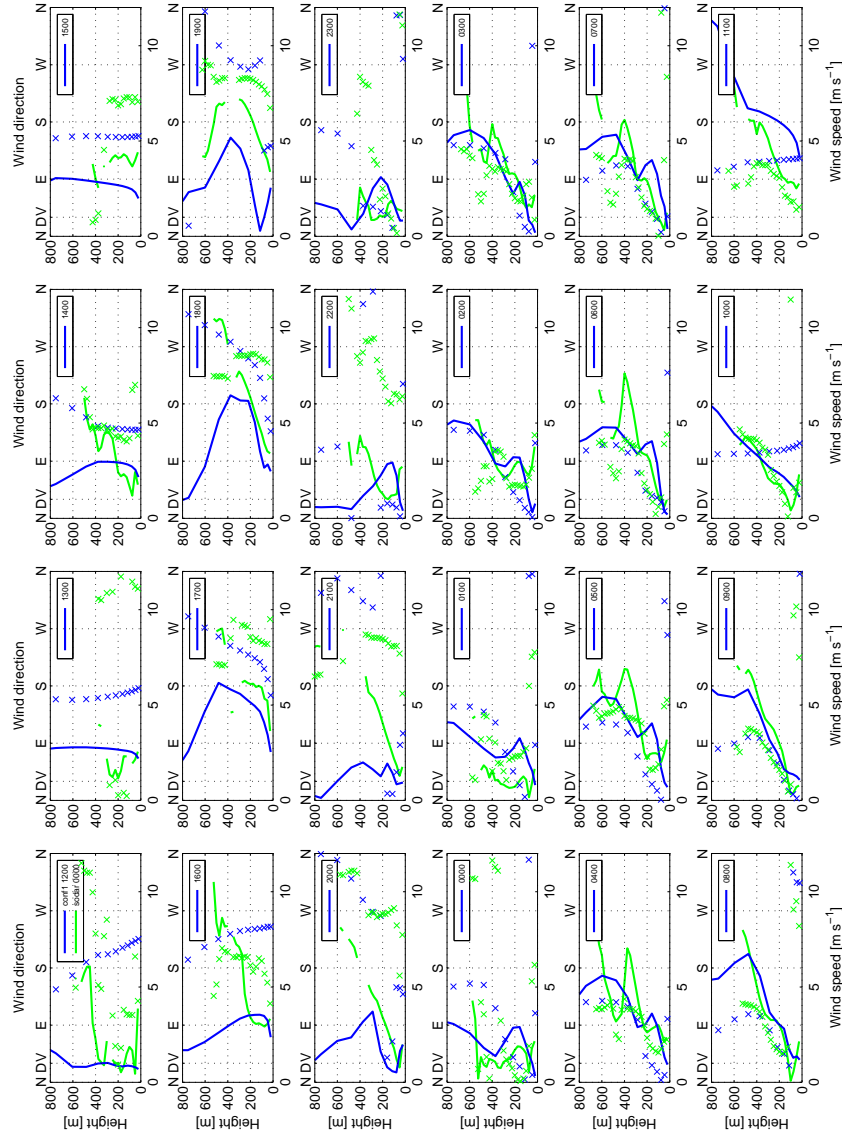


Figure 7.14: Comparison of wind speed (lines) and wind direction (crosses) between Sodar observations (green) and simulations (blue) for the reference configuration at the VER site during IOP 21; the times (in UTC) are indicated in each box.

however regularly observed in the afternoons (see Chap. 4).

Less than 4 hours later at 21:00 UTC, the wind above 400 m has weakened and a DDV directed wind is already simulated throughout the valley (Fig. 7.13b). The DDV wind is 800 m thick in the middle DV, but in the lower valley it extends up to 400 m, which is high for this location. Above this layer in the lower valley, the westerly wind remained. Along the full DV, the DDV wind is represented as LLJs of different size and with different magnitude: a strong one (7 m s^{-1}) after la Bléone, a weaker one (4 m s^{-1}) between l'Asse and le Verdon, and also a small jet is found in the lower valley. Finding LLJs at this time in the lower valley is surprising, as their onset was not even expected in the middle valley before midnight (see Chap. 4). Nevertheless, at the Cadarache site (Fig. 7.14) a weak LLJ is formed, and Fig. 7.14 clearly shows that this LLJ in the model develops gradually below 400 m with its peak at 250 m.

Just before midnight, in the middle valley above 400 m the wind has somewhat strengthened and turned to a southeasterly direction (Fig. 7.14), and easterly winds are found in the lower

valley throughout the vertical (Fig. 7.13c). This corresponds well to the synoptic situation. At 600 m in the middle valley the wind speeds are still very weak (Fig. 7.14). However the DDV wind was maintained and deepened to 400 m, the corresponding LLJs strengthened to more than 5 m s^{-1} . Above this layer, a weak up-valley wind is found.

During the course of the night, the southeasterly wind develops in the model. Above the DV depth at 600 m agl, LLJ-like structures develop with windspeed peaks of around 5 m s^{-1} (Fig. 7.14). Their direction departs from the direction less than 90° of the DDV direction and makes flow channeling as extra contribution to the already developed DDV wind very well possible. Within the valley, at 04:30 UTC the LLJs belonging to the DDV wind at 200 m have strengthened to $6 - 7 \text{ m s}^{-1}$, while maintaining their height at 200 m agl (Fig. 7.13d). Ultimately they were at their maximum at sunrise (06:16 UTC) and continued well into the morning two hours after sunrise (Figs. 7.13e and f), with speeds reaching 10 m s^{-1} . At the Cadarache site in the model lower wind speeds are also found which corresponds well to observations, where wind speeds below 200 m did not exceed 4 m s^{-1} . Easterly wind is found in the lower valley throughout the rest of the IOP on the whole vertical.

7.3.4 Summary

A methodology is developed in Sect. 7.3 which allows to see the development of the DDV wind inside the DV in a single figure despite the DV curvatures. However, one should be cautious when interpreting winds above the valley flow around the direction of the DV, i.e. up-valley and down-valley. In spite of this, inside the valley itself it is a robust tool to detect up-valley and down-valley winds and their jet-like behavior.

The IOPs investigated in more detail by this method showed differences in the DDV wind development. IOP 16 showed a typical behavior of a drainage flow origin with low wind speeds. During IOP 16, several hours were needed for the DDV wind to develop, to thicken and to reach ultimately the Cadarache site just before sunrise. The DDV wind did not reach the lower Durance valley, which was caused by the opposite synoptic wind in the open lower valley. During IOP 21, a DDV wind was initiated very quickly after sunset with strong LLJs inside the valley, reaching up to 10 m s^{-1} in the early morning. The winds above the valley showed a LLJ-like behavior at the Cadarache site as well. With their direction being within 90° from the DDV direction, they can contribute to flow channeling within the valley.

The methodology suits to highlight the behavior of the DDV wind along the valley. However, it cannot be used to infer the origin of the DDV flow. We try to point out the origin by taking up a different procedure, which will be explained in the next section.

7.4 The origin of the flow

Whiteman and Doran (1993) proposed several relationships between bottom valley winds and above-valley winds (see also Sect. 1.3.3). They classified them into fully independent - a thermally driven flow - and (quasi-) dependent flows. In the latter class, features as downward momentum transport, forced channeling and pressure-driven channeling are proposed. In Fig. 7.15 these are indicated for the DV orientation at the Cadarache site. As the DV is curved close to Cadarache, a different pattern could be found for up-valley and down-valley flow relationships to above-valley winds. Therefore in the figure two colors are visible: in black the DV orientation is north-northeast - south-southwest and in red it is west-east oriented.

Small valleys enhance decoupling from above-valley patterns, which facilitates the development of a daily pattern in them. These are called thermally driven flows (Fig. 7.15a). Downward momentum transport plays a large role in unstable and neutral stratification and is favored in wider valleys (Whiteman and Doran, 1993). It is independent from the valley orientation (Fig.

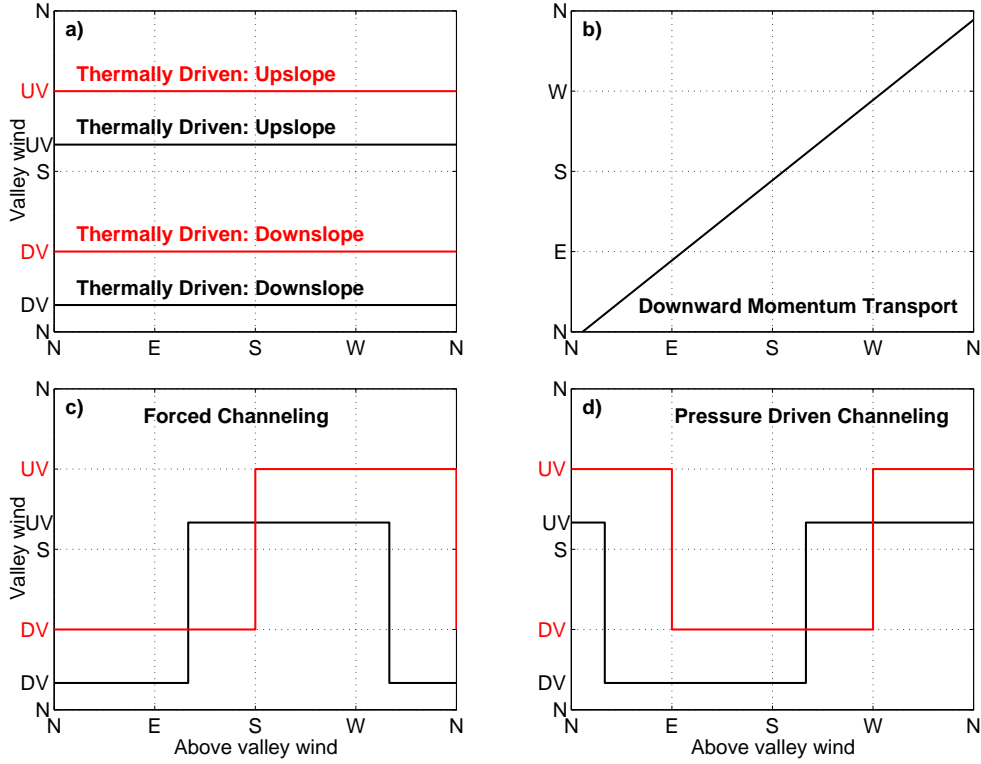


Figure 7.15: Valley wind direction and its relation to above valley wind according to Whiteman and Doran (1993), adapted for the Durance Valley in a 30° - 210° (black) and a 90° - 270° orientation (red). These two orientations are those of the Durance river up- and downstream of the Cadarache site, respectively. Up-valley (UV) and down-valley (DV) are indicated on the y-axis. For downward momentum transport the valley's orientation is not important.

7.15b). Narrow valleys during unstable or neutral conditions facilitate the forced channeled flow relation (Weber and Kaufmann, 1998), see Fig. 7.15c. Pressure-driven channeling (Fig. 7.15d) can be of importance in wide and shallow valleys in cloudy climates under slightly to moderately stable atmospheric conditions (Whiteman, 2000; Carrera et al., 2009). The figures show that there is an overlap for the forced and pressure-driven channeling features when accounting for the curvature in the valley.

Our analysis starts with location DV13 as it is in the heart of the middle DV and along a relatively straight fetch of the DV, see Fig. 7.3 for its location. At DV13 the valley depth is around 200 m. We want to analyze above the valley as high as possible, but in the range of Sodar observations to make a comparison later on. Thus, we set our above-valley flow height at 485 m, which is a best-of-both-worlds choice: the just below level in the model, at 380 m, comes close to the valley influence; the just above level in the model, at 600 m, does not benefit from fully available Sodar observations data.

At the DV13 location, the DDV winds are mostly simulated during the night and early morning and are only observed when above-valley winds are in the range $[300^\circ$ and $120^\circ]$ (clockwise - Fig. 7.16a). This strongly complies with features of forced channeling. It should be noted however that these above-valley winds are mainly coming from the higher surrounding mountains and the Plateau de Valensole, and so the above-valley winds should be linked to drainage currents or LLJs created either by the mountains or this sloping plateau. So at DV13, a channeled flow mechanism is the most important one, but with a drainage origin involving an area larger than the DV itself. In fact, regarding the above-valley wind direction and the timing, this leads to suspect a mountain-to-plain circulation. However, an up-valley flow pattern is missing in the

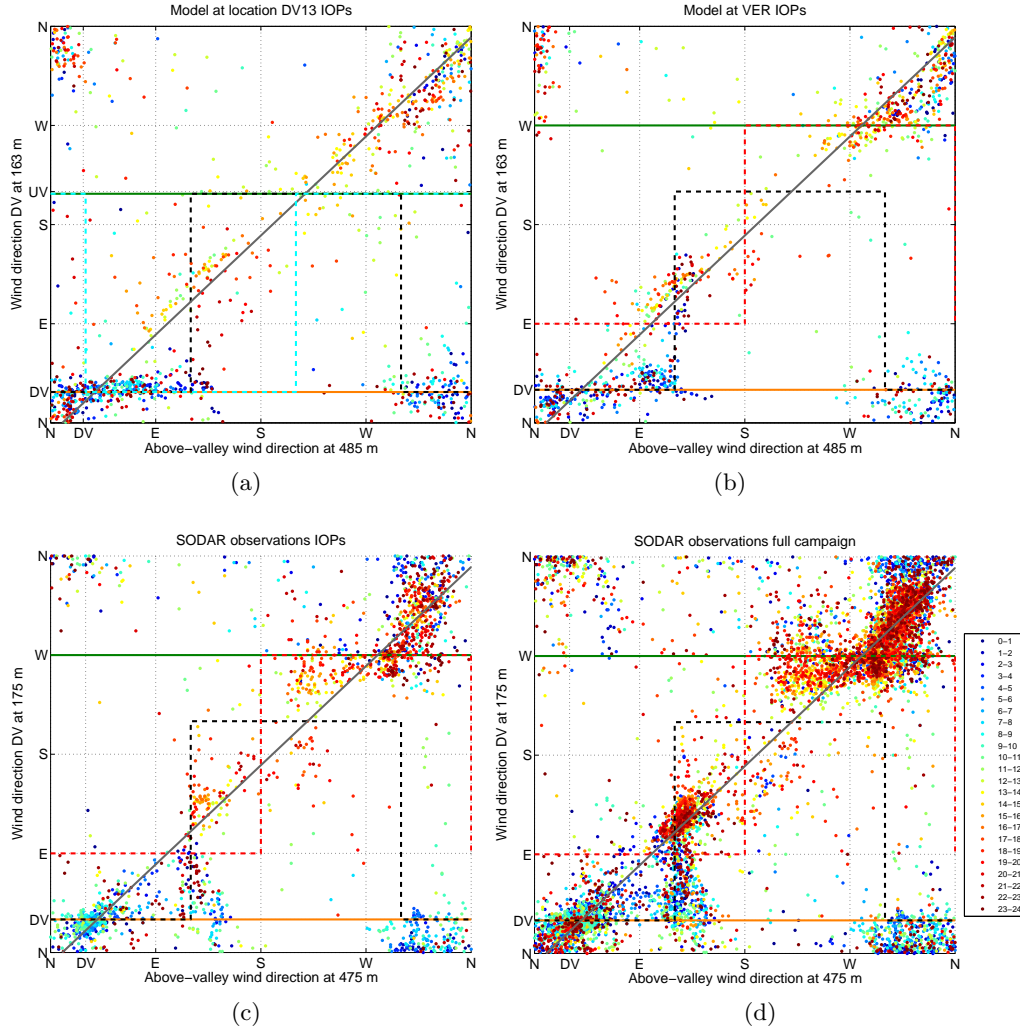


Figure 7.16: Durance Valley wind dependency on above-valley winds for two locations in the model ((a) and (b) for DV13 and VER, respectively) and for Sodar observations at VER ((c) and (d)) as classified in hourly bins (UTC). The lines indicate the idealized relationships between valley winds and above-valley winds, gray: downward momentum transport; green and orange: thermally driven up-valley and down-valley flow, respectively; black: forced channeling for north-northeast - south-southwest oriented valley and red: forced channeling for east-west oriented valley; cyan: pressure driven channeling (only in a). See Fig. 7.15 for the theoretical signatures.

simulations at DV13, as well as a plain-to-mountain circulation: during the day, the downward momentum transport dominates the wind direction within the valley. This figure also shows that pressure-driven channeling is not a dominant mechanism in the valley. For simplicity we have excluded this theoretical line in the next Figs. 7.16b to 7.16d.

Figure 7.16b shows the model results at location VER, where the Sodar is. Due to the DV curvature close to this location, this picture is somewhat more complicated, as up-valley winds are westerly oriented. Therefore an overlap of the forced channeling relationship is found in the direction range $[300^\circ - 360^\circ]$ for the above-valley flow (Fig. 7.16b). Keeping this in mind, at the VER site a signature is found similar to that at DV13, although less clearly. Remember that VER is 20 km to the south of DV13. Here the DV is a bit less deep and there is less influence of the 'protecting' higher mountains of the Southern Prealps, like Mourre de Chanier (Fig. 7.10). However, also for simulations at VER the DDV wind can be linked to the drainage current mechanism, and so the mountain-to-plain circulation, as was found at the DV13 location.

The Sodar observations show a good correspondence with the VER simulations for the above-

valley wind relationship (Fig. 7.16c). This is extended to the full KASCADE campaign data in Fig. 7.16d. In both diagrams there is a clear signature of the forced channeling mechanism: for up-valley flows it corresponds to above-valley wind directions in the range $[210^\circ - 360^\circ]$ (clockwise), and for down-valley flows to above-valley wind directions in the range $[300^\circ - 120^\circ]$ (clockwise). These above-valley winds belong in fact to a mountain-to-plain circulation. Remark that this is found on all figures, excluding Fig. 7.16a. We can then conclude that the Durance valley winds are also a consequence of a mountain-to-plain circulation during the night and a plain-to-mountain circulation during the day.

Note that on all figures there are two clusters of quasi-identical directions for above- and inside-valley winds, translating as a downward momentum transport mechanism. This occurs for northwesterly and southeasterly winds, which correspond to the Mistral wind and cloudy and precipitation related synoptic events, respectively. They are also the most pronounced during the day, which corresponds well with the theory.

Lastly, the two Sodar observation diagrams reveal that the IOPs data subset is quite similar to the full dataset. It reinforces the relevance of the analysis of the IOPs in this section and throughout this thesis.

7.5 Summary and conclusions

In this chapter the DDV wind has been characterised in terms of timing and space and further analysed to clarify its main driver. The DDV wind analysis was made based on the reference configuration (see previous chapter) alone, which was already satisfactory concerning the flow characteristics. The well represented valley depth leads to DDV wind characteristics which correspond well to observations at the Cadarache site. However, the DDV wind onset and cessation are early in the model even if biased observations could not be excluded here. Based on the ensemble of the 23 simulated IOPs, a spatial pattern approach was developed and showed that the wind is present throughout the valley - from 60 km north of Cadarache to the lower valley beyond the Clue de Mirabeau - and is well constricted to the valley depth in most cases studied. The valley gets less deep towards Cadarache and the distance to high surrounding mountains increases, which adds to the uncertainty for predicting the onset of a DDV wind at the site.

A directional vector approach allows to investigate the DDV wind development all along the curved valley bottom and at all heights. This method showed that differences in DDV wind development patterns can be large between different IOPs studied. One IOP showed a clear development of the DDV wind as a drainage current. A second IOP showed drainage flow signatures but with a combination of LLJs aloft which developed under the influence of the synoptic situation. The method further allowed to show that LLJs can exist all along the valley.

A final study to point out the general origin of the DDV wind was based on the relation of valley winds to above valley winds. Two locations were considered: one in the middle valley 20 km north of Cadarache and one at the VER site to allow comparison with the Sodar observations. For the different locations in the model similar origins could be observed for a down-valley directed flow: strong signatures of channeled flow and thermally driven down-valley winds are found. The model at the VER site matches well with the Sodar observations, which reinforced our confidence in the model configuration. For Sodar observations, the full 3-month dataset is very similar to the IOPs data subset, which warrants the analysis of the DDV wind by means of the IOPs. All diagrams show a mix of channeled and thermally driven flows for the onset of DDV wind. This leads to the conclusion that flow channeling and thermally driven winds are the most dominant mechanisms for the DDV wind. However, the flow channeling is probably mostly triggered by LLJs and drainage flows originating from a larger area that includes the high surrounding mountains and plateaus, and thus belongs to a mountain-to-plain circulation.

General conclusions and perspectives

Conclusions

Atmospheric stability in complex terrain, and subsequent valley wind formation, strongly influence the dispersion of effluents. Therefore, the characterization of these valley winds is indispensable for impact assessment studies and risk management procedures. This thesis focused on the characterization of down-valley winds in two perpendicular shallow of different sizes. Its main objectives were first to observe and analyse the valley winds by means of the field observation campaign KASCADE, then to set up a mesoscale model which can be used to analyse the wind characteristics at a larger scale than the observation frame.

The KASCADE campaign was designed to gain insight in the local valley wind pattern developing under stable stratification periods during weak synoptic forcing with an emphasis on down-valley winds. The focus of the experiment was on the Cadarache site and its region, and particularly the Durance Valley and its small tributary: the Cadarache valley. The Cadarache site is located in a rather complex orography. The region is characterized by valleys of 100 to 200 m depth and is situated in between the Mediterranean Sea, Rhône Valley and Southern Alps, all approximately 60 km away as the crow flies. The region is further characterized by west-east oriented mountain ridges of around 1000 m height which largely influence the wind pattern. In the region clear skies are more than regular, and under weak synoptic forcing conditions, stability sets in and builds up easily. This is enhanced by the fairly dry atmosphere due to the Mistral wind that regularly dries out the upper soil, and transports air masses away, making the sky dry and bright.

The campaign has been conducted in the winter of 2013, from mid-December 2012 to mid-March 2013 and proved successful to observe the stability and valley winds onset and cessation. According to the regional monthly climatology by MétéoFrance the winter was characterized as fresh to cold, dry, with frequent clear skies. December was close to normal regarding temperature, frequent Mistrals were experienced, and the rain amount only reached 75% of its normal value. January was characterized as fresh, dry and sunny also with frequent Mistral events. February was cold, dry and sunny, and snow covered the region for several days. Again, frequent Mistral events occurred. From March, the region was mainly subjected to easterly winds and concomitant rain events which lead to precipitation amounts higher than normal. Overall, the winter of 2013 was close to normal, with some colder periods enhancing the stability expected for our flow characterization.

The continuous observations relied on a divergence flux tower, a Sodar and the meteorological observation network of Cadarache. The 30 m high flux tower was set up in the smaller Cadarache Valley and was equipped with three sonic anemometers, two net radiometers and two thermohygrometers at different levels. The Sodar observed the wind and turbulence profiles between 100 and 500 m at La Verrerie (VER), which is outside the Cadarache Valley. The Cadarache meteorological facilities consist of a 110 m high tower (temperature at the top and bottom, wind speed and direction at the top) and a 15 m high tower at VER. From mid-January to the end of February, intensive observations periods (IOPs) were conducted. During IOPs atmospheric

profiles were obtained by means of tethered balloon soundings and radio-sonde releases. An IOP was carried out whenever a clear sky and weak synoptic forcing were forecasted, started at 12:00 UTC and lasted for 24 hours. In total 23 IOPs were conducted.

To fulfill the demand of high quality data, shortly after the campaign an inter-comparison experiment was conducted at the Centre de Recherche Atmosphérique, Lannemezan, France. A combination of observations done there supplemented observations during KASCADE itself, and allowed to inter-calibrate and correct the sensors relatively to each other. After this, a specific data post-processing was performed. From this point, analyses could be made and the data served as a basis for the modelling objective.

The local valley winds along the Durance valley and Cadarache valley developed regularly during the campaign and proved to be dominant. Two specific down-valley winds were investigated: the Durance down-valley (DDV) wind and the Cadarache down-valley (CDV) wind. Despite the fact that the smaller Cadarache valley is shallow, it revealed its own local meteorology, characterized by early onsets of stability, consequent down-valley winds and delayed onset of the up-valley wind pattern in the following early morning. When synoptic forcing is weak and sky is clear, the CDV wind sets in around astronomical sunset. Its depth is regularly found to be up to half the valley depth. However in extremely calm situations it can grow up to valley depth. Low level jets (LLJs) develop and are strongest at around 30 m in height, with wind speeds of around $2 - 3 \text{ m s}^{-1}$. Once established, it remains in a quite steady state until cessation in the early morning. Even in weak Mistral conditions (i.e. moderate synoptic forcing), the down-valley wind develops, although with less depth and strength due to valley inflow upslope. As the facilities of the Cadarache site are mostly situated inside the Cadarache Valley and do not have high stacks, the characterization of this wind is essential for local crisis management.

The existence of the CDV wind was indeed known, but neither documented in literature, nor studied before by means of continuous observations with the adequate instrumentation. A threshold test developed in this thesis proved successful to nowcast this wind by means of the available instrumentation existing at Cadarache. Three potential indicators were investigated: a vertical temperature difference, the wind speed at 110 m in height and a bulk Richardson number. The vertical temperature difference showed the best performance to nowcast the CDV wind with a score of 91%. The combination of results proved that the CDV flow is primarily thermally driven. The threshold based on a single direct measurement should help to greatly facilitate instant crisis management.

The DDV wind had never been thoroughly studied before, only short remarks were made in literature as a by-product of campaigns in the region which focused on meteorological situations other than stable stratification periods (e.g. sea breezes during the ESCOMPTE campaign). The DDV wind appeared to be less dominant than the CDV wind for the period of observations. The onset of the DDV wind is more uncertain than that of the CDV wind: on average it sets in 6 to 9 hours after sunset, but sometimes it sets in earlier or later. Nevertheless, the DDV wind appeared to be dominant and strongest around sunrise, when convectively driven winds are not yet well developed. At this time, LLJs are regularly observed with wind speeds of around $4 - 8 \text{ m s}^{-1}$ at 175 - 225 m agl.

The second objective was to set up a meso-scale model able to capture the regional meteorological characteristics. The main goal in this exercise however was to test the model's capability to simulate the DDV wind as it is expected to be a dominant driver for larger scale dispersion. As its origin could not be inferred from the localized observations of KASCADE, the WRF model was used to figure further the DDV wind characteristics. The model appeared to be very resistant to the performed sensitivity tests. Model deficiencies were recognized and not surprising, according to literature regarding simulations for stable stratification in complex terrain: high underestimations of diurnal temperature range, biases on atmospheric turbulent fluxes, overestimation of LLJ strength, problems with the afternoon-evening transition period

and a general lack of clouds in the model. Some of the problems were investigated. Sensitivity tests for surface-atmosphere coupling and soil moisture content did improve the atmospheric profiles, but this was at the cost of a reliable partitioning of the fluxes, as compared to observations. A sensitivity test on a lower horizontal resolution (3 km) showed that the DDV wind is simulated in the heart of the DV, but the model fails to represent it as good at the Cadarache site.

The observations done during the campaign were local. Moreover, they were done in a valley which is not represented in the model simulations. This constituted one of the biggest problems for the modelling purpose. Therefore, an attempt was made to include region meteorological station data in the model evaluation. However, the available quantities were scarce and as the region is complex in the inner domain, only some generalities could be recognized. Nevertheless, the Sodar profiles could be used to validate the locally modelled winds throughout the boundary layer.

Despite the model general deficiencies, it is capable with a 1 km resolution to simulate the DDV wind to a reasonable extent in terms of onset, decay, wind depths as compared to observations at Cadarache. The DDV wind may develop in different patterns and be present throughout the DV. Its depth is constricted to the valley depth. As the valley depth varies greatly, and diminishes towards Cadarache, the DDV wind itself also diminishes in depth accordingly. The development of the wind was found to be close to down-valley wind theory as a consequence of stability, slowly but gradually thickening as time passes by, so that it reaches the CEA centre around sunrise. A second possible origin for the DDV wind is forced channelling consecutive to the existence of LLJs. The latter can develop on the sloping plateaus between the DV and surrounding higher mountains and belongs to a mountain-to-plain circulation. This additionally explains the great delay of the DDV wind at the Cadarache site.

Although the principle objectives were reached, a lot of work can still be envisaged to better understand the regional meteorology. Some ideas are suggested in the next section.

Perspectives

This thesis opens perspectives for both experimentalists and model users.

First of all, the KASCADE dataset has provided a mix of slow and high frequency measurements in a region which has not been intensively studied before especially during stable stratification periods. In this section some ideas are presented that could be relevant either to the scientific community or for local risk management purposes.

The tethered balloon observations are in a large database with high quality measurements of the CDV wind. Although general patterns were analysed here, the depth and strength differed throughout the observations and so far no attempt has been made to link these to above-valley wind patterns or to heat budget calculations. Doing so, a characterization of the CDV wind might be elaborated with respect to the valley geometry and stability strength.

To simulate the CDV wind, the Cadarache Valley must be resolved and WRF employed at a subkilometer resolution. This usage questions the WRF physical limitations which are not fully agreed on in the scientific community, but is the only way to study the CDV wind and its interaction with the DDV wind.

In order to forecast the CDV wind with WRF anyway, the threshold test method proposed in Chap. 5 can also be used in a statistical downscaling procedure. A trial attempt has been made on this by using the 23 simulated IOPs and showed promising results (not shown in this thesis). However, these simulations were IOP-based and have therefore a bias towards calm weak synoptic forcing and stability. To get a general threshold valid for all meteorological situations, a larger set of model output would be needed.

The DDV wind has been revealed as a dominant wind. To find its relation to terrain geometry, it would be interesting to simulate an idealized case study: it would suffice to shut down the synoptic forcing during, for example, IOP16.

The DDV wind has been intensively investigated by observations but only for the winter of 2013. To detect and clarify a seasonal behaviour one should go to year-round observations as has been performed by the Sodar. Additionally these are available at different locations and for two years. The characteristics could be linked to stability by means of GBA tower observations. As this tower contains a long-term dataset, a climatology of the DDV wind could subsequently be made.

The WRF model can be coupled with FLEXPART to study dispersion (nb. this is envisaged in a future thesis). It would be interesting to do a real case study using an atmospheric tracer when stable situations occur. By doing so, the dilution of the tracer could be monitored on site and give insight on the exchange processes between stable layers and transport by a down-valley wind. Such an experiment could be part of a future KASCADE II campaign (see below).

Improvements on Cadarache meteorological network

The Cadarache site deploys two meteorological stations equipped with classical instrumentation on which the site currently relies for crisis management. This thesis has shown that for proper crisis management, some adaptations could be done to the current meteorological network:

1) The boundary layer evolves greatly during the day, from stable to unstable situations in a daily pattern. Besides, closer to the ground, stability is higher than above. Sometimes stability is observed inside the Cadarache Valley but not in the Durance Valley (c.f. IOP 5). To better capture these different features, it is proposed to increase the instrumentation at the GBA tower from the current two levels (at 2 and 110 m) to at least six levels (e.g. 2, 10, 20, 40, 80 and 110 m). This would cover the CDV wind by far to a better extent than it is done currently. Improving the distribution on the tower should give better insight in boundary layer (in)stability and notably the CDV wind from which we have seen that it occurs mostly under 50 m.

2) LMTE should install an atmospheric flux station at the M30 location. This will cover the CDV wind in the heart of the Cadarache Valley. But it is recommended to extend observations with soil heat flux and soil moisture sensors to better understand the overestimation of the ground temperature and check model behavior with these additional data.

KASCADEux

It has been confirmed that the region is very susceptible for stability and the development of valley winds. Although KASCADE proved successful to a large extent, we have seen that questions remain unanswered. Therefore a future campaign could be very fruitful to atmospheric scientists interested in processes in complex terrain.

Flux towers shielded from the CV influences are strongly recommended for proper model evaluation. From the observational perspective little is known about all spatial characteristics and about the onset of the DDV wind below 100 m. For a future campaign, it would be interesting to put boundary layer profiling and atmospheric flux systems along the DV, at least at three locations: close to Cadarache, in between the valleys of l'Asse and la Bléone, and close to St. Auban. If appropriate, profiling systems and flux stations should be installed on the Plateau de Valensole to monitor possible LLJs. Some of these duties can also be achieved by Unmanned Air Vehicles or light aircrafts. It would also be interesting to check the behavior of the DDV wind on the west bank.

One could also think of the yet unexplored interaction between the DDV and CDV winds (see Chap. 4). Finally, the spatial structure of the CDV wind itself remains a question, since it cannot be readily simulated with WRF as was done for the DDV wind.

Alternative wind energy

The DDV wind occurs regularly, and reaches its highest wind speeds in the morning at around 175 to 250 m agl. Without prejudging the relevance of producing wind energy with such characteristics, it should be noticed that the analysis and modelling tools developed and used in this thesis can contribute to assess the wind energy resource in the southern Alps valleys considering the specific climatology they addressed.

The KASCADE-dataset

The thesis was focused on stability and valley winds, but the dataset can also be used by scientists interested in exploring Mistral occurrences, precipitation events, and in valley winds, heat budget, flux divergence, etc. Therefore, the database will be made available on a web site soon (<http://kascade.sedoo.fr/>).

Conclusions générales et perspectives

Conclusions générales

La dispersion des rejets en terrain complexe est largement dépendante des conditions de stratification atmosphérique et de la formation de vents de vallée, dont la caractérisation est par conséquent indispensable pour les études d'impact et la mise au point des procédures de gestion des risques. L'étude présentée dans ce travail est relative aux écoulements de deux vallées perpendiculaires. Ceux-ci ont été analysés grâce à la campagne d'observations KASCADE, et à un modèle météorologique de méso-échelle utilisé en particulier pour étendre l'étude au-delà de la zone d'observations.

Le dispositif d'observation de la campagne KASCADE a été conçu pour appréhender les écoulements de vallée (plus spécifiquement les vents descendants) qui se mettent en place en conditions de stratification stable quand le forçage est faible à l'échelle synoptique. La région-cible était le site de Cadarache et les alentours, et tout particulièrement la vallée de Durance ainsi que la petite vallée de Cadarache qui y débouche. Cette région est complexe, à la fois par son relief local avec des vallées d'une profondeur de 100 à 200 m, par l'impact sur les vents régionaux de chaînes de montagnes orientées Est-Ouest et atteignant 1000 m de hauteur, et enfin par le fait qu'elle est située à une soixantaine de kilomètres à peine de la Méditerranée, de la Vallée du Rhône et des Alpes du Sud. Le climat local se caractérise par une faible nébulosité, ce qui favorise les stratifications stables. Cet effet est renforcé par la présence régulière du Mistral qui rend l'atmosphère plus transparente au rayonnement sous l'effet de l'évacuation des aérosols et de l'assèchement de la surface et de la couche limite.

La campagne d'observations s'est déroulée de mi-décembre 2012 à mi-mars 2013, soit un hiver complet. Les cycles de mise en place et de disparition, à la fois des différentes conditions de stratification et des vents de vallée ont été observés avec succès. Par rapport à la climatologie du site établie par Météo-France, l'hiver en question était plutôt froid et sec quoique proche de la normale, avec une nébulosité faible. En décembre, la température a été proche de la normale, le Mistral fréquent, et les précipitations déficitaires de 25%. Janvier a été légèrement froid, sec et ensoleillé, avec un Mistral fréquent. En février le temps a été froid, sec et ensoleillé, le Mistral fréquent, et une chute de neige a couvert le sol pour plusieurs jours. Les conditions ont été très différentes en mars, avec des flux d'est fréquents apportant des pluies supérieures à la normale. D'une façon générale, le déficit de température a été favorable aux conditions de stabilité recherchées pour cette étude.

Les observations continues comportaient un mât de 30 m équipé pour la mesure des flux et un Sodar, installés pour la campagne, ainsi que le dispositif permanent du site. Le mât de 30 m, implanté dans la vallée de Cadarache, était équipé de trois anémomètres soniques, deux radiomètres pour le rayonnement net, et deux capteurs de température-humidité. Le Sodar mesurait le vent et la turbulence entre 100 et 500 m de hauteur, sur le site de la Verrerie situé en dehors de la vallée de Cadarache. Le dispositif permanent du site comporte une tour de 110 m mesurant la température à la base et au sommet et le vent au sommet, ainsi qu'une mesure de vent à 15 m sur le site de la Verrerie. Entre mi-janvier et fin février, chaque fois qu'une

situation de ciel clair avec un forçage synoptique faible était annoncée, était déclenchée une POI pour une durée de 24 h (1200 UTC - 1200 UTC) au cours de laquelle des profils étaient réalisés grâce à un ballon captif et des lâchers de radiosondes.

Un exercice d'inter-comparaison des capteurs a été réalisé peu de temps après la campagne au Centre de Recherche Atmosphérique, à Lannemezan, afin d'améliorer la qualité du jeu de données. Ceci a permis de corriger et/ou d'inter-calibrer les différents signaux, avant d'entreprendre la phase de traitement proprement dite. Le jeu de données élaborées ainsi obtenu est maintenant libre d'accès et peut être récupéré sur le portail <http://kascade.sedoo.fr/>. C'est sur ce jeu que se sont appuyées les analyses et le travail de modélisation présentés dans ce mémoire.

On a pu observer que les écoulements le long des vallées de Durance et de Cadarache se sont mis en place très régulièrement et se sont révélés être un caractère dominant de la météorologie locale. On s'est plus précisément intéressé aux flux descendants dans la vallée de Cadarache (vent CDV) et de Durance (DDV). Malgré sa largeur et sa profondeur modestes, la vallée de Cadarache présente une météorologie très signée, avec la mise en place du vent CDV dès l'apparition de la stratification stable, mais en revanche le report bien après le lever du jour de la mise en place du vent remontant la vallée. Le vent CDV se développe en général jusqu'à une hauteur de l'ordre de la moitié de la profondeur de la vallée, mais peut parfois la remplir entièrement si le flux synoptique est très faible. Le profil de vent présente un jet de $2\text{--}3\text{ m s}^{-1}$ observé vers 30 m de hauteur. Une fois établi, ce profil perdure jusqu'au lever du soleil. Le vent CDV a été observé même par conditions de faible Mistral (reflétant un forçage synoptique modéré). Dans ce cas, toutefois, l'écoulement est plus mince et moins fort à cause de la présence du flux contraire. Cette connaissance précise et détaillée des écoulements dans cette vallée de Cadarache est indispensable pour la gestion des crises, car c'est à cet endroit que sont situées la plupart des installations du CEA sur ce site, avec de faibles hauteurs de rejets potentiels.

Si l'existence du vent CDV était connue avant ce travail, il n'était pas documenté dans la littérature, et n'avait jamais été observé avec une instrumentation appropriée. Il a été montré dans ce mémoire que sur la base des observations de routine réalisées sur le site il était possible de prévoir son apparition grâce à une méthode basée sur le seuillage d'un indicateur pertinent. Trois d'entre eux ont été testés - une différence de température sur la verticale, la vitesse du vent à 110 m de hauteur et un nombre de Richardson "bulk". La meilleure performance a été obtenue avec la différence de température, pour un taux de réussite de 91%. Au passage, cette technique de prévision immédiate suggère que le vent CDV est principalement un courant de densité. De plus, étant basée sur un indicateur très simple, elle offre un potentiel intéressant pour faciliter la gestion immédiate de crise.

Le vent DDV n'avait jamais été auparavant étudié de façon approfondie. Tout au plus trouve-t-on dans la littérature de rapides commentaires à l'occasion d'analyses d'expériences conduites dans cette région mais focalisées sur des situations météorologiques différentes (par exemple la pénétration de la brise de mer pendant la campagne ESCOMPTE). Par rapport au vent CDV, celui-ci s'est révélé moins dominant pendant la campagne de mesures. Son établissement se produit en général entre 6 et 9 heures après le coucher du soleil, mais peut largement déborder cette plage horaire. Toutefois, c'est un mécanisme dominant de la circulation locale, et il est à son apogée au lever du soleil quand les écoulements générés par la convection ne sont pas encore développés. A ce moment, on observe fréquemment un jet de basse couche entre 175 et 225 m de hauteur, pour des vitesses comprises entre $4\text{ et }8\text{ m s}^{-1}$.

L'objectif suivant a été de mettre en place un modèle à méso-échelle à même de décrire les caractéristiques météorologiques de la région. Plus spécifiquement, il s'agissait d'évaluer les capacités du modèle à simuler le vent DDV, puisqu'au-delà de l'échelle très locale c'est un des principaux pilotes de la dispersion. Le modèle devait permettre de déterminer la genèse de cet écoulement, puisque celle-ci ne pouvait être étudiée à partir des observations trop locales de la

campagne KASCADE. Le modèle WRF s'est révélé peu réactif aux tests de sensibilité réalisés. Des défauts ont été identifiés, mais conformément à ce que la littérature laissait entrevoir compte tenu des conditions de stratification stable et de terrain complexe: une nette surestimation de l'amplitude thermique, des biais dans les flux turbulents, une surestimation des jets de basse couche, des difficultés dans la période de transition de fin d'après-midi et, enfin, une couverture nuageuse sous-estimée. Certains de ces problèmes ont été analysés plus en détail. Des tests de sensibilité sur le couplage sol-atmosphère et le contenu en eau du sol ont parfois permis d'améliorer les profils atmosphériques, mais la confrontation aux observations a montré que c'était au détriment de la partition des flux. Un test sur la résolution horizontale a montré qu'une dégradation de 1 à 3 km permettait encore de générer un vent DDV au coeur de la vallée, mais en aval, à Cadarache, l'écoulement n'était plus représenté correctement.

L'une des principales difficultés dans ces travaux de modélisation a été liée au caractère très local des observations réalisées, de plus dans une vallée que la résolution kilométrique ne permet pas de représenter. Par conséquent une tentative de validation des simulations a été faite à partir des stations météorologiques réparties dans la région. Cette validation ne pouvait qu'être limitée, puisque ces stations sont peu nombreuses et ont une représentativité très locale du fait de la complexité de la région. De ce fait, seules de grandes tendances peuvent être étudiées. Les profils obtenus avec le Sodar se sont révélés mieux appropriés pour la validation du vent dans la couche limite.

Malgré ses défauts, le modèle à 1 km de résolution, confronté aux observations, se révèle capable de simuler correctement le vent DDV à la fois pour son établissement, sa disparition et son extension verticale. Ce vent peut présenter différentes configurations, et souffler tout le long de la vallée de Durance. Son extension verticale suit celle de la vallée, et de fait elle diminue vers l'aval jusqu'à Cadarache. Son comportement est conforme à la théorie des vents de vallée résultant de la stratification, avec un écoulement qui se renforce progressivement au cours du temps, et atteint le site de Cadarache à la fin de la nuit. Une autre origine possible de cet écoulement est une canalisation forcée par un jet de basse couche qui s'est développé sur les plateaux inclinés entre la vallée de Durance et les montagnes plus hautes des environs, et donc correspond à un écoulement de la montagne vers la plaine. Ceci explique en outre l'arrivée tardive du DDV à Cadarache.

A ce stade, les principaux objectifs fixés pour ce travail ont été atteints. Toutefois, la poursuite de cette étude peut être envisagée afin d'améliorer la connaissance des processus de la météorologie régionale. Les paragraphes qui suivent présentent quelques idées dans ce sens.

Perspectives

Ce travail de thèse ouvre des perspectives tant pour les expérimentateurs que pour les modélisateurs.

Tout d'abord les données de KASCADE comprennent un ensemble de mesures obtenues à haute et à basse fréquence d'échantillonnage dans une région relativement peu étudiée auparavant, particulièrement en conditions stables. Aussi cette section présente quelques idées convenant soit à la communauté scientifique soit aux besoins de la gestion de crise.

Les observations avec le ballon captif figurent dans une base de données de qualité pour le vent descendant de vallée de Cadarache. Bien que son aspect général ait été décrit dans la thèse, la force et la profondeur de ce vent de vallée ont varié au cours des observations et il n'a pas été tenté jusqu'ici de les relier aux conditions de vent au-dessus de la vallée ou à des bilans de flux thermiques. Ce travail permettrait de généraliser la caractérisation du vent descendant de vallée de Cadarache en fonction de la géométrie de la vallée et de l'ampleur de la stabilité.

Pour pouvoir simuler le vent descendant de Cadarache, la vallée doit être spatialement résolue et WRF utilisé sur une grille d'échelle horizontale sub-kilométrique (par exemple 200 m,

voire moins). Ainsi le vent de vallée de Cadarache et son interaction avec le vent de Durance pourraient être étudiés par simulation, soulevant toutefois la question débattue des limitations d'emploi de WRF à ce niveau de résolution.

La procédure de descente d'échelle, par test de seuil à partir des observations, proposée au Chap. 5 peut aussi être utilisée pour prédire le vent dans la vallée de Cadarache à partir des simulations numériques actuelles limitées à une résolution de un kilomètre. Une tentative a été faite sur les 23 POIs simulées et a montré des résultats prometteurs (non présentés dans la thèse). Cependant, ces simulations étant basées sur des POIs réalisées en conditions calmes et stables, la généralisation de la validité du seuil à toutes les situations météorologiques nécessiterait une plus grande base de données de simulations.

Le vent descendant de vallée de Durance s'est révélé être un vent dominant. Pour mieux comprendre sa relation avec la géométrie du terrain, il serait intéressant de simuler un cas théorique "idéal", par exemple en se basant sur le POI 16 dont on annulerait le forçage synoptique.

Le vent descendant de vallée de Durance a été mesuré intensivement mais seulement pendant l'hiver 2013. Pour mettre en évidence son comportement saisonnier, il faudrait analyser des observations continues sur l'année comme celles dont on dispose avec le SODAR sur deux années complètes et en deux lieux différents. De cette façon, une étude dédiée à la saisonnalité pourrait être faite en y associant la stabilité connue au moyen des mesures au pylône GBA. Les données GBA étant stockées depuis 50 ans, une climatologie du vent de Durance pourrait être construite.

WRF peut être couplé au modèle lagrangien FLEXPART pour les études de dispersion (sujet envisagé pour une future thèse) et il serait par conséquent intéressant de simuler une dispersion de traceur atmosphérique sur un cas réel basé sur un épisode météorologique en situation stable. Ce faisant, la dilution du traceur pourrait être suivie sur le site et fournir une connaissance approfondie sur les processus de transfert entre couches stables et de transport par le courant descendant la vallée. Ce travail pourrait figurer conjointement à une future campagne KASCADE II (voir plus loin).

Amélioration des mesures météorologiques de Cadarache

Le centre de Cadarache s'appuie sur les données d'instrumentation classique d'une station météorologique pour la gestion de crise. Cette thèse a montré que dans une telle situation, quelques adaptations pourraient être apportées au réseau actuel de surveillance météorologique.

1) La couche limite évolue amplement au cours du temps, de stable à instable suivant un rythme circadien. De plus la stabilité est plus forte à proximité du sol qu'en hauteur. Il peut arriver que la stabilité soit observée dans la vallée de Cadarache alors qu'elle ne l'est pas dans la vallée de la Durance (voir POI 5 dans cette thèse). Pour mieux saisir ces différents aspects, il est proposé d'accroître l'instrumentation du pylône GBA des deux niveaux actuels instrumentés en mesure de température (à 2 et 110 m) et du vent à 110 m jusqu'à au moins six niveaux: 2, 10, 20, 40, 80 et 110 m. Cela permettrait de considérablement mieux appréhender la couche limite, sa stabilité, sa capacité de transport et de mélange des rejets. Mais cela permettrait d'abord de s'assurer de la présence du vent de vallée de Cadarache, ce qui n'est pas le cas actuellement, puisque nous avons vu qu'il s'étendait sur la verticale jusqu'à 50 m la plupart du temps.

2) Le LMTE installera une station météorologique classique à la position M30. Celle-ci permettra d'observer le vent de Cadarache au cœur même de la vallée. Il est alors recommandé d'ajouter une mesure du flux de chaleur et d'humidité au niveau du sol pour mieux comprendre les échanges d'énergie avec le sol et les confronter aux calculs opérationnels (ou de recherche) dans le futur. Ceci dans le but de résoudre une des déficiences du modèle WRF : sa capacité à prédire correctement l'amplitude journalière de température.

KASCADEux

Il est confirmé que la région est propice à la stabilité atmosphérique et au développement des vents de vallée. Bien que la campagne KASCADE ait atteint ses objectifs dans une large mesure avec succès, des questions restent sans réponse. Par conséquent une nouvelle campagne serait très profitable aux physiciens de l'atmosphère concernés par les processus en terrain complexe.

Par exemple, on dispose de fort peu d'observations sur le commencement du vent descendant la vallée de Durance et ses caractéristiques spatiales dans la première centaine de mètres de hauteur. Dans une future campagne, il serait intéressant de mesurer les profils de couche limite et les flux atmosphériques le long de la DV, au moins pour trois positions: proche de Cadarache, entre les vallées de l'Asse et de la Bléone, et à hauteur de St. Auban. Le même type de mesure sur le Plateau de Valensole permettrait l'observation de possibles jets de basse couche. Notons que certaines de ces données peuvent être acquises par des drones ou avions légers. Enfin il faudrait vérifier le comportement de vent de Durance sur sa rive gauche et y disposer d'une station en un lieu non soumis à l'influence de la vallée de Cadarache. Des mesures de flux turbulent de même type que M30 dans DV en-dehors de CV sont aussi nécessaires pour différencier l'influence des 2 vallées sur les flux turbulents.

L'interaction entre les vents descendants de Durance et de Cadarache n'a pas été explorée (cf Chap. 4). Finalement, la structure spatiale du vent de Cadarache reste une source de questionnement, puisqu'il ne peut pas être simulé avec WRF comme cela l'a été pour le vent de Durance.

Energie alternative

Le vent descendant de la vallée de Durance se manifeste régulièrement et atteint son maximum de vitesse en matinée entre 175 to 250 m au-dessus du sol. Sans préjuger de l'intérêt de ces caractéristiques pour produire de l'énergie éolienne, on remarquera que les outils de modélisation développés et utilisés dans la thèse peuvent contribuer à l'évaluation du gisement éolien dans les vallées des Alpes du Sud du fait de leur climatologie spécifique.

La base de données KASCADE

La thèse s'est concentrée sur la stabilité et les vents de vallée, mais les données accumulées peuvent être exploitées par les scientifiques intéressés par l'étude du Mistral, des événements avec précipitation, et particulièrement les thématiques de vent de vallée, bilan de chaleur, divergence de flux thermique. En conséquence, la base de données sera prochainement mise à disposition sur un serveur ouvert à la communauté scientifique (<http://kascade.sedoo.fr/>).

Bibliography

- Anfossi, D., P. Bacci, and A. Longhetto (1976). Forecasting of vertical temperature profiles in the atmosphere during nocturnal radiation inversions from air temperature trend at screen height. *Q. J. Roy. Meteor. Soc.* 102(431), 173–180.
- Angevine, W., E. Bazile, D. Legain, and D. Pino (2014). Land surface spinup for episodic modeling. *Atmos. Chem. Phys.* 14(15), 8165–8172.
- Arnold, D., D. Morton, I. Schicker, P. Seibert, M. Rotach, K. Horvath, J. Dudhia, T. Satomura, M. Müller, G. Zängl, et al. (2012). *High resolution modelling in complex terrain: report on the HiRCOT 2012 Workshop, Vienna, 21-23 February 2012*. Institut für Meteorologie, Department Wasser-Atmosphäre-Umwelt, Univ. f. Bodenkultur.
- Atkinson, B. (1995). Orographic and stability effects on valley-side drainage flows. *Bound.-Lay. Meteorol.* 75(4), 403–428.
- Baghi, R., P. Durand, C. Jambert, C. Jarnot, C. Delon, D. Serça, N. Striebig, M. Ferlicoq, and P. Keravec (2012). A new disjunct eddy-covariance system for BVOC flux measurements - validation on CO₂ and H₂O fluxes. *Atmospheric Measurement Techniques* 5(12), 3119–3132. 10.5194/amt-5-3119-2012.
- Barry, R. G. (2013). *Mountain weather and climate, 3rd edition*. Cambridge University Press.
- Bastin, S., P. Drobinski, A. Dabas, P. Delville, O. Reitebuch, and C. Werner (2005). Impact of the Rhône and Durance valleys on sea-breeze circulation in the Marseille area. *Atmos. Res.* 74(1), 303–328.
- Beljaars, A. (1995). The parametrization of surface fluxes in large-scale models under free convection. *Q. J. Roy. Meteor. Soc.* 121(522), 255–270.
- Blackadar, A. K. (1957). Boundary layer wind maxima and their significance for the growth of nocturnal inversions. *B. Am. Meteorol. Soc.* 38(5), 283–290.
- Bowen, B. M., J. A. Baars, and G. L. Stone (2000). Nocturnal wind direction shear and its potential impact on pollutant transport. *J. Appl. Meteorol.* 39(3), 437–445.
- Brioude, J., W. Angevine, S. McKeen, and E.-Y. Hsie (2012). Numerical uncertainty at mesoscale in a Lagrangian model in complex terrain. *Geoscientific Model Development* 5(5), 1127–1136.
- Bromwich, D. H. (1989). An extraordinary katabatic wind regime at Terra Nova Bay, Antarctica. *Mon. Wea. Rev.* 117(3), 688–695.
- Brutsaert, W. (1972). Radiation, evaporation and the maintenance of turbulence under stable conditions in the lower atmosphere. *Bound.-Lay. Meteorol.* 2(3), 309–325.
- Burns, P. and C. Chemel (2014). Evolution of cold-air-pooling processes in complex terrain. *Bound.-Lay. Meteorol.* 150(3), 423–447.
- Businger, J. (1982). Equations and concepts. In *Chapt. 1 in Atmospheric turbulence and air pollution modelling*, pp. 1–36. Springer.
- Büttner, G., T. Soukup, and A. Sousa (2007). CLC2006 technical guidelines. Technical Report 17, European Environment Agency.
- Carrera, M. L., J. R. Gyakum, and C. A. Lin (2009). Observational study of wind channeling within the St. Lawrence River Valley. *J. Appl. Meteorol. Clim.* 48(11), 2341–2361.

- Chen, F. and J. Dudhia (2001). Coupling an advanced land surface-hydrology model with the Penn State-NCAR MM5 modeling system. Part I: Model implementation and sensitivity. *Mon. Wea. Rev.* 129(4), 569–585.
- Chen, F., Z. Janjić, and K. Mitchell (1997). Impact of atmospheric surface-layer parameterizations in the new land-surface scheme of the NCEP mesoscale Eta model. *Bound.-Lay. Meteorol.* 85(3), 391–421.
- Chou, M.-D. and M. J. Suarez (1994). An efficient thermal infrared radiation parameterization for use in general circulation models. *NASA Tech. Memo* 104606(3), 85.
- Clements, C. B., C. D. Whiteman, and J. D. Horel (2003). Cold-air-pool structure and evolution in a mountain basin: Peter Sinks, Utah. *J. Appl. Meteorol.* 42(6), 752–768.
- Collins, W. D., P. J. Rasch, B. A. Boville, J. J. Hack, J. R. McCaa, D. L. Williamson, J. T. Kiehl, B. Briegleb, C. Bitz, S. Lin, et al. (2004). Description of the NCAR community atmosphere model (CAM 3.0). Technical report, Tech. Rep. NCAR/TN-464+ STR.
- Cros, B., P. Durand, H. Cachier, P. Drobinski, E. Frejafon, C. Kottmeier, P. Perros, V.-H. Peuch, J.-L. Ponche, D. Robin, et al. (2004). The ESCOMPTE program: an overview. *Atmos. Res.* 69(3), 241–279.
- Cuxart, J., L. Conangla, and M. Jiménez (2015). Evaluation of the surface energy budget equation with experimental data and the ECMWF model in the Ebro Valley. *J. Geophys. Res.-Atmos.* 120(3), 1008–1022.
- De Meij, A., E. Bossioli, C. Penard, J. Vinuesa, and I. Price (2014). The effect of Corine Land Cover data on calculated gas and PM10 concentrations in WRF-Chem. *Atmos. Environ.* 101, 177–193.
- Delage, Y., P. A. Bartlett, and J. H. McCaughey (2002). Study of ‘soft’ night-time surface-layer decoupling over forest canopies in a land-surface model. *Bound.-Lay. Meteorol.* 103(2), 253–276.
- Doran, J., J. D. Fast, and J. Horel (2002). The VTMX 2000 campaign. *B. Am. Meteorol. Soc.* 83(4), 537–551.
- Draxler, R. R. and G. D. Rolph (2003). HYSPLIT (HYbrid Single-Particle Lagrangian Integrated Trajectory) model access via NOAA ARL READY website (<http://www.arl.noaa.gov/ready/hysplit4.html>). NOAA Air Resources Laboratory, Silver Spring.
- Drobinski, P., V. Ducrocq, P. Alpert, E. Anagnostou, K. Béranger, M. Borga, I. Braud, A. Chanzy, S. Davolio, G. Delrieu, et al. (2013). HyMeX, a 10-year multidisciplinary program on the Mediterranean water cycle. *B. Am. Meteorol. Soc.*
- Dudhia, J. (1989). Numerical study of convection observed during the winter monsoon experiment using a mesoscale two-dimensional model. *J. Atmos. Sci.* 46(20), 3077–3107.
- Dudhia, J. (1996). A multi-layer soil temperature model for MM5. In *Preprint from the Sixth PSU/NCAR Mesoscale Model Users’ Workshop*, pp. 22–24.
- Durrán, D. R. (2002). Downslope winds. In J. R. Holton, J. A. Curry, and J. A. Pyle (Eds.), *Encyclopedia of Atmospheric Sciences*, pp. 644–650. London, UK: Elsevier Science Ltd.
- Farr, T. G., P. A. Rosen, E. Caro, R. Crippen, R. Duren, S. Hensley, M. Kobrick, M. Paller, E. Rodriguez, L. Roth, et al. (2007). The shuttle radar topography mission. *Rev. Geophys.* 45(2). doi:10.1029/2005RG000183.
- Fernando, H. J., B. Verhoef, S. Di Sabatino, L. S. Leo, and S. Park (2013). The Phoenix evening transition flow experiment (TRANSFLEX). *Bound.-Lay. Meteorol.* 147(3), 443–468.
- Foken, T. (2008). The energy balance closure problem: an overview. *Ecol. Appl.* 18(6), 1351–1367.
- García-Díez, M., J. Fernández, L. Fita, and C. Yagüe (2013). Seasonal dependence of WRF model biases and sensitivity to PBL schemes over Europe. *Q. J. Roy. Meteor. Soc.* 139(671), 501–514.
- Geerts, B. (2003). Empirical estimation of the monthly-mean daily temperature range. *Theor. Appl. Climatol.* 74(3–4), 145–165.
- Gross, G. and F. Wippermann (1987). Channeling and countercurrent in the upper Rhine Valley: Numerical simulations. *J. Climate Appl. Meteor.* 26(10), 1293–1304.
- Guenard, V., P. Drobinski, J.-L. Caccia, B. Campistron, and B. Bench (2005). An observational study of the mesoscale mistral dynamics. *Bound.-Lay. Meteorol.* 115(2), 263–288.

- Haiden, T. and C. D. Whiteman (2005). Katabatic flow mechanisms on a low-angle slope. *J. Appl. Meteorol.* *44*(1), 113–126.
- Hanna, S. R. and R. Yang (2001). Evaluations of mesoscale models’ simulations of near-surface winds, temperature gradients, and mixing depths. *J. Appl. Meteorol.* *40*(6), 1095–1104.
- Hoch, S., P. Calanca, R. Philipona, and A. Ohmura (2007). Year-round observation of longwave radiative flux divergence in Greenland. *J. Appl. Meteorol. Clim.* *46*(9), 1469–1479.
- Holtslag, A., G. Svensson, P. Baas, S. Basu, B. Beare, A. Beljaars, F. Bosveld, J. Cuxart, J. Lindvall, G. Steeneveld, et al. (2013). Stable atmospheric boundary layers and diurnal cycles: challenges for weather and climate models. *B. Am. Meteorol. Soc.* *94*(11), 1691–1706.
- Holtslag, A. A. (2003). Atmospheric turbulence. In *Encyclopedia of Physical Science and Technology (Third Edition)*, pp. 707 – 719. New York: Academic Press.
- Hong, S.-Y. and J.-O. J. Lim (2006). The WRF single-moment 6-class microphysics scheme (WSM6). *J. Korean Meteor. Soc.* *42*(2), 129–151.
- Hong, S.-Y., Y. Noh, and J. Dudhia (2006). A new vertical diffusion package with an explicit treatment of entrainment processes. *Mon. Wea. Rev.* *134*(9), 2318–2341.
- Horst, T. and J. Doran (1986). Nocturnal drainage flow on simple slopes. *Bound.-Lay. Meteorol.* *34*(3), 263–286.
- Iacono, M. J., J. S. Delamere, E. J. Mlawer, M. W. Shephard, S. A. Clough, and W. D. Collins (2008). Radiative forcing by long-lived greenhouse gases: Calculations with the AER radiative transfer models. *J. Geophys. Res.-Atmos.* *113*(D13). doi:10.1029/2008JD009944.
- Jammalamadaka, S. R. and A. Sengupta (2001). *Topics in circular statistics*, Volume 5. World ScientificPub Co Inc.
- Janjic, Z. I. (1994). The step-mountain eta coordinate model: Further developments of the convection, viscous sublayer, and turbulence closure schemes. *Mon. Wea. Rev.* *122*(5), 927–945.
- Jiménez, M. A. and J. Cuxart (2014). A study of the nocturnal flows generated in the north side of the Pyrenees. *Atmos. Res.* *145*, 244–254.
- Jiménez, P. A. and J. Dudhia (2012). Improving the representation of resolved and unresolved topographic effects on surface wind in the WRF model. *Journal of Applied Meteorology and Climatology* *51*(2), 300–316.
- Kain, J. S. (2004). The Kain-Fritsch convective parameterization: an update. *J. Appl. Meteorol.* *43*(1), 170–181.
- Kalthoff, N., C. Kottmeier, J. Thürauf, U. Corsmeier, F. Said, E. Fréjafon, and P. Perros (2005). Mesoscale circulation systems and ozone concentrations during ESCOMPTE: a case study from IOP 2b. *Atmos. Res.* *74*(1), 355–380.
- Kalverla, P., G.-J. Duine, G.-J. Steeneveld, and T. Hedde (2015). Evaluation of the Weather Research and Forecasting model for contrasting diurnal cycles in the Durance Valley complex terrain during the KASCADE field campaign. *submitted to J. Appl. Meteorol. Climatol.*
- Kleczeck, M. A., G.-J. Steeneveld, and A. A. Holtslag (2014). Evaluation of the weather research and forecasting mesoscale model for GABLS3: impact of boundary-layer schemes, boundary conditions and spin-up. *Bound.-Lay. Meteorol.* *152*(2), 213–243.
- Kraus, H., J. Malcher, and E. Schaller (1985). A nocturnal low level jet during PUKK. *Bound.-Lay. Meteorol.* *31*(2), 187–195.
- Largerion, Y. (2010). *Dynamique de la couche limite atmosphérique stable en relief complexe. Application aux épisodes de pollution particulaire des vallées alpines*. Ph. D. thesis, Grenoble University.
- Largerion, Y., C. Staquet, and C. Chemel (2013). Characterization of oscillatory motions in the stable atmosphere of a deep valley. *Bound.-Lay. Meteorol.* *148*(3), 439–454.
- Lothon, M., F. Lohou, D. Pino, F. Couvreux, E. Pardyjak, J. Reuder, J. Vilà-Guerau de Arellano, P. Durand, O. Hartogensis, D. Legain, et al. (2014). The BLLAST field experiment: Boundary-layer late afternoon and sunset turbulence. *Atmospheric Chemistry and Physics* *14*(20), 10931–10960.
- Mahrt, L. (1982). Momentum balance of gravity flows. *J. Atmos. Sci.* (39), 2701–2711.

- Mahrt, L. (1999). Stratified atmospheric boundary layers. *Bound.-Lay. Meteorol.* 90(3), 375–396.
- Mahrt, L. (2014). Stably stratified atmospheric boundary layers. *Annu. Rev. Fluid Mech.* 46, 23–45.
- Mahrt, L. and S. Larsen (1990). Relation of slope winds to the ambient flow over gentle terrain. *Bound.-Lay. Meteorol.* 53(1-2), 93–102.
- Mahrt, L., J. Sun, W. Blumen, T. Delany, and S. Oncley (1998). Nocturnal boundary-layer regimes. *Bound.-Lay. Meteorol.* 88, 255–278.
- Manins, P. and B. Sawford (1979). Katabatic winds: A field case study. *Q. J. Roy. Meteor. Soc.* 105(446), 1011–1025.
- Margerit, Y. (2004). Analyse des données météorologiques dans la région de Cadarache. Technical Report CEA DEN CAD DTN SMTM LMTE NT 2004(90) 90, Commissariat à l’Energie Atomique.
- Margerit, Y. (2006). Analyse des données météorologiques, gradient thermique, pluviométrie et humidité sur la zone de Cadarache. Technical Report CEA DEN CAD DTN SMTM LMTE NT 2006(07) 30, Commissariat à l’Energie Atomique.
- McTaggart-Cowan, R. and A. Zadra (2014). Representing Richardson Number Hysteresis in the NWP Boundary Layer. *Mon. Wea. Rev.* 143(4), 1232–1258.
- Mestayer, P. G., P. Durand, P. Augustin, S. Bastin, J.-M. Bonnefond, B. Bénéch, B. Campistron, A. Coppalle, H. Delbarre, B. Dousset, et al. (2005). The urban boundary-layer field campaign in Marseille (UBL/CLU-ESCOMPTE): set-up and first results. *Bound.-Lay. Meteorol.* 114(2), 315–365.
- Milliez, M. and B. Carissimo (2007). Numerical simulations of pollutant dispersion in an idealized urban area, for different meteorological conditions. *Bound.-Lay. Meteorol.* 122(2), 321–342.
- Mlawer, E. J., S. J. Taubman, P. D. Brown, M. J. Iacono, and S. A. Clough (1997). Radiative transfer for inhomogeneous atmospheres: RRTM, a validated correlated-k model for the longwave. *J. Geophys. Res.-Atmos.* 102(D14), 16663–16682.
- Moene, A. F. and J. C. van Dam (2014). *Transport in the atmosphere-vegetation-soil continuum*. Cambridge University Press.
- Monti, P., H. Fernando, M. Princevac, W. Chan, T. Kowalewski, and E. Pardyjak (2002). Observations of flow and turbulence in the nocturnal boundary layer over a slope. *J. Atmos. Sci.* 59(17), 2513–2534.
- Nadeau, D. F., E. R. Pardyjak, C. W. Higgins, H. Huwald, and M. B. Parlange (2013). Flow during the evening transition over steep alpine slopes. *Q. J. Roy. Meteor. Soc.* 139(672), 607–624.
- Nakanishi, M. and H. Niino (2006). An improved Mellor–Yamada level-3 model: Its numerical stability and application to a regional prediction of advection fog. *Bound.-Lay. Meteorol.* 119(2), 397–407.
- Nappo, C. J. (2012). *An introduction to atmospheric gravity waves*, Volume 102. Academic Press.
- Nieuwstadt, F. T. (1984). The turbulent structure of the stable, nocturnal boundary layer. *J. Atmos. Sci.* 41(14), 2202–2216.
- Ogura, Y. and N. A. Phillips (1962). Scale analysis of deep and shallow convection in the atmosphere. *Journal of the atmospheric sciences* 19(2), 173–179.
- Oke, T. R. (1987). *Boundary layer climates: second edition*. Routledge, London.
- Pardyjak, E. R., H. J. S. Fernando, J. C. Hunt, A. A. Grachev, and J. Anderson (2009). A case study of the development of nocturnal slope flows in a wide open valley and associated air quality implications. *Meteorol. Z.* 18(1), 85–100.
- Pielke, R. A. (2013). *Mesoscale meteorological modeling*, Volume 98. Academic press.
- Pineda, N., O. Jorba, J. Jorge, and J. Baldasano (2004). Using NOAA AVHRR and SPOT VGT data to estimate surface parameters: application to a mesoscale meteorological model. *Int. J. Remote Sens.* 25(1), 129–143.
- Pleim, J. E. (2006). A simple, efficient solution of flux-profile relationships in the atmospheric surface layer. *J. Appl. Meteorol. Clim.* 45(2), 341–347.

- Pleim, J. E. (2007). A combined local and nonlocal closure model for the atmospheric boundary layer. Part I: Model description and testing. *J. Appl. Meteorol. Clim.* 46(9), 1383–1395.
- Price, J., S. Vosper, A. Brown, A. Ross, P. Clark, F. Davies, V. Horlacher, B. Claxton, J. McGregor, J. Hoare, et al. (2011). COLPEX: field and numerical studies over a region of small hills. *B. Am. Meteorol. Soc.* 92(12), 1636–1650.
- Quénol, H. and G. Beltrando (2008). Impact of a new railway line embankment (Mediterranean TGV) on the frequency of spring frosts in a fruit-growing area of the Durance Valley (south of France). *Meteorol. Appl.* 15(3), 389–398.
- Reiter, E. (1971). Digest of Selected Weather Problems of the Mediterranean. Technical Report 9-71, Navy Weather Research Facility.
- ReVelle, D. O. (1993). Chaos and "bursting" in the planetary boundary layer. *J. Appl. Meteorol.* 32(7), 1169–1180.
- Rotach, M. W., P. Calanca, G. Graziani, J. Gurtz, D. G. Steyn, R. Vogt, M. Andretta, A. Christen, S. Cieslik, R. Connolly, et al. (2004). Turbulence Structure and Exchange Processes in an Alpine Valley: The Riviera Project. *B. Am. Meteorol. Soc.* 85(9), 1367–1385.
- Salmond, J. and I. McKendry (2005). A review of turbulence in the very stable nocturnal boundary layer and its implications for air quality. *Prog. Phys. Geog.* 29(2), 171–188.
- Santos-Alamillos, F., D. Pozo-Vázquez, J. Ruiz-Arias, V. Lara-Fanego, and J. Tovar-Pescador (2013). Analysis of WRF model wind estimate sensitivity to physics parameterization choice and terrain representation in Andalusia (Southern Spain). *Journal of Applied Meteorology and Climatology* 52(7), 1592–1609.
- Santos-Alamillos, F., D. Pozo-Vázquez, J. Ruiz-Arias, and J. Tovar-Pescador (2015). Influence of land-use misrepresentation on the accuracy of WRF wind estimates: Evaluation of GLCC and CORINE land-use maps in the southern Spain. *Atmos. Res.* 157, 17–28.
- Savijärvi, H. (2006). Radiative and turbulent heating rates in the clear-air boundary layer. *Q. J. Roy. Meteor. Soc.* 132(614), 147–161.
- Schmid, H., H. Cleugh, C. Grimmond, and T. Oke (1991). Spatial variability of energy fluxes in suburban terrain. *Bound.-Lay. Meteorol.* 54, 249–276.
- Sertel, E., A. Robock, and C. Ormeci (2010). Impacts of land cover data quality on regional climate simulations. *Int. J. Climatol.* 30(13), 1942–1953.
- Shin, H. H. and S.-Y. Hong (2011). Intercomparison of planetary boundary-layer parametrizations in the WRF model for a single day from CASES-99. *Bound.-Lay. Meteorol.* 139(2), 261–281.
- Skyllingstad, E. D. (2003). Large-eddy simulation of katabatic flows. *Bound.-Lay. Meteorol.* 106(2), 217–243.
- Smedman, A.-S. (1988). Observations of a multi-level turbulence structure in a very stable atmospheric boundary layer. *Bound.-Lay. Meteorol.* 44(3), 231–253.
- Smith, C. M. and E. D. Skillingstad (2005). Numerical simulation of katabatic flow with changing slope angle. *Mon. Wea. Rev.* 133(11), 3065–3080.
- Steeneveld, G., M. Wokke, C. G. Zwaafink, S. Pijlman, B. Heusinkveld, A. Jacobs, and A. Holtslag (2010). Observations of the radiation divergence in the surface layer and its implication for its parameterization in numerical weather prediction models. *J. Geophys. Res.* 115, D06107. doi:10.1029/2009JD013074.
- Steeneveld, G.-J. (2014). Current challenges in understanding and forecasting stable boundary layers over land and ice. *Front. Environ. Sci.* 2, 41.
- Sterk, H., G. Steeneveld, and A. Holtslag (2013). The role of snow-surface coupling, radiation, and turbulent mixing in modeling a stable boundary layer over arctic sea ice. *J. Geophys. Res.-Atmos.* 118(3), 1199–1217.
- Stull, R. B. (1988). *An Introduction to Boundary Layer Meteorology*. Kluwer Academic Publishers.
- Stull, R. B. (2000). *Meteorology: For Scientists and Engineers*. Thomson Learning.
- Sukoriansky, S., B. Galperin, and V. Perov (2005). Application of a new spectral theory of stably stratified turbulence to the atmospheric boundary layer over sea ice. *Bound.-Lay. Meteorol.* 117(2), 231–257.

- Sun, J., S. Burns, A. C. Delany, S. Oncley, T. Horst, and D. Lenschow (2003). Heat balance in the nocturnal boundary layer during CASES-99. *J. Appl. Meteorol.* 42, 1649–1666.
- Svensson, G., A. Holtslag, V. Kumar, T. Mauritsen, G. Steeneveld, W. Angevine, E. Bazile, A. Beljaars, E. de Bruijn, A. Cheng, et al. (2011). Evaluation of the diurnal cycle in the atmospheric boundary layer over land as represented by a variety of single-column models: the second GABLS experiment. *Bound.-Lay. Meteorol.* 140(2), 177–206.
- Tewari, M., F. Chen, W. Wang, J. Dudhia, M. LeMone, K. Mitchell, M. Ek, G. Gayno, J. Wegiel, and R. Cuenca (2004). Implementation and verification of the unified NOAA land surface model in the WRF model. In *20th conference on weather analysis and forecasting/16th conference on numerical weather prediction*, pp. 11–15.
- Triantafyllou, A. and P. Kassomenos (2002). Aspects of atmospheric flow and dispersion of air pollutants in a mountainous basin. *Sci. Total Environ.* 297(1), 85–103.
- Tuononen, M., V. Sinclair, and T. Vihma (2015). A climatology of low-level jets in the mid-latitudes and polar regions of the northern hemisphere. *Atmos. Sci. Lett.*. doi: 10.1002/asl.587.
- Van de Wiel, B., A. Moene, O. Hartogensis, H. De Bruin, and A. Holtslag (2003). Intermittent turbulence in the stable boundary layer over land. Part III: A classification for observations during CASES-99. *J. Atmos. Sci.* 60(20), 2509–2522.
- Van Heerwaarden, C. C., J. Vilà-Guerau de Arellano, A. F. Moene, and A. A. Holtslag (2009). Interactions between dry-air entrainment, surface evaporation and convective boundary-layer development. *Q. J. Roy. Meteor. Soc.* 135(642), 1277–1291.
- Vecchi, R., G. Marazzan, and G. Valli (2007). A study on nighttime–daytime PM10 concentration and elemental composition in relation to atmospheric dispersion in the urban area of Milan (Italy). *Atmos. Environ.* 41(10), 2136–2144.
- Viterbo, P., A. Beljaars, J.-F. Mahfouf, and J. Teixeira (1999). The representation of soil moisture freezing and its impact on the stable boundary layer. *Q. J. Roy. Meteor. Soc.* 125(559), 2401–2426.
- Warner, R. F. (2006). Natural and artificial linkages and discontinuities in a Mediterranean landscape: Some case studies from the Durance Valley, France. *Catena* 66(3), 236–250.
- Weber, R. O. and P. Kaufmann (1998). Relationship of synoptic winds and complex terrain flows during the MISTRAL field experiment. *J. Appl. Meteorol.* 37(11), 1486–1496.
- Whiteman, C. D. (1982). Breakup of temperature inversions in deep mountain valleys: Part I. Observations. *J. Appl. Meteorol.* 21(3), 270–289.
- Whiteman, C. D. (2000). *Mountain meteorology: fundamentals and applications*. Oxford University Press.
- Whiteman, C. D. and J. C. Doran (1993). The relationship between overlying synoptic-scale flows and winds within a valley. *J. Appl. Meteorol.* 32(11), 1669–1682.
- Whiteman, C. D., S. W. Hoch, M. Hahnenberger, A. Muschinski, V. Hohreiter, M. Behn, Y. Cheon, S. Zhong, W. Yao, D. Fritts, et al. (2008). METCRAX 2006: Meteorological experiments in Arizona’s Meteor crater. *B. Am. Meteorol. Soc.* 89(11), 1665–1680.
- Wrathall, J. (1985). The Mistral And Forest Fires In Provence - Côte D’Azur, Southern France. *Weather* 40, 119–124. doi: 10.1002/j.1477-8696.1985.tb07493.x.
- Zanetti, P. (1990). Air pollution modelling. *Southampton-UK: Comp. Mech. Publications*.
- Zhang, D.-L. and W.-Z. Zheng (2004). Diurnal cycles of surface winds and temperatures as simulated by five boundary layer parameterizations. *J. Appl. Meteorol.* 43(1), 157–169.
- Zilitinkevich, S. (1995). Non-local turbulent transport pollution dispersion aspects of coherent structure of convective flows. *Air Pollution III, Air pollution theory and simulation (H Power, N Moussiopoulos, CA Brebbia, eds) Computational Mechanics Publ, Southampton, Boston* 1, 53–60.

Appendices

Appendix A

Terminology

In literature the terminology used for winds over slopes or inside valleys or mountains is various and sometimes improperly used. This appendix provides the definitions taken from the Glossary of Meteorology from the American Meteorological Society (<http://glossary.ametsoc.org/>).

Katabatic wind

1. Most widely used in mountain meteorology to denote a downslope flow driven by cooling at the slope surface during periods of light larger-scale winds; the nocturnal component of the along-slope wind systems.

The surface cools a vertical column of the atmosphere starting at the slope surface and reaching perhaps 10-100 m deep. This column is colder than the column at equivalent levels over the valley or plain, resulting in a hydrostatic pressure excess over the slope relative to over the valley or plain. The horizontal pressure gradient, maximized at the slope surface, drives an acceleration directed away from the slope, or downslope. Although the pressure-gradient forcing is at its maximum at the slope, surface friction causes the peak in the katabatic wind speeds to occur above the surface, usually by a few meters to a few tens of meters. The depth of the downslope flow layer on simple slopes has been found to be 0.05 times the vertical drop from the top of the slope. Surface-wind speeds in mountain-valley katabatic flows are often $3\text{--}4\text{ m s}^{-1}$, but on long slopes, they have been found to exceed 8 m s^{-1} . Slopes occur on many scales, and consequently katabatic flows also occur on many scales. At local scales katabatic winds are a component of mountain-valley wind systems. At scales ranging from the slopes of individual hills and mountains to the slopes of mountain ranges and massifs, katabatic flows represent the nocturnal component of mountain-plains wind systems. Besides diurnal-cycle effects, surface cooling can also result from cold surfaces such as ice and snow cover. Katabatic flows over such surfaces have been studied as glacier winds in valleys and as large-scale slope flows in Antarctica and Greenland. The large-scale katabatic wind blowing down the ice dome of the Antarctic continent has sometimes reached 50 m s^{-1} on the periphery of the continent. The persistence of the surface forcing and the great extent of the slopes on these great landmasses means that the flows are subject to Coriolis deflection, and thus they are not pure katabatic flows.

See *downslope wind*, *gravity wind*, *drainage wind*.

2. Occasionally used in a more general sense to describe cold air flowing down a slope or incline on any of a variety of scales, including phenomena such as the *bora*, in addition to thermally forced flows as described above.

From its etymology, the term means simply 'going down' or 'descending,' and thus could refer to any descending flow; some authors have further generalized it to include downslope

flows such as the *foehn* or chinook even though they do not represent a flow of cold air. This concept has given rise to the expression *katafront*, which indicates flow down a sloped cold-frontal surface.

Downslope wind

1. A wind directed down a slope, often used to describe winds produced by processes larger in scale than the slope.

Because this flow produces subsidence, downslope winds experience warming, drying, increasing stability, and clearing if clouds are present.

2. Flow directed down a mountain slope and driven by cooling at the earth's surface: a component of the mountain-valley or mountain-plains wind systems.

same as *katabatic wind*.

The many synonyms for downslope flow are sometimes used interchangeably, and this gives rise to ambiguity and confusion. Downslope can be used generically to denote any wind flow blowing down a slope, or it is used specifically for katabatic flows on any scale, such as the nocturnal slope-wind component of mountain-valley wind systems or mountain-plains wind systems.

See *katabatic wind*, *gravity wind*, *drainage wind*, *fall wind*, *bora*, *foehn*.

Down-valley wind

(Same as mountain breeze.) A nocturnal, thermally forced along-valley wind produced as a result of nocturnal cooling of the valley air; a nocturnal component of the fair-weather mountain-valley wind systems encountered during periods of light synoptic or other larger-scale flow.

Valley cooling is accomplished by the combined effects of draining cold air off the slopes by early-evening downslope (katabatic) winds, and upward motion with upward cold-air advection from the convergence of katabatic flows in the valley center. Air in the valley thus becomes cooler than air at the same level over the adjacent plain (see topographic amplification factor), producing higher pressure in the valley. The pressure gradient drives a downvalley wind that begins one to four hours after sunset, persists for the rest of the night until after sunrise, and often reaches $7\text{--}10\text{ m s}^{-1}$ or more above the surface. The downvalley wind tends to fill the valley, that is, its depth is approximately the depth of the valley, and where mountains end and a valley empties onto the plains, the downvalley wind can become a cold-air valley outflow jet flowing out of the mouth of the valley.

See *drainage wind*, *along-valley wind systems*.

Drainage wind

Cold-air-runoff winds that are produced when air in contact with terrain surfaces is cooled and flows downslope and/or downvalley.

This generic term is often used to indicate aggregate downslope (katabatic) and downvalley flows, when it is difficult to distinguish between the two. This happens frequently in basins, at the upper end of valleys, in complicated topography where the downslope and downvalley directions are not perpendicular, and in simple valleys when the weaker and shallower downslope flows are masked or overwhelmed by the stronger downvalley flow. Over even gently sloping topography, drainage winds also refer to gravity winds that drain cold air into frost hollows, river valleys, and other lower-lying terrain.

See *downslope wind*.

Along-slope wind systems

Thermally forced winds that blow up or down the sidewall slopes in a mountain valley, and the accompanying countercurrents when present; the slope-wind components of the mountain-valley wind system.

During the daytime this system consists of upslope (anabatic) flow adjacent to the slope and often a compensatory return current directed downslope just above the upslope layer. At night it is a *downslope* (*katabatic*) flow layer near the slope, sometimes with a return flow aloft.

Along-valley wind systems

Thermally forced winds blowing along the main (longitudinal) axis of a valley, sometimes accompanied by countercurrents aloft; the up- and down-valley components of the mountain-valley wind systems.

During the daytime, this system comprises an up-valley wind and its countercurrent if present. At night it is a *down-valley wind* and return flow if present.

Gravity wind

(Also called *drainage wind*.) A wind resulting from cold air running or flowing down a slope, caused by greater air density near the slope than at the same altitude some distance horizontally from the slope.

Generally used when cold air is locally generated by a chilled slope surface during periods of weak synoptic or other larger-scale winds, as with *katabatic* or *drainage* winds. Slopes can be gentle as found over rolling topography or into river valleys, or steep as on mountains or mountain ranges. Although usually applied to smaller (individual slope) scale flows, the term is occasionally used to include fall winds, or air advected from a cold source region elsewhere, then spilling over and accelerating down a slope, as with a bora or a cold front passage over orography.

See *downslope wind*.

Density current

The intrusion of a denser fluid beneath a lighter fluid, due mainly to the hydrostatic forces arising from gravity and the density differences.

This term is used principally in engineering for such cases as the intrusion of saltwater below freshwater in an estuary, or for currents caused by the presence of denser water with suspended silt at the bottom of a lake or ocean. Many of the phenomena are quite analogous to some of those associated with cold fronts in the atmosphere.

Gravity flow

1. In general, water flow in which gravitational forces predominate.
2. In glaciology, glacial movement in which ice flow results from the downslope component of gravitational force.

Fall wind

A wind that accelerates as it moves downslope because of its low temperature and greater density.

A fall wind is a larger-scale phenomenon than the individual-slope scale and is produced by accumulated cold air spilling down a slope or over a mountain range. The cold air often either accumulates on a plateau or other elevated terrain, or is part of an extensive cold air mass approaching a mountain range as a cold front. Fall winds may have a hydraulic character similar to water flowing over a dam, and one of the details of this flow is that the acceleration of the cold air begins to occur before the crest of the mountain range and therefore before the down-sloping portion of the topography. Fall winds are especially well developed as strong easterly winds on the coast of Norway, and for some distance inland; here they give a narrow strip of fine weather along the shore. They are also well developed on the northern coast of the Aegean Sea. At the southeastern tip of rocky Hagion Oros Peninsula in Greece, Mt. Athos rises to 2033 m and descends steeply to the sea; northerly winds are disturbed by this great mass and descend as the cold northeasterly Athos fall wind, often of gale force, extending several kilometers out to sea. In the Antarctic fall winds off the inland ice form violent blizzards. Other examples of fall winds are the *mistral*, papagayo, and vardar. Some authors have generalized this term to refer to downslope winds forced by large meso- and synoptic-scale processes (i.e., scales larger than that of an individual slope), even if they do not represent flows of colder air. Thus, under this nonstandard definition, the *foehn* and chinook could be considered fall winds.

Smith, R. B. 1987. Aerial observations of the Yugoslavian bora. *J. Atmos. Sci.* 44. 269-297.

Mistral

A north wind that blows down the Rhone valley south of Valence, France, and into the Gulf of Lions.

It is strong, squally, cold, and dry, the combined result of the basic circulation, a fall wind, and jet-effect wind. It blows from the north or northwest in the Rhône Delta, where it is strongest, from west to northwest in Provence. A general mistral usually begins with the development of a depression over the Tyrrhenian Sea or Gulf of Genoa with an anticyclone advancing from the Azores to central France. It often exceeds 27 m s^{-1} and reaches 38 m s^{-1} in the lower Rhône valley and 22 m s^{-1} at Marseille, decreasing both east and west and out to sea. It remains strong to a height of 2-3 km. In the absence of a strong pressure gradient, a weaker *katabatic* local mistral develops in the Rhône valley. A general mistral usually lasts for several days, sometimes with short lulls. It is most violent in winter and spring, and may do considerable damage. Market gardens and orchards are protected from it by windbreaks, and rural houses are built with only a few openings on the side exposed to it. The mistral has a variety of local names: mangofango in Provence; sécaire, maistrau, maistre, or magistral in Cévennes; dramundan in Perpignan; cierz in Spain; cers in the Pyrenees, etc. South of Mont Ventoux a similar wind is named bise. A local west wind of mistral type that descends from Mt. Canigou to the plains of Roussillon is called canigonenc.

Defant, F. 1951. *Compendium of Meteorology*. p. 670.

Foehn wind

(Or föhn.) A warm, dry, *downslope wind* descending the lee side of the Alps as a result of synoptic-scale, cross-barrier flow over the mountain range.

Bora

A fall wind with a source so cold that, when the air reaches the lowlands or coast, the dynamic warming is insufficient to raise the air temperature to the normal level for the region; hence it appears as a cold wind.

Appendix B

Background for Chapter 6

This Appendix consists out of two sections. The first section is dedicated to the IOP descriptions. The second part contains the figures as a back-up.

B.1 IOP descriptions

Here descriptions are given for each IOP. We base ourselves on a combination of the previous findings from Sects. 6.3.2 to 6.3.4.5. Additionally, results were checked from meteograms and atmospheric profiles (see Appendix B.2 for the background figures). When important, other variables will be detailed as the combination with other criteria is needed to check whether the model has detected clouds, snow, rain, etc. correctly.

Note that this section is background information only. The most important information is given in normal font size in the first sentences after the IOP number, then a description of the IOP observations and simulations follows in smaller font size. It is primarily background information for the IOP selected to test the model on DDV wind sensitivity, whose results were shown in Sect. 6.2.2. The IOP dates can be found in Table 2.2.

IOP 1: We do not consider this IOP for further investigation on DDV wind development.

IOP with a short period of DDV wind observations before a precipitation event came in, which was missed in the simulations. Clouds are missing in the model. Wind directions are poorly simulated (Fig. 6.26).

IOP 2: This IOP was dominated by a strong Mistral event, thus no DDV wind was observed (Fig. 6.27). It will therefore not be considered for DDV wind development.

However, *DACC* shows the highest values of all IOPs (Fig. 6.26). Strong synoptic forcing leads to good modeling results regarding wind direction. A confirmation of a good modeling skill is comforting, even though this type of event is not the goal of this study. It further can give more information on the model behavior. The model slightly underestimates wind speed for most heights available (Fig. 6.25). Atmospheric radiation, notably SW^\uparrow and SW^\downarrow , have the lowest errors (Fig. 6.19). Low errors for SW -components in Mistral conditions mean that solar insolation is well captured for clear skies. u^* is underestimated to a large extent, which is due to the fact that wind speeds are underestimated at the surface. It leads to an underestimation of H . The 2 m minimum temperatures are underestimated (Fig. 6.21), as well as the mean temperature (Fig. 6.22), both acting in opposition to the behavior expected under stable boundary layer formation. It can be used however for other purposes as it points out the differences between stable nocturnal boundary layer formation and mixed BL formation.

IOP 3: IOP 3 is poorly modeled for wind direction in general and the DDV wind was not observed. It was therefore not selected for the sensitivity tests.

A rain event occurred in the second part of the IOP. Although clouds were observed, these are not simulated regarding the large biases for SW^\downarrow and LW^\downarrow from Figs. 6.19 and 6.20. The error for $L_v E$ is also high, but cannot be trusted because the gas analyzer LICOR 7500A is not proper for observations during precipitation.

IOP 4: This IOP was subjected to Mistral conditions in the beginning but in the second part of the night DDV wind started and was simulated properly. It was therefore selected for the sensitivity simulations. See Fig. B.1 for comparison with sodar observations.

This IOP shows a large bias for SW^\downarrow , coming from observed clouds which have not been modeled. The absence of clouds in the model is also reflected in the error on LW^\downarrow , which is underestimated in the model (e.g. IOP 2 and 16). The clouds were observed in the afternoon at the start of the IOP, therefore a mismatch may not be the biggest problem for proper SBL formation. Nevertheless, other fluxes do not show high discrepancies between model and observations. The DDV wind is simulated properly. Note that the DDV wind here extends up to 600 m agl, and so is not restricted to the DV depth only (200 m deep at the observation site).

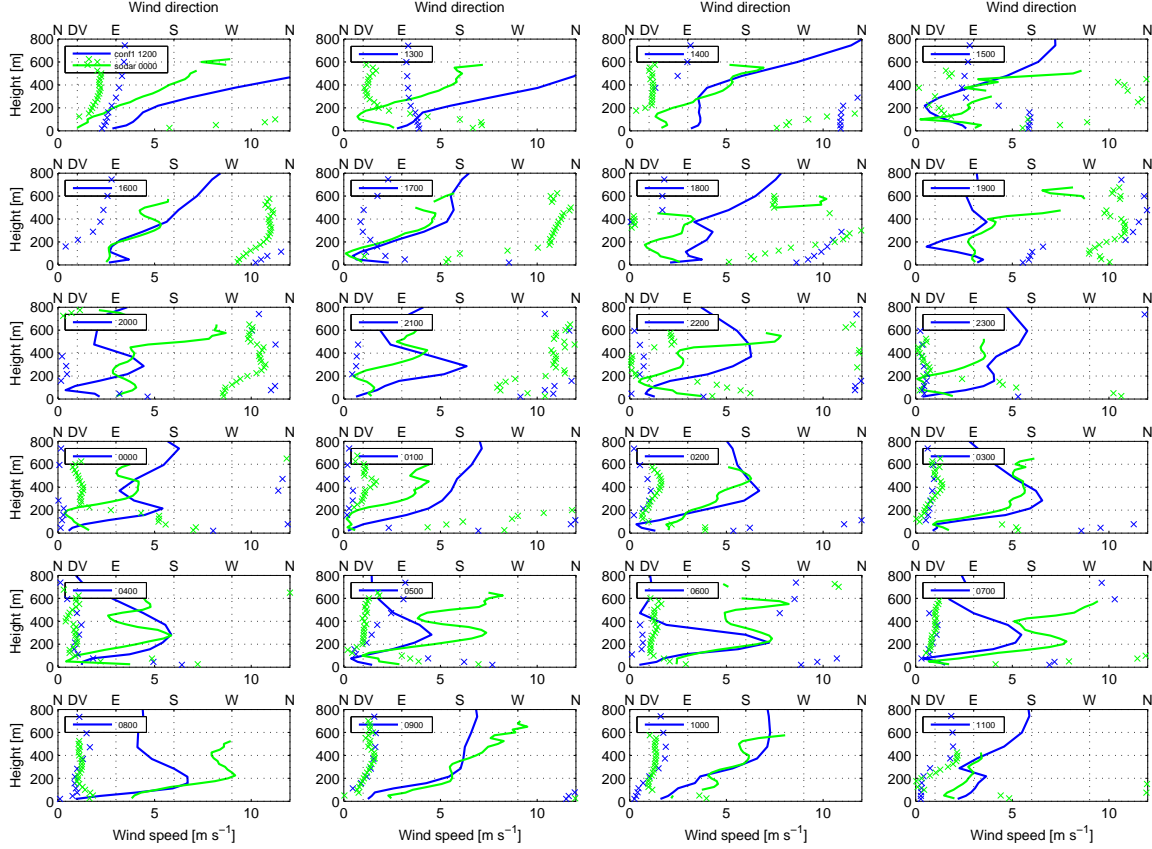


Figure B.1: Comparison for wind speed (lines) and wind direction (crosses) between Sodar observations (green) and simulations (blue) at the VER site during IOP 4; the times (in UTC) are indicated in each box.

IOP 5: This IOP was subjected to light Mistral wind all along the IOP and was therefore not interesting to simulate the DDV wind.

This IOP has been treated to a large extent in Chap. 4 to point out the difference between an IOP recognized as representative regarding observations (IOP 21) and one which had no representative behavior (IOP 5). It was subjected to light Mistral, with winds around the northerly direction in the DV itself. Above the DV depth, the DDV wind directions are observed and simulated. Errors for atmospheric fluxes are considerably small, as is also the case for 2 m humidity.

IOP 6: A DDV wind is observed and simulated. So it was considered for the DDV wind sensitivity study.

The IOP 6 started under Mistral conditions, winds at GBA were observed up to 14 m s^{-1} and were underestimated at this height. H and u^* are simulated with relatively large errors. The Mistral lasted until midnight after which the wind turned to the DDV direction up to 600 m; this wind shift was 3 hours too early in the model. So for this IOP the high winds in the afternoon are underestimated, but the DDV wind is ultimately obtained by the model.

IOP 7: IOP with a DDV wind up to 300 m in observations and simulations. It was considered for the DDV wind sensitivity study.

This IOP has very good performance for the general wind direction of more than 80% at the 150, 200, 275 and 350 m layer (Fig. 6.26). Also above the DV depth a DDV wind is observed and simulated, although the score is less high. At the GBA location and height of 110 m the model performs quite well. The errors for wind speed at all heights (Fig. 6.25) are relatively low. Up to 150 m the wind is slightly overestimated, whereas above this height it is underestimated. The underestimation of wind speed above the DV depth is peculiar, as this wind is usually overestimated for other IOPs. So for wind alone this seems a very good IOP. The atmospheric fluxes are relatively well simulated regarding the mean error for all IOPs, except for SW^\downarrow . Scattered clouds were observed at the beginning of the IOP (i.e. the afternoon), which mainly contribute to the error. However, it does not have a big influence on the results for the DDV wind development. One issue arises regarding the humidity at the regional stations network (Fig. 6.23), IOP 7 shows the largest overestimations for all

stations. However, the onset of the DDV wind is correctly timed, and a jet development is obtained along the night in the model and observations. The fact that this IOP has been initiated with a spin up time during Mistral conditions from IOP 6 might positively influence the results.

IOP 8: Not relevant for DDV wind development research.

Dominated by westerly winds, no DDV wind development. Atmospheric fluxes are considerably small.

IOP 9: The model is not capable to simulate the DDV wind, which is only observed very shortly due to a Mistral wind. We do not consider this IOP for further investigation.

A heavy Mistral dominated this IOP until midnight. The observations of the DDV wind in Fig. 6.27 are obtained after sunrise (Sodar, not shown). The errors are found for atmospheric fluxes are identical to those of IOP 2.

IOP 10: DDV wind simulated but not observed. It was treated for the DDV wind sensitivity test.

Cloudless IOP dominated by westerly winds, very stable conditions are measured at the M30 site. Overall wind directions are not modeled to a good extent, at all heights $DACC$ and $DACC_{DDV}$ values are lower than average (Figs. 6.26 and 6.27). Fluxes are modeled to a good extent. Although DDV wind is not observed, it is simulated with winds up to 400 m depth in DDV direction. This is not revealed by Fig. 6.27, as this direction was lacking in observations.

IOP 11: DDV wind are observed up to the DV depth and some of them are modeled (Fig. 6.27). It was therefore used for the DDV wind sensitivity test.

For the general wind direction ($DACC$), the IOP scores around the mean, i.e. 40-60%. A proper comparison with fluxes is impossible due to a rain event just before the start of the IOP. Clouds were observed during the IOP, but not simulated. Although for a short amount of time, the DDV wind has been both observed and simulated. To discover the DDV wind origin, this IOP can be used.

IOP 12: Considering the very scarce amount of DDV wind observations, the model performs quite well. However, this IOP was not chosen because in the simulations the DDV wind only showed up late after sunset for a very short amount of time.

The $DACC$ wind directions are a bit higher than average at every height. Errors on wind speeds are also of the same order as the mean of observations for each height, with low biases. For the fluxes this IOP scores the worst concerning L_vE . The IOP had a windy start, which was not present in the simulation and leads to negative biases for u^* , as seen in IOP 2, 6 and 9. This is one of the reasons why H is underestimated as well.

IOP 13: The DDV wind was present in observations up to 500 m agl. It has been simulated to a good extent, and therefore was used for the DDV wind sensitivity test.

The best correspondences with the model are found at the DV depth. Higher up in the profile, the representation for the DDV direction is less good. Considering all wind directions ($DACC$) the same pattern can be observed: highest occurrences up to DV depth, above the valley the correspondences with observations are less good. The radio-soundings show that we are dealing with a northerly synoptic forcing (not shown), but under relatively low wind speeds (less than 10 m s^{-1} at 2 km height). In both observations and simulations a strong LLJ is found in the DDV direction. The IOP started with a light Mistral, which was well captured (not shown), nevertheless wind speeds are underestimated. Note that this underestimation comes mainly from the early morning profiles. The wind speeds in observations had increased to around 12 m s^{-1} in the DDV direction, which leads to the suspicion that the DDV wind was synoptically forced.

IOP 14: Clearly shows a DDV wind in simulations, but this is not visible in $DACC_{DDV}$ due to the lack of any DDV wind in the observations. The $DACC$ is also very low for this IOP. However, this IOP was taken into consideration for the DDV wind sensitivity tests.

IOP 15: High scores for $DACC_{DDV}$ are found for the layers within the DV. The IOP was considered for the DDV wind sensitivity test.

Concerning all wind directions (Fig. 6.26), this IOP shows the best scores up to 350 m. By means of the Sodar the DDV wind has been observed well above the DDV depth, the model shows features typical of flow channeling, i.e. wind directions above the DV depart by less than 90° from the DDV direction. Wind speeds are overestimated, more than the average. Also for this IOP clouds were present in the observations, but not in the model, leading to higher biases than average for SW^\downarrow and LW^\downarrow . Big outliers are found for L_vE . Temperatures are underestimated.

IOP 16: The reference set-up was focused on this IOP. Although the DDV wind occurrence was scarce in the early morning, the model simulations captured it extremely well.

The set-up of the model was focused on the processes occurring during this very calm and clear sky IOP. It has been investigated thoroughly in Sect. 3.3.1. Surprisingly it shows high scores for $DACC_{DDV}$ concerning the minimal number of observations in the DDV direction. The combination with the fact that $DACC$ is very high for this IOP, especially at the heights with high $DACC_{DDV}$ implies that the high score for the latter is not a coincidence. The timing of the DDV wind onset is very good. Wind speeds are also very well estimated. Relatively small errors are found for the fluxes. Overall, the IOP is very well simulated.

IOP 17: Only interesting from an observational point of view as DDV winds occur regularly. The model behaves very poorly for overall wind direction and was therefore not considered.

For this IOP the DDV wind is completely missed by the model. For $DACC_{DDV}$ and $DACC$ the model behaves very poorly, only at GBA at 110 m we see some simulated DDV wind. In the model, winds above the DV are southeasterly throughout the night, whereas this has been observed for only a short amount of time. Wind speeds are overestimated for all layers. Fluxes are modeled to a good extent.

IOP 18: This IOP is interesting from an observational point of view for DDV wind study. However, with high wind speed overestimations it is poorly simulated and so was not further considered for the DDV wind investigation.

DDV wind to DV depth, observed and simulated. A typical case for observing the development of a DDV wind during the second part of the night. It is however poorly simulated: this IOP scores poorly for all layers for $DACC$. Wind speeds are overestimated to a large extent. The longwave radiative fluxes indicate that clouds are missed, there was radiation fog which developed in the early morning and was not simulated. Nevertheless a good example of DDV wind channeling.

IOP 19: Shows a proper DDV wind development in both observations and modeling. It was retained for the DDV wind sensitivity study, but it should be remarked that simulations were far from observations due to a snow layer which was not incorporated in the model.

This IOP was conducted after a snow event two days earlier. The snow layer of around 10 cm persisted and affected all measurements of this IOP. The snow layer was not present in the model, and therefore SW^\uparrow is largely underestimated. Nevertheless, a DDV wind has been observed and simulated. Relatively to the average of all IOPs, the overall wind direction is poorly modeled. Besides, larger biases on wind speed are found, with overestimations of wind speeds in every layer. A 'positive' consequence of the snow layer is the fact that the error and bias of LW^\uparrow is decreased to a minimum. The temperatures simulated show the largest errors of all IOPs. So, DDV wind directions are simulated to a considerable agreement with observations, but the model behaves poorly on other properties.

IOP 20: DDV wind observed on the full vertical up to 600 m, but in simulations only up to DDV depth. This IOP was retained for the sensitivity tests.

Most of the snow layer has disappeared and therefore simulations are closer to observations. An IOP with a high number of occurrences for the DDV wind direction; throughout the vertical profile in observations, but in the model up to the DV depth only. Above 400 m, the direction was easterly, in coherence with the synoptic flow. Wind speeds are overestimated, but with errors less than the mean.

IOP 21: This IOP has been considered as one with good DDV wind development and has been studied by means of observations in detail (Chap. 4). Relatively to the mean of all IOPs, we can consider this IOP as rather well simulated. It was therefore considered for the sensitivity test.

The DDV wind exists up to the DV depth for both observations and simulations although $DACC_{DDV}$ is not that high. Nevertheless, $DACC$ is quite high relative to the mean. Wind speeds are slightly underestimated, although the error is small, also relatively to other IOPs. Atmospheric fluxes are modeled to a good extent.

IOP 22: This IOP was not considered in model sensitivity study. Although it shows high values for $DACC_{DDV}$ and $DACC$, flow channeling was found to be the main mechanism. Wind speeds were very high in the model (e.g. $> 12 \text{ m s}^{-1}$ at 200 m).

High values for $DACC_{DDV}$ are found up to the DV depth, above the DDV wind is observed but not modeled. For all wind directions, the model scores highest for almost all layers, together with IOP 7. However, wind speeds are overestimated greatly, biggest errors are found for almost all layers especially at 600 m height. The fluxes indicate that clouds were observed but they were not modeled. Note that a rain event occurred in the early morning which was not simulated. This is together with IOP 23 the only IOP which underestimates humidity for all stations (Fig. 6.23). This IOP is not taken for the next step, because the simulated wind came at extremely high wind speed which does not match the observed DDV wind (Chap. 4). However, this can be a good candidate for flow channeling studies, as IOP 18 is.

IOP 23: DDV wind is both observed and simulated. The IOP was retained for the sensitivity tests.

The DDV wind is observed above the DV depth, however not in the model. For general wind direction the model scores poorly. Wind speeds are overestimated in the DV itself. The fluxes show again that clouds are not modeled leading to high errors in SW^\downarrow and LW^\downarrow . This is together with IOP 22 the only IOP which underestimates humidity for all stations (Fig. 6.23).

B.2 Figures

This section contains the figures serving as background information. Three types of figures are presented:

- 1 Meteograms containing observations and simulation output for Configuration 1 (see Sect. 6.2 for its definition). Every page contains two meteograms (Figs. B.2 to B.11). The first one is dedicated to the GBA 110 m observations and simulations (temperature, wind speed and direction), the second one contains the surface fluxes at the locations M30 (observations are from the CSAT and Li-COR at 30 m). IOP numbers are indicated at each figure.
- 2 The second set of figures (from Fig. B.12 to B.24) contains wind profiles from the Sodar compared with model output from the three configurations for the subset of 13 IOPs. IOP-numbers are indicated at the top of each graph.
- 3 The third set of figures (from Fig. B.25) contains profiles of potential temperature, humidity mixing ratio, wind speed and direction for the subset of 13 IOPs for observations and simulations in configuration 1 and 2. IOP-numbers are indicated at the top of each graph.

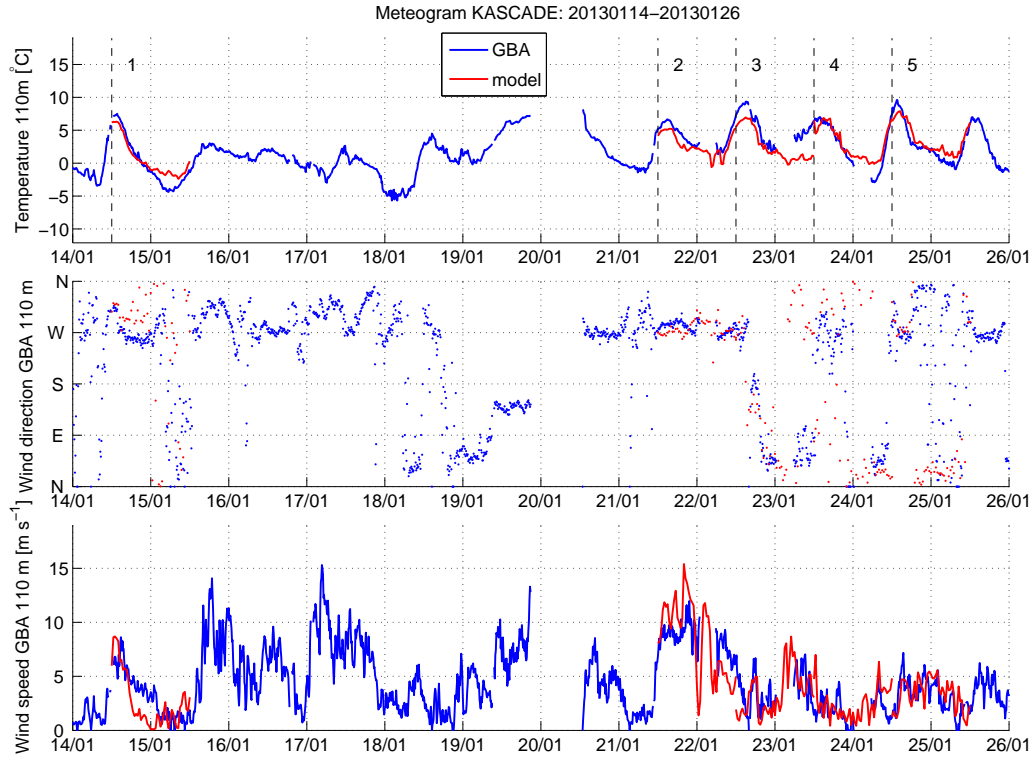


Figure B.2

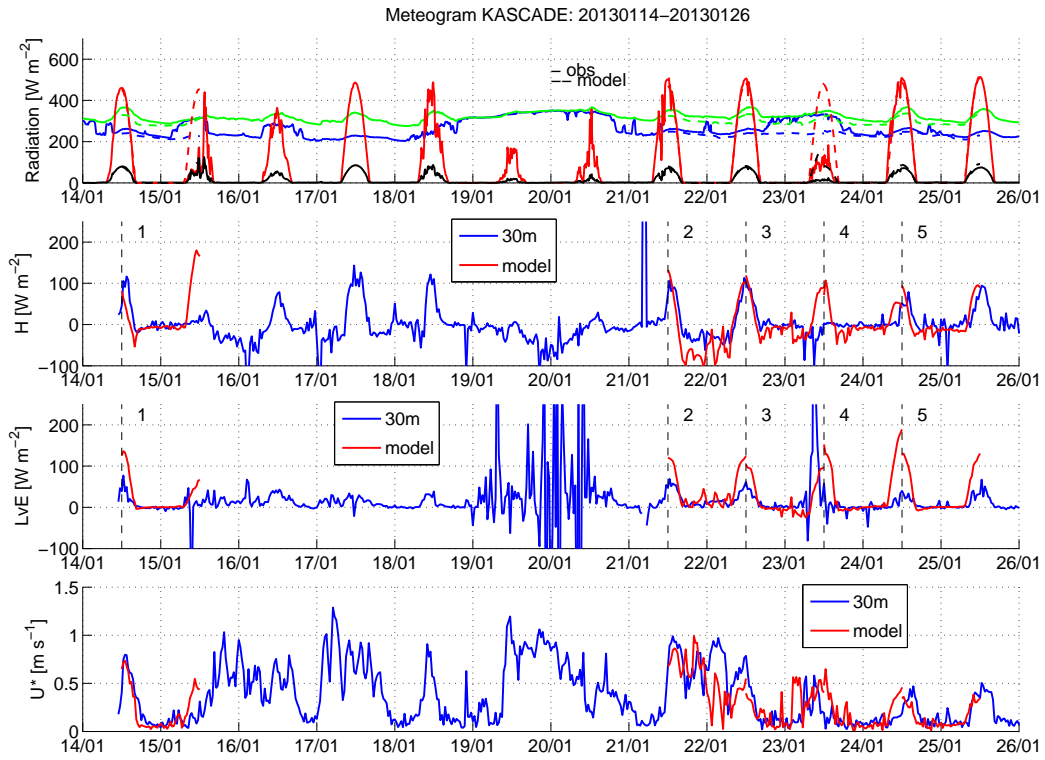


Figure B.3

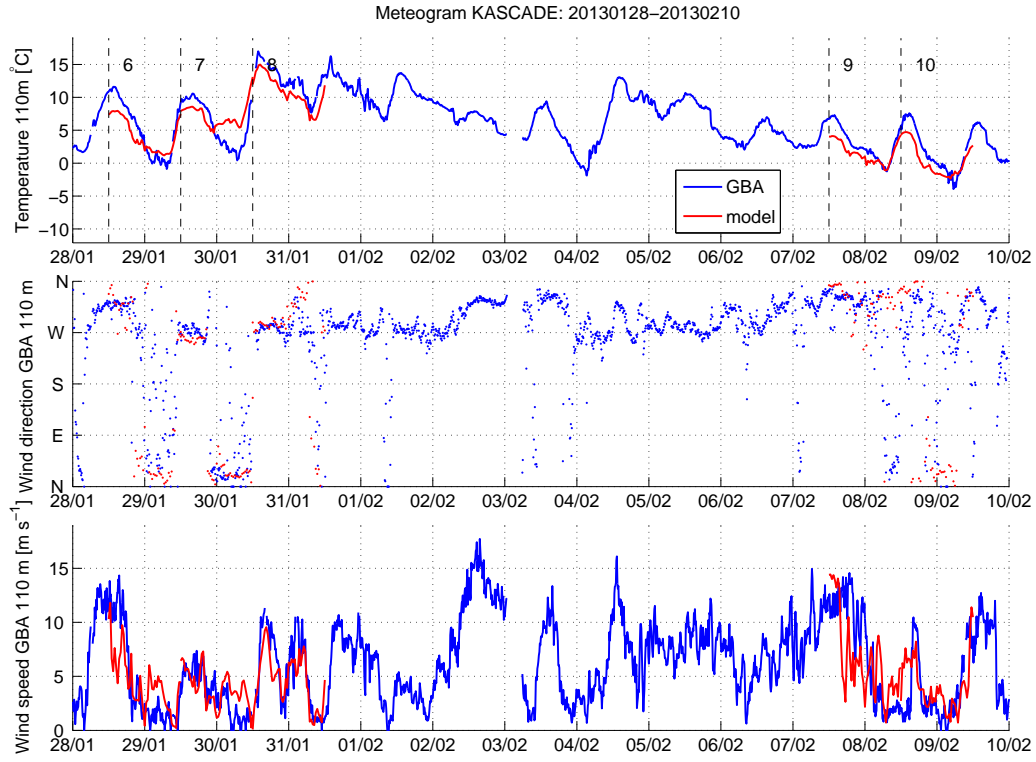


Figure B.4

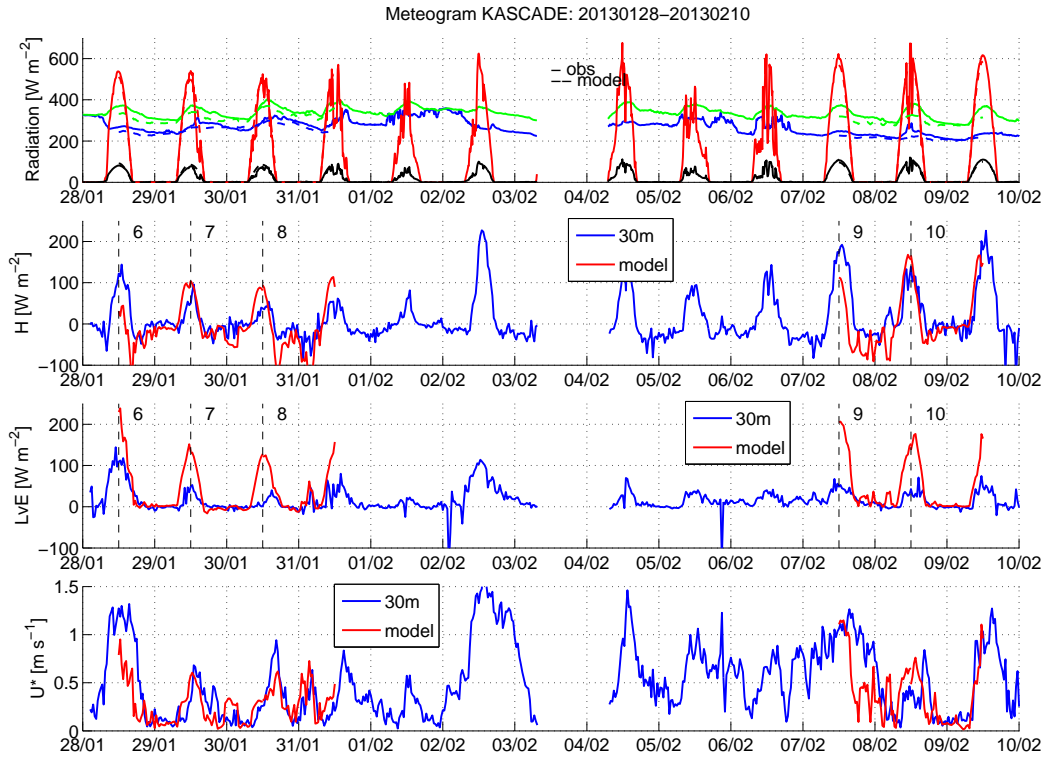


Figure B.5

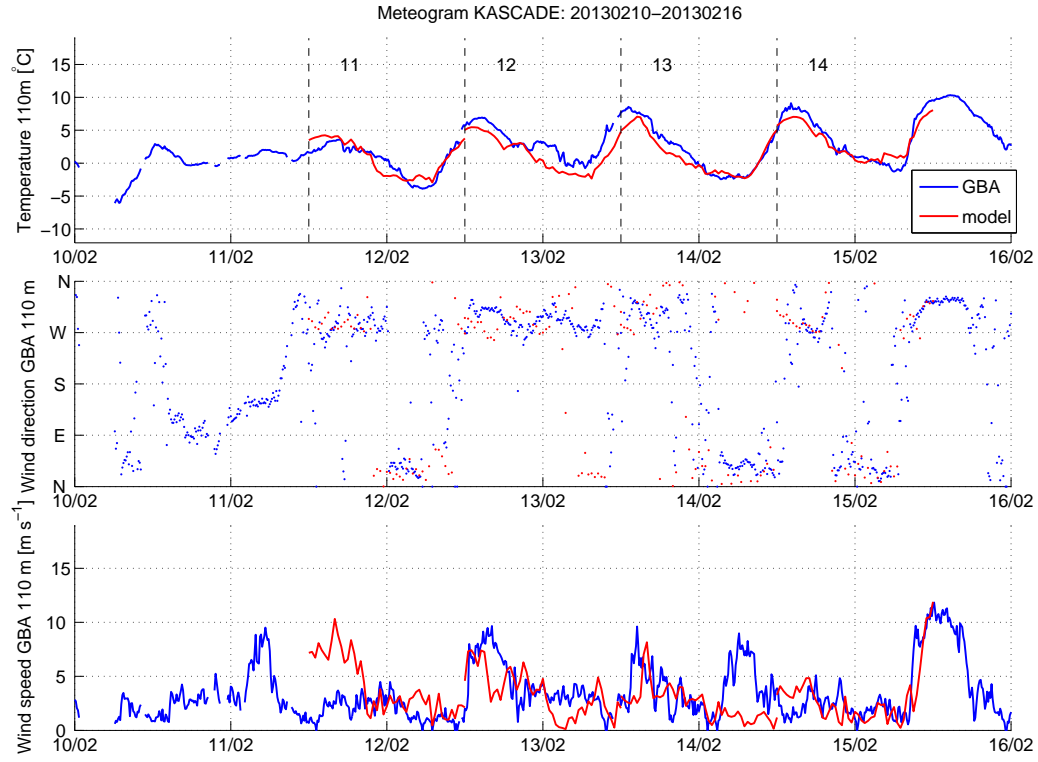


Figure B.6

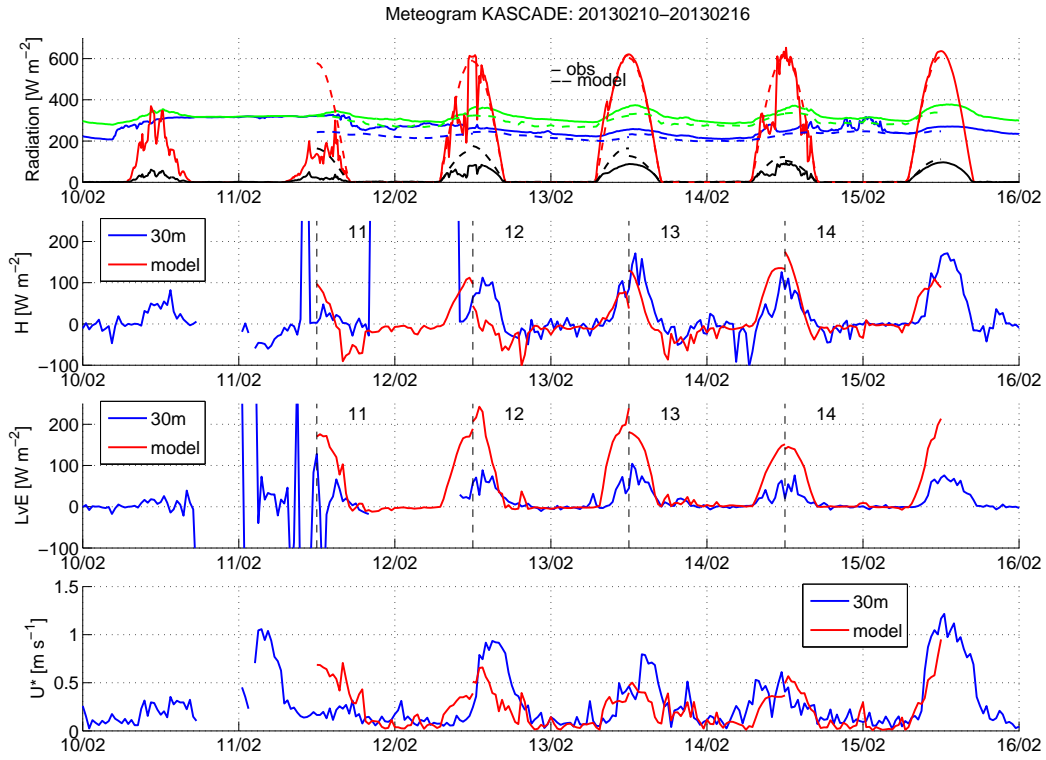


Figure B.7

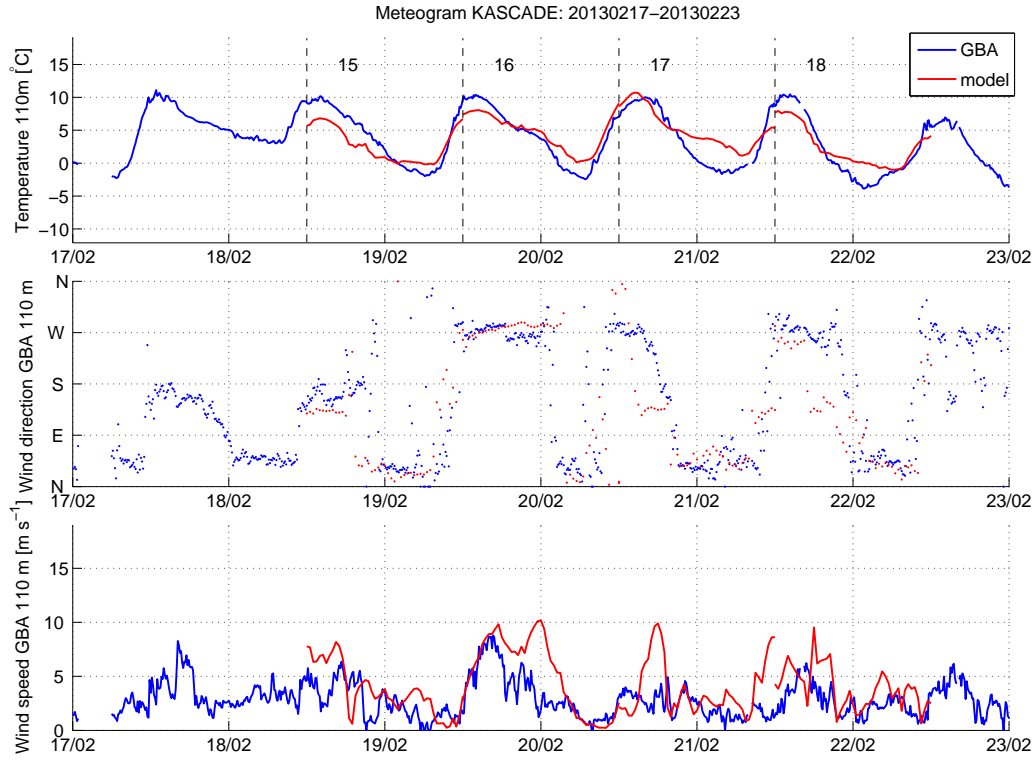


Figure B.8

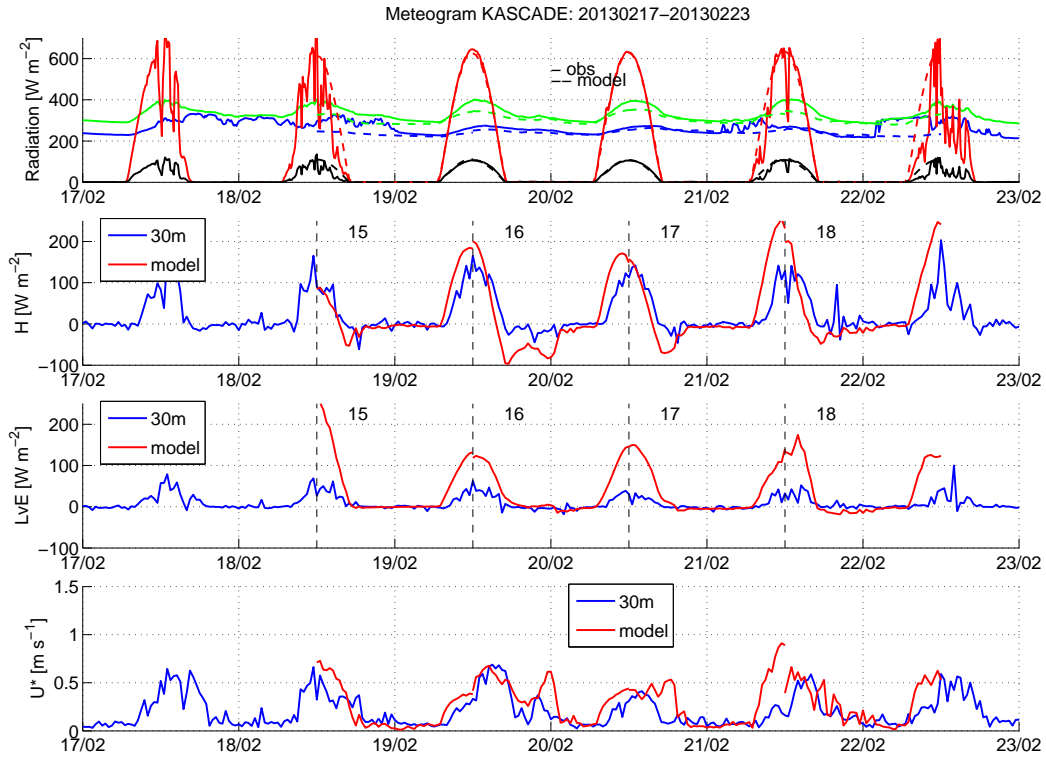


Figure B.9

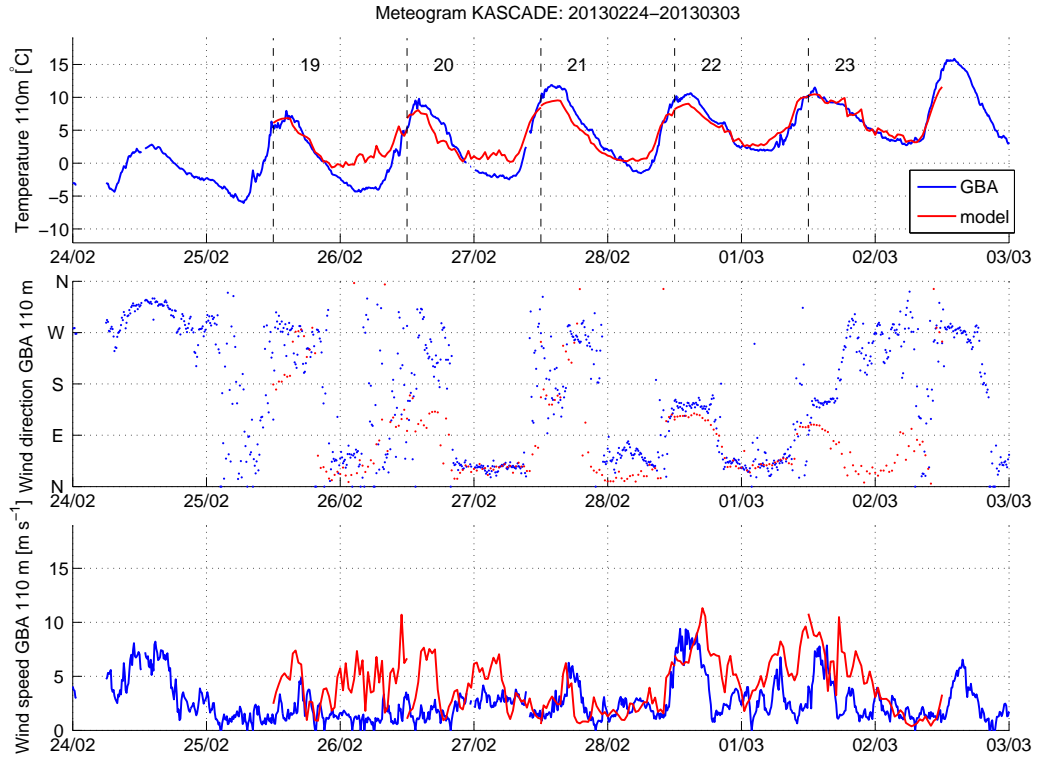


Figure B.10

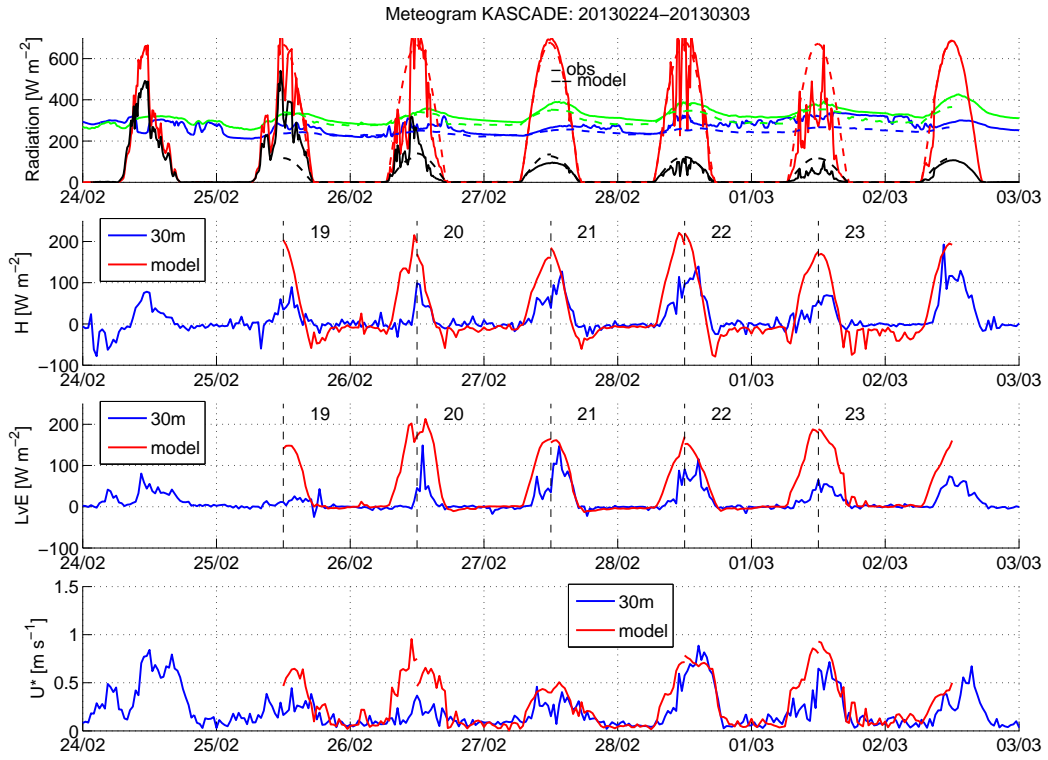


Figure B.11

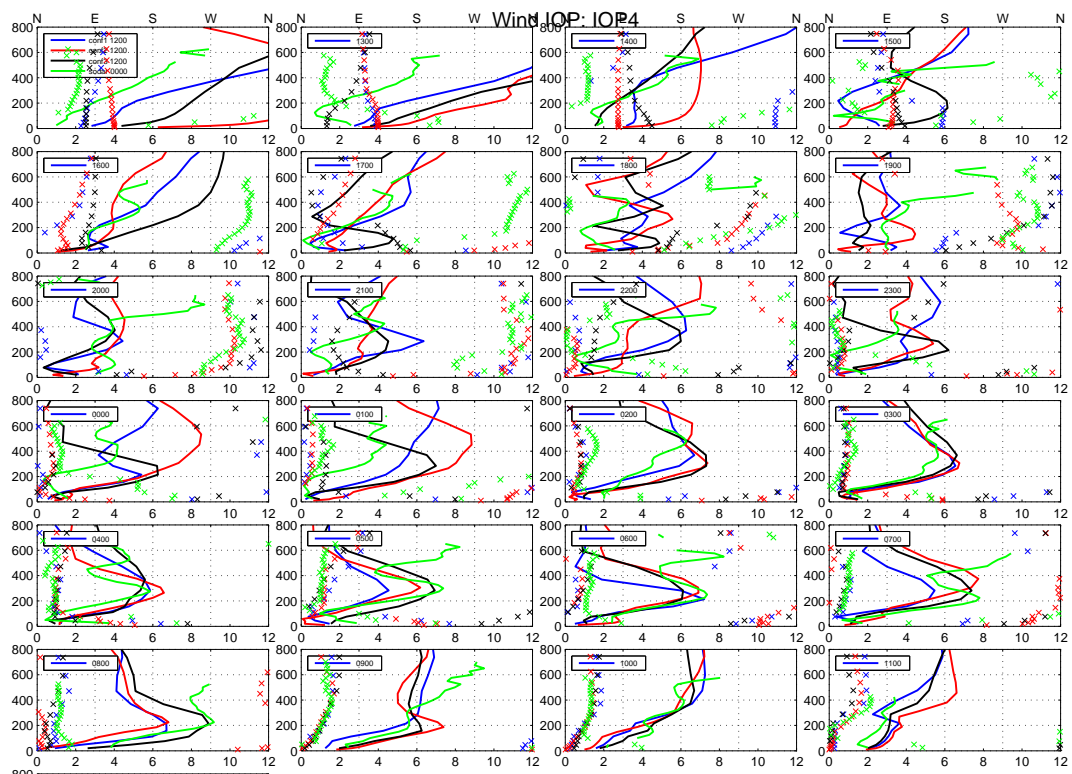


Figure B.12

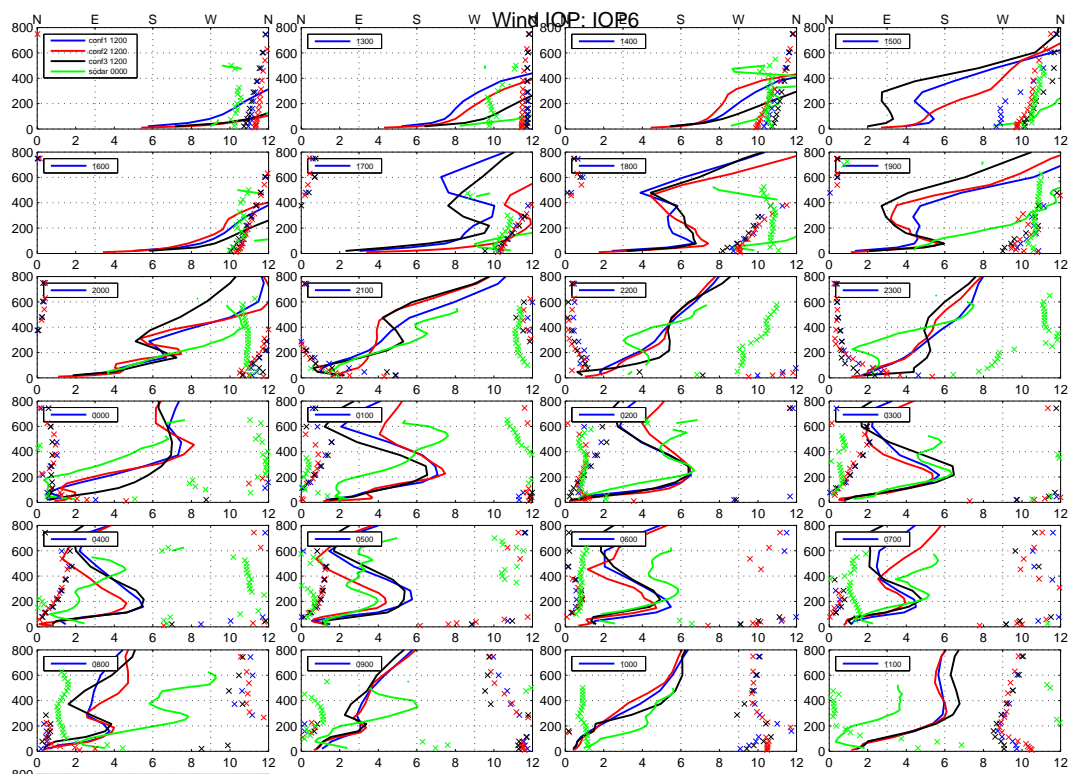


Figure B.13

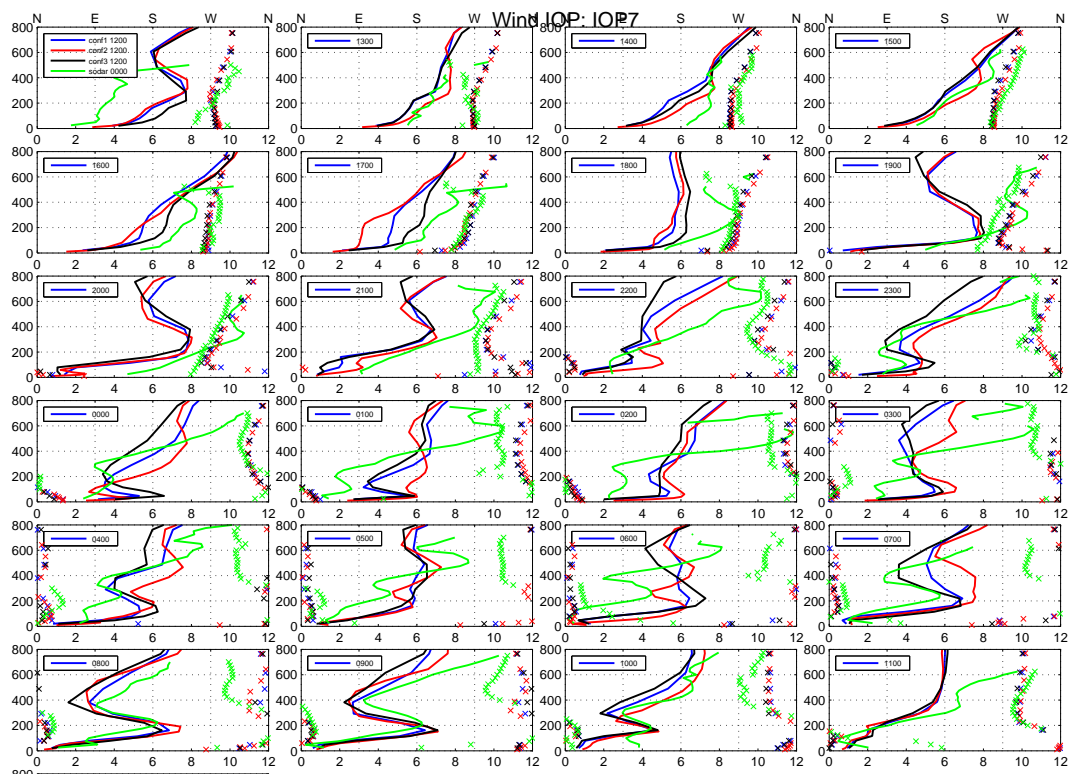


Figure B.14

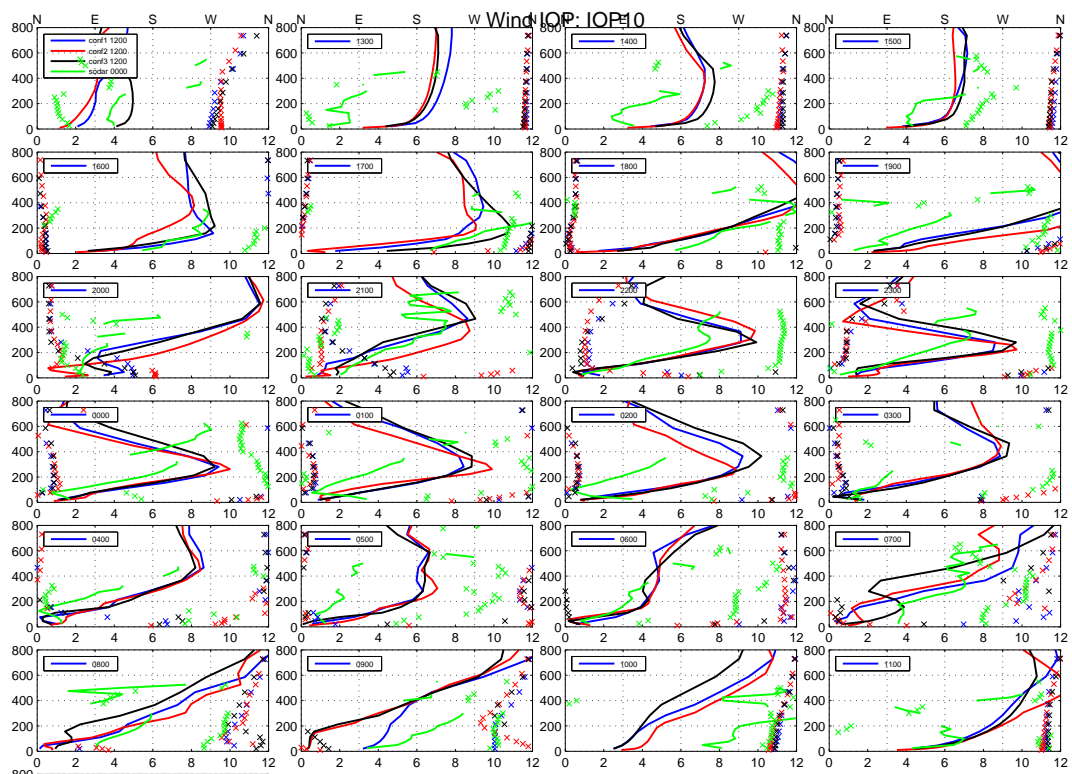


Figure B.15

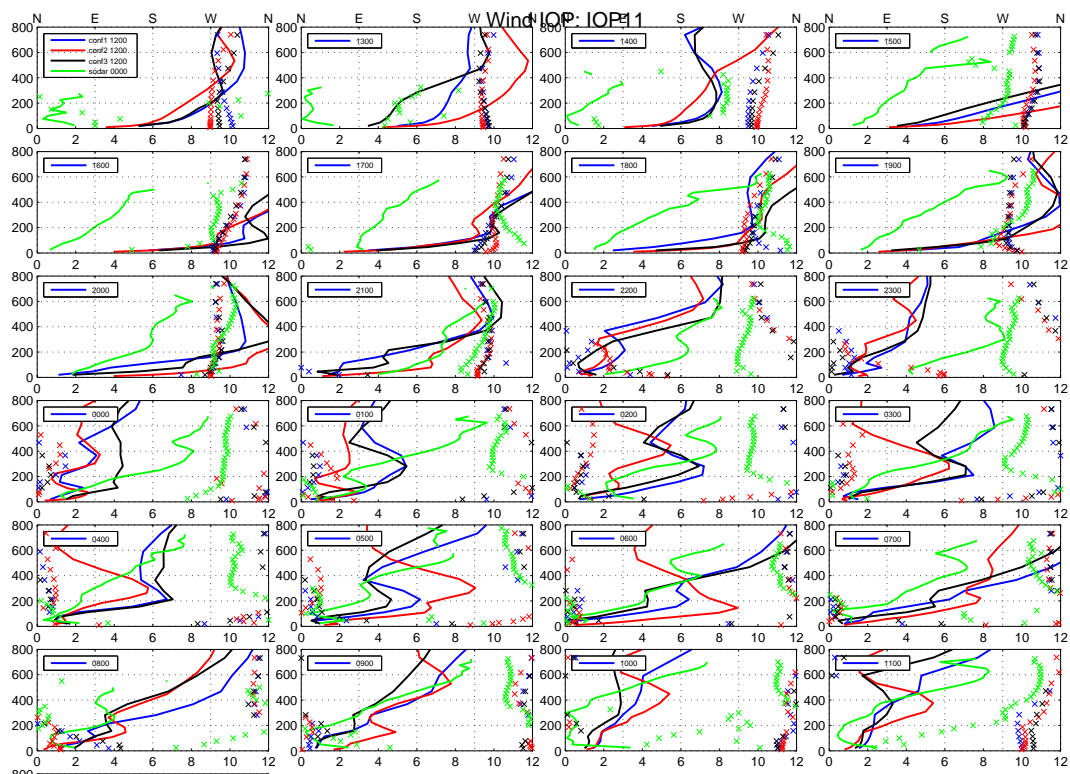


Figure B.16

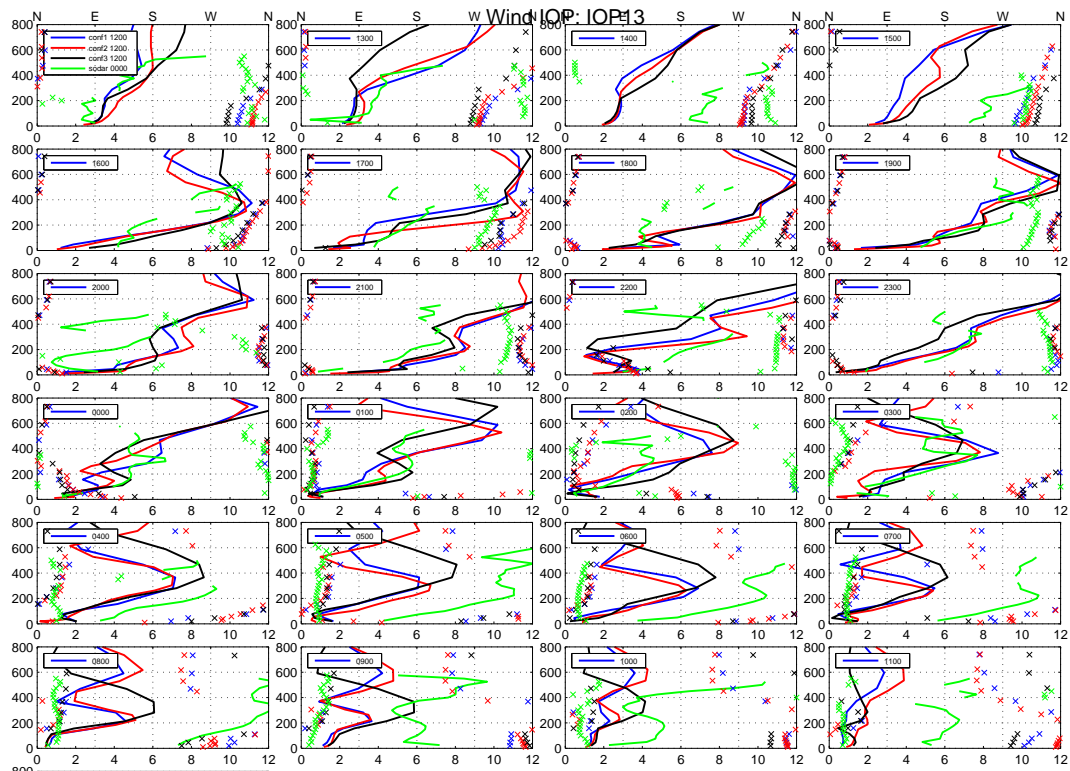


Figure B.17

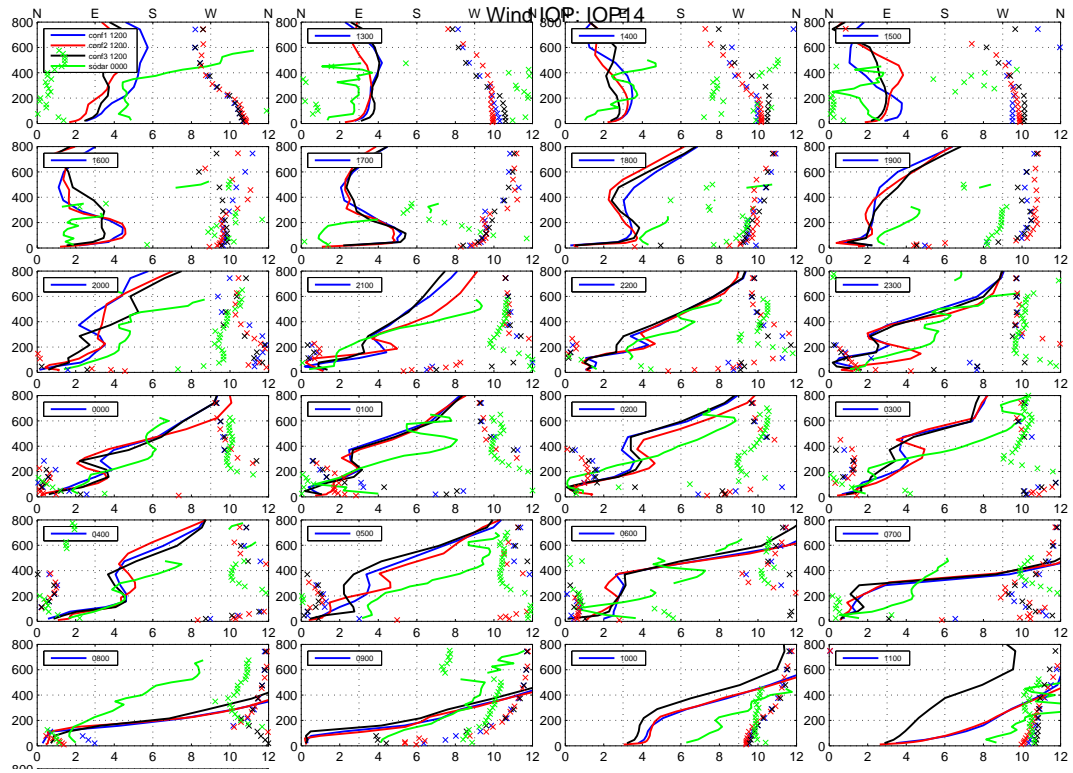


Figure B.18

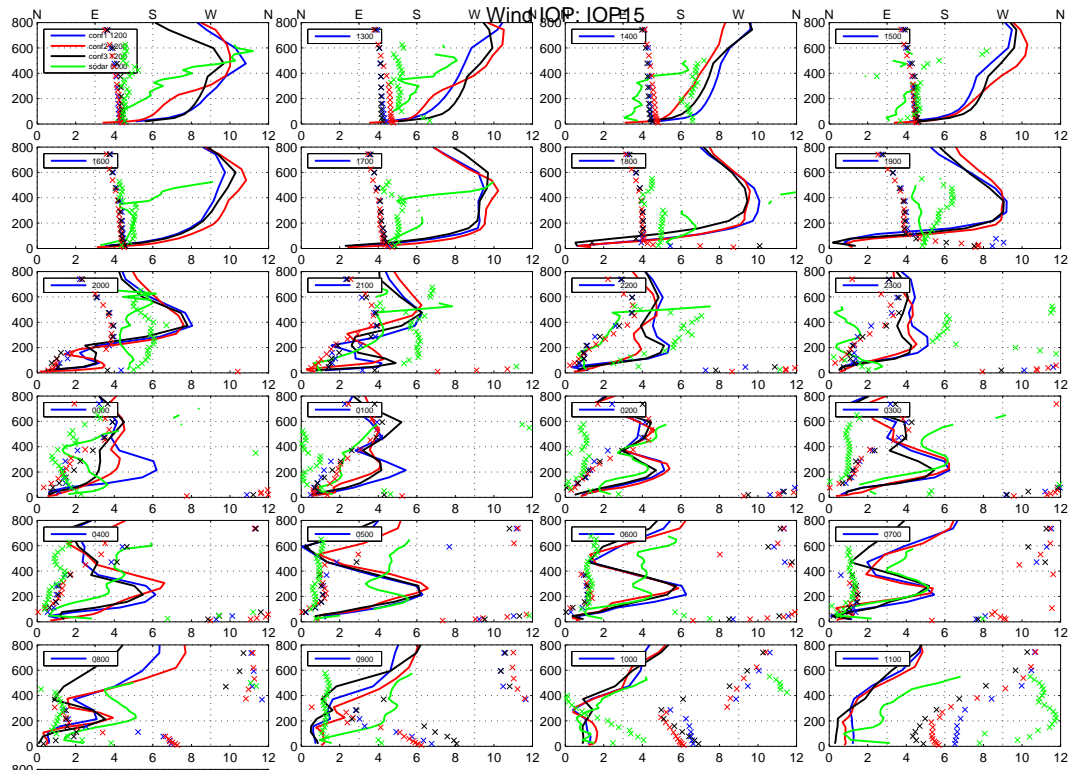


Figure B.19

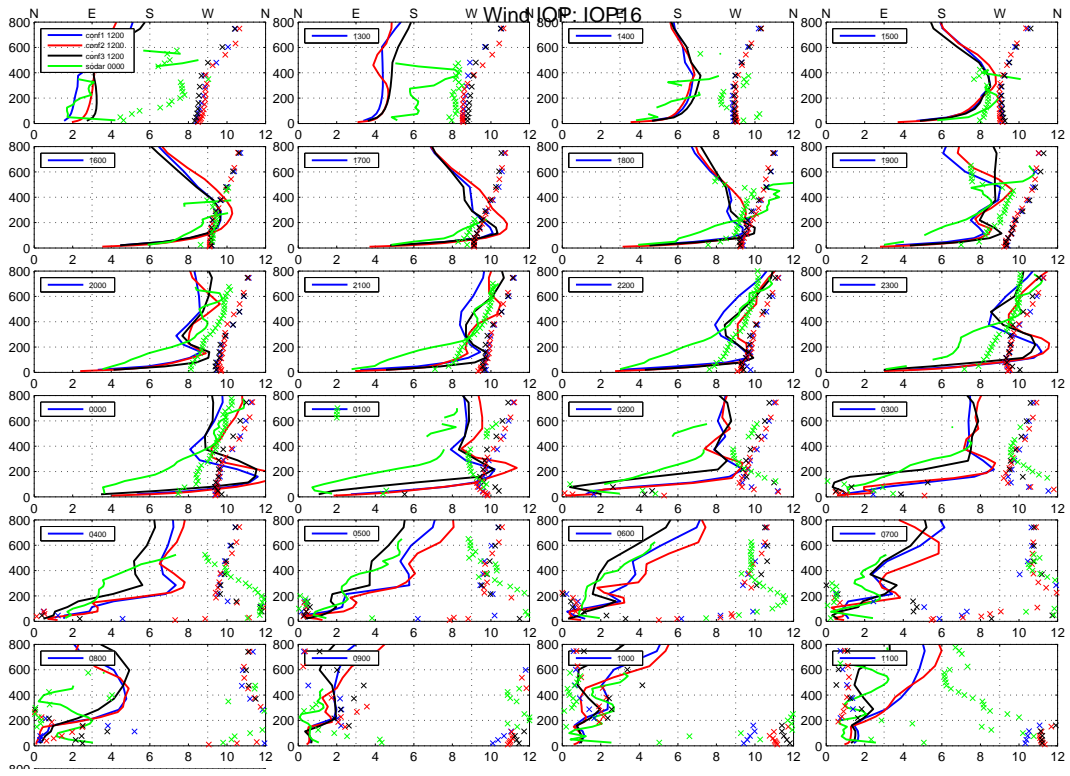


Figure B.20

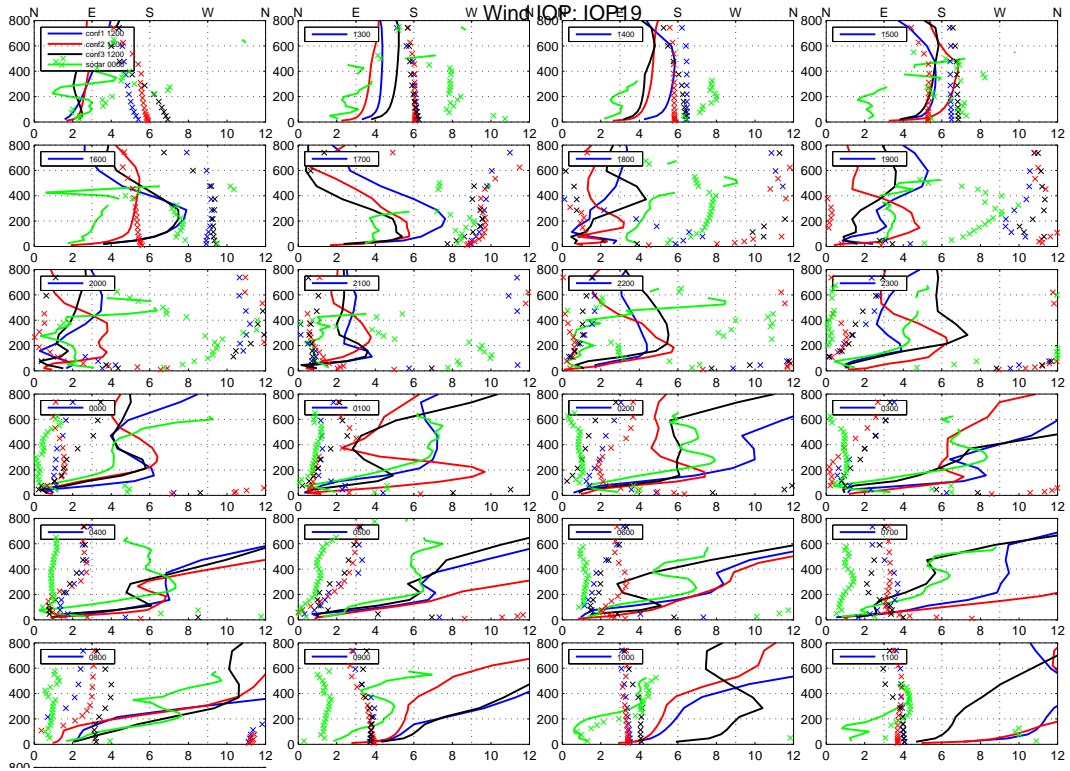


Figure B.21

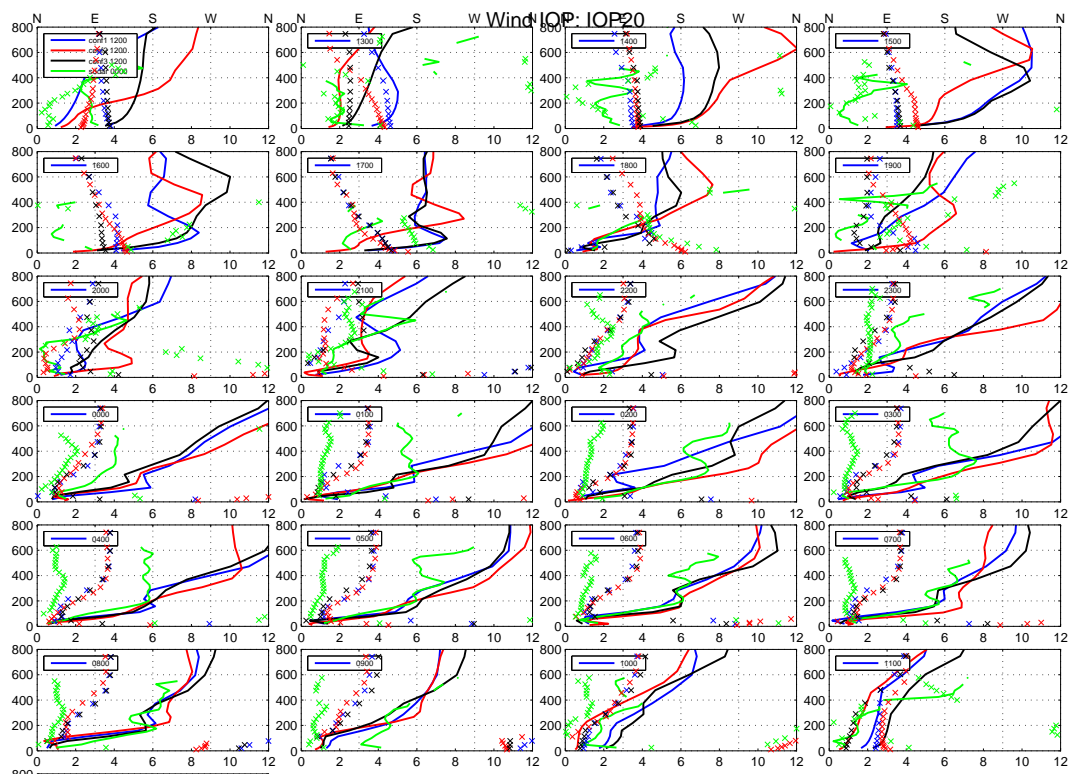


Figure B.22

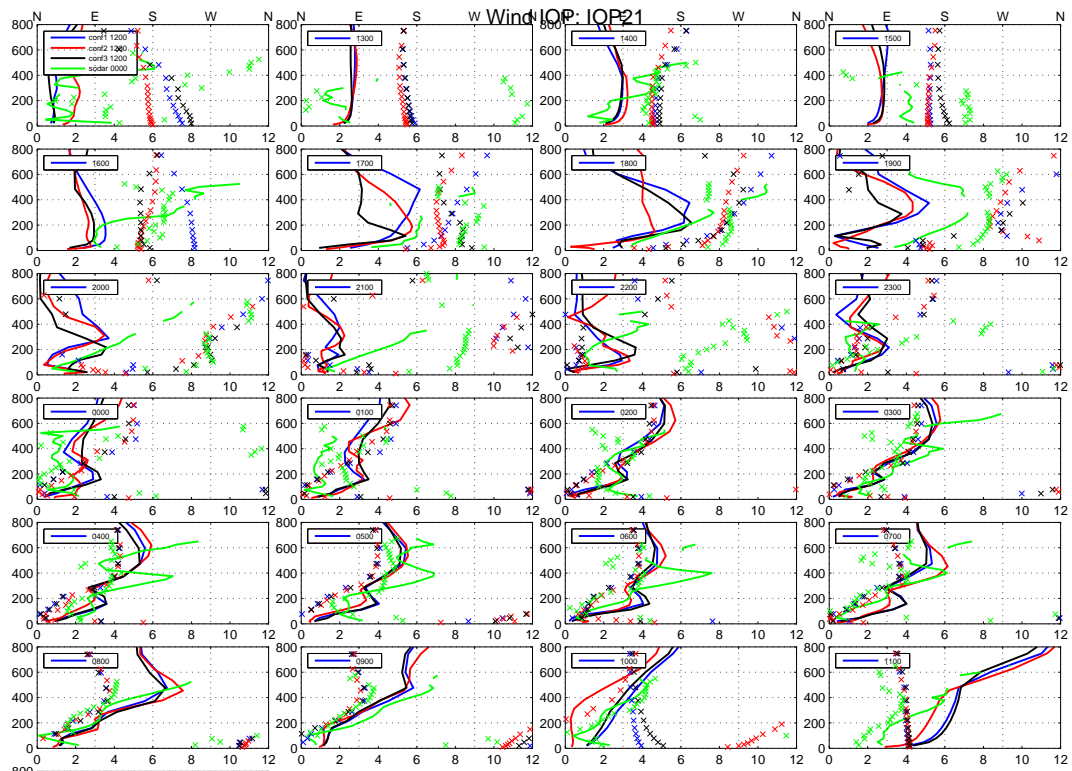


Figure B.23

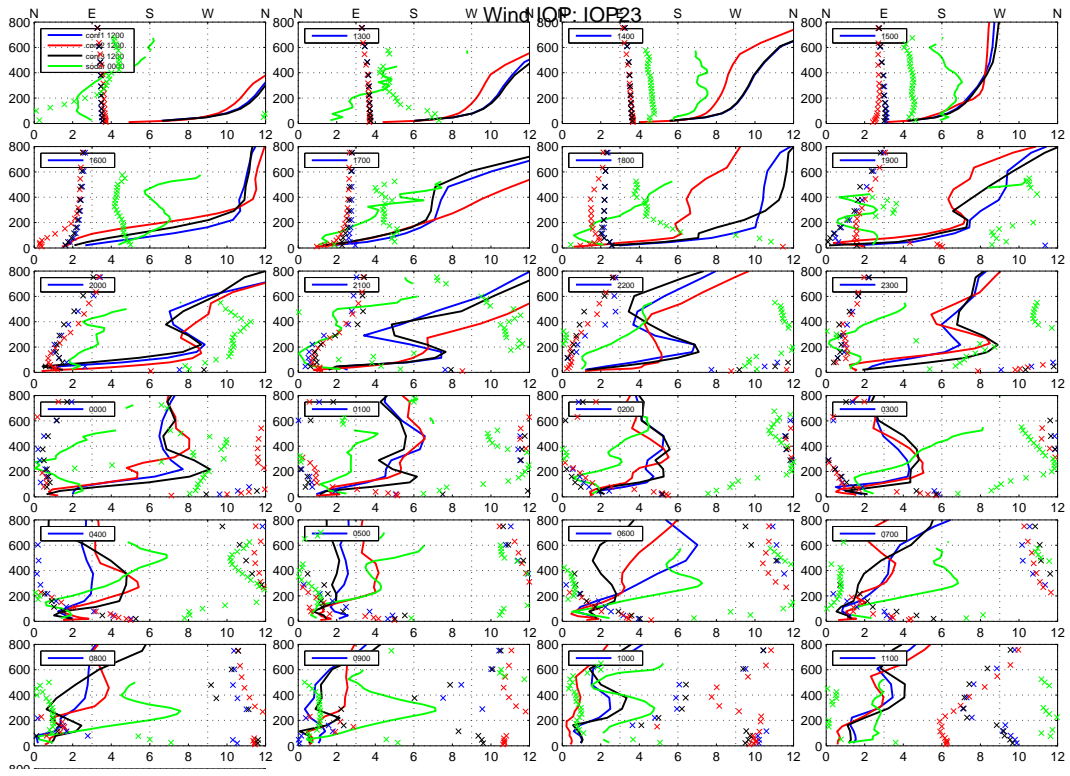


Figure B.24

IOP 4

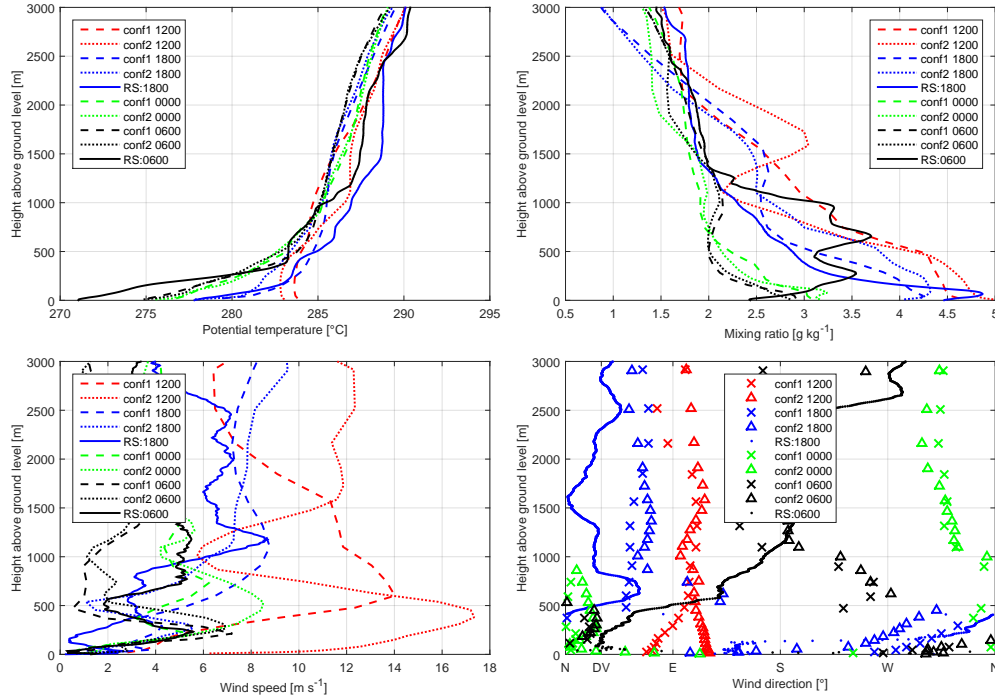


Figure B.25

IOP 6

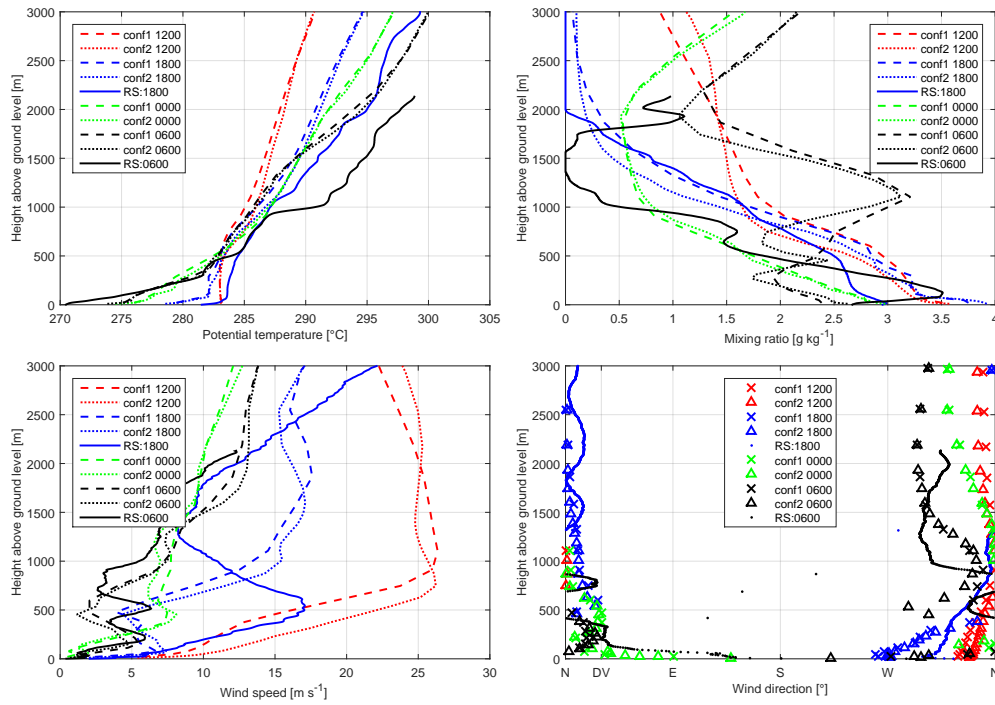


Figure B.26

IOP 7

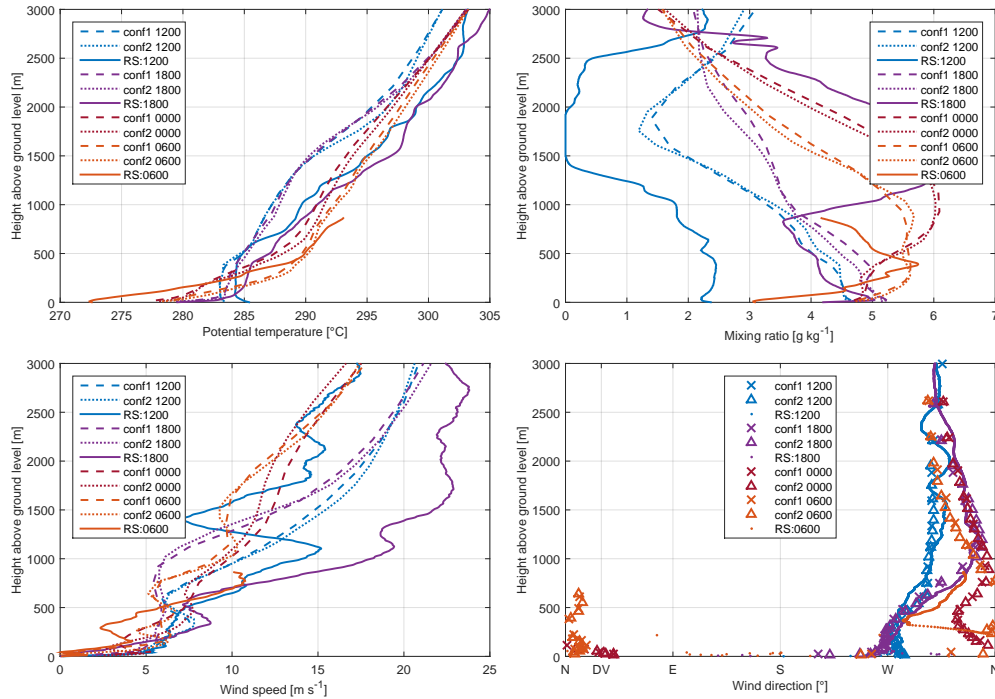


Figure B.27

IOP 10

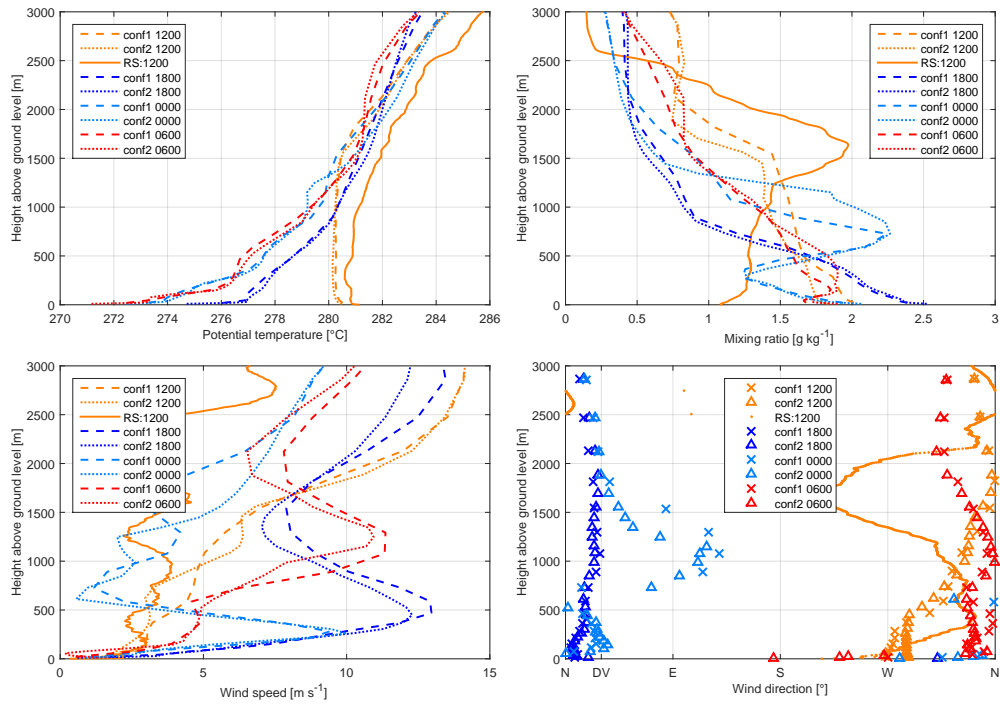


Figure B.28

IOP 11

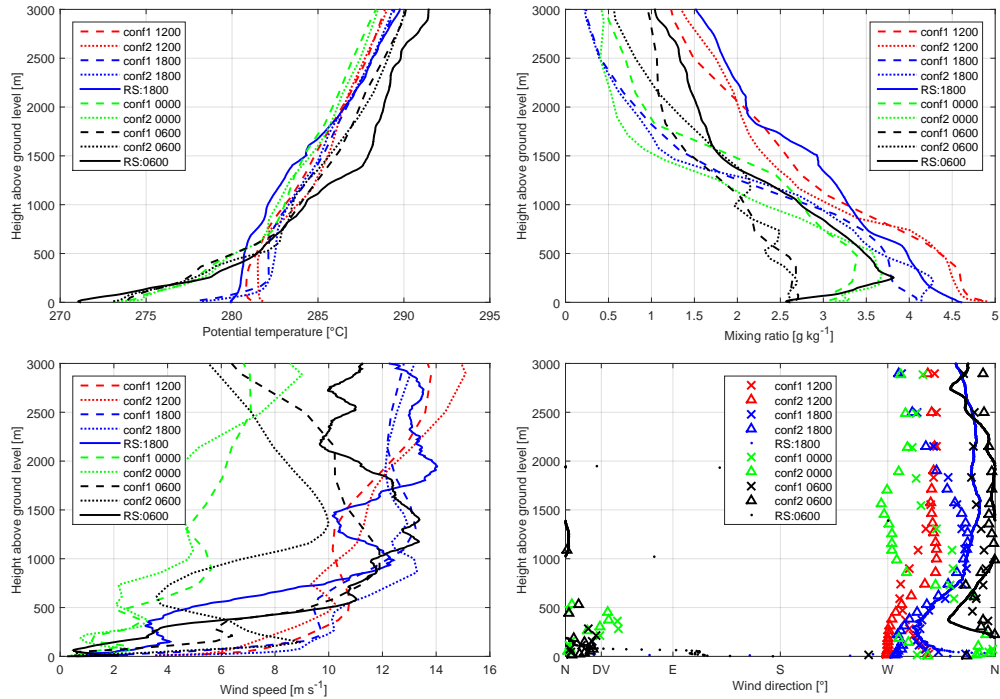


Figure B.29

IOP 13

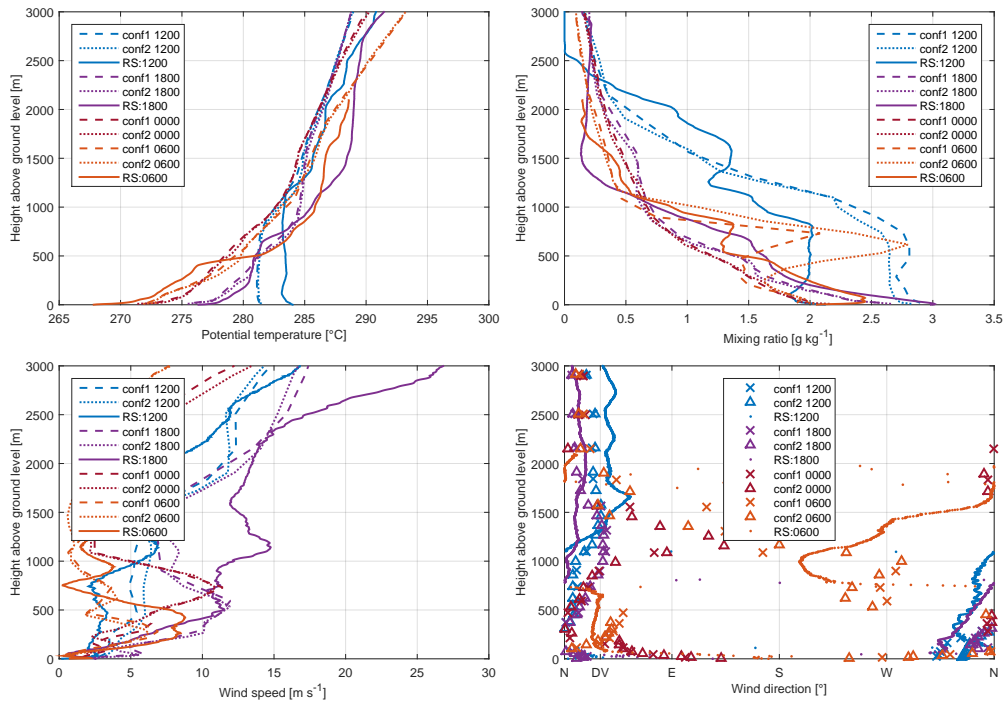


Figure B.30

IOP 14

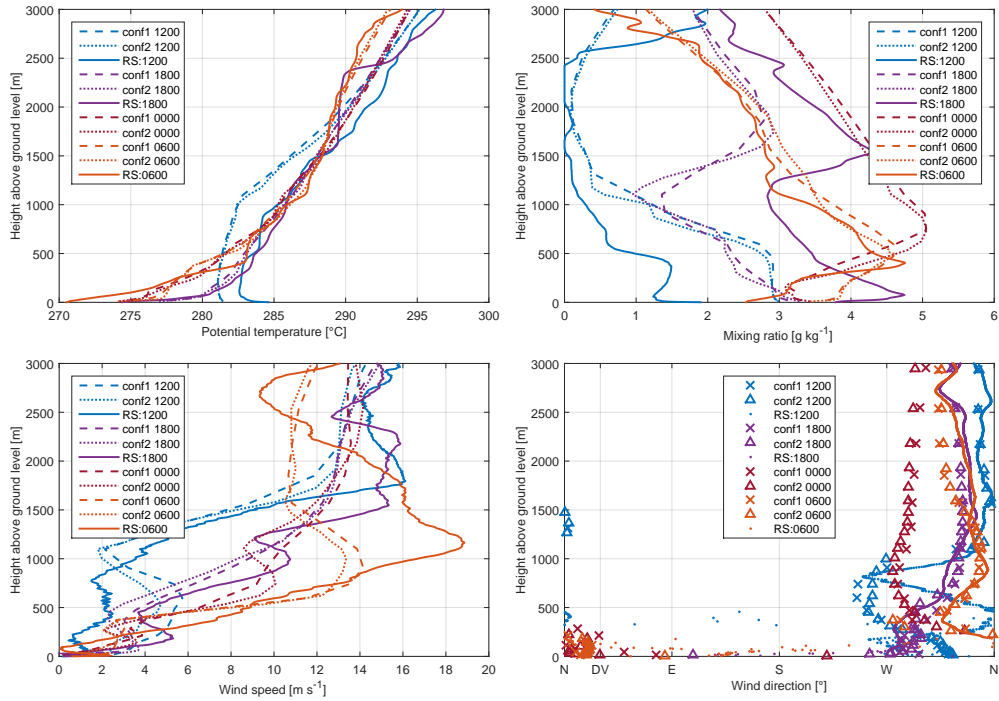


Figure B.31

IOP 15

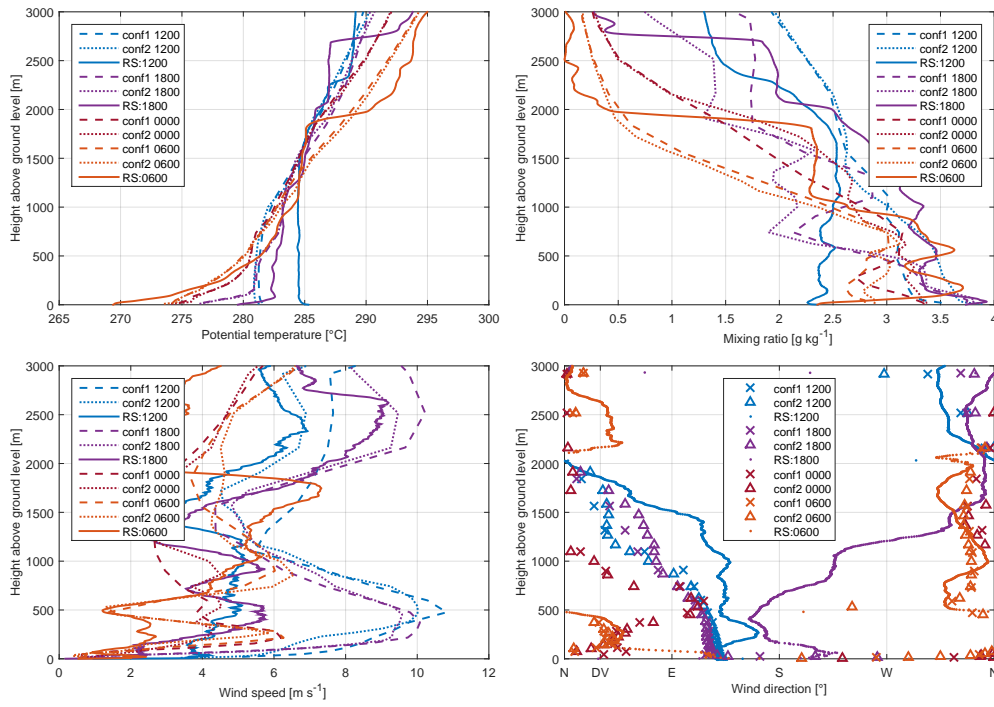


Figure B.32

IOP 16

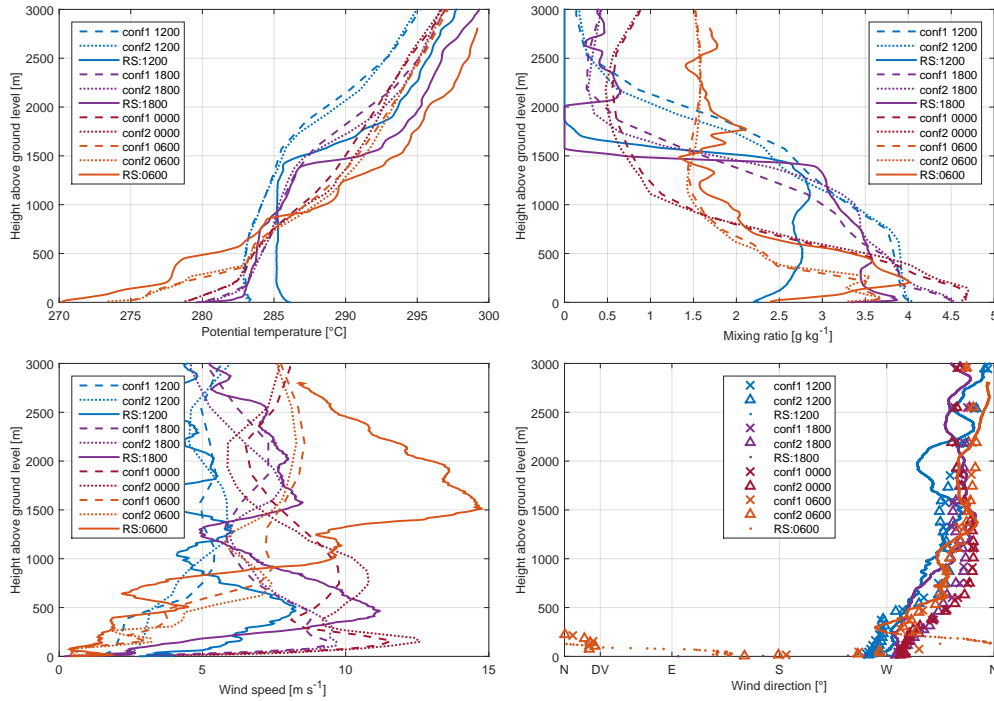


Figure B.33

IOP 19

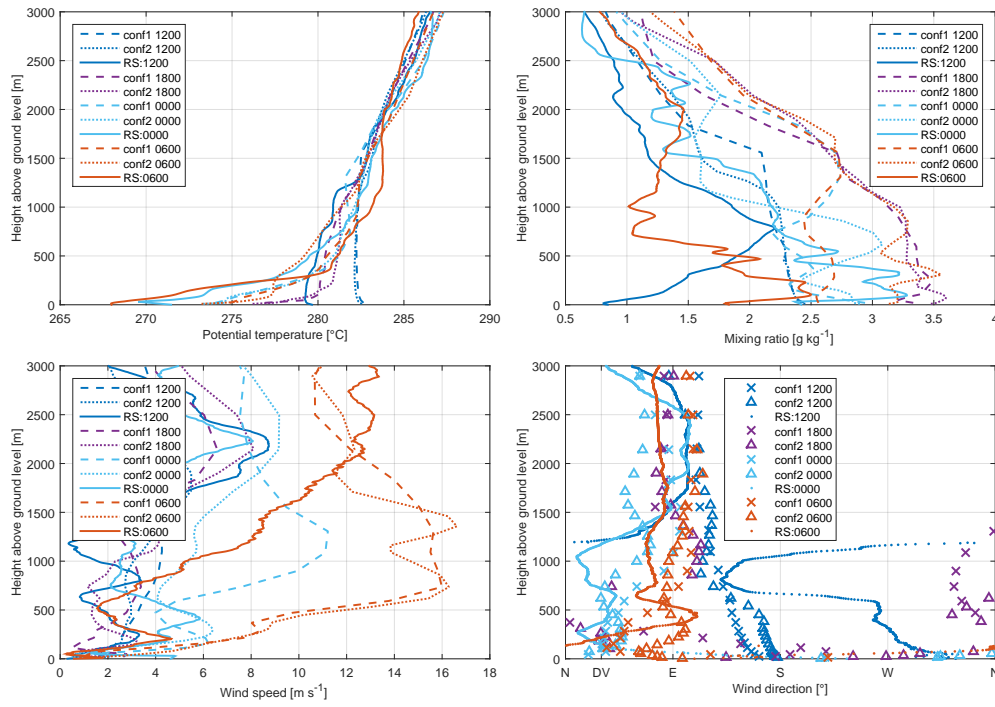


Figure B.34

IOP 20

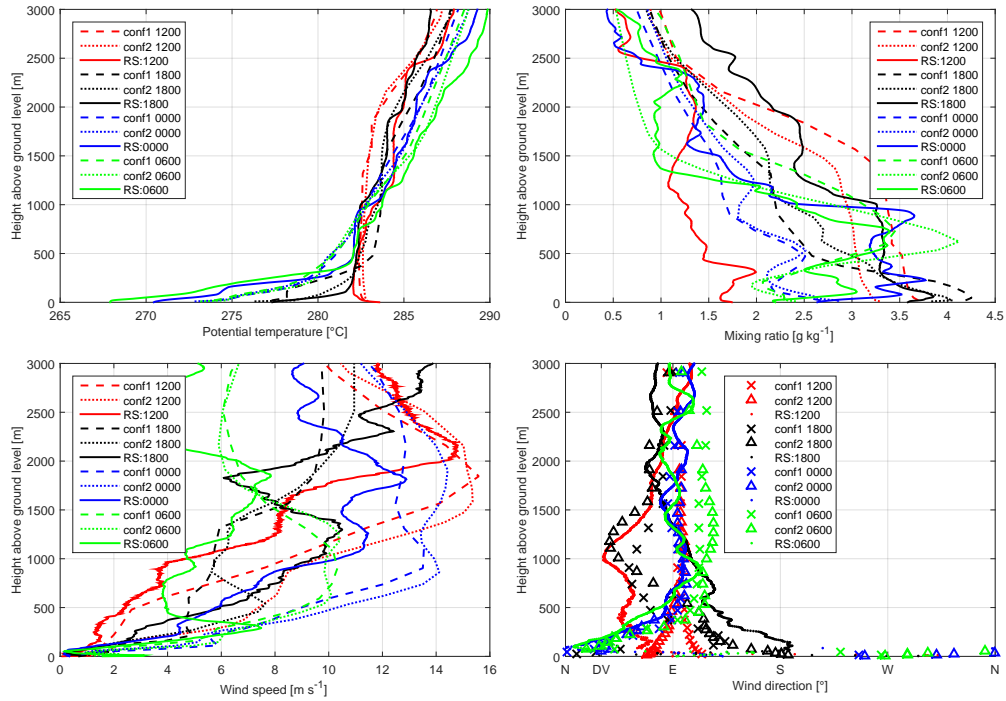


Figure B.35

IOP 21

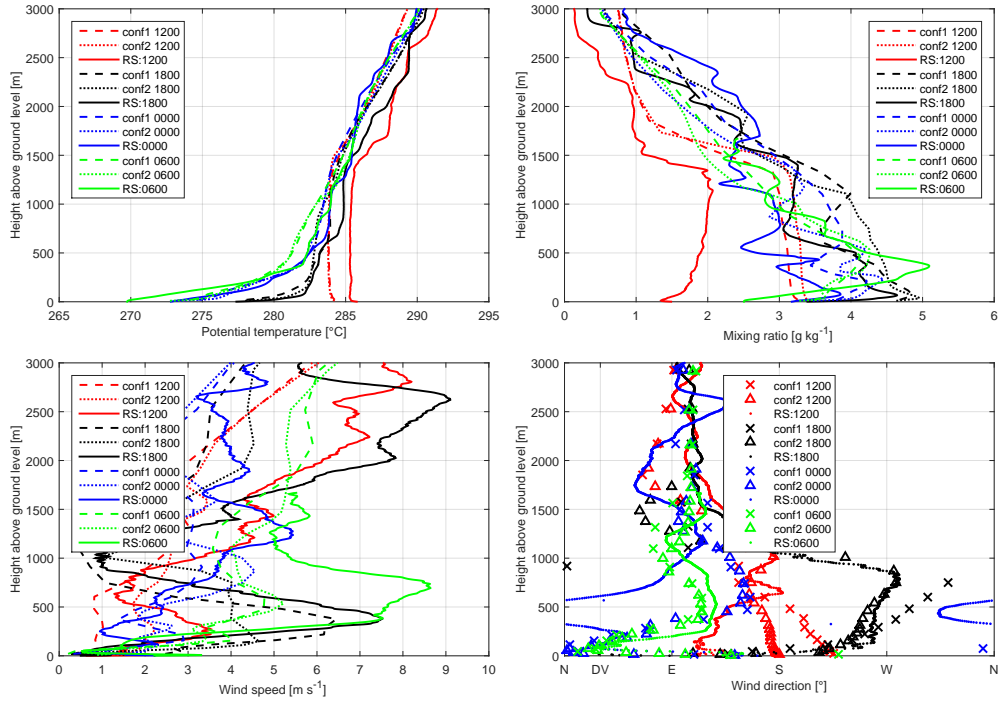


Figure B.36

IOP 23

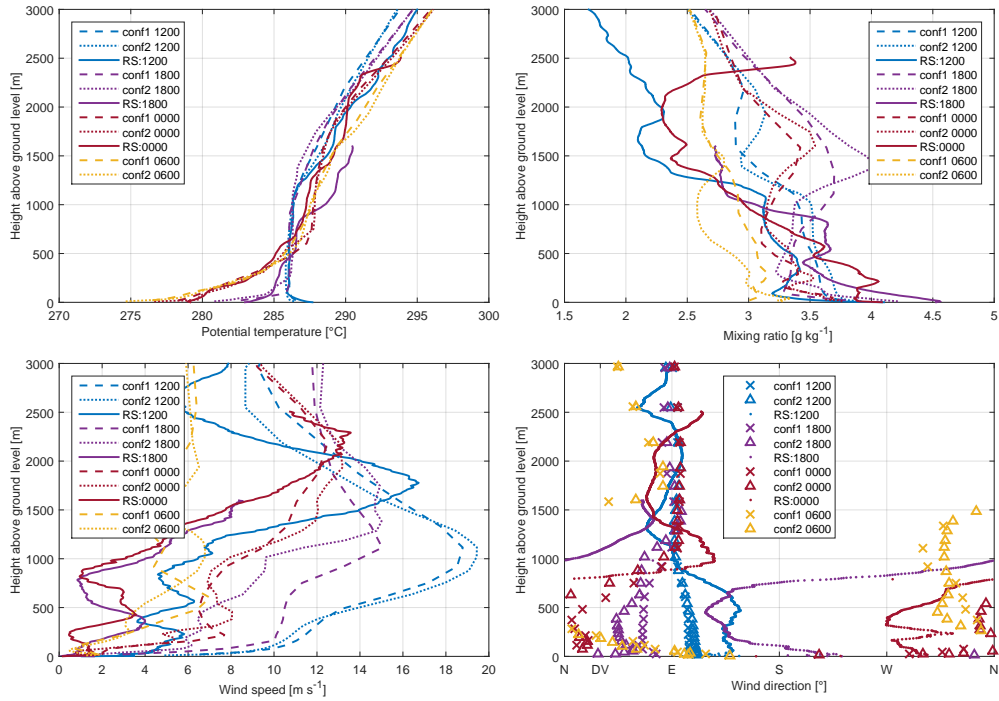



Figure B.37

Appendix C

Technical Report: Instruments calibration experiment and results

		
	TECHNICAL REPORT CEA/DEN LMTE	Page 1/67


Nuclear Energy Sector
Cadarache Center
Department of Nuclear Technology
Division of Measurements and modeling of Transfers and severe Accidents
Laboratory of Environmental Transfer Modeling

KASCADE 2013 Instruments Calibration Campaign

DUINE Gert-Jan

Reference CEA/DEN/CAD/DTN/SMTA/LMTE/NT 2014-11

This document issued by CEA falls within the scope of agreement CEA V4013.001
and V4001.001

		TECHNICAL REPORT CEA/DEN	Page 2/67
		<u>Agreement</u> : CEA V4013.001 and V4001.001 <u>Ref.</u> : CEA/DEN/CAD/DTN/SMTA/LMTE/NT/2014-11	
		<u>Date</u> : 05/02/2014	<u>Version</u> : A
	KASCADE 2013: Instruments Calibration Campaign		


LEVEL OF CONFIDENTIALITY				
DO	DR	CCEA	CD	SD
X				

PARTNERS/CUSTOMERS	AGREEMENT	TYPE OF ACTION

CEA INTERNAL REFERENCES			
MANAGEMENT BY OBJECTIVES	FIELD	PROJECT	EOTP
DISN	MCIS	MRISQ	A-MRISQ-01-02
MILESTONE	MILESTONE TITLE	TIME LIMIT OF CONFIDENTIALITY	LABORATORY SPECIFICATIONS

AMENDMENT RECORD SHEET			
VERSION	DATE	DESCRIPTION	PAGES, CHAPTERS, APPENDICES
A	05/02/2014	FIRST EDITION	

	NAME	POSITION	DATE	SIGNATURE
WRITTEN BY	G. DUINE	PHD-STUDENT	5/2/2014	
CHECKED BY	T. HEDDE	ENGINEER	5/2/2014	
APPROVED BY	F. JOURDAIN	HEAD OF THE LAB		
ISSUED BY	D. PECHEUR	HEAD OF THE DIVISION		

	TECHNICAL REPORT CEA/DEN		Page 3/67
	<u>Agreement</u> : CEA V4013.001 and V4001.001 <u>Ref.</u> : CEA/DEN/CAD/DTN/SMTA/LMTE/NT/2014-11		
	<u>Date</u> : 05/02/2014		<u>Version</u> : A
KASCADE 2013: Instruments Calibration Campaign			

KEY WORDS

KASCADE, meteorological field experiment, sensor calibration, sensor corrections, longwave & shortwave radiation, relative humidity, temperature, pressure, wind speed, radiation divergence

ABSTRACT/CONCLUSION (subject to the same level of confidentiality as the rest of the document)

The sensors used at the meteorological field experiment KASCADE, conducted during the winter of 2013 in Cadarache, are checked for inconsistencies and corrected where necessary. In order to achieve, two complementary intercomparison experiments have been conducted at Centre de Recherche Atmosphérique (Lannemezan) and Laboratoire d'Aérodologie (LA) in Toulouse in spring 2013. Also the data collected during KASCADE itself has been used to be able to calibrate the tethered balloon sondes.

A resolution issue for the net radiometer CNR1 has been solved. It appears that the WMO-agreement of 10-minute averaging for meteorological measurements is sufficient to suppress the spikes detected.

The longwave components of the net radiometer CNR4 has been checked on inconsistencies for the calibration coefficients k supplied by the manufacturer. For this check, a CG4-pyrgeometer was used. The supplied k 's were approved to be correct and so the CNR4 can be used as a reference for relative calibration against the net radiometer CNR1.


The relative calibration of CNR1 for LW has been done in 2 steps: The classical correction for k which is supplied by the manufacturer and in a second step, a body temperature T_{body} correction has been applied. For the lower sensor $k=11.238 \mu V/(W.m^{-2})$ and $T_{body}=0.6196K$. For the upper sensor: $k=10.032 \mu V/(W.m^{-2})$ and $T_{body}=0.5324K$. The improvements after corrections are clearly seen by the mean differences, which are stepwise decreasing from -4.53 (no correction applied) to -3.22 (k -corrected) to 0.03 $W.m^{-2}$ (both k - and T_{body} -corrections applied) for the calibration of the lower sensor. A similar improvement is shown for the upper sensor (-4.17 to -2.80 to -0.07 $W.m^{-2}$). Uncertainties for LW-divergence and LHR are estimated at 0.93 $W.m^{-2}$ and 0.15 $^{\circ}C.h^{-1}$, respectively. Considering only incoming and outgoing LW, these quantities can be calculated at 1.36 and 0.69 $W.m^{-2}$ and 0.21 and 0.11 $^{\circ}C.h^{-1}$, respectively.

Also SW-radiation for CNR1 has been calibrated for both incoming and outgoing components and both are estimated by a 2nd order polynomial fit, see Equations 11 and 12 for correction coefficients.

The thermohygrometers have been calibrated relatively against their average for relative humidity only (17 to 19), for temperature no correction was needed. The tethered balloon sondes needed no correction for wind speed and temperature, for relative humidity (Table 14) and pressure (Table 15) a correction has been performed for all sondes. For relative humidity it concerns a relative correction against the corrected thermohygrometers and for pressure this was a relative correction against their average. In order to achieve the latter corrections, the KASCADE-dataset has been used.

This report will feed the quality of the dataset collected at the field experiment KASCADE.

ABSTRACT/CONCLUSION (if the DEN technical document is of a higher level of confidentiality)

	TECHNICAL REPORT CEA/DEN		Page 4/67
	<u>Agreement</u> : CEA V4013.001 and V4001.001		
	<u>Ref.</u> : CEA/DEN/CAD/DTN/SMTA/LMTE/NT/2014-11		
	<u>Date</u> : 05/02/2014		<u>Version</u> : A
KASCADE 2013: Instruments Calibration Campaign			

DISTRIBUTION (BY E-MAIL)

Full document:

CEA/DEN/CAD/DTN/STMA/DIR
CEA/DEN/CAD/DTN/STMA/LMTE

D. PECHEUR
GJ. DUINE
P. ROUBIN
T. HEDDE
Y. MARGERIT
F. JOURDAIN
E. COHENNY
S. BONTEMPS

LA TOULOUSE

P. DURAND

LA LANNEMEZAN

C. JARNOT

S. DERRIEN

F. LOHOU

LPCA DUNKERQUE

M. LOTHON

P. AUGUSTIN

P. FOURMENTIN

First page and abstract :

CEA/DEN/CAD/DTN/Dir
CEA/DEN/CAD/DTN/STCP/Dir
CEA/DEN/CAD/DTN/SMTA/Dir
CEA/DEN/CAD/DTN/SMTA/LMN/Dir
CEA/DEN/CAD/DTN/SMTA/LMTR/Dir
CEA/DEN/CAD/DTN/SMTA/LIPC/Dir
CEA/DEN/CAD/DTN/SMTA/LPMA/Dir
CEA/DEN/CAD/DTN/SMTA/LMTE
CEA/DEN/DQE

Tout le personnel

T. DE BRUYNE

H. CHERIN

CEA/DEN/DISN/MCIS

C. DELLIS

F. LEFEVRE




	TECHNICAL REPORT CEA/DEN		Page 5/67
	Agreement : CEA V4013.001 and V4001.001		
	Ref. : CEA/DEN/CAD/DTN/SMTA/LMTE/NT/2014-11		
	Date : 05/02/2014		Version : A
KASCADE 2013: Instruments Calibration Campaign			

TABLE OF CONTENTS

Chapter 1. Introduction	10
1.1 Set-up Lannemezan	10
1.2 Intercomparison experiments during KASCADE	13
Chapter 2. Radiation	15
2.1 Atmospheric radiation budget	15
2.1.1 Measuring longwave radiation and radiation divergence	16
where ρ is the air density in kg.m^{-3} and C_p the specific heat of dry air ($=1005 \text{ J.kg}^{-1}.\text{K}^{-1}$)	16
2.1.2 Measuring shortwave radiation	16
2.2 General remarks concerning CNR1 and CNR4	16
2.2.1 Offsets radiation	16
	18
2.2.2 Resolution issue	18
2.3 Calibration longwave radiation CNR4 vs. CG4	19
2.3.1 Materials & Methods	20
2.3.1.1 Instruments	20
2.3.1.2 Time frame & remarks	22
2.3.1.3 Weather during calibration set-up	23
2.3.1.4 Data selection	23
2.3.2 Results	23
2.3.2.1 Testing the hypothesis	23
2.4 Calibration longwave radiation CNR1	27
2.4.1 Upper sensor	28
2.4.2 Lower sensor	30
2.5 Correction shortwave radiation for CNR1	31
2.5.1 Upper sensor	32
2.5.2 Lower sensor	34
2.6 Comparison radiation components CRA-experiment	36
2.7 Uncertainty Longwave Heating Rate	38
2.8 Summary	38
Chapter 3. Thermohygrometers	39
3.1 General remarks	39
3.2 Temperature correction	39
3.3 Relative Humidity correction	41
Chapter 4. TTB-SONDES	43
4.1 General description and approach	43
4.2 Temperature	43
4.2.1 Temperature correction 402	43
4.2.1.1 Correction during IC-experiment Lannemezan	43
4.2.1.2 Correction during neutral conditions using KASCADE dataset	44
4.2.2 Correction TTSS 405, 404, 403 and 401	46
4.3 Wind speed	48
4.4 Relative Humidity	50
4.4.1 Relative Humidity correction TTS 402	50
4.4.2 Correction TTSS 405, 404, 403 and 401	52
4.5 Pressure	53
Chapter 5. Summary and Conclusions	56
References	56
Acknowledgements	57
Appendix A. staggering of tethersondes during IOPs	58
Appendix B. Flow charts sensor corrections	59
Appendix C-1. Technical specifications radiometers CNR1, CNR4 and CG4	64

		TECHNICAL REPORT CEA/DEN	Page 6/67
		<u>Agreement</u> : CEA V4013.001 and V4001.001	
		<u>Ref.</u> : CEA/DEN/CAD/DTN/SMTA/LMTE/NT/2014-11	
		<u>Date</u> : 05/02/2014	<u>Version</u> : A
KASCADE 2013: Instruments Calibration Campaign			

Appendix C-2. Technical specifications thermohygrometers	66
Appendix C-3. Technical specifications tethersondes.....	67

	TECHNICAL REPORT CEA/DEN		Page 7/67
	Agreement : CEA V4013.001 and V4001.001		
	Ref. : CEA/DEN/CAD/DTN/SMTA/LMTE/NT/2014-11		
	Date : 05/02/2014		Version : A
KASCADE 2013: Instruments Calibration Campaign			

LIST OF FIGURES

Figure 1 Schematical drawing of the calibration experimental set-up. Young 1.5 & 10 refer to the measurement height during KASCADE. The angles for α and β are 31° and -18° , respectively, with South as reference.....	13
Figure 2 Impression of an IC-experiment of the TTS performed during KASCADE.	14
Figure 3 Comparison of the emission spectra for the Sun and the Earth.	15
Figure 5 Same as Figure 4, for shortwave radiation components.	18
Figure 6 Recalculated voltage signals for longwave radiation components of CNR1 and CNR4 on 06/05 during the IC-campaign at CRA. Up represents the upper sensors, while dn represents the lower ones.	19
Figure 7 Longwave radiation calibration set-up at the terrace of LA in normal order. Pictures taken the 06/06	21
Figure 8 Longwave radiation calibration set-up at the terrace of LA for the CNR4 upside down. Picture taken the 12/06	22
Figure 9 All radiation components measured (manufacturer coefficients, e.g. frequency in seconds) during June 12 and 13 in the infrared calibration set-up at the terrace of Laboratoire d'Aérodynamique, when CNR4 was in normal order set-up. For CNR4, all components have been shown with their KASCADE-set-up (e.g. incorrect coefficients). For CNR4-LW-in-new the correct coefficient has been used.	25
Figure 10 Comparison of CNR4 and CG4 values, the period from Figure 9 is divided into two parts : Night-time (2030 – 0730 UTC) in blue and daytime (1200 – 1925 UTC) in red.	25
Figure 11 As Figure 9 but for CNR4 in reversed sensors and for the night from 11 to 12 June.	26
Figure 12 As Figure 10 but for 12th of June. Periods for night-time in blue and daytime in red are 0000 – 0500 UTC and 0600 – 1144 UTC, respectively.	26
Figure 13 New calibration coefficient for CNR1 upper sensor (k_{CNR1up}). The slope indicates the value for k	29
Figure 14 Validation dataset, longwave radiation reference CNR4 and CNR1 upper sensors before and after applying the calibration coefficient (k-corrected) and body temperature (k- and body T-corrected).	29
Figure 15 As Figure 13, for the lower sensor: k_{dnCNR1}	30
Figure 16 Validation dataset, longwave radiation reference CNR4 and CNR1 lower sensors before and after applying the calibration coefficient (k-corrected) and body temperature (k- and body T-corrected).	31
Figure 17 Incoming shortwave radiation regression curve.....	33
Figure 18 Incoming shortwave radiation, for validation dataset.	34
Figure 19 Outgoing shortwave radiation, CNR1 vs. CNR4	35
Figure 20 Outgoing shortwave radiation, for validation dataset.	35
Figure 19 Outgoing shortwave radiation correction	35
Figure 21 Nighttime radiative components for a radiative cooling night with original and corrected (-corr) values.	36
Figure 22 All radiation components for CNR1 and CNR4, after corrections explained in this chapter, for 06/05, LW_{in} and LW_{out} from 00-05 UTC.....	37
Figure 24 10 minute averages of temperature between HMP45 and HC2S3, all data, 2-13 May excluded (see text for explanation). 24 and 25 April were excluded as well. The blue line is defined as the 1:1 line.	40
Figure 25 RH_{ref} vs. RH_{HC2S3} (blue) ; RH_{ref} vs. RH_{HMP45} (purple) and the corrected values for $\text{RH}_{\text{HMP45New}}$ vs. $\text{RH}_{\text{HC2S3New}}$ (orange), red line gives the linear trend for the latter. 1:1 line is given in green. See Table 9 for data selection.	41
Figure 26 Relative humidity for both thermohygrometers before and after correction. The mean difference values show a large improvement after corrections. For this validation, all data measured during the intercomparison campaign has been used.	42
Figure 27 IC-experiment for TTS in Lannemezan at 14/05, temperature for the both thermohygrometers and all working sondes of the TTB.....	44
Figure 28 Schematical drawing to determine the range between the thermohygrometers at 30 meters (z_1) and 1.90m (z_2) for which neutral conditions are valid.	45




	TECHNICAL REPORT CEA/DEN		Page 8/67
	Agreement : CEA V4013.001 and V4001.001		
	Ref. : CEA/DEN/CAD/DTN/SMTA/LMTE/NT/2014-11		
	Date : 05/02/2014		Version : A
KASCADE 2013: Instruments Calibration Campaign			

Figure 29 Regression curve for temperature between the tethersonde 402 (W4834334) and the thermohygrometer HC2S3. a determines the slope of the regression curve (represented by the green line), b the intercept, r2 the regression coefficient, mean-diff the mean difference between the two and diff-RMS the difference between the Root Mean Square of both sensor's measurements. The blue line represents the 1:1 line.	46
Figure 30 Regression curves for temperature correction between the reference tethersonde 402 and the sondes 405 (left top), 404 (right top), 403 (left bottom), 401 (right bottom). See text from Figure 28 for explanation on the variables given in the pictures.	47
Figure 31 Correction values a for all sondes when compared with the averages. The periods are taken from the ICs during IOPs 16-23. See text from Figure 28 for explanation on the variables given in the pictures.	49
Figure 32 Calibration coefficients for TTB sonde 401, calibrated against sonde 404, the most reliable sonde out of calibration shown in Figure 30.	49
Figure 33 Measured RH during IC-experiment during Lannemezan at May 14th. See text for details.	51
Figure 34 Polynomial regression curve for relative humidity correction of sonde 402, the ground level probe, with thermohygrometer HC2S3. Data selected from 20-22 Feb, coinciding with IOPs 17 & 18.	51
Figure 35 Validation regression curve for reference thermohygrometer and RH corrected sonde 402 (W4834334). Hence, it is applied on data from IOPs 6 to 21, during neutral conditions. See text from Figure 28 for explanation on the variables given in the pictures.	52
Figure 36 Relative humidity correction coefficients for every tethersonde (TTS) used during KASCADE. TTS 402 was used as reference, after correction against thermohygrometer.	53
Figure 37 Pressure correction regression curves, with a being the correction coefficient, b the intercept, r2 the coefficient of determination, ofs the offset (average of the differences) and diff-RMS the difference between the Root Mean Square. The blue line represents the 1:1 line; the green represents the regression line. The dataset consisted out of all ICs during the IOPs 16-23.	54
Figure 38 Same as Figure 36, but for the sonde 401, which has been corrected with the corrected sonde 405.	55
Figure 39 Flow chart on correction for longwave radiation CNR1. Can be used for both upper and lower sensor. Green squared variables are new quantities. The red square signifies the original volt signal which cannot be changed.	59
Figure 42 Flow chart on relative humidity correction for thermohygrometers HC2S3 and TTS sensors 405, 404, 403, 402, 401.	62
Figure 43 Flow chart on pressure and wind speed correction for TTS sensors.	63
Figure 44 The net radiometers CNR1 (left) and CNR4 (right).	64
Figure 45 Pyrgeometer CG4, provided by CNRM.	64
Figure 46 The Campbell HMP45 probe (left) and HC2S3 probe (right).	66
Figure 47 The Tethersonde TTS111.	67

	TECHNICAL REPORT CEA/DEN		Page 9/67
	Agreement : CEA V4013.001 and V4001.001		
	Ref. : CEA/DEN/CAD/DTN/SMTA/LMTE/NT/2014-11		
	Date : 05/02/2014		Version : A
KASCADE 2013: Instruments Calibration Campaign			

LIST OF TABLES

Table 1 Installation of the sensors of turbulent flux mast M30 used during the intercomparison experiment in Lannemezan. In the 2 nd column the heights in meters are given for which the measurements were taken during KASCADE.	11
Table 2 Tethered balloon sondes used during the intercomparison experiment in Lannemezan	11
Table 3 Sensors horizontal separation.....	12
Table 4 Calibration specifications of the several radiometers used.....	20
Table 6 Final data selection for determination and validation of the corrections made.....	23
Table 7 Selected data during intercomparison experiment at CRA, used for the calibration of CNR1.	28
Table 8 Selected data for the calibration of the shortwave components from CNR1	32
Table 9 Summary of the calibration coefficients (k) and body temperature correction (T_{offs}), determined for CNR1's radiation components and their regression coefficients (R^2). coeff1 and coeff2 refer to the correction coefficients from Equations 11 and 12. For body temperature correction a standard deviation is given. The last 2 columns show the validity range of the coefficients (LAN) and the range measured during KASCADE (KCD). The * for SW_{out} was measured when a fresh snow layer covered the surface, the value between brackets represents the highest value measured for a bare surface.	38
Table 10 Data selection for thermohygrometer's temperature correction.....	39
Table 11 Tethered balloon sondes used during the intercomparison experiment in Lannemezan	43
Table 12 Temperature correction coefficients and their statistics for TTS. The last column indicates whether the the correction coefficients will be applied or not.	48
Table 13 Wind speed correction coefficients and their statistics for TTS. The last column indicates whether the correction coefficients will be applied or not.	50
Table 14 Relative humidity correction coefficients for all tethersondes used in KASCADE together with the regression coefficient. See text for explanation and Equation 21 for application	53
Table 15 Pressure correction coefficients and their statistics for TTS. The last column indicates whether the the correction coefficients will be applied or not.	55
.....	64
Table 16 Manufacturer's technical specifications for the radiometers CNR1 and CNR4	65
Table 17 Technical specifications on the both thermohygrometers used in this report.....	66
Table 18 General specifications of tethersonde TTS111.....	67
Table 19 Manufacturer's sensor's specifications for TTS111.....	67

	TECHNICAL REPORT CEA/DEN		Page 10/67
	<u>Agreement</u> : CEA V4013.001 and V4001.001 <u>Ref.</u> : CEA/DEN/CAD/DTN/SMTA/LMTE/NT/2014-11		
	<u>Date</u> : 05/02/2014		<u>Version</u> : A
KASCADE 2013: Instruments Calibration Campaign			

CHAPTER 1. INTRODUCTION

In this calibration report the sensors used for the winter field campaign KASCADE have been intercompared, calibrated and/or corrected. From January to mid-March 2013, the atmospheric measurement campaign KASCADE (Katabatic winds and Atmospheric Stability over CAdarache for Dispersion of Effluents) has been conducted at the CEA-center of Cadarache, South-Eastern France. The purpose of the campaign was to characterize the local stable boundary layer (SBL) and its main drivers, in order to feed future planned numerical dispersion studies. A flux measurement tower of 30 meters was present for continuous measurements, where sonic anemometers, a gas analyzer, thermohygrometers and net radiometers were present to cover surface layer variables. During Intensive Observational Periods (IOPs) a tethered balloon (TTB) was treated with several tethersondes (TTS), and radiosoundings were launched. Table 1 and 2 show the sensors which are considered in this report (with an exception on the sonic anemometers).

The sensors to be tested have been installed in an Intercomparison/Calibration campaign (IC-experiment) at the Centre de Recherche Atmosphérique (CRA) at Lannemezan from late April to early June 2013, see Section 1.1. Hence, the IC-experiment has been conducted at a different location and during a different time of the year, so the conditions were far from the conditions desired in comparison with KASCADE. Therefore, in some cases the Intercomparison experiments (ICs) taken during KASCADE itself are used to compare and correct the sensors, see Section 1.2 on the general approach. The radiometers are calibrated in Section 2, Section 3 covers the calibration for the thermohygrometers, and the sensors of the tethered balloon sondes are covered by Section 4. A conclusion is given in Section 5. Flow charts on correction procedures are given in Appendix B, technical specifications on all sensors are given in Appendix C.

1.1 SET-UP LANNEMEZAN

This section represents intercomparison set-up performed at CRA, Lannemezan.

Date of installation: 24/25 April 2013

Date of de-installation: 5th of June 2013

Duration: 41 days

For 41 days the set-up was installed at CRA, according to Table 1. The TTB-sondes were intercompared at May 14th 2013; see Table 2 for the sondes used during this experiment.


	TECHNICAL REPORT CEA/DEN		Page 11/67
	Agreement : CEA V4013.001 and V4001.001		
	Ref. : CEA/DEN/CAD/DTN/SMTA/LMTE/NT/2014-11		
	Date : 05/02/2014		Version : A
KASCADE 2013: Instruments Calibration Campaign			

Table 1 Installation of the sensors of turbulent flux mast M30 used during the intercomparison experiment in Lannemezan. In the 2nd column the heights in meters are given for which the measurements were taken during KASCADE.

Sensor	Manufacturer	Model	Type	Height (cm)	Alignment to pole (cm)	Sample freq
Sonic anemometer	Young1 (1.90)	81000	omni	298.5	0	10 Hz
Sonic anemometer	Young2 (10.0)	81000	omni	298	0	"
Sonic anemometer	Campbell (30.0)	CSAT3	C-clamp	291.5	0	"
Gas analyzer	LI-COR (30.29)	LI-7500A		240	48.0	"
Net radiometer	Kipp&Zonen (1.18)	CNR1		185.5	63.5	0.1 Hz
Net radiometer	Kipp&Zonen (20.11)	CNR4		190.5	64.5	"
Thermohygrometer	Campbell (30.0)	HC2S3		243.5	50.0	"
Thermohygrometer	Campbell (1.90)	HMP45		247.5	57.0	"

Table 2 Tethered balloon sondes used during the intercomparison experiment in Lannemezan


Manufacturer	Frequency	Serial nr.	Remarks
Vaisala	405	W4834144	
Vaisala	404	C0829547	Relative Humidity not reliable
Vaisala	403	W4834323	Sensor used from IOP 16
Vaisala	402	W4834334	
Vaisala	401	W4834332	Wire is broken, not used

Experimental set-up:

All M30-sensors are placed on a scaffold to reach a measurement height of around 3m. The radiometers are placed on a different mast 10 meters southward to reduce the scaffold's influence. The TTB-sondes are used in one intensive experiment.

M30-sensors:

The sonic anemometers are placed together on a mount above the scaffold, horizontal separation 65cm, facing prevailing (westerly) wind direction. See Figure 1. The thermohygrometers and gas analyzer are grouped together on the South-East corner of the scaffold. Easterly to be out of the range of the sonic anemometer as far as possible. Southerly, as this will have the least influence of shadow effects of the scaffold's integrated bars. Further details are given in Table 3.

		TECHNICAL REPORT CEA/DEN	Page 12/67
		<u>Agreement</u> : CEA V4013.001 and V4001.001	
		<u>Ref.</u> : CEA/DEN/CAD/DTN/SMTA/LMTE/NT/2014-11	
		<u>Date</u> : 05/02/2014	<u>Version</u> : A
KASCADE 2013: Instruments Calibration Campaign			

Net radiometers:


The net radiometers are placed on 1 mast, located south of the calibration scaffold and facing southward. Horizontal separation is 51 cm between the radiometer's cores. Vertical separation is 3 cm because they are placed on the same pole. To obtain a wider range for the calibration measurement (approx. -10°C to 20°C around April), there is an ability to turn both radiometers upside down halfway the measurement.

Tethered balloon sondes:

Placed in the field close to the other sensors. The intercomparison is done in 1 part: Sunrise transition. Conducted at May 14th. See Figure 2 for the set-up.

Table 3 Sensors horizontal separation

<i>Sensor</i>	<i>Horizontal separation (cm)</i>
CNR1 - CNR4	51
Sonic anemometers	65
HC2S3 - LI-COR	40
HC2S3 - HMP45	88
LI-COR - HMP45	50

	TECHNICAL REPORT CEA/DEN		Page 13/67
	<u>Agreement</u> : CEA V4013.001 and V4001.001 <u>Ref.</u> : CEA/DEN/CAD/DTN/SMTA/LMTE/NT/2014-11		
	<u>Date</u> : 05/02/2014		<u>Version</u> : A
KASCADE 2013: Instruments Calibration Campaign			

view from above



Climatological
prevailing wind: West

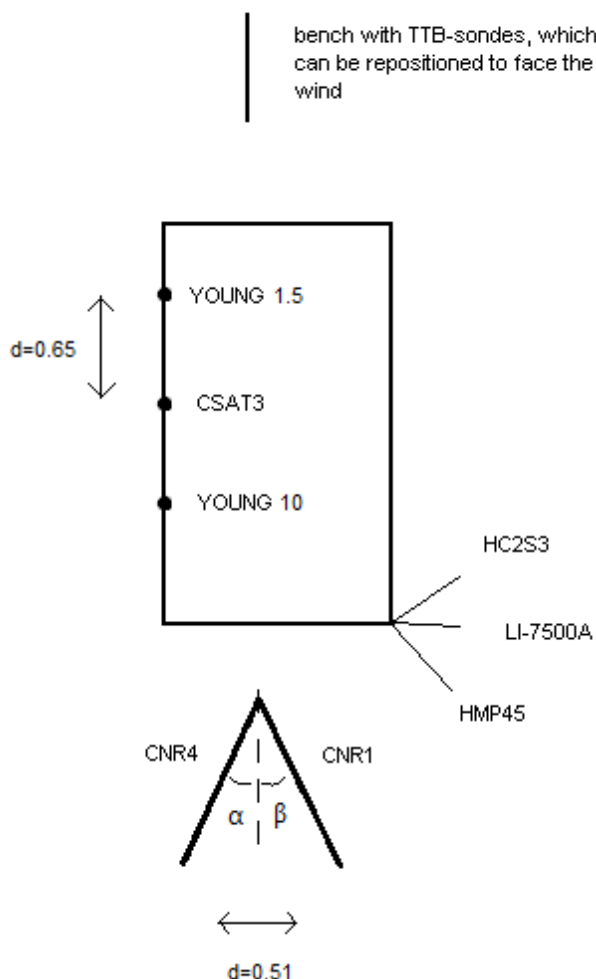


Figure 1 Schematical drawing of the calibration experiment set-up. Young 1.5 & 10 refer to the measurement height during KASCADE. The angles for α and β are 31° and -18° , respectively, with South as reference, d = the distance between sensors in m.

1.2 INTERCOMPARISON EXPERIMENTS DURING KASCADE

Before and after every IOP during KASCADE there were short intercomparison periods (ICs) for the TTS. At least for 3 minutes the sondes used during that IOP, were placed together on the small wooden bench showed in Figure 2. Some ICs took 2 hours. These ICs allow us to correct the sondes to each other. Please note that during KASCADE the wooden bench was placed on a vegetation free ground.


	TECHNICAL REPORT CEA/DEN		Page 14/67
	<u>Agreement</u> : CEA V4013.001 and V4001.001 <u>Ref.</u> : CEA/DEN/CAD/DTN/SMTA/LMTE/NT/2014-11		
	<u>Date</u> : 05/02/2014		<u>Version</u> : A
KASCADE 2013: Instruments Calibration Campaign			



Figure 2 Impression of an IC-experiment of the TTS performed during KASCADE.

CHAPTER 2. RADIATION

2 net radiometers were used during KASCADE, a CNR1 and CNR4 both produced by Kipp&Zonen. The CNR4 was installed at the M30 at 20.11 meters height, while the CNR1 was installed at a separate mast at 1.18 meters height. The horizontal distance between the both masts of CNR4 and CNR1 was 23.60 meters. See Appendix C-1 for further technical specifications. In this chapter, the methodology for calibrating CNR1 and CNR4 are described. The first section is dedicated to the principles of atmospheric radiation and its measurements with a net radiometer.

2.1 ATMOSPHERIC RADIATION BUDGET

Each body with a temperature above zero degrees Kelvin emits electromagnetic energy. Wien's law states that for a given black body temperature T you can find the maximum of the wavelength λ_m for a radiation curve:

$$\lambda_m T = c \quad (1)$$

where $c = 2897 \mu\text{m.K}$.

We identify 2 radiation emitting bodies influencing processes in the atmosphere: the Sun and the Earth. With the Sun's surface temperature of 6000K and the Earth's temperature of 288K we come up to 0.5 and 10.0 μm for λ_m , respectively. Planck's law states how radiation emitted from a black body is divided over the different wavelengths; see Figure 3 for a visualization of the concept. Considering the radiation curves according to Planck's law for both body's in one diagram – on the left hand the radiation curve for the Sun and on the right hand side the one for the Earth – we can distinguish the atmospheric radiation into two separate parts: the radiation emitted by the sun or directly reflected by the Earth's surface – shortwave radiation (SW) – and radiation emitted by the Earth or its atmosphere – longwave radiation (LW) (Stull, 2000).

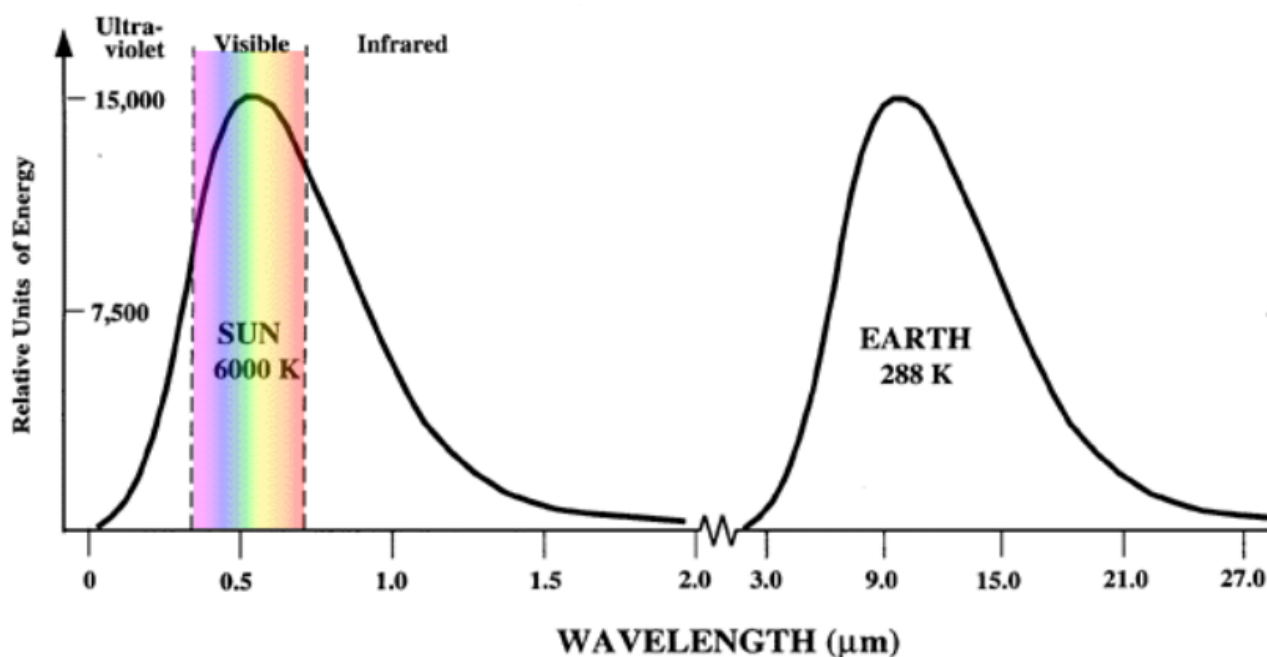



Figure 3 Comparison of the emission spectra for the Sun and the Earth.

	TECHNICAL REPORT CEA/DEN		Page 16/67
	<u>Agreement</u> : CEA V4013.001 and V4001.001		
	<u>Ref.</u> : CEA/DEN/CAD/DTN/SMTA/LMTE/NT/2014-11		
	<u>Date</u> : 05/02/2014		<u>Version</u> : A
KASCADE 2013: Instruments Calibration Campaign			

For the total energy budget Q^* this holds that:

$$Q^* = SW_{in} - SW_{out} + LW_{in} - LW_{out} \quad (2)$$

Where the terms on the right hand side represent the shortwave (SW) and longwave (LW) incoming ($_{in}$) and outgoing ($_{out}$) radiation, all terms are in $W.m^{-2}$. These terms can be measured separately by a net radiometer, which is explained in the next section.

2.1.1 Measuring longwave radiation and radiation divergence

We use a pyrgeometer to measure atmospheric longwave, or infrared, radiation. The pyrgeometer can be integrated also in a net radiometer, the purpose and features of the sensor remain the same. The signal of a pyrgeometer represents the exchange of longwave infrared radiation between the pyrgeometer and the object that it is facing. When the pyrgeometer faces an object which is warmer than its own sensor housing, it will generate a positive voltage V . A negative voltage is generated when the pyrgeometer is facing an object which is colder than itself. This implies that we need to take the pyrgeometer temperature T_{body} into account. To calculate the longwave radiation we use the following equation:

$$LW = V/k + \sigma T_{body}^4 \quad (3)$$

With the Stefan-Boltzmann constant $\sigma = 5.67 \cdot 10^{-8} W.m^{-2}.K^{-4}$, k denotes the sensitivity in $\mu V/W.m^{-2}$, which is different for every pyrgeometer. A net radiometer has two pyrgeometers: An upper and a lower one. The upward looking (upper) pyrgeometer measures the longwave radiation received from the sky. This can be sky or cloud temperature, both are typically colder than the instrument. The downward looking (lower) sensor is measuring the longwave radiation received from the Earth's surface. A detailed description of the principles on longwave measurements are described in *Phillipona et al. (1995)*.

For SBL-formation, LW-radiation divergence is one of the crucial drivers. LW-radiation divergence is in KASCADE measured as a difference, by putting the two net radiometers at different levels z_1 and z_2 ($z_2 > z_1$). By considering the difference we can calculate a Longwave Heating Rate (LHR), which is an estimation of the atmospheric heating per time unit controlled by radiative loss:

$$LHR = \frac{1}{\rho C_p} \frac{LW_{z2}^{\downarrow} - LW_{z1}^{\downarrow} + LW_{z1}^{\uparrow} - LW_{z2}^{\uparrow}}{z_2 - z_1} \left[\frac{K}{s} \right] \quad (4)$$

where ρ is the air density in $kg.m^{-3}$ and C_p the specific heat of dry air ($=1005 J.kg^{-1}.K^{-1}$).

2.1.2 Measuring shortwave radiation

To measure shortwave radiation, we use a pyranometer which is integrated too in the net radiometer. As for the pyrgeometer, it consists out of two parts, an upper and a lower pyranometer. The upper one is facing the sky and measuring the downwelling solar radiation, it gives a voltage signal V which is proportional to this radiation. The same holds for the lower one, but this is upwelling solar radiation, reflected by the surface it is facing. To calculate the shortwave radiation SW we use the equation:

$$SW = V/k \quad (5)$$

Every pyranometer has its unique calibration coefficient k .

2.2 GENERAL REMARKS CONCERNING CNR1 AND CNR4

2.2.1 Offsets radiation

A first outlook on raw data measurements of radiation is shown in Figures 4 (longwave radiation) and 5 (shortwave radiation). In the figures, all measured components for the both radiometers CNR1 and CNR4 are

compared for May 6th, on which a clear sky was present during the night and morning. By the end of the afternoon, some fair weather clouds appeared and the evening was cloudy.

From the figures it can be concluded that the 2 radiometers used at KASCADE do not coincide. The longwave incoming radiation (LW_{in}) for both radiometers differ by about 40-60 $W \cdot m^{-2}$ for clear sky during night-time. LW_{out} shows the same behavior though with a smaller discrepancy. At the measurement site there is an extra radiometer available at a 60m mast, also shown in Figure 4. For this permanently installed net radiometer, only incoming radiation components are shown. Comparing the different outputs for LW_{in} , we conclude that the measured bias is attributable mainly to CNR4. CNR1's measurements are more in agreement with the radiometer at the 60 meter mast. It will however not be used as a reference for CNR4 because its calibration date is unknown. The difference for LW between CNR1 and CNR4 is found throughout the calibration experiment and present in the KASCADE-dataset as well. Probably it is caused by a wrong input of the calibration coefficient. An extra calibration experiment is performed, focused on the longwave radiation components of CNR4. See Section 2.3 for results.

Also for shortwave radiation (incoming and outgoing) there is a bias between the 2 net radiometers, illustrated by Figure 5. As the CNR4 is new (purchased late 2012) it will be of reference to CNR1. See results on this in Section 2.3.

To serve the desired purpose of radiation divergence during KASCADE, LW_{CNR1} will be calibrated relatively to LW_{CNR4} for incoming and outgoing components. See Section 2.4.

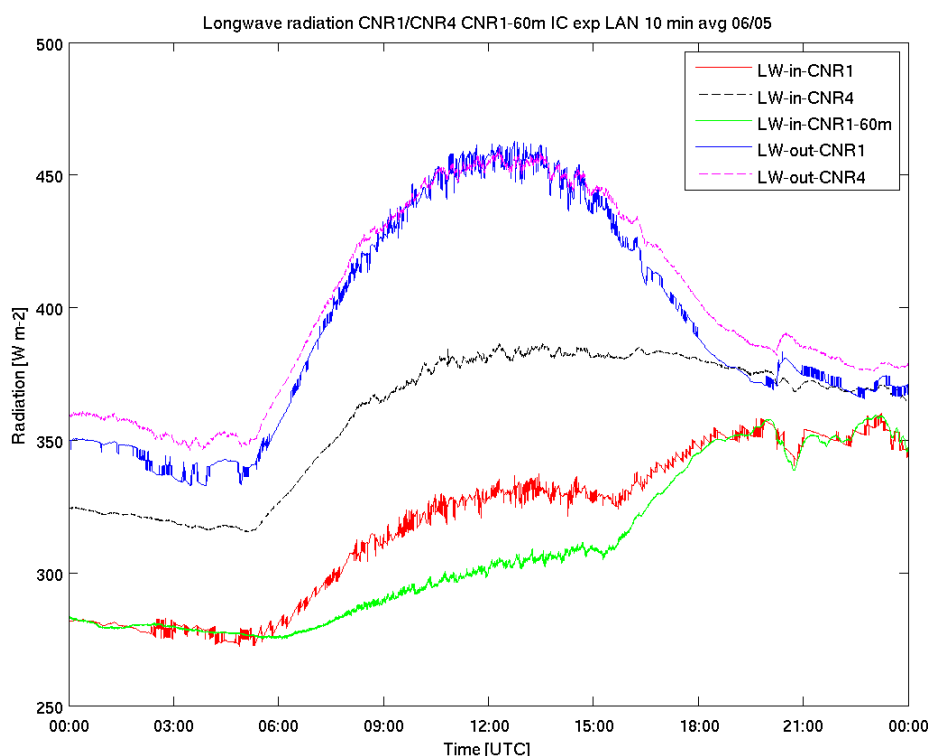


Figure 4 LW-radiation components for CNR1, CNR4 – both used during Kascade – and CNR1-60, a radiometer which is permanently installed at Lannemezan at 60 meters height.

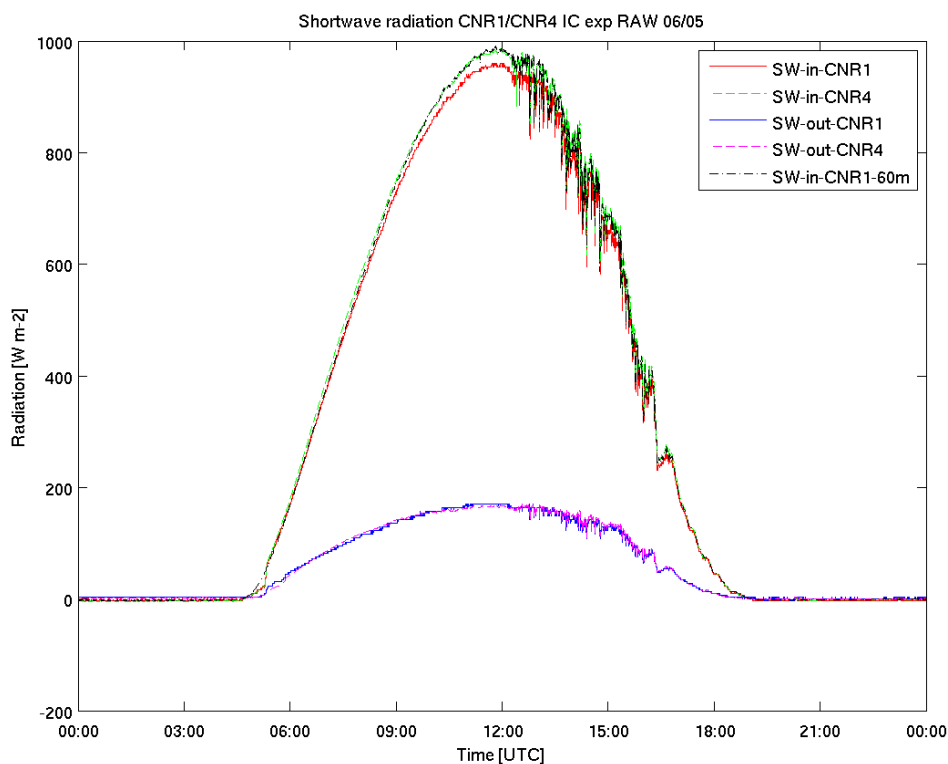


Figure 5 Same as Figure 4, for shortwave radiation components.

2.2.2 Resolution issue

The raw data for CNR1 (Figures 4 and 5) show a very jumpy behavior. When values should be constant, or should show a trend, the output signal for all terms on radiation creates spikes which are of the order of 4 W.m^{-2} . After a voltage check, by calculating backwards to obtain the original voltage output of the CNR1, it was concluded that the resolution in the acquisition of the datalogger was not set high enough, see Figure 6. For CNR1-data treatment, 10-min averages will be used. Figure 21 shows clearly there are no problems when averaging over this time lapse.

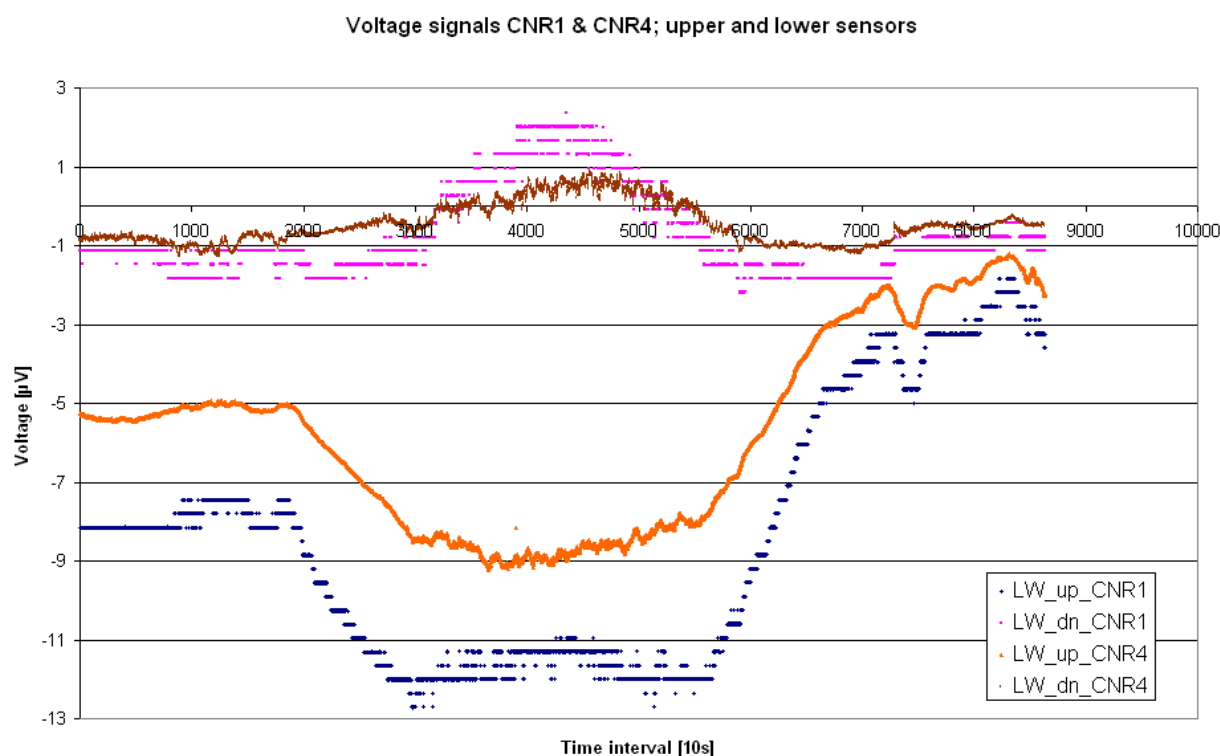



Figure 6 Recalculated voltage signals for longwave radiation components of CNR1 and CNR4 on 06/05 during the IC-campaign at CRA. Up represents the upper sensors, while dn represents the lower ones.

2.3 CALIBRATION LONGWAVE RADIATION CNR4 vs. CG4

In this calibration experiment conducted at CRA, 2 radiometers (CNR1 and CNR4 – Kipp&Zonen, Delft) were positioned aside each other for calibration. Specifications on calibration coefficients are given in Table 4. Technical specifications are given in Appendix C-1. The experiment at CRA revealed a bias between the 2 net radiometers used for KASCADE. The bias was at the range of $40 - 60 \text{ W.m}^{-2}$ for longwave incoming radiation during nighttime (LW_{in}). Although it is less distinct, the outgoing longwave radiation (LW_{out}) showed the same behavior. It is suspected that the reason for the bias is probably a wrong input of the calibration coefficient of CNR4.

After communication with Campbell Sci. – the provider of the net radiometer in France – this suspicion proved correct: The datalogger CR3000 appeared to be wrongly encoded and it therefore applied the k coefficient from shortwave upper sensor (SW_{in}) to all separate components of the CNR4, while every component should have its own dedicated k (Table 4) instead. As this was not known by the first instance, and due to the importance of longwave radiation for this study, an additional calibration was set-up and installed at the terrace of Laboratoire d'Aérodynamique (LA) in Toulouse, between June 7 and June 13 in 2013. For this set-up, a CG4 Pyrgeometer has been used, supplied by Centre National de Recherches Météorologiques (CNRM).

The purpose of Chapter 2.3 is to test whether longwave radiation of CNR4 with the manufacturer calibration coefficients holds when compared with the pyrgeometer CG4.

		TECHNICAL REPORT CEA/DEN	Page 20/67
		<u>Agreement</u> : CEA V4013.001 and V4001.001 <u>Ref.</u> : CEA/DEN/CAD/DTN/SMTA/LMTE/NT/2014-11	
		<u>Date</u> : 05/02/2014	<u>Version</u> : A
	KASCADE 2013: Instruments Calibration Campaign		


2.3.1 Materials & Methods

2.3.1.1 Instruments

During the calibration set-up, the CNR4 has been put together with a Pyrgeometer CG4 (Kipp&Zonen) which was lent to us by CNRM. As both upper and lower sensor of the CNR4 needed a test and calibration, the CNR4 was put several days in normal order, and several days it was turned upside down, see Figures 7 and 8, respectively. The orientation for both net radiometer and pyrgeometer was such to reduce the influence from surrounding buildings and trees. Therefore the sensors were put in Easterly direction, while a traditional orientation for a radiometer should be southward. Hence, no exact measurement on this orientation was performed. When the CNR4 was turned upside down, its orientation remained the same. Data acquisition frequency was set to 1 second. As we are interested in clear sky conditions during KASCADE, the CNR4 will be tested as close to these conditions as possible.

Table 4 Calibration specifications of the several radiometers used

	Serial no.	Calibration coefficient ($\mu\text{V/W.m}^{-2}$)	Calibration date
CNR1	980149	9.72	unknown
CNR4	121005	-	
“ – LW _{upper}	-	7.79	31/07/2012
“ – LW _{lower}	-	7.56	31/07/2012
“ – SW _{upper}	-	14.97	31/07/2012
“ – SW _{lower}	-	14.79	31/07/2012
CG4	060898	8.35	23/04/2008 (CNRM)

	TECHNICAL REPORT CEA/DEN		Page 21/67
	<u>Agreement</u> : CEA V4013.001 and V4001.001 <u>Ref.</u> : CEA/DEN/CAD/DTN/SMTA/LMTE/NT/2014-11		
	<u>Date</u> : 05/02/2014		<u>Version</u> : A
KASCADE 2013: Instruments Calibration Campaign			

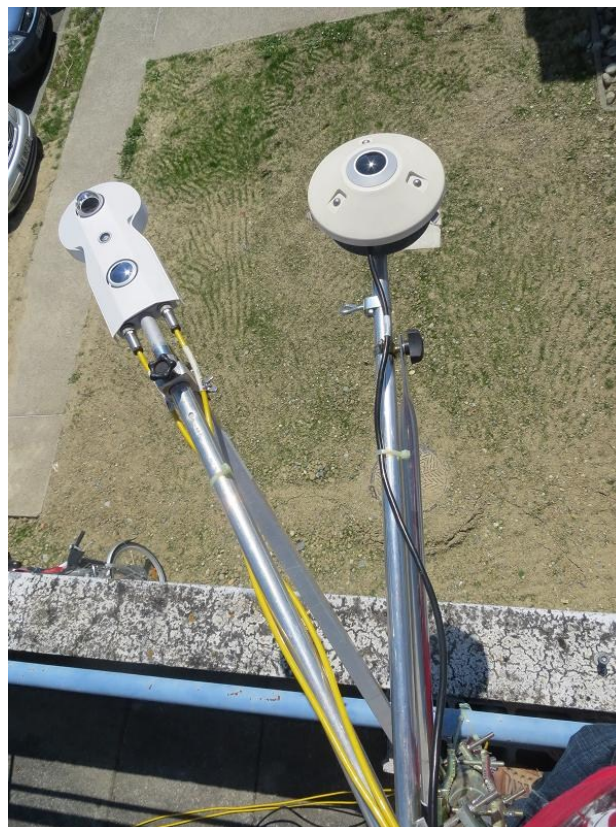


Figure 7 Longwave radiation calibration set-up at the terrace of LA in normal order. Pictures taken the 06/06


	TECHNICAL REPORT CEA/DEN		Page 22/67
	<u>Agreement</u> : CEA V4013.001 and V4001.001 <u>Ref.</u> : CEA/DEN/CAD/DTN/SMTA/LMTE/NT/2014-11		
	<u>Date</u> : 05/02/2014		<u>Version</u> : A
KASCADE 2013: Instruments Calibration Campaign			



Figure 8 Longwave radiation calibration set-up at the terrace of LA for the CNR4 upside down. Picture taken the 12/06

2.3.1.2 Time frame & remarks


The calibration campaign has been divided in 3 parts.

CNR4, normal order (NO) :	07 June 1230 UTC – 10 June 0808 UTC
	12 June 1200 UTC – 13 June 0730 UTC
CNR4, upside down (UD) :	10 June 2030 UTC – 12 June 1145 UTC

The first period for NO lacked a radiative cooling night, therefore at the end of the measurements the radiometer has been put at NO again.

A failure of the data acquisition system, source unknown, has led to a data gap of 12 hours at June 10, 0808 UTC – 2030 UTC.

At June 11th (upside down sensors set-up), from 00 to 06 UTC, there is no correlation at all between the both LW-sensors. The direct source is unknown, this data will not be used.

	TECHNICAL REPORT CEA/DEN		Page 23/67
	Agreement : CEA V4013.001 and V4001.001		
	Ref. : CEA/DEN/CAD/DTN/SMTA/LMTE/NT/2014-11		
	Date : 05/02/2014		Version : A
KASCADE 2013: Instruments Calibration Campaign			

2.3.1.3 Weather during calibration set-up

Table 5 Weather during the calibration set-up at LA in Toulouse.

Date	Weather conditions, with cloud cover in okta's
07 June	Sunny, with clear sky (CS). Windy afternoon. CS night until 0100 UTC.
08 June	Cloudy (8/8) and some (heavy) rain. Early night some spells.
09 June	Cloudy (8/8) and dry. Afternoon 5/8. Cloudy night afterwards.
10 June	6/8 during day. From afternoon 0/8 with a clear sky following.
11 June	6/8. No extra information.
12 June	CS with parts of light clouds, sunny morning, 0/8. CS during evening
13 June	Clear sky during night, 8/8 from ~0545 UTC.

2.3.1.4 Data selection

In order to test the quality for upper and lower sensor of CNR4 during night-time, a dataset is selected containing dry and clear sky conditions. Another point of importance is that when the CNR4 is turned, the lower part of the sensor is exposed directly to the sun. The sun's influence on the body temperature is not known – in normal order it is protected – and the body temperature is not trustworthy. This part of the dataset will therefore not be used for calibration. See Table 6 for details on the data selection, where the training dataset refers to the dataset used for determination of the calibration coefficients. After correction, the data has been tested using a validation dataset.

Table 6 Final data selection for determination and validation of the corrections made


	Date	Time [UTC]
Upper sensor (training)	07/06/2013	2200 - 2400
Lower sensor (training)	12/06/2013	0000 – 0430
Upper sensor (validation)	13/06/2013	0000 – 0600
Lower sensor (validation)	10/06/2013	2030 – 2400

2.3.2 Results

2.3.2.1 Testing the hypothesis

See Figures 9 and 11 for the measurements of CNR4 and CG4 on 2 particular days, as reference, all radiation parts are shown. Shortwave radiation and outgoing longwave radiation only give information in qualitative sense.

Both figures confirm the aforementioned bias, the difference between LW_{in_CG4} and LW_{in_CNR4} during a radiative cooling night is around 40 W.m^{-2} . $CNR4-LW-in-new$ in Figure 9 represents LW_{in_CNR4} re-calculated with the correct coefficient supplied by the manufacturer. The improvement is clearly visible: During night-time conditions the values of LW_{in_CNR4} approach LW_{in_CG4} to a small difference of $1-3 \text{ W.m}^{-2}$. This is also shown by Figure 10, the blue dots in this figure represent the night-time part and the red dots are during daytime. LW_{in_CG4} is considered as reference value, so LW_{in_CNR4} behaves during daytime conditions not as good as during night-time conditions. During daytime the differences between the both sensors can come up to $10-15 \text{ W.m}^{-2}$. Probably these

		TECHNICAL REPORT CEA/DEN	Page 24/67
		<u>Agreement</u> : CEA V4013.001 and V4001.001 <u>Ref.</u> : CEA/DEN/CAD/DTN/SMTA/LMTE/NT/2014-11	
		<u>Date</u> : 05/02/2014	<u>Version</u> : A
	KASCADE 2013: Instruments Calibration Campaign		

differences are due to differences in body temperature. But as we are interested in night-time conditions, this is not a big issue.

The same conclusions from the previous paragraph can be drawn for the lower sensor, see Figures 11 and 12. Altogether, it means that the values for CNR4 longwave radiation can be used to calibrate CNR1 longwave radiation. This is done in Section 2.4.

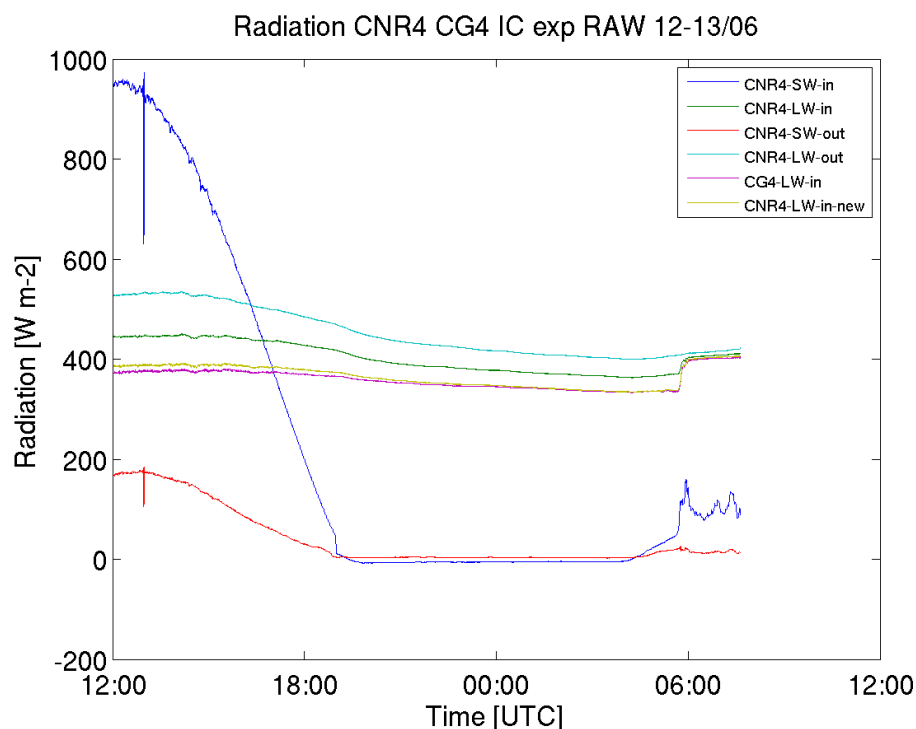


Figure 9 All radiation components measured (manufacturer coefficients, e.g. frequency in seconds) during June 12 and 13 in the infrared calibration set-up at the terrace of Laboratoire d'Aérodynamique, when CNR4 was in normal order set-up. For CNR4, all components have been shown with their Cascade-set-up (e.g. incorrect coefficients). For CNR4-LW-in-new the correct coefficient has been used.

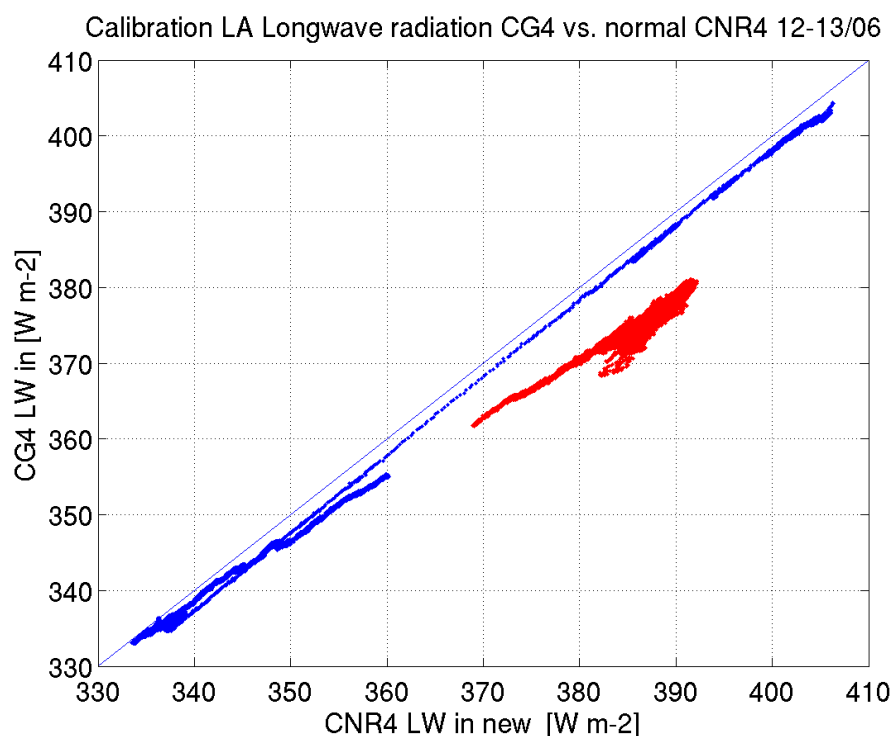


Figure 10 Comparison of CNR4 and CG4 values, the period from Figure 9 is divided into two parts : Night-time (2030 – 0730 UTC) in blue and daytime (1200 – 1925 UTC) in red.

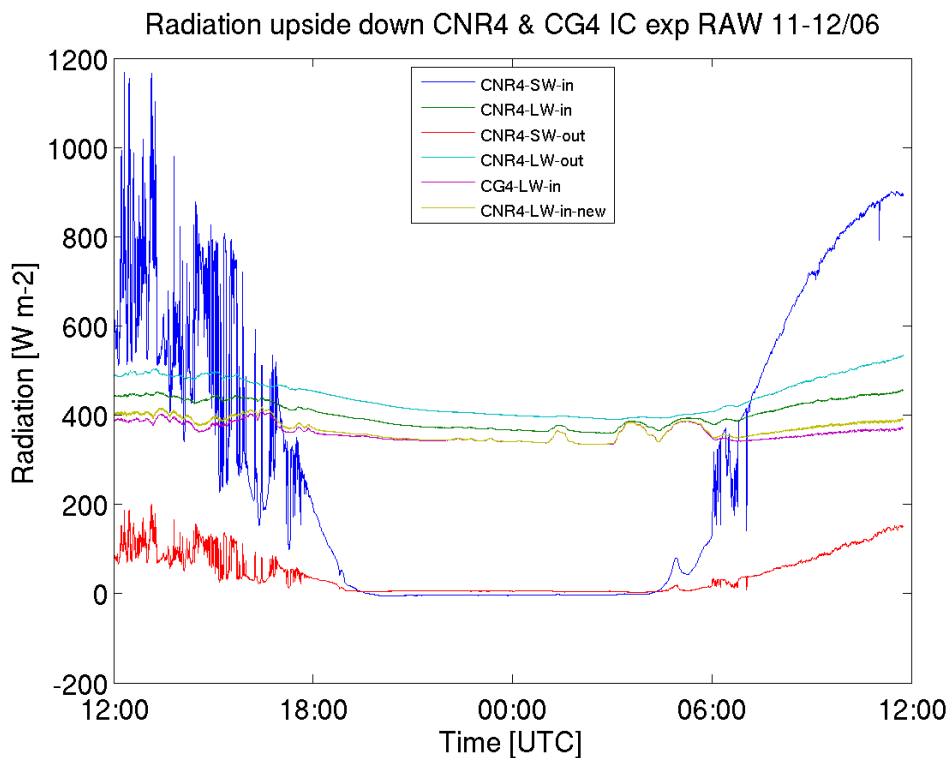


Figure 11 As Figure 9 but for CNR4 in reversed sensors and for the night from 11 to 12 June.

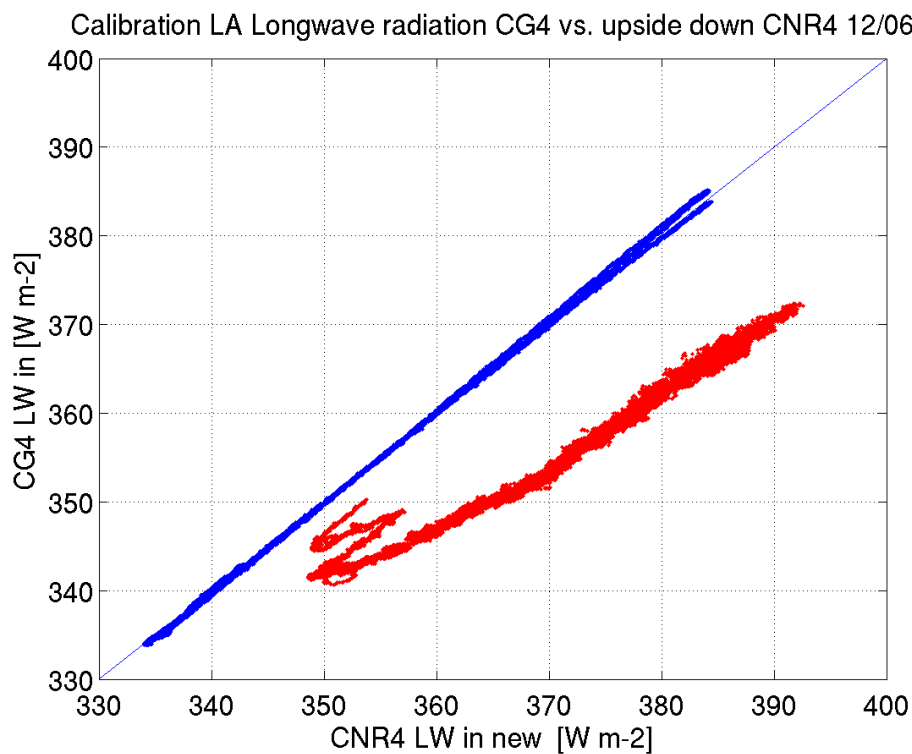



Figure 12 As Figure 10 but for 12th of June. Periods for night-time in blue and daytime in red are 0000 – 0500 UTC and 0600 – 1144 UTC, respectively.

	TECHNICAL REPORT CEA/DEN		Page 27/67
	<u>Agreement</u> : CEA V4013.001 and V4001.001		
	<u>Ref.</u> : CEA/DEN/CAD/DTN/SMTA/LMTE/NT/2014-11		
	<u>Date</u> : 05/02/2014		<u>Version</u> : A
KASCADE 2013: Instruments Calibration Campaign			

2.4 CALIBRATION LONGWAVE RADIATION CNR1

After checking the calibration coefficients for CNR4's LW_{in} and LW_{out} of Section 2.3, the CNR1 can be calibrated using the method described in this section. Both radiometers were put in the calibration experiment described in Section 1.1. 10-minute averages are used to determine the correction coefficients. A flow chart for correction procedure is given in Appendix B.

Infrared signals for CNR1 upper and lower sensors are tested for the calibration coefficient with CNR4 upper and lower sensors as reference. The method described below is applied for both upper and lower sensors, so up can be exchanged to dn , referring to upper and lower sensors, respectively. Firstly, a new calibration coefficient is approximated. For this, we plot $LW_{CNR4} - \sigma T_{CNR1}^4$ vs. V_{upCNR1} (y vs. x axis, respectively). LW_{CNR4} is our reference LW_{in} , T_{CNR1} is the CNR1's internal body temperature in Kelvin and V_{upCNR1} is the voltage output signal of CNR1 upper sensor. The inverse value of the slope will be the new coefficient k_{upCNR1} .

Hereafter, the newly found coefficient k_{upCNR1} will be applied on upper sensor (k_{dnCNR1} on lower sensor), according to the following formula:

$$LW_{CNR1int}(i) = V_{upCNR1}(i) / k_{upCNR1} + \sigma T_{CNR1}^4(i) \quad (6)$$

where $LW_{CNR1int}$ is an intermediate corrected value for longwave radiation in $W.m^{-2}$. i stands for an individual measurement. After finding the new coefficient, a likewise procedure can be followed for the body temperature correction:

$$T_{upRef}(i) = \sqrt[4]{\frac{LW_{CNR4}(i) - V_{upCNR1}(i) / k_{upCNR1}}{\sigma}} \quad (7)$$

T_{upRef} now represents the corrected body temperature for CNR1 with longwave radiation measurement corrected for the calibration coefficient in Kelvin. T_{upRef} is the value to aim for, so we perform an additional correction from T_{upRef} to the measured body temperature T_{CNR1} by calculating an offset on the mean difference between T_{upRef} and T_{CNR1} (Equation 8) and by adding this offset to the original body temperature (Equation 9). Finally the corrected value for longwave radiation is given by Equation 10.

$$\overline{T_{offsetUp}} = \frac{1}{N} \sum (T_{upRef}(i) - T_{CNR1}(i)) \quad (8)$$

$$T_{corrUp}(i) = T_{CNR1}(i) + \overline{T_{offsetUp}} \quad (9)$$

$$LW_{CNR1corr}(i) = V_{upCNR1}(i) / k_{upCNR1} + \sigma T_{corrUp}^4(i) \quad (10)$$

Data selection

Data selection was mainly focused on nights with clear skies. As the period of measurement did not have these conditions in a sufficient amount, half cloudy or cloudy dry periods were added. The data was split into 2 parts : the 1st part as a training dataset for the determination of new calibration coefficients k_{upCNR1} en k_{dnCNR1} and for correction of the radiometer's body temperature; the 2nd part serves as a validation dataset. See Table 7 for details on the data selection. In total 65.5 hours are selected for the training dataset, and 49.5 hours for the validation dataset.


		TECHNICAL REPORT CEA/DEN	Page 28/67
		<u>Agreement</u> : CEA V4013.001 and V4001.001 <u>Ref.</u> : CEA/DEN/CAD/DTN/SMTA/LMTE/NT/2014-11	
		<u>Date</u> : 05/02/2014	<u>Version</u> : A
	KASCADE 2013: Instruments Calibration Campaign		

Table 7 Selected data during intercomparison experiment at CRA, used for the calibration of CNR1.

	Date	hhhh-hhhh	Observations (cloud cover in okta's)
<i>Training dataset</i>	24/04 – 25/04	1630-0520	0/8
	25/04 – 26/04	1840-0540	4/8 at start, gradually getting to 8/8 at night
	29/04 – 30/04	1900-0520	6/8 to 8/8
	04/05	0000-0520	No sky view available
	04/05 – 05/05	1850-0430	No sky view available
	11/05	0000-0420	6/8
	11/05 – 12/05	1850-0430	6/8
<i>Validation dataset</i>	05/05	0000-0540	No sky view available
	05/05 – 06/05	1840-0430	No sky view available
	06/05 – 07/05	1840-0440	No sky view available
	07/05	1900-2350	4/8 ; some spells during night
	14/05	0000-0420	5/8 to 8/8.
	14/05	1900-2350	No observations available
	26/05 – 27/05	1920-0410	0/8

2.4.1 Upper sensor

The calibration coefficient k_{upCNR1} for night-time data was defined as $10.0321027 \mu V/(W.m^{-2})$. Measured data for determination is shown in Figure 13. We are interested in the slope only, therefore outlying data points were excluded from the dataset.

The offset for body temperature was defined as $T_{offsetUpCNR1} = 0.53238676$ Kelvin, after applying equations 8 to 10. The new LW_{inCNR1} was calculated with the validation dataset and compared with LW_{inCNR4} . See Figure 14 for the performance of the corrections.

The mean difference between the sensors is improving every correction, visible in the validation dataset. Without correction this value is $-4.17 W.m^{-2}$. When we correct for the calibration coefficient, the mean difference is $-2.80 W.m^{-2}$ whereas it comes to $-0.07 W.m^{-2}$ when we apply the correction for body temperature.

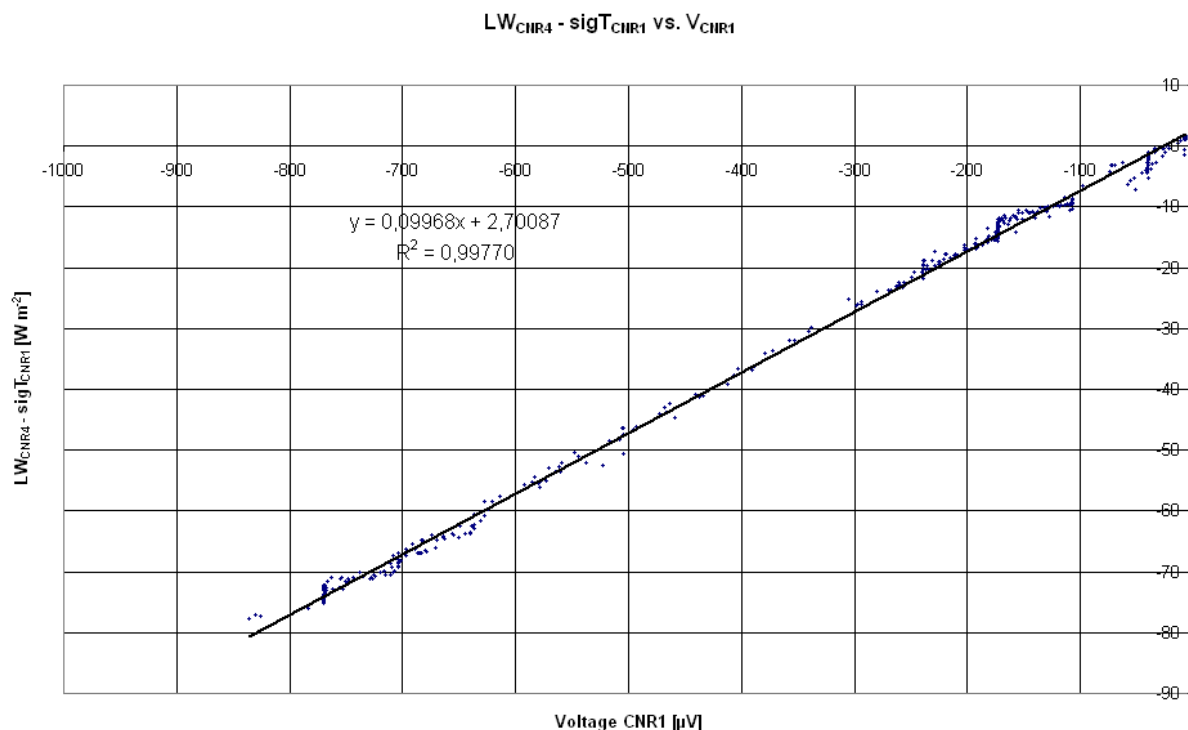


Figure 13 New calibration coefficient for CNR1 upper sensor (k_{CNR1up}). The slope indicates the value for k .

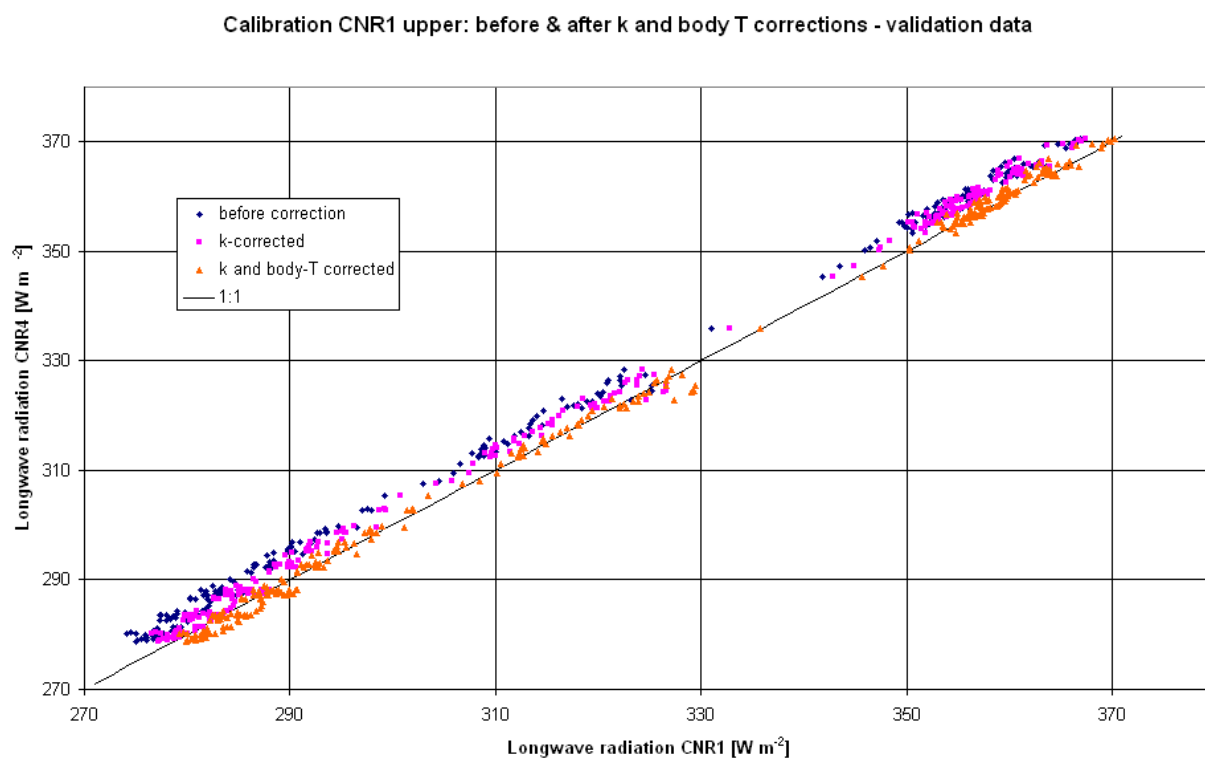



Figure 14 Validation dataset, longwave radiation reference CNR4 and CNR1 upper sensors before and after applying the calibration coefficient (k -corrected) and body temperature (k - and body T -corrected).

	TECHNICAL REPORT CEA/DEN		Page 30/67
	Agreement : CEA V4013.001 and V4001.001		
	Ref. : CEA/DEN/CAD/DTN/SMTA/LMTE/NT/2014-11		
	Date : 05/02/2014		Version : A
KASCADE 2013: Instruments Calibration Campaign			

2.4.2 Lower sensor

For the determination of the lower sensor of CNR1, the same procedure has been followed as for the upper sensor, see Section 2.4.1. Also the same dataset has been used, resulting in $k_{dnCNR1} = 11.2384806 \mu V/(W.m^{-2})$ and $T_{offsetDnCNR1} = 0.61959007$. Determination of k_{dnCNR4} is shown in Figure 15 and the performance of the corrections is demonstrated in Figure 16.

Also here the improvement is clearly visible after every correction, regarding the validation dataset: The mean difference of non-corrected sensors is $-4.53 W.m^{-2}$. After correction for k_{dnCNR1} : $-3.22 W.m^{-2}$. When applying the body temperature correction the mean difference has been reduced to $0.03 W.m^{-2}$.

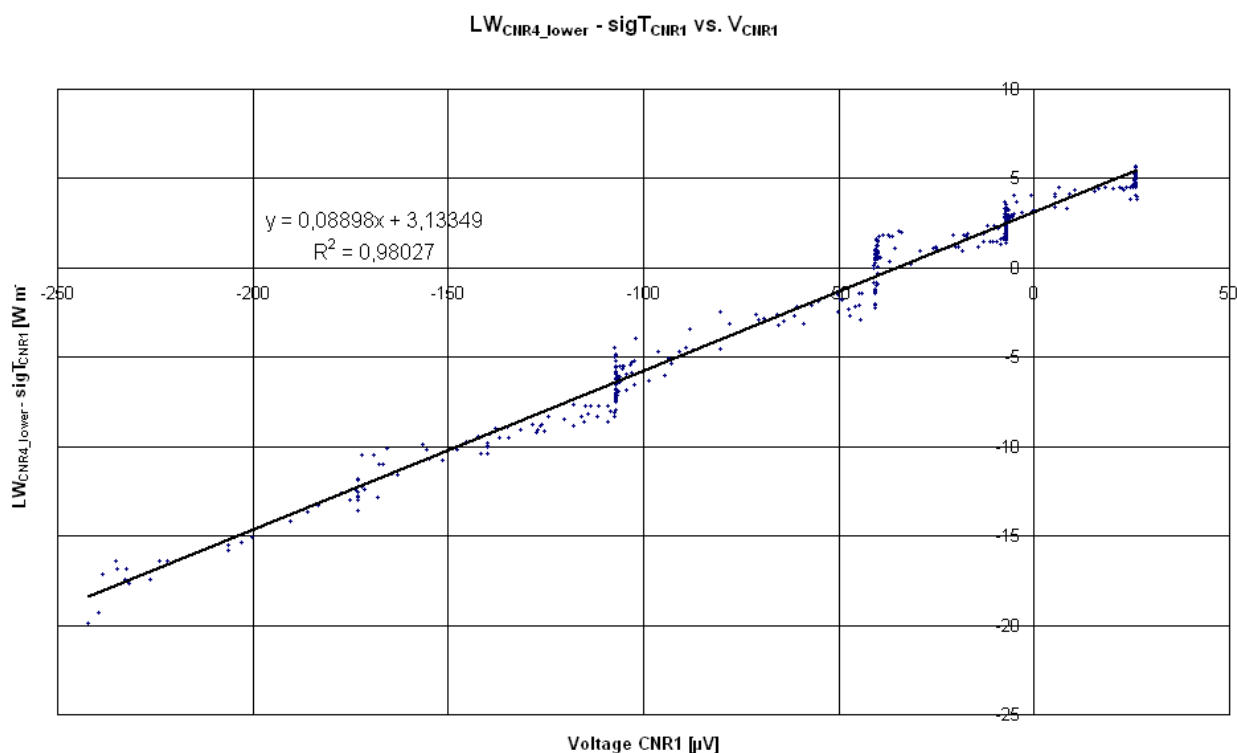


Figure 15 As Figure 13, for the lower sensor: k_{dnCNR1}

Calibration CNR1 lower: before & after k and body T corrections - validation data

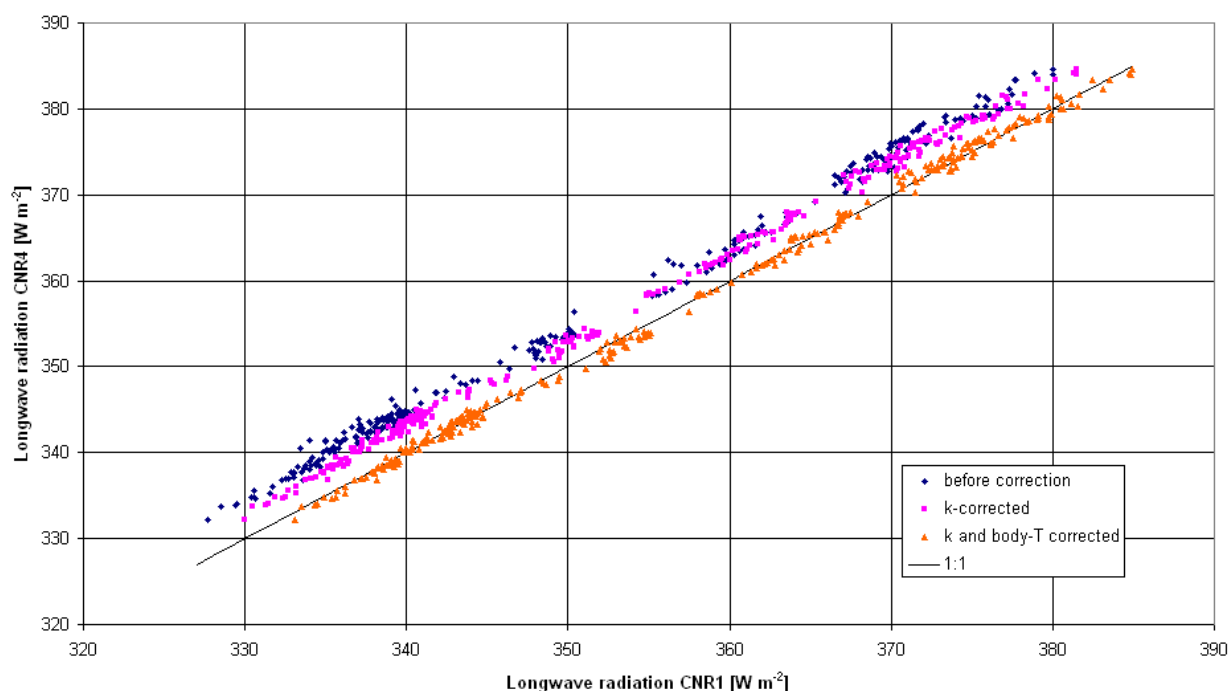


Figure 16 Validation dataset, longwave radiation reference CNR4 and CNR1 lower sensors before and after applying the calibration coefficient (k-corrected) and body temperature (k- and body T-corrected).

2.5 CORRECTION SHORTWAVE RADIATION FOR CNR1

The incoming and outgoing shortwave radiation components of CNR4 (SW_{inCNR1} and $SW_{outCNR1}$) will be of reference for calibration of CNR1's shortwave radiation components SW_{inCNR1} and $SW_{outCNR1}$. For data selection all sunny days were used with extensions of lightly cloudy to cloudy days. See Table 8 for the distinction between the training and validation dataset.

Table 8 Selected data for the calibration of the shortwave components from CNR1


	<i>Data</i>	<i>Hours [UTC]</i>	<i>Remarks</i>
<i>Training dataset</i>	24/04	1630 – 1840	0/8 Partly : Installation day
	05/05	0440 – 1850	2/8 Fair weather clouds
	06/05	0440 – 1850	0/8 Fair weather clouds in afternoon
	26/05	0530 – 1900	0/8
	27/05	0420 – 0720	2/8 Malfunction CR3000 : only early morning data available
<i>Validation dataset</i>	25/04	0520 – 1840	0/8 at start, gradually getting to 8/8 at night.
	29/04	0450 – 0920	6/8 to 8/8
	01/05	0900 – 1830	No sky view available ; before 09 UTC dew
	04/05	0450 – 1850	No sky view available
	07/05	0440 – 1850	8/8 ; some spells during night
	11/05	0430 – 1830	6/8
	14/05	0440 – 1900	5/8 to 8/8

2.5.1 Upper sensor

For the determination, 287 bins of 10 minute averages were used. The regression curve has been forced to 0. After several tries with linear and polynomial regression, the correction of CNR1's upper sensor ($SW_{inCNR1corr}$) appeared to have the best result by using a 2nd order polynomial fit:

$$SW_{inCNR1Corr} = 1.06545 \cdot SW_{inCNR1} + -3.69973E - 5 \cdot SW_{inCNR1}^2 \quad (11)$$

See Figure 17 for the regression curve on the training data. The quality of correction according to equation 11 has been tested with the validation dataset from Table 8. Results are shown in Figure 18.

	TECHNICAL REPORT CEA/DEN		Page 33/67
	<u>Agreement</u> : CEA V4013.001 and V4001.001		
	<u>Ref.</u> : CEA/DEN/CAD/DTN/SMTA/LMTE/NT/2014-11		
	<u>Date</u> : 05/02/2014		<u>Version</u> : A
KASCADE 2013: Instruments Calibration Campaign			

Incoming shortwave radiation correction CNR1 vs. CNR4

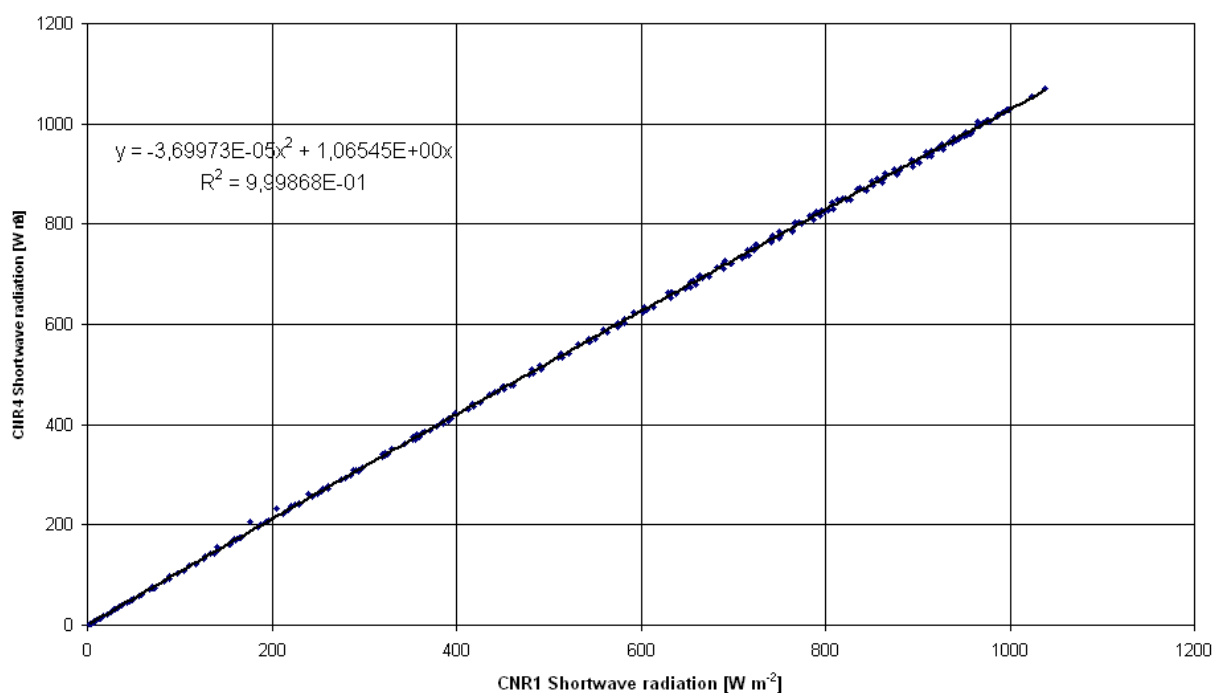


Figure 17 Incoming shortwave radiation regression curve.

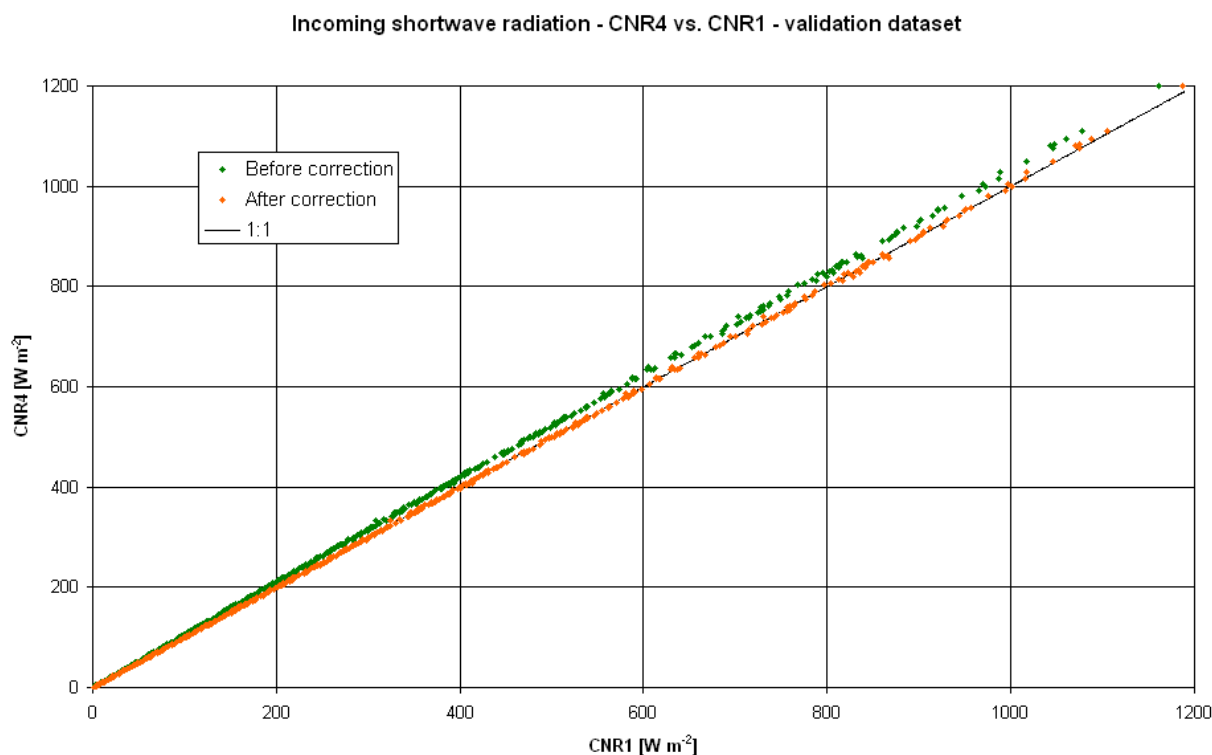


Figure 18 Incoming shortwave radiation, for validation dataset.

2.5.2 Lower sensor

For the correction of SW_{out} , mainly the same dataset has been used as for SW_{in} , in total 283 bins of 10 minute averages were used. The regression curve has been forced to 0. After several tries with linear and polynomial regression, a 2nd order polynomial fit appeared to yield the best result for correction of CNR1's lower sensor ($SW_{outCNR1corr}$) :

$$SW_{outCNR1Cor} = 1.06637 \cdot SW_{outCNR1} + -3.27150E-4 \cdot SW_{outCNR1}^2 \quad (12)$$

See Figure 19 for the regression curve of equation 12 and the training dataset. Validation dataset results are shown in Figure 20.

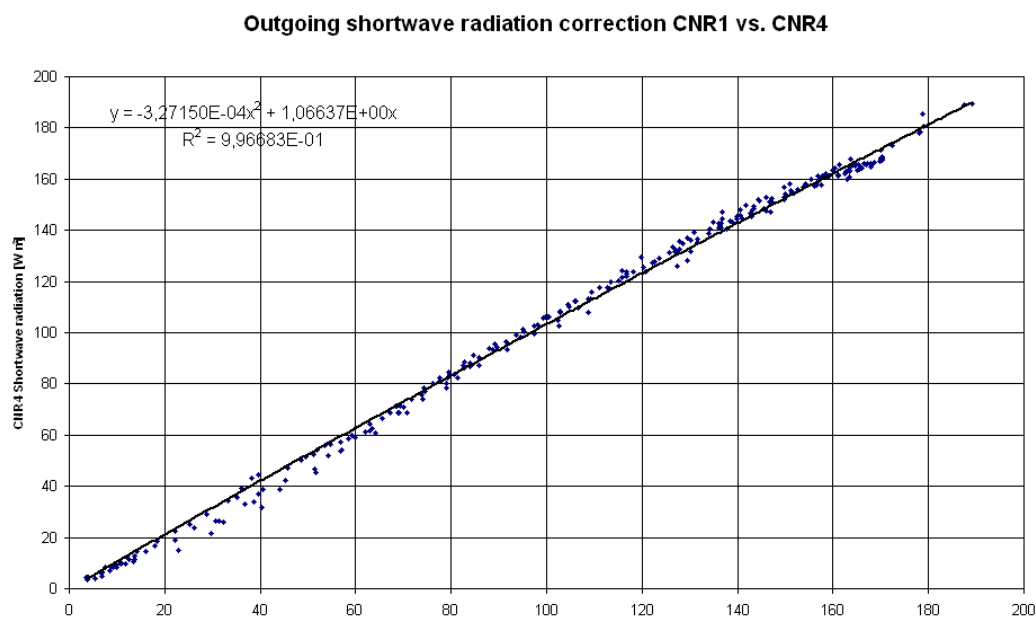


Figure 19 Outgoing shortwave radiation correction

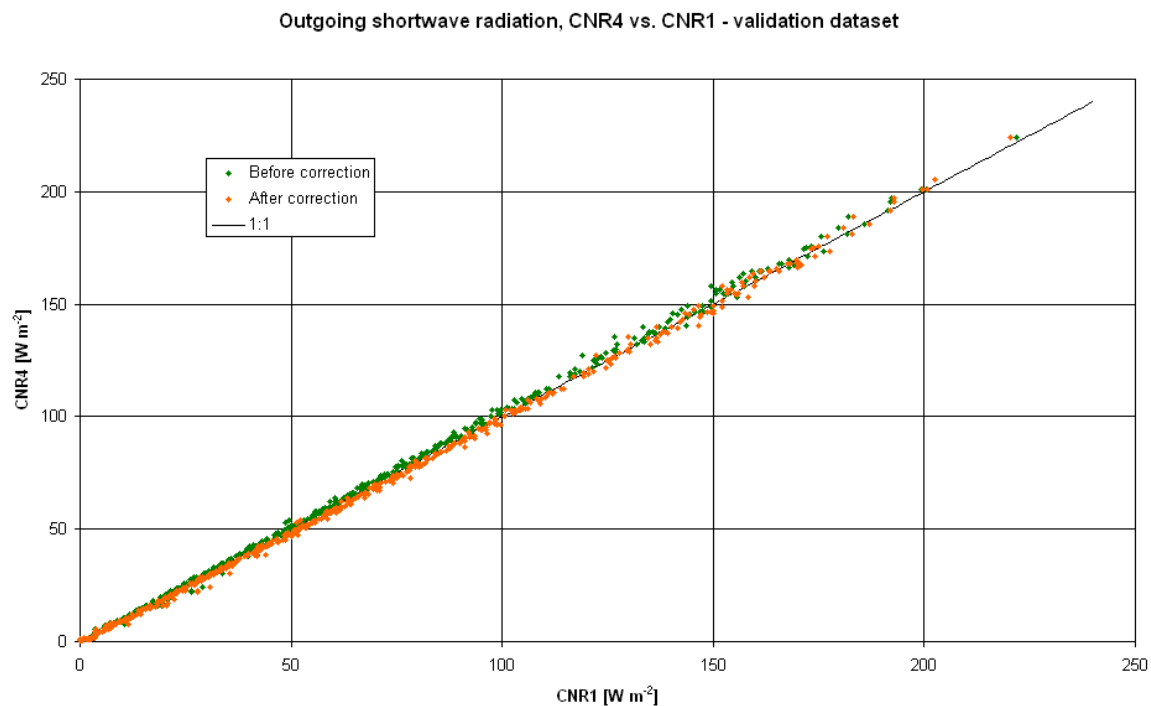


Figure 20 Outgoing shortwave radiation, for validation dataset.

2.6 COMPARISON RADIATION COMPONENTS CRA-EXPERIMENT

See Figure 21 for a comparison between LW-radiation components of CNR1 and CNR4 during a clear sky period present in the intercomparison set-up at CRA. A permanently installed CNR1 at 60m height ($LW_{in-CNR1-60m}$) is shown as an extra reference for LW_{in} . The corrected LW_{in} for CNR1 show good agreement with CNR4 during nighttime conditions (e.g. 00-05 UTC). Measurement differences are around $1-3 \text{ W.m}^{-2}$, also demonstrated in Figure 23 (top left). This difference lies within the range of uncertainty for longwave radiation measurements (Phillipona et al. 1995). Also shown in Figure 23 are the comparisons between the other radiative components corrected for CNR1. The difference between $LW_{outCNR4corr}$ and $LW_{outCNR1corr}$ has been reduced from $\sim 10 \text{ W.m}^{-2}$ to less than 2 W.m^{-2} . The corrections for $SW_{inCNR1corr}$ and $SW_{outCNR1corr}$ lead to improvement in biases from 20 (not shown) to less than 5 W.m^{-2} .

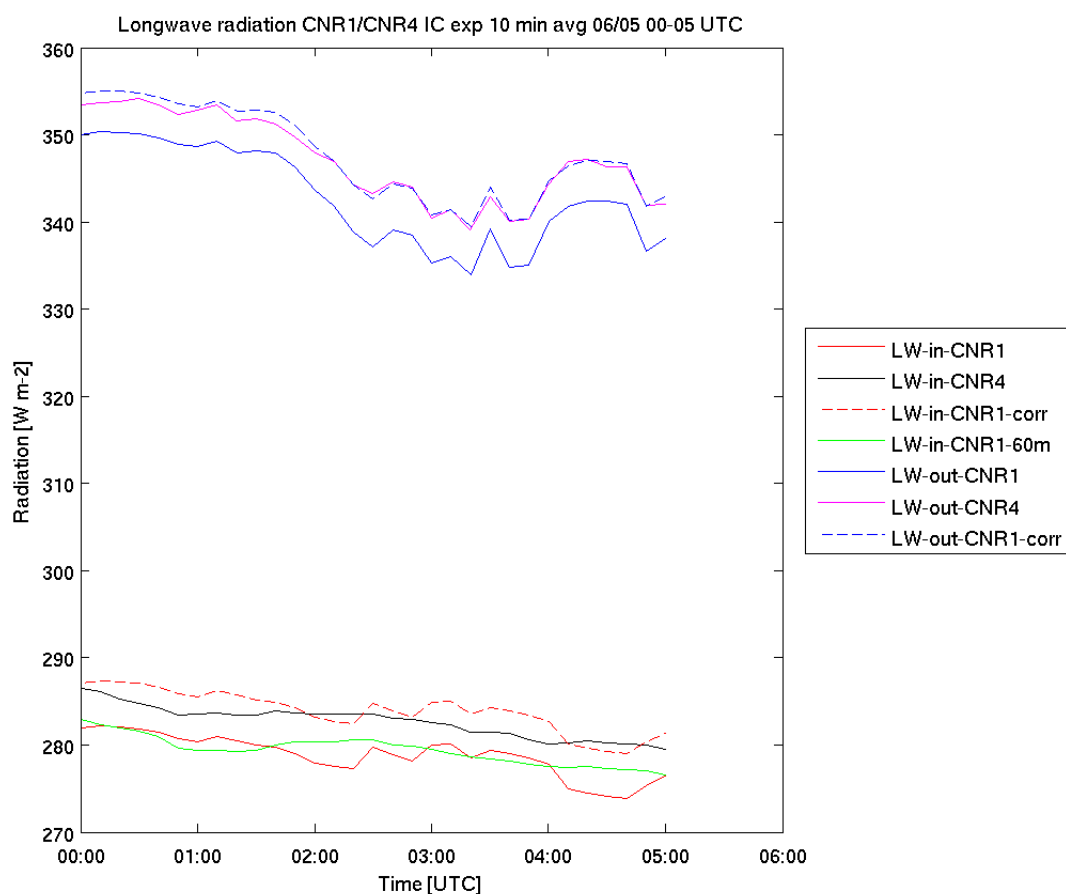


Figure 21 Nighttime radiative components for a radiative cooling night with original and corrected (-corr) values.

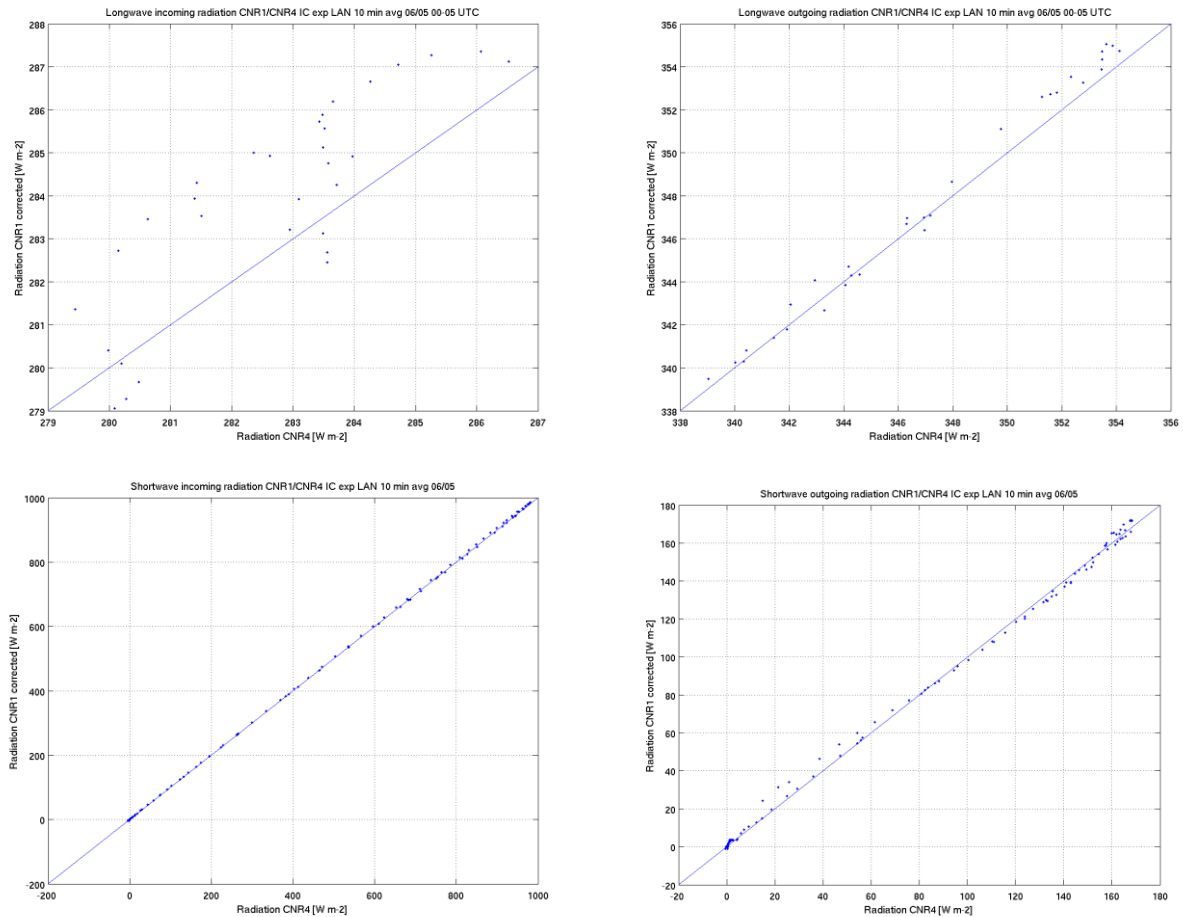


Figure 22 All radiation components for CNR1 and CNR4, after corrections explained in this chapter, for 06/05, LW_{in} and LW_{out} from 00-05 UTC.

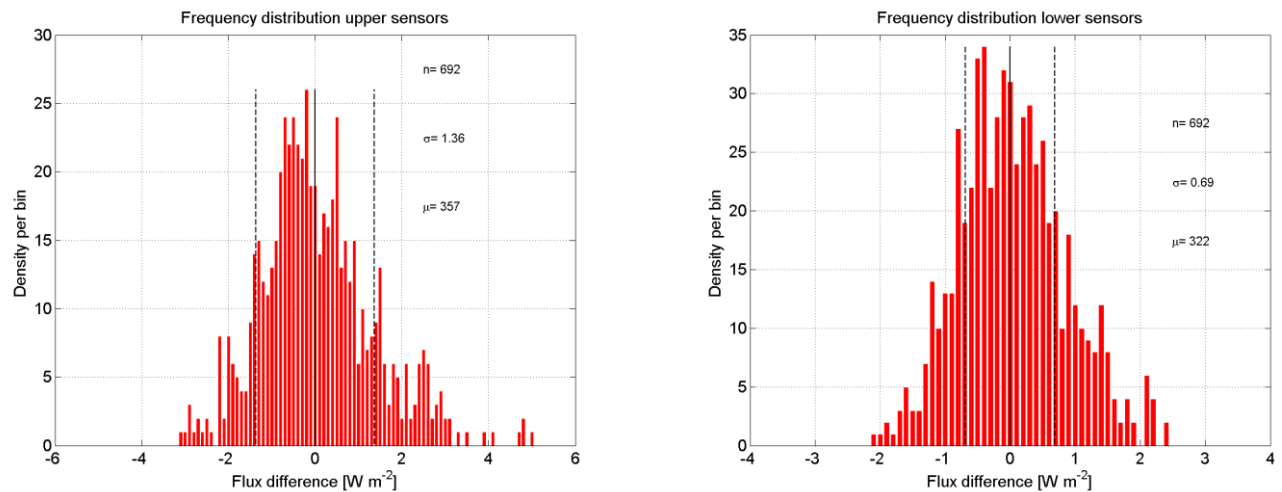



Figure 23 Flux difference distribution between CNR1 and CNR4 for upper and lower infrared sensors during IC-campaign in Lannemezan.

	TECHNICAL REPORT CEA/DEN		Page 38/67
	Agreement : CEA V4013.001 and V4001.001		
	Ref. : CEA/DEN/CAD/DTN/SMTA/LMTE/NT/2014-11		
	Date : 05/02/2014		Version : A
KASCADE 2013: Instruments Calibration Campaign			

2.7 UNCERTAINTY LONGWAVE HEATING RATE

It's beyond the scope of this report to go into detail of the concept of LW-divergence (see Introduction), but because of its importance for SBL-development during the KASCADE-experiment, we devote this section to the uncertainty of LW-difference, defined by:

$$\delta \Delta L W_{z_1}^{z_2} = [(\delta \Delta L W^{\downarrow})^2 + (\delta \Delta L W^{\uparrow})^2]^{1/2} \quad (13)$$

Where each term on the right hand side represents the measurement error of the flux difference between the two net radiometers CNR4 and CNR1 for its incoming or outgoing component, respectively. The term on the left hand side of the equation represents the total measurement uncertainty for LW-divergence between CNR4 at z_2 and CNR1 at z_1 .


The uncertainties $\delta \Delta L W^{\downarrow}$ and $\delta \Delta L W^{\uparrow}$ are estimated at 1.36 and 0.69 W.m⁻², respectively (see Figure 23). For this estimation both training and validation dataset were used after applying the corrections for k and T_{offs} . This leads to a total measurement uncertainty of 0.94 W.m⁻². With Equation 4 we come to a total uncertainty for LHR of 0.15 °C.h⁻¹. The uncertainties for LHR by its separate components for incoming and outgoing LW-radiation are estimated 0.21 and 0.11 °C.h⁻¹, respectively.

2.8 SUMMARY

Table 9 gives an outlook on all calibration coefficients and body temperature offset for the CNR1 determined in this chapter. In addition it provides the regression coefficient and standard deviations calculated for the derived components. The calibration range is given in the last 2 columns. Please note that these ranges of validity are not wide enough to extrapolate to the KASCADE-dataset. Differences are quickly obtained, as the measurement campaign and the intercomparison experiment were not conducted at the same time and location. However, other possible influences (clear sky, radiative cooling nights) during the calibration experiments were set as close to the desired conditions as possible. Consequently the found correction coefficients can be used confidently.

Table 9 Summary of the calibration coefficients (k) and body temperature correction (T_{offs}), determined for CNR1's radiation components and their regression coefficients (R^2). *coeff1* and *coeff2* refer to the correction coefficients from Equations 11 and 12. For body temperature correction a standard deviation is given. The last 2 columns show the validity range of the coefficients (LAN) and the range measured during KASCADE (KCD). The * for SW_{out} was measured when a fresh snow layer covered the surface, the value between brackets represents the highest value measured for a bare surface.

	k	R^2	T_{offs}	<i>stdev</i>	Range (LAN)	Range (KCD)
	[μV/W.m ⁻²]	[-]	[K]	[W.m ⁻²]	[W.m ⁻²]	[W.m ⁻²]
CNR1 LW_{in}	10.0321027	0.9977	0.53238676	0.2500	278 – 369	194.6 – 409.2
CNR1 LW_{out}	11.2384806	0.98027	0.61959007	0.1701	333 – 385	244.0 – 434.1
	<i>coeff1</i>	<i>coeff2</i>	R^2		Range (LAN)	Range (KCD)
	[-]	[-]	[-]		[W.m ⁻²]	[W.m ⁻²]
CNR1 SW_{in}	1.06545	-3.69973E-05	0.99987		0 – 1100	0 – 1135.0
CNR1 SW_{out}	1.06637	-3.27150E-04	0.99668		0 – 200	0 – 593.3* (146.7)

	TECHNICAL REPORT CEA/DEN		Page 39/67
	Agreement : CEA V4013.001 and V4001.001		
	Ref. : CEA/DEN/CAD/DTN/SMTA/LMTE/NT/2014-11		
	Date : 05/02/2014		Version : A
KASCADE 2013: Instruments Calibration Campaign			

CHAPTER 3. THERMOHYGROMETERS

3.1 GENERAL REMARKS

Two thermohygrometers were used during KASCADE, HMP45 (Campbell – LA) and HC2S3 (Campbell – LMTE) and installed on a 30 meter mast at 2 different levels : HMP45 at 30.36 meters and HC2S3 at 1.90 meters. As both thermohygrometers are different sensors measuring at different heights, it is important to compare and potentially calibrate these sensors before, which is done in the intercomparison experiment at CRA. See Table 2 for properties, measurement heights and pole alignments during this experiment. Figure 1 and Table 3 show the measurement set-up, and horizontal separation between the 2 sensors, respectively.

The first two days, April 24 and 25, were installation days and therefore excluded from the analysis. In addition, due to equipment malfunction of HC2S3, between May 2 (0300 UTC) and May 13 (1530 UTC) there is no data available: the wiring inside the sensor was damaged, probably due to water which had infiltrated inside the sensor. After detection, the problem has been solved rapidly. However, this part of the data cannot be used for the corrections and is therefore excluded as well.

For data selection used for the determination of the correction coefficients, see Table 10. The selection was mainly focused on getting the full range of values measured during the experiment to be able to get a good correction coefficient. For the determination 10-minute averages are used, in total this is 158 hours of measurements.

Also for validation of the thermohygrometers 10-minute averages have been used.

Section 3.2 deals with the procedure on temperature, section 3.3 for relative humidity. In Appendix B a flow chart is given on the correction procedures for thermohygrometers. In Appendix C-2 technical specifications for both sensors are given.

Table 10 Data selection for thermohygrometer's temperature correction

date	Hours [UTC]	Remarks
28/04	0000-2400	-
29/04	0000-2400	-
14/05	0000-2400	-
25/05	0000-2400	-
26/05	0000-2400	-
27/05	0000-0720	Acquisiton failure
04/06	0000-2400	-
05/06	0000-1140	End of measurements

3.2 TEMPERATURE CORRECTION

The measurement range during KASCADE was from -11°C during cold nights to +15°C during sunny afternoons. Unfortunately, by the time of installation of the intercomparison experiment it was impossible to observe temperatures below zero degrees, the range of temperature measurements was between 1°C and 22 °C. For the final intercomparison, days were selected to obtain a range as close as possible to the actual KASCADE range, see Table 10 for period of interest.

For the correction, first the average was taken between the measured values for temperature for HMP45 (T_{HMP45}) and HC2S3 (T_{HC2S3}) which is considered to be the reference temperature T_{ref} .

$$T_{ref}(i) = (T_{HMP45}(i) + T_{HC2S3}(i)) / 2 \quad (14)$$

Again i denotes an individual measurement. The measured value T_{HMP45} will be extracted from T_{ref} and after averaging we get the correction value T_{corr} , which is a constant:

$$T_{corrHMP45} = \overline{T_{ref}(i) - T_{HMP45}(i)} \quad (15)$$

Adding the correction value T_{corr} to the the measured T_{HMP45} we get our new corrected temperature value T_{HMP45} :

$$T_{HMP45New}(i) = T_{corrHMP45} + T_{HMP45}(i) \quad (16)$$

For T_{HC2S3} the same method is followed, but basically this is the opposite value of T_{HMP45} .

After calculation, $T_{corrHMP45} = 0.0013$ and $T_{corrHC2S3} = -0.0013$. It is a minor difference. Figure 24 shows all measured values during the experiment, except the first two days and 2 to 13 May, as explained in Section 3.1.

$R^2 = 0.99974$ and the offset = -0.00072 °C. Considering the measurement accuracy (+/- 0.2°C at 20°C to +/- 0.3 °C at 0°C, given by the sensor documentation in Appendix C-2), the values show that a correction is unnecessary. The temperature values for the thermohygrometers will not be corrected.

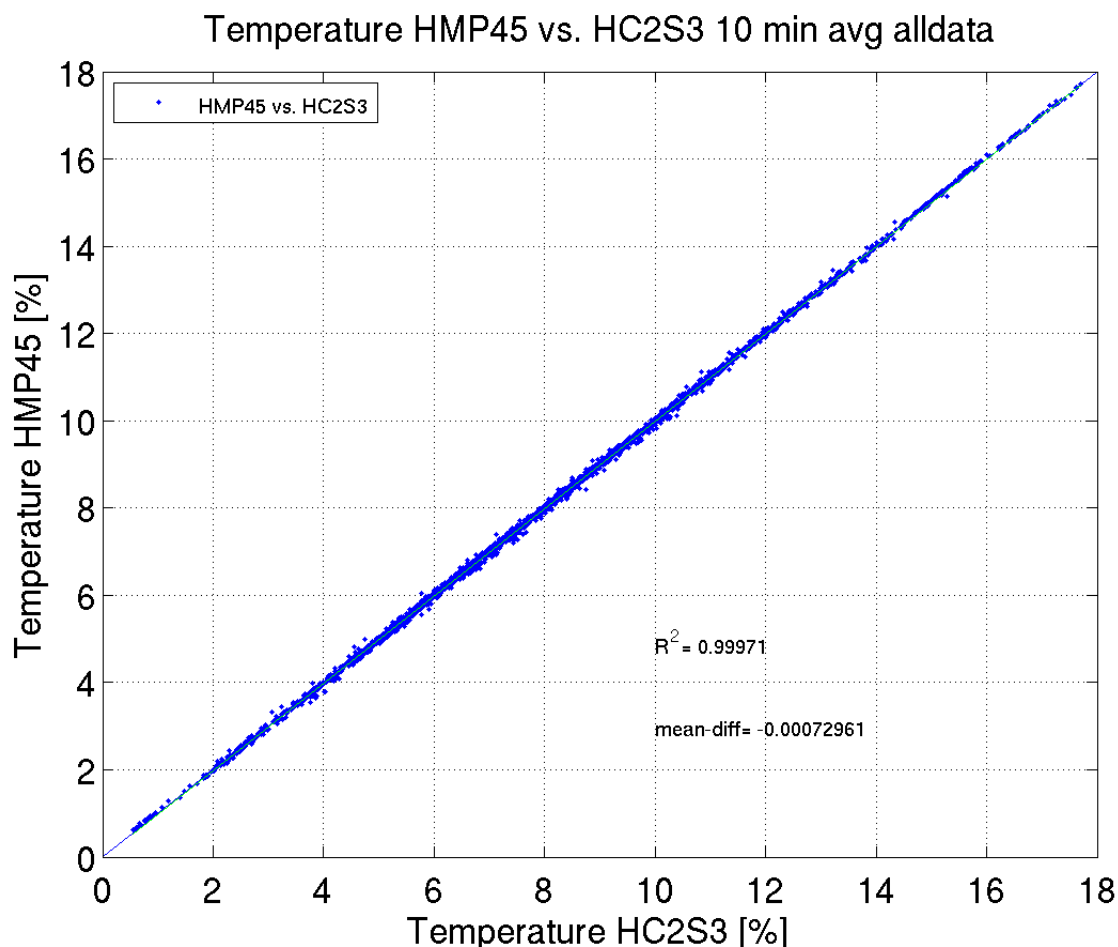


Figure 24 10 minute averages of temperature between HMP45 and HC2S3, all data, 2-13 May excluded (see text for explanation). 24 and 25 April were excluded as well. The blue line is defined as the 1:1 line.

3.3 RELATIVE HUMIDITY CORRECTION

For correction of relative humidity measured with the thermohygrometers, mainly the same strategy is followed as for temperature, Section 3.2. Also the same time range of the dataset was selected for the correction. First we define a reference value which is the average of the 2 measurements values at the same time:

$$RH_{ref}(i) = (RH_{HMP45}(i) + RH_{HC2S3}(i)) / 2 \quad (17)$$

The best performance for correcting RH_{HMP45} and RH_{HC2S3} could be yield by performing a 2nd order polynomial fit regression against RH_{ref} , see Figure 25. The regression curve has been forced to zero. The correction coefficients for this polynomial fit for $RH_{HMP45New}$ and $RH_{HC2S3New}$ are defined as:

$$RH_{HMP45New}(i) = 0.929888 \cdot RH_{HMP45}(i) + 4.45229E-04 \cdot RH_{HMP45}^2(i) \quad (18)$$

$$RH_{HC2S3New}(i) = 1.08136 \cdot RH_{HC2S3}(i) + (-6.00573E-04) \cdot RH_{HC2S3}^2(i) \quad (19)$$

Intercomparison hygrometers HMP45 and HC2S3: Relative Humidity

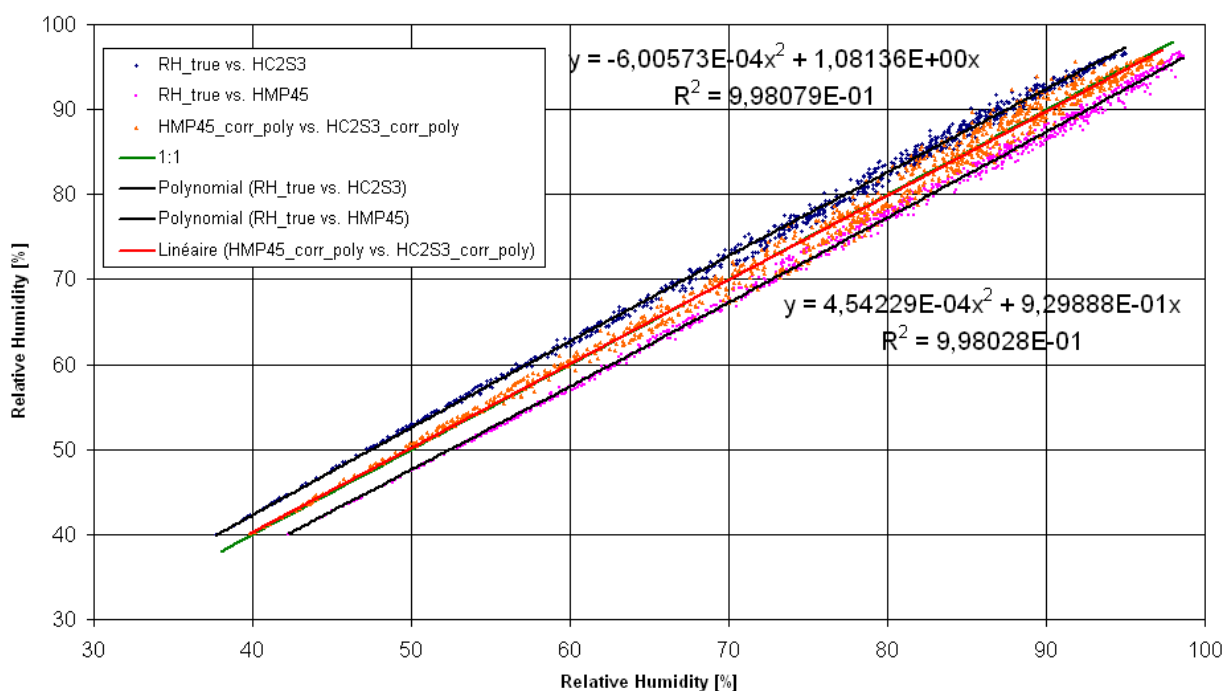


Figure 25 RH_{ref} vs. RH_{HC2S3} (blue) ; RH_{ref} vs. RH_{HMP45} (purple) and the corrected values for $RH_{HMP45New}$ vs. $RH_{HC2S3New}$ (orange), red line gives the linear trend for the latter. 1:1 line is given in green. See Table 10 for data selection.

Figure 26 shows the values for both thermohygrometers before and after correction for all data selected in Table 10. However the broken wire of HC2S3 seemed to affect only temperature values directly, it is unclear what could be the influence for relative humidity. Hence, these data are not used in the figure and this analysis.

The mean difference before correction between both thermohygrometers was determined at 5.263 %, after correction it is 0.08043 %. The improvement after correction is significant, so the correction coefficients will be used.

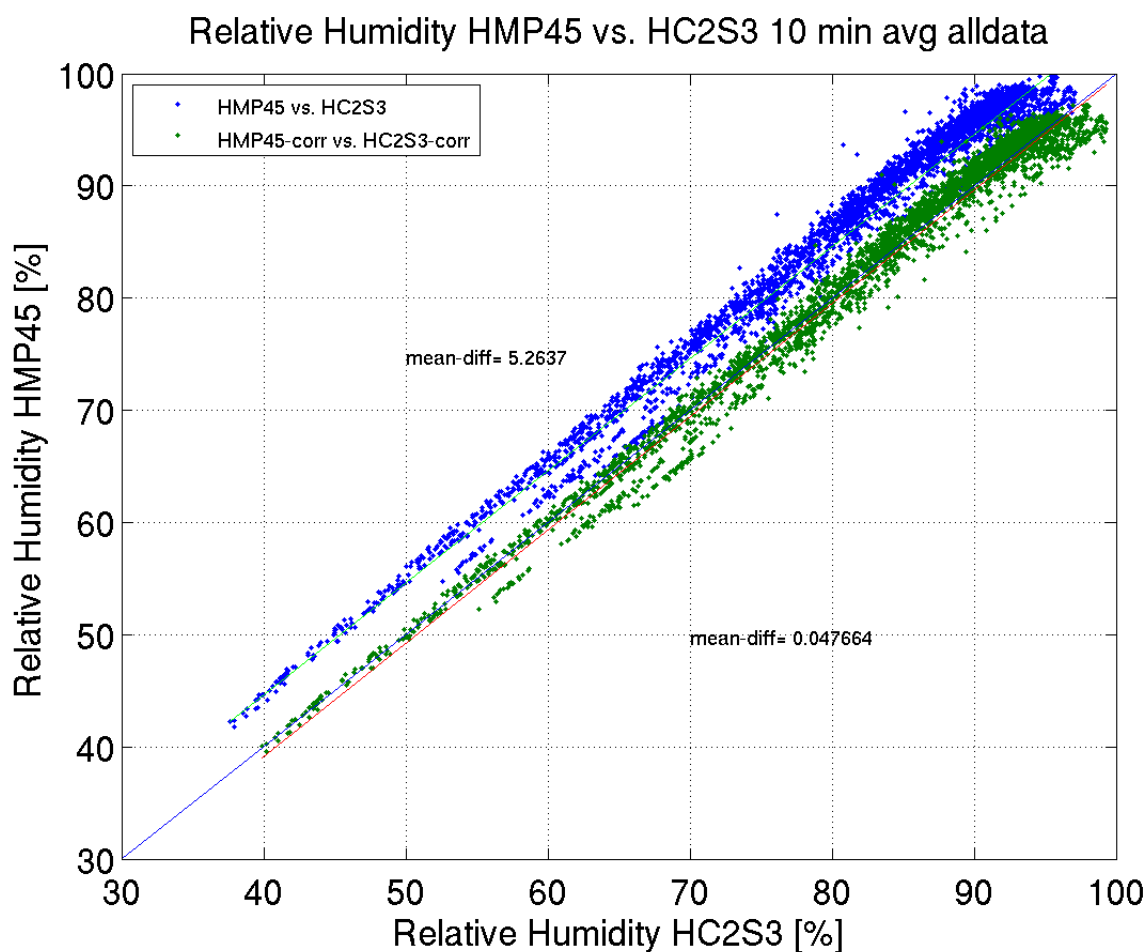



Figure 26 Relative humidity for both thermohygrometers before and after correction. The mean difference values show a large improvement after corrections. For this validation, all data measured during the intercomparison campaign has been used.

	TECHNICAL REPORT CEA/DEN		Page 43/67
	Agreement : CEA V4013.001 and V4001.001		
	Ref. : CEA/DEN/CAD/DTN/SMTA/LMTE/NT/2014-11		
	Date : 05/02/2014		Version : A
KASCADE 2013: Instruments Calibration Campaign			

CHAPTER 4. TTB-SONDES

4.1 GENERAL DESCRIPTION AND APPROACH

One calibration/intercomparison experiment was conducted for the 4 working TTS on the 14th of May, between 0400 and 1345 UTC, see Table 11 for details and Figure 2 for an impression. At the start, a clear sky was present with 2m-temperatures around 10°C at a low wind speed (< 1 m/s). After sunrise, temperature and wind speed gradually increase till 20°C and between 2-4 m/s, respectively. Atmospheric pressure decreased from ~947 to 940 hPa. Relative humidity decreased from 80-90 % to 60-80 % at the end of the experiment.

The TTSs measure pressure, temperature, wind speed, wind direction and relative humidity (RH). The wind direction has been calibrated before every IOP by performing a standard procedure, and this data is directly ready to use.

For corrections of the sondes temperature and relative humidity, an analogous procedure has been followed : The Ground Level sonde (GL-sonde) 402, present at almost every IOP, has been calibrated against the thermohygrometer HC2S3, which was fixed at the flux tower at 1.90 meters height. Subsequently, the corrected GL-sonde acts as a reference probe for the other sondes mentioned in Table 11. In this part, the sondes were corrected by using all intercomparison experiments conducted during KASCADE and the IC-experiment in Lannemezan in which sonde 402 and the sonde-to-correct were present. Details on these procedures are explained in the section on Temperature (4.2) and Relative Humidity (4.4).

For pressure and wind speed first averages were calculated between the sondes 405, 404, 403, 402 which were present during the consecutive IOPs 16-23. After this, correction coefficients were found by comparing to this average. Sonde 401 was corrected against one corrected sonde. See sections 4.3 (wind speed) and 4.5 (pressure) for details. A detailed table on the sequence of the TTSs during ICs is given in Appendix A. Flow charts for the correction procedures are given in Appendix B. Technical specifications of the TTSs are given in Appendix C-3.

Table 11 Tethered balloon sondes used during the intercomparison experiment in Lannemezan

Manufacturer	Frequency [MHz]	Serial nr.	Remarks
Vaisala	405	W4834144	
Vaisala	404	C0829547	RH not reliable
Vaisala	403	W4834323	Sensor used from IOP 16
Vaisala	402	W4834334	
Vaisala	401	W4834332	Wire is broken, not used


4.2 TEMPERATURE

4.2.1 Temperature correction 402

4.2.1.1 Correction during IC-experiment Lannemezan

See Figure 27 for the measurements of temperature during the IC-experiment in Lannemezan. At first it was the set-up intended for the correction of the TTSs. For temperature and relative humidity (see Section 4.4) it was impossible to use the dataset collected in this manner. There were 2 main reasons for this:

The difference in height between both thermohygrometers and the TTSs appeared to be too large. The thermohygrometers were installed at around 2.50 meters (see Table 1) while the tethersondes were placed at the wooden bench on top of two chairs, and had a measurement height of 0.50 meter. The measurements at different

	TECHNICAL REPORT CEA/DEN		Page 44/67
	Agreement : CEA V4013.001 and V4001.001		
	Ref. : CEA/DEN/CAD/DTN/SMTA/LMTE/NT/2014-11		
	Date : 05/02/2014		Version : A
KASCADE 2013: Instruments Calibration Campaign			

heights in this part of the surface layer will cause an undesired offset, clearly shown by Figure 27.

Secondly, the IC-experiment has been conducted too late in the year, and therefore it was impossible to have the same temperatures measured as during KASCADE, a crucial need for a quantity as temperature. Correction coefficients would not be valid because the measurements during the IC-experiment were between 10 – 18 °C while the sondes during the campaign measured temperatures between minus 8 to plus 12 °C. Therefore, another procedure is needed.

Nonetheless, the data obtained during the IC-experiment at Lannemezan can be used for the intercomparison between the corrected GL-sonde 402 and the other sondes, see Section 4.2.2.

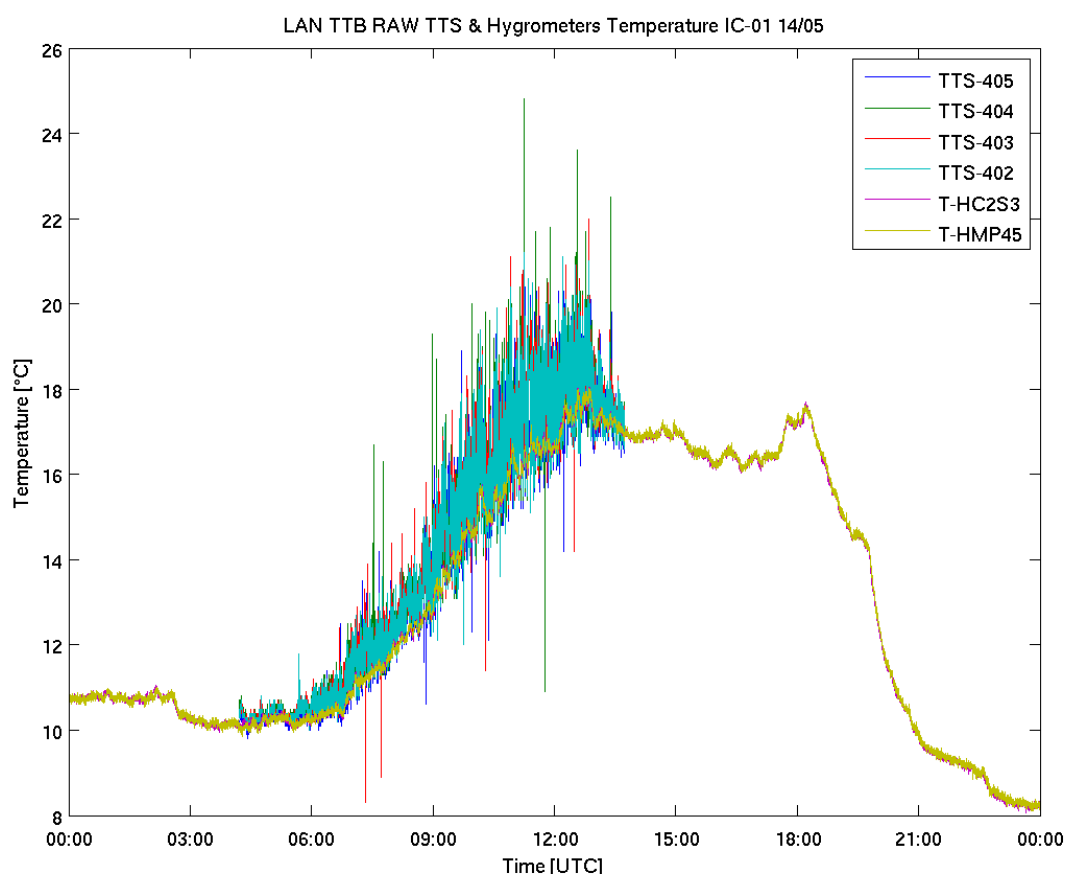



Figure 27 IC-experiment for TTS in Lannemezan at 14/05, temperature for the both thermohygrometers and all working sondes of the TTB.

4.2.1.2 Correction during neutral conditions using KASCADE dataset

We can use the KASCADE-dataset in order to correct the tethersondes with a thermohygrometer. During most of the IOPs conducted for KASCADE, there was a ground level sonde installed at a height of 1.3-1.5 meter as a reference for the sondes which were aloft. In total there were 14 IOPs where sonde 402 was used as GL-probe. From these IOPs, 11 are appropriate to be used for comparison with the thermohygrometers at the 30m-mast. The IOPs used for this comparison were 6 – 9, 14, 16 – 21.

At M30 the thermohygrometer HC2S3 was installed at an height of 1.90m. So, there is a difference in measurement height of 0.4 – 0.6 meters between the thermohygrometer and ground level sonde. This difference

	TECHNICAL REPORT CEA/DEN		Page 45/67
	<u>Agreement</u> : CEA V4013.001 and V4001.001		
	<u>Ref.</u> : CEA/DEN/CAD/DTN/SMTA/LMTE/NT/2014-11		
	<u>Date</u> : 05/02/2014		<u>Version</u> : A
KASCADE 2013: Instruments Calibration Campaign			

is smaller than in the experiment during Lannemezan, but still this difference will cause an offset during stable or unstable conditions. The sonde was located around 70 meters from the M30-mast, which makes the horizontal distance between the thermohygrometer and the GL-sonde large.

Because of these present differences in measurement height and horizontal distance, it is important to calibrate the sonde during neutral conditions. The state of the atmosphere can be determined by comparison of the two thermohygrometers installed at the M30: The aforementioned HC2S3 at 1.90m and the HMP45 at 30.36m. The difference in height between these sensors is around 30 meters, therefore, assuming the adiabatic temperature profile γ (+/- 1°C decrease per 100m increase) in neutral conditions we come to a difference of -0.3°C between height z_1 and z_2 , see the drawing in Figure 28. Because we are in the surface layer, we assume for unstable conditions a lapse rate γ_u of -2°C/100m or lower, while stability is defined with a lapse rate γ_s of 0°C/100m and higher. By doing so, we come to a temperature range between the two hygrometers where the atmosphere is assumed to be neutral: -0.6 and 0°C. As long as we have neutral conditions, we can use the lower hygrometer at 1.90 meters to compare and correct the tethered sonde.

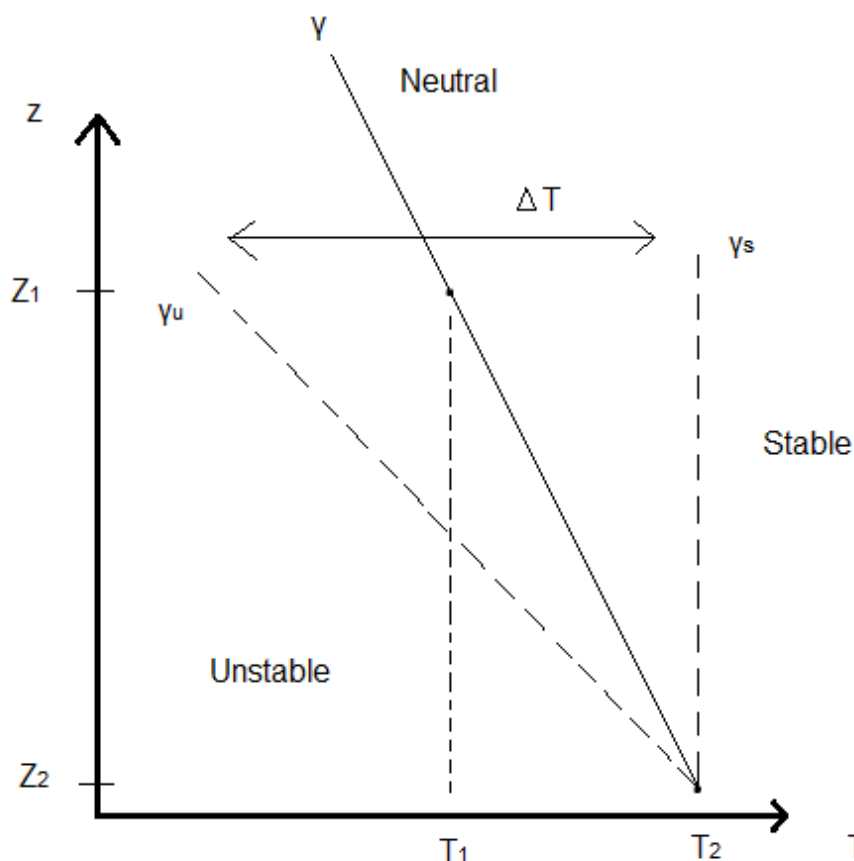


Figure 28 Schematic drawing to determine the range between the thermohygrometers at 30 meters (z_1) and 1.90m (z_2) for which neutral conditions are valid.

The approach described seems promising in two ways: firstly this is a very large potential dataset for calibration ; secondly, we calibrate the sonde over a period where we actually measured. Consequently the calibration will be done in a range of measurements for temperature which are valid within KASCADE.

It appeared that no correction is needed; see Figure 29 where all measured data for the GL-probe is set out against the thermohygrometer. 7630 measurement points were used to yield the regression. Hence, the good R^2 of 0.99 obtained. Comparing intercept b of the regression curve with the difference of the RMS indicates whether a correction is needed. The intercept is lower than RMS-difference, 0.048 °C against 0.449 °C, respectively and

therefore a correction of the tethersonde is unnecessary.

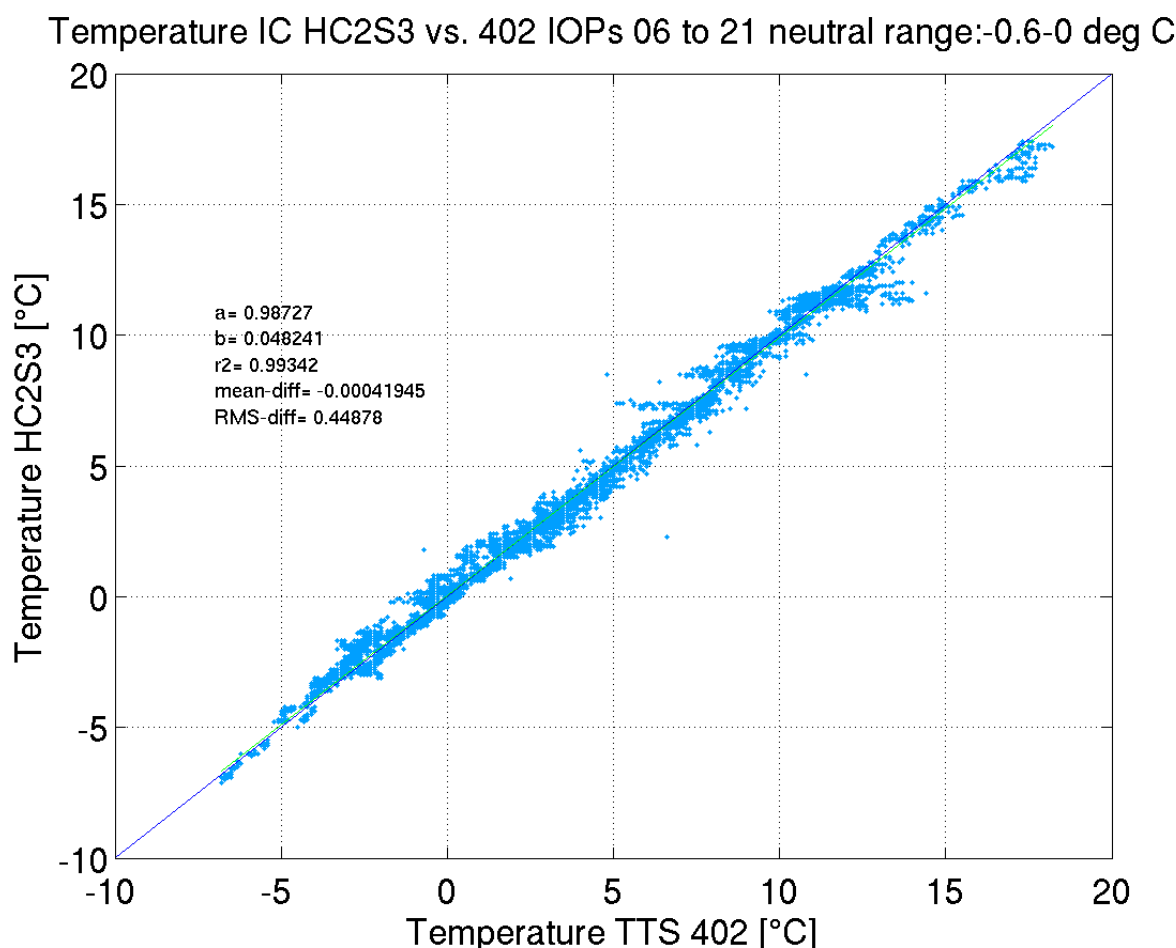


Figure 29 Regression curve for temperature between the tethersonde 402 (W4834334) and the thermohygrometer HC2S3. **a** determines the slope of the regression curve (represented by the green line), **b** the intercept, **r2** the regression coefficient, **mean-diff** the mean difference between the two and **diff-RMS** the difference between the Root Mean Square of both sensor's measurements. The blue line represents the 1:1 line.

4.2.2 Correction TTSs 405, 404, 403 and 401

One of the goals during the IOPs of KASCADE was to have an intercomparison between all used tethersondes, before and after every IOP. During these intercomparisons (ICs) the sondes are placed together on a wooden bench and are compared for a minimum of 3 minutes. Some ICs had a duration 2 hours. See Figure 2 for an impression of the sondes when they are placed on this bench during the IC-experiment at Lannemezan. During the IOPs at KASCADE, the bench was placed on the ground at measurement height of approximately 10cm.

Combining these ICs, potentially a large dataset becomes available which makes it possible to compare the sondes to the calibrated sonde 402 (section 4.2.1) and evaluate whether corrections are needed or not. A large benefit of taking this dataset is that the meteorological conditions are already appropriate: normally an IOP has been conducted when having appropriate meteorological conditions.

See Figure 30 for results on the correction for the tethersondes 405, 404, 403 and 401 against 402. Table 12 shows an overview for the correction coefficients for the TTS. The differences between the sondes to correct and the corrected sonde 402 are minor. Correction coefficients are close to 1, with the differences of RMS being lower

than the intercept b . The regression coefficients R^2 for all sondes are 0.99. These combinations allow us to conclude that the sondes do not need any correction.

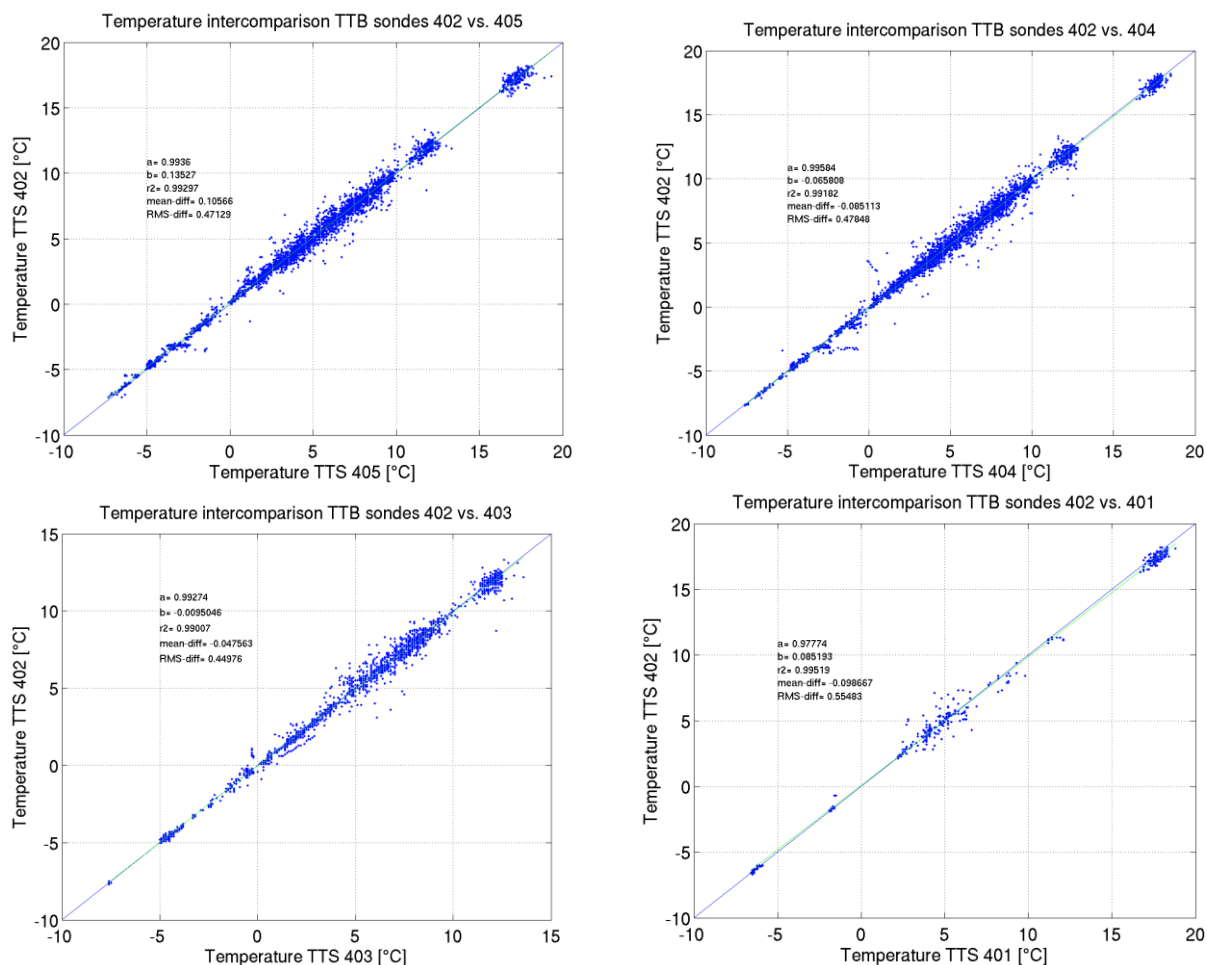


Figure 30 Regression curves for temperature correction between the reference tether sonde 402 and the sondes 405 (left top), 404 (right top), 403 (left bottom), 401 (right bottom). See text from Figure 29 for explanation on the variables given in the pictures.


			TECHNICAL REPORT CEA/DEN	Page 48/67
	<u>Agreement</u> : CEA V4013.001 and V4001.001			
	<u>Ref.</u> : CEA/DEN/CAD/DTN/SMTA/LMTE/NT/2014-11			
	<u>Date</u> : 05/02/2014		<u>Version</u> : A	
KASCADE 2013: Instruments Calibration Campaign				

Table 12 Temperature correction coefficients and their statistics for TTS. The last column indicates whether the the correction coefficients will be applied or not.

TTS	Serial number	a [-]	b [-]	R^2 [-]	mean-diff [K]	diff-RMS [K]	Apply ?
405	W4834144	0.9936	0.13527	0.993	0.10566	0.47129	No
404	C0829547	0.99584	-0.065808	0.992	-0.085113	0.47848	No
403	W4834323	0.99274	-9.5046E-03	0.990	-0.0476	0.44976	No
402	W4834334	0.98727	0.048241	0.993	-4.1945E-04	0.44878	No
401	W4834332	0.97774	0.085193	0.995	-0.098667	0.55483	No

4.3 WIND SPEED

The starting speed for cup anemometers for the Vaisala tethersondes is 0.5 m/s, so only values above this threshold will be used for the correction. A disadvantage from the intercomparison set-up during KASCADE is that it has been performed at 10cm above the ground where generally the wind is weak. Throughout the IC-experiments we recorded values up to 4 m/s. During the IC-experiment in Lannemezan the bench was placed at around 50cm above ground level, but no larger values than 4 m/s have been measured.

There is no direct reference for wind speed, so a calibration dataset will be obtained by taking the average of the values measured during the intercomparison sessions of KASCADE. During the IOPs 16-23, there were 4 sondes active at the same time: 405, 404, 403 and 402. The ICs from these IOPs will be taken to calculate the averages. Hence, the lower limit of 0.5 m/s has not been taken into account for the average. The sondes will be corrected against this average.

Results are shown in Figure 31, Table 13 gives a summary. In this figure, the y-axis shows the values after averaging. The averaged values do not show a discretization, because they have not been rounded after averaging. As for all sondes the intercept is lower than the RMS-difference, it can be concluded that no correction is needed.

In addition, sonde 401 was also used but could not be included in the calculation above. Instead, it will be calibrated against sonde 404, which appeared to be the 'most correct' sonde against the average, see Figure 31. For this, the ICs from IOPs 5 – 10 are taken; the result is shown in Figure 32. There are no corrections needed for wind speed.

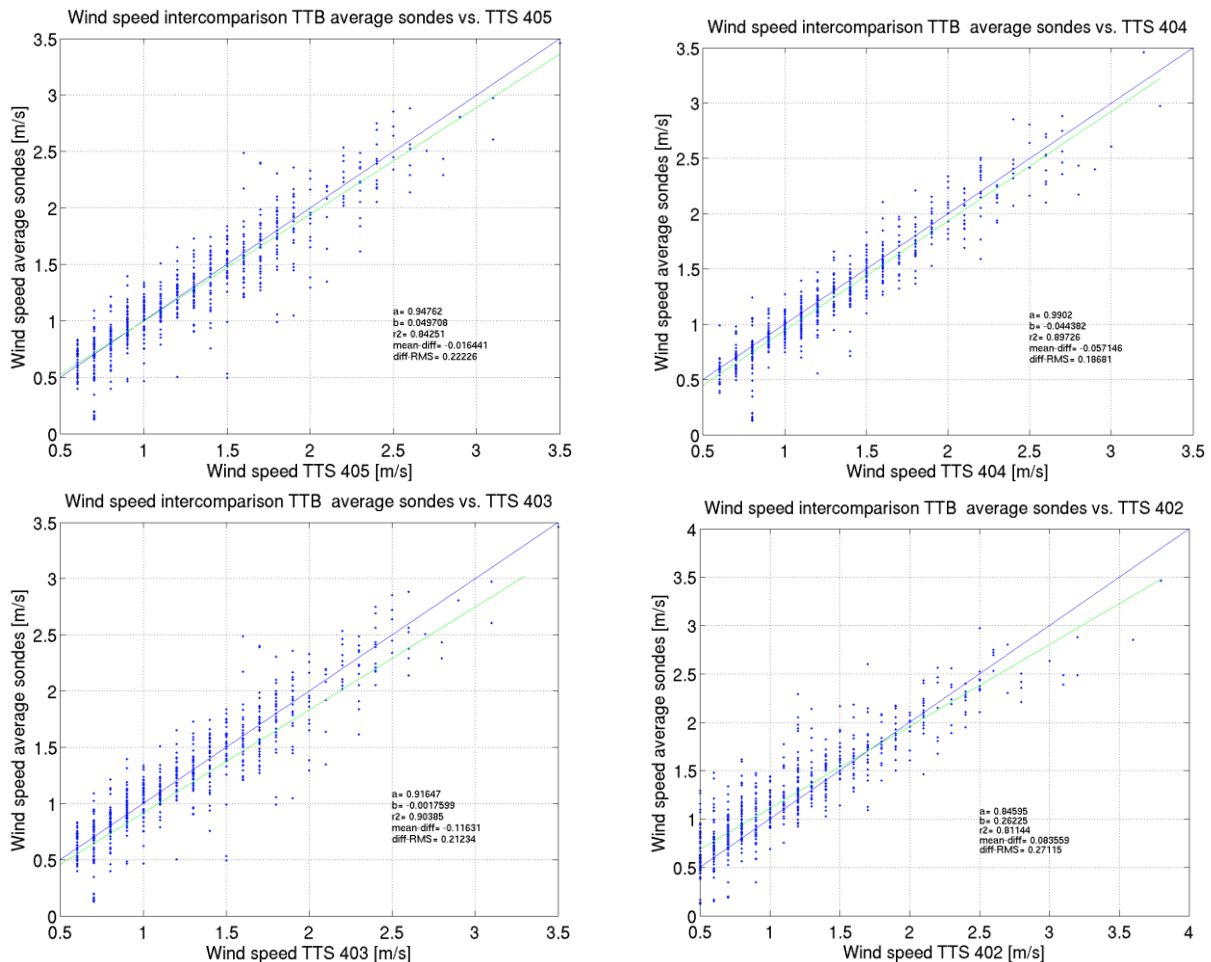


Figure 31 Correction values a for all sondes when compared with the averages. The periods are taken from the ICs during IOPs 16-23. See text from Figure 28 for explanation on the variables given in the pictures.

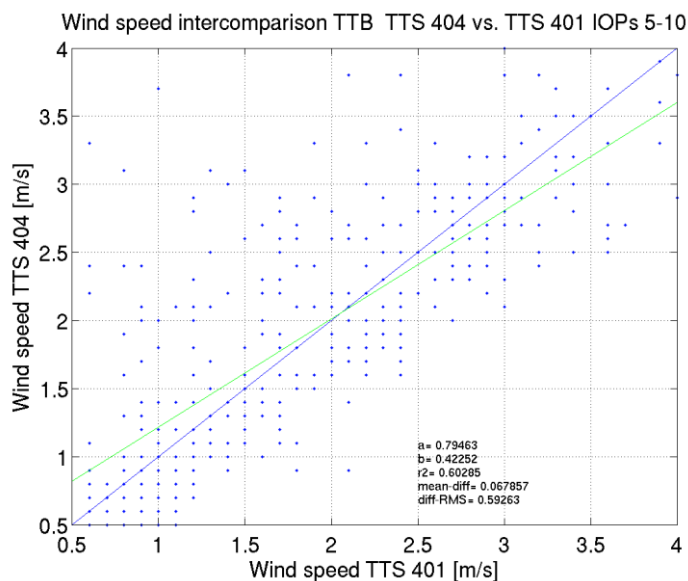


Figure 32 Calibration coefficients for TTB sonde 401, calibrated against sonde 404, the most reliable sonde out of calibration shown in Figure 30.


	TECHNICAL REPORT CEA/DEN		Page 50/67
	Agreement : CEA V4013.001 and V4001.001		
	Ref. : CEA/DEN/CAD/DTN/SMTA/LMTE/NT/2014-11		
	Date : 05/02/2014		Version : A
KASCADE 2013: Instruments Calibration Campaign			

Table 13 Wind speed correction coefficients and their statistics for TTS. The last column indicates whether the correction coefficients will be applied or not.

TTS	Serial number	a [-]	b [-]	R^2 [-]	mean-diff [m/s]	diff-RMS [m/s]	Apply ?
405	W4834144	0.94762	0.049708	0.843	-0.016441	0.22226	No
404	C0829547	0.9902	-0.044382	0.897	-0.057146	0.18681	No
403	W4834323	0.91647	0.0017599	0.904	-0.11631	0.21234	No
402	W4834334	0.84595	0.26225	0.811	0.083559	0.27115	No
401	W4834332	0.79463	0.42252	0.603	0.067857	0.59263	No

4.4 RELATIVE HUMIDITY

4.4.1 Relative Humidity correction TTS 402

Figure 33 shows the original values measured for relative humidity during the IC-experiment in Lannemezan. It clearly shows the offsets between the different sensors, including the saturation for sonde 404. For this sensor, saturation occurs when other sensors are between 80 and 100 %. These offsets were present during KASCADE as well.

For the correction of the relative humidity for the sondes, approximately the same procedure has been followed as for correction of temperature. We compare the measured values for the tethersonde 402 at ground level near the winch with the thermohygrometer values at the mast recorded under neutral atmospheric conditions, obtained at KASCADE. See Section 4.2 for further details on this part of the approach. For the thermohygrometer HC2S3, the measured values are used after application of the corrections determined in Section 3.3.

Figure 34 shows the 2nd order polynomial regression curve for the correction. For this regression the IOPs 17 and 18 were used. The 2nd order is chosen as it appeared to have the highest regression coefficient and is defined by the coefficients used in the following equation for the final correction of the tethersonde 402:

$$RH_{TTS-402_{new}}(i) = -18.0445 \cdot RH_{TTS-402}(i) + 2.02047 \cdot RH_{TTS-402}(i) - 0.00841669 \cdot RH_{TTS-402}^2(i) \quad (20)$$

Figure 35 shows the validation after correction of the tethersonde 402. The validation dataset consists of a comparison between the TTS402 and thermohygrometer HC2S3 during KASCADE in neutral conditions.

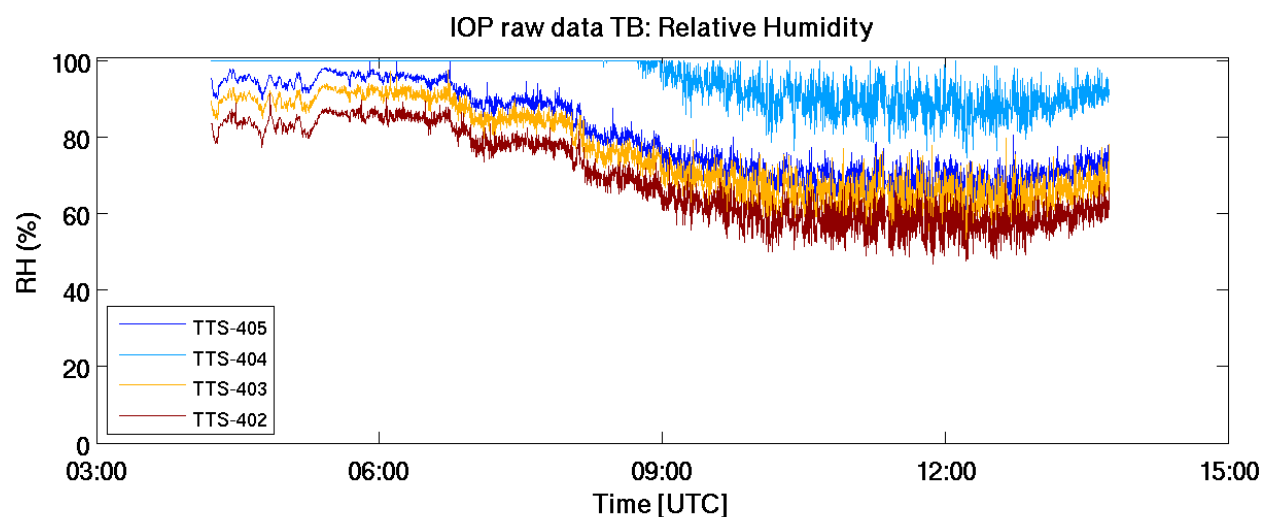


Figure 33 Measured RH during IC-experiment during Lannemezan at May 14th. See text for details.

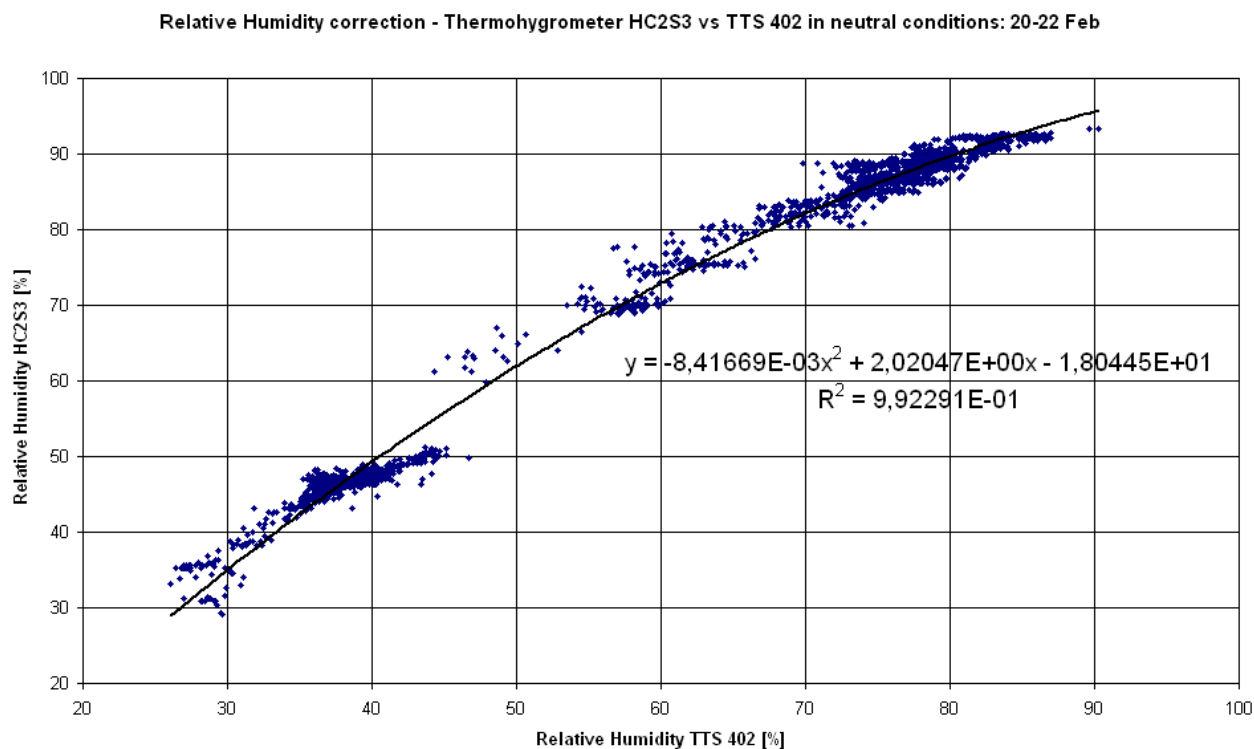


Figure 34 Polynomial regression curve for relative humidity correction of sonde 402, the ground level probe, with thermohygrometer HC2S3. Data selected from 20-22 Feb, coinciding with IOPs 17 & 18.

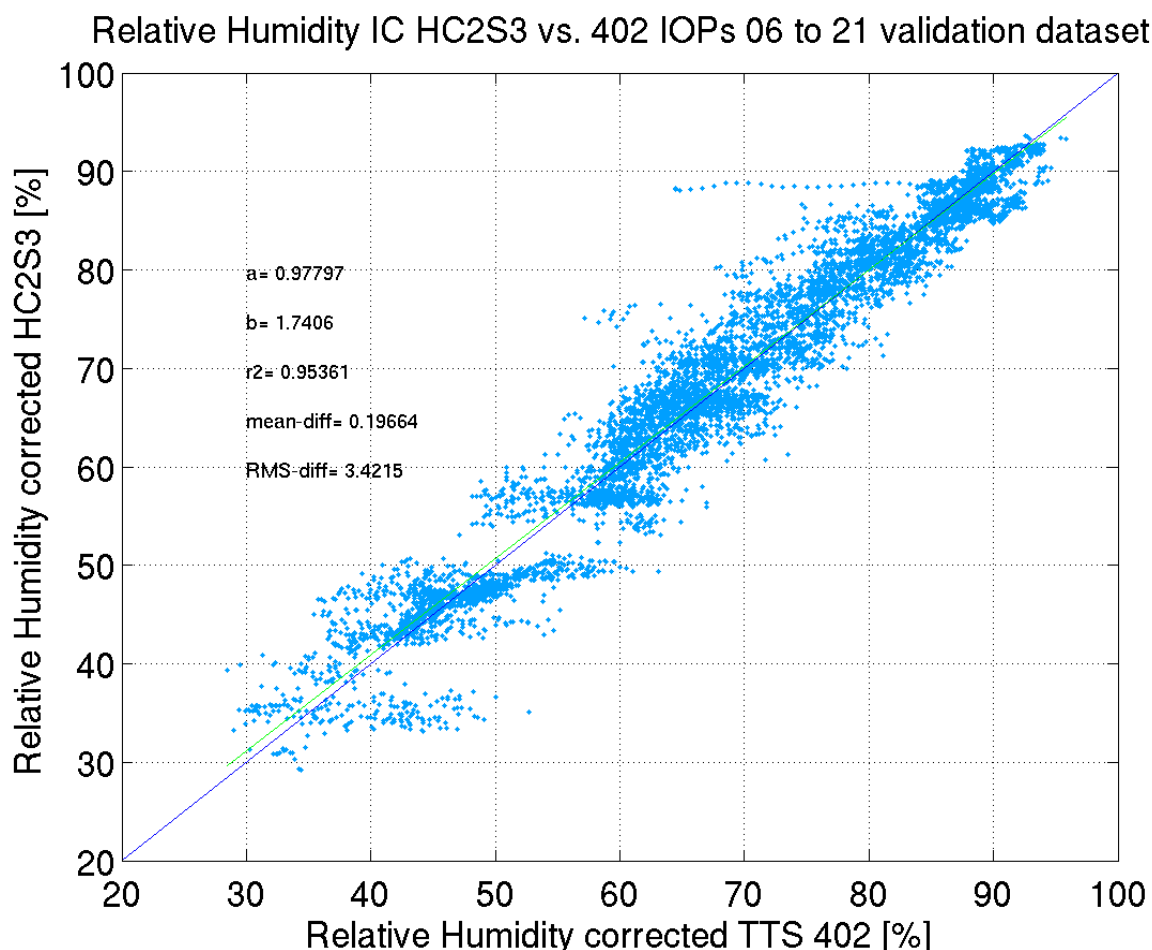


Figure 35 Validation regression curve for reference thermohygrometer and RH corrected sonde 402 (W4834334). Hence, it is applied on data from IOPs 6 to 21, during neutral conditions. See text from Figure 28 for explanation on the variables given in the pictures.

4.4.2 Correction TTSs 405, 404, 403 and 401

With the correction coefficients for TTS 402 determined in the previous section, it was possible to calibrate the other tethered balloon sondes used during KASCADE. For this, the same procedure as for the correction for temperature of the other TTSs has been followed, see Section 4.2. All intercomparison data available between the sondes to calibrate and TTS 402 are used to determine a correction coefficient dedicated to the tethered sonde.

Although desired, not every IOP had the same sequence of the TTSs and therefore the datasets for determination of correction coefficients vary widely. Figure 36 shows the regression curves which determine the correction coefficients. These are duplicated in Table 14, where for the complete picture also TTS 402 is shown. These coefficients can be applied using equation 21 where RH stands for the measured value of $TTS \#$, leading to the corrected value for $RH_{TTS\#corrected}$. For every sonde, an optimal polynomial fit was determined by finding the highest regression coefficient.

$$RH_{TTS\#corrected}(i) = coeff1_{TTS\#}(i) + coeff2 \cdot RH_{TTS\#}(i) + coeff3 \cdot RH_{TTS\#}^2(i) + coeff4 \cdot RH_{TTS\#}^3(i) \quad (21)$$

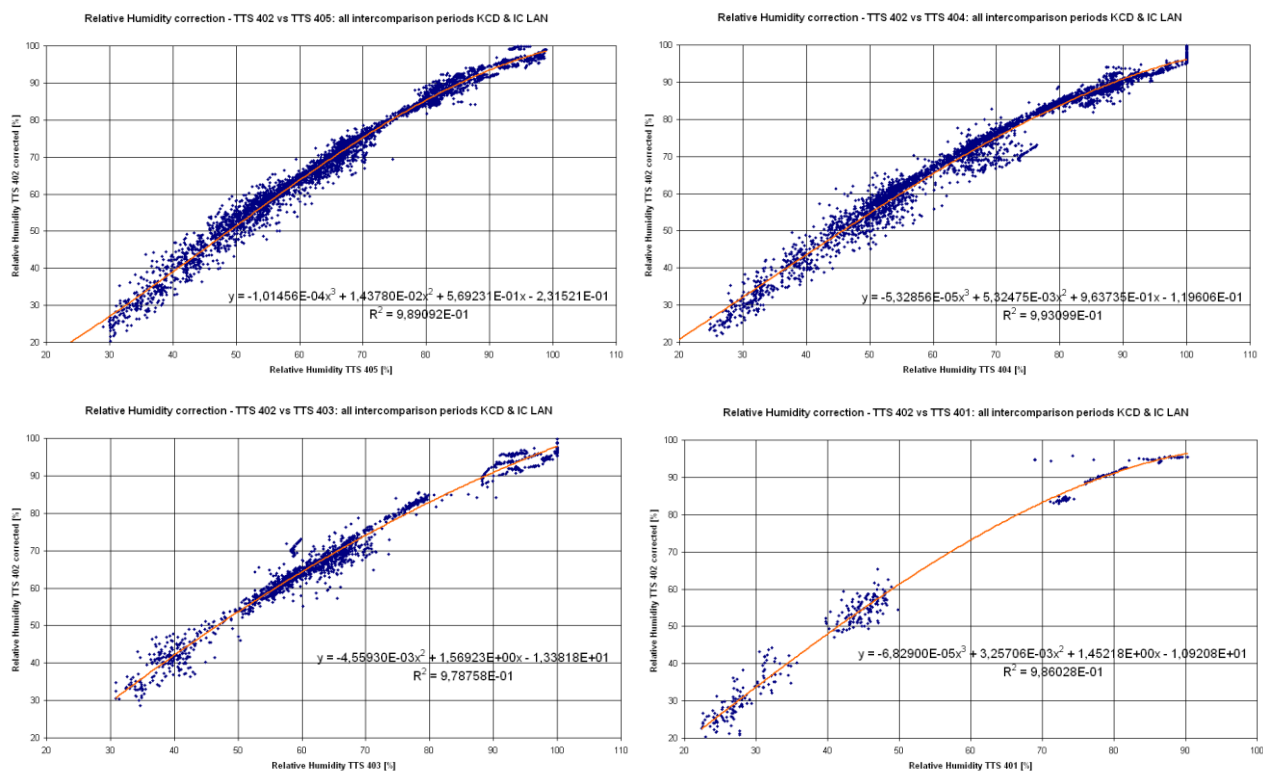


Figure 36 Relative humidity correction coefficients for every tether sonde (TTS) used during KASCADE. TTS 402 was used as reference, after correction against thermohygrometer.

Table 14 Relative humidity correction coefficients for all tethersondes used in KASCADE together with the regression coefficient. See text for explanation and Equation 21 for application

TTS	Serial number	coeff1	coeff2	coeff3	coeff4	R ²
405	W4834144	-2.31521E-01	5.69231E-01	1.43780E-02	-1.01456E-04	0.998
404	C0829547	-1.19606E-01	9.63735E-01	5.32475E-03	-5.32856E-05	0.993
403	W4834323	-1.33818E+01	1.56923E+00	-4.55930E-03	--	0.979
402	W4834334	-1.80445E+01	2.02047E+00	-8.41669E-03	--	0.992
401	W4834332	-1.09208E+01	1.45218E+00	3.25706E-03	-6.82900E-05	0.986

Although corrected, it should be remarked that sonde 404 remains a troublemaker, because it gives 100 % values in non-saturated air. Unfortunately, this is unsolvable. Therefore, one should be cautious when using the value of 96.21 % for TTS 404 after corrections; this is the value where the air is already saturated.

4.5 PRESSURE

In this paragraph the TTS correction for pressure are evaluated. The same procedure as for wind speed (Section 4.3) has been followed: For the sondes most frequently used (405, 404, 403, 402) average values for the ICs 16 – 23 are obtained. The sondes mentioned are subsequently corrected to this average. Results are shown in Figure

37 and a summary is given in Table 15. Every sonde must be corrected according to the coefficients a and b given in this table, as the intercept are larger than the RMS-difference.

The sonde 401 was not used during IOPs 16 – 23, but in IOPs 5 – 10 only. Therefore this sonde is corrected against sonde 405, which in itself has been corrected by the coefficients given in Table 15. Figure 38 shows the regression constants and their statistics. It is concluded that sonde 405 should be corrected.

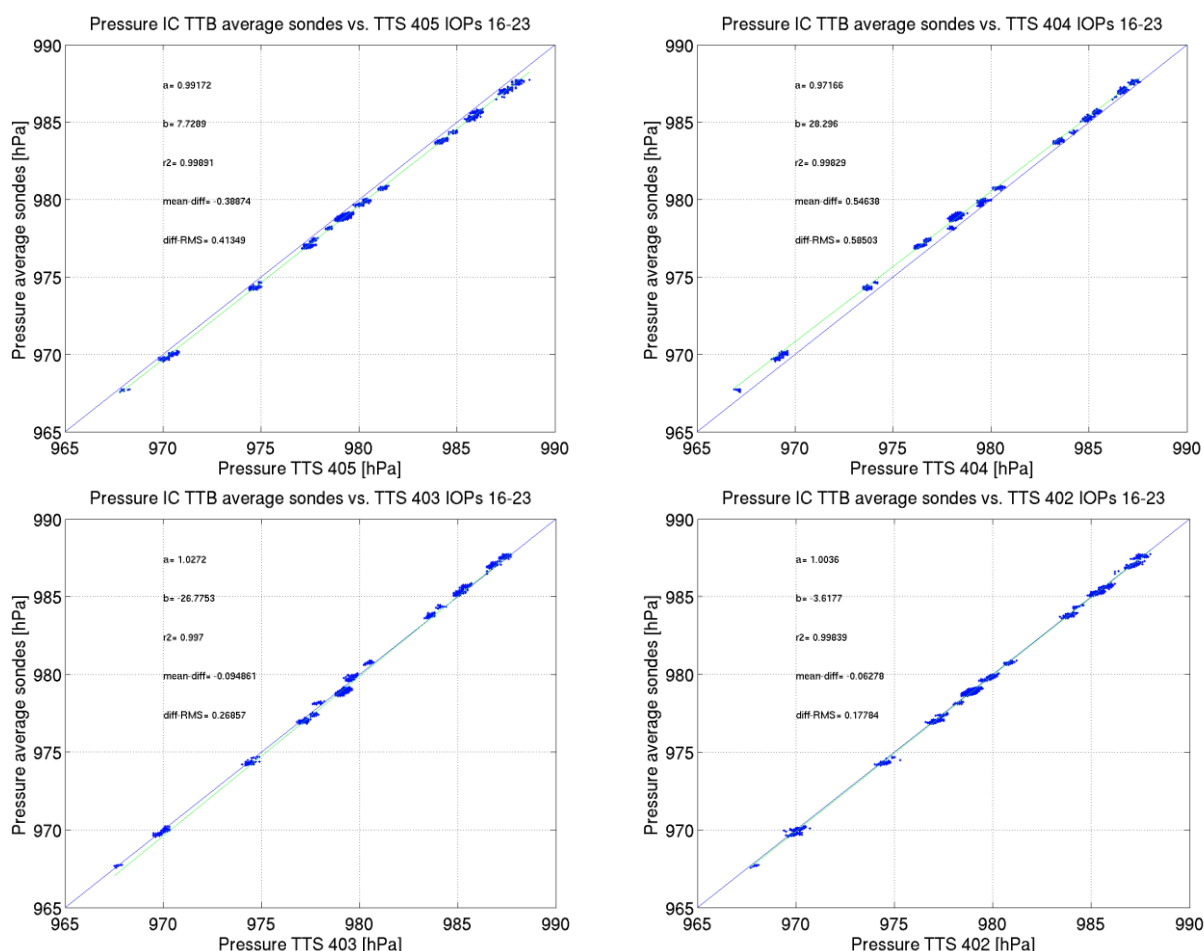


Figure 37 Pressure correction regression curves, with a being the correction coefficient, b the intercept, r^2 the coefficient of determination, of the offset (average of the differences) and diff-RMS the difference between the Root Mean Square. The blue line represents the 1:1 line; the green represents the regression line. The dataset consisted out of all ICs during the IOPs 16-23.

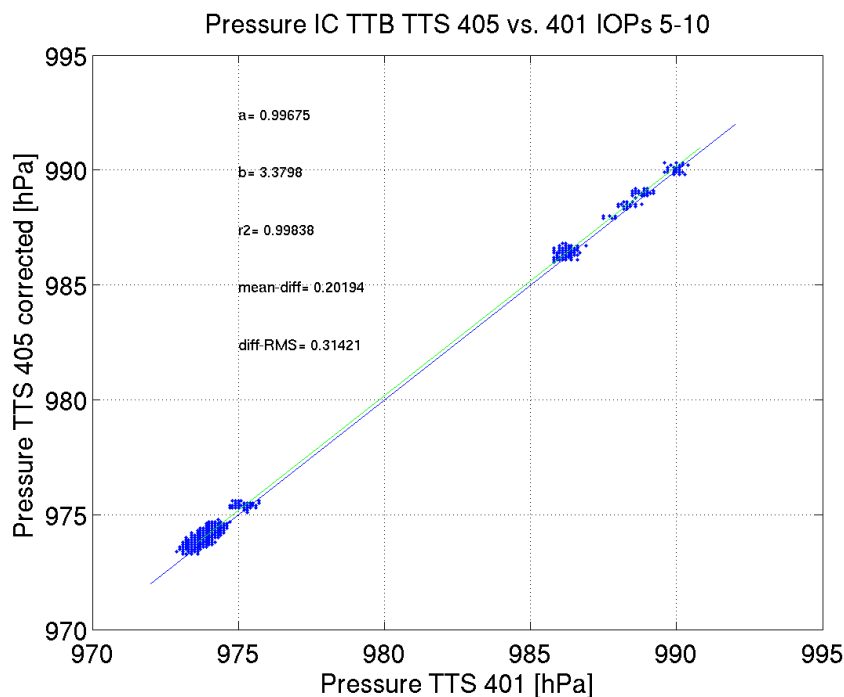



Figure 38 Same as Figure 36, but for the sonde 401, which has been corrected with the corrected sonde 405.

Table 15 Pressure correction coefficients and their statistics for TTS. The last column indicates whether the correction coefficients will be applied or not.

TTS	Serial number	a	b	R^2	mean-diff	diff-RMS	Apply ?
405	W4834144	0.99172	7.7289	0.999	-0.38874	0.41349	Yes
404	C0829547	0.97166	28.296	0.998	0.54638	0.58503	Yes
403	W4834323	1.0272	-26.7753	0.997	-0.094861	0.26857	Yes
402	W4834334	1.0036	-3.6177	0.998	-0.06278	0.17784	Yes
401	W4834332	0.99675	3.3798	0.998	0.20194	0.31421	Yes

	TECHNICAL REPORT CEA/DEN		Page 56/67
	Agreement : CEA V4013.001 and V4001.001		
	Ref. : CEA/DEN/CAD/DTN/SMTA/LMTE/NT/2014-11		
	Date : 05/02/2014		Version : A
KASCADE 2013: Instruments Calibration Campaign			

CHAPTER 5. SUMMARY AND CONCLUSIONS

The sensors used at the meteorological field experiment KASCADE, conducted during the winter of 2013 in Cadarache, are checked for inconsistencies and corrected where necessary. In order to achieve, two complementary intercomparison experiments have been conducted at Centre de Recherche Atmosphérique (Lannemezan) and Laboratoire d'Aérodynamique (LA) in Toulouse in spring 2013. Also the data collected during KASCADE itself has been used to be able to calibrate the tethered balloon sondes.

A resolution issue for the net radiometer CNR1 has been solved. It appears that the WMO-agreement of 10-minute averaging for meteorological measurements is sufficient to suppress the spikes detected.


The longwave components of the net radiometer CNR4 has been checked on inconsistencies for the calibration coefficients k supplied by the manufacturer. For this check, a CG4-pyrgeometer was used. The supplied k 's were approved to be correct and so the CNR4 can be used as a reference for relative calibration against the net radiometer CNR1.

The relative calibration of CNR1 for LW has been done in 2 steps: The classical correction for k which is supplied by the manufacturer and in a second step, a body temperature T_{body} correction has been applied. For the lower sensor $k=11.238 \mu V/(W.m^{-2})$ and $T_{body}=0.6196K$. For the upper sensor: $k=10.032 \mu V/(W.m^{-2})$ and $T_{body}=0.5324K$. The improvements after corrections are clearly seen by the mean differences, which are stepwise decreasing from -4.53 (no correction applied) to -3.22 (k -corrected) to 0.03 $W.m^{-2}$ (both k - and T_{body} -corrections applied) for the calibration of the lower sensor. A similar improvement is shown for the upper sensor (-4.17 to -2.80 to -0.07 $W.m^{-2}$). Uncertainties for LW-divergence and LHR are estimated at 0.93 $W.m^{-2}$ and 0.15 $^{\circ}C.h^{-1}$, respectively. Considering only incoming and outgoing LW, these quantities can be calculated at 1.36 and 0.69 $W.m^{-2}$ and 0.21 and 0.11 $^{\circ}C.h^{-1}$, respectively.

Also SW-radiation for CNR1 has been calibrated for both incoming and outgoing components and both are estimated by a 2nd order polynomial fit, see Equations 11 and 12 for correction coefficients.

The thermohygrometers have been calibrated relatively against their average for relative humidity only (17 to 19), for temperature no correction was needed. The tethered balloon sondes needed no correction for wind speed and temperature, for relative humidity (Table 14) and pressure (Table 15) a correction has been performed for all sondes. For relative humidity it concerns a relative correction against the corrected thermohygrometers and for pressure this was a relative correction against their average. In order to achieve the latter corrections, the KASCADE-dataset has been used.

This report will feed the quality of the dataset collected at the field experiment KASCADE.

	TECHNICAL REPORT CEA/DEN		Page 57/67
	<u>Agreement</u> : CEA V4013.001 and V4001.001 <u>Ref.</u> : CEA/DEN/CAD/DTN/SMTA/LMTE/NT/2014-11		
	<u>Date</u> : 05/02/2014		<u>Version</u> : A
KASCADE 2013: Instruments Calibration Campaign			

REFERENCES

Phillipona, R., C. Fröhlich, and C. Betz (1995), Characterization of pyrgeometers and the accuracy of atmospheric long-wave radiation measurements, *Appl. Opt.*, **34**, 1598 – 1605, doi:10.1364/AO.34.001598.

Stull, R. B. (2000), Meteorology for Scientists and Engineers, Second Edition, *Brooks/Cole*, 502 pp.

ACKNOWLEDGEMENTS


Special thanks to...

...Solene, Eric, Fabienne & Marie from CRA, Lannemezan for their help and advice during KASCADE and the calibration set-up in Lannemezan.

...Christian Jarrot for the installation for the longwave radiation calibration held at the terrace of LA, Toulouse.

...CNRM for lending CG4.

...Pierre Durand for his advices and comments.

		TECHNICAL REPORT CEA/DEN	Page 58/67
		<u>Agreement</u> : CEA V4013.001 and V4001.001 <u>Ref.</u> : CEA/DEN/CAD/DTN/SMTA/LMTE/NT/2014-11	
		<u>Date</u> : 05/02/2014	<u>Version</u> : A
KASCADE 2013: Instruments Calibration Campaign			

APPENDIX A. STAGGERING OF TETHERSONDES DURING IOPS

IOP_nr	sondes used											
	IOP a				IOP b				IOP c			
	t	m	b	GL	t	m	b	GL	t	m	b	GL
1	--	--	--	--	402	404	405	--				
2	--	--	--	--								
3	402	404	405	--	--	--	--	--				
4	402				402	404	405	--				
5	--	404	405		401	404	405	--				
6	--	--	--	--	401	404	405	402				
7	401	404	405	402	401	404	405	402				
8	401	404	--	402	--	--	--	--				
9	--	--	--	--	401	404	405	402				
10	401	404	405	402	--	--	--	--				
11	--	--	--	--	405	404	402	--				
12	405	404	402	--	405	404	402	--				
13	405	404	402	--	405	404	402	--				
14	405	404	402	--	405	404	402	--				
15	405	404	402	--	405	404	402	--				
16	405	404	403	402	405	404	403	402				
17	405	404	403	402	405	404	403	402				
18	405	404	403	402	405	404	403	402				
19	405	404	403	402	405	404	403	--	405	404	403	402
20	405	404	403	402	405	404	403	402	405	403		402
21	405	404	403	402	405	404	403	402	405	404	403	402
22	405	404	403	402	405	404	403	402				
23	405	404	403	402								

APPENDIX B. FLOW CHARTS SENSOR CORRECTIONS

Longwave radiation

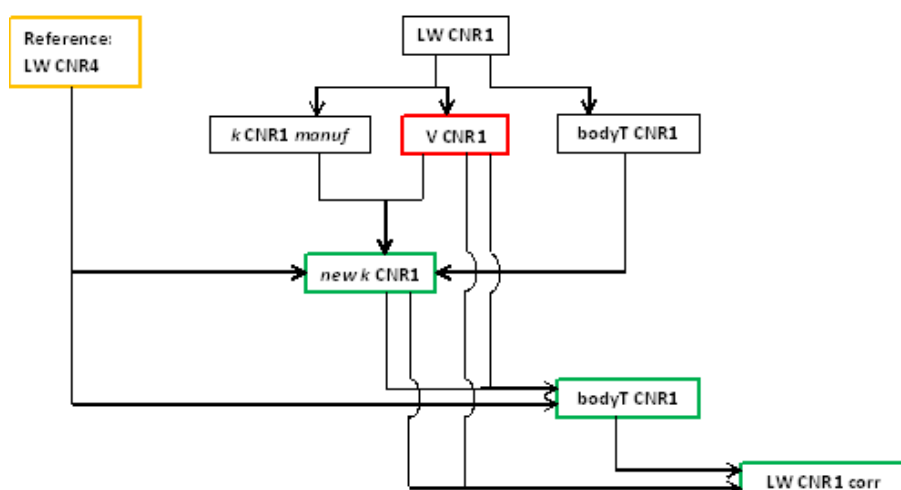



Figure 39 Flow chart on correction for longwave radiation CNR1. Can be used for both upper and lower sensor. Green squared variables are new quantities. The red square signifies the original volt signal which cannot be changed.

	TECHNICAL REPORT CEA/DEN		Page 60/67
	<u>Agreement</u> : CEA V4013.001 and V4001.001 <u>Ref.</u> : CEA/DEN/CAD/DTN/SMTA/LMTE/NT/2014-11		
	<u>Date</u> : 05/02/2014		<u>Version</u> : A
KASCADE 2013: Instruments Calibration Campaign			

Shortwave radiation

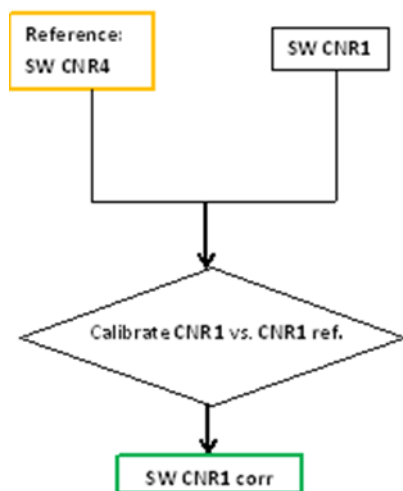


Figure 40 Flow chart on correction for shortwave radiation CNR1.
Can be used for both upper and lower sensor.

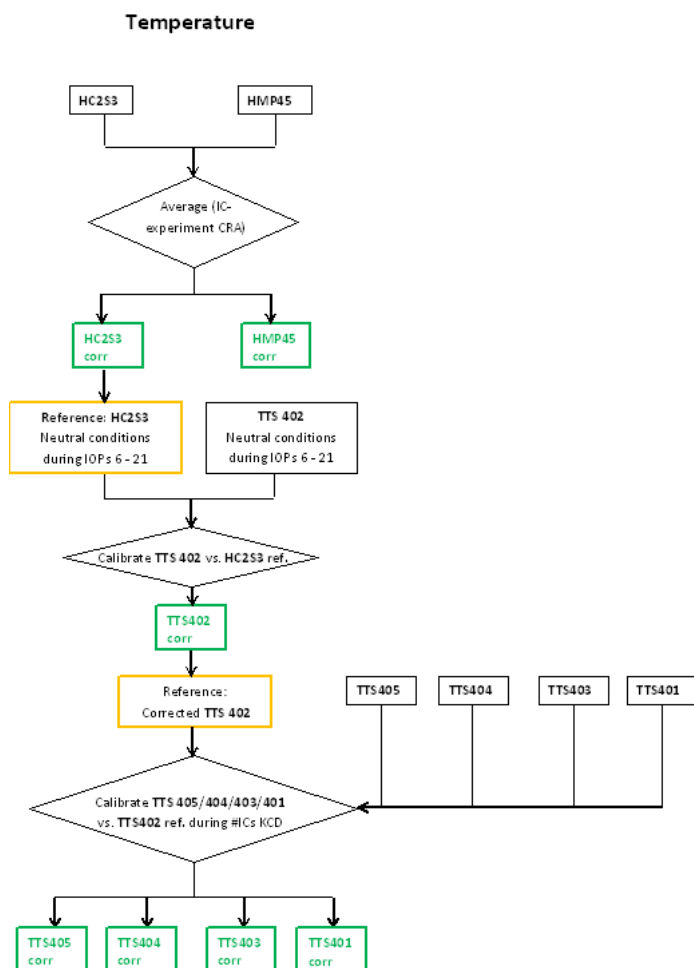


Figure 41 Flow chart on temperature correction for thermohygrometers HC2S3 and TTS sensors 405, 404, 403, 402, 401

Relative Humidity

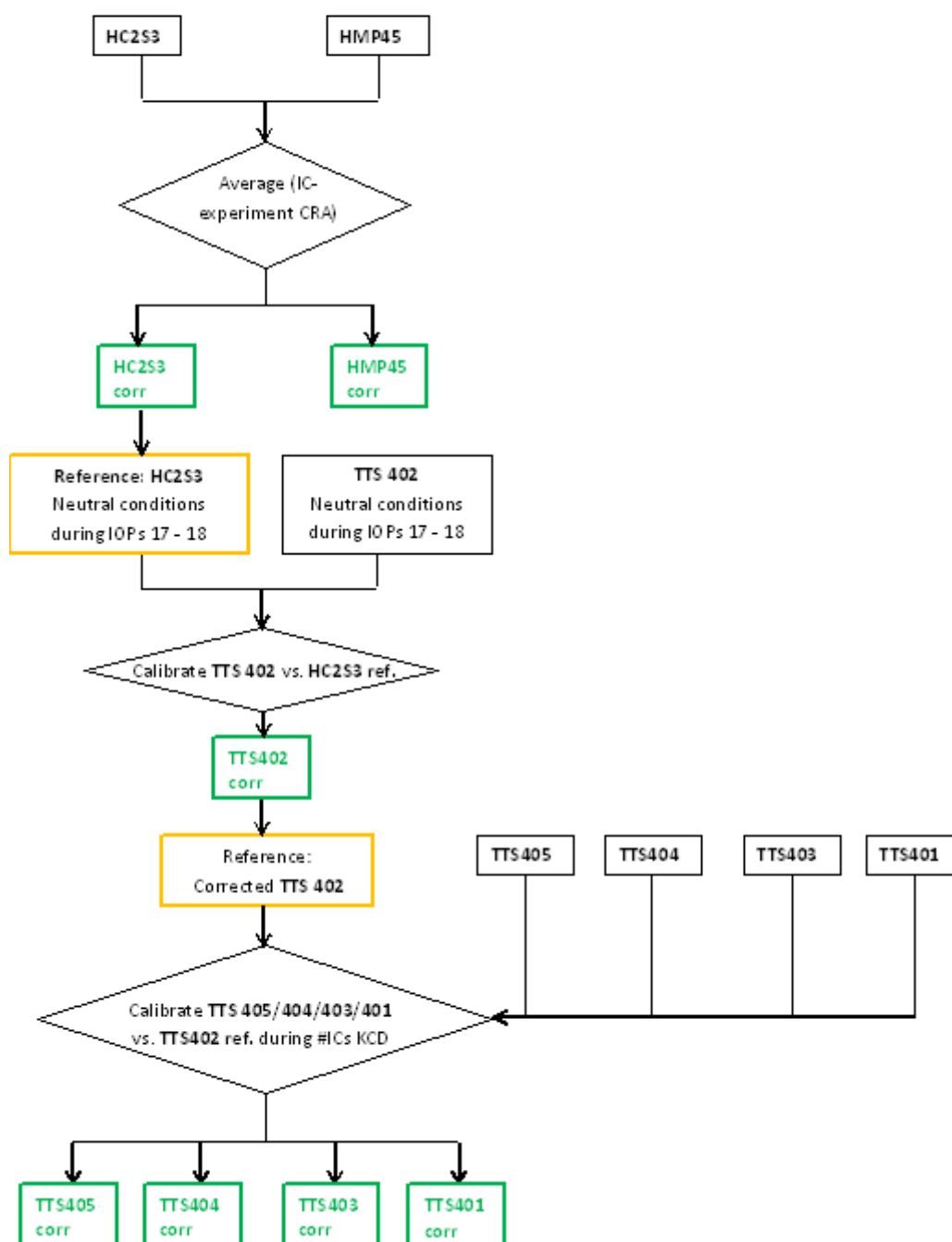


Figure 42 Flow chart on relative humidity correction for thermohygrometers HC2S3 and TTS sensors 405, 404, 403, 402, 401

Pressure and wind speed

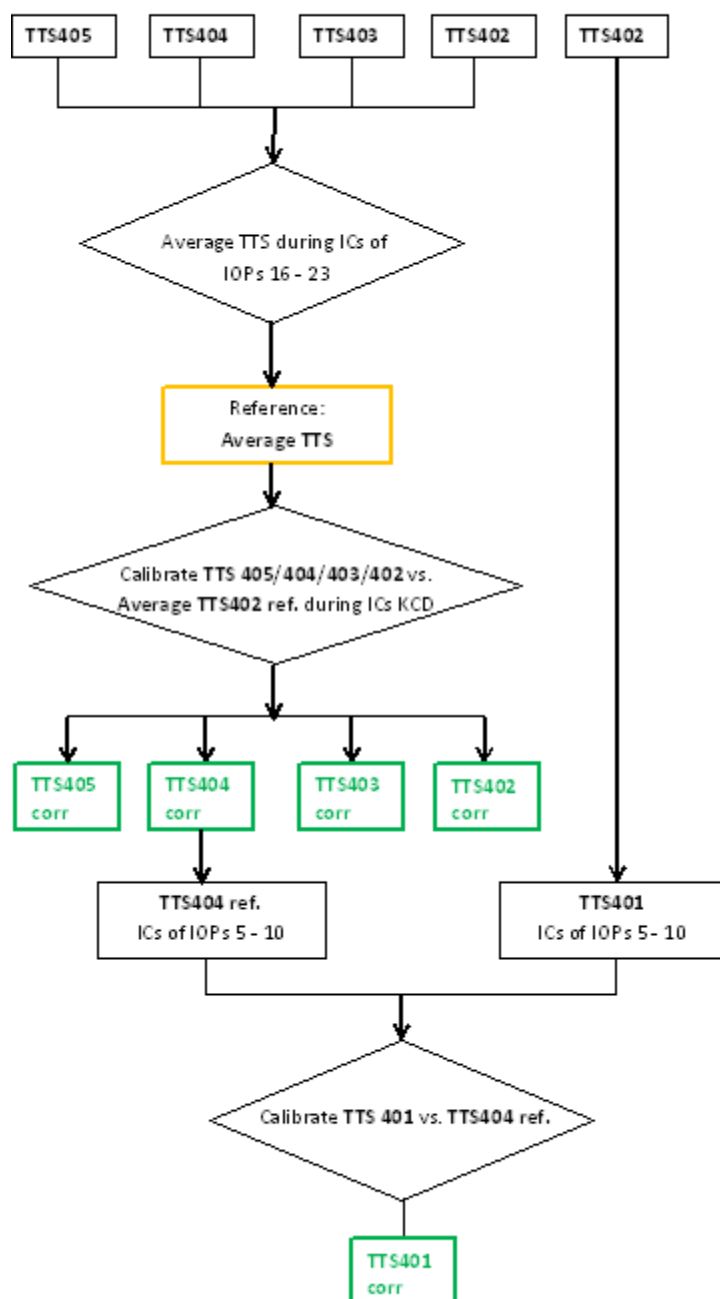



Figure 43 Flow chart on pressure and wind speed correction for TTS sensors

	TECHNICAL REPORT CEA/DEN		Page 64/67
	<u>Agreement</u> : CEA V4013.001 and V4001.001 <u>Ref.</u> : CEA/DEN/CAD/DTN/SMTA/LMTE/NT/2014-11		
	<u>Date</u> : 05/02/2014		<u>Version</u> : A
KASCADE 2013: Instruments Calibration Campaign			

APPENDIX C-1. TECHNICAL SPECIFICATIONS RADIOMETERS CNR1, CNR4 AND CG4

See Table 16 on a comparison on the technical specifications of the net radiometers CNR1 and CNR4 and the pyrgeometer CG4. All three sensors are from the manufacturer Kipp & Zonen, Delft, the Netherlands. The CNR1 and CNR4 are purchased by LA, the CG4 is from CNRM.



Figure 44 The net radiometers CNR1 (left) and CNR4 (right)



Figure 45 Pyrgeometer CG4, provided by CNRM.


		TECHNICAL REPORT CEA/DEN	Page 65/67
		<u>Agreement</u> : CEA V4013.001 and V4001.001 <u>Ref.</u> : CEA/DEN/CAD/DTN/SMTA/LMTE/NT/2014-11	
		<u>Date</u> : 05/02/2014	<u>Version</u> : A
	KASCADE 2013: Instruments Calibration Campaign		

Table 16 Manufacturer's technical specifications for the radiometers CNR1 and CNR4

	CNR1	CNR4	CG4
Spectral response pyranometer " " pyrgeometer	305 to 2.800 nm 5.000 to 50.000 nm	305 to 2.800 nm 4.500 to 42.000 nm	4.500 to 42.000 nm
Response time	< 18 s	< 18 s	18 s
Sensitivity Range: Pyranometer Pyrgeometer	10 to 35 $\mu\text{V W}^{-1} \text{m}^{-2}$ 5 to 35 $\mu\text{V W}^{-1} \text{m}^{-2}$	10 to 20 $\mu\text{V W}^{-1} \text{m}^{-2}$ 5 to 15 $\mu\text{V W}^{-1} \text{m}^{-2}$	5 to 10 $\mu\text{V W}^{-1} \text{m}^{-2}$
Field of view: Upper sensor Lower sensor	150 degrees	180 degrees 150 degrees	180 degrees
Accuracy/uncertainty daily total	$\pm 10\%$	Pyranometer (uncertainty) <5% Pyrgeometer (uncertainty) < 10 %	< 3 % (95% confidence interval)
Directional error (pyranometer at 1000 W.m^{-2})	< 25 W.m^{-2}	< 20 W.m^{-2}	not defined
Temperature dependence of sensitivity (-10° to +40°C)	6 %	< 4 %	< 1 % (-20° to +50°C)
Non-Linearity pyrano (0-1000 W.m^{-2}) pyrgeo (-250 to +250 W.m^{-2})	< 2.5 % < 2.5 %	< 1 % < 1 %	< 1 %
Height ; dome-to-dome	4 cm ; 15.6 cm	- ; 6.6 cm	7.25 cm
Width	8.0 cm	11.1 cm	6.5 cm
Length	23.2 cm	23.5 cm	6.5 cm
Length with CNF		40.5 cm	
Weight	2500 g	850 g	600 g
Heating resistor	24 Ohms, 6 W at 12 Vdc		

APPENDIX C-2. TECHNICAL SPECIFICATIONS THERMOHYGROMETERS

For slow response measurements on temperature and humidity two different types of thermohygrometers are used: HMP45 and HC2S3. Both are produced by Campbell Scientific.



Figure 46 The Campbell HMP45 probe (left) and HC2S3 probe (right)

Table 17 Technical specifications on the both thermohygrometers used in this report

	HMP45	HC2-S3
Supply voltage	12 Vdc nominal	12 Vdc
Power consumption	< 4 mA at 12V	< 2 mA at 12V
Probe dimensions	Diameter 2.5 cm Length 25.4 cm	Diameter 1.5 cm Length 8.5 cm 18.3 cm (incl. connector)
Probe weight	0.27 kg	10 g
Filter	0.2 µm Teflon membrane	Polyethylene or Teflon (unknown)
Filter diameter	1.9 cm	
Operating temperature	-40° to + 60 °C	-40° to + 100 °C
AIR TEMPERATURE		
Temperature sensor	1000 Ω PRT	PT100 RTD
Measurement range	-40 to + 60 °C	Default -40 to + 60 °C
Output signal range	0.008 to 1.0 V	0 to 1.0 V
Accuracy	±0.2°C (at 20°C)	±0.1 °C (at 23 °C)
RELATIVE HUMIDITY		
Sensor	HUMICAP 180	ROTRONIC Hygromer IN1
Measurement range	0 to 100% RH non-condensing	0 to 100% RH non-condensing
RH output signal range	0.008 to 1 Vdc	0 to 1 Vdc
Accuracy	At 20 °C: ±2% RH (0 – 90% RH) ±3% RH (90 – 100 % RH)	±0.8% RH (at 23 °C in standard configuration settings)
Temperature dependence	±0.05% RH/ °C	
Response time	15 s with membrane filter (at 20 °C, 90% response)	<22s with PE-filter <30s with Teflon filter

APPENDIX C-3. TECHNICAL SPECIFICATIONS TETHERSONDES

The tethered balloon was operated with the TTS111 Tethersonde from Vaisala Inc.



Figure 47 The Tethersonde TTS111

Table 18 General specifications of tethersonde TTS111

Property	Description/Value
Dimensions	Approx. 145 cm x 32 cm x 32 cm
Power source	9 V battery
Power consumption	100 mA
Weight (incl. sensors and internal battery)	300 g
Operating temperature	0 ... + 50 °C
Storage conditions	RH < 85%, +5 ... +40 °C

Table 19 Manufacturer's sensor's specifications for TTS111.

Variable	Range	Resolution	Accuracy	Response time
Temperature	-50 ... +60 °C	0.1°C	0.1°C	0.2 s
Humidity	0 ... 100 %	0.1%	2.0 %	0.5 s
Pressure	500 ... 1080 hPa	0.1hPa	0.4 hPa	
Wind speed	0 ... 20 m/s	0.1 m/s		
Wind direction	0 ... 360°	1°		

Résumé

Cette thèse est dédiée à la caractérisation des vents descendants de vallée dans une région de moyenne latitude caractérisée par un terrain complexe d'orographie modérée, et dans le contexte de la réglementation des rejets atmosphériques du centre de Cadarache. Cadarache est un des centres de recherche du 'Commissariat à l'Énergie Atomique et aux Énergies Alternatives' (CEA), installé dans une petite vallée (CV) confluyente à la vallée majeure de la Durance (DV). Ces deux vallées se distinguent par leur largeur (1 à 2 kms et 5 kms respectivement pour CV et DV), leur longueur (5 kms et plus de 50 kms), leur profondeur (environ 100 m et plus de 200 m) et leur pente moyenne (1.2° et 0.2°), et par conséquent sont le siège d'écoulements aux caractéristiques différentes en stratification stable. En effet, un forçage synoptique faible associé à un ciel dégagé sont dans la région des conditions fréquentes qui favorisent la stabilité atmosphérique et consécutivement la mauvaise dispersion des polluants, faisant de cette situation un sujet d'intérêt majeur pour l'impact sanitaire et environnemental du centre.

La campagne de mesure KASCADE (KAtabatic winds and Stability over CAdarache for Dispersion of Effluents) constitue le volet expérimental de l'étude. Réalisée pendant l'hiver 2013 elle a couvert 3 mois d'observation continue (avec un mât pour la mesure des flux turbulents et radiatifs, un sodar et les observations météorologiques du site de Cadarache) complétée de 23 périodes d'observation intensive (POI). Pendant ces POI des profils ont été réalisés par ballon captif et radiosondages. Une POI était déclenchée en conditions de forçage synoptique faible et de ciel clair, démarrait à 12 UTC et durait 24 heures. Une phase de calibration des capteurs a permis les corrections nécessaires à la qualité des données et la constitution d'une base de données bien documentée (<http://kascade.sedoo.fr/>). Les analyses ont été basées sur ces observations et sur un volet de simulation numérique de la météorologie régionale avec le code WRF.

L'analyse montre que les écoulements descendant les vallées de Cadarache (CDV) et de la Durance (DDV) dominent pendant toute la période d'étude. La stabilité s'installant dès le coucher du soleil, le courant CDV s'établit et s'épaissit progressivement. Le profil de vent en forme de jet présente son maximum à environ 30 m où il atteint 2 à 3 m s⁻¹. C'est un courant de densité qui se maintient toute la nuit et disparaît avec l'inversion de stabilité au lever du soleil. Comme la station météorologique du centre manque de capteur de vent dans la CV même, une méthode a été développée pour diagnostiquer le CDV en exploitant l'instrumentation disponible. Ainsi, si la prévision de ce vent n'est pas à la portée du modèle méso-échelle WRF avec une résolution kilométrique, cette méthode le permet en combinant une descente d'échelle dynamique et statistique.

Le vent DDV a été étudié grâce aux observations et aux simulations - toutes les POI ont été simulées avec une résolution de 1 km. C'est un vent qui suit l'axe de la vallée, fortement corrélé à la stabilité à l'échelle régionale car il n'apparaît que la nuit lorsque le forçage synoptique est faible. Ce vent n'arrive à Cadarache que 6 à 9 heures après le coucher du soleil avec une grande variabilité. D'un autre côté, il est à son maximum au lever du soleil avant que les processus convectifs ne démarrent, et présente un jet entre 175 et 225 m avec des vitesses de 4 à 8 m s⁻¹ et dont la hauteur est corrélée à la profondeur variable de la vallée. Les simulations s'avèrent imparfaites avec une sous-estimation de l'amplitude diurne de température, une surestimation des flux turbulents et un décalage dans la chronologie du DDV par rapport à l'observation. Mais malgré ces défauts, la DV étant bien résolue avec une maille de 1 km, l'occurrence de ce vent est assez bien simulée. Par ailleurs l'examen de ses caractéristiques spatiales montre qu'il s'agit soit d'un écoulement de drainage, soit d'un écoulement canalisé forcé. Ce dernier trouve son origine dans des jets de basse couche naissant sur les plateaux inclinés situés entre la vallée même et les montages voisins des Préalpes du sud. Ces jets présentent des vitesses significatives, principalement au niveau des confluences de la Durance et de ses affluents. Bien qu'on ne dispose pas de données suffisantes pour élucider le mécanisme dominant de déclenchement du vent DDV, il est clair que les deux précédemment identifiés sont de bons candidats.

Abstract

This thesis investigates down-valley wind characteristics in complex terrain of moderate orography for a mid-latitude area. The work was motivated by safety regulation in the context of sanitary impact of the Cadarache centre on its close surroundings. Cadarache is one of the research centres of 'Commissariat à l'Énergie Atomique et aux Energies Alternatives' (CEA), located in southeastern France. It is embedded in a small valley, the Cadarache Valley (CV), which is one of the tributaries of the larger Durance Valley (DV). The two valleys are distinct in width (1 - 2 vs. 5 km for CV and DV, respectively), length (5 vs. more than 60 km), depth (100 vs. 200 m and higher) and slope angle (1° vs. 0.2° on average along the valleys main axis), and therefore react differently under stable conditions. Stable stratifications regularly occur in the region due to frequent weak synoptic forcing and clear sky conditions. During such conditions, dilution of pollutants can become weak; this is one of the major motivations of the present study.

To investigate the valley wind behaviour, the KASCADE (KAtabatic winds and Stability over CAadarache for Dispersion of Effluents) campaign has been designed. It was conducted in the winter of 2013 including continuous observations (flux tower, Sodar and Cadarache observational network) covering a 3-month period and 23 intensive observation periods (IOPs). During the IOPs tethered balloon experiments were conducted and radio-soundings were launched. An IOP was carried out when weak synoptic forcing periods and clear skies were expected, started at 12 UTC and lasted 24 hours. A calibration experiment served for sensor correction purposes, resulting in a high quality data set of a well-documented campaign (<http://kascade.sedoo.fr/>). The valley flows at the local and regional scale are characterized from observations analysis and IOP simulations with the non-hydrostatic WRF model.

The analysis shows that the Cadarache and Durance down-valley (CDV and DDV, respectively) winds are both dominating flows during the period of investigation. Once stable stratification has set around sunset, CDV wind continuously grows and thickens. The profile forms in a jet which is mostly observed at around 30 m agl with $2 - 3 \text{ m s}^{-1}$. CDV wind is a thermally driven flow, which persists regularly throughout the night and disappears in the early morning alongside stable stratification. Though the Cadarache current observational network lacks means of measurement for inside CDV wind, this work shows that it can be nowcasted from available meteorological tower observations. Although the forecast of CDV wind is out of reach of mesoscale modeling on a kilometer-scale resolution, the nowcasting methodology developed here could be used to forecast it by means of a combination of dynamical and statistical downscaling.

The DDV wind has been investigated by means of observations and modeling - all IOPs were simulated with an optimized WRF configuration at a 1-km horizontal grid spacing. The DDV wind has been recognized as down-valley oriented, and strongly related to stability at a regional scale, as it exists only after sunset when synoptic forcing is very weak. On the one hand, though highly variable, the DDV wind arrival at Cadarache is mostly observed 6 to 9 hours after sunset. On the other hand, it is dominantly present around sunrise, when convectively driven processes are not yet established. Jets are observed mostly at around 175 - 225 m agl with wind speeds between 4 and 8 m s^{-1} . DDV wind depth appears to be closely related to valley depth, which varies throughout the DV. Some deficiencies of the simulations are found, including underestimations of diurnal temperature ranges, overestimations of atmospheric turbulent fluxes, too early timing for onset and cessation of DDV wind. Despite these, the DDV wind is simulated close to reality thanks to the 1-km resolution allowing a correct representation of the Durance valley orography. Spatial characteristics show different types of DDV winds: it may appear as shallow drainage, but also as channelled flow resulting from a mountain-to-plain circulation. The latter finds its origin in low level jets (LLJs) simulated at the sloping plateau in between Southern Alps and DV itself. High wind speeds within the valley are seen in LLJs especially after tributary valley inlets. Data was not abundant enough to fully clarify the most dominant mechanism that causes the flow, but drainage and flow channelling are the most important candidates.